ACOUSTIC DAMPING MECHANISMS OF HALF-WAVE RESONATORS IN A ROCKET ENGINE ENVIRONMENT

A Dissertation
Presented to
The Academic Faculty

By

Shane V. Lympany

In Partial Fulfillment
of the Requirements for the Degree
Doctor of Philosophy in the
School of Aerospace Engineering

Georgia Institute of Technology

August 2018

ACOUSTIC DAMPING MECHANISMS OF HALF-WAVE RESONATORS IN A ROCKET ENGINE ENVIRONMENT

Approved by:

Prof. K. K. Ahuja, Advisor
School of Aerospace Engineering
Georgia Institute of Technology

Prof. Vigor Yang
School of Aerospace Engineering
Georgia Institute of Technology

Prof. Massimo Ruzzene
School of Aerospace Engineering
Georgia Institute of Technology

Prof. Kenneth A. Cunefare
School of Mechanical Engineering
Georgia Institute of Technology

Dr. Joseph R. Gavin
Preliminary Design
Gulfstream Aerospace Corporation

Mr. Michael G. Jones
Structural Acoustics Branch
NASA Langley Research Center

Date Approved: June 12, 2018

ACKNOWLEDGEMENTS

First, I would like to thank my graduate research advisor, Prof. Krish Ahuja, for guiding me through my graduate research, teaching me about aeroacoustics, and always challenging me to produce my best quality work. Special thanks are due to Joseph Mattingly for first introducing me to Dr. Ahuja.

I would also like to thank Prof. Vigor Yang, Prof. Massimo Ruzzene, Prof. Kenneth Cunefare, Dr. Joseph Gavin, and Mr. Michael Jones for reading this dissertation and providing their technical expertise to help me improve the quality of this work.

This material is based upon work supported by the National Science Foundation Graduate Research Fellowship Program under Grant No. DGE-1650044. This work would not have been possible without the support of numerous people at the Georgia Tech Research Institute (GTRI). I would like to thank the management of the Aerospace, Transportation, and Advanced Systems Laboratory at GTRI for allowing me to use their world-class research facilities. Special thanks are due to Dr. Aharon Karon and Madison Wadsworth for their significant efforts in the design and development of the new experimental facility and to Michael Mayo for conducting the particle image velocimetry presented in this work. The contributions of principal research engineer Dr. Rob Funk, student assistants Max Barnett and Jonathan Gillis, and the members of the GTRI machine shop are also gratefully acknowledged. Additionally, I would like to thank my fellow graduate students and office mates, Nick Breen and Jonathan Carroll, for making every day at the lab more enjoyable.

I am fortunate to be surrounded by an incredible group of family and friends who support me and keep me grounded. Thank you to my parents, Steve and Laurie, and my brother, Aaron, for their continued love and support. I would especially like to thank my fiancée, Sarah, for encouraging me and patiently loving me throughout this Ph.D. process.

Most importantly, thanks be to God for graciously giving me the opportunity to pursue a Ph.D. and sustaining me through this time in my life.

TABLE OF CONTENTS

Acknowledgments iii

List of Tables x

List of Figures xii

Nomenclature xxiii

Summary xxx

Chapter 1: Introduction 1
1.1 Motivation 1
1.2 Objectives 3
1.3 Technical Approach 4
1.4 Outline 6

Chapter 2: Literature Review 7
2.1 Overview 7
2.2 Background and Definitions 7
2.2.1 Definitions of Impedance Terms 8
2.2.2 End Corrections 9
2.2.3 Acoustic Resonators 10
2.3 Acoustic Damping of Propellant Injectors 15
2.3.1 Effect of the Geometric Features 15
2.3.2 Effect of the Open Area Ratio and the Number of Injectors 18
2.3.3 Effect of the Position and Distribution of the Injectors 22
2.3.4 Effect of Bias Flow 25
2.3.5 Effect of High Temperature 30
2.3.6 Effect of Amplitude 32
2.3.7 Effect of Higher-Order Modes 39
2.4 Concluding Remarks 43

Chapter 3: Methodology 44
3.1 Overview 44
3.2 The Impedance Tube as a Combustion Chamber 44
3.2.1 Classical Impedance Tube 45
3.2.2 Two-Sided Impedance Tube 48
3.3 Mode Propagation in Cylindrical Ducts 48
3.4 Wavenumber 51
3.4.1 Non-Dissipative Wavenumber 52
3.4.2 Kirchhoff Model 53

3.4.3 Weng-Bake Model . . . 54
3.5 Modal Decomposition . . . 55
3.6 Scattering Matrix . . . 58
3.7 Acoustic Power Quantities . . . 62
3.8 Impedance . . . 65
3.9 Modifications to the Methodology for a One-Sided Impedance Tube . . . 67
3.10 Simplifications to the Methodology for Plane Waves . . . 69
3.11 Summary . . . 71

Chapter 4: Experimental Setup . . . 72
4.1 Overview . . . 72
4.2 One-Sided Experimental Facilities . . . 72
4.3 Two-Sided Experimental Facility . . . 74
4.3.1 Overview of the Experimental Facility . . . 74
4.3.2 Sound Sources . . . 78
4.3.3 Acoustic Pressure Measurements . . . 81
4.3.4 Velocity and Temperature Measurements . . . 85
4.3.5 Data Acquisition and Post-Processing . . . 89
4.4 Particle Image Velocimetry . . . 91
4.5 Test Articles . . . 93
4.5.1 Injectors with Unique Geometric Features . . . 93
4.5.2 Cylindrical Half-Wave Resonators . . . 94
4.6 Summary . . . 97

Chapter 5: Analytical and Numerical Models . . . 99
5.1 Overview . . . 99
5.2 Analytical Expressions . . . 99
5.2.1 Absorption Coefficient as a Function of Impedance . . . 101
5.2.2 Impedance at a Simple Area Discontinuity . . . 103
5.2.3 Input Impedance . . . 107
5.2.4 Impedance at an Area Discontinuity with a Side Branch . . . 108
5.2.5 Impedance Near Resonance . . . 110
5.2.6 Sound Power Coefficients . . . 115
5.2.7 Absorption Frequency Bandwidth . . . 116
5.3 Numerical Model . . . 117
5.4 Summary . . . 118

Chapter 6: Effect of Geometric Parameters . . . 120
6.1 Overview . . . 120
6.2 Effect of the Geometric Features . . . 121
6.2.1 Straight Injector . . . 122
6.2.2 Inlet Protrusion . . . 123
6.2.3 Recess . . . 124
6.2.4 Annulus and Fuel Holes . . . 124
6.3 Effect of the Open Area Ratio . . . 125

6.4 Comparison Between the One- and Two-Sided Impedance Tubes 128
6.5 Effect of the Number of Injectors 130
6.5.1 Effect of the Number of Injectors on the Absorption Coefficient . . 131
6.5.2 Effect of the Number of Injectors on the Resonance Frequency . . . 133
6.5.3 Sound Power Dissipation and Transmission of Multiple Injectors . . 134
6.6 Effect of the Position of the Injectors 135
6.7 Validation of the Numerical Model 138
6.7.1 Numerical Model for a Single Propellant Injector 139
6.7.2 Numerical Model for Multiple Half-Wave Resonators 141
6.8 Summary 142

Chapter 7: Effect of Bias Flow 146
7.1 Overview 146
7.2 Analytical Expressions in the Presence of Flow 147
7.2.1 Effect of Flow on the Resonance Frequency 147
7.2.2 Normalized Resistance at the Inlet and Outlet of a Duct 148
7.2.3 Impedance Near Resonance in the Presence of Flow 149
7.2.4 Sound Power Coefficients in the Presence of Flow 152
7.3 On the Numerical Model in the Presence of Flow 154
7.4 Effect of the Geometric Features in the Presence of Flow 156
7.4.1 Normalized Resistance of Unique Injectors in the Presence of Flow 156
7.4.2 Absorption Coefficient of Unique Injectors in the Presence of Flow . 158
7.4.3 Resonance Frequency of Unique Injectors in the Presence of Flow . 161
7.5 Effect of the Number of Injectors in the Presence of Flow 165
7.5.1 Normalized Resistance of Multiple Injectors in the Presence of Flow 165
7.5.2 Sound Power Coefficients of Multiple Injectors in the Presence of Flow 168
7.5.3 Resonance Frequency of Multiple Injectors in the Presence of Flow 171
7.6 Discussion of Underdamping and Overdamping 172
7.7 Summary 175

Chapter 8: Effect of Temperature 178
8.1 Overview 178
8.2 Acoustic Dissipation Mechanisms at High Temperatures 179
8.2.1 Dissipation at the Walls and Within the Fluid 179
8.2.2 Application to Half-Wave Resonators 180
8.3 Acoustic Measurements at High Temperatures 184
8.3.1 Effect of Temperature 184
8.3.2 Effect of Temperature Gradient 185
8.4 On the Numerical Model at High Temperatures 189
8.5 Summary 190

Chapter 9: Effect of High Amplitude 192
9.1 Overview 192
9.2 Nonlinear Wave Propagation 193
9.3 Effect of the Geometric Features at High Amplitudes 194
9.3.1 Normalized Resistance of Unique Injectors at High Amplitudes . . 194
9.3.2 Absorption Coefficient of Unique Injectors at High Amplitudes . . . 196
9.3.3 Resonance Frequency of Unique Injectors at High Amplitudes . . . 200
9.4 Effect of the Number of Injectors at High Amplitudes 201
9.4.1 Normalized Resistance of Multiple Injectors at High Amplitudes . . 201
9.4.2 Sound Power Coefficients of Multiple Injectors at High Amplitudes 201
9.4.3 Resonance Frequency of Multiple Injectors at High Amplitudes . . 204
9.5 Particle Image Velocimetry Measurements 206
9.5.1 PIV Measurements for the Straight Injector 207
9.5.2 PIV Measurements for the Recess Injector 213
9.6 Sound Power Dissipation: Acoustic Measurements 219
9.7 Sound Power Dissipation: PIV Measurements 221
9.7.1 Dissipation by the Coriolis Force 221
9.7.2 Acoustic Particle Velocity 223
9.7.3 Dissipation Due to the Formation of Vortices 225
9.7.4 Dissipation Due to the Formation of a Jet 231
9.8 Quantitative Comparison Between the Acoustic and PIV Measurements . . 232
9.8.1 Calculation of the Sound Power Dissipation 232
9.8.2 Additional Sound Power Dissipation Mechanisms 235
9.9 Summary 239

Chapter 10: Higher-Order Modes 242
10.1 Overview 242
10.2 Mode-Matching Method 243
10.3 Numerical Model for Higher-Order Modes 244
10.4 Effect of Higher-Order Evanescent Modes on the Length Correction at an Area Discontinuity 246
10.4.1 Effect of the Position of the Resonators 246
10.4.2 Calculation of the Length Correction 247
10.4.3 Application to the Half-Wave Resonators 250
10.4.4 The Role of Evanescent Modes 252
10.5 Measurements of the Acoustic Damping of Higher-Order Modes 258
10.5.1 Scattering Matrix of a Single Half-Wave Resonator 259
10.5.2 Absorption Coefficient of a Single Half-Wave Resonator 264
10.5.3 Sound Power Coefficients of Three Half-Wave Resonators 266
10.6 Validation of the Numerical Model for Higher-Order Modes 268
10.7 Effect of the Side Branch 273
10.7.1 Multiple Absorption Peaks Due to the Side Branch 274
10.7.2 One-Way Absorption Due to the Side Branch 276
10.8 Summary 277

Chapter 11: Conclusions and Future Research . . . 280
11.1 Conclusions . . . 280
11.2 Recommendations for Future Research . . . 285

Appendix A: Uncertainty Analysis . . . 289
A.1 Background . . . 289
A.1.1 Definitions . . . 289
A.1.2 Literature Survey . . . 291
A.2 Methodology . . . 292
A.2.1 Experimental Uncertainties . . . 292
A.2.2 Multivariate Uncertainty Analysis of the Transfer Functions . . . 294
A.2.3 Monte Carlo Method . . . 296
A.2.4 Confidence Intervals . . . 299
A.3 Applications of the Uncertainty Analysis . . . 302
A.3.1 Open Duct: Microphones Versus Pressure Transducers . . . 302
A.3.2 Uncertainty Analysis of a Straight Injector . . . 305
A.3.3 Uncertainty Analysis in Heated Flow . . . 307

Appendix B: Evaluation of the Wavenumber Models . . . 309
B.1 Dissipative Versus Non-Dissipative Wavenumbers . . . 309
B.2 Accounting for the Excess Dissipation . . . 312

Appendix C: Development of a Numerical Model for Plane Waves . . . 315
C.1 Relationship Between Transfer Matrices . . . 315
C.2 Transfer Matrix of a Straight Cylinder . . . 317
C.3 Transfer Matrix of an Area Discontinuity . . . 317
C.4 Length Correction at an Area Discontinuity . . . 321
C.5 Development of the Transfer Matrix of a Propellant Injector . . . 323
C.6 Development of the Scattering Matrix of a Propellant Injector . . . 325

Appendix D: Higher-Order Mode-Matching Method . . . 327
D.1 Application of the Boundary and Continuity Conditions . . . 327
D.2 Solution to the System of Equations . . . 330
D.2.1 Truncation of the Number of Modes . . . 330
D.2.2 Scattering Matrix Solution to the Mode-Matching Method . . . 331
D.2.3 Transfer Matrix Solution to the Mode-Matching Method . . . 332

Appendix E: Development of a Numerical Model for Higher-Order Modes . . . 334
E.1 Overview of the Numerical Model for Higher-Order Modes . . . 334
E.2 Mode-Matching Method for Multiple Ducts . . . 335
E.3 Mode-Matching Method for Ducts with a Side Branch . . . 336
E.4 Mode Shapes in the Side Branch . . . 338
E.5 Scattering Matrix Solution to the Numerical Model for Higher-Order Modes 340
E.5.1 Truncation of the Number of Modes . . . 340
E.5.2 Matrix Solution to the System of Equations . . . 341

E.5.3 Scattering Matrix of Half-Wave Resonators for Higher-Order Modes 342

Appendix F: Formulas for the Length Correction at an Area Discontinuity . . . 344
F.1 Peat's Length Correction 344
F.2 Ando's Length Correction 346

Appendix G: Derivation of the Mode Normalization Factor 349

References 352

Vita 367

LIST OF TABLES

3.1 Properties of the first six cut-on modes in a circular duct. 53

4.1 Coordinates of the acoustic driver closest to $\theta = 0^\circ$ in each source section. 80

4.2 Coordinates of the optimized sensor locations. 84

6.1 Open area ratios of the injectors with different geometric features in each of the impedance tubes. 126

6.2 Percentage errors between the numerical model and the measured data for the injectors with different geometric features. 141

6.3 Percent errors between the numerical model and the measured data for different numbers of half-wave resonators. 141

6.4 Effect of realistic geometric features on the acoustic properties of a propellant injector. 143

9.1 Nonlinear sound power dissipation, in milliwatts, calculated from the acoustic and PIV measurements at an incident sound pressure level of 150 dB. . 233

10.1 Measured and predicted length corrections of the resonators for the configurations shown in Figure 10.1. 252

A.1 Summary of the experimental bias and random uncertainties. 293

C.1 Relationship between the numbered duct sections in Figure C.3 and the geometric features of the "recess" injector. 324

E.1 Reference origin for the acoustic waves in each duct section defined in Figure E.1. 335

E.2 Definitions of the matrices in Eq. (E.10). 342

F.1 Coefficients of the double Chebyshev series for a simple area discontinuity (Ref. [70]). 345

F.2 Coefficients of the double Chebyshev series for an extended inlet or outlet with an extension length of $L_e/a_1 \geq 0.5$ (Ref. [164]). 346

F.3 Multiplicative factor for the effect of wall thickness on the end correction of a pipe as a function of the Helmholtz number and wall thickness ratio (extracted from Ref. [25]). 348

LIST OF FIGURES

1.1 Cross-sectional view of a combustion chamber. 2

2.1 Helmholtz resonator. 11

2.2 Quarter-wave resonator. 12

2.3 Half-wave resonator. 13

2.4 Comparison of the absorption coefficients of Helmholtz, quarter-wave, and half-wave resonators. 14

2.5 Geometric features of a propellant injector. 15

2.6 Amplitude and frequency of the first circumferential acoustic mode in a model combustion chamber as a function of injector length (Ref. [8]). . . . 16

2.7 Absorption coefficient of a half-wave resonator (Ref. [11]). 17

2.8 Absorption coefficient of injectors with various amounts of inlet protrusion (Ref. [11]). 18

2.9 Axial acoustic pressure profiles inside injectors with different geometric features (Ref. [12]). 19

2.10 Absorption coefficient of injectors of various diameters (Ref. [11]). 20

2.11 Absorption coefficient of various numbers of injectors (Ref. [11]). 21

2.12 Absorption coefficient for underdamped, optimally damped, and overdamped Helmholtz resonators (Ref. [6]). 22

2.13 Absorption coefficient of different injector configurations with identical open area ratio (Ref. [11]). 23

2.14 Length correction as a function of the offset distance between a resonator and the centerline of the duct calculated using the "double-duct model" of Selamet and Ji [31] and the "single-duct model" of Ingard [30] (Ref. [31]). 24

2.15 Comparison of the attenuation coefficients (α_{wall}) given by the models of Ronneberger and Ahrens [34] and Howe [37] in ($+$) and against ($-$) the flow direction in a duct (Ref. [41]). 27

2.16 Specific acoustic resistance as a function of the bias flow velocity through the orifice. For curve 1, the orifice was open to the ambient air, but for curve 2, an external duct was present (Ref. [54]). 29

2.17 Normalized length correction as a function of mean flow Strouhal number at an area discontinuity in a circular duct based on experimental results from Ref. [71]. The solid lines represent different frequencies, and the dashed and dotted lines represent theoretical values for the no-flow low-frequency limit (Ref. [63]). 31

2.18 Temperature, pressure, and frequency conditions (shaded region) for which the attenuation within the fluid is at least one-tenth of the attenuation at the walls of a duct with a 0.01 m radius for a water vapor concentration of 0.05% and no flow (Ref. [41]). 33

2.19 Absorption coefficient at resonance of a Helmholtz resonator array as a function of open area ratio at high amplitudes (Ref. [54]). 35

2.20 Nonlinear resistance of Helmholtz and quarter-wave resonators at high amplitudes (Ref. [6]). 35

2.21 PIV measurements of the velocity (arrows) and vorticity (color) fields at the open end of a tube at 170 dB at (a) 0.0 T, (b) 0.3 T, (c) 0.6 T, and (d) 0.9 T (Ref. [93]). 37

2.22 Mode shapes of (a) the two degenerate 1T modes of a circular chamber and (b) the 1Tσ and 1Tπ modes of a chamber coupled to a quarter-wave resonator (Ref. [29]). 42

3.1 Cross-sectional view of a combustion chamber. 46

3.2 Schematic of an impedance tube. 46

3.3 Mode shapes of several representative circular modes. 51

3.4 Acoustic reflection and transmission of modes across a test article in a duct. 58

4.1 101.6-mm diameter (top) and 28.5-mm diameter (bottom) one-sided impedance tubes. 73

4.2 Top-view drawing of HOTMESS. 76

4.3 Male-to-female alignment system between adjacent sections. 76

4.4 Photograph of HOTMESS. 77

4.5 Partial cutaway view of the canister and finned-pipe heat exchanger assembly for the acoustic drivers. 81

4.6 Weighting function and condition number of the M-matrix for the optimized sensor locations. 85

4.7 Drawing of the instrumented measurement sections in HOTMESS. 86

4.8 Data acquisition and post-processing flowchart. 90

4.9 Schematic of the particle image velocimetry experimental setup. 92

4.10 Section views of the (a) “straight”, (b) “protrusion”, (c) “recess”, (d) “annulus”, and (e) “fuel holes” propellant injectors with labeled geometric features and dimensions (in mm). 94

4.11 A single propellant injector mounted to the end of each one-sided impedance tube. 95

4.12 Front and sectional views of the mounting plate for the injectors with unique geometric features installed in the two-sided impedance tube, with dimensions (in mm). 96

4.13 Front and sectional views of the mounting assembly for the single straight half-wave resonator installed in the two-sided impedance tube, with dimensions (in mm). 96

4.14 Front and sectional views of the mounting assembly for multiple straight half-wave resonators installed in the two-sided impedance tube, with dimensions (in mm). 97

5.1 Schematic of the analytical model for a half-wave resonator (not to scale). 100

5.2 Absorption coefficient versus normalized termination resistance for different values of the normalized termination reactance. 102

5.3 Simple area discontinuity between two ducts. 104

5.4 Area discontinuity between two ducts with a side branch. 109

6.1 Absorption coefficients of the injectors with different geometric features measured in the 101.6-mm diameter one-sided impedance tube. 122

6.2 Absorption coefficients of the injectors with different geometric features measured in the 28.5-mm diameter one-sided impedance tube. 126

6.3 Comparison of the absorption coefficients of the injectors with different geometric features measured in the 101.6-mm diameter one-sided and two-sided impedance tubes. 130

6.4 Absorption coefficients of various numbers of half-wave resonators measured in the two-sided impedance tube. 131

6.5 Normalized termination resistance at resonance and absorption frequency bandwidth of various numbers of half-wave resonators measured in the two-sided impedance tube and calculated using the simplified analytical expressions developed in Section 5.2. 133

6.6 Power dissipation coefficients of various numbers of half-wave resonators measured in the two-sided impedance tube. 135

6.7 Power transmission coefficients of various numbers of half-wave resonators measured in the two-sided impedance tube. 136

6.8 Power absorption, dissipation, and transmission coefficients of various numbers of half-wave resonators at resonance in the two-sided impedance tube. 136

6.9 Number and positions of the half-wave resonators. 137

6.10 Absorption coefficients of various numbers of half-wave resonators in different positions measured in the two-sided impedance tube. 138

6.11 Comparison between the numerical model prediction and the measured absorption coefficients for the injectors with different geometric features. . 139

6.12 Comparison between the numerical model prediction and the measured power dissipation coefficients for the injectors with different geometric features. 140

6.13 Comparison between the numerical model prediction and the measured power transmission coefficients of the injectors with different geometric features. 140

6.14 Comparison between the numerical model prediction and the measured absorption coefficients of different numbers of half-wave resonators. . . . 142

7.1 Absorption coefficient versus normalized termination resistance at resonance for different values of the Mach number. 153

7.2 Normalized termination resistance at resonance as a function of the bias flow Mach number in the main body of the injector for the propellant injectors with different geometric features. 157

7.3 Absorption coefficient of the "straight" injector at different bias flow Mach numbers in the main body of the injector. 159

7.4 Absorption coefficient of the "protrusion" injector at different bias flow Mach numbers in the main body of the injector. 160

7.5 Absorption coefficient of the "recess" injector at different bias flow Mach numbers in the main body of the injector. 161

7.6 Ratio of the absorption frequency bandwidth with mean flow to the absorption frequency bandwidth with no flow as a function of the bias flow Mach number in the main body of the injector for the propellant injectors with different geometric features. 162

7.7 Percentage change in resonance frequency as a function of the bias flow Mach number in the main body of the injector for the propellant injectors with different geometric features. 163

7.8 Normalized length correction as a function of Strouhal number for the "straight" injector shown in Figure 4.12 and the single half-wave resonator shown in Figure 4.13. 165

7.9 Normalized termination resistance at resonance as a function of the bias flow Mach number in the resonators for different numbers of half-wave resonators. 166

7.10 Change in the normalized input resistance at resonance as a function of the bias flow Mach number in the resonators for different numbers of half-wave resonators. 167

7.11 Absorption coefficient of three and twelve half-wave resonators at different bias flow Mach numbers in the resonators. 169

7.12 Dissipation coefficient of three and twelve half-wave resonators at different bias flow Mach numbers in the resonators. 170

7.13 Power transmission coefficient of three and twelve half-wave resonators at different bias flow Mach numbers in the resonators. 171

7.14 Power absorption, dissipation, and transmission coefficients of three half-wave resonators at resonance as a function of the bias flow Mach number in the resonators. 172

7.15 Percentage change in resonance frequency as a function of the bias flow Mach number in the resonators for different numbers of half-wave resonators. 173

8.1 Temperatures and frequencies (shaded region) in which the attenuation in the bulk fluid is at least 10% of the attenuation in the acoustic boundary layer for a 6.275-mm diameter resonator at a constant concentration of water vapor of $h = 0.07\%$. 181

8.2 Temperatures and frequencies (shaded region) in which the attenuation in the bulk fluid is at least 10% of the attenuation in the acoustic boundary layer for a 6.275-mm diameter resonator at a constant concentration of water vapor of $h = 0.10\%$. 182

8.3 Temperatures and frequencies (shaded region) in which the attenuation in the bulk fluid is at least 10% of the attenuation in the acoustic boundary layer for a 6.275-mm diameter resonator at a constant concentration of water vapor of $h = 0.25\%$. 182

8.4 Temperatures and frequencies (shaded region) in which the attenuation in the bulk fluid is at least 10% of the attenuation in the acoustic boundary layer for a 6.275-mm diameter resonator at a constant concentration of water vapor of $h = 0.50\%$. 183

8.5 Absorption coefficient of three half-wave resonators at different temperatures with a Mach 0.2 mean flow through the resonators. 185

8.6 Absorption coefficient of twelve half-wave resonators at different temperatures with a Mach 0.1 mean flow through the resonators. 186

8.7 Number and positions of the half-wave resonators. 187

8.8 Absorption coefficient of one half-wave resonator at different temperatures with a Mach 0.1 mean flow through the resonator. 188

8.9 Absorption coefficient of three half-wave resonators at different temperatures with a Mach 0.1 mean flow through the resonators. 189

9.1 Normalized termination resistance at resonance as a function of incident amplitude for the propellant injectors with different geometric features. . . 195

9.2 Absorption coefficient of the "straight" injector at different incident amplitudes. 197

9.3 Absorption coefficient of the "protrusion" injector at different incident amplitudes. 198

9.4 Absorption coefficient of the "recess" injector at different incident amplitudes. 199

9.5 Absorption frequency bandwidth as a function of incident amplitude for the propellant injectors with different geometric features. 199

9.6 Percentage change in the resonance frequency as a function of incident amplitude for the propellant injectors with different geometric features. . . 200

9.7 Normalized termination resistance at resonance as a function of incident amplitude for different numbers of half-wave resonators. 202

9.8 Absorption coefficient of three and twelve half-wave resonators at different incident amplitudes. 203

9.9 Power dissipation coefficient of three and twelve half-wave resonators at different incident amplitudes. 204

9.10 Power dissipation coefficient of three and twelve half-wave resonators at different incident amplitudes. 204

9.11 Percentage change in the resonance frequency as a function of incident amplitude for different numbers of half-wave resonators. 205

9.12 Representative two-dimensional spatial grid for the PIV measurements at the open end of an injector. 207

9.13 Velocity (arrows) and vorticity (colors) flow field outside the open end of the "straight" injector at an incident SPL of 140 dB. 209

9.14 Velocity profiles at various distances downstream of the open end of the "straight" injector at an incident SPL of 140 dB. 210

9.15 Velocity (arrows) and vorticity (colors) flow field outside the open end of the "straight" injector at an incident SPL of 150 dB. 211

9.16 Velocity profiles at various distances downstream of the open end of the "straight" injector at an incident SPL of 150 dB. 212

9.17 Velocity (arrows) and vorticity (colors) flow field outside the open end of the "recess" injector at an incident SPL of 130 dB. 214

9.18 Velocity profiles at various distances downstream of the open end of the "recess" injector at an incident SPL of 130 dB. 215

9.19 Velocity (arrows) and vorticity (colors) flow field outside the open end of the "recess" injector at an incident SPL of 150 dB. 217

9.20 Velocity profiles at various distances downstream of the open end of the "recess" injector at an incident SPL of 150 dB. 218

9.21 (a) Velocity (arrows) and energy (colors) flow field outside the open end of the "straight" injector at an incident SPL of 150 dB; (b) Sum of the kinetic energy over the y-coordinate, where the shaded region corresponds to one acoustic period for attached vortices. 228

9.22 (a) Velocity (arrows) and energy (colors) flow field outside the open end of the "recess" injector at an incident SPL of 150 dB; (b) Sum of the kinetic energy over the y-coordinate, where the shaded region corresponds to one acoustic period for shed and convected vortices. 230

10.1 Number and positions of the half-wave resonators. 247

10.2 Absorption coefficients of various numbers of half-wave resonators in different positions measured in the two-sided impedance tube. 248

10.3 COMSOL models of the area discontinuity between the impedance tube and one and three resonators. 249

10.4 Normalized length correction of a single resonator as a function of its offset distance from the centerline of the duct. 251

10.5 Normalized length correction of three equally distributed resonators as a function of their offset distance from the centerline of the duct. 252

10.6 Calculated relative amplitudes of the evanescent modes formed at the area discontinuity between one 12.55-mm diameter resonator and the 101.6-mm diameter impedance tube for various offset distances between the centerlines of the ducts. 254

10.7 Calculated relative amplitudes of the evanescent modes formed at the area discontinuity between three equally distributed 12.55-mm diameter resonators and the 101.6-mm diameter impedance tube for various offset distances between the centerlines of the ducts. 256

10.8 Calculated normalized length correction and scaled power of the evanescent modes at an area discontinuity between one or three resonators and the impedance tube as a function of their offset distances from the centerline of the tube. 257

10.9 Absolute value of the pressure reflection matrix of a single half-wave resonator at various offset distances from the center of the impedance tube. . 260

10.10 Absolute value of the pressure transmission matrix of a single half-wave resonator at various offset distances from the center of the impedance tube. 261

10.11 Absorption coefficient of a single half-wave resonator at various offset distances from the center of the impedance tube. 265

10.12 Absorption coefficient of three half-wave resonators at various offset distances from the center of the impedance tube. 267

10.13 Total power transmission coefficient of three half-wave resonators at various offset distances from the center of the impedance tube. 268

10.14 Absolute value of the pressure reflection matrix of one half-wave resonator at an offset distance of 65.8% radius (the "1, outer" configuration shown in Figure 10.1b). 270

10.15 Absolute value of the pressure reflection matrix of three half-wave resonators at an offset distance of 65.8% radius (the "3, outer" configuration shown in Figure 10.1d). 271

10.16 Absorption coefficient of twelve half-wave resonators. 273

10.17 Absorption coefficient on side B for three half-wave resonators at an offset distance of 24.9% radius (see Figure 10.1c). The "No Extension" curve is the numerical model without a side branch. 275

10.18 Absorption coefficient on side A for three half-wave resonators at an offset distance of 24.9% radius (see Figure 10.1c). The "No Extension" curve is the numerical model without a side branch. 275

A.1 Flowchart of the Monte Carlo method (adapted from Refs. [156] and [159]).297

A.2 True value and 95% confidence interval for the dissipation coefficient of the (0,0) mode in the open duct at 2500 Hz measured using the microphones.300

A.3 True value and 95% confidence region for the complex pressure transmission coefficient of the (0,0) mode in the open duct at 1000 Hz measured using the microphones. 301

A.4 True value and 95% confidence region for the complex pressure transmission coefficient of the (1,0) mode in the open duct at 2500 Hz measured using the microphones. 302

A.5 Comparison of the power transmission coefficients of the (0,0) mode in the open duct measured using the microphones and pressure transducers. . 304

A.6 Estimate of the 95% confidence interval for the dissipation coefficient of the (0,0) mode in the open duct measured using the microphones. 305

A.7 Estimate of the 95% confidence interval for the dissipation coefficient of the (0,0) mode in the open duct measured using the pressure transducers. . 306

A.8 Estimate of the 95% confidence interval for the plane-wave absorption coefficient of the "straight" injector in quiescent air measured using the microphones. 307

A.9 Estimate of the 95% confidence interval for the plane-wave absorption coefficient of three half-wave resonators at 500°F with a Mach 0.2 mean flow through the resonators measured using the pressure transducers. . . . 308

B.1 Comparison of the power transmission coefficients of the (0,0), (1,0), (2,0) and (0,1) modes in the open duct using different wavenumber models. . . . 310

B.2 Contours of the relative attenuation in the bulk fluid compared to the attenuation in the acoustic boundary layer for the 101.6-mm diameter impedance tube at a constant concentration of water vapor of $h = 0.15\%$. . 313

B.3 Comparison of the dissipation coefficients of the (0,0) mode in the open duct using different wavenumber models. 314

C.1 Flow expansion with a side branch (the flow direction is in the positive axial direction). 318

C.2 Flow contraction with a side branch (the flow direction is in the positive axial direction). 318

C.3 Schematic of the duct sections in the numerical model for the "recess" injector (not to scale). 324

D.1 Area discontinuity between two offset ducts. 328

E.1 Schematic of the duct sections in the numerical model for multiple half-wave resonators with a side branch at one end (not to scale). 334

E.2 Degenerate circumferential mode shapes in the side branch formed by the extension of the resonators into the impedance tube. 339

E.3 Radial mode shapes in the side branch formed by the extension of the resonators into the impedance tube. 339

E.4 Split (3,0)-like mode shapes in the side branch formed by the extension of the resonators into the impedance tube. 340

F.1 End correction as a function of Helmholtz number for wall thickness ratios $a_{\text{out}}/a_{\text{in}}$ of (a) 1.00, (b) 0.85, (c) 0.75, and (d) 0.70 (Ref. [25]). 347

NOMENCLATURE

Latin Symbols

$\mathbf{0}$	Zero matrix
$\hat{\mathbf{A}}$	Matrix of modal pressure amplitudes for multiple sound pressure fields
$\mathbf{A}_i$	Diagonal matrix containing the wavenumber parameters $\alpha_{i,mn}$
A	Absorption coefficient
$\hat{a}_{mn}$	Pressure amplitude of mode (m, n)
$\hat{\mathbf{a}}$	Vector of modal pressure amplitudes
a	Radius of a cylindrical duct
BW	Frequency bandwidth, $BW = f_{+1/2} - f_{-1/2}$, Hz
$\hat{b}_{mn}$	Axial particle velocity amplitude of mode (m, n)
$\hat{\mathbf{b}}$	Vector of modal axial particle velocity amplitudes
C_{mn}	Normalization factor of mode (m, n)
c	Speed of sound
D^{Π}	Power dissipation coefficient
$\mathbf{E}_i$	Diagonal matrix containing the propagation parameters $e^{-jk_{i,mn}L}$
E_k	Kinetic energy
F	Force
$\tilde{f}$	Normalized frequency, $\tilde{f} = f(2L/c)$
f	Frequency, Hz
f_0	Resonance frequency, Hz
$f_{\pm 1/2}$	Frequencies at which a function equals half its peak value, Hz
$\mathbf{G}$	Monopole source excitation matrix
G_{xx}	Auto-spectral density of signal x
G_{xy}	Cross-spectral density of signals x and y

H_{xy} Transfer function, $H_{xy} = G_{xy}/G_{xx}$

$\mathbf{h}$ Vector of transfer functions between microphones

h Concentration of water vapor

$\mathbf{I}$ Identity matrix

I Total number of acoustic pressure measurement locations

i Index of grid points in the horizontal direction

$\mathbf{J}$ Jacobian matrix

J_m Bessel function of the first kind of order m

j Imaginary number, $j = \sqrt{-1}$

j Index of grid points in the vertical direction

$\overline{k}$ Mean wavenumber, $\overline{k} = (k^+ + k^-)/2$

k Wavenumber

k_{mn} Axial wavenumber of mode (m, n)

ΔL Length correction

L Length

L_{eff} Effective length of an acoustic resonator

$L_{\text{nonlinear}}$ Discontinuity distance

L_e Extension length of a smaller-diameter duct into a larger-diameter duct

$\mathbf{M}$ Matrix of mode shape weights

M Mean flow Mach number, $M = \overline{U}/c$

M_a Acoustic Mach number, $M_a = u/c$

M_F Mach number at which flow losses become non-negligible

m Circumferential mode order

N Total number of propagating modes above cut-on

n Radial mode order

Pr Prandtl number

$\hat{\mathbf{p}}$ Vector of acoustic pressure amplitude measurements

p	Acoustic pressure
p_0	Stagnation pressure
p_a	Ambient pressure
Q	Monopole source strength
Q	Total number of independent sound sources
$\mathbf{R}$	Pressure reflection matrix
R	Pressure reflection coefficient
R^{Π}	Power reflection coefficient
R_s	Surface resistance, $R_s = (1/2)\sqrt{2\mu\rho\omega}$
Re	Reynolds number
$\hat{\mathbf{r}}$	Unit vector in the outward radial direction
r	Radial coordinate
r_0	Offset distance between the centerlines of two ducts
$\mathbf{S}$	Scattering matrix
S	Cross-sectional area
S_X	Sample standard deviation of the variable X
St	Mean flow Strouhal number, $St = \omega a/\overline{U}$ or $St = ka/M$
St_a	Acoustic Strouhal number, $St = \omega a/\lvert u\rvert$ or $St = ka/M_a$
$\mathbf{Tr}$	Transfer matrix
$\mathbf{T}$	Pressure transmission matrix
T	Period, s
T	Pressure transmission coefficient
T	Temperature
T^{Π}	Power transmission coefficient
T_i	Chebyshev polynomial of the first kind of degree i
t	Time, s
$\overline{U}$	Mean flow velocity

U Acoustic volume velocity

U_X 95% confidence estimate of the uncertainty of the variable X

$\mathbf{u}$ Acoustic particle velocity vector in the flow field

u Acoustic particle velocity

V Volume

$\mathbf{v}$ Velocity vector in the flow field

v Component of the velocity vector

$\mathbf{X}_{i,j}$ Modal coupling matrix between ducts i and j

$\overline{X}$ Sample mean of the variable X

$\hat{\mathbf{x}}$ Unit vector in the x-direction

$\hat{\mathbf{y}}$ Unit vector in the y-direction

$\mathbf{Z}$ Normalized impedance matrix

Z Acoustic impedance, $Z = p/U$

Z_m Mechanical impedance, $Z_m = F/u$

Z_r Radiation (mechanical) impedance

$\hat{\mathbf{z}}$ Unit vector in the z-direction

z Axial coordinate

z Specific acoustic impedance, $z = p/u$

z_0 Axial coordinate of the reference origin

Greek Symbols

α_{mn} Wavenumber parameter for mode (m, n)

β Attenuation coefficient

β_{fluid} Attenuation coefficient due to losses within the fluid itself

β_{wall} Attenuation coefficient due to losses within the acoustic boundary layer

β_X Bias error of the measured variable X

γ Ratio of specific heats

$\Gamma_{mn}^{\pm}$ Weng-Bake wavenumber model parameter

δ Acoustic boundary layer thickness, $\delta = \sqrt{2\nu/\omega}$

ε_X Random error of the measured variable X

ζ Normalized impedance, $\zeta = \theta + j\chi$

ζ_0 Normalized input impedance

ζ_T Normalized termination impedance

$\zeta_{0,\text{eff}}$ Effective normalized input impedance, $\zeta_{0,\text{eff}} = \zeta_0 + \zeta_{i,j}$

θ Azimuthal coordinate

θ Normalized resistance

θ_F Normalized resistance due to mean flow at an area expansion

κ Coverage factor relating the uncertainty and sample standard deviation

κ_{mn} Eigenvalue of mode (m, n)

λ Wavelength

μ Dummy variable for circumferential mode order m

μ Dynamic viscosity

μ_X True mean of the variable X

ν Dummy variable for radial mode order n

ν Kinematic viscosity

Ξ Number of resonators

Π Sound power

ρ Density

$\mathbf{\Sigma}$ Covariance matrix

σ Open area ratio

σ_X True standard deviation of the variable X

Φ Velocity potential

χ Normalized reactance

Ψ_{mn} Mode shape function for mode (m, n)

$\mathbf{\Omega}$ Vorticity, $\mathbf{\Omega} = \nabla \times \mathbf{v}$

ω Angular frequency, rad/s

$\omega_{\pm 1/2}$ Angular frequencies at which a function equals half its peak value, rad/s

Other Symbols

$\Im$ Imaginary part of a complex argument

$\Re$ Real part of a complex argument

$\hat{X}$ Fourier transform of the variable X (Amplitude of X at a single frequency)

Superscripts

$+$ Associated with propagation in the positive axial direction

$-$ Associated with propagation in the negative axial direction

H Complex conjugate (Hermitian) transpose

Π Power quantity

Subscripts

A Upstream ($z < 0$) side of the impedance tube

B Downstream ($z > 0$) side of the impedance tube

body Main body of the injector

C Side branch formed by the extension of the resonators into the duct

D Dissipated

down Downstream side of the impedance tube

exit Exit of the impedance tube

I Imaginary part of a complex quantity

I Incident

i, j Area discontinuity between ducts i and j

in Incoming acoustic waves propagating towards the test article

inlet Inlet protrusion of the injector

J Associated with the formation of a jet

L Boundary condition at $z = -L$

mn Mode (m, n)

out	Outgoing acoustic waves propagating away from the test article
R	Real part of a complex quantity
R	Reflected
ref	Reference microphone
T	Transmitted
test	Test article
true	True value of a measured variable
up	Upstream side of the impedance tube
V	Associated with the formation of vortices
ξ	Resonator index
Ω	Associated with the Coriolis term of vorticity

Acronyms

FS	Full Scale
HOTMESS	Heated, Optimized Tube for Multimodal Evaluation of Sound Scattering
PIV	Particle Image Velocimetry
POD	Proper Orthogonal Decomposition
SPL	Sound Pressure Level, dB

SUMMARY

Combustion instabilities in rocket engines are caused by coupling between the combustion processes and pressure oscillations in a combustor, and they are characterized by the frequencies and shapes of the acoustic modes of the combustion chamber. Acoustic resonators are commonly installed in combustors to provide passive acoustic damping and prevent combustion instabilities. Previously, it has been proposed that the propellant injectors in a combustor can be tuned to act as half-wave resonators and provide acoustic damping. This requires a thorough understanding of the acoustic damping mechanisms of injectors, and producing this understanding forms the basis of the work described in this dissertation.

In this work, the acoustic damping of propellant injectors is measured experimentally. A new experimental facility is developed and employed to measure the sound power reflection, transmission, and dissipation under the conditions of mean flow, high temperature, high acoustic amplitude, and higher-order modes. The effects of common design parameters—namely, the typical features of an injector, the ratio between the cross-sectional area of the injectors and the combustion chamber, the number of injectors, and the relative position of the injectors within the cross-section of the combustion chamber—on the acoustic absorption coefficient are investigated experimentally using the new facility. Measurements of the fraction of sound power dissipated by the injectors and the velocity flow fields at the ends of the injectors are used to elucidate the physical mechanisms responsible for the acoustic damping. Attempts are made to quantify the separate contributions of viscothermal dissipation and the conversion of acoustic energy into vorticity. Analytical and numerical models incorporating some of these dissipation mechanisms are developed to predict the absorption coefficient of the injectors.

CHAPTER 1
INTRODUCTION

1.1 Motivation

Combustion instabilities have plagued rocket engine development programs throughout history and continue to present challenges today. Such instabilities are caused by coupling between the combustion processes and pressure oscillations in a combustor, and they are characterized by the frequencies and shapes of the acoustic modes of the combustion chamber [1, 2]. These instabilities can produce severe vibration and high rates of heat transfer, which may ultimately lead to failure of the combustion system [3]. To prevent combustion instabilities, the damping in the system must be large enough to dissipate energy more rapidly than the combustion process supplies energy. Acoustic resonators, which are narrowband acoustic damping devices, are commonly installed in combustors to provide passive acoustic damping, and they have proved successful at preventing combustion instabilities [4, 5].

Historically, Helmholtz and quarter-wave resonators have been installed in combustion chambers to increase the acoustic damping [4–7]. Unlike Helmholtz and quarter-wave resonators, which serve no additional purpose for combustion, propellant injectors are necessary for combustion and are already present in combustors, as indicated by the cross-sectional view of a combustion chamber shown in Figure 1.1. Kim and Sohn [8] proposed that these propellant injectors can be tuned to act as half-wave resonators and thus provide acoustic damping in a combustion chamber.

There are a number of factors that affect the acoustic damping of propellant injectors in a rocket engine. Although Kim and Sohn [8] showed that a propellant injector nominally behaves like a half-wave resonator with a resonance frequency determined by the length of

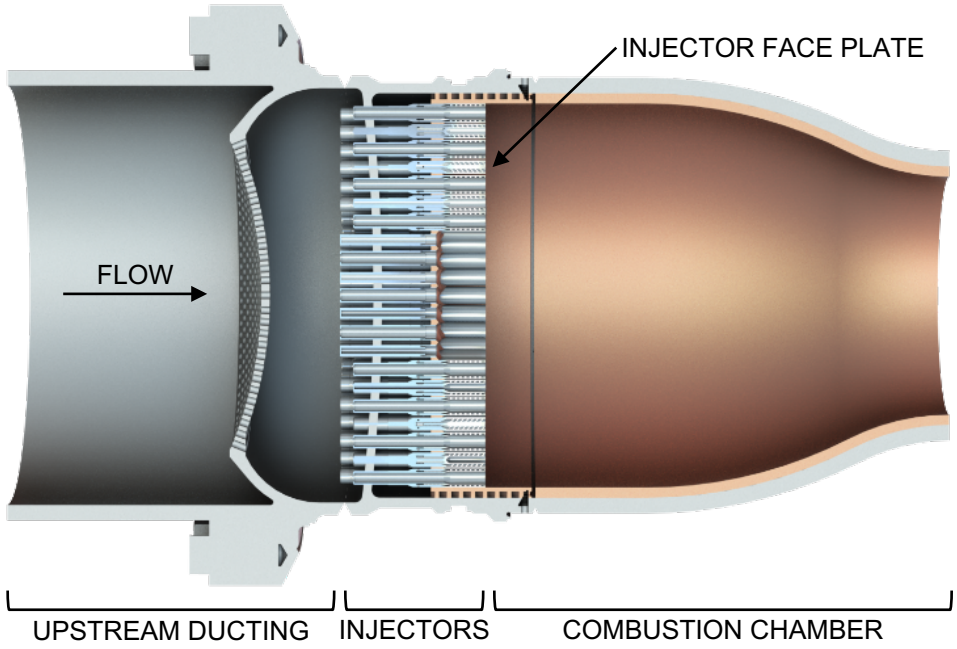

Figure 1.1: Cross-sectional view of a combustion chamber.

the injector, the geometric features of a realistic injector cause its behavior to deviate from that of a perfect half-wave resonator [9–13]. The acoustic damping is not only a function of the geometry of the injector, but it also depends on the ratio between the open area of the injectors and the cross-sectional area of the combustion chamber, so the acoustic damping is a function of the number of injectors and the diameter of each injector [9, 11, 13, 14]. In addition to the geometric parameters of the injectors, the conditions in the combustion chamber play a significant role in the acoustic damping of the propellant injectors. There is a nonzero mean flow of gaseous oxidizer through a rocket engine, which induces a bias flow through the propellant injectors and affects their acoustic damping [15]. The temperature in a combustion chamber is extremely high, and the behavior of the injectors depends on the temperature at the face of the injectors and the temperature gradient within each injector [4, 6]. The sound pressure level in a combustion chamber reaches extremely high amplitudes [2], and it is well known that the performance of acoustic dampers, including propellant injectors, is a function of amplitude at high sound pressure levels due to so-called nonlinearities [13, 16]. Experience has shown that the frequencies and mode shapes

of combustion instabilities in existing rocket engines tend to correspond to higher-order acoustic modes within the combustion chamber [2], so the damping effectiveness of an injector depends on its position relative to the nodes and antinodes of the three-dimensional acoustic modes [17, 18].

A thorough understanding of the acoustic damping mechanisms of propellant injectors is required if injectors are to be designed to prevent combustion instabilities. In particular, the effects of realistic geometric parameters and operating conditions on the acoustic damping must be well understood to accurately predict the acoustic behavior of the injectors during the design phase. However, there are only a few studies reported in the literature on the acoustic damping of propellant injectors, and none of these studies include experimental measurements of the effects of mean flow, high temperature, high amplitude, or higher-order modes. Therefore, the acoustic damping mechanisms of propellant injectors and the dependence of these physical mechanisms on the injector geometry and operating conditions are not yet completely understood. Understanding these mechanisms is the basis of the work described in this dissertation. Although the motivation for this work stems from propellant injectors in a rocket engine, the results are applicable, more generally, to any end-mounted half-wave resonators in a duct.

1.2 Objectives

The overall objective of this work is to experimentally investigate the acoustic damping of propellant injectors in order to gain an understanding of the physical mechanisms governing their acoustic damping. There are a number of variables that may affect the acoustic damping of propellant injectors in a rocket engine, including the physical design and operating conditions of the combustor. The specific objectives of this work are to individually investigate the effects of each of these relevant variables on the acoustic damping. The following geometric parameters based on the physical design of a combustor are considered in this work:

- Geometric features of the injectors
- Ratio between the open area of the injectors and the cross-sectional area of the combustion chamber
- Number of injectors
- Position and distribution of the injectors on the injector faceplate

The following realistic operating conditions also considered in this work:

- Bias flow through the injectors
- High temperatures
- High acoustic amplitudes
- Higher-order mode propagation

1.3 Technical Approach

The objectives described in the previous section are accomplished using a new experimental facility called the Heated, Optimized Tube for Multimodal Evaluation of Sound Scattering (HOTMESS), which was developed as part of this work to measure the acoustic scattering matrix of a test article under mean flow, high temperature, high amplitude, and higher-order mode propagation conditions. HOTMESS is currently the only known experimental facility in the world that is capable of measuring the acoustic scattering matrix—and hence the power reflection, transmission, dissipation, and absorption coefficients—of a test article under all of the aforementioned conditions. The acoustic damping of the propellant injectors is quantified using the absorption coefficient, which is the fraction of the incident sound power that is not reflected from the injectors. The absorption coefficient is commonly used in the design and analysis of acoustic dampers [1, 6, 11, 19]. The effects of the geometric parameters on the absorption coefficient are investigated using test articles

that contain different numbers and layouts of propellant injectors with unique geometric features. The effects of the operating conditions on the absorption coefficient are measured by varying the following conditions in HOTMESS:

- Velocity of the bias flow through the injectors
- Temperature of the flow
- Amplitude of the acoustic waves incident on the injectors
- Modes of the acoustic waves incident on the injectors

Kim and Sohn [8] showed that propellant injectors nominally behave like half-wave resonators, so the effects of some of the aforementioned parameters are tested using straight cylindrical half-wave resonators in place of propellant injectors with realistic geometric features. Thus, the results are applicable to both propellant injectors and, more generally, to any end-mounted half-wave resonators in a duct.

In addition to the absorption coefficient, the fraction of the incident sound power that is reflected from, transmitted through, and dissipated by the propellant injectors is measured using HOTMESS. Measurements of the sound power dissipation coefficient and the velocity flow fields at the ends of the propellant injectors are used to quantitatively separate the effects of the following physical mechanisms responsible for the acoustic damping:

- Viscous and thermal losses in the acoustic boundary layer
- Acoustic radiation from the open end of the injectors opposite the incident acoustic waves in the combustion chamber, i.e., acoustic radiation into the upstream ducting
- Dissipation due to turbulence
- Conversion of acoustic energy to vorticity at the open ends of the injectors
- Acoustic attenuation within the bulk fluid

1.4 Outline

This dissertation contains a total of eleven chapters, including the present chapter. Chapters 2–5 provide the background material required for a thorough understanding of the experiments and results presented in this work. Chapter 2 contains a review of the existing literature on the acoustic damping of propellant injectors, including background material on acoustic resonators and a discussion of the effects of the geometric parameters and operating conditions on the acoustic damping. The methodology used to conduct the experiments is presented in Chapter 3, and a description of the experimental facilities is given in Chapter 4. The experiments are based on the assumption that an impedance tube can be used to model the acoustic behavior of a combustion chamber. Chapter 5 acts as a bridge between the background material and the experimental results, in which the analytical and numerical models for the acoustic damping of propellant injectors are developed. The interpretations of the results are presented in subsequent chapters and are based upon these models.

Chapters 6–10 contain the experimental results for the acoustic damping of propellant injectors. The effects of the geometric parameters on the acoustic damping are presented in Chapter 6. The effects of the operating conditions on the acoustic damping are divided between different chapters: the effects of bias flow are presented in Chapter 7, the effects of temperature are presented in Chapter 8, the effects of high amplitude are presented in Chapter 9, and the effects of higher-order modes are presented in Chapter 10. Finally, the conclusions and recommendations for future research are presented in Chapter 11.

CHAPTER 2
LITERATURE REVIEW

2.1 Overview

This chapter provides a review of the literature on the acoustic damping of propellant injectors. The outline of this chapter is as follows: First, in Section 2.2, relevant terms required for understanding the literature are defined, and additional background material on acoustic resonators is provided. Next, a review of the literature on the acoustic damping of propellant injectors is presented in Section 2.3. The literature review is organized into sections corresponding to the geometric parameters and operating conditions that are investigated in this work for their effects on the acoustic damping. Sections in which there is a dearth of studies on the acoustic damping of propellant injectors or half-wave resonators are supplemented with literature on the acoustic damping of Helmholtz and quarter-wave resonators, orifices, and open ducts if the results are applicable to propellant injectors. Finally, in Section 2.4, the gaps in the existing literature that are filled by this work are noted.

2.2 Background and Definitions

The purpose of this section is to provide the necessary background material required for understanding the literature on the acoustic damping of propellant injectors and other acoustic resonators. Many studies report results in terms of the impedance and the end correction (or length correction) of a resonator. In this section, the different types of impedance used in this work are defined, and expressions for the end correction at the open end of a resonator are given based on the impedance. Finally, the common types of acoustic resonators—namely, Helmholtz, quarter-wave, and half-wave resonators—are described, and expressions for their resonance frequencies are given in terms of their end corrections.

2.2.1 Definitions of Impedance Terms

There are several definitions of impedance that are common in the acoustics literature, but the definitions are not always used consistently. For the sake of completeness, and to avoid confusion, the different types of impedance used in this work are defined in this section. The impedance is a complex frequency-domain parameter that is useful for analyzing the performance of acoustic resonators. The definitions used in this work are those given by Kinsler, et al. [20], which are summarized below:

- The *specific acoustic impedance*, $z = p/u$, at a given point is the complex ratio of the acoustic pressure, p, to the particle velocity, u, at that point.

- The *acoustic impedance*, $Z = p/U$, at a given surface is the complex ratio of the acoustic pressure, p, to the volume velocity, $U = uS$, averaged over that surface, where S is the cross-sectional area of the surface.

- The *mechanical impedance*, $Z_m = F/u$, is the complex ratio of the force, F, acting on an acoustic medium or a mechanical device to the resulting particle velocity of the medium or the velocity of the device. The acoustic force is given by $F = pS$.

In general, the impedance is complex if the pressure (or force) fluctuations and the particle velocity fluctuations are not in phase.

There are additional impedance terms that can be defined from the aforementioned impedance definitions. The *characteristic impedance* of a medium, ρc, is the specific acoustic impedance of plane wave propagation in an unbounded medium, where ρ is the density and c is the speed of sound in the medium. The *normalized impedance*, ζ, is a non-dimensional impedance, which is given by the specific acoustic impedance normalized by the characteristic impedance, or

$$\zeta = \frac{z}{\rho c} = \theta + j\chi \tag{2.1}$$

where the real part, θ, is the normalized resistance, and the imaginary part, χ, is the normalized reactance. Finally, the *radiation impedance*, Z_r, is the mechanical impedance associated with the radiation of sound [20].

2.2.2 End Corrections

The radiation impedance is useful for describing the boundary condition at the open end of a resonator or a pipe. The boundary condition at the open end of a pipe is often approximated as a pressure node since the free boundary cannot support a net force. In reality, the fluctuating pressure and particle velocity inside the pipe cause the medium outside the open end to fluctuate due to the radiation of sound from the open end of the pipe. Therefore, a pressure node does not form precisely at the open end of the pipe, and the boundary condition is instead given by the radiation impedance. The radiation impedance is a function of the geometry at the open end. If the open end of the pipe is surrounded by an infinite flange, then in the low-frequency limit ($ka \ll 1$), the approximate normalized impedance due to the radiation of sound, as given by Kinsler, et al. [20], is

$$\zeta_r = \frac{Z_r}{\rho c S} = \frac{1}{2}(ka)^2 + j\frac{8}{3\pi}ka \qquad \text{(flanged)} \tag{2.2}$$

where S is the cross-sectional area of the pipe, a is the radius of the pipe, and $k = \omega/c$ is the wavenumber. The imaginary part of the normalized radiation impedance increases the effective length of the pipe, which implies that the pressure node is located outside the open end of the pipe. This change in the effective length in the pipe is called the length correction and is related to the normalized reactance by $\chi_r = jk\Delta L$. Nomura, et al. [21] calculated an exact value for the length correction at a flanged open end, which was reported by Peters, et al. [22] to be

$$\frac{\Delta L}{a} = 0.8217 - 0.367(ka)^2, \quad ka < 0.5 \qquad \text{(flanged)} \tag{2.3}$$

In the low-frequency limit ($ka \ll 1$), Kinsler, et al. [20] reported that the approximate normalized radiation impedance of an unflanged pipe is

$$\zeta_r = \frac{Z_r}{\rho c S} = \frac{1}{4}(ka)^2 + j0.6ka \qquad \text{(unflanged)} \tag{2.4}$$

Levine and Schwinger [23] derived an exact expression for the length correction of the open end of an unflanged pipe, and Davies [24] approximated their expression using the empirical fit

$$\frac{\Delta L}{a} = \begin{cases} 0.6133 - 0.1168(ka)^2, & ka < 0.5 \\ 0.6393 - 0.1104ka, & 0.5 < ka < 2 \end{cases} \qquad \text{(unflanged)} \tag{2.5}$$

In many realistic cases, the open end of a pipe does not terminate in a large flange; instead, the pipe itself has a finite wall thickness, which may be treated as a small flange. Ando [25] studied the radiation of sound from a circular pipe with finite wall thickness and found that the length correction increases with increasing wall thickness from the unflanged limit towards the flanged limit. However, Ando did not provide a simple analytical expression for the length correction as a function of wall thickness, so the length correction for the open end of a pipe with finite wall thickness must be interpolated from the results plotted in Ref. [25] and tabulated in Appendix F.

2.2.3 Acoustic Resonators

Acoustic resonators are commonly installed in rocket engines to provide passive acoustic damping, and they have proved successful at preventing combustion instabilities [4, 5]. However, acoustic resonators are narrowband devices, so they provide significant acoustic damping only near their resonance frequencies. The resonance frequency, which is defined as the frequency at which a positive-going zero crossing occurs in the reactance, is a function of the geometry of the resonator and the end correction at the open end(s)

of the resonator. There are many possible acoustic resonator geometries, but historically, Helmholtz and quarter-wave resonators have been used most frequently in industrial applications [26], including rocket engines [4–7]. An overview of Helmholtz, quarter-wave, and half-wave resonators is given here.

Helmholtz Resonator

A Helmholtz resonator consists of a neck or a thin orifice backed by a cavity, as shown in Figure 2.1. If the dimensions of the resonator are much smaller than the wavelengths of the frequencies of interest, then the Helmholtz resonator can be treated as a lumped-element acoustic device with an equivalent mass, stiffness, and resistance. Under these conditions, the resonance frequency of a Helmholtz resonator is [27]

$$f_0 = \frac{c}{2\pi}\sqrt{\frac{S}{(L+\Delta L)V}} \tag{2.6}$$

where S is the cross-sectional area of the neck, L is the length of the neck, V is the volume of the cavity, and ΔL is the length correction due to the radiation impedance, which is discussed in Section 2.2.2. The total length correction, $\Delta L = \Delta L_{\text{in}} + \Delta L_{\text{out}}$, is the sum of the length corrections of the inner and outer openings of the neck; the inner opening to the cavity is assumed to be flanged, and the length correction of the outer opening depends on how the Helmholtz resonator is installed [20].

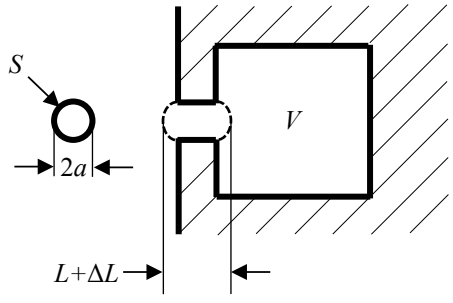

Figure 2.1: Helmholtz resonator.

Quarter-Wave Resonator

A quarter-wave resonator is a cylindrical tube that is closed at one end and open at the other end, as shown in Figure 2.2. The particle velocity must be zero at the closed end of the resonator since the wall is impermeable, so the closed end has an infinite impedance. Sound radiates into the surrounding medium from the open end of the resonator, so the boundary condition at the open end is given by the radiation impedance. Solving the acoustic wave equation for these boundary conditions gives an expression for the resonance frequencies of a quarter-wave resonator as [20, 27]

$$f_0 = \frac{nc}{4(L + \Delta L)}, \quad n = 1, 3, 5, ... \tag{2.7}$$

where n is any odd integer. A quarter-wave resonator has multiple resonance frequencies at approximately the odd harmonics of the fundamental resonance frequency, where the fundamental is given by $n = 1$. The length correction is given by Eq. (2.3) or Eq. (2.5) depending on whether the open end of the resonator is flanged or unflanged.

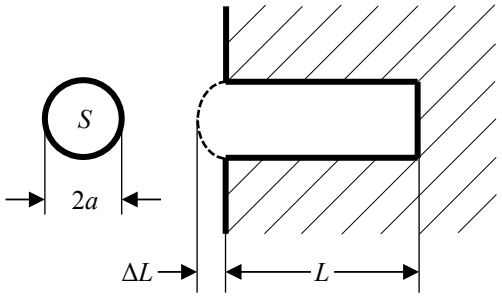

Figure 2.2: Quarter-wave resonator.

Substitution of the relation $c = \lambda f$ into Eq. (2.7) reveals that the effective length of the quarter-wave resonator at its fundamental resonance frequency is $(L + \Delta L) = \lambda/4$, where λ is the wavelength. The effective length of the resonator is equal to one-quarter of the wavelength of the fundamental resonance frequency, and hence the resonator is called a "quarter-wave" resonator.

Half-Wave Resonator

The acoustic damping mechanisms of propellant injectors are investigated in this work, and injectors have been shown to behave like half-wave resonators [8]. A half-wave resonator is a cylindrical tube that is open at both ends, as shown in Figure 2.3. Sound radiates into the surrounding medium from both open ends of the resonator, so the boundary condition at each open end is given by the radiation impedance. Solving the acoustic wave equation for these boundary conditions gives an expression for the resonance frequencies of a half-wave resonator as [20, 27]

$$f_0 = \frac{nc}{2(L + \Delta L)}, \quad n = 1, 2, 3, ... \tag{2.8}$$

where n is any integer. A half-wave resonator has multiple resonance frequencies at approximately the integer harmonics of the fundamental resonance frequency, where the fundamental is given by $n = 1$. The total length correction, $\Delta L = \Delta L_{\text{in}} + \Delta L_{\text{out}}$, is the sum of the length corrections at the inlet and outlet of the resonator. The length correction at each open end is given by Eq. (2.3) or Eq. (2.5) depending on whether the end is flanged or unflanged.

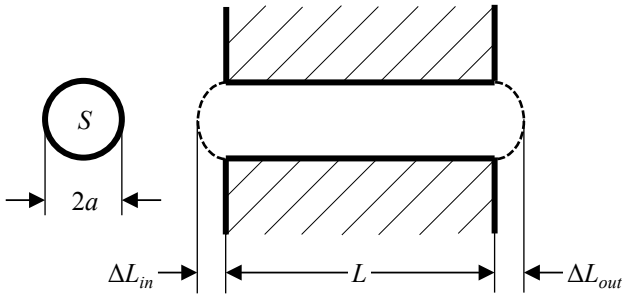

Figure 2.3: Half-wave resonator.

Substitution of the relation $c = \lambda f$ into Eq. (2.8) reveals that the effective length of the half-wave resonator at the fundamental resonance frequency is $(L + \Delta L) = \lambda/2$. The effective length of the resonator is equal to one-half of the wavelength of the fundamental resonance frequency, and hence the resonator is called a "half-wave" resonator.

Comparison of the Acoustic Damping

Sohn and Park [26] experimentally compared the acoustic damping of Helmholtz, quarter-wave, and half-wave resonators using the absorption coefficient, as shown in Figure 2.4. In their experiments, all three resonators were tuned to the same frequency, and the diameter of the neck of the Helmholtz resonator was identical to the diameter of the quarter-wave and half-wave resonators. Their results showed that a Helmholtz resonator has the highest absorption coefficient, and a half-wave resonator has the lowest absorption coefficient. This suggests that injectors are not as efficient as other types of resonators at providing acoustic damping. However, Helmholtz and quarter-wave resonators serve no purpose for combustion, so they must be installed in a combustion chamber for the sole purpose of providing acoustic damping, whereas propellant injectors, which act like half-wave resonators, are already present in combustors because they are required for combustion. Therefore, it would be advantageous if the injectors themselves could be designed to provide sufficient acoustic damping to prevent combustion instabilities, even if the acoustic damping of each individual injector is less than that of a comparable Helmholtz resonator. The existing literature on the factors that enhance and diminish the acoustic damping of propellant injectors is discussed in the following sections.

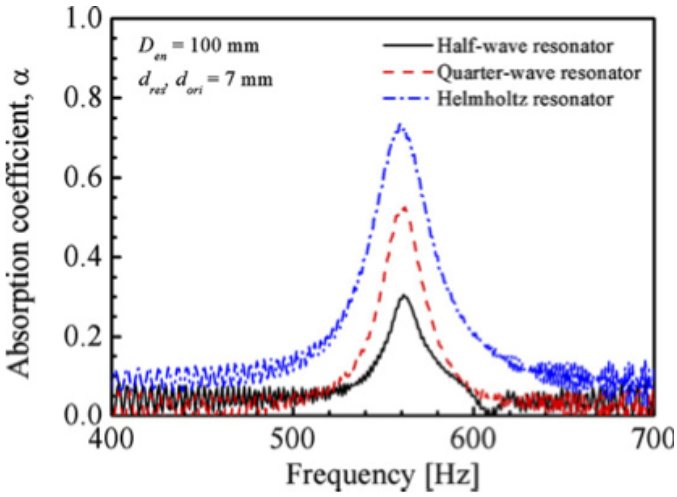

Figure 2.4: Comparison of the absorption coefficients of Helmholtz, quarter-wave, and half-wave resonators.

2.3 Acoustic Damping of Propellant Injectors

A review of the literature on the acoustic damping of propellant injectors is presented in this section. The literature review is organized into subsections corresponding to the effects of the different geometric parameters and operating conditions on the acoustic damping.

2.3.1 Effect of the Geometric Features

First, the literature on the effects of the geometric features of a propellant injector is reviewed. Figure 2.5 shows an example of a propellant injector with several realistic geometric features, including the main body of the injector, an inlet protrusion, and a recess. The flow direction is from left to right in Figure 2.5, so the left side of the injector is the inlet, and the right side is the outlet. The inlet protrusion forms an area contraction, or partial blockage, at the inlet, and the recess forms an area expansion at the outlet. Real propellant injectors contain additional features that are not shown in Figure 2.5, but the existing literature summarized below only discusses the effects of the main body, the inlet protrusion, and the recess on the acoustic damping.

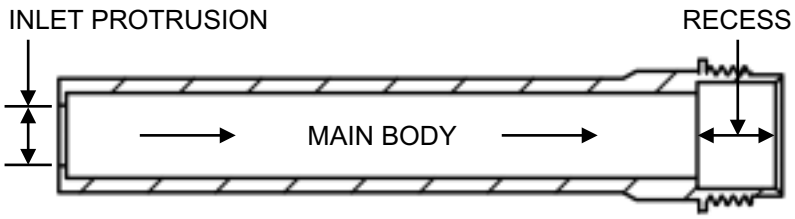

Figure 2.5: Geometric features of a propellant injector.

Propellant Injectors as Half-Wave Resonators

A number of studies on the role of propellant injectors as acoustic resonators have been performed in quiescent air at standard atmospheric conditions [8–14]. Kim and Sohn [8] proposed that an injector behaves like a half-wave resonator because acoustic pressure nodes are formed near the open boundaries at each end. Kim and Sohn [8] tested this hypothesis

by mounting a variable-length straight cylindrical injector to a model combustion chamber to investigate the acoustic damping of the injector as a function of its length. They generated broadband noise using a loudspeaker to excite the acoustic modes in the model chamber and measured the amplitude of the first circumferential mode in the chamber as a function of the length of the injector. Figure 2.6 shows the amplitude and frequency of the first circumferential acoustic mode in the model combustion chamber as a function of the length of the injector. The minimum amplitude occurred when the length of the injector was approximately equal to one-half the wavelength of the acoustic waves at the frequency of the first circumferential mode in the model chamber. The second local minimum in the amplitude occurred when the length of the injector was approximately equal to the wavelength of the acoustic waves at the frequency of the first circumferential mode in the model chamber. From these results, Kim and Sohn [8] showed that a single straight injector indeed behaves like a half-wave resonator and is most effective for acoustic damping when its length is close to a half wavelength of the frequency of the combustion instability, and the injector also provides acoustic damping when its length is an integer multiple of a half wavelength.

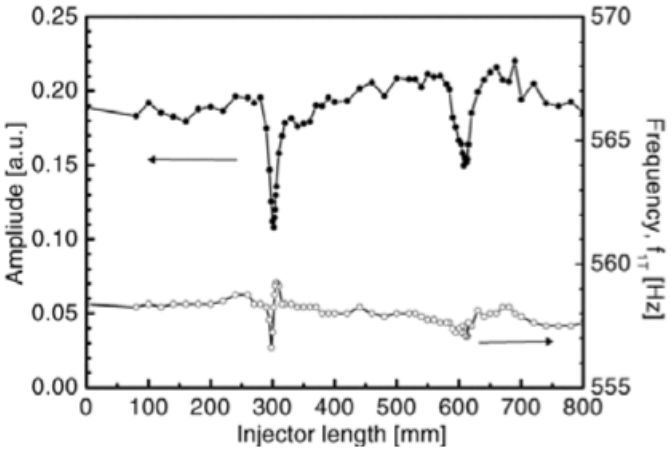

Figure 2.6: Amplitude and frequency of the first circumferential acoustic mode in a model combustion chamber as a function of injector length (Ref. [8]).

The absorption coefficient quantifies the fraction of the incident sound power that is not reflected from a test article, and it is often used in practice to design resonators for acoustic

damping in a combustion chamber [1]. Park and Sohn [11] adopted the absorption coefficient as a quantitative measure of the acoustic damping of an injector. Figure 2.7 shows the absorption coefficient of a single straight cylindrical injector, where the maximum absorption coefficient corresponds to the resonance frequency of the injector.

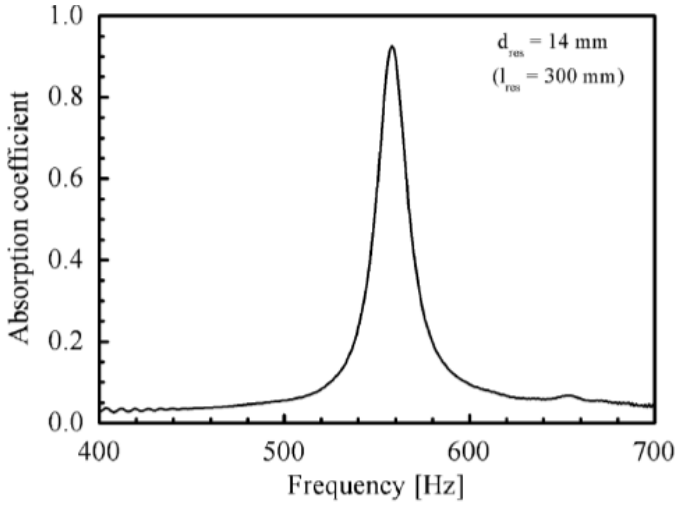

Figure 2.7: Absorption coefficient of a half-wave resonator (Ref. [11]).

Effect of Inlet Protrusion: Resonance Frequency Decreases

Multiple investigators [9–11] studied the effect of an inlet protrusion (which they called "inlet blockage") on the acoustic damping using a model injector. Several of these investigators [9, 10] showed, using linear numerical analysis, that the addition of the inlet protrusion decreases the resonance frequency of the injector. Park and Sohn [11] measured the absorption coefficient of injectors with different amounts of inlet protrusion and reported the results as a function of the blockage ratio, which they defined as the ratio between the area of the inlet to the area of the main body of the injector. Their experimental results, which are shown in Figure 2.8, confirm that the resonance frequency continues to decrease as the percentage of the inlet area blocked by the protrusion increases. Park and Sohn [11] stated that this phenomenon occurs as a result of the change in the acoustically open boundary condition at the inlet of the injector.

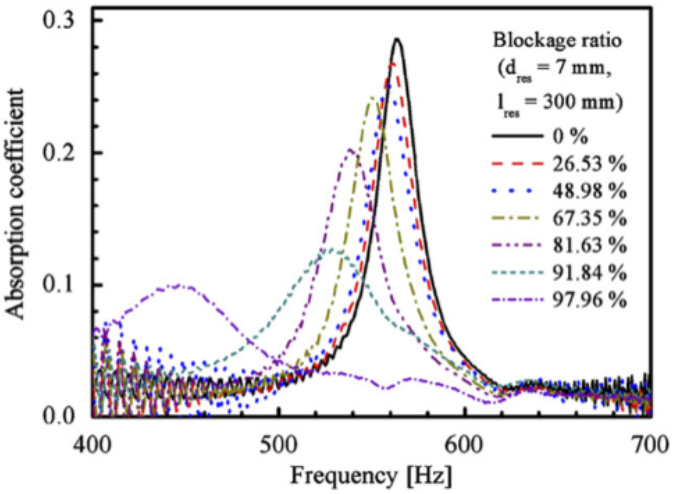

Figure 2.8: Absorption coefficient of injectors with various amounts of inlet protrusion (Ref. [11]).

Effect of a Recess: Resonance Frequency Increases

Kim, et al. [12] computationally modeled the effect of a recess on the acoustic damping of a propellant injector. The axial pressure profiles of the standing wave in a straight cylindrical injector, an injector with inlet protrusion (or inlet blockage), an injector with an induction bulge (which is the region of the injector shown in Figure 2.5 with diameter d_{res}), and an injector of actual shape, including a recess, are compared in Figure 2.9. Kim, et al. [12] found from this comparison that the addition of a recess changes the shape of the standing wave in an injector, which increases the resonance frequency of the injector. However, they did not calculate the effect of the geometric features on the absorption coefficient or measure the effects of the recess experimentally.

2.3.2 Effect of the Open Area Ratio and the Number of Injectors

In the previous section, a propellant injector was shown to behave nominally like a half-wave resonator. The realistic geometric features were shown to change the resonance frequency but not significantly alter the acoustic damping behavior of the injector. In the studies presented in this section, the injectors were modeled as straight cylindrical half-

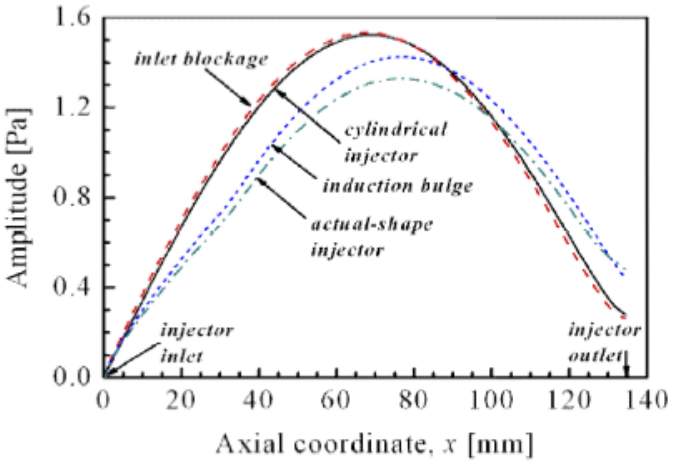

Figure 2.9: Axial acoustic pressure profiles inside injectors with different geometric features (Ref. [12]).

wave resonators, and the diameter and number of the resonators were varied to investigate the open area ratio and number effects on the acoustic damping. Related studies on the acoustic damping of multiple Helmholtz resonators are also presented in this section.

Effect of the Open Area Ratio for Propellant Injectors

Several investigators [9, 11, 14, 26] have studied the effect of the open area ratio on the acoustic damping of propellant injectors. The open area ratio is the ratio between the area of the open ends of the injectors and the cross-sectional area of the combustion chamber, so it is a function of the diameter of the injectors, the number of injectors, and the dimensions of the combustion chamber. Park and Sohn [11] measured the absorption coefficient of injectors of various diameters, as shown in Figure 2.10. They found that as the diameter of the injector—and hence the open area ratio—increases, the frequency bandwidth of the absorption coefficient and the peak value of the absorption coefficient both increase. However, they found that the peak absorption coefficient decreases with increasing diameter for injectors with diameters larger than 20 mm. They noted that the resonance frequency of the injector decreases slightly with increasing diameter, which they attributed to the increase in the length correction ΔL in Eq (2.3) or Eq. (2.5) with diameter. Park and Sohn

[11] also measured the absorption coefficient of various numbers of injectors, as shown in Figure 2.11. They found that as the number of injectors—and hence the open area ratio—increases, the frequency bandwidth of the absorption coefficient increases monotonically, but the peak absorption coefficient increases until it reaches a maximum value of one and then decreases as additional injectors are added. These two sets of experiments demonstrate that there is an optimal open area ratio that maximizes the peak value of the absorption coefficient for a particular experimental configuration. However, Park and Sohn [11] found that there is no universal optimal open area ratio because the acoustic damping of the injectors depends on the boundary absorption at the walls of the injectors, which is a function of the diameter and shape of the individual injectors.

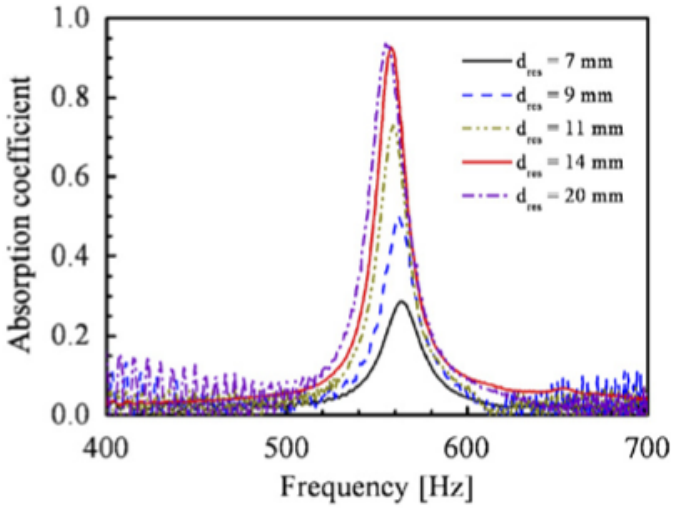

Figure 2.10: Absorption coefficient of injectors of various diameters (Ref. [11]).

Underdamping and Overdamping as a Function of the Open Area Ratio

Park and Sohn [11] found that the frequency bandwidth of the absorption coefficient increases monotonically with the open area ratio, but the peak absorption coefficient is maximized at a certain open area ratio. Other investigators [6, 19, 28] have observed similar behavior for Helmholtz and quarter-wave resonators. Laudien, et al. [6] measured the absorption coefficient of various numbers of Helmholtz resonators and classified the configu-

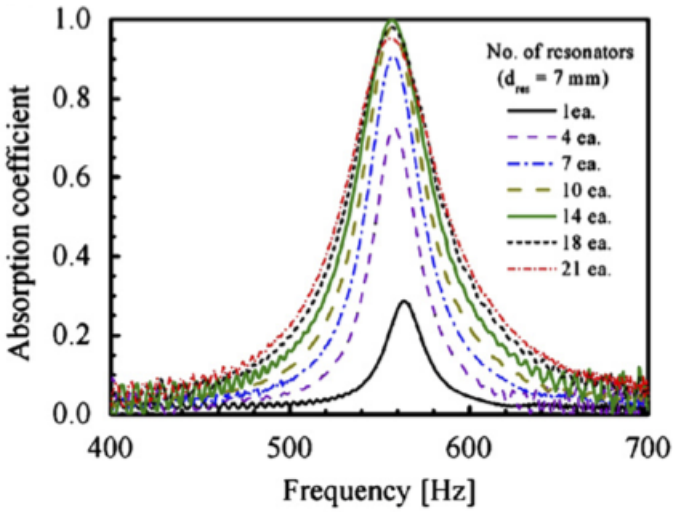

Figure 2.11: Absorption coefficient of various numbers of injectors (Ref. [11]).

rations as underdamped, optimally damped, or overdamped, as shown in Figure 2.12. They found that for a small number of resonators with a small open area ratio, the peak absorption coefficient is less than one, and the absorption frequency bandwidth is relatively narrow, so they termed this configuration as underdamped. For a greater number of resonators with a large open area ratio, they found that the peak absorption coefficient is also less than one, but the absorption frequency bandwidth is wider, so they termed this configuration as overdamped. At some intermediate open area ratio, the peak absorption coefficient reaches a maximum value of one, so they classified this configuration as optimally damped.

However, the open area ratio at which the peak absorption coefficient is maximized may not be optimal for preventing combustion instabilities if the frequency bandwidth of the absorption coefficient is relatively small. In the monograph edited by Harrje and Reardon [1], the optimal open area ratio is defined as the ratio that maximizes both the peak value and the frequency bandwidth of the absorption coefficient. A wide frequency bandwidth is important due to uncertainty in the exact frequency of the combustion instability in a real combustion chamber, especially in the presence of strong temperature gradients [1, 5]. For example, the addition of acoustic dampers to a combustion chamber can shift the frequency and the mode of the combustion instability [1]. Several investigators found

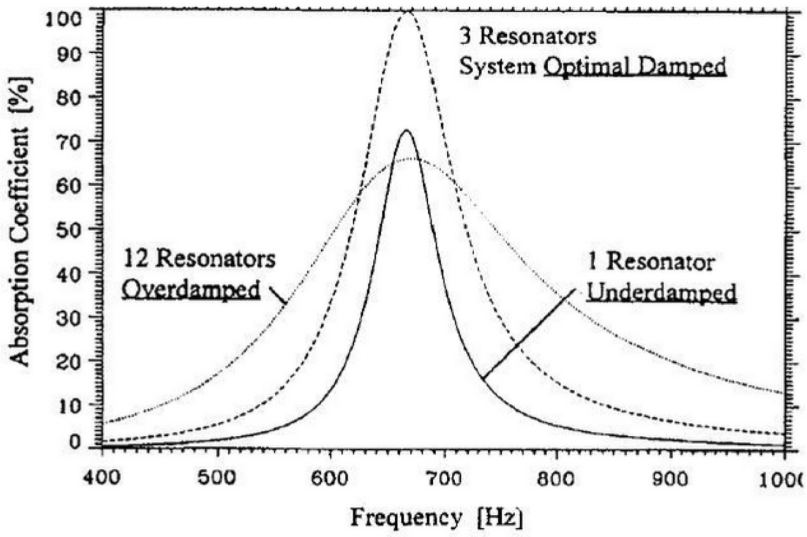

Figure 2.12: Absorption coefficient for underdamped, optimally damped, and overdamped Helmholtz resonators (Ref. [6]).

that the addition of an acoustic resonator to a chamber causes additional resonant acoustic modes to appear, even in the absence of combustion [4, 29]. The frequencies and shapes of the acoustic modes in the chamber are particularly affected by the addition of resonators with large open area ratios because the resonators begin to act like the interior volume of the combustion chamber [9, 17].

2.3.3 Effect of the Position and Distribution of the Injectors

In the previous section, the open area ratio and number of injectors were shown to have a significant effect on the absorption coefficient. In the studies presented in this section, the open area ratio of the injectors was held constant, but the position and distribution of the injectors on the injector faceplate were varied. The effects of the position of the injectors on the acoustic damping are discussed for both the plane wave mode and higher-order modes.

Effect of Position for the Plane Wave Mode

Park and Sohn [11] measured the absorption coefficient of several injectors placed in close proximity to one another and the same number of injectors distributed uniformly within the

cross-section of the termination of a normal-incidence impedance tube. They found that the spatial distribution of the injectors has a negligible effect on the absorption coefficient for plane-wave propagation, as shown in Figure 2.13. By definition, the acoustic pressure and particle velocity of a plane wave is uniform over the cross-section of the impedance tube, so the position of the injectors was not expected to significantly affect the acoustic damping for the plane-wave mode.

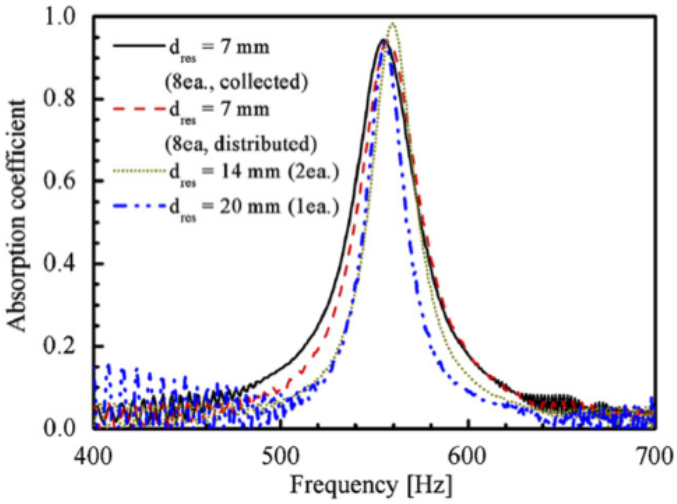

Figure 2.13: Absorption coefficient of different injector configurations with identical open area ratio (Ref. [11]).

However, Ingard [30] showed that the length correction—and hence the resonance frequency—of a resonator is indeed a function of its position within the cross section of the duct, even in the plane wave regime, because the length correction is related to the excitation of higher-order evanescent modes at the area discontinuity between the resonator and the duct. Unlike Ingard, who assumed a uniform particle velocity distribution in the mouth of the resonator, Selamet and Ji [31] accounted for higher-order evanescent modes in the mouth of the resonator. Selamet and Ji computed the length correction as a function of the offset distance between the resonator and the centerline of the duct using their "double-duct model," which included evanescent modes in both the resonator and the duct, and Ingard's "single-duct model," which only included evanescent modes in the duct. Their results, which are shown in Figure 2.14, indicate that the length correction is smallest when

the resonator is located at the centerline of the duct, and the length correction increases as the resonator approaches the wall of the duct.

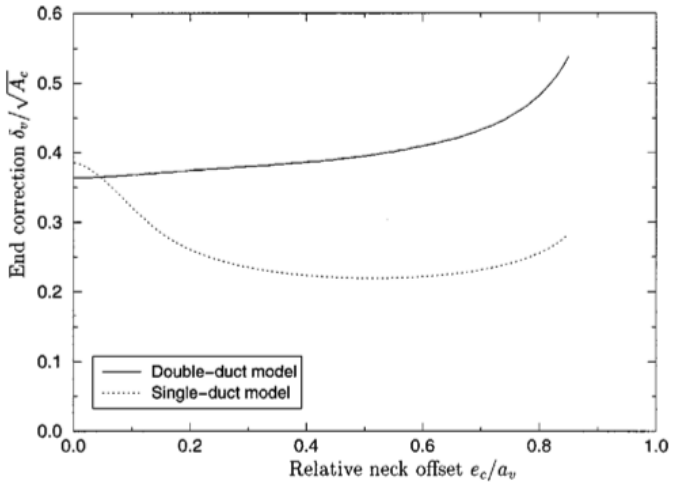

Figure 2.14: Length correction as a function of the offset distance between a resonator and the centerline of the duct calculated using the "double-duct model" of Selamet and Ji [31] and the "single-duct model" of Ingard [30] (Ref. [31]).

Effect of Position for Higher-Order Modes

Experience has shown that the frequencies and mode shapes of combustion instabilities in existing rocket engines tend to correspond to higher-order acoustic modes within the combustion chamber [2]. An acoustic damper is most effective when it is located at a pressure antinode, which provides the maximum driving force for interactions between the acoustic damper and the oscillating pressure [17, 18]. The optimal location for acoustic dampers in a combustion chamber is near the boundary of the chamber wall and the injector faceplate, which is a pressure antinode for the higher-order modes within the combustion chamber [1, 5, 17]. Reference [1] also suggests that acoustic resonators can be installed in the injector faceplate itself, which has the additional benefit of simplifying the cooling requirements for the resonators. Propellant injectors installed near the outer wall of the combustion chamber are thus already located in the optimal position for maximum acoustic damping.

As discussed in Section 2.3.2, the addition of an acoustic resonator to a combustion chamber can cause the frequencies of the acoustic modes in the chamber to shift and new injector-coupled modes to appear. The frequencies and shapes of the resulting coupled modes—especially higher-order modes—depend on the location of the resonator. The damping effectiveness of the resonator is then affected by the shapes of the resulting coupled modes because the acoustic damper is most effective when it is located at a pressure antinode [17, 18]. These phenomena are discussed in more detail in Section 2.3.7.

2.3.4 Effect of Bias Flow

The studies presented in the previous sections were each conducted in a quiescent medium. In this section, the literature on the effects of bias flow on the acoustic damping of propellant injectors is reviewed. The term "bias" refers to flow through the injectors and is included to distinguish between studies on the effects of through-flow and studies on the effects of grazing flow. Studies on the effects of bias flow on the dissipation and the end correction of a duct are also presented.

Effect of Bias flow on the Acoustic Damping of Propellant Injectors

There is only one known study in the literature on the acoustic damping of propellant injectors that considers the effects of mean flow. Kim, et al. [12] performed a numerical analysis on the effects of bias flow on the tuning length of a propellant injector, and they showed that the resonance frequency decreases by the factor $(1 - M^2)$, where M is the Mach number of the flow through the injector. However, they stated that the mean flow only has "secondary effects" on the performance of the injector, so they did not calculate the change in the magnitude of the acoustic damping due to the mean flow, and they neglected changes to the end corrections at the open ends of the injector due to the mean flow.

Effect of Mean Flow on the Dissipation in a Duct

Although there are few studies in the literature on the acoustic damping of propellant injectors with bias flow, there are a number of studies on the effects of flow on the propagation of acoustic waves in a duct. Ingard and Singhal [32, 33] found that bias flow has two main effects on the acoustic propagation in a duct: convection of sound by the mean flow and attenuation of sound due to turbulence. Davies [24] discussed the effect of convection on the acoustic propagation. Ronneberger and Ahrens [34] measured the sound attenuation in a turbulent pipe flow and proposed a quasi-laminar model for the attenuation. Peters, et al. [22], showed that the quasi-laminar model fits the experimental data well when the acoustic boundary layer is thinner than the viscous sublayer. However, when the acoustic boundary layer is thicker than the viscous sublayer, the attenuation due to the turbulent boundary layer is significant and can be approximately modeled by adding the eddy viscosity to the kinematic viscosity [22]. Howe [35–37] developed a detailed theoretical model for the acoustic damping in a turbulent boundary layer, which agrees well with many experiments [22] and is the most widely accepted model in the current literature [38]. Figure 2.15 compares the attenuation coefficients given by the models of Ronneberger and Ahrens [34] and Howe [37] in the upstream and downstream directions in a duct. Figure 2.15 shows that the attenuation coefficient against the flow direction is greater than the attenuation coefficient in the flow direction at all frequencies. At low frequencies, the attenuation coefficient predicted by Howe [37] exceeds that predicted by Ronneberger and Ahrens [34], so the attenuation due to the turbulent boundary layer is significant at low frequencies. Other researchers, such as Dokumaci [39] and Knutsson and Åbom [40], have continued to extend Howe's model.

Effect of Mean Flow on the Dissipation at the Open End of a Duct

In addition to the sound attenuation by the turbulent boundary layer in a duct, numerous studies have been conducted on the sound dissipation that occurs when the mean flow exits

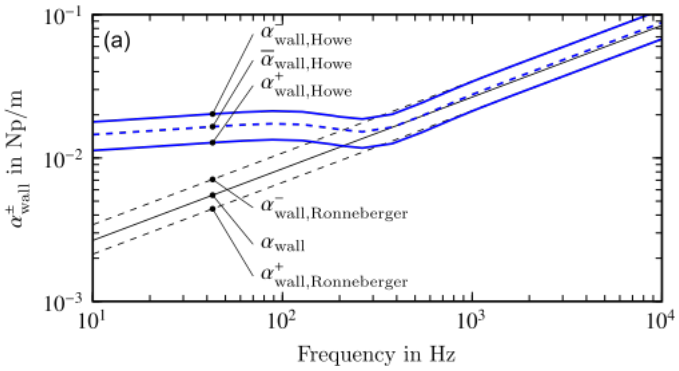

Figure 2.15: Comparison of the attenuation coefficients (α_{wall}) given by the models of Ronneberger and Ahrens [34] and Howe [37] in ($+$) and against ($-$) the flow direction in a duct (Ref. [41]).

the open end of a duct. Ingard and Singhal [33] found that the absorption coefficients at the open ends of a pipe are roughly proportional to the Mach number at low frequencies and low Mach numbers. They also found that the absorption coefficient at the outlet is larger than at the inlet, which they attributed to interactions between the acoustic waves and the outflow. Bechert [42] and Salikuddin and Ahuja [43] demonstrated that the sound dissipation mechanism at the outlet of a pipe with mean flow involves the conversion of acoustic energy into the kinetic energy of fluctuating vortices, which shed from the edge of the pipe and convect downstream. Morfey [44] showed theoretically that acoustic energy is not necessarily conserved in flows with vorticity, and according to Howe [45], vorticity can act as either a sound source or sink.

Munt [46, 47] developed an exact theory for the reflection and transmission of acoustic waves from the open end of a pipe with a mean flow assuming that the shear layer is thin. Cargill [48, 49] and Rienstra [50] simplified Munt's theory for small Strouhal numbers. Munt's theory depends on the application of the Kutta condition at the exit of the pipe; this unsteady Kutta condition was reviewed by Crighton [51]. Peters, et al. [22] and Allam and Åbom [38] showed that Munt's theory agrees well with experimental measurements. Howe [36, 52, 53] also applied the Kutta condition to develop a theory for the dissipation of sound at the exit of a pipe with a mean flow, but he assumed that the shear layer is thick.

Howe's theory explicitly shows that the dissipation mechanism at the exit of the pipe is the conversion of acoustic energy into the kinetic energy of the vortices that shed from the edge of the pipe and convect downstream.

Effect of Mean Flow on the Dissipation at an Area Discontinuity in a Duct

Numerous studies have also been conducted on the sound dissipation that occurs at an area discontinuity in a duct with mean flow. These studies are applicable to propellant injectors because the open ends of the injectors form area discontinuities with the upstream ducting and the combustion chamber. One type of area discontinuity that has received considerable attention in the literature is an orifice. Ingard and Ising [54] found that the specific acoustic resistance increases linearly with the velocity of the bias flow through the orifice above some nonzero velocity, as shown in Figure 2.16. Ingard [55] gave a simple expression for the increase in resistance and the resulting behavior of the absorption coefficient. Ahuja, et al. [56] showed that the absorption coefficient is maximized at an optimal frequency-dependent bias flow velocity. Yang and Morgans [57] modeled the acoustic impedance of finite-length orifices with mean flow, but they did not extend their model to include half-wave resonances. Lahiri and Bake [58] reviewed a number of additional theoretical, experimental, and numerical studies on bias flow acoustic liners and discussed the acoustic damping mechanisms.

Another type of area discontinuity in a duct that is particularly applicable to propellant injectors is a flow expansion. Cummings [59] analyzed the sound transmission through a flow expansion using the continuity, momentum, and energy equations, and Davies [24] followed a similar approach. Cummings and Haddad [60] later showed that only the continuity and momentum equations are necessary because the entropy fluctuations are small. A number of more recent theoretical and computational studies on the scattering and absorption of sound waves at an area expansion have also been performed [61–65]. For example, Boij and Nilsson [62] showed that the absorption coefficient at an area expansion in a duct

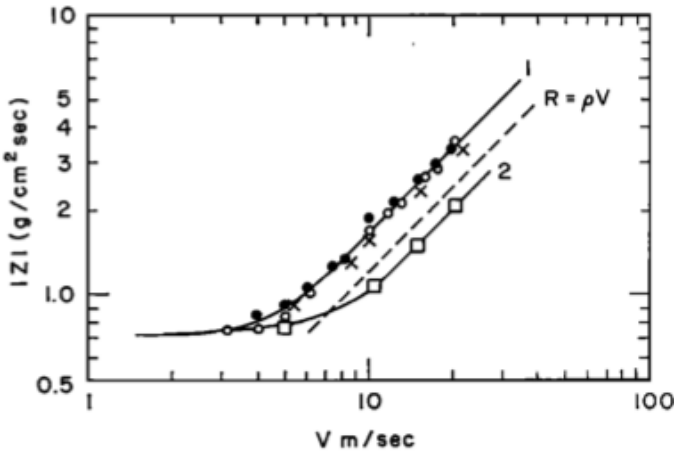

Figure 2.16: Specific acoustic resistance as a function of the bias flow velocity through the orifice. For curve 1, the orifice was open to the ambient air, but for curve 2, an external duct was present (Ref. [54]).

with mean flow is a function of the mean flow Strouhal number, and their results indicated that main dissipation mechanism is the interaction between the acoustic waves and the vortex shedding. Kierkegaard, et al. [65] showed that the mean flow profile downstream of the area expansion also has a significant effect on the acoustic losses. Note that the Kutta condition is imposed at the area expansion in each of these studies.

The aforementioned studies considered the behavior of acoustic waves propagating in the same direction as the mean flow at an area expansion. However, at the area discontinuity between the propellant injectors and the combustion chamber, the incident acoustic waves propagate in the opposite direction as the mean flow. Bodén, et al. [66] showed that the flow direction has a significant effect on the measured impedance of acoustic liners. Scarpato, et al. [67] investigated the reflection coefficient of a perforate backed by a cavity near its quarter-wave resonance with a bias flow in the opposite direction as the incident acoustic waves. Dupère and Dowling [68] modeled the case in which the acoustic waves propagate in the opposite direction as the mean flow at an area expansion, and they applied their model to predict the absorption coefficient of a half-wave resonator with bias flow.

Effect of Mean Flow on the End Correction

Davies [24, 69] showed experimentally that the end correction at the inlet of a pipe scales with the factor $(1 - M^2)$ at low to moderate Mach numbers. Davies [24] noted that the experimental evidence is inconclusive regarding the effect of flow on the end correction at the outlet of the pipe; some investigators, such as Peat [70], found that the Mach number has a negligible effect, whereas others, such as Ingard and Singhal [33], showed that the end correction at the outlet also scales with $(1 - M^2)$. Peters, et al. [22] measured the end correction at the outlet for very low Helmholtz numbers ($0 < ka < 0.06$) and found that the end correction is a function of the mean flow Strouhal number, which is defined as $St = ka/M$. At high Strouhal numbers (low Mach numbers), the end correction approaches the value derived by Levine and Schwinger [23] given in Eq. (2.5), but at low Strouhal numbers (higher Mach numbers), the limiting value is found to be $\Delta L = 0.19a$, which is close to the value predicted by Rienstra [50]. Cargill [49] stated that there is no simple expression for the end correction in the intermediate regime at which $St \sim 1$, which was confirmed experimentally by Peters, et al. [22]. Boij [63] showed using experimental results obtained by Ronneberger [71] and the numerical model developed by Boij and Nilsson [62] that the end correction at a sudden area expansion in a duct with mean flow is also a function of the Strouhal number. In the limiting cases of low or high Strouhal numbers, Boij [63] found that the end correction of the area expansion approaches that of an open pipe, but in the intermediate regime at which $St \sim 1$, there is a dip in the end correction below either of the limiting values, as shown in Figure 2.17.

2.3.5 Effect of High Temperature

The studies presented in the previous section were performed for unheated flows. In the studies presented in this section, the acoustic damping mechanisms in resonators and ducts were investigated at high temperatures.

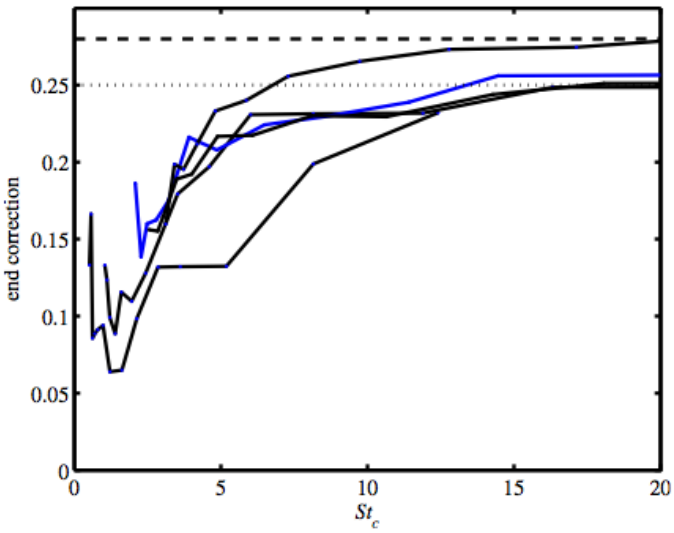

Figure 2.17: Normalized length correction as a function of mean flow Strouhal number at an area discontinuity in a circular duct based on experimental results from Ref. [71]. The solid lines represent different frequencies, and the dashed and dotted lines represent theoretical values for the no-flow low-frequency limit (Ref. [63]).

Effect of Temperature on the Acoustic Damping of Resonators

There is only one known study in the literature on the acoustic damping of propellant injectors that considers the effects of high temperatures. Kim, et al. [12] numerically analyzed the acoustic tuning of a propellant injector at a specific high-temperature condition that is realistic for a combustor. Furthermore, they calculated the change in the resonance frequency due to a non-uniform temperature distribution. However, the purpose of their study was not to identify the effect of temperature on the acoustic damping, so they did not vary the temperature or discuss the effect of temperature on the absorption coefficient.

Laudien, et al. [6] demonstrated that the physical damping mechanisms of an acoustic resonator do not qualitatively change with temperature, so acoustic tests at standard atmospheric conditions in a model combustion chamber are useful for predicting the acoustic damping of resonators in a combustion chamber under hot-fire conditions. However, Sohn and Cho [72] showed that spatial temperature variations in a combustion chamber affect the fine tuning of resonators for acoustic damping. A number of studies have also shown that steep temperature gradients exist within the acoustic resonators themselves under hot-fire

conditions [4–6]. Bies and Wilson [73] found that the absorption of very high amplitude acoustic waves causes the temperature in a Helmholtz resonator to increase, which affects its resonance frequency. Acker and Mitchell [17] showed that the mean temperature in a resonator can be used for acoustic tuning if the temperature gradient within the resonator is not too steep. However, they also found that quarter-wave resonators are sensitive to small changes in temperature, and their damping effectiveness decreases rapidly at off-design temperature conditions.

Effect of Temperature on the Attenuation in Ducts

Lahiri, et al. [74] measured the sound attenuation in a hard-walled duct and found that the attenuation increases with temperature, which could not be explained by the viscothermal losses at the wall of the duct alone. In duct acoustics, the viscothermal dissipation at the walls of the duct is typically much larger than the dissipation within the fluid itself, so the losses within the fluid are neglected [75]. However, Lahiri, et al. [41] analyzed the dissipation within the fluid itself, including the classical attenuation coefficient due to viscosity and thermal conductivity, attenuation due to rotational relaxation, and attenuation due to vibrational relaxation. They found that the attenuation due to vibrational relaxation increases significantly at high temperatures and pressures, so the acoustic losses within the fluid are non-negligible compared to the viscothermal dissipation at the walls of the duct at these conditions. For example, Figure 2.18 shows the shaded region in which the attenuation within the fluid is at least one-tenth of the attenuation at the walls of a duct with a 0.01 m radius for a water vapor concentration of 0.05% and no flow [41].

2.3.6 Effect of Amplitude

The studies presented in the previous sections were conducted at low acoustic amplitudes in the linear regime. In this section, the literature on the nonlinearities in propellant injectors, orifices, and other acoustic resonators at high amplitudes is reviewed. Experimental and

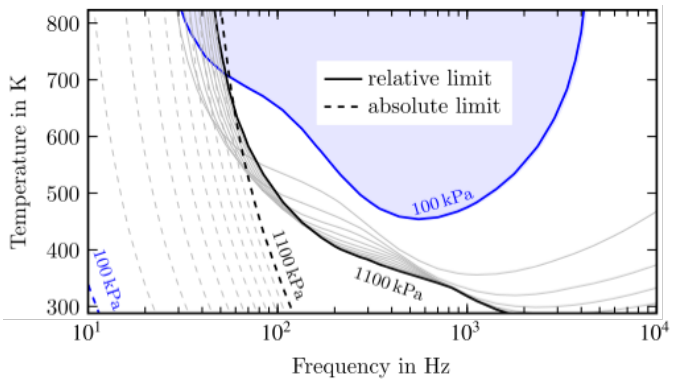

Figure 2.18: Temperature, pressure, and frequency conditions (shaded region) for which the attenuation within the fluid is at least one-tenth of the attenuation at the walls of a duct with a 0.01 m radius for a water vapor concentration of 0.05% and no flow (Ref. [41]).

numerical studies that attempted to elucidate the acoustic damping mechanisms at high amplitudes are also presented.

Nonlinearities in Propellant Injectors at High Amplitudes

The sound pressure level in a combustion chamber reaches extremely high amplitudes [1, 2], so nonlinearities can have a significant effect on the acoustic damping of a propellant injector. At low amplitudes, the linearized acoustic wave equation is valid, and properties such as the acoustic impedance and absorption coefficient are independent of amplitude. However, at higher amplitudes, the governing equations for acoustic propagation are nonlinear, and certain acoustic properties may vary with amplitude, which is called *nonlinearity*. In one of the few studies reported in the literature on the acoustic damping of half-wave resonators at high amplitude, Park and Sohn [16] showed using a numerical analysis that nonlinearities began to occur at sound pressure levels between 120 dB and 130 dB for their half-wave resonator configuration. However, they did not calculate the acoustic impedance or absorption coefficient of the resonator, and they did not confirm their nonlinear analysis experimentally.

Nonlinearities of an Orifice at High Amplitudes

Although there are few studies reported in the literature on the nonlinearities of propellant injectors or half-wave resonators, there are a number of studies on orifices, which are helpful for understanding the phenomena that produce nonlinearities in injectors. Sivian [76] first discovered that the acoustic resistance of an orifice at high amplitudes is a function of the fluctuating particle velocity in the orifice. Ingard and Labate [77] showed that vortices and jets are formed at an orifice at very high acoustic amplitudes, and they suggested that the increase in the acoustic resistance is caused by the conversion of acoustic energy into the kinetic energy of the jet and the rotational energy of the vortices. Ingard and Ising [54] measured the acoustic resistance and reactance of an orifice at high incident sound pressure levels in air. Thurston and Martin [78] and Thurston, et al. [79] performed flow visualization experiments and measured the acoustic resistance and reactance of an orifice at high particle velocities in a liquid. Panton and Goldman [80] collapsed the nonlinear acoustic resistance and reactance measured by these other investigators in terms of a reduced set of nondimensional parameters. Sturtevant [81] measured the reflection coefficients of orifices at amplitudes up to 190 dB using a test apparatus that could be considered a nonlinear impedance tube, and his results showed good agreement with those of Ingard and Ising [54]. Additional studies are summarized by Melling [82], who reviewed the literature that existed in 1973 on the nonlinearity of an orifice, and Gaeta and Ahuja [83], who provided a more recent review.

Nonlinearities of Helmholtz and Quarter-Wave Resonators at High Amplitudes

The nonlinearities of Helmholtz and quarter-wave resonators at high amplitudes have also been studied extensively. Bies and Wilson [73] and Ingard and Ising [54] measured the acoustic impedance of a Helmholtz resonator as a function of the sound pressure level, and Ingard and Ising [54] demonstrated that the absorption coefficient is a function of the sound pressure level at high amplitudes, as shown in Figure 2.19. Laudien, et al. [6] showed ex-

perimentally that the acoustic resistance and absorption frequency bandwidth of Helmholtz and quarter-wave resonators increase with sound pressure level at high amplitudes, which they attributed to acoustic energy losses due to the formation of vortices at the open end of the resonator. Figure 2.20 shows the ratio of the total resistance to the linear resistance as a function of sound pressure level for a Helmholtz and quarter-wave resonator.

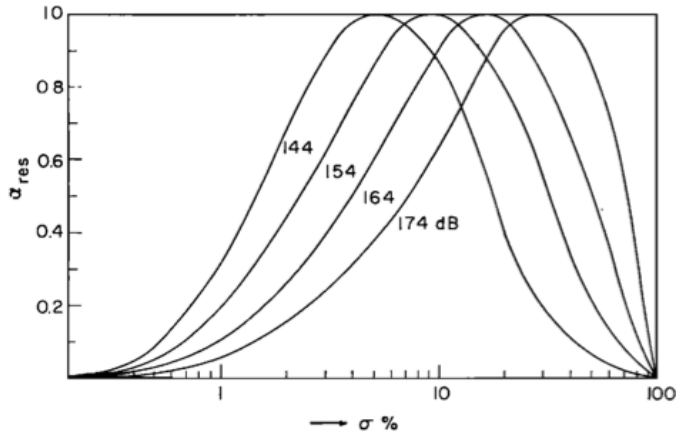

Figure 2.19: Absorption coefficient at resonance of a Helmholtz resonator array as a function of open area ratio at high amplitudes (Ref. [54]).

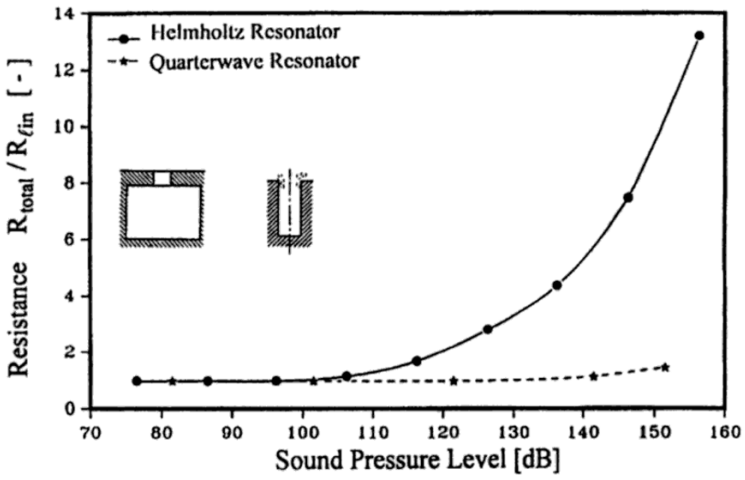

Figure 2.20: Nonlinear resistance of Helmholtz and quarter-wave resonators at high amplitudes (Ref. [6]).

Förner, et al. [84–86] also showed that the acoustic resistance and the absorption frequency bandwidth of quarter-wave resonators increase with sound pressure level at high amplitudes, but the peak absorption coefficient only increases until it is maximized at a cer-

tain amplitude; at even higher amplitudes, the peak absorption coefficient decreases with increasing amplitude. They classified these regimes as "normally damped," "optimally damped," and "overdamped" based on the behavior of the absorption coefficient.

Formation of Vortices at the Open End of a Tube at High Amplitudes

Numerous experimental and theoretical studies have been conducted on the behavior of the flow at the open end of a straight tube at high sound pressure levels. These studies are particularly relevant to the open ends of a half-wave resonator. Disselhorst and van Wijngaarden [87] captured schlieren photographs of the vortices at the open end of a tube at resonance, and they developed a model for the vortex formation and shedding process. Peters and Hirschberg [88] refined this model. Peters, et al. [22] measured the reflection coefficient of the open end of a tube at high amplitudes and confirmed the influence of vortex shedding on the sound power dissipation predicted by Disselhorst and van Wijngaarden [87], but they showed that amplitude has little effect on the end correction. Disselhorst and van Wijngaarden [87] and Peters, et al. [22] each proposed models for the nonlinear acoustic resistance that vary with the acoustic Strouhal number, $St_a = \omega a/|u|$. Their models are qualitatively similar but differ by a factor of approximately three.

Atig, et al. [89] measured the impedance of the open end of a cylindrical tube using the two-microphone method and showed that the acoustic resistance increases with sound pressure level. Skulina [90] used particle image velocimetry (PIV) to measure the flow field at the end of a cylindrical tube at high amplitudes, and he applied the theory of Howe [53] to calculate the sound power dissipated by the vortices. However, the dissipation that he calculated from the flow field was significantly lower than the dissipation determined by the corresponding acoustic measurements in the impedance tube. Macdonald, et al. [91] applied proper orthogonal decomposition (POD) to PIV measurements at the open end of a tube at high amplitudes. They analyzed the energy transfer between the first and second POD modes based on the results of Marx, et al. [92], who identified the first and second

POD modes as the nonlinear acoustic flow field and the vortex structures, respectively. Buick, et al. [93] investigated the nonlinear losses from the open end of a tube at high sound pressure levels using PIV, a two-dimensional lattice Boltzmann simulation, and an analytical model. Figure 2.21 shows their PIV measurements of the flow field at the open end of a tube with an incident sound pressure level of 170 dB. However, neither their PIV measurements, their lattice Boltzmann simulation, nor their analytical model accurately predicted the magnitude of the nonlinear acoustic losses. Therefore, there are additional loss terms that were not considered in their investigation.

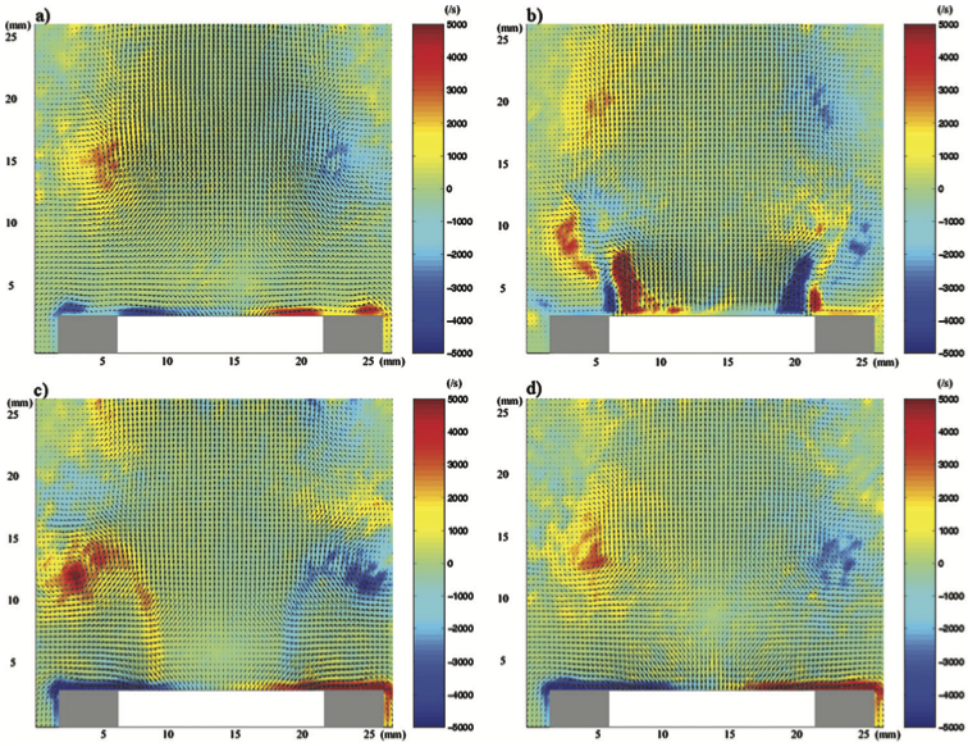

Figure 2.21: PIV measurements of the velocity (arrows) and vorticity (color) fields at the open end of a tube at 170 dB at (a) 0.0 T, (b) 0.3 T, (c) 0.6 T, and (d) 0.9 T (Ref. [93]).

Sound Power Dissipation Mechanisms at High Amplitudes

As discussed in Section 2.3.4, several investigators [42, 52, 53] showed that acoustic energy in a mean flow is converted into vortical energy due to flow separation at a sharp trailing edge. The flow separates to satisfy the unsteady Kutta condition, which represents

the mechanism for the sound power dissipation in a mean flow [51]. Even in the absence of a mean flow, sound power can be dissipated by the same mechanism if the acoustic velocity is high enough to cause flow separation [43, 94]. Experimental evidence for this statement was provided by Salikuddin and Ahuja [43], who measured the sound power dissipated by an orifice at high amplitudes and simultaneously captured flow visualization photographs that showed the formation of vortices at the orifice. Cummings and Eversman [94] and Cummings [95] developed a theory for the nonlinear losses, which matched the experiments reasonably well. Salikuddin and Brown [96] conducted additional experiments, which showed that both the sound power losses and the intensity of the vortices at the orifice increased with amplitude.

More recently, Tam, et al. [97] conducted a coordinated numerical and experimental investigation of the power dissipation mechanisms of an orifice at high acoustic amplitudes. They obtained good agreement between their numerical and experimental results, which showed that the nonlinear dissipation due to the conversion of acoustic energy into the kinetic energy of the vortices dominates the viscous dissipation at high amplitudes. However, measurements of the flow field at the open end of a tube have not been able to quantitatively account for the acoustic losses. Buick, et al. [93] measured the nonlinear dissipation due to vortex shedding from the open end of a tube at high amplitudes, but their PIV measurements significantly underestimated the acoustic losses. Sturtevant and Keller [98] also reported that the energy in the vortices shed from the open end of a tube at high amplitudes only accounted for approximately one-tenth of the acoustic losses in their experiments. These findings suggest that there are other mechanisms that contribute to the acoustic dissipation at high amplitudes.

Whereas orifices and Helmholtz resonators are typically short compared to the acoustic wavelength, quarter-wave and half-wave resonators have lengths of the same order of magnitude as the wavelength. Tang, et al. [99] found that the nonlinear acoustic dissipation mechanisms are dominant for Helmholtz resonators at high amplitudes, but the linear

viscous losses at the walls of quarter-wave resonators cannot be neglected, even at high amplitudes. Chester [100] showed that the dissipation mechanisms in a resonating open tube include the viscosity within the fluid, acoustic radiation at the open end, thermoviscous losses in the acoustic boundary layer at the wall of the tube, and nonlinear dissipation at high amplitudes due to the formation of vortices at the open end. According to Van Wijngaarden [101], the nonlinear dissipation due to vortex shedding dominates the acoustic radiation at the open end of a tube at high amplitudes. Ilinskii, et al. [102] showed that the boundary layer becomes turbulent if the acoustic velocity is sufficiently high, and this additional dissipation mechanism can be modeled using the eddy viscosity.

2.3.7 Effect of Higher-Order Modes

The studies presented in the previous sections were primarily conducted for the plane wave mode, or the effects of higher-order modes were not specifically discussed. In this section, the literature on the effects of higher-order modes on the acoustic damping of resonators is reviewed. Studies on analytical and experimental methods for calculating and measuring the propagation of higher-order modes are also presented.

Effect of Higher-Order Modes on the Acoustic Damping of Resonators

Shimizu, et al. [103] analyzed the acoustic damping of the longitudinal and circumferential modes of an open-ended cylindrical combustion chamber equipped with a single injector, but the injector was detuned to a non-resonant condition, so it did not function as a half-wave resonator. Nevertheless, they showed that the acoustic damping of the first circumferential mode due to acoustic radiation from the open end of the combustion chamber is significantly smaller than the damping of the first longitudinal mode. Experience has shown that the frequencies and mode shapes of combustion instabilities in existing rocket engines tend to correspond to circumferential modes within the combustion chamber [2], so the damping effectiveness of an injector depends on its position relative to the nodes

and antinodes of the higher-order acoustic modes [17, 18]. However, few studies have been conducted on the effect of higher-order modes on the acoustic damping of resonators. Sohn, et al. [9] acoustically tuned a propellant injector to the resonance frequency of the first circumferential mode in a model combustion chamber, but they simply adopted the resonance frequency as the tuning frequency and did not study the effects of the mode shape on the acoustic damping. Acker and Mitchell [17] found that the method for tuning quarter-wave resonators for any higher-order mode is qualitatively similar to the method for tuning resonators for the first circumferential mode.

Analytical Mode-Matching Methods for Higher-Order Modes

In 1944, Miles [104] proposed an analytical higher-order mode-matching method to calculate the reflection and transmission of sound at an area discontinuity in a circular duct, which describes the boundary between an acoustic resonator and the combustion chamber (or impedance tube). El-Sharkawy and Nayfeh [105] applied the higher-order mode-matching technique to predict the propagation of sound through an expansion chamber. An expansion chamber is comprised of smaller-diameter inlets and outlets that open into a larger-diameter chamber, which is the inverse problem compared to propellant injectors mounted between the combustion chamber and the upstream ducting (or between the two sides of a two-sided impedance tube). However, the methods developed for expansion chambers can be adapted to analyze the acoustic damping of propellant injectors for higher-order modes. Ih and Lee [106] and Åbom [107] calculated the scattering matrix, or four-pole parameters, of an expansion chamber using the mode-matching method, so the mode-matching method can be adapted to compute the higher-order scattering matrix of injectors. Eriksson [108] showed that specific higher-order modes in an expansion chamber are suppressed or excited based on the locations of the inlet and outlet relative to the nodes and antinodes of the mode shapes in the chamber, so higher-order modes in the combustion chamber are likely to be suppressed or excited based on the locations of the injectors.

Selamet and Ji [31, 109] applied the mode-matching method to analyze the acoustic performance of expansion chambers with offset inlets and outlets and Helmholtz resonators with offset necks, which excite different higher-order modes than concentric configurations. Selamet and Ji [31] also showed that the length correction at an area discontinuity in a duct varies with the offset distance between the duct centerlines.

Coupling of Higher-Order Modes Between the Injectors and Combustion Chamber

As discussed in Section 2.3.2, the addition of an acoustic resonator to a combustion chamber can cause the frequencies of the acoustic modes in the chamber to shift and new modes to appear. The frequencies and shapes of the resulting coupled modes—especially higher-order modes—depend on the location of the resonator. Oschwald, et al. [29] numerically calculated the frequencies and shapes of the acoustic modes in a combustion chamber of circular cross-section due to the addition of a quarter-wave resonator. In a circular chamber with no resonator, the first circumferential (1T) mode has two degenerate solutions with perpendicular nodal lines, as shown in Figure 2.22a. Because of the rotational symmetry, the nodal lines have no preferred orientation. However, when a quarter-wave resonator is added to the chamber, the rotational symmetry of the chamber is broken, and the first circumferential modes are no longer degenerate; instead, the first circumferential mode has a symmetric and an antisymmetric solution with respect to the resonator axis, as shown in Figure 2.22b. Oschwald, et al. [29] designated the symmetric and antisymmetric components of the first circumferential mode as 1Tσ and 1Tπ, respectively. The axis of symmetry of the 1Tσ mode is aligned with the resonator axis, but for the 1Tπ mode, its nodal line is aligned with the resonator axis. Because an acoustic damper is most effective when it is located at a pressure antinode [17], the damping effectiveness of the resonator is significantly reduced for the antisymmetric 1Tπ mode compared to the symmetric 1Tσ mode [18]. These results also apply to other higher-order circumferential modes, such as the 2T mode, but radial modes cannot have antisymmetric solutions [18].

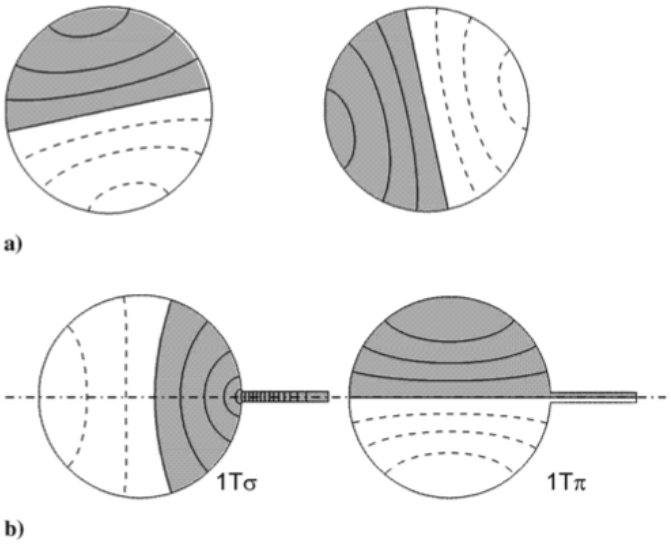

Figure 2.22: Mode shapes of (a) the two degenerate 1T modes of a circular chamber and (b) the 1Tσ and 1Tπ modes of a chamber coupled to a quarter-wave resonator (Ref. [29]).

Methods for Measuring Higher-Order Modes

The development of measurement techniques for the reflection and transmission of higher-order modes is a topic of ongoing research interest. Åbom [110] proposed a modal decomposition technique for measuring the higher-order mode reflection matrix using only wall-mounted microphones in a circular duct. Watson and Jones [111] developed an impedance eduction method for acoustic liners in the presence of higher-order modes in a rectangular duct. Schultz, et al. [112] measured the higher-order mode reflection matrix of an acoustic liner in a square duct, and Akoum and Ville [113] measured the higher-order mode reflection matrix of an area discontinuity at the open end of a circular duct. Sitel, et al. [114] measured the higher-order mode reflection and transmission matrices of a reactive silencer installed in a circular duct, and Sack, et al. [115] conducted similar measurements of an orifice plate in a circular duct. The methods developed in these studies are useful for measuring the acoustic damping of propellant injectors for higher-order modes.

2.4 Concluding Remarks

A review of the literature on the acoustic damping of propellant injectors was presented in the previous section. However, there are numerous gaps in the existing literature, so a complete understanding of the acoustic damping mechanisms of propellant injectors is currently lacking. For example, the acoustic damping of a propellant injector with realistic geometric features other than an inlet protrusion has not been measured experimentally. Although there are several studies on the effects of the position and distribution of the injectors on the injector faceplate, these studies reported contradictory results for the effect of position on the resonance frequency. Most importantly, there are no experimental results in the existing literature on the effects of bias flow, high temperatures, high amplitudes, and higher-order modes on the acoustic damping of propellant injectors or half-wave resonators. This work fills the aforementioned gaps in the existing literature and represents a considerable advancement in the state of the art.

CHAPTER 3
METHODOLOGY

3.1 Overview

In this chapter, the acoustic measurement methodology for the experiments conducted in this work is presented. The outline of this chapter is as follows: First, the use of an impedance tube to measure the acoustic damping of propellant injectors is discussed in Section 3.2. Next, the acoustic measurement methodology in a two-sided impedance tube is presented in its entirety, starting from the theory of higher-order mode propagation in circular ducts in Section 3.3 and theoretical models for the wavenumber in Section 3.4, from which the procedures for the modal decomposition and the determination of the acoustic scattering matrix are developed in Sections 3.5–3.6. The acoustic power quantities—namely, the power reflection, transmission, dissipation, and absorption coefficients—and the acoustic impedance are calculated from the scattering matrix in Sections 3.7–3.8. Finally, modifications to the methodology for a one-sided impedance tube and simplifications for the plane wave mode are presented in Sections 3.9–3.10. The methodology is based on contributions by a number of authors, but this is believed to be the first time that the complete methodology for measuring the scattering matrix and acoustic power quantities for higher-order modes has been presented in a single work.

3.2 The Impedance Tube as a Combustion Chamber

In this section, justifications are provided for using an impedance tube to measure the acoustic damping of propellant injectors and for quantifying the acoustic damping by the absorption coefficient. The arguments are initially presented for a classical impedance tube, in which acoustic drivers and microphones are mounted on one side of a test article; this is

followed by a brief description of a two-sided impedance tube and the rationale for using such an experimental setup.

3.2.1 Classical Impedance Tube

The key assumption for the experiments conducted in this work is that an impedance tube can be used to model the acoustics of a combustion chamber and accurately measure the acoustic damping of propellant injectors. In the combustion chamber of a rocket engine, as shown in Figure 3.1, the combustion process generates broadband noise, which propagates in all directions, including in the direction of the injector faceplate. Some fraction of the sound power incident on the injector faceplate is reflected back into the combustion chamber, while the remaining sound power is either transmitted upstream through the injectors or dissipated into heat. Broadband noise produced by acoustic drivers in a classical impedance tube, as shown in Figure 3.2, mimics combustion noise. One or more injectors are mounted to the end of the impedance tube opposite the acoustic drivers so that the termination of the impedance tube is made up of a portion of the injector faceplate. The broadband noise generated by the drivers propagates along the impedance tube, and some fraction of the sound power incident on the injectors is reflected back into the impedance tube, while the remaining sound power is either transmitted through the injectors or dissipated into heat.

Since combustion instabilities involve coupling between the combustion processes and the acoustic pressure oscillations within the combustion chamber, if the acoustic reflection from the injector faceplate is eliminated, then the feedback mechanism that leads to instability is broken, and the combustion instabilities can be eliminated [1]. Therefore, it is desirable to design the propellant injectors so that the sound power incident on the injector faceplate is not reflected back into the combustion chamber. Conservation of energy requires that the incident sound power be reflected, transmitted, or dissipated, which can be expressed as

$$\Pi_I = \Pi_R + \Pi_T + \Pi_D \tag{3.1}$$

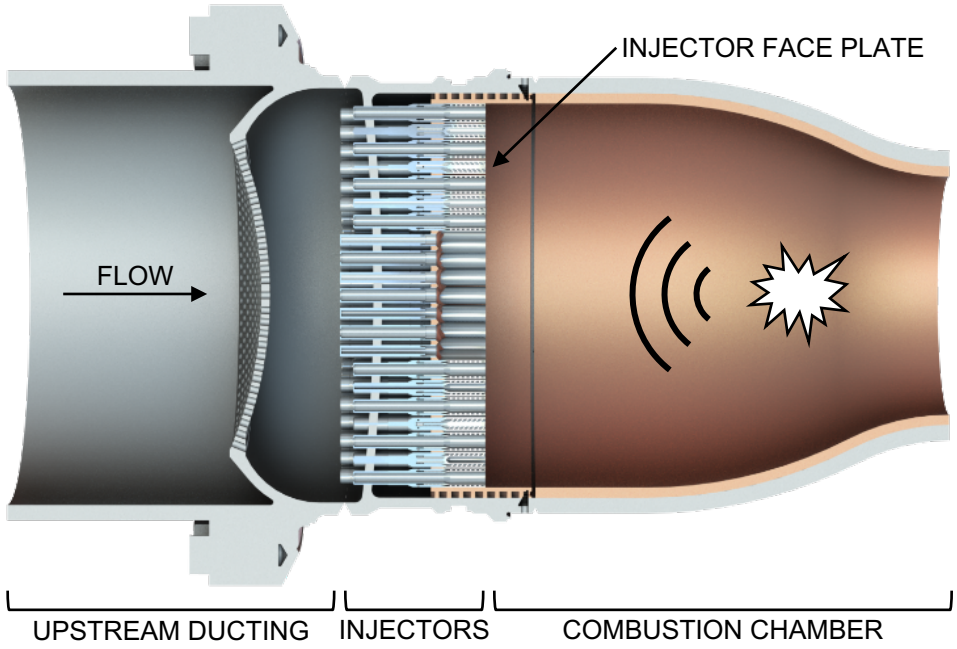

Figure 3.1: Cross-sectional view of a combustion chamber.

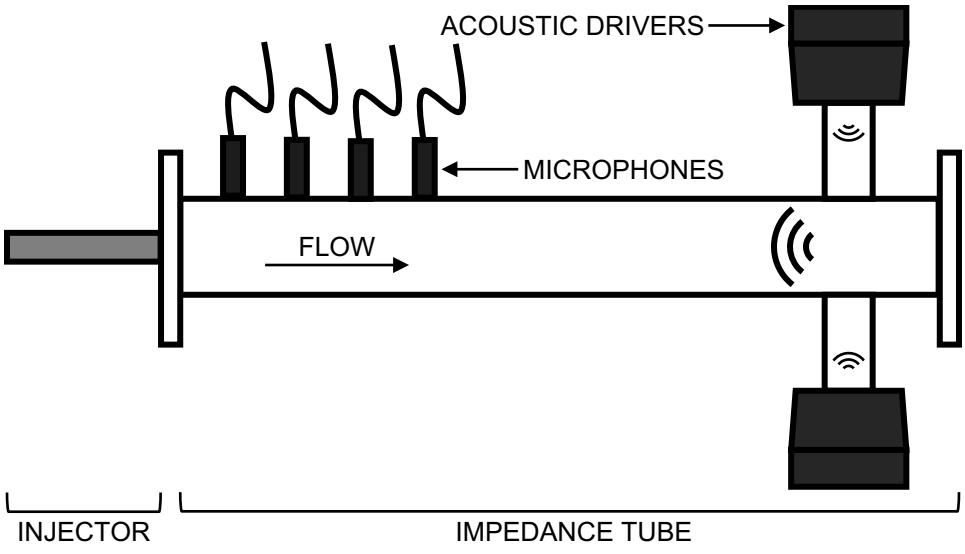

Figure 3.2: Schematic of an impedance tube.

where Π_I, Π_R, Π_T, and Π_D represent the sound power of the incident, reflected, transmitted, and dissipated acoustic waves, respectively. If the sound power incident on the injector faceplate is not reflected back into the combustion chamber, then it is instead transmitted through or dissipated by the injectors. Fundamentally, the injectors provide acoustic damping in this way by removing sound power from the combustion chamber. The acoustic damping of the injectors can be characterized by using an impedance tube to measure the fraction of sound power incident on the injectors that is not reflected. The parameter that quantifies this fraction is the absorption coefficient, which is defined as

$$A = \frac{\Pi_I - \Pi_R}{\Pi_I} \tag{3.2}$$

where Π_I is the sound power of the acoustic waves incident on a surface and Π_R is the sound power of the acoustic waves reflected from that surface. In this study, the surface is the plane at which the injectors are mounted to the impedance tube, so the absorption coefficient is a function of the injectors, their boundary conditions, and how they are mounted to the impedance tube. Previous studies have also adopted the absorption coefficient as a measure of the acoustic damping of resonators [6, 11, 19], and the absorption coefficient is often used in practice to design resonators to provide acoustic damping in a combustion chamber [1].

Substitution of the energy conservation expression in Eq. (3.1) into the absorption coefficient definition in Eq. (3.2) yields

$$A = \frac{\Pi_T + \Pi_D}{\Pi_I} \tag{3.3}$$

which shows that the absorption coefficient measures the fraction of the incident sound power that is both transmitted through and dissipated by the injectors. One may question whether it is appropriate to include transmission in the acoustic damping. For the purpose of preventing combustion instabilities, however, it is only important that as little as possible

of the incident sound power be reflected into the combustion chamber, so the method by which the incident sound power is removed from the combustion chamber is irrelevant. Therefore, it is argued that the absorption coefficient—which includes both transmission and dissipation—is the appropriate measure of the acoustic damping. For this reason, the terms "absorption coefficient," which is common in the acoustics literature, and "acoustic damping," which is common in the combustion literature, are used interchangeably in this work.

3.2.2 Two-Sided Impedance Tube

Although the absorption coefficient is appropriate for characterizing the acoustic damping of propellant injectors, measurements of the fraction of the incident sound power that is reflected from, transmitted through, and dissipated by the injectors are also required to elucidate the physical mechanisms responsible for the acoustic damping. The fraction of the incident sound power that is reflected from the injectors can be measured using a classical impedance tube, as shown in Figure 3.2. However, as suggested by Eq. (3.3), the transmitted and dissipated sound power cannot be separated using a classical impedance tube. Instead, the sound power of the acoustic waves transmitted through the injectors must be measured directly, and then the dissipated sound power can be calculated from Eq. (3.1). The following sections describe the acoustic measurement methodology for conducting experiments in a two-sided impedance tube, in which the fraction of the incident sound power that is reflected from, transmitted through, and dissipated by the injectors is measured in addition to the absorption coefficient.

3.3 Mode Propagation in Cylindrical Ducts

The acoustic measurement methodology for conducting experiments in a two-sided impedance tube is developed from the theory of higher-order mode propagation in ducts. The sound field in a duct of constant cross-section is the superposition of an infinite number of modes.

It is assumed that the fluid in the duct is ideal and inviscid, the flow in the duct is uniform, and the amplitude of the acoustic waves is small enough that linear acoustic theory is valid. The acoustic pressure at a single frequency, f, in a hard-walled straight duct of circular cross section is described by

$$p(r,\theta,z,t) = \Re[\hat{p}(r,\theta,z,f)e^{j\omega t}] \tag{3.4}$$

where $\Re$ represents the real part of a complex argument, and $\omega = 2\pi f$ is the angular frequency. The sound pressure amplitude, $\hat{p}$, is given by [116]

$$\hat{p}(r,\theta,z,f) = \sum_{m=-\infty}^{\infty}\sum_{n=0}^{\infty}\left[\hat{a}^{+}_{mn}(f)e^{-jk^{+}_{mn}z} + \hat{a}^{-}_{mn}(f)e^{jk^{-}_{mn}z}\right]\Psi_{mn}(r,\theta) \tag{3.5}$$

where r, θ, and z are the radial, azimuthal, and axial coordinates, respectively. The modes in a cylindrical duct are designated by the ordered pair (m,n), where $m \in (-\infty,+\infty)$ is the circumferential mode order, and $n \in [0,+\infty)$ is the radial mode order. The parameter $\hat{a}^{\pm}_{mn}$ is the complex pressure amplitude, $k^{\pm}_{mn}$ is the axial wavenumber, and Ψ_{mn} is the mode shape of mode (m,n), where the superscript "$+$" designates propagation in the positive axial direction, and the superscript "$-$" designates propagation in the negative axial direction. The hat symbol above a variable represents a complex amplitude in the frequency domain, which is obtained from the corresponding variable in the time domain using the Fourier transform.

Alternatively, Eq. (3.5) can be written as

$$\hat{p}(r,\theta,z,f) = \sum_{m=-\infty}^{\infty}\sum_{n=0}^{\infty}\left[\hat{p}^{+}_{mn}(z,f) + \hat{p}^{-}_{mn}(z,f)\right]\Psi_{mn}(r,\theta) \tag{3.6}$$

where

$$\hat{p}^{\pm}_{mn}(z,f) = \hat{a}^{\pm}_{mn}(f)e^{\mp k^{+}_{mn}z} \tag{3.7}$$

describes the amplitude of the forward- or rearward-propagating mode (m,n) at a single

frequency at any axial location in the duct. Note that $\hat{p}^{\pm}_{mn}(0,f) = \hat{a}^{\pm}_{mn}(f)$.

The mode shape function Ψ_{mn} in Eq. (3.5) describes the variation of the acoustic pressure across the cross-section of the duct. By definition, the pressure is uniform across the cross-section for the plane wave mode, but the pressure varies with the azimuthal and radial coordinates for higher-order modes [117]. The mode shapes in a duct with a circular cross-section are described by [118]

$$\Psi_{mn}(r,\theta) = C_{mn} J_m(\kappa_{mn} r) e^{-jm\theta} \tag{3.8}$$

where C_{mn} is a normalization factor, J_m is the Bessel function of the first kind of order m, and κ_{mn} is the eigenvalue of mode (m,n). The eigenvalues κ_{mn} are given by the roots of the equation [117]

$$J'_m(\kappa_{mn} a) = 0 \tag{3.9}$$

where J'_m is the first derivative of the Bessel function of the first kind of order m, and a is the radius of the duct. The normalization factor is defined such that

$$\frac{1}{S}\int_S \Psi_{mn}\Psi^*_{\mu\nu} dS = \begin{cases} 1, & (m,n) = (\mu,\nu) \\ 0, & (m,n) \neq (\mu,\nu) \end{cases} \tag{3.10}$$

where S is the cross-sectional area of the duct, and $*$ denotes the complex conjugate. An explicit expression for the normalization factor is derived in Appendix G, and the result is

$$C_{mn} = \left[\left(1 - \left(\frac{m}{\kappa_{mn} a}\right)^2\right) J_m^2(\kappa_{mn} a)\right]^{-1/2} \tag{3.11}$$

Figure 3.3 shows the mode shapes of a representative set of circumferential and radial modes. The shaded colors represent pressure amplitude, where red and blue designate opposite phase, and the black curves represent pressure nodes. The variation of the acoustic pressure with the azimuthal coordinate is governed by the exponential term $e^{-jm\theta}$ in

Eq. (3.8). The circumferential mode order, m, is equal to the number of nodal lines that pass through the center of the cross-section of the circular duct. Due to the exponential term, modes with positive m spin counterclockwise, and modes with negative m spin clockwise. These circumferential modes are the spinning modes originally described by Tyler and Sofrin [117]. The variation of the acoustic pressure with the radial coordinate is governed by the Bessel function $J_m(\kappa_{mn}r)$ in Eq. (3.8). The radial mode order, n, is equal to the number of concentric nodal circles within the cross-section of the circular duct.

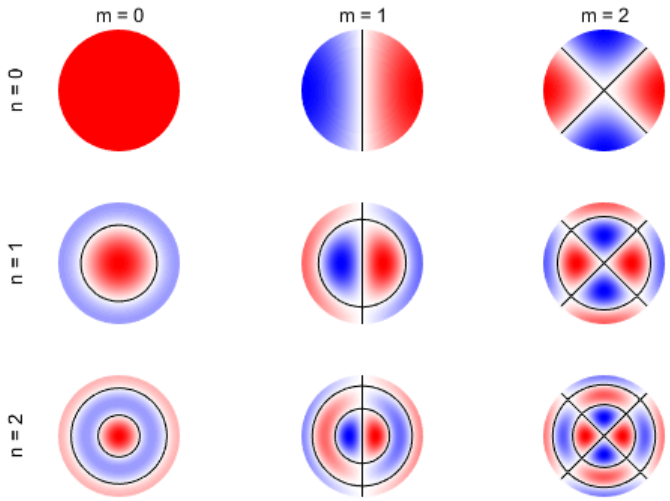

Figure 3.3: Mode shapes of several representative circular modes.

3.4 Wavenumber

The exponential functions $e^{\mp jk^{\pm}_{mn}z}$ in Eq. (3.5) describe the variation of the acoustic pressure along the axial coordinate of the duct. The axial wavenumber, $k^{\pm}_{mn}$, describes the spatial frequency of the acoustic waves of mode (m, n) propagating in the positive and negative axial directions in the duct. In the following subsections, three different models for the axial wavenumber are given: the non-dissipative wavenumber, which is the simplest model and is used to define the cut-on frequency; the Kirchhoff wavenumber, which incorporates the effects of viscothermal losses for the plane wave mode; and the Weng-Bake

wavenumber, which extends the Kirchhoff wavenumber to higher-order modes.

3.4.1 Non-Dissipative Wavenumber

The axial wavenumber of the (m, n) mode in the upstream and downstream directions as given by Morfey [116] is

$$k_{mn}^{\pm} = \frac{\omega}{c}\left(\frac{\alpha_{mn} \mp M}{1 - M^2}\right) \tag{3.12}$$

where c is the speed of sound, M is the Mach number of the flow in the duct, and

$$\alpha_{mn} = \sqrt{1 - (\kappa_{mn}c/\omega)^2(1 - M^2)} \tag{3.13}$$

In Eqs. (3.12)–(3.13), the Mach number is positive if the mean flow is in the positive axial direction and negative if the mean flow is in the negative axial direction. The axial wavenumber is real when the term inside the radical of Eq. (3.13) is greater than or equal to zero, which occurs at frequencies given by [116]

$$\omega \geq \kappa_{mn}c\sqrt{1 - M^2} \tag{3.14}$$

However, if the inequality in Eq. (3.14) is not satisfied, then the axial wavenumber is imaginary, and the pressure amplitude decays exponentially along the duct axis. In this case, the mode is evanescent, and it does not propagate acoustic energy along the duct [116]. The equality in Eq. (3.14) defines the cut-on frequency of the (m, n) mode. At frequencies higher than the cut-on frequency, the mode propagates energy along the duct axis [116]. Table 3.1 lists the eigenvalues and normalization factors of the first six cut-on modes in a cylindrical duct. Higher-order circumferential modes can spin in either the clockwise or counterclockwise direction, so the $(\pm 1, 0)$ modes are actually two degenerate modes with different spin directions. Note that $\kappa_{00} = 0$ for the plane wave mode, so according to Eq. (3.14), the plane wave mode propagates at all frequencies.

Table 3.1: Properties of the first six cut-on modes in a circular duct.

m	n	$\kappa_{mn}a$	C_{mn}
0	0	0	1
±1	0	1.8412	2.0468
±2	0	3.0542	2.7197
0	1	3.8317	2.4829

3.4.2 Kirchhoff Model

In general, the wavenumber can be complex, where the real part of the wavenumber governs the spatial fluctuations of the waveforms, and the imaginary part accounts for attenuation as the wave propagates. The wavenumber given by Eq. (3.12) is strictly real at frequencies satisfying the cut-on criterion of Eq. (3.14), so Eq. (3.12) predicts that a cut-on mode propagates along the duct with no attenuation; thus, Eq. (3.12) describes a non-dissipative wavenumber. In reality, viscous and thermal losses within the acoustic boundary layer at the walls of the duct cause the amplitude of a wave to decay as the mode propagates. Kirchhoff [119, 120] obtained a solution for the dissipative wavenumber of the plane wave mode propagating in a wide duct in the absence of flow. The wide duct assumption is valid if the width of the duct is much greater than the thickness of the acoustic boundary layer. Under these assumptions, the Kirchhoff wavenumber as given by Blackstock [27] is

$$k = \frac{\omega}{c}\left[1 + (1-j)\frac{1}{a}\sqrt{\frac{\mu}{2\rho\omega}}\left(1 + \frac{\gamma - 1}{\sqrt{Pr}}\right)\right] \tag{3.15}$$

where a is the radius of the duct, μ is the dynamic viscosity, γ is the ratio of specific heats, and Pr is the Prandtl number. The Kirchhoff wavenumber can also be written as

$$k = \frac{\omega}{c} + (1-j)\beta \tag{3.16}$$

where

$$\beta = \frac{1}{ac}\sqrt{\frac{\mu\omega}{2\rho}}\left(1 + \frac{\gamma - 1}{\sqrt{Pr}}\right) \tag{3.17}$$

is the attenuation coefficient due to the viscothermal losses in the acoustic boundary layer at the walls.

The viscothermal dissipation at the walls of the duct is typically much larger than the dissipation within the fluid itself, so the losses within the fluid are commonly neglected [75]. Therefore, the Kirchhoff wavenumber given by Eq. (3.15) is an excellent approximation for the attenuation of the plane wave mode in a wide duct in the absence of flow. Weng and Bake [121] suggested incorporating the convective effects of a uniform mean flow into the Kirchhoff wavenumber by

$$k^{\pm} = \frac{\omega/c}{1 \pm M} + \frac{(1 - j)\beta}{(1 \pm M)^{3/2}} \tag{3.18}$$

which agrees well with more exact theories for the attenuation of the plane wave mode in the presence of a uniform mean flow.

3.4.3 Weng-Bake Model

The Kirchhoff wavenumber models the acoustic dissipation due to viscothermal losses in the acoustic boundary layer for the plane wave mode, but not for higher-order modes. Beatty [122] was the first to extend the Kirchhoff model to the higher-order circumferential and radial modes in a circular duct, and Doak and Vaidya [75] derived the viscothermal attenuation more generally for ducts of arbitrary cross-section. More recently, Dokumaci [123] obtained a dispersion relation for the acoustic propagation of higher-order modes with viscothermal losses in a duct with mean flow, which Sack, et al. [115] used in their measurements of higher-order modes. However, Dokumaci's equation must be solved iteratively using a root-finding algorithm. Weng and Bake [121] derived an analytical solution for the viscothermal attenuation in a wide duct with a uniform mean flow, and they showed

that their model closely matches Dokumaci's model under these assumptions. The Weng-Bake wavenumber model can be written as [121]

$$k_{mn}^{\pm} = \frac{\omega}{c}\left(\frac{\alpha_{mn} \mp M}{1 - M^2}\right) + (1 - j)\beta_{mn}^{\pm} \tag{3.19}$$

where α_{mn} is defined in Eq. (3.13), and the attenuation coefficient, $\beta_{mn}^{\pm}$, is adapted from Ref. [121] as

$$\beta_{mn}^{\pm} = \pm\frac{1}{ac}\sqrt{\frac{\mu\omega}{2\rho}}\left[\frac{(\Gamma_{mn}^{\pm})^{3/2}\left(1 - \frac{(\kappa_{mn}a)^2 - m^2}{a^2(a\Gamma_{mn}^{\pm}\omega/c)^2} + \frac{\gamma - 1}{\sqrt{Pr}}\right)}{\alpha_{mn}\left(1 - \left(\frac{m}{\kappa_{mn}a}\right)^2\right)}\right] \tag{3.20}$$

where

$$\Gamma_{mn}^{\pm} = \left(\frac{1 \mp M\alpha_{mn}}{1 - M^2}\right) \tag{3.21}$$

Note that $\Gamma_{mn}^{\pm}$ is not the same as the nondimensional parameter Γ defined by Weng and Bake in Ref. [121].

Equation (3.19) reduces to Eq. (3.18) for the plane wave mode, which is the reason why Weng and Bake recommended Eq. (3.18) as the most accurate method of incorporating the convective effects of a uniform mean flow into the Kirchhoff model [121]. The Weng-Bake wavenumber model is therefore equivalent to the Kirchhoff wavenumber model for plane wave propagation.

3.5 Modal Decomposition

In the previous sections, the theory of higher-order mode propagation in circular ducts and theoretical models for the axial wavenumber were presented. The purpose of this section is to determine the modal amplitudes $\hat{a}_{mn}^{\pm}$ of the pressure field described by Eq. (3.5). Åbom [110] introduced a general modal decomposition method for higher-order modes based on transfer functions between microphones, which is an extension of the two-microphone

method [124]. There are other modal decomposition techniques discussed in the literature [113, 125], but the technique proposed by Åbom is well-suited for wall-mounted microphones. The following discussion in this section is adapted from Åbom [110].

At a given frequency, if there are N modes that satisfy the cut-on criterion of Eq. (3.14), then the pressure field described by Eq. (3.5) becomes a finite sum over N propagating modes. The purpose of the modal decomposition is to determine the $2N$ unknown modal amplitudes $\hat{a}^{+}_{mn}$ and $\hat{a}^{-}_{mn}$. If measurements of the pressure field are acquired at I independent spatial locations, then every term in Eq. (3.5) is known except the $2N$ modal amplitudes, and Eq. (3.5) is a system of I equations in $2N$ unknowns. The number of measurement locations must be greater than or equal to the number of unknown modal amplitudes in order to obtain a unique solution. If $I = 2N$, then there is an exact solution to the system of equations, and if $I > 2N$, then the system of equations is overdetermined and can be solved using a least-squares approximation. The system of equations can be written in matrix form as

$$\begin{bmatrix} \hat{p}_1 \\ \vdots \\ \hat{p}_i \end{bmatrix} = \begin{bmatrix} M^{+}_{1,00} & M^{-}_{1,00} & \dots & M^{+}_{1,mn} & M^{-}_{1,mn} \\ \vdots & \vdots & & \vdots & \vdots \\ M^{+}_{i,00} & M^{-}_{i,00} & \dots & M^{+}_{i,mn} & M^{-}_{i,mn} \end{bmatrix} \begin{bmatrix} \hat{a}^{+}_{00} \\ \hat{a}^{-}_{00} \\ \vdots \\ \hat{a}^{+}_{mn} \\ \hat{a}^{-}_{mn} \end{bmatrix} \tag{3.22}$$

where i designates the number of the spatial measurement location, and mn designates the circumferential and radial mode ordered pair. Therefore, $\hat{p}_i = \hat{p}(r_i, \theta_i, z_i, f)$ is the acoustic pressure measured at location i, $\hat{a}^{\pm}_{mn}$ are the modal amplitudes of the (m, n) mode propagating in the positive and negative z-directions, and the weights of the mode shapes at each measurement location are given by

$$M^{\pm}_{i,mn} = \Psi_{mn}(r_i, \theta_i) e^{\mp j k^{\pm}_{mn} z_i} \tag{3.23}$$

Equation (3.22) can also be written compactly as

$$\hat{\mathbf{p}} = \mathbf{M}\hat{\mathbf{a}} \tag{3.24}$$

where $\hat{\mathbf{p}}$ is an $I \times 1$ vector of the pressure measurements, $\mathbf{M}$ is an $I \times 2N$ matrix of the weighted mode shapes at the measurement locations, and $\hat{\mathbf{a}}$ is a $2N \times 1$ vector of the unknown modal amplitudes. The modal amplitudes in vector $\hat{\mathbf{a}}$ are arranged in order of increasing cut-on frequency.

The two-microphone method is based on the transfer function between two microphones [124]. Åbom [110] expressed the pressure vector in Eq. (3.24) in terms of the transfer functions between microphone pairs such that

$$\hat{\mathbf{p}} = \hat{p}_{\text{ref}}\mathbf{h} \tag{3.25}$$

where $\hat{p}_{\text{ref}}$ is the acoustic pressure amplitude measured at a reference microphone, and $\mathbf{h}$ is an $I \times 1$ vector of the transfer functions between the reference microphone and every other microphone. The transfer functions are defined by

$$H_{xy} = \frac{G_{xy}}{G_{xx}} \tag{3.26}$$

where G_{xx} is the auto-spectral density of the reference microphone, and G_{xy} is the cross-spectral density between the reference and another microphone. The modal amplitudes are then calculated by

$$\hat{\mathbf{a}} = \hat{p}_{\text{ref}}\mathbf{M}^{-1}\mathbf{h} \tag{3.27}$$

If the number of measurement locations is greater than the number of unknown modal amplitudes, then a least-squares approximation is used to obtain the modal amplitudes, and $\mathbf{M}^{-1}$ is replaced by the Moore-Penrose pseudoinverse [126], $\mathbf{M}^{+} = (\mathbf{M}^{H}\mathbf{M})^{-1}\mathbf{M}^{H}$, where the superscript H designates the complex conjugate (or Hermitian) transpose. This

is the well-known least-squares solution to an overdetermined system of equations [127].

3.6 Scattering Matrix

In the previous section, a general method was presented for decomposing the amplitudes of the modes propagating in a duct based on acoustic measurements. The purpose of this section is to determine the acoustic scattering matrix from measurements of the modal amplitudes in a two-sided impedance tube. Figure 3.4 depicts a two-sided duct with a test article mounted between the two sides. The test article is treated as a black box, so the coordinate system is defined such that the axial coordinates at the upstream and downstream boundaries of the element are $z = 0^-$ and $z = 0^+$, respectively. The coordinate system is oriented so that the mean flow through the duct is aligned with the positive z-direction. Thus, side A ($z < 0$) and side B ($z > 0$) are the upstream and downstream sides of the duct, respectively.

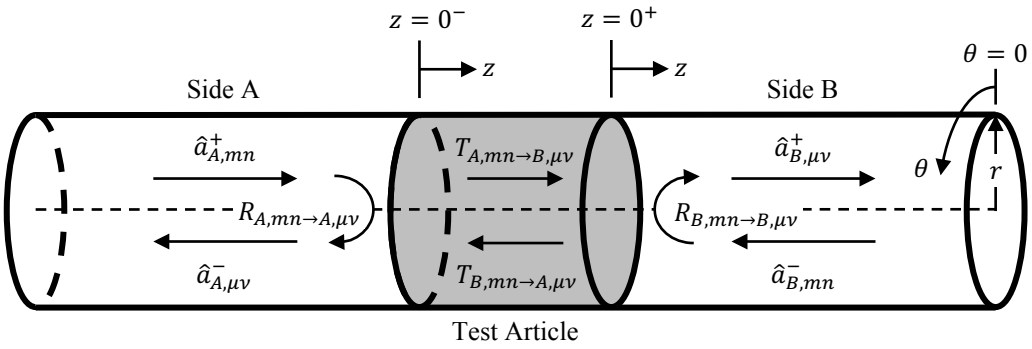

Figure 3.4: Acoustic reflection and transmission of modes across a test article in a duct.

The amplitudes of the modes propagating in the positive and negative axial directions and the acoustic pressure reflection and transmission coefficients across the test article are labeled in Figure 3.4. The acoustic scattering matrix completely describes the pressure reflection and transmission coefficients of the test article [24, 128]. If there are N propagating modes on each side of the duct that satisfy the cut-on criterion of Eq. (3.14), then

the scattering matrix of the test article shown in Figure 3.4 is defined by [114, 115, 128]

$$\begin{bmatrix} \hat{\mathbf{a}}_A^- \\ \hat{\mathbf{a}}_B^+ \end{bmatrix} = \begin{bmatrix} \mathbf{R}_{A\to A} & \mathbf{T}_{B\to A} \\ \mathbf{T}_{A\to B} & \mathbf{R}_{B\to B} \end{bmatrix} \begin{bmatrix} \hat{\mathbf{a}}_A^+ \\ \hat{\mathbf{a}}_B^- \end{bmatrix} \tag{3.28}$$

Each $\hat{\mathbf{a}}_X^{\pm}$ is an $N \times 1$ vector of the amplitudes of the modes propagating in the positive or negative axial direction on side X of the duct, where X represents either side A or side B. The vector on the left-hand side of Eq. (3.28) is comprised of the amplitudes of the outgoing modes propagating away from the test article, whereas the vector on the right-hand side of Eq. (3.28) is comprised of the amplitudes of the incoming modes propagating towards the test article. Therefore, Eq. (3.28) implies that the outgoing waves are caused by the reflection and transmission—the acoustic scattering—of the incoming waves through the scattering matrix. The scattering matrix is a block matrix comprised of four individual reflection or transmission matrices: $\mathbf{R}_{X\to X}$ is the $N \times N$ matrix of pressure reflection coefficients between modes on side X, and $\mathbf{T}_{X\to Y}$ is the $N \times N$ matrix of pressure transmission coefficients from modes on side X to modes on side Y.

If the only incoming waves are those on side A of the duct, then Eq. (3.28) reduces to $\mathbf{a}_A^- = \mathbf{R}_{A\to A}\mathbf{a}_A^+$ for the pressure reflection on side A, which can be expanded in terms of the individual modal amplitudes and reflection coefficients as

$$\begin{bmatrix} \hat{a}_{A,00}^- \\ \vdots \\ \hat{a}_{A,\mu\nu}^- \end{bmatrix} = \begin{bmatrix} R_{A,00\to A,00} & \cdots & R_{A,mn\to A,00} \\ \vdots & & \vdots \\ R_{A,00\to A,\mu\nu} & \cdots & R_{A,mn\to A,\mu\nu} \end{bmatrix} \begin{bmatrix} \hat{a}_{A,00}^+ \\ \vdots \\ \hat{a}_{A,mn}^+ \end{bmatrix} \tag{3.29}$$

Furthermore, if mode (m, n) on side A is the only incident mode, then the pressure reflection coefficient defined at $z = 0$ between the incident mode (m, n) and the reflected mode (μ, ν) on side A is

$$R_{A,mn\to A,\mu\nu} = \frac{\hat{a}_{A,\mu\nu}^-}{\hat{a}_{A,mn}^+} \tag{3.30}$$

Therefore, elements on the main diagonal of the pressure reflection matrix, for which $(m,n) = (\mu,\nu)$, represent the pure reflection of an incident mode into the same reflected mode, whereas off-diagonal elements, for which $(m,n) \neq (\mu,\nu)$, represent scattering from one incident mode into a different reflected mode [114, 115]. The pressure reflection matrix on side B of the duct is similarly defined.

If the only incoming waves are those on side A of the duct, then Eq. (3.28) reduces to $\mathbf{a}_B^+ = \mathbf{T}_{A\to B}\mathbf{a}_A^+$ for the pressure transmission from side A to side B, which can be expanded in terms of the individual modal amplitudes and transmission coefficients as

$$\begin{bmatrix} \hat{a}^+_{B,00} \\ \vdots \\ \hat{a}^+_{B,\mu\nu} \end{bmatrix} = \begin{bmatrix} T_{A,00\to B,00} & \dots & T_{A,mn\to B,00} \\ \vdots & & \vdots \\ T_{A,00\to B,\mu\nu} & \dots & T_{A,mn\to B,\mu\nu} \end{bmatrix} \begin{bmatrix} \hat{a}^+_{A,00} \\ \vdots \\ \hat{a}^+_{A,mn} \end{bmatrix} \tag{3.31}$$

Furthermore, if mode (m,n) on side A is the only incident mode, then the pressure transmission coefficient defined at $z = 0$ between the incident mode (m,n) on side A and the transmitted mode (μ,ν) on side B is

$$T_{A,mn\to B,\mu\nu} = \frac{\hat{a}^+_{B,\mu\nu}}{\hat{a}^+_{A,mn}} \tag{3.32}$$

Therefore, elements on the main diagonal of the pressure transmission matrix, for which $(m,n) = (\mu,\nu)$, represent pure transmission of a single mode, whereas off-diagonal elements, for which $(m,n) \neq (\mu,\nu)$, represent scattering from one incident mode into a different transmitted mode [114, 115]. The pressure transmission matrix from side B to side A of the duct is similarly defined.

Equation (3.28) can be written compactly as

$$\hat{\mathbf{a}}_{\text{out}} = \mathbf{S}\hat{\mathbf{a}}_{\text{in}} \tag{3.33}$$

where the modal amplitude vectors, $\hat{\mathbf{a}}_{\text{in}}$ and $\hat{\mathbf{a}}_{\text{out}}$, are $2N \times 1$ vectors, and the scattering ma-

trix, $\mathbf{S}$, is a $2N \times 2N$ matrix. Recall that N is the number of propagating modes that satisfy the cut-on criterion of Eq. (3.14). The subscripts "in" and "out" designate the incoming and outgoing waves, respectively. The modal amplitudes are known from the result of the modal decomposition method given by Eq. (3.27), but the elements of the scattering matrix in Eq. (3.33) are unknown. Therefore, Eq. (3.33) is a system of $2N$ equations in $(2N)^2$ unknowns.

Munjal and Doige [129] proposed a two-source method to obtain a sufficient number of known modal amplitudes to solve the system of equations described in Eq. (3.33) for plane wave propagation, and Åbom [128, 130] showed that the two-source method is superior to alternative methods. Sitel, et al. [114] extended the two-source method to a multiple-source method for higher-order modes. In the multiple-source method, Q distinct sound sources at independent spatial locations are used to excite Q unique acoustic pressure fields in the duct (with $Q/2$ sound sources, and hence $Q/2$ incident acoustic pressure fields, on each side of the test article). Each acoustic pressure field q is defined as the vector of incoming modal amplitudes $\hat{\mathbf{a}}^q_{\text{in}}$. Each linearly independent acoustic pressure field contributes $2N$ additional equations to the system described by Eq. (3.33), so at least $2N$ sound sources are required for the system to have a unique solution. If $Q = 2N$, then Eq. (3.33) is a system of $(2N)^2$ equations in $(2N)^2$ unknowns, and there is an exact solution to the system of equations. If $Q > 2N$, then the system of equations is overdetermined and can be solved using a least-squares approximation. The system of equations given by Eq. (3.33) becomes

$$\left[\hat{\mathbf{a}}^1_{\text{out}},\ \ldots,\ \hat{\mathbf{a}}^q_{\text{out}}\right] = \mathbf{S}\left[\hat{\mathbf{a}}^1_{\text{in}},\ \ldots,\ \hat{\mathbf{a}}^q_{\text{in}}\right] \tag{3.34}$$

where $\hat{\mathbf{a}}^q_{\text{in}}$ and $\hat{\mathbf{a}}^q_{\text{out}}$ are the incoming and outgoing modal amplitude vectors for the sound pressure field q. In matrix form, Eq. (3.34) can be written as

$$\hat{\mathbf{A}}_{\text{out}} = \mathbf{S}\hat{\mathbf{A}}_{\text{in}} \tag{3.35}$$

where $\hat{\mathbf{A}}_{\text{in}}$ and $\hat{\mathbf{A}}_{\text{out}}$ are $2N \times Q$ matrices. Finally, the scattering matrix is calculated by

$$\mathbf{S} = \hat{\mathbf{A}}_{\text{out}} \hat{\mathbf{A}}_{\text{in}}^{-1} \tag{3.36}$$

If the number of sound sources is greater than twice the number of propagating modes, then a least-squares approximation is used to obtain the scattering matrix, and $\hat{\mathbf{A}}_{\text{in}}^{-1}$ is replaced by the Moore-Penrose pseudoinverse [126, 127], $\hat{\mathbf{A}}_{\text{in}}^{+} = \hat{\mathbf{A}}_{\text{in}}^{H} (\hat{\mathbf{A}}_{\text{in}} \hat{\mathbf{A}}_{\text{in}}^{H})^{-1}$, where the superscript H represents the complex conjugate (or Hermitian) transpose. Overdetermination of the number of sound sources has been shown to reduce experimental errors [114, 130, 131]. Note that the scattering matrix solution in Eq. (3.36) depends only on the amplitudes of the incoming and outgoing modes, and is independent of the reflection from the upstream and downstream end terminations of the duct. Therefore, anechoic terminations are not required to obtain accurate measurements.

3.7 Acoustic Power Quantities

The acoustic scattering matrix given by Eq. (3.36) is the most complete description of the pressure reflection and transmission coefficients of a test article [24, 128]. However, the acoustic damping of the propellant injectors is quantified using the absorption coefficient, and the physical mechanisms responsible for the damping are elucidated using the power reflection, transmission, and dissipation coefficients. The fraction of the incident sound power that is reflected from, transmitted through, and dissipated by the test article in each direction can be determined from the scattering matrix. Using the definition of sound power proposed by Morfey [44], which conserves sound power in an isentropic, irrotational flow, the sound power of the upstream- and downstream-propagating waves of mode (m, n) is [116]

$$\Pi_{mn}^{\pm} = \frac{S}{2\rho c} |\hat{a}_{mn}^{\pm}|^2 \alpha_{mn} \left(\frac{1 - M^2}{1 \mp \alpha_{mn} M} \right)^2 \tag{3.37}$$

If mode (m, n) on side A of the duct is the only incoming mode, then the power reflec-

tion coefficient between the incident mode (m,n) and the reflected mode (μ,ν) on side A can be derived from Eqs. (3.30) and (3.37) as

$$R^{\Pi}_{A,mn\to A,\mu\nu} = \frac{\Pi^{-}_{A,\mu\nu}}{\Pi^{+}_{A,mn}} = |R_{A,mn\to A,\mu\nu}|^2 \frac{\alpha_{A,\mu\nu}}{\alpha_{A,mn}} \left(\frac{1-\alpha_{A,mn}M}{1+\alpha_{A,\mu\nu}M}\right)^2 \tag{3.38}$$

Similarly, the power reflection coefficient between the incident mode (m,n) and the reflected mode (μ,ν) on side B is

$$R^{\Pi}_{B,mn\to B,\mu\nu} = \frac{\Pi^{+}_{B,\mu\nu}}{\Pi^{-}_{B,mn}} = |R_{B,mn\to B,\mu\nu}|^2 \frac{\alpha_{B,\mu\nu}}{\alpha_{B,mn}} \left(\frac{1+\alpha_{B,mn}M}{1-\alpha_{B,\mu\nu}M}\right)^2 \tag{3.39}$$

The total power reflection coefficient between the incident mode (m,n) and all of the reflected modes on side A is given by

$$R^{\Pi}_{A,mn\to A} = \frac{\Pi^{-}_{A}}{\Pi^{+}_{A,mn}} = \sum_{\mu,\nu} R^{\Pi}_{A,mn\to A,\mu\nu} \tag{3.40}$$

where Π^{-}_{A} is the total outgoing sound power propagating in the negative axial direction on side A as a result of reflection from the incident mode (m,n). An expression similar to Eq. (3.40) can be derived for the total power reflection coefficient on side B.

If mode (m,n) on side A of the duct is the only incoming mode, then the power transmission coefficient between the incident mode (m,n) on side A and the transmitted mode (μ,ν) on side B of the duct can be derived from Eqs. (3.32) and (3.37) as

$$T^{\Pi}_{A,mn\to B,\mu\nu} = \frac{\Pi^{+}_{B,\mu\nu}}{\Pi^{+}_{A,mn}} = |T_{A,mn\to B,\mu\nu}|^2 \frac{\rho_A c_A}{\rho_B c_B} \frac{\alpha_{B,\mu\nu}}{\alpha_{A,mn}} \left[\frac{(1-M_B^2)\,(1-\alpha_{A,mn}M_A)}{(1-M_A^2)\,(1-\alpha_{B,\mu\nu}M_B)}\right]^2 \tag{3.41}$$

Similarly, the power transmission coefficient between the incident mode (m,n) on side B

and the transmitted mode (μ, ν) on side A is

$$T^{\Pi}_{B,mn\to A,\mu\nu} = \frac{\Pi^{-}_{A,\mu\nu}}{\Pi^{-}_{B,mn}} = |T_{B,mn\to A,\mu\nu}|^2 \frac{\rho_B c_B}{\rho_A c_A} \frac{\alpha_{A,\mu\nu}}{\alpha_{B,mn}} \left[\frac{(1-M_A^2)\,(1+\alpha_{B,mn}M_B)}{(1-M_B^2)\,(1+\alpha_{A,\mu\nu}M_A)} \right]^2 \tag{3.42}$$

In general, the density, speed of sound, and Mach number can vary between sides A and B. The total power transmission coefficient between the incident mode (m, n) on side A and all of the transmitted modes on side B is given by

$$T^{\Pi}_{A,mn\to B} = \frac{\Pi^{+}_{B}}{\Pi^{+}_{A,mn}} = \sum_{\mu,\nu} T^{\Pi}_{A,mn\to B,\mu\nu} \tag{3.43}$$

where Π^{+}_{B} is the total outgoing sound power propagating in the positive axial direction on side B as a result of transmission from the incident mode (m, n) on side A. An expression similar to Eq. (3.43) can be derived for the total power transmission coefficient from side B to side A.

The power dissipation coefficient is the fraction of the sound power in the incoming mode (m, n) that is neither reflected nor transmitted, but instead is dissipated into heat. Energy conservation requires that the sound power in the incoming wave be equal to the sum of the sound power that is reflected, transmitted, and dissipated, as expressed in Eq. (3.1). Therefore, the power dissipation coefficient for the incident mode (m, n) on side A of the duct is given by [74, 132]

$$D^{\Pi}_{A,mn} = 1 - R^{\Pi}_{A,mn\to A} - T^{\Pi}_{A,mn\to B} \tag{3.44}$$

and a similar expression can be derived for side B.

The absorption coefficient is defined as the fraction of the incoming sound power that is not reflected from the test article. However, it is a function of the duct and end termination downstream of the test article if measured using conventional methods [132]. The power reflection, transmission, and dissipation coefficients have the advantage that they are prop-

erties only of the test article, and not the downstream duct or end termination. In this work, the absorption coefficient is defined so that it, too, is only a property of the test article. Therefore, the absorption coefficient for the incident mode (m, n) on side A of the duct is given by

$$A_{A,mn} = \frac{\Pi^{+}_{A,mn} - \Pi^{-}_{A}}{\Pi^{+}_{A,mn}} = 1 - R^{\Pi}_{A,mn\to A} \tag{3.45}$$

and a similar expression can be derived for side B. Note that a superscript Π is not included in the notation because the absorption coefficient is understood to be a power quantity.

The absorption coefficient given by Eq. (3.45) is used to quantify the acoustic damping of the propellant injectors in this work. Additionally, the total power reflection coefficient given by Eq. (3.40), total power transmission coefficient given by Eq. (3.43), and the power dissipation coefficient given by Eq. (3.44) are particularly useful for elucidating the physical mechanisms responsible for the acoustic damping.

3.8 Impedance

Although the acoustic power quantities described in the previous section are used to quantify the acoustic damping of the propellant injectors and elucidate the acoustic damping mechanisms, the impedance is a useful parameter that is commonly reported in the literature. For example, the resonance frequency is defined as the frequency at which the imaginary part of the impedance is zero, and the real part of the impedance is useful for understanding the effects of many of the geometric parameters and operating conditions considered in this work. The normalized impedance is defined in Eq. (2.1) as the specific acoustic impedance normalized by the characteristic impedance of the medium, or

$$\zeta = \frac{\hat{p}/\hat{u}}{\rho c} \tag{3.46}$$

where $\hat{p}$ is the acoustic pressure amplitude given by Eq. (3.5), and $\hat{u}$ is the axial particle velocity amplitude of the acoustic oscillations. Under the same assumptions used in the

derivation of Eq. (3.5), the axial particle velocity at a single frequency, f, in a hard-walled straight duct of circular cross-section is given by

$$\hat{u}(r,\theta,z,f) = \sum_{m=-\infty}^{\infty}\sum_{n=0}^{\infty}\left[\hat{b}^{+}_{mn}(f)e^{-jk^{+}_{mn}z} - \hat{b}^{-}_{mn}(f)e^{jk^{-}_{mn}z}\right]\Psi_{mn}(r,\theta) \tag{3.47}$$

where $\hat{b}^{\pm}_{mn}$ is the complex axial particle velocity amplitude given by Morfey [116] as

$$\hat{b}^{\pm}_{mn} = \frac{\hat{a}^{\pm}_{mn}}{\rho c}\left(\frac{\alpha_{mn} \mp M}{1 \mp \alpha_{mn}M}\right) \tag{3.48}$$

The mode shape function Ψ_{mn} appears in the equations for both the acoustic pressure and the axial particle velocity, so the normalized impedance of a given mode (m,n) is independent of the position (r and θ) within the cross-section of the duct. The normalized impedance of the test article measured at $z = 0$ for mode (m,n) is

$$\zeta_{mn} = \frac{\hat{a}^{+}_{mn} + \hat{a}^{-}_{mn}}{\pm\rho c(\hat{b}^{+}_{mn} - \hat{b}^{-}_{mn})} \tag{3.49}$$

where the denominator is positive on side A of the duct and negative on side B such that the particle velocity is always defined in the direction of the test article.

In general, the relationship between the acoustic pressure and particle velocity of each mode can be described by a normalized impedance matrix, which is the inverse of the modal admittance matrix given by Åbom [110]. The normalized impedance matrix, $\mathbf{Z}$, is defined by the relation

$$(\hat{\mathbf{a}}^{+} + \hat{\mathbf{a}}^{-}) = \pm\rho c\mathbf{Z}(\hat{\mathbf{b}}^{+} - \hat{\mathbf{b}}^{-}) \tag{3.50}$$

If there are N propagating modes, then $\mathbf{Z}$ is an $N \times N$ matrix, each $\hat{\mathbf{a}}^{\pm}$ is an $N \times 1$ vector of the pressure amplitudes, and each $\hat{\mathbf{b}}^{\pm}$ is an $N \times 1$ vector of the axial particle velocity amplitudes of the modes propagating in the positive or negative direction. The right-hand side of Eq. (3.50) is positive on side A of the duct and negative on side B so that the particle velocity is defined in the direction of the test article. The normalized impedance matrix on

side A of the duct can be derived from the relationship between the pressure amplitude and axial particle velocity amplitude given by Eq. (3.48) as

$$\mathbf{Z}_A = (\mathbf{I} + \mathbf{R}_{A\to A})(\mathbf{Z}^+ - \mathbf{Z}^-\mathbf{R}_{A\to A})^{-1} \tag{3.51}$$

and the normalized impedance matrix on side B can be derived as

$$\mathbf{Z}_B = (\mathbf{I} + \mathbf{R}_{B\to B})(\mathbf{Z}^- - \mathbf{Z}^+\mathbf{R}_{B\to B})^{-1} \tag{3.52}$$

where each $\mathbf{Z}^{\pm}$ term is an $N \times N$ diagonal matrix given by

$$\mathbf{Z}^{\pm} = \text{diag}\left(\frac{\alpha_{mn} \mp M}{1 \mp \alpha_{mn} M}\right) \tag{3.53}$$

Thus, the normalized impedance of the modes on both sides of the test article can be determined directly from the pressure reflection matrices.

3.9 Modifications to the Methodology for a One-Sided Impedance Tube

In a classical impedance tube, as shown in Figure 3.2, acoustic measurements are conducted on only one side of the test article, so the full scattering matrix cannot be determined, and some modifications to the methodology are warranted. It is assumed that the flow is in the positive z-direction, so the one-sided impedance tube shown in Figure 3.2 corresponds to side B of the two-sided impedance tube shown in Figure 3.4. The modal decomposition described in Section 3.5 still applies to a one-sided impedance tube, so the modal amplitudes of the incident and reflected acoustic waves are still given by Eq. (3.27). However, the only part of the scattering matrix equation given in Eq. (3.28) that is applicable to the one-sided impedance tube is $\hat{\mathbf{a}}_B^+ = \mathbf{R}_{B\to B}\hat{\mathbf{a}}_B^-$, which can be expanded in terms of the individual reflection coefficients as in Eq. (3.29). Since there is only one side to the duct, the

subscript B can be dropped, and reflection matrix equation can be written as

$$\hat{\mathbf{a}}_R = \mathbf{R}\hat{\mathbf{a}}_I \tag{3.54}$$

If there are N propagating modes, then $\hat{\mathbf{a}}_I$ and $\hat{\mathbf{a}}_R$ are the $N \times 1$ modal amplitude vectors of the incident and reflected acoustic waves, respectively, and $\mathbf{R}$ is the $N \times N$ reflection matrix. The modal amplitudes are known from the result of the modal decomposition given by Eq. (3.27), but the elements of the reflection matrix in Eq. (3.54) are unknown, so Eq. (3.54) is a system of N equations in N^2 unknowns. Based on the discussion in Section 3.6, if there are Q distinct sound sources at independent spatial locations that are used to excite Q independent acoustic pressure fields, then a unique solution to the system of equations can be obtained if $Q \geq N$. The reflection matrix is calculated following the same steps as Eqs. (3.34)–(3.36), which yields

$$\mathbf{R} = \hat{\mathbf{A}}_R \hat{\mathbf{A}}_I^{-1} \tag{3.55}$$

where $\hat{\mathbf{A}}_I$ and $\hat{\mathbf{A}}_R$ are $N \times Q$ matrices of the incident and reflected modal amplitudes, respectively, of the Q acoustic pressure fields. If the number of sources is greater than the number of propagating modes, then a least-squares approximation is used to obtain the reflection matrix, and $\hat{\mathbf{A}}_I^{-1}$ is replaced by the Moore-Penrose pseudoinverse [126, 127].

For a one-sided impedance tube, the power reflection coefficient between the incident mode (m, n) and the reflected mode (μ, ν) is calculated using Eq. (3.38). Likewise, the total power reflection coefficient for the incident mode (m, n) is calculated using Eq. (3.40). However, neither the transmission nor dissipation coefficients can be measured using a one-sided impedance tube. The expression for the absorption coefficient given in Eq. (3.45) is still valid in a one-sided impedance tube, but the measured absorption coefficient is a function of the end termination and boundary conditions downstream of the measurement surface. The modifications to the methodology described in this section are used for the

experiments in the one-sided impedance tubes.

3.10 Simplifications to the Methodology for Plane Waves

At frequencies below the cut-on frequency of the first higher-order mode in the impedance tube, only the plane wave mode propagates, and many of the expressions presented in Sections 3.3–3.8 can be simplified. Although these simplifications are not strictly necessary since the acoustic measurement methodology is a general method for all modes, including the plane wave mode, the simplified expressions remove the complications introduced by higher-order modes and aid in the physical understanding of the acoustic measurements. For the plane wave mode, the mode shape function defined in Eq. (3.8) is no longer a function of the position (r and θ) within the cross-section of the duct and reduces to $\Psi_{mn} = 1$. Similarly, the wavenumber parameter defined in Eq. (3.13) reduces to $\alpha_{mn} = 1$. The Kirchhoff wavenumber model given by Eq. (3.18) is appropriate for plane waves. Additionally, the scattering matrix defined in Eq. (3.28) becomes a 2×2 matrix, and the pressure reflection and transmission coefficients are scalars.

The acoustic power quantities defined in Section 3.7 can be greatly simplified for the plane wave mode. The sound power given by Eq. (3.37) reduces to

$$\Pi_{00}^{\pm} = \frac{S}{2\rho c}|\hat{a}^{\pm}|^2(1 \pm M)^2 \tag{3.56}$$

for the plane wave mode. The expressions for the sound power reflection and transmission coefficients can also be simplified for the plane wave mode. The sound power reflection coefficient on side A of the duct becomes

$$R_{A\to A}^{\Pi} = |r_{A\to A}|^2 \left(\frac{1-M}{1+M}\right)^2 \tag{3.57}$$

and the sound power reflection coefficient on side B becomes

$$R^{\Pi}_{B\to B} = |r_{B\to B}|^2 \left(\frac{1+M}{1-M}\right)^2 \tag{3.58}$$

for the plane wave mode. Thus, the power reflection coefficient for the plane wave mode only depends on the pressure reflection coefficient and the Mach number. Likewise, the sound power transmission coefficient from side A to side B of the duct becomes

$$T^{\Pi}_{A\to B} = |t_{A\to B}|^2 \frac{\rho_A c_A}{\rho_B c_B} \left(\frac{1+M_B}{1+M_A}\right)^2 \tag{3.59}$$

and the sound power transmission coefficient from side B to side A becomes

$$T^{\Pi}_{B\to A} = |t_{B\to A}|^2 \frac{\rho_B c_B}{\rho_A c_A} \left(\frac{1-M_A}{1-M_B}\right)^2 \tag{3.60}$$

for the plane wave mode, where the density, speed of sound, and Mach number can vary between sides A and B. There is no need to separately define the total power reflection and transmission coefficients since the plane wave mode is the only propagating mode. Finally, the dissipation and absorption coefficients for the plane wave mode are given by Eqs. (3.44) and (3.45), respectively.

The normalized impedance matrix defined in Section 3.8 is a scalar for the plane wave mode, and Eqs. (3.51)–(3.52) can be expressed in terms of the reflection coefficient as

$$\zeta_X = \frac{1+R_{X\to X}}{1-R_{X\to X}} \tag{3.61}$$

where the subscript X signifies either side A or B of the duct.

The simplified expressions developed in this section aid in the physical understanding of the parameters that affect the acoustic power quantities and the impedance by removing the complications introduced by higher-order modes. These expressions have useful

applications that will be discussed in future chapters.

3.11 Summary

The acoustic measurement methodology for the experiments conducted in this work was presented in this chapter. The key assumption in the experiments is that an impedance tube can be used to measure the acoustic damping of propellant injectors. The acoustic measurement methodology in a two-sided impedance tube was presented in its entirety, starting from the theory of higher-order mode propagation in circular ducts and theoretical models for the wavenumber, from which the procedures for the modal decomposition and the determination of the acoustic scattering matrix were developed. The acoustic power quantities—namely, the power reflection, transmission, dissipation, and absorption coefficients—and the acoustic impedance were calculated from the scattering matrix. Finally, modifications to the methodology for a one-sided impedance tube and simplifications for the plane wave mode were presented. The methodology presented in this chapter was based on contributions by a number of authors, but this is believed to be the first time that the complete methodology for measuring the scattering matrix and acoustic power quantities for higher-order modes has been presented in a single work.

CHAPTER 4
EXPERIMENTAL SETUP

4.1 Overview

In this chapter, the experimental facilities and procedures used in this work are presented. The outline of this chapter is as follows: First, the one-sided impedance tubes used to measure the absorption coefficient of propellant injectors at different open area ratios are discussed in Section 4.2. Next, a detailed description of the design and operation of the Heated, Optimized Tube for Multimodal Evaluation of Sound Scattering (HOTMESS) is provided in Section 4.3. HOTMESS was developed as part of this work to measure the acoustic scattering matrix—and hence the acoustic power quantities—of a test article under mean flow, high temperature, high amplitude, and higher-order mode propagation conditions. The procedure for conducting particle image velocimetry (PIV) measurements is presented in Section 4.4 following the description of HOTMESS. Finally, the propellant injector test articles used in this work are described in Section 4.5.

4.2 One-Sided Experimental Facilities

Two different one-sided experimental facilities—or classical impedance tubes—are used in this work to measure the absorption coefficient of propellant injectors. Figure 4.1 shows the two impedance tubes instrumented with microphones and acoustic drivers and with a single injector mounted to the end of each tube. The smaller impedance tube, which has an inner diameter of 28.5 mm, has one acoustic driver attached to the end of the tube and two microphones mounted flush with the inner wall of the tube at two different axial locations. The larger impedance tube, which has an inner diameter of 101.6 mm, has four acoustic drivers distributed circumferentially around the tube and four microphones

mounted flush with the inner wall of the tube at four uniformly spaced axial locations. These two impedance tubes of different diameters are selected so that the same propellant injectors can be measured at two different open area ratios.

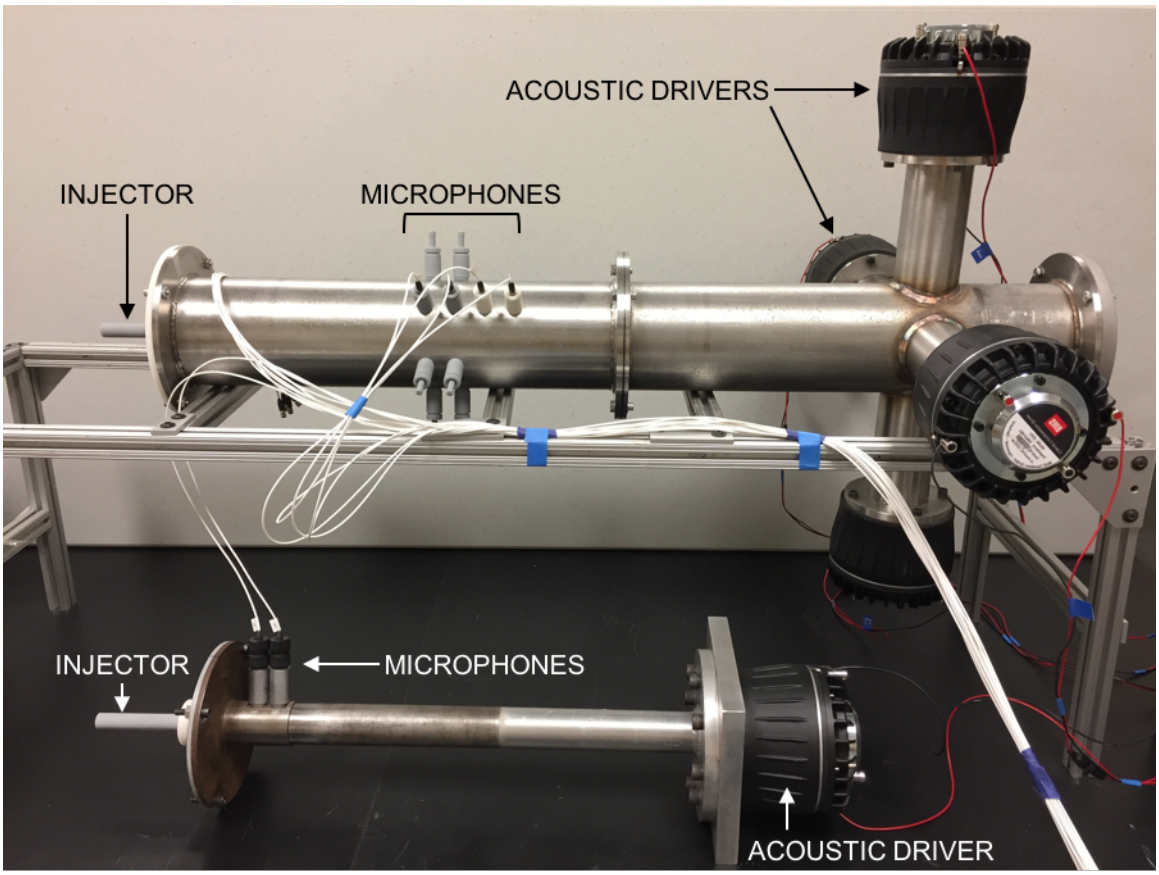

Figure 4.1: 101.6-mm diameter (top) and 28.5-mm diameter (bottom) one-sided impedance tubes.

The data acquisition and post-processing are performed using LabVIEW and MATLAB, respectively. The source signals are generated using LabVIEW and are converted to analog voltage signals using an NI-9263 output module. The voltage signals are amplified by dual-channel Behringer Europower EP2000 power amplifiers, and the amplified signals drive BMS 4592ND compression drivers. The BMS 4592ND driver has both a midrange and a high-frequency diaphragm, but only the midrange diaphragm is used because its operating frequency range is sufficient for the experiments in this work. For broadband testing, the acoustic drivers are driven with high-pass filtered Gaussian noise so that all frequencies

of interest can be tested simultaneously. The high-pass filter has a cut-off frequency of 500 Hz. For high-amplitude testing, the acoustic drivers are driven with single-frequency sinusoidal tones, so each frequency of interest must be tested individually. The time histories of the acoustic pressures are measured by PCB 378A14 microphones and are read to LabVIEW using an NI-9234 input module. These time histories are exported from LabVIEW to a file. Custom MATLAB software is used to read the raw data file, perform the post-processing based on the methodology described in Section 3.9, and analyze and plot the acoustic results.

4.3 Two-Sided Experimental Facility

4.3.1 Overview of the Experimental Facility

A new experimental facility called the Heated, Optimized Tube for Multimodal Evaluation of Sound Scattering (HOTMESS) was developed to measure the acoustic scattering matrix of a test article under mean flow, high temperature, high amplitude, and higher-order mode propagation conditions. There are several other experimental facilities described in the literature that are capable of measuring the properties of a test article under some combination of these conditions. For example, measurements of the performance of acoustic liners under mean flow, high temperature, and high amplitude conditions have been conducted in the Hot Acoustic Test rig at DLR in Germany [74, 133], the hot stream acoustic liner testing facility at NLR in the Netherlands [134], and an impedance tube with hot air blowers at KTH in Sweden [135]. However, acoustic measurements in these three facilities are limited to plane waves. Measurements of the performance of acoustic liners for higher-order mode propagation conditions have been conducted in the rectangular Curved Duct Test Rig at the NASA Langley Research Center in the USA [136, 137] and facilities with circular cross-sections at the University of Compiegne in France [138] and KTH in Sweden [115]. Although the Curved Duct Test Rig and the KTH facility can produce mean flows and high amplitudes, none of these three facilities are capable of conducting measurements at high

temperatures. Therefore, HOTMESS is currently the only known experimental facility in the world that is capable of measuring the acoustic scattering matrix—and hence the power reflection, transmission, and dissipation—of a test article under all of the conditions of mean flow, high temperature, high amplitude, and higher-order mode propagation.

A top-view drawing of HOTMESS is shown in Figure 4.2. The experimental facility is comprised of several main components: a heater duct, a 90° bend and flow-straightening pipe, four upstream source sections, an upstream measurement section, the test article, a downstream measurement section, and four downstream source sections. The upstream and downstream source and measurement sections act like a two-sided impedance tube with a circular cross-section that is capable of measuring the acoustic scattering matrix of a test article. The purpose of the heater duct and the 90° bend and flow-straightening pipe is to deliver clean heated flow to the two-sided impedance tube. Because of the wide variety of possible experiments that could be conducted using HOTMESS, the facility is designed to be modular. The source sections, measurement sections, and test article are individual pieces, which are interconnected using flanges with twelve screw holes equally spaced at 30° intervals and a one-way male-to-female alignment system, as shown in Figure 4.3. The male-to-female alignment system prevents steps and gaps between adjacent sections, which reduces the risk of acoustic reflections and leaks. A photograph of the entire HOTMESS experimental facility is shown in Figure 4.4.

The total length of the two-sided impedance tube, which is made up of the upstream and downstream source and measurement sections, is roughly 3.35 m (11 ft) excluding the test article, which can change in length depending on the experiment. The impedance tube has an inner diameter of 101.6 mm (4 in) and a wall thickness of 6.35 mm (0.25 in). Each of the components of HOTMESS is constructed using type 304 stainless steel, which has a high melting point and good resistance to corrosion. The exterior of the heater duct is covered with thick insulating material, and the circular pipe sections are each insulated with two or three layers of Fiberfrax® ceramic fiber blankets to reduce the heat loss along

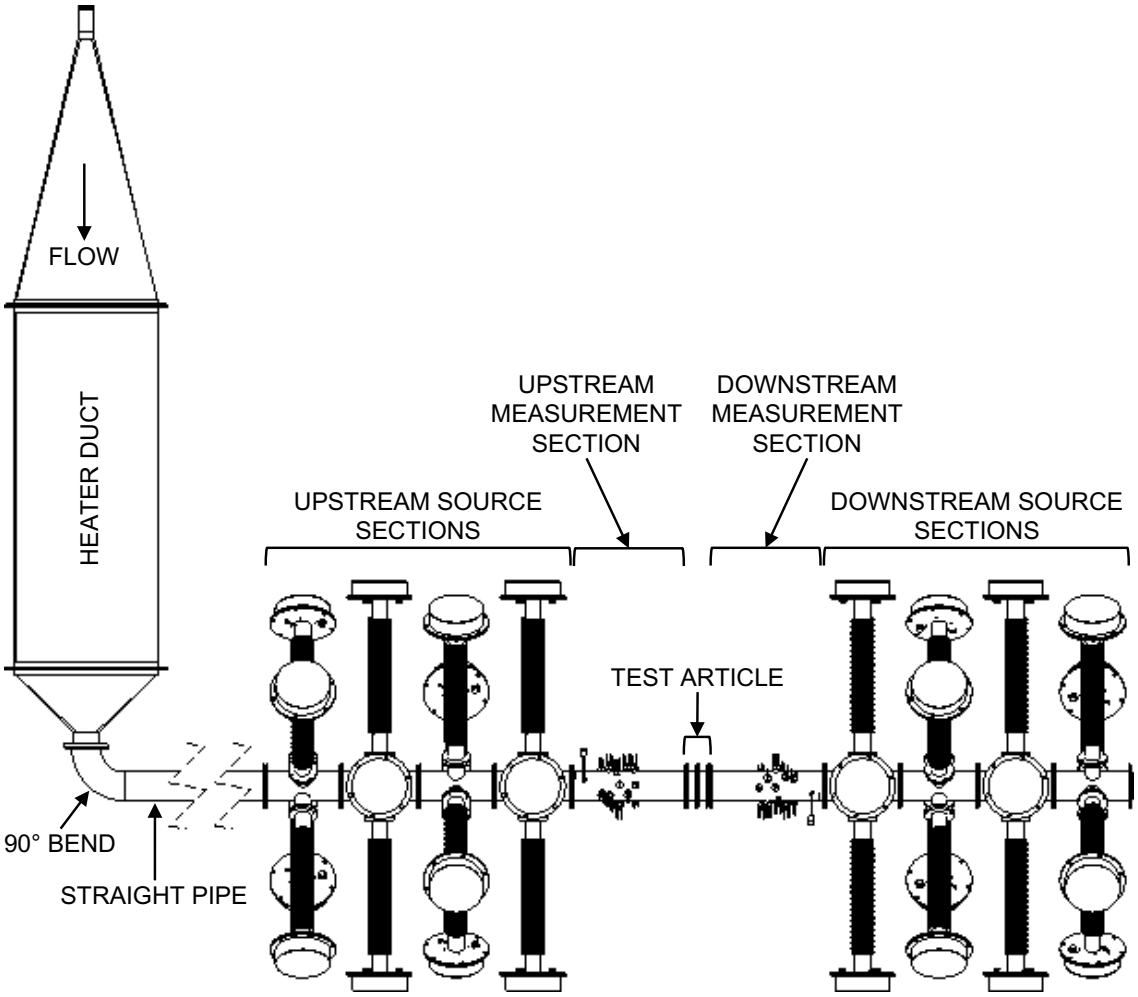

Figure 4.2: Top-view drawing of HOTMESS.

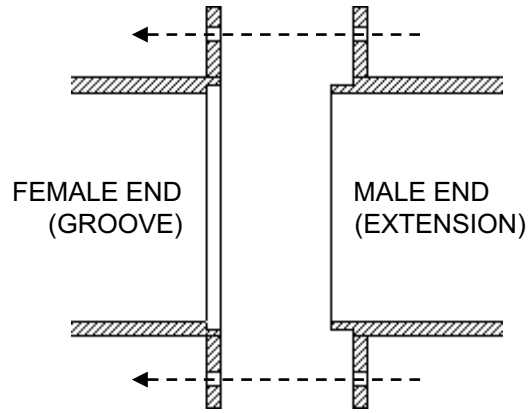

Figure 4.3: Male-to-female alignment system between adjacent sections.

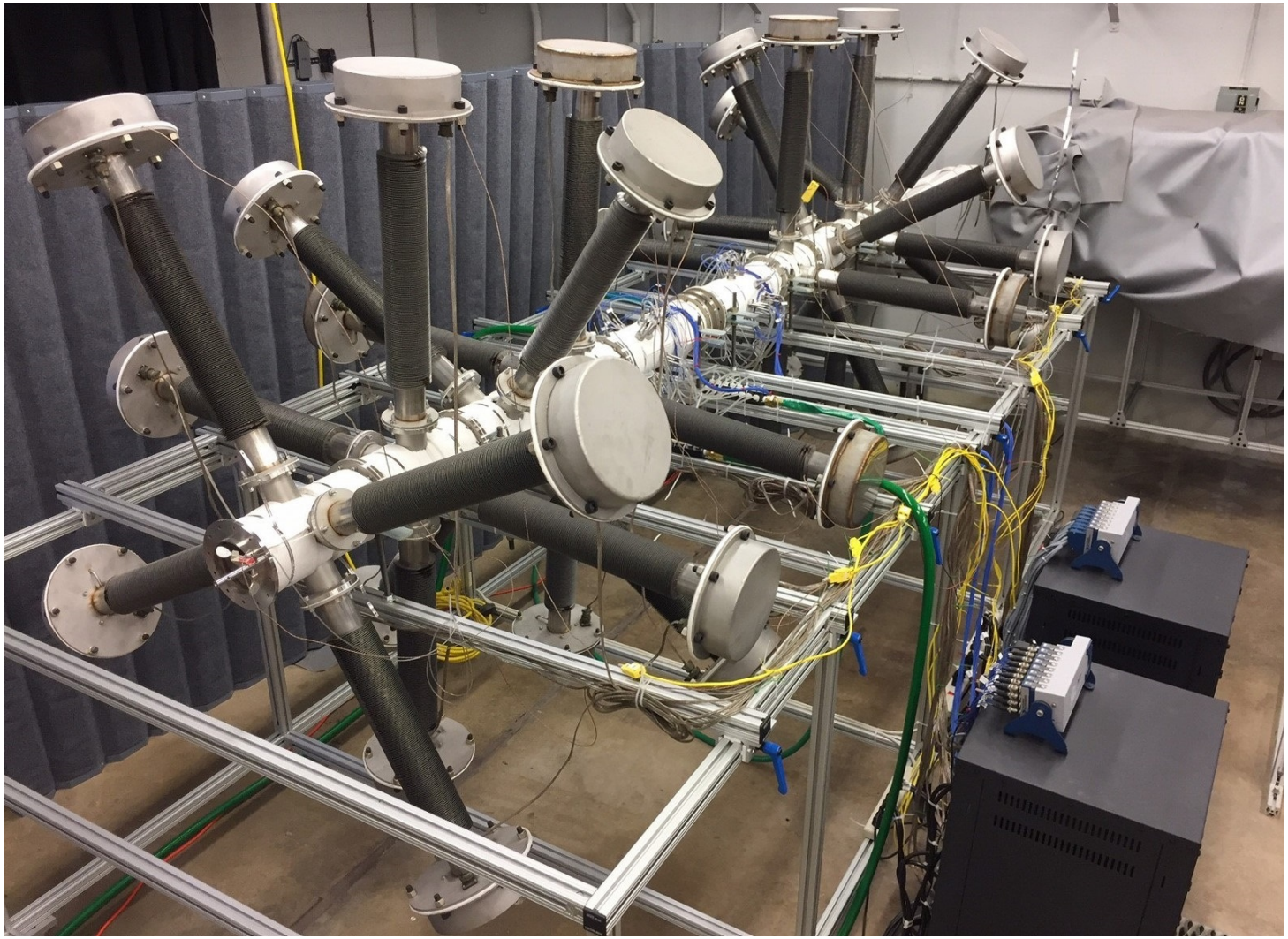

Figure 4.4: Photograph of HOTMESS.

the tube. Fiberfrax® ceramic fiber blankets are also used as gaskets between each pair of flanges.

The mean flow of air originates from a 100-psia pressure source, and a 4-in valve controls the air flow to several experimental facilities at GTRI, including HOTMESS. However, for the current experiments, a 2-in regulating valve upstream of the heater duct is used as a throttle to provide fine velocity control of low subsonic flow rates through HOTMESS. Within the heater duct, the air flow is heated by a 45 kW Heatrex HX-164N-118-101U tubular electric heater that is rated for heating air up to temperatures of 650°C (1200°F). The heater has its own proportional-integral-derivative (PID) controller that sets and maintains a programmed temperature based on a process thermocouple installed in the heater duct downstream of the heater.

As shown in Figure 4.4, the heater duct and two-sided impedance tube are mounted on independent 80/20® T-slotted aluminum frames. The two-sided impedance tube is secured by pipe clamps attached to threaded rods raised above the 80/20® support structure. The upstream and downstream sides of the two-sided impedance tube can slide independently along the 80/20® frame to facilitate the installation of test articles of different lengths. Practically, however, the upstream side remains fixed because it is attached to the 90° bend and flow-straightening pipe, so the downstream side slides to accommodate different test articles. A photograph of the entire HOTMESS experimental facility is shown in Figure 4.4.

4.3.2 Sound Sources

As discussed in Section 3.6, if there are N propagating modes on each side of the two-sided impedance tube that satisfy the cut-on criterion of Eq. (3.14), then at least $2N$ sound sources are required to measure the acoustic scattering matrix. HOTMESS is designed to measure the first six cut-on modes, so at least twelve sound sources are required, with at least six sources on each side of the test article. However, additional sources cause the system of equations described by Eq. (3.36) to become overdetermined, which can improve

the accuracy of the results [115, 131]. Additional sound sources also increase the maximum incident sound pressure level that can be produced.

For these reasons, thirty-two Radian 760NEOPB neodymium compression drivers are used as the sound sources for HOTMESS, with sixteen drivers on each side of the test article. The acoustic drivers are mounted to eight individual source sections, which each have four drivers distributed at 90° intervals around the circumference. Four of the source sections are located on the upstream side of the two-sided impedance tube, and the other four sections are on the downstream side. The source sections are connected using flanges with twelve screw holes equally spaced at 30° intervals and the one-way male-to-female alignment system. Because the flange screw holes are spaced at 30° intervals, the source sections can be independently rotated at 30° angles relative to one another.

Design of the Source Positions

Sack, et al. [115] showed that the ability of the acoustic drivers to excite all of the cut-on modes in a duct is related to the condition number of the monopole source excitation matrix, $\mathbf{G}^{\pm}$, with elements $G^{\pm}_{q,mn} = \alpha_{mn}(M^{\pm}_{q,mn})^*$, where α_{mn} is the wavenumber parameter defined in Eq. (3.13), $M^{\pm}_{q,mn}$ are the elements of the matrix of the weighted mode shapes at the source locations as defined in Eq. (3.23), and $*$ denotes the complex conjugate. Theoretically, the positions of the acoustic drivers could be optimized to minimize the condition number of the monopole source excitation matrix. The condition number provides a measure of the sensitivity of the outputs of a linear system due to small changes in the inputs, so a small condition number is desirable [139]. However, there are practical constraints due to the size of the drivers and the manufacturability of the source sections. In addition, this matrix formulation assumes that each acoustic driver behaves like a monopole and neglects the effects of internal reflections within the impedance tube [115]. Therefore, an optimization was not performed for the source positions. However, based on an analysis of the condition number of the monopole source excitation matrix, the source sections are rotated at $\pm 30°$

angles relative to each other to prevent singular source spacing for the ($\pm$2,0) mode. The axial and azimuthal coordinates of the acoustic driver closest to $\theta = 0^\circ$ in each of the eight sections are listed in Table 4.1 based on the coordinate system defined in Figure 3.4, where $\theta = 0^\circ$ is the vertical upward direction; the other acoustic drivers in each section are at 90° intervals relative to the driver at $\theta = 0^\circ$. Note that the axial spacing between each set of four acoustic drivers is not identical due to manufacturing tolerances.

Table 4.1: Coordinates of the acoustic driver closest to $\theta = 0^\circ$ in each source section.

Upstream Sources			Downstream Sources		
Section	z (m)	θ (deg.)	Section	z (m)	θ (deg.)
1	–1.60	–30	5	0.619	0
2	–1.30	0	6	0.924	–30
3	–0.914	30	7	1.22	0
4	–0.619	0	8	1.53	30

Cooling Considerations

The acoustic drivers are not rated for high temperatures, so the drivers must be actively cooled or be isolated from the heated flow. For example, another experimental facility in which similar tests with heated flow are conducted keeps the acoustic drivers cool by actively blowing cold air over the faces of the drivers [133]. However, HOTMESS was designed to conduct measurements even at low flow rates, so actively blowing cold air across thirty-two acoustic drivers could significantly change the temperature and velocity of the flow through the test article. Therefore, the acoustic drivers are mounted at the ends of 50.8-mm (2-in) diameter finned pipes that are approximately 0.61 m (2 ft) long. The fins increase the surface area of the pipes, so the finned pipes act as heat exchangers with the ambient air. A mounting plate is welded to the end of each finned pipe, and an encapsulating canister is secured to the mounting plate around the acoustic driver. A small steel tube connects the finned pipe in front of the acoustic driver to the canister to

equalize the pressure across the diaphragm. An electrical bulkhead connector is attached to the mounting plate so that the driving voltage signal can be delivered to the acoustic driver inside the canister. A partial cutaway view drawing of the finned pipe and canister assembly is shown in Figure 4.5.

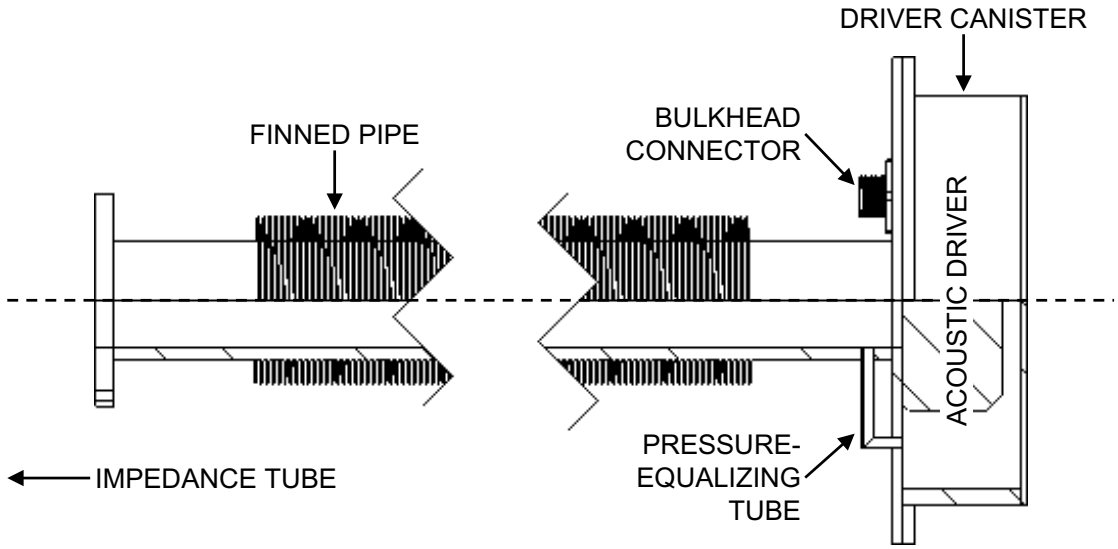

Figure 4.5: Partial cutaway view of the canister and finned-pipe heat exchanger assembly for the acoustic drivers.

In each of the eight source sections, the acoustic driver within $\pm 30^\circ$ of the vertical upward direction is likely to be exposed to the highest temperature and thus is instrumented with a thermocouple in front of the face of the driver. If the temperature of the air in front of the acoustic drivers becomes too high, then the heater is turned off, and the acoustic drivers are allowed to cool.

4.3.3 Acoustic Pressure Measurements

As discussed in Section 3.5, if there are N propagating modes that satisfy the cut-on criterion of Eq. (3.14), then a minimum of $2N$ measurements of the acoustic pressure field at independent spatial locations are required to decompose the modal amplitudes. HOTMESS is designed to measure the first six cut-on modes, so at least twelve acoustic pressure measurements are required on each side of the two-sided impedance tube. However, additional

measurements cause the system of equations described by Eq. (3.27) to become overdetermined, and Sack, et al. [115] showed that this can improve the accuracy of the results.

For this reason, thirty-two sensors are used to measure the acoustic pressure field at independent spatial locations in HOTMESS, with sixteen sensors mounted on each side of the test article. For unheated experiments, PCB 378A14 1/4-in diameter pressure microphones are used to measure the acoustic pressure field, but for high-temperature experiments, PCB 113B28 pressure transducers with PCB 064B01 water-cooled adapters are used instead. The nominal sensitivity of the microphones (1 mV/Pa) is significantly greater than the nominal sensitivity of the pressure transducers (0.0145 mV/Pa), so the microphones have a significantly lower noise floor than the pressure transducers and thus are used for unheated experiments. However, the maximum operating temperature of the microphones is only 70°C (158°F), so the pressure transducers and water-cooled adapters are required for high-temperature acoustic tests. The cold water for the water-cooled adapters is fed by two garden hoses, which distribute the water through two manifolds with sixteen outlets apiece. After circulating through the water-cooled adapters, the water then flows into two additional manifolds with sixteen inlets apiece and exits the facility through two additional garden hoses.

Magnitude and Phase Corrections

The sensor-switching procedure proposed by Chung and Blaser [124] is performed in the 28.5-mm diameter one-sided impedance tube for each PCB 378A14 microphone relative to a single reference microphone in order to correct for the magnitude and phase mismatches between the transducers. A highly absorptive foam sample is placed at the termination of the impedance tube per the ASTM E1050 standard to reduce reflections and improve the accuracy of the method [140], and the transfer function between the reference microphone and the microphone under test is measured. The physical locations of the two microphones are then switched, and the transfer function is measured again. The correction for the mag-

nitude and phase mismatch is determined from the two transfer function measurements according to the ASTM E1050 standard [140]. The sensor-switching procedure is only valid for plane wave propagation, so the smaller-diameter impedance is used because the cut-on frequency of its (1,0) mode is higher than the cut-on frequency of the (3,0) mode in the two-sided impedance tube, and thus the magnitude and phase mismatches between microphones can be corrected for the entire frequency range of interest. The sensor-switching procedure is not performed for the PCB 113B28 pressure transducers because their magnitude and phase responses depend on the recessed water-cooled adapters as well, and the water-cooled adapters cannot be installed in the smaller-diameter impedance tube due to size limitations. Although this means that the uncertainty in measurements using the pressure transducers is greater than the uncertainty in measurements using the microphones, the uncertainty analysis provided in Appendix A suggests that the uncertainty is sufficiently small that the pressure transducers provide useful acoustic measurements.

Optimization of the Sensor Positions

Sack, et al. [115] used a genetic algorithm to optimize the axial and azimuthal positions of wall-mounted microphones by minimizing the condition number of the matrix of weighted mode shapes, which is the $\mathbf{M}$-matrix in Eq. (3.24). The condition number provides a measure of the sensitivity of the outputs of a linear system due to small changes in the inputs, so a small condition number is desirable for accurate acoustic measurements [139]. The locations of the sixteen microphones on each side of the test article in HOTMESS were also optimized using the built-in MATLAB genetic algorithm function to minimize the weighted mean condition number of the $\mathbf{M}$-matrix across the measured frequency range at room temperature with no flow. A weighting function was applied to the condition number so that neither low frequencies nor frequencies just above the cut-on frequency of each higher-order mode overly penalized the optimizer. The weighting function excluded all frequencies below 500 Hz, increased linearly between 500 Hz and 1000 Hz, and remained

constant between 1000 Hz and the cut-on frequency of the (3,0) mode, with the exception of frequencies between the cut-on frequency and 2% above the cut-on frequency of the (1,0), (2,0), and (0,1) modes, which were excluded from the weighted mean. Figure 4.6 shows a plot of the weighting function and the condition number of the $\mathbf{M}$-matrix as a function of frequency for the optimized microphone positions. The resulting condition number is large near the cut-on frequencies of the higher-order modes, but the modal decomposition method is known to be inaccurate at these frequencies [110]. As the number of propagating modes increases, the condition number also increases because the degree of overdetermination in the number of microphones compared to the number of modes decreases. However, the condition number remains small (on the order of one) up to the cut-on frequency of the (3,0) mode, which suggests that the acoustic measurements will not be overly sensitive to experimental errors; the full uncertainty analysis is presented in Appendix A. Table 4.2 lists the optimized axial and azimuthal coordinates of the sixteen microphones on the upstream side of HOTMESS based on the coordinate system defined in Figure 3.4; the downstream measurement section is identical to the upstream measurement section but is flipped in the opposite direction, so the axial and azimuthal coordinates of the downstream microphones are the negatives of the values listed in Table 4.2.

Table 4.2: Coordinates of the optimized sensor locations.

Upstream Sensors			Downstream Sensors		
Mic	z (mm)	θ (deg.)	Mic	z (mm)	θ (deg.)
1	–200	0	9	–265	93
2	–203	144	10	–275	308
3	–206	274	11	–288	136
4	–232	30	12	–304	35
5	–235	267	13	–306	273
6	–238	167	14	–319	147
7	–263	0	15	–336	29
8	–265	220	16	–338	245

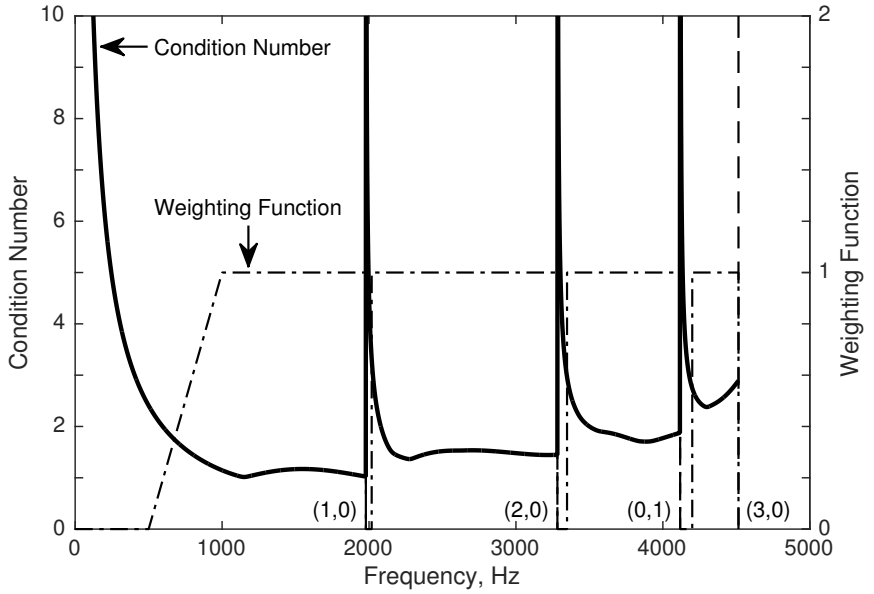

Figure 4.6: Weighting function and condition number of the M-matrix for the optimized sensor locations.

4.3.4 Velocity and Temperature Measurements

The modal decomposition—and thus all resulting acoustic measurements—depends on the wavenumber, which is a function of the Mach number and the speed of sound in the duct near the sensors used to measure the acoustic pressure field. The speed of sound is determined by the temperature. Although HOTMESS is well-insulated, there is heat loss within the measurement sections due to the water-cooled adapters, and there may be additional heat loss across the test article. In general, the Mach number and the temperature may differ between the upstream and downstream sides of the test article. Therefore, measurements of the Mach number and temperature in both the upstream and downstream measurement sections are required to obtain accurate acoustic data.

Figure 4.7 shows a drawing of the instrumented measurement sections. Thermocouple ports and static pressure taps are located immediately upstream of the upstream microphones and immediately downstream of the downstream microphones. In addition, a pitot probe is positioned at the centerline of the flow at the exit of HOTMESS. Type K thermocouples are inserted into the flow at the upstream and downstream thermocouple ports, and

a type K thermocouple is attached to the pitot probe at the exit of the impedance tube. The static pressures at the upstream and downstream pressure taps and the stagnation pressure at the pitot probe are measured using 1 psig pressure transducers, and the ambient pressure at the GTRI facility is measured using a Netscan 9032 barometer. The transducers are not mounted between the microphones and the test article so that they do not create spurious reflections and contaminate the acoustic measurements.

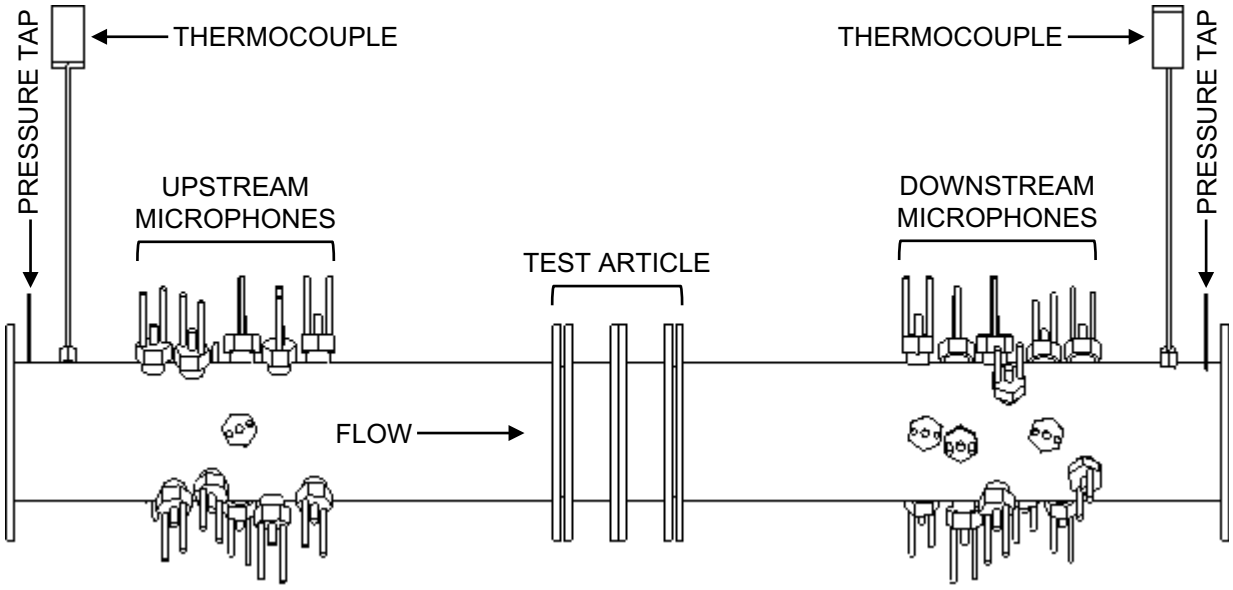

Figure 4.7: Drawing of the instrumented measurement sections in HOTMESS.

To simplify the modal decomposition, the temperature measured at the upstream thermocouple is assumed to remain constant throughout the upstream measurement section; likewise, the temperature measured at the downstream thermocouple is assumed to be constant throughout the downstream measurement section. The Mach number is calculated using different methods depending on the velocity of the flow and the cross-sectional area of the test article as described below.

Mach Number Calculation Using the Pitot Probe

If the cross-sectional area of the test article is comparable to that of the impedance tube, the Mach number is calculated using the stagnation pressure measured by the pitot probe

at the exit of HOTMESS. Assuming isentropic flow, the Mach number at the exit is

$$M_{\text{exit}} = \sqrt{\frac{2}{\gamma - 1}\left[\left(\frac{p_0}{p_a}\right)^{\frac{\gamma-1}{\gamma}} - 1\right]} \tag{4.1}$$

where p_0 is the stagnation pressure, p_a is the ambient pressure, and γ is the ratio of specific heats. The Mach numbers in the upstream and downstream measurement sections are calculated based on the assumption that the mass flow rate, $\dot{m} = \rho S \overline{U}$, is constant throughout the impedance tube. Noting that $\overline{U} = Mc$ and $c \propto \sqrt{T}$, the ratio of the Mach numbers between any two points 1 and 2 may be written as

$$\frac{M_2}{M_1} = \frac{S_1}{S_2}\frac{p_1}{p_2}\sqrt{\frac{T_2}{T_1}} \tag{4.2}$$

The cross-sectional area, S, is the same in the upstream and downstream measurement sections as at the exit, and the static pressure and temperature in the upstream and downstream measurement sections are measured at the locations shown in Figure 4.7. The temperature at the exit is measured by the thermocouple attached to the pitot probe, and the static pressure at the exit is equal to the ambient pressure, so the Mach numbers in the upstream and downstream measurement sections can be calculated directly from Eq. (4.2).

Although the temperature and Mach number of the flow through the test article are not required for the modal decomposition, the acoustic results are reported based on the conditions in the test article. It is assumed that most of the heat loss between the upstream and downstream thermocouples is due to the water-cooled adapters, so the temperature in the test article is assumed to be the mean value of the upstream and downstream thermocouple measurements. The Mach number in the test article is then estimated using Eq. (4.2), where point 1 is the pitot probe at the exit of the impedance tube and point 2 is the test article.

Mach Number Calculation Using the Static Pressures

For the initial experiments on propellant injectors conducted using HOTMESS, the cross-sectional areas of the propellant injector test articles are significantly smaller than the cross-sectional area of the impedance tube. Furthermore, these experiments are conducted at relatively low subsonic Mach numbers through the injectors, so the velocity of the flow through the impedance tube is very low. The difference between the stagnation pressure and the static pressure is small at low velocities, so the Mach number measured using the pitot probe is likely to have a relatively large percentage error due to the resolution of the pressure transducers. This results in even larger errors in the calculation of the Mach number in the test article because the pitot probe error is multiplied by the large area ratio between the impedance tube and the test article.

Therefore, if the cross-sectional area of the test article is much smaller than that of the impedance tube, and the Mach number of the flow through the test article is relatively low, the velocity of the flow in the impedance tube is low enough that the upstream side can be approximated as a plenum chamber. The upstream static pressure measurement is assumed to be equal to the stagnation pressure, and the downstream static pressure measurement is equal to the static pressure at the exit of the test article, so the Mach number in the test article is calculated by

$$M_{\text{test}} = \sqrt{\frac{2}{\gamma - 1}\left[\left(\frac{p_{\text{up}}}{p_{\text{down}}}\right)^{\frac{\gamma-1}{\gamma}} - 1\right]} \tag{4.3}$$

Equation (4.3) assumes isentropic flow between the upstream and downstream measurement sections. In reality, the flow is neither adiabatic, because there is heat loss due to the water-cooled adapters, nor reversible, because the abrupt area change between the impedance tube and test article creates flow losses. However, the isentropic assumption is considered sufficiently accurate to obtain a reasonable estimate for the Mach number in the test section at low velocities.

The Mach numbers in the upstream and downstream measurement sections, which are required for the modal decomposition, are calculated using Eq. (4.2), where point 1 is the test article, and point 2 is either the upstream or downstream measurement section. The stagnation temperature in the test article is assumed to be the mean value of the upstream and downstream thermocouple measurements, and the static temperature is extracted from the stagnation temperature using the isentropic equations.

4.3.5 Data Acquisition and Post-Processing

Figure 4.8 depicts a flowchart of the process for acquiring and post-processing acoustic data using HOTMESS. The user sets the velocity and temperature conditions using the 2-in regulating valve and the PID controller on the electric heater. The pressures are measured using a Measurement Specialties DTC Initium pressure system outfitted with 1 psig pressure transducers, and these measurements are imported into LabVIEW. The temperatures are measured using type K thermocouples, which are read to LabVIEW by NI-9211 temperature input modules in an NI-cDAQ-9174 chassis. The Mach number and temperature in the test article and the upstream and downstream measurement sections are calculated internally within the custom LabVIEW software.

The source signals are generated using LabVIEW and are converted to analog voltage signals using eight NI-9263 output modules installed in an NI cDAQ-9178 chasis. The voltage signals are amplified by sixteen dual-channel Behringer Europower EP2000 power amplifiers, and the amplified signals drive the Radian 760NEOPB compression drivers. For broadband testing, the acoustic drivers are driven with high-pass filtered Gaussian noise so that all frequencies of interest can be tested simultaneously. The high-pass filter has a cut-off frequency of 500 Hz, which is the lowest rated frequency of the acoustic drivers. For high-amplitude testing, the acoustic drivers are driven with single-frequency sine tones, so each frequency of interest must be tested individually. A mode generator was implemented in LabVIEW so that the amplitude of a desired mode can be specified at a single

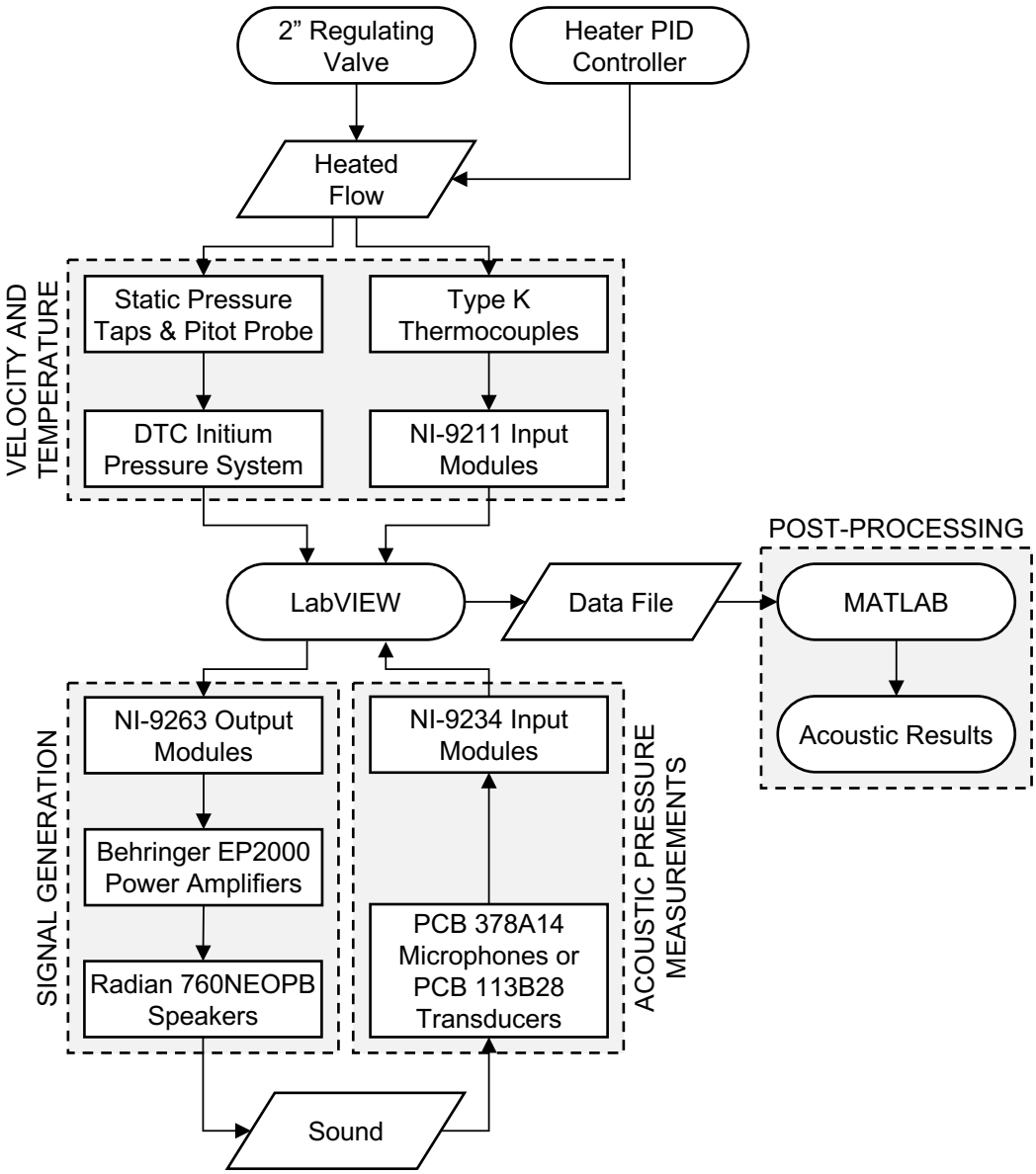

Figure 4.8: Data acquisition and post-processing flowchart.

frequency. The mode generator sets the phase of each acoustic driver based on its position, and the amplitudes of the acoustic drivers are adjusted within a feedback loop based on the microphone measurements.

The time histories of the acoustic pressures measured by the thirty-two PCB 378A14 microphones or PCB 113B28 pressure transducers are read to LabVIEW using eight NI-9234 input modules installed in an NI cDAQ-9178 chassis. These time histories, as well as the pressure and temperature measurements, are exported to a file. Custom MATLAB software is used to read the raw data files, perform the post-processing based on the methodology described in Chapter 3, and analyze and plot the acoustic results.

4.4 Particle Image Velocimetry

Particle image velocimetry (PIV) is a non-intrusive technique for measuring instantaneous velocity flow fields. Hann and Greated [141, 142] showed that the acoustic particle velocity could be measured using PIV, and other investigators [90–93, 143] have applied PIV to measure the flow field generated by high amplitude acoustic waves. In this work, PIV is used to measure the particle velocity generated by high amplitude acoustic oscillations at the open end of a propellant injector. The PIV measurements are conducted using the 101.6-mm diameter one-sided impedance tube because it is easier to conduct optical measurements at the open end of the one-sided impedance tube than inside the two-sided impedance tube.

A schematic of the experimental setup for the PIV measurements is shown in Figure 4.9. Although it is not shown in Figure 4.9, a box lined with nonreflective black material is placed over the open end of the injector to provide a containing volume for the seeding particles and to reduce reflections. Holes are cut in the box for the laser, the camera, and the seeder. A Laskin nozzle seeder is used to seed the interior volume of the box with mineral oil particles of less than 1.0 μm mean diameter. A New Wave Solo III Nd:YAG pulsed laser with a 532 nm wavelength is located 30 cm downstream of the open end of

the injector, and a LaVision adjustable light sheet optic attachment is used to create a laser sheet that bisects the open end of the injector. A LaVision Imager Intense high-speed camera with a Nikon Nikkor Zoom lens is positioned at a distance of 10 cm perpendicular to the laser sheet and is focused on the plane of the laser sheet, which produces a 29 mm $\times$ 21 mm viewing window at the open end of the injector.

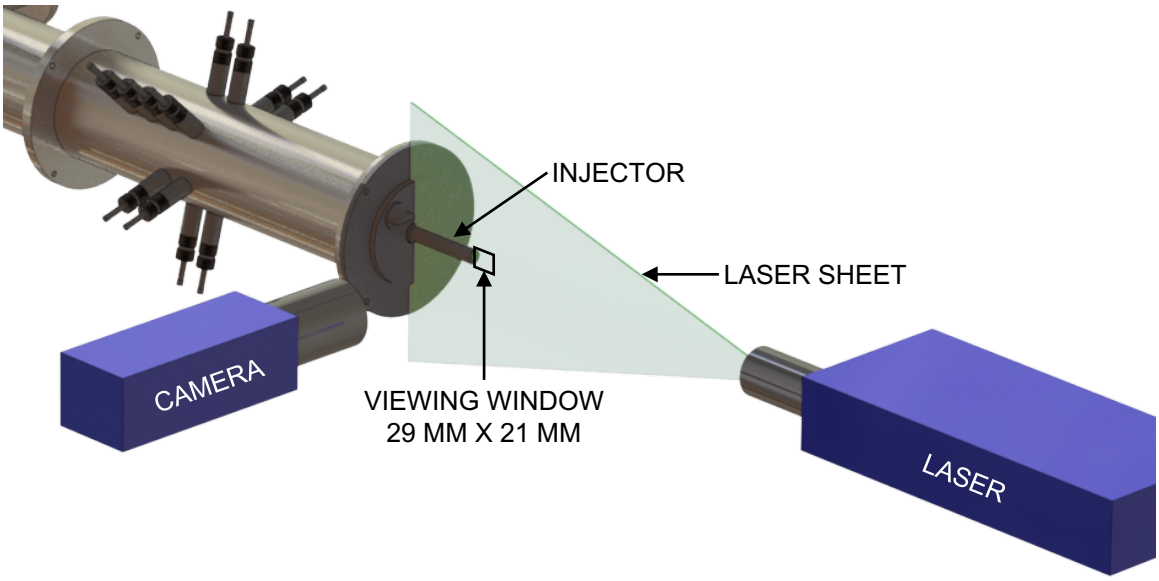

Figure 4.9: Schematic of the particle image velocimetry experimental setup.

Since the high-amplitude acoustic tests are conducted using pure sinusoidal tones, the laser is triggered using the driving signal for the acoustic drivers. The measurements are conducted at evenly spaced time intervals within the acoustic period by setting the delay between the sinusoidal source signal and the laser pulse. The laser is pulsed twice in quick succession each time it is triggered, and a cross-correlation technique is used to track the motion of the illuminated particles between the two snapshots. The velocity flow field is obtained by dividing the particle displacement by the time between the pulses. One hundred such image pairs are obtained at a single phase of the acoustic period, and the results are averaged to obtain the needed results. All images are collected and processed using LaVision Davis 8.3 imaging PIV software.

4.5 Test Articles

4.5.1 Injectors with Unique Geometric Features

Five unique propellant injectors were constructed out of ABS-like plastic material using 3D printing. Each injector contains one additional geometric feature compared to the previous injector, as shown in Figure 4.10. The baseline injector, designated as the "straight" injector, is a simple straight cylinder, which models the main body of a typical propellant injector. The "protrusion" injector has the same dimensions as the "straight" injector, but it also includes a protrusion, or area contraction, at the inlet. The "recess" injector adds a recess and taper region to the "protrusion" injector geometry. The recess forms an area expansion at the injector outlet, and the taper region is a chamfer at the open end of the recess. In addition to the features of the "recess" injector, the "annulus" injector includes shielding, which forms a small annulus adjacent to the recess surrounding the main body. Finally, the "fuel holes" injector includes small holes through the exterior wall surrounding the annulus through which fuel would be injected in a real injector. The "fuel holes" injector accurately models the size and geometric features of a realistic propellant injector.

The external threads at the outlet of each of the injectors allow the injectors to be securely attached to internally threaded mounting plates, which mate with the one-sided impedance tubes. The mounting plates for each one-sided impedance tube were constructed out of ABS-like plastic material using 3D printing. Figure 4.11 shows single propellant injectors attached to the ends of the 101.6-mm diameter and 28.5-mm diameter one-sided impedance tubes using these mounting plates. The inlet of each injector is open to the ambient air, and the outlet of each injector is installed in the mounting plate, which forms the termination of the impedance tube.

A mounting plate for the two-sided impedance tube was also constructed out of ABS-like plastic material using 3D printing. The mounting plate has male connectors of the type shown in Figure 4.3 on each side so that it can be placed between the microphones

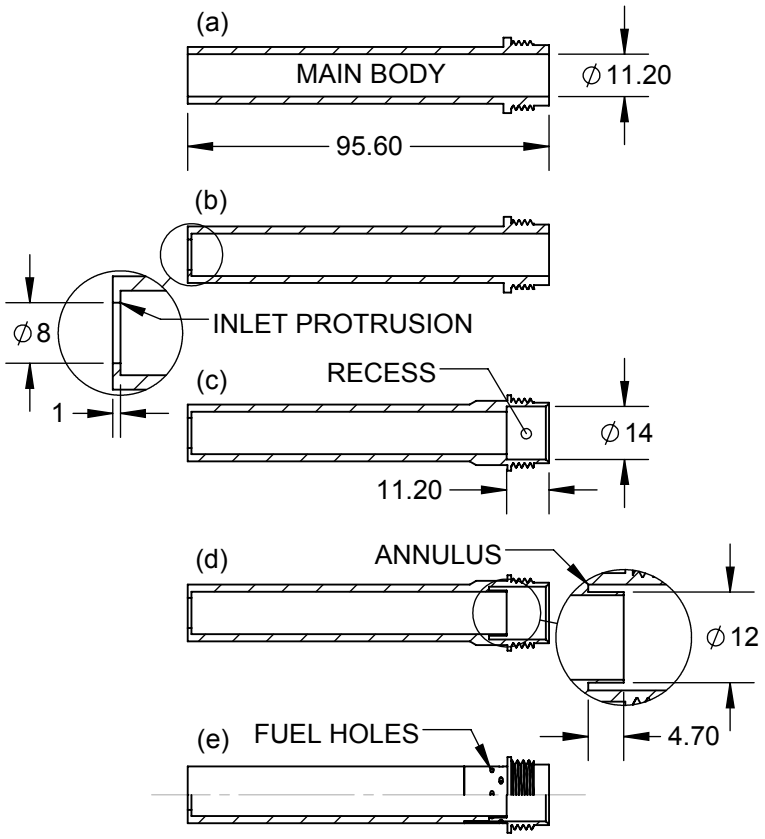

Figure 4.10: Section views of the (a) “straight”, (b) “protrusion”, (c) “recess”, (d) “annulus”, and (e) “fuel holes” propellant injectors with labeled geometric features and dimensions (in mm).

sections of the two-sided impedance tube. There are two internally threaded holes in the mounting plate so that an injector can be installed in different positions within the cross-section of the impedance tube, and a threaded plug is used to fill the unused hole. Front and sectional views of the mounting plate installed in the two-sided impedance tube are shown in Figure 4.12. The inlet of each injector extends into side A of the two-sided impedance tube, and the outlet of each injector is installed in the mounting plate, which forms the termination of side B of the two-sided impedance tube.

4.5.2 Cylindrical Half-Wave Resonators

In addition to the plastic injectors with unique geometric features, test articles were also constructed out of type 304 stainless steel so that high-temperature measurements could

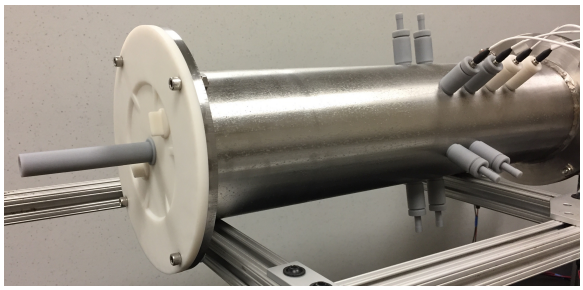

(a) 101.6-mm diameter impedance tube.

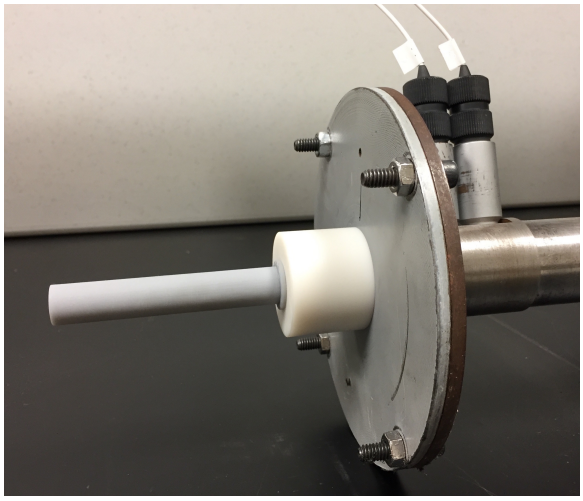

(b) 28.5-mm diameter impedance tube.

Figure 4.11: A single propellant injector mounted to the end of each one-sided impedance tube.

be performed. The metal test articles are straight cylindrical half-wave resonators with dimensions representative of realistic propellant injectors. A single metal half-wave resonator was constructed using 3D printing, and a structure for mounting the resonator in the two-sided impedance tube was machined. The mounting structure has two internally threaded holes so that the resonator can be positioned either at the centerline or near the wall of the impedance tube, and a plug is inserted into the unused threaded hole in the face-plate. Figure 4.13 shows front and sectional views of the mounting structure installed in the two-sided impedance tube. The inlet of the resonator extends into side A of the two-sided impedance tube, and the outlet of the resonator is installed in the mounting plate, which forms the termination of side B of the two-sided impedance tube.

An assembly for up to twelve type 304 stainless steel straight cylindrical half-wave

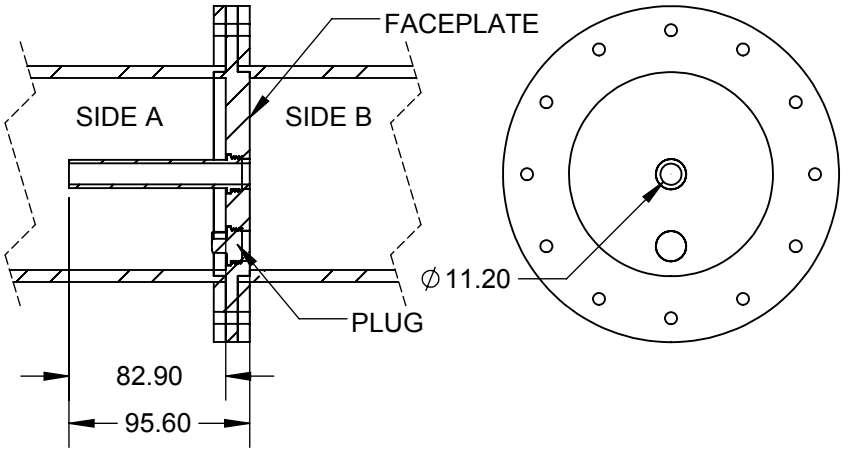

Figure 4.12: Front and sectional views of the mounting plate for the injectors with unique geometric features installed in the two-sided impedance tube, with dimensions (in mm).

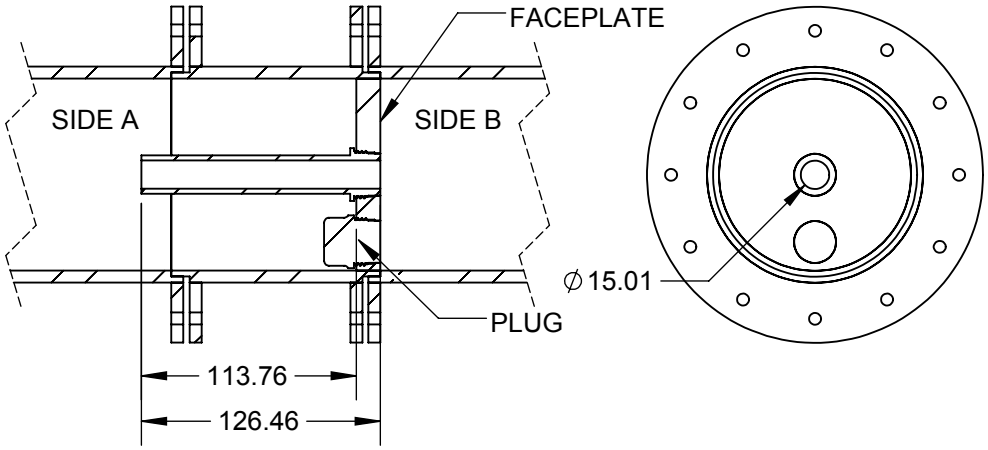

Figure 4.13: Front and sectional views of the mounting assembly for the single straight half-wave resonator installed in the two-sided impedance tube, with dimensions (in mm).

resonators was also machined, as shown in Figure 4.14. The resonators are mounted to the interpropellant plate using threaded connections, and the outer wall of each resonator is tapered at the outlet end so that the resonators fit snugly into the faceplate. Cylindrical plugs of the same outer dimensions as the resonators were also machined out of type 304 stainless steel, and the resonators can each be replaced by plugs so that any configuration of zero to twelve resonators can be tested. The inlets of the resonators and plugs extend from the interpropellant plate into side A of the two-sided impedance tube, and the outlets of the resonators are installed in the faceplate, which forms the termination of side B of the two-sided impedance tube. This geometry is representative of the injector mounting scheme in liquid-propellant combustion chambers, such as the one shown in Figure 3.1. Note that the inner diameter and the length of the half-wave resonators in the multiple-injector assembly shown in Figure 4.14 are different than the inner diameter and the length of the single half-wave resonator shown in Figure 4.13.

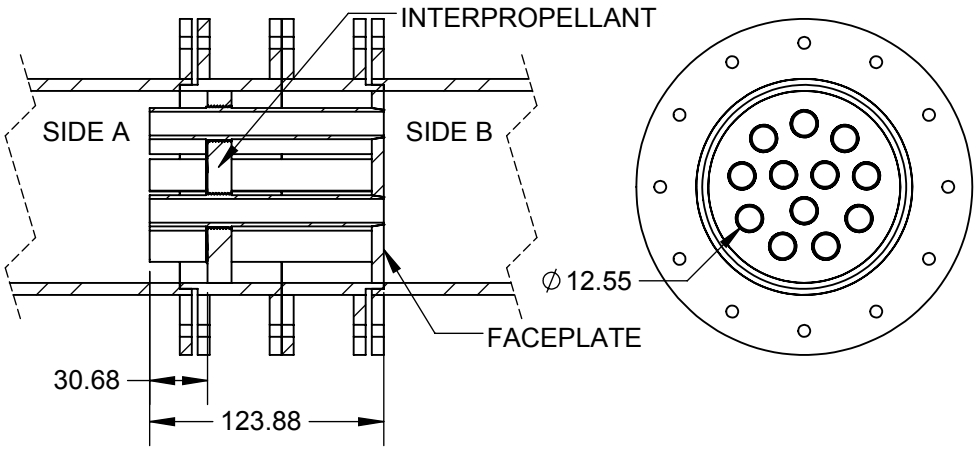

Figure 4.14: Front and sectional views of the mounting assembly for multiple straight half-wave resonators installed in the two-sided impedance tube, with dimensions (in mm).

4.6 Summary

The experimental facilities and procedures used in this work were presented in this chapter. Two different one-sided impedance tubes are used to measure the absorption coefficient

of propellant injectors at different open area ratios. However, most of the experiments are conducted using the Heated, Optimized Tube for Multimodal Evaluation of Sound Scattering (HOTMESS). HOTMESS was developed as part of this work to measure the acoustic scattering matrix of a test article under mean flow, high temperature, high amplitude, and higher-order mode propagation conditions. It is currently the only known experimental facility in the world that is capable of measuring the acoustic scattering matrix—and hence the power reflection, transmission, dissipation, and absorption coefficients—of a test article under all of the aforementioned conditions. The procedure for conducting particle image velocimetry (PIV) measurements and a description of the propellant injector test articles used in this work were also provided in this chapter.

CHAPTER 5
ANALYTICAL AND NUMERICAL MODELS

5.1 Overview

The purpose of this chapter is to establish the analytical and numerical methods that will inform the interpretation of the results in subsequent chapters. The outline of this chapter is as follows: First, analytical results for the acoustic damping of a half-wave resonator are derived in Section 5.2, and the results are simplified for frequencies near resonance. This approximate analysis is intended to be sufficiently simple to provide a physical understanding of the acoustic damping mechanisms of a half-wave resonator in quiescent air at standard atmospheric conditions and low acoustic amplitudes. Next, in Section 5.3, a numerical model for the acoustic damping of a propellant injector with several geometric features is developed using transfer matrices. The numerical model is intended to accurately predict the sound power absorption, dissipation, and transmission coefficients of one or more propellant injectors. The effects of mean flow, high amplitudes, high temperatures, and higher-order modes are neglected in this chapter; instead, these effects will be considered individually in subsequent chapters.

5.2 Analytical Expressions

The purpose of this section is to derive analytical expressions for the acoustic damping of a half-wave resonator. The geometry shown in Figure 5.1 represents the experimental setups shown in Figures 4.12–4.14. A half-wave resonator of length L is installed in the two-sided impedance tube, and it extends into side A by a distance of L_e. The amplitude of the incident acoustic wave is a_B^-, the reflected wave amplitude is a_B^+, and the transmitted wave amplitude is a_A^-, where all acoustic waves are assumed to be plane waves. The coordinate

system is defined such that the origin, $z = 0$, is at the axial plane at which the resonator is mounted to side B of the impedance tube. The remaining subscripts and normalized impedance terms shown in Figure 5.1 are defined as follows:

- The subscript L is associated with the conditions at $z = -L$, so ζ_L is the normalized impedance based on the acoustic pressure and particle velocity just inside the resonator at $z = -L$. Thus, ζ_L represents the boundary condition of the resonator at $z = -L$.

- The subscript 0 is associated with the conditions just inside the resonator at $z = 0$ (or $z = 0^-$), so ζ_0 is called the *normalized input impedance*, which is defined based on the acoustic pressure and particle velocity just inside the resonator at $z = 0$.

- The subscript T designates the termination conditions of the impedance tube and is associated with the conditions just inside the impedance tube at $z = 0$ (or $z = 0^+$), so ζ_T is called the *normalized termination impedance*, which is defined based on the acoustic pressure and particle velocity just inside the impedance tube at $z = 0$.

The normalized input impedance and the normalized termination impedance are both defined at $z = 0$, but their values differ because the particle velocity inside the resonator is greater than the particle velocity in the impedance tube by a factor of the area ratio.

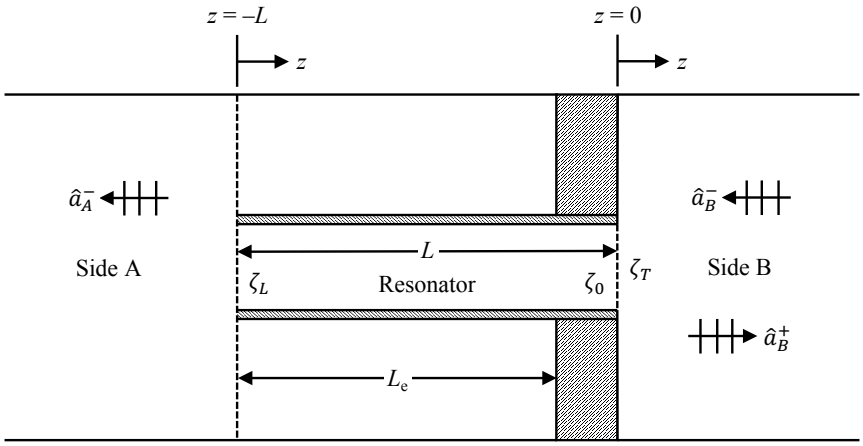

Figure 5.1: Schematic of the analytical model for a half-wave resonator (not to scale).

In the following section, the absorption coefficient is shown to be related to the normalized termination impedance, which is a function of the normalized input impedance. The relationships between the impedance terms defined above with the help of Figure 5.1 are then applied to obtain an expression for the normalized input impedance of a half-wave resonator. This expression is approximated at frequencies near resonance, and the resulting simplified expression is used to estimate the power dissipation and transmission coefficients and the absorption frequency bandwidth of a half-wave resonator. This simplified analysis provides physical insights into the acoustic damping mechanisms of a half-wave resonator.

5.2.1 Absorption Coefficient as a Function of Impedance

The absorption coefficient is defined in Eq. (3.2) as the fraction of sound power incident on a surface that is not reflected from that surface. In this study, the surface is the axial plane at which the injectors are mounted in the impedance tube, which is the $z = 0$ plane in Figure 5.1. From Eqs. (3.45) and (3.58), the absorption coefficient for the plane wave mode in the absence of flow can be expressed as

$$A = 1 - |R|^2 \tag{5.1}$$

where $R = \hat{a}_B^+ / \hat{a}_B^-$ is the pressure reflection coefficient. From Eq. (3.61), the normalized termination impedance for the plane wave mode at $z = 0$ can also be expressed in terms of the pressure reflection coefficient as

$$\zeta_T = \frac{1 + R}{1 - R} \tag{5.2}$$

In general, the normalized termination impedance is complex and may be expressed as $\zeta_T = \theta_T + j\chi_T$, where θ_T and χ_T are the normalized termination resistance and reactance, respectively. Since both the absorption coefficient and the normalized termination impedance are functions of only the reflection coefficient, the absorption coefficient can be

expressed directly as function of the normalized termination resistance and reactance by

$$A = \frac{4\theta_T}{(1+\theta_T)^2 + {\chi_T}^2} \tag{5.3}$$

Figure 5.2 shows the absorption coefficient given by Eq. (5.3) plotted as a function of the normalized termination resistance for different values of the normalized termination reactance. The maximum possible absorption coefficient is $A = 1$, which means that no sound power is reflected from the termination. This condition only occurs when $\theta_T = 1$ and $\chi_T = 0$. Resonance is defined as the frequency at which the reactance is zero, so the absorption coefficient is maximized if the normalized termination resistance is unity at resonance; otherwise, the absorption coefficient at resonance is less than one. Likewise, the absorption coefficient is always less than one at frequencies away from resonance, at which the normalized termination reactance is nonzero. These relationships are key to understanding the behavior of the absorption coefficient of propellant injectors described in subsequent chapters.

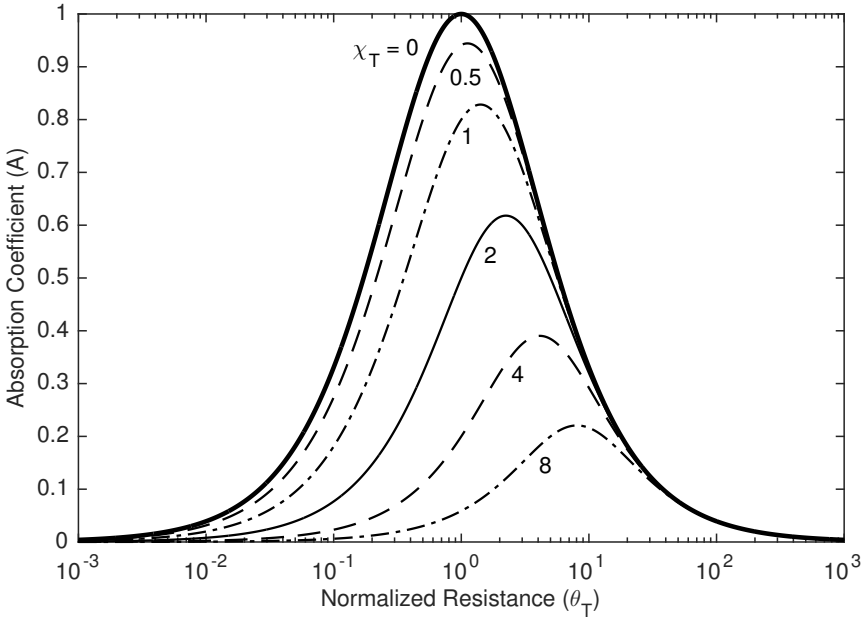

Figure 5.2: Absorption coefficient versus normalized termination resistance for different values of the normalized termination reactance.

5.2.2 Impedance at a Simple Area Discontinuity

In the previous section, the absorption coefficient was shown to be related to the normalized termination impedance by Eq. (5.3). In this section, the continuity conditions at an area discontinuity and corrections for additional accuracy are presented to relate the normalized termination impedance to the normalized input impedance of the half-wave resonator. The absorption coefficient is then rewritten in terms of the normalized input impedance of the half-wave resonator.

Continuity Conditions at a Simple Area Discontinuity

In Figure 5.1, a simple area discontinuity is formed at $z = 0$ between the half-wave resonator and side B of the impedance tube. Figure 5.3 shows a generic schematic of the acoustic waves and the cross-sectional areas, S, at a simple area discontinuity between ducts 1 and 2. In the following discussion, it is assumed that all waves are plane waves, so the acoustic pressure and particle velocity are constant across the cross-section of each duct. In addition, it is assumed that there is no mean flow through the ducts, and the characteristic impedance of the medium in each region is identical. The resulting boundary conditions at the area discontinuity are that no net force can be supported at the boundary, so the pressure in each region at the boundary must be identical, and continuity must be satisfied, so the volume velocity remains constant between the two ducts.

In general, an area discontinuity is formed at the boundary between any number of ducts of different cross-sectional areas, so the area discontinuity shown in Figure 5.3 can be generalized to an area discontinuity formed at the boundary between region 1 and regions 2 to N. This general area discontinuity is representative of the boundary between the impedance tube (region 1) and multiple resonators (regions 2 to N). The pressure boundary condition for this general case is $p_1 = p_2 = \cdots = p_N$ at $z = 0$, and continuity requires that $U_1 = U_2 + \cdots + U_N$ at $z = 0$. The acoustic velocity is defined such that it is positive in the direction of the incident acoustic waves, which in this case is the negative z-direction.

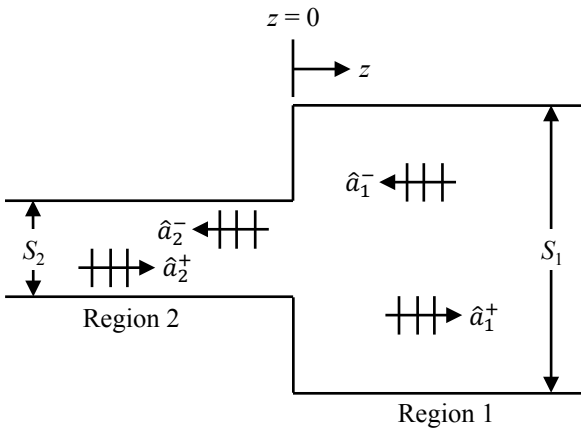

Figure 5.3: Simple area discontinuity between two ducts.

Dividing the continuity equation by the pressure equation yields

$$\frac{1}{Z_1} = \sum_{i=2}^{N} \frac{1}{Z_i} \tag{5.4}$$

where Z_i is the acoustic impedance of region i at $z = 0$, and the summation starts at 2 because the multiple resonators are designated as regions 2 to N. Since the characteristic impedance in each region is assumed to be identical, Eq. (5.4) can be expressed in terms of the normalized impedance as

$$\zeta_1 = S_1 \left(\sum_{i=2}^{N} \frac{S_i}{\zeta_i} \right)^{-1} \tag{5.5}$$

where ζ_i is the normalized impedance of region i at $z = 0$, and S_i is the cross-sectional area of region i.

Reactance Correction at an Area Discontinuity

In reality, evanescent higher-order modes are formed at the area discontinuity, even in the plane wave regime. Therefore, the boundary conditions represented by Eq. (5.4) are inexact. Karal [144] showed that the evanescent modes formed at the area discontinuity introduce an impedance, which can be represented by applying a length correction to the

smaller-diameter duct. Kergomard and Garcia [145] developed an approximation for the length correction, $\Delta L_{1,2}$, due to the evanescent modes at a simple area discontinuity between two concentric cylindrical waveguides 1 and 2. Their length correction is an involved function of the frequency and the radii of the two waveguides that form the discontinuity, but in the low-frequency limit ($ka \ll 1$), their length correction can be approximated as

$$\frac{\Delta L_{1,2}}{\pi a_2} \approx 0.26154 - 0.3512(a_2/a_1), \quad a_2/a_1 \leq 0.55 \tag{5.6}$$

where a_2 is the radius of the smaller-diameter duct, and a_1 is the radius of the larger-diameter duct. In general, the length correction is related to the normalized reactance by $\chi_{1,2} = k\Delta L_{1,2}$, which can be added to the input impedance of the smaller-diameter duct at the area discontinuity to account for the added effective length.

Resistance Correction at an Area Discontinuity

At the area discontinuity, the particle velocity in the larger-diameter duct has a nonzero radial component that is not modeled under the one-dimensional assumptions. Ingard [30] analyzed the viscous losses due to this oscillatory particle velocity over the flat wall at the discontinuity using the surface resistance, which is given by Rayleigh [146] as

$$R_s = \frac{1}{2}\sqrt{2\mu\rho\omega} \tag{5.7}$$

However, Ingard [30] measured the specific acoustic resistance of an orifice and found that it was approximately twice what his analysis predicted. Allam and Åbom [147] showed that discontinuities with sharp edges, such as the discontinuity between the impedance tube and propellant injectors considered in this work, require this factor of two. Therefore, the normalized resistance correction due to the viscous losses at an area discontinuity between

waveguides 1 and 2 is given by [30, 147]

$$\theta_{1,2} = \frac{4R_s}{\rho c} \tag{5.8}$$

Note that Eq. (5.8) is exactly one-half the value given by Allam and Åbom [147] because they analyzed the viscous losses on the two planar surfaces on either side of an orifice, whereas an area discontinuity between two ducts has only one planar surface.

Impedance Correction at an Area Discontinuity

The resistance and reactance corrections at the area discontinuity between waveguides 1 and 2 can be written as a normalized impedance correction, $\zeta_{1,2} = \theta_{1,2} + j\chi_{1,2}$, which is added to the input impedance of the smaller-diameter duct at the area discontinuity. The addition of this correction term to the denominator of Eq. (5.5) yields

$$\zeta_1 = S_1 \left(\sum_{i=2}^{N} \frac{S_i}{\zeta_i + \zeta_{1,i}} \right)^{-1} \tag{5.9}$$

where $\zeta_{1,i}$ is the impedance correction for the area discontinuity between regions 1 and i. For an area discontinuity between just two waveguides, as shown in Figure 5.3, Eq. (5.9) simplifies to

$$\zeta_1 = \frac{S_1}{S_2} \left(\zeta_2 + \zeta_{1,2} \right) \tag{5.10}$$

where, again, $\zeta_{1,2}$ is the impedance correction for the area discontinuity between regions 1 and 2. Thus, the *effective normalized input impedance* of region 2 can be defined as the sum of the normalized input impedance and the impedance correction at the discontinuity, or $\zeta_{2,\text{eff}} = \zeta_2 + \zeta_{1,2}$.

Application to the Resonator

For the area discontinuity formed between the resonator and side B of the impedance tube at $z = 0$ in Figure 5.1, the normalized termination impedance is given by rewriting Eq. (5.10) as

$$\zeta_T = \frac{\zeta_{0,\text{eff}}}{\sigma} \tag{5.11}$$

where the open area ratio, σ, is defined as the ratio between the cross-sectional area of the resonator and the cross-sectional area of the impedance tube, and

$$\zeta_{0,\text{eff}} = \zeta_0 + \zeta_{1,2} \tag{5.12}$$

is the effective normalized input impedance of the resonator. The absorption coefficient can then be written as a function of the effective normalized input resistance and reactance of the resonator by substituting Eq. (5.11) into Eq. (5.3), which produces

$$A = \frac{4\sigma\theta_{0,\text{eff}}}{(\sigma + \theta_{0,\text{eff}})^2 + \chi_{0,\text{eff}}^2} \tag{5.13}$$

This form of the absorption coefficient is preferred to Eq. (5.3) because it makes the dependence on the open area ratio explicit.

5.2.3 Input Impedance

In the previous section, the absorption coefficient was related to the normalized input impedance of a half-wave resonator through Eq. (5.13); thus, the absorption coefficient can be determined if the normalized input impedance is known. For a propellant injector, the normalized input impedance depends on the geometry of the injector itself and the boundary condition at the end of the injector at $z = -L$. There is no simple formula for the input impedance of a propellant injector containing multiple geometric features. However, the half-wave resonator shown in Figure 5.1 is a simple straight cylinder of length L, for

which the normalized input impedance is given by [20]

$$\zeta_0 = \frac{\zeta_L + j\tan(kL)}{1 + j\zeta_L\tan(kL)} \tag{5.14}$$

where ζ_L is the normalized impedance at the end of the resonator at $z = -L$, and k is the wavenumber. Note that this expression applies when the particle velocity is defined such that it is positive in the direction of the incident acoustic waves, which in this case is the negative z-direction in Figure 5.1. The acoustic dissipation of the plane wave mode due to viscothermal losses in the acoustic boundary layer at the walls of the resonator can be modeled using the complex Kirchhoff wavenumber given by Eq. (3.15).

5.2.4 Impedance at an Area Discontinuity with a Side Branch

In the previous section, the normalized input impedance of a half-wave resonator was shown to be a function of the length of the resonator, the complex wavenumber, and the boundary condition at $z = -L$ based on Eq. (5.14). The length of the resonator is known from geometry, and the complex wavenumber is given by Eq. (3.15). However, the boundary condition at $z = -L$ remains to be determined, which is the purpose of this section.

Continuity Conditions at an Area Discontinuity with a Side Branch

In Figure 5.1, an area discontinuity is formed at $z = -L$ between the resonator, side A of the impedance tube, and a side branch of length L_e. Figure 5.4 shows a schematic of the acoustic waves and the critical dimensions of a general area discontinuity between ducts 1 and 2 with a side branch designated by region 3.

Applying Eq. (5.9) to the area discontinuity shown in Figure 5.4 and solving for ζ_2 yields

$$\zeta_2 = S_2\left(\frac{S_1}{\zeta_1} - \frac{S_3}{\zeta_3}\right)^{-1} + \zeta_{1,2} \tag{5.15}$$

The area of the side branch is given by $S_3 = S_1 - S_2$. The impedance correction for the

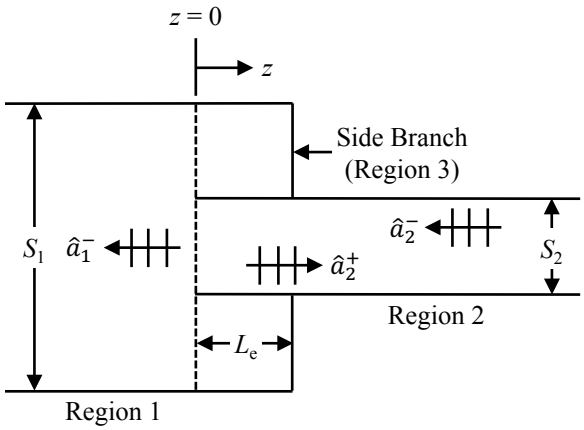

Figure 5.4: Area discontinuity between two ducts with a side branch.

area discontinuity between the side branch and region 1 is assumed to be zero because the difference in area between regions 1 and 3 is significantly less severe than the difference in area between regions 1 and 2 for the half-wave resonators considered in this work. Since there is no planar wall surface at the area discontinuity with a side branch, the resistance correction due to viscous losses between regions 1 and 2 is also assumed to be zero; thus, $\zeta_{1,2} = j\chi_{1,2}$, and Eq. (5.15) can be rewritten as

$$\zeta_2 = S_2 \left(\frac{S_1}{\zeta_1} - \frac{S_3}{\zeta_3} \right)^{-1} + j\chi_{1,2} \tag{5.16}$$

If the termination of the side branch at $z = L_e$ is assumed to be a hard wall, then the normalized input impedance of the side branch is obtained by solving Eq. (5.14) for ζ_L when $\zeta_0 = \infty$ to show that [20]

$$\zeta_3 = j \cot(kL_e) \tag{5.17}$$

The acoustic waves are assumed to only propagate away from the area discontinuity in region 1, so the normalized impedance of region 1 is simply $\zeta_1 = 1$. Substituting these expressions for ζ_1 and ζ_3 into Eq. (5.16) produces

$$\zeta_2 = \frac{S_2}{S_1 + j(S_1 - S_2)\tan(kL_e)} + j\chi_{1,2} \tag{5.18}$$

Application to the Resonator

For the area discontinuity with a side branch formed between the resonator and side A of the impedance tube at $z = -L$ in Figure 5.1, Eq. (5.18) can be rewritten as

$$\zeta_L = \frac{\sigma}{1 + j(1-\sigma)\tan(kL_e)} + j\chi_{1,2} \tag{5.19}$$

Recall that the open area ratio, σ, is defined as the ratio between the cross-sectional area of the resonator and the cross-sectional area of the impedance tube. Note that $L_e = 0$ for the simple area discontinuity shown in Figure 5.3, so the normalized impedance of the end of the resonator would reduce to $\zeta_L = \sigma + \zeta_{1,2}$ for a simple area discontinuity with no side branch.

5.2.5 Impedance Near Resonance

In the previous sections, the building blocks required to obtain an analytical expression for the absorption coefficient of a half-wave resonator were developed: the absorption coefficient is expressed in Eq. (5.13) in terms of the normalized input impedance, the normalized input impedance of the half-wave resonator is given by Eq. (5.14), and the boundary condition of the end of the resonator at $z = -L$ is given by Eq. (5.19). The expression for the normalized input impedance given by Eq. (5.14) can be simplified near resonance to provide a physical understanding of the acoustic damping mechanisms of a half-wave resonator. Kinsler, et al. [20] performed a more straightforward simplification for a pipe with a rigid termination, but a half-wave resonator has open boundaries at each end, which requires a different analysis. The following discussion is specific to a half-wave resonator near resonance.

Frequencies Near Resonance

First, the meaning of "near resonance" must be defined. If the length correction, ΔL, is neglected in Eq. (2.8), then the resonance frequencies of a half-wave resonator can be written in terms of the angular frequency as

$$\omega_0 = \frac{n\pi c}{L}, \quad n = 1, 2, 3, ... \tag{5.20}$$

where n is any integer. The angular frequency can be expressed as

$$\omega = \omega_0 + \Delta\omega \tag{5.21}$$

where ω_0 is given by Eq. (5.20), and $\Delta\omega$ is some change in the angular frequency. "Near resonance" means that $\Delta\omega$ is assumed to be small, so the validity of the near-resonance approximations will depend on the size of the $\Delta\omega$ term.

Order of Magnitude of the Impedance Boundary Condition at $z = -L$

The first term in the numerator of the expression for the normalized input impedance given by Eq. (5.14) is $\zeta_L = \theta_L + j\chi_L$, which is the normalized impedance boundary condition at the end of the resonator at $z = -L$. For the case shown in Figure 5.1, in which the resonator is installed in the two-sided impedance tube, ζ_L is given by Eq. (5.19). Thus, the normalized resistance at the end of the resonator is approximately of the order $\theta_L \sim \sigma$ based on Eq. (5.19). For the injectors considered in this work, the open area ratio is small, so θ_L is also small.

If, instead, the end of the resonator is open to the ambient air, as is the case for the experiments using the one-sided impedance tubes shown in Figure 4.11, the normalized impedance of the open end is equal to the radiation impedance of an unflanged pipe, which

is given by Eq. (2.4) and is repeated here:

$$\zeta_L = \zeta_r = \frac{1}{4}(ka)^2 + j0.6ka \qquad \text{(unflanged)} \tag{5.22}$$

where a is the radius of the resonator. If the end of the resonator at $z = -L$ is open to the ambient air, the normalized resistance at the end is of the order $\theta_L \sim (ka)^2$. The radiation impedance given by Eq. (5.22) is strictly valid in the limit $ka \ll 1$. Based on Eq. (5.20), the wavenumber, $k = \omega/c$, is of the order $k \sim n\pi/L$ near resonance, so $ka \sim n\pi(a/L)$, which is small at the fundamental resonance frequency of the injectors used in this work. Therefore, θ_L is small, regardless of whether the resonator is installed in the one-sided or two-sided impedance tubes.

Approximation of the Tangent Term in Eq. (5.14)

The other term in Eq. (5.14) is the tangent of the argument kL. The wavenumber is generally complex due to the viscothermal losses in the acoustic boundary layer at the walls of the resonator. The complex wavenumber obtained by Kirchhoff [119, 120] for the plane wave mode in the absence of flow is given by Eq. (3.16) and is repeated here:

$$k = \frac{\omega}{c} + (1 - j)\beta \tag{5.23}$$

The attenuation coefficient, β, is given by Eq. (3.17) and is of the order $\beta \sim (\omega/c)(\delta/a)$, where $\delta = \sqrt{2\nu/\omega}$ is the thickness of the acoustic boundary layer. The wide duct assumption used in the derivation of the Kirchhoff wavenumber requires that $\delta/a \ll 1$, which is satisfied for the injectors used in this work. Therefore, $\beta \ll \omega/c$, and the Kirchhoff wavenumber can be approximated as $k \approx \omega/c - j\beta$. The tangent of the complex argument kL in Eq. (5.14) can then be expanded as

$$\tan(kL) \approx \frac{\sin(2\omega L/c) + j\sinh(-2\beta L)}{\cos(2\omega L/c) + \cosh(-2\beta L)} \tag{5.24}$$

Based on the orders of magnitude of terms described previously, $\beta L \sim n\pi(\delta/a)$, which is small for the injectors used in this work at all frequencies of interest, including the fundamental resonance frequency and the first several harmonics. Making the small-angle approximations $\sinh(-2\beta L) \approx -2\beta L$ and $\cosh(-2\beta L) \approx 1$ and using the trigonometric identity $\sin(2x)/(\cos(2x)+1) = \tan(x)$ yields

$$\tan(kL) \approx \tan(\omega L/c) - j\frac{2\beta L}{\cos(2\omega L/c)+1} \tag{5.25}$$

The angular frequency near resonance can be expanded in the form given by Eq. (5.21) such that $\omega L/c = n\pi + \Delta\omega L/c$. The near-resonance approximations assume that $\Delta\omega L/c$ is relatively small. Making the small-angle approximation $\tan(\omega L/c) \approx \Delta\omega L/c$ and using the Taylor series approximation $\cos(2\omega L/c) \approx 1 - 2(\Delta\omega L/c)^2$ produces the result

$$\tan(kL) \approx (\Delta\omega L/c) - j\frac{\beta L}{1-(\Delta\omega L/c)^2} \tag{5.26}$$

Approximate Normalized Input Impedance

Substitution of the result obtained in Eq. (5.26) into Eq. (5.14) shows that the input impedance of the half-wave resonator can be approximated as

$$\zeta_0 \approx \frac{[\theta_L + (\beta L/\xi)] + j\,[\chi_L + (\Delta\omega L/c)]}{[1 + \theta_L(\beta L/\xi) - \chi_L(\Delta\omega L/c)] + j\,[\theta_L(\Delta\omega L/c) + \chi_L(\beta L/\xi)]} \tag{5.27}$$

where the numerator and denominator are grouped into real and imaginary components, and the parameter $\xi = 1 - (\Delta\omega L/c)^2$ is introduced for simplicity of notation. In these experiments, higher-order terms of θ_L and $\beta L/\xi$ can be neglected compared to the first-order terms because both terms were shown to be small in previous sections. After some

algebraic manipulation, Eq. (5.27) can be expressed in the form $\zeta_0 = \theta_0 + j\chi_0$ given by

$$\zeta_0 \approx \frac{\theta_L + (\beta L/\xi) + \theta_L(\Delta\omega L/c)^2 + \chi_L^2(\beta L/\xi)}{(1 - \chi_L \Delta\omega L/c)^2} + j\frac{\chi_L + (\Delta\omega L/c) - \chi_L(\Delta\omega L/c)^2 - \chi_L^2(\Delta\omega L/c)}{(1 - \chi_L \Delta\omega L/c)^2} \quad (5.28)$$

Equation (5.28) is a good approximation of Eq. (5.14) at frequencies near resonance, but it is too cumbersome to provide a physical understanding of the acoustic damping mechanisms of a half-wave resonator. Therefore, additional approximations are required to simplify the expression. From Eqs. (5.6) and (5.22), the normalized reactance at the end of the resonator at $z = -L$ is on the order of $\chi_L \sim ka$ for resonators installed in either the one-sided or two-sided impedance tubes, and ka was already shown to be small at the fundamental resonance frequency. In addition, $\Delta\omega L/c$ is small at frequencies very close to resonance. If higher-order terms of χ_L and $\Delta\omega L/c$ are also neglected, then Eq. (5.28) becomes

$$\zeta_0 \approx [\theta_L + \beta L] + j\,[\chi_L + \Delta\omega L/c] \quad (5.29)$$

The effective normalized input impedance, which is defined by Eq. (5.12), is obtained by adding the impedance correction at the area discontinuity to the normalized input impedance of the injector. Therefore, the effective normalized input resistance and reactance of the resonator are given by

$$\begin{aligned} \theta_{0,\text{eff}} &\approx \theta_L + \beta L + \theta_{1,2} \\ \chi_{0,\text{eff}} &\approx \chi_L + \Delta\omega L/c + \chi_{1,2} \end{aligned} \quad (5.30)$$

Even though these expressions are remarkably simple, Eq. (5.29) is a reasonable approximation of Eq. (5.14) at frequencies very close to resonance.

Resonance Frequency

The resonance frequency is defined as the frequency at which the reactance is zero. If the approximate normalized input reactance given by Eq. (5.30) is set to zero, the resonance frequencies of the half-wave resonator are found to be

$$f_0 = \frac{nc}{2(L + \Delta L_L + \Delta L_{1,2})}, \quad n = 1, 2, 3, \ldots \tag{5.31}$$

which is identical to Eq. (2.8), as expected. This gives confidence in the validity of the approximations in the previous sections. Alternatively, the resonance frequency can be expressed as $f_0 = nc/(2L_{\text{eff}})$, where the effective length of the resonator is the sum of the physical length and the length corrections, or $L_{\text{eff}} = L + \Delta L_L + \Delta L_{1,2}$.

5.2.6 Sound Power Coefficients

The absorption coefficient near resonance is estimated by substituting the effective normalized input resistance and reactance approximated by Eq. (5.30) into the form of the absorption coefficient given by Eq. (5.13) to show that

$$A \approx \frac{4\sigma(\theta_L + \beta L + \theta_{1,2})}{(\sigma + \theta_{0,\text{eff}})^2 + \chi_{0,\text{eff}}^2} \tag{5.32}$$

Estimates of the power dissipation and transmission coefficients may be obtained using this form of the absorption coefficient. Searby, et al. [18] showed that the sound power that is not reflected from a resonator can be expressed in terms of the normalized input resistance of the resonator. The absorption coefficient is equal to the sum of the power dissipation and transmission coefficients, or $A = D^{\Pi} + T^{\Pi}$, so it stands to reason that the effective normalized input resistance of the resonator can be decomposed into two components, $\theta_{0,\text{eff}} = \theta_{0,\text{eff},D} + \theta_{0,\text{eff},T}$, where $\theta_{0,\text{eff},D}$ is the part of the resistance that describes the dissipation, and $\theta_{0,\text{eff},T}$ is the part of the resistance that describes the transmission. The effective

normalized input resistance of a half-wave resonator near resonance is approximated by Eq. (5.30). In Eq. (5.30), the term θ_L is due to the radiation—or transmission—of sound from the free end of the resonator, so it is suggested that $\theta_{0,\text{eff},T} \approx \theta_L$. The remaining terms, βL and $\theta_{1,2}$, are due to viscothermal dissipation in the acoustic boundary layer inside the resonator and viscous dissipation on the wall of the area discontinuity, respectively, so it is suggested that $\theta_{0,\text{eff},D} \approx \beta L + \theta_{1,2}$. Estimates of the power dissipation and transmission coefficients are then given by splitting Eq. (5.32) into

$$D^{\Pi} \approx \frac{4\sigma(\beta L + \theta_{1,2})}{(\sigma + \theta_{0,\text{eff}})^2 + \chi_{0,\text{eff}}^2} \tag{5.33}$$

and

$$T^{\Pi} \approx \frac{4\sigma\theta_L}{(\sigma + \theta_{0,\text{eff}})^2 + \chi_{0,\text{eff}}^2} \tag{5.34}$$

5.2.7 Absorption Frequency Bandwidth

The frequency bandwidth of the absorption coefficient is defined quantitatively as the difference between the higher and lower frequencies at which the value of the absorption coefficient equals half its peak value. A simplified expression for the absorption frequency bandwidth can be obtained from Eq. (5.32). The effective normalized input resistance does not vary significantly with frequency near resonance, and half-wave resonators tend to have relatively narrow frequency bandwidths, so the effective normalized input resistance is treated as a constant. The effective normalized input reactance, which does vary with frequency, is approximated by Eq. (5.30). The frequencies at which the value of the absorption coefficient equals half its peak value are determined by setting the denominator of Eq. (5.32) equal to twice its value at resonance. Recalling that the length correction and the reactance are related by $\chi = k\Delta L$ and that $\Delta\omega L/c = \omega L/c - n\pi$, this condition can

be written, after some algebraic manipulation, as

$$\left[\frac{\omega}{c}(L + \Delta L_L + \Delta L_{1,2}) - n\pi\right]^2 - (\sigma + \theta_{0,\text{eff}})^2 = 0 \tag{5.35}$$

This equation can be solved using the quadratic formula to find that the frequencies at which the value of the absorption coefficient equals half its peak value are given by

$$\omega_{\pm 1/2} \approx \frac{c\left[n\pi \pm (\sigma + \theta_{0,\text{eff}})\right]}{L_{\text{eff}}} \tag{5.36}$$

where $L_{\text{eff}} = L + \Delta L_L + \Delta L_{1,2}$ is the effective length of the resonator. The absorption frequency bandwidth is defined as $\omega_{+1/2} - \omega_{-1/2}$ in terms of the angular frequency, and the absorption frequency bandwidth in Hertz is given by

$$BW = f_{+1/2} - f_{-1/2} \approx \frac{2f_0}{n\pi}(\sigma + \theta_{0,\text{eff}}) \tag{5.37}$$

where f_0 is the resonance frequency given by Eq. (5.31).

5.3 Numerical Model

In Section 5.2, approximate analytical expressions for the resonance frequency, sound power coefficients, and absorption frequency bandwidth of a half-wave resonator were derived. These results are simple enough to provide a basic physical understanding of the acoustic damping mechanisms of a half-wave resonator. However, the analytical expressions are limited to a straight cylindrical half-wave resonator.

Therefore, a numerical model is developed to predict the acoustic reflection, transmission, and dissipation of propellant injectors with realistic geometric features including the main body, inlet protrusion, and recess. Each of the included geometric features is modeled as a straight cylindrical duct, and adjacent geometric features form area discontinuities where they meet. It is assumed that the acoustic waves remain plane waves at the area dis-

continuity, and the effects of the evanescent higher-order modes that are formed at the area discontinuity can be represented by adding a length correction to the smaller-diameter duct. In Section 5.2.2, the length correction was expressed as a normalized reactance and was added directly to the input impedance of the smaller-diameter duct. However, this is a simplification of the procedure described by Davies [24], who proposed that the smaller-diameter duct should be extended into the larger-diameter duct by an amount equal to the length correction, $\Delta L_{1,2}$, to form an area discontinuity with a side branch. Munjal [148] presented a transfer matrix formulation for calculating the acoustic reflection and transmission properties of extended-tube resonators, which are comprised of straight ducts and area discontinuities with side branches. The transfer matrix defined by Munjal relates the acoustic pressure and particle velocity on both sides of a test article. However, the experiments conducted in this work measure the scattering matrix, which relates the acoustic pressure amplitudes of the inward- and outward-propagating waves on both sides of the test article, so a transfer matrix formulation in terms of the pressure amplitudes of the acoustic waves propagating in the positive and negative axial directions is adopted for the numerical model. Finally, the transfer matrix is rearranged into a scattering matrix, from which the reflection and transmission coefficients are obtained. The details of the development of the numerical model are contained in Appendix C. Note that the numerical model does not include the effects of flow or combustion because a quiescent medium with constant properties is assumed.

5.4 Summary

In this chapter, analytical and numerical models for the acoustic damping of propellant injectors were developed. The effects of mean flow, high amplitudes, high temperatures, and higher-order modes were neglected in this chapter; instead, these effects will be considered individually in subsequent chapters.

In the analytical model, a simplified expression for the impedance of a half-wave res-

onator near resonance was derived. This simplified impedance was used to obtain estimates for the power absorption, dissipation, and transmission coefficients near resonance, as well as the resonance frequency and absorption frequency bandwidth. The results of the analytical model are simple enough to provide a physical understanding of the damping mechanisms of a half-wave resonator in quiescent air at low amplitudes.

The numerical model was constructed using transfer matrices to model the acoustic behavior of straight cylindrical tubes and area discontinuities. A propellant injector with multiple geometric features was modeled as a collection of straight cylindrical tubes joined together at area discontinuities, so the component transfer matrices were combined into the overall transfer matrix for an injector with an inlet protrusion and a recess. The scattering matrix for the injector was obtained by rearranging the transfer matrix, and the reflection and transmission coefficients were given directly by the scattering matrix. The details of the development of the numerical model are contained in Appendix C. The accuracy of the numerical model will be verified in subsequent chapters.

CHAPTER 6
EFFECT OF GEOMETRIC PARAMETERS

6.1 Overview

In this chapter, the effects of the following geometric parameters on the acoustic damping of propellant injectors are investigated:

- Geometric features of the injectors
- Open area ratio between the cross-sectional areas of the injectors and impedance tube
- Number of injectors
- Position and distribution of the injectors on the injector faceplate

The experiments presented in this chapter are conducted in both the one-sided and two-sided impedance tubes using the 3D-printed propellant injectors with unique geometric features (see Figures 4.10–4.12) and multiple stainless steel half-wave resonators (see Figure 4.14). The experiments are conducted in quiescent air at ambient conditions in the linear acoustic regime for the plane wave mode. These results establish the baseline measurements required before the effects of bias flow, high amplitude incident acoustic waves, high temperatures, and higher-order modes are investigated in subsequent chapters. The primary physical mechanisms responsible for the acoustic damping in the experiments described in this chapter include:

- Viscous and thermal losses in the acoustic boundary layer
- Acoustic radiation from the open end of the injectors opposite the incident acoustic waves

The outline of this chapter is as follows: First, the effects of each geometric feature are investigated in Section 6.2 using measurements of the absorption coefficients of the five propellant injectors with unique geometric features in the one-sided impedance tube. In Section 6.3, the absorption coefficients of several of these injectors are compared between the 101.6-mm and 28.5-mm diameter one-sided impedance tubes to examine the effect of the open area ratio. Next, in Section 6.4, the measurements in the 101.6-mm diameter one-sided impedance tube are compared to those in the two-sided impedance tube, and the differences are discussed. The effect of multiple resonators is investigated in Section 6.5 using measurements in the two-sided impedance tube, and the results are explained analytically. The effect of the position of the resonators is also briefly discussed in Section 6.6. Finally, in Section 6.7, the numerical model described in Chapter 5 is applied to predict the sound power coefficients for several cases, and the numerical predictions are compared to the experimental results.

6.2 Effect of the Geometric Features

A number of studies have shown that a propellant injector can be tuned to behave like a half-wave resonator and provide acoustic damping near its resonance frequency, as discussed in Section 2.3.1. The purpose in this section is not to tune an injector to a particular frequency, however, but to investigate the effects of the geometric features of a typical propellant injector on its absorption coefficient. Figure 6.1 shows the absorption coefficients of the five unique injectors with different geometric features, which are depicted in Figure 4.10, measured using the 101.6-mm diameter one-sided impedance tube shown earlier in Figure 4.11a. The absorption coefficients are plotted in the neighborhood of the fundamental resonance frequencies of the injectors. The results indicate that the frequency and amplitude of the peak absorption coefficient of each injector are different. At frequencies away from resonance, the absorption coefficients are small. The differences between the injectors are the manifestations of the effects of each geometric feature on the acoustic

damping. Changes in the resonance frequency, the peak absorption coefficient, and the absorption frequency bandwidth due to each geometric feature are analyzed in detail in the following subsections.

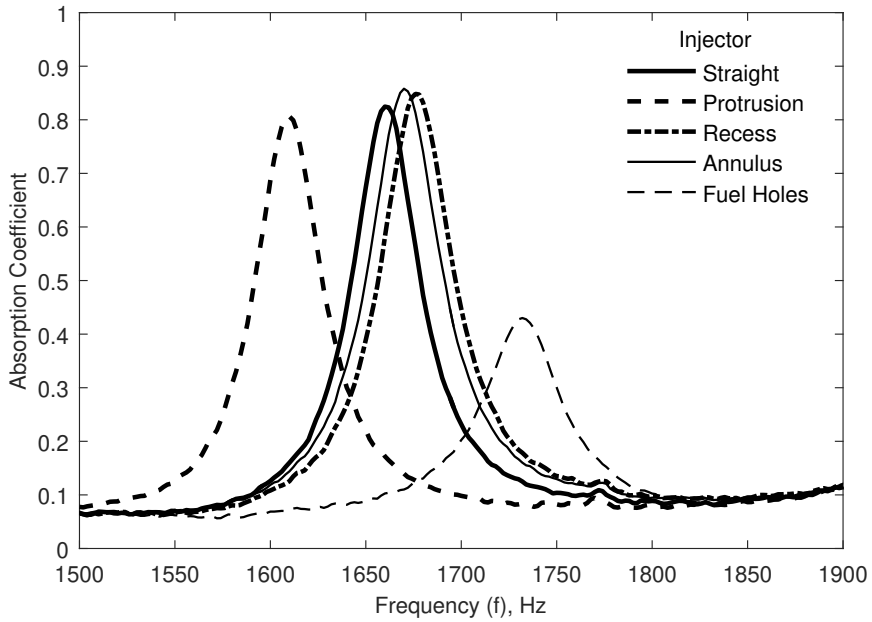

Figure 6.1: Absorption coefficients of the injectors with different geometric features measured in the 101.6-mm diameter one-sided impedance tube.

6.2.1 Straight Injector

The absorption coefficient spectrum of the "straight" injector in Figure 6.1 indicates that it behaves like a simple half-wave resonator: it has a high peak absorption coefficient that decreases rapidly as the frequency moves away from resonance. The resonance frequency, which is defined as the frequency at which the reactance is zero, is nearly identical to the frequency of the peak absorption coefficient, which is typical behavior for a narrowband acoustic resonator. The fundamental resonance frequency of the "straight" injector can be estimated using Eq. (2.8), which gives the resonance frequencies of a half-wave resonator as a function of its geometry. The "straight" injector has a length of 95.6 mm and a radius of 5.6 mm. The inlet of the injector is open to the ambient air, so the length correction at the inlet is the unflanged length correction given by Eq. (2.5). The outlet forms a sim-

ple area discontinuity with the impedance tube, and the length correction due to the area discontinuity is given by Eq. (5.6). Including these length corrections, the effective length of the resonator is about 103.0 mm. The speed of sound is approximately 344 m/s in the experimental facility, so the resonance frequency predicted by Eq. (2.8) is 1670 Hz, which is very close to the measured value of 1659 Hz. A more accurate prediction of both the resonance frequency and the absorption coefficient is given by the numerical model described in Section 5.3; the comparison between the numerical model and experimental results is presented in Section 6.7.

6.2.2 Inlet Protrusion

Figure 6.1 also indicates that the addition of the inlet protrusion decreases the resonance frequency of the "protrusion" injector compared to the "straight" injector. This is consistent with the trend observed by Park and Sohn [11], who examined the absorption coefficient as a function of the blockage ratio, which they defined as the percentage of the cross-sectional area of the main body of the injector that is blocked by the inlet protrusion. In the current experiments, the blockage ratio is 49% for the "protrusion" injector. In the limit as the blockage ratio approaches 100%, the inlet protrusion would become a hard-wall boundary, and the injector would behave like a quarter-wave resonator, which has a fundamental resonance frequency of approximately half that of a half-wave resonator. Therefore, the addition of the inlet protrusion causes the behavior of the propellant injector to shift from that of a pure half-wave resonator towards that of a quarter-wave resonator, and hence the resonance frequency of the injector decreases. For the blockage ratio of 49% measured in these experiments, the addition of the inlet protrusion slightly decreases the peak absorption coefficient and causes no observable change in the absorption frequency bandwidth of the "protrusion" injector compared to the "straight" injector. At even higher blockage ratios, Park and Sohn [11] observed that the peak absorption coefficient continues to decrease and the frequency bandwidth increases.

6.2.3 Recess

Figure 6.1 shows that the addition of a recess increases the resonance frequency of the "recess" injector compared to the "protrusion" injector, which is consistent with the numerical results of Kim, et al. [12]. The recess has a larger cross-sectional area than the main body of the injector. In the limit as the diameter of the recess approaches the diameter of the impedance tube, the recess would become indistinguishable from the impedance tube, and the injector would act like it is comprised only of the main body and the inlet protrusion. Since the limiting behavior physically shortens the length of the injector, the addition of a recess shortens the effective length of the injector, which causes the resonance frequency to increase. For the size of the recess measured in these experiments, the addition of the recess also slightly increases the peak absorption coefficient and causes no observable change in the absorption frequency bandwidth of the "recess" injector compared to the "protrusion" injector.

6.2.4 Annulus and Fuel Holes

Figure 6.1 shows that the small annulus around the main body of the injector causes slight changes in both the resonance frequency and the peak absorption coefficient, but the difference between the measured absorption coefficients of the "annulus" and "recess" injectors is small for the size of the annulus measured in these experiments. Fuel holes, however, are shown to significantly affect the acoustic damping of the propellant injector by increasing the resonance frequency and decreasing the peak absorption coefficient. The normalized reactance of the "fuel holes" injector does not cross the zero axis, so the frequency at which the normalized reactance reaches its closest value to zero is taken as the resonance frequency. There is a 1.4% difference between the frequency of minimum reactance and the frequency of the peak absorption coefficient, so the "fuel holes" injector deviates from the behavior of an ideal narrowband acoustic resonator.

The effects of the annulus and fuel holes on the absorption coefficient of a propellant

injector have not been previously reported in the literature. It is noted that these measurements were conducted using quiescent air as the medium inside the injector, but the fuel holes and the annulus in a real propellant injector would contain liquid propellant. Since the impedance of liquid propellant is significantly greater than the impedance of gaseous oxidizer, the liquid propellant is expected to act like an acoustically hard boundary compared to the gaseous oxidizer in the main body, inlet protrusion, and recess. Therefore, the "recess" injector, which contains a physical hard wall where the annulus and fuel holes would otherwise be, is likely the best model for the acoustic damping of a real propellant injector in these experiments with no flow and no combustion.

6.3 Effect of the Open Area Ratio

The open area ratio, σ, is the ratio between the open area of the injectors and the cross-sectional area of the combustion chamber or impedance tube. It has been shown to affect the absorption coefficient of propellant injectors in a model combustion chamber, as discussed in Section 2.3.2. Open area ratio effects have previously been studied by changing the injector diameter [11] and the number of injectors [9, 11, 14], but in this study, impedance tubes of two different diameters are used to achieve two different open area ratios for the same propellant injector. The absorption coefficients of the five unique propellant injectors with different geometric features measured in the larger 101.6-mm diameter one-sided impedance tube are shown in Figure 6.1. The absorption coefficients of these same injectors were also measured using the smaller 28.5-mm diameter one-sided impedance tube to vary the open area ratio, and the results are shown in Figure 6.2. The diameter of each propellant injector remains constant between the two sets of measurements, but the cross-sectional areas of the two impedance tubes are different, so the open area ratio of each injector is larger in the 28.5-mm diameter impedance tube than in the 101.6-mm diameter tube, as listed in Table 6.1. The open area ratios of each of the five injectors are not identical because the "straight" and "protrusion" injectors do not include the recess, which has a

larger cross-sectional area than the main body of the injector.

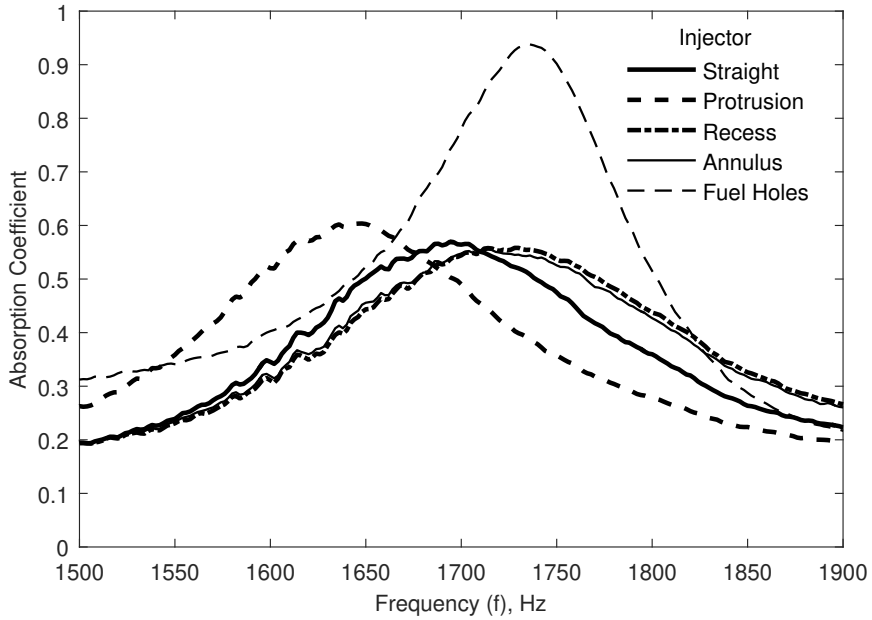

Figure 6.2: Absorption coefficients of the injectors with different geometric features measured in the 28.5-mm diameter one-sided impedance tube.

Table 6.1: Open area ratios of the injectors with different geometric features in each of the impedance tubes.

Injector	Impedance Tube	
	101.6-mm diameter	28.5-mm diameter
Straight	1.2%	15.4%
Protrusion	1.2%	15.4%
Recess	1.9%	24.1%
Annulus	1.9%	24.1%
Fuel Holes	1.9%	24.1%

A comparison between the results shown in Figures 6.1 and 6.2 demonstrates that several properties of the absorption coefficient vary with the open area ratio. Namely, the effect of the open area ratio on the absorption frequency bandwidth, the resonance frequency, and the peak absorption coefficient are discussed below.

Effect of the Open Area Ratio on the Absorption Frequency Bandwidth

A comparison of the absorption frequency bandwidth of each injector shown in Figures 6.1 and 6.2 indicates that the absorption frequency bandwidth of the injectors increases with increasing open area ratio, which is consistent with the results reported by Park and Sohn [11]. This means that a given propellant injector provides acoustic damping over a wider range of frequencies in a combustion chamber with a smaller cross-sectional area. This effect is described analytically by Eq. (5.37), which suggests that the absorption frequency bandwidth increases approximately linearly with increasing open area ratio.

Effect of the Open Area Ratio on the Resonance Frequency

A comparison of the resonance frequency of each injector shown in Figures 6.1 and 6.2 shows that the resonance frequency of each injector also increases with open area ratio. This is attributable to the fact that as the open area ratio increases, the area discontinuity between the injector and the impedance tube becomes less severe, so the length correction at the area discontinuity given by Eq. (5.6) decreases. For a resonator of a given radius, this means that the pressure node outside the open end of the resonator moves closer to the resonator, and the effective length of the resonator decreases. Since the resonance frequency is inversely proportional to the effective length of the resonator based on Eq. (5.31), this should increase the resonance frequency as observed here.

Effect of the Open Area Ratio on the Peak Absorption Coefficient

The absorption coefficient does not seem to vary uniformly with the open area ratio: the value of the peak absorption coefficient of the "fuel holes" injector is larger in the 28.5-mm diameter impedance tube than in the 101.6-mm diameter tube, but the reverse is true for the other propellant injectors. These observations can be explained by analyzing the normalized termination impedance. The peak absorption coefficient occurs at or very close to resonance. At resonance, the normalized termination reactance is zero, so the normal-

ized termination impedance is equal to the normalized termination resistance. Based on Eq. (5.11), the normalized termination resistance is given by $\theta_T = \theta_{0,\text{eff}}/\sigma$, where $\theta_{0,\text{eff}}$ is the effective normalized input resistance of the injector. The approximate expression for the effective normalized input resistance of a half-wave resonator given by Eq. (5.30) indicates that $\theta_{0,\text{eff}}$ does not vary strongly with the open area ratio. Thus, the normalized termination resistance varies approximately inversely with the open area ratio such that $\theta_T \propto \sigma^{-1}$. In the larger 101.6-mm diameter impedance tube, the normalized termination resistance of each injector is greater than one, and the normalized resistance of the "fuel holes" injectors is larger than that of the other injectors. The relationship between the absorption coefficient and the normalized termination resistance at resonance is governed by Eq. (5.3); this relationship is plotted in Figure 5.2. Based on the $\chi_T = 0$ curve shown in Figure 5.2, the peak absorption coefficient of the "fuel holes" injectors is lower than that of the other injectors measured in the 101.6-mm diameter impedance tube, as shown in Figure 6.1. The normalized termination resistance is less than one for each injector in the smaller 28.5-mm diameter impedance tube, but the normalized resistance of the "fuel holes" is still greater than that of the other injectors. Based on the $\chi_T = 0$ curve plotted in Figure 5.2, the peak absorption coefficient of the "fuel holes" injectors is greater than that of the other injectors measured in the 28.5-mm diameter impedance tube, as shown in Figure 6.2. Therefore, the normalized termination resistance varies monotonically with the open area ratio, but the behavior of the peak absorption coefficient depends on the normalized termination resistance through Eq. (5.3).

6.4 Comparison Between the One- and Two-Sided Impedance Tubes

The measurements discussed in Sections 6.2 and 6.3 were conducted in two different one-sided impedance tubes in order to elucidate the effect of the open area ratio on the acoustic damping of the propellant injectors. Although the one-sided impedance tubes are capable of measuring the absorption coefficient, the two-sided impedance tube is required to sepa-

rate the absorption coefficient into the power transmission and dissipation coefficients, as explained in Section 3.2. The remaining measurements discussed in this chapter and subsequent chapters were all conducted in the two-sided experimental facility, HOTMESS, to understand the reflection, transmission, and dissipation properties of the injectors.

Figure 6.3 compares the absorption coefficients of three of the unique injectors with different geometric features measured in the 101.6-mm diameter one-sided and two-sided impedance tubes. The two-sided experimental facility is not climate controlled, so the ambient temperature within the facility may vary between measurements. Therefore, the horizontal axis of Figure 6.3 is plotted in terms of the normalized frequency, which is defined as

$$\tilde{f} = \frac{f}{c/(2L)} \tag{6.1}$$

where the denominator is the theoretical resonance frequency of a half-wave resonator given by Eq. (2.8) neglecting the length corrections. The normalized frequency accounts for the effect of temperature on the resonance frequency, and thus it allows measurements conducted at different temperatures to be compared to one another.

Even though Figure 6.3 is plotted in terms of the normalized frequency, the resonance frequencies and peak absorption coefficients of the injectors show differences between the one- and two-sided impedance tubes. These differences are due to the change in the boundary condition at the injector inlet. In the one-sided impedance tube, the injector inlet is open to the ambient air, and the normalized impedance of the end of the injector is given by Eq. (5.22). In the two-sided impedance tube, the injector inlet extends into side A of the impedance tube (see Figure 4.12), and a reasonable approximation for the normalized impedance of the end of the injector is given by Eq. (5.19). For each of the measured configurations, the normalized resistance of the injector inlet at resonance is greater in the two-sided impedance tube than in the one-sided impedance tube. The measured normalized termination resistance of each injector is greater than one in both impedance tubes, so the peak absorption coefficient of each injector is smaller in the two-sided impedance tube

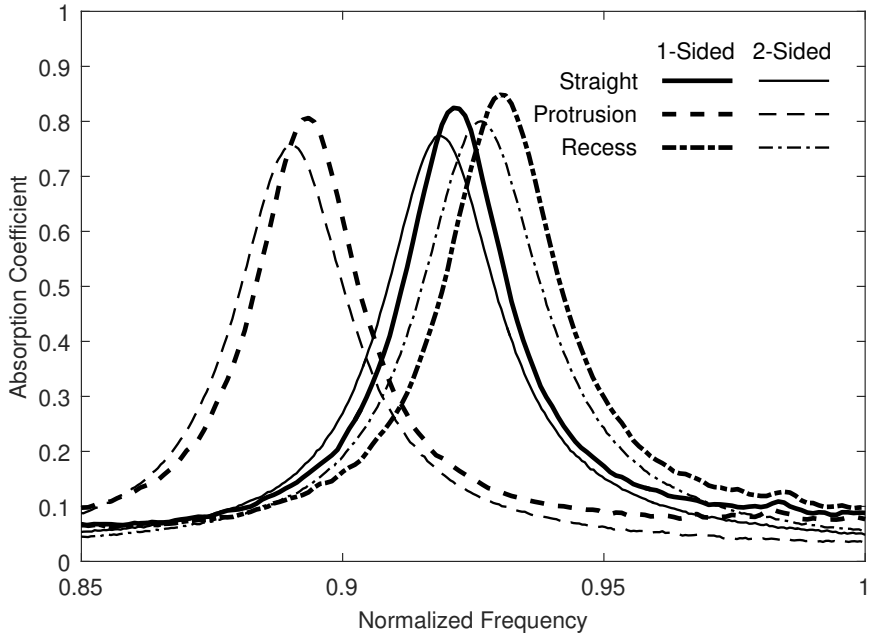

Figure 6.3: Comparison of the absorption coefficients of the injectors with different geometric features measured in the 101.6-mm diameter one-sided and two-sided impedance tubes.

than in the one-sided impedance tube based on the $\chi_T = 0$ curve plotted in Figure 5.2. A comparison between the results of Eqs. (2.5) and (5.6) indicates that the length correction at the injector inlet due to the area discontinuity between the injector and the impedance tube is larger than the length correction due to acoustic radiation into the ambient air, so the resonance frequency of each injector is lower in the two-sided impedance tube than in the one-sided impedance tube. Therefore, the differences between the measurements in the one- and two-sided impedance tubes can be fully explained by the change in the boundary condition at the injector inlet, and the two-sided impedance tube is used with confidence to investigate the reflection, transmission, and dissipation of the injectors for the remainder of the experiments in the sections that follow.

6.5 Effect of the Number of Injectors

As described in Section 6.3, impedance tubes of two different diameters were used to achieve two different open area ratios for the same propellant injector. The open area ratio

is also a function of the number of injectors, and in this section, the effect of the number of injectors on the acoustic damping is investigated.

6.5.1 Effect of the Number of Injectors on the Absorption Coefficient

Figure 6.4 shows the absorption coefficients of one, three, six, nine, and twelve stainless steel half-wave resonators measured in the two-sided impedance tube. As the number of injectors increases, the peak absorption coefficient first increases and then decreases slightly. More importantly, the absorption frequency bandwidth increases monotonically with the number of injectors. Both observations agree qualitatively with the measurements of Park and Sohn [11].

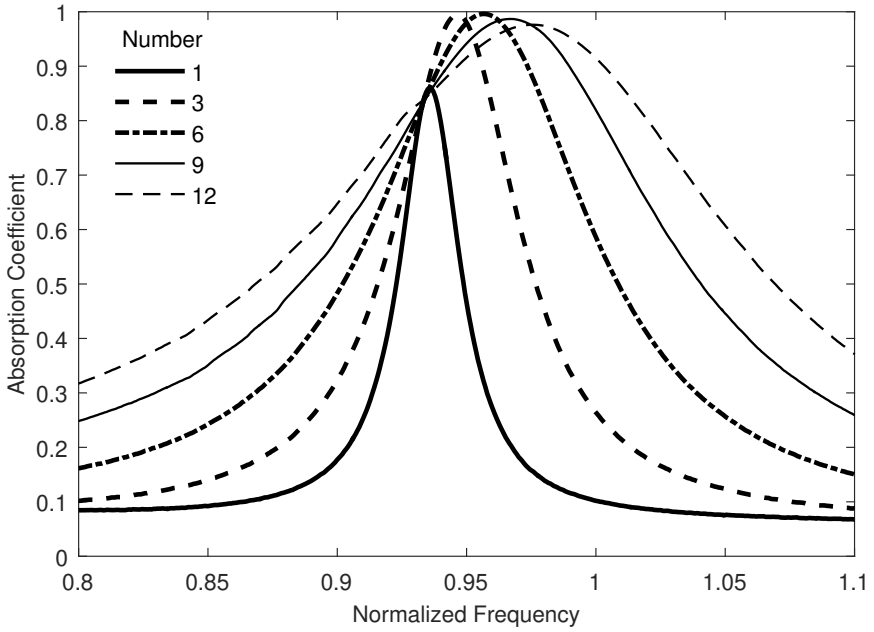

Figure 6.4: Absorption coefficients of various numbers of half-wave resonators measured in the two-sided impedance tube.

The behavior of the peak absorption coefficient can be explained by analyzing the normalized termination impedance. The peak absorption coefficient occurs at or very close to resonance. At resonance, the normalized termination reactance is zero, so the normalized termination impedance is equal to the normalized termination resistance. Based on Eq. (5.11), the normalized termination resistance is given by $\theta_T = \theta_{0,\text{eff}}/\sigma$, where $\theta_{0,\text{eff}}$

is the effective normalized input resistance of one of the resonators. The combined open area ratio for multiple resonators is given by $\sigma = N(S_2/S_1)$, where N is the number of resonators, S_1 is the cross-sectional area of the impedance tube, and S_2 is the open area of a single resonator. This analysis seems to suggest that the normalized termination resistance of the resonators varies as $\theta_T \propto \sigma^{-1}$. However, the simplified expression for the effective normalized input resistance of each resonator given by Eq. (5.30) shows that $\theta_{0,\text{eff}}$ depends on the normalized resistance of the inlet end of the resonator, θ_L, which varies with the open area ratio according to the real part of Eq. (5.19). Substitution of the real part of Eq. (5.19) into Eq. (5.30) and division by σ yields an approximate expression for the normalized termination resistance of multiple half-wave resonators in the two-sided impedance tube:

$$\theta_T = \frac{1}{1 + (1-\sigma)^2 \tan^2(kL_e)} + \frac{\beta L + \theta_{1,2}}{\sigma} \tag{6.2}$$

where L_e is the distance that the resonators extend into the impedance tube. The tangent in the denominator of the first term in this expression accounts for the change in the impedance boundary condition at the inlet end of the resonators due to acoustic oscillations within the cavity surrounding the extension of the resonators into the impedance tube, so the tangent vanishes if $L_e = 0$.

Figure 6.5 compares the measured normalized termination resistance of the various numbers of half-wave resonators to the corresponding values predicted by Eq. (6.2). The normalized termination resistance decreases monotonically as the number of resonators increases, and the simplified analytical expression given by Eq. (6.2) agrees remarkably well with the measured results. The resulting behavior of the peak absorption coefficient as a function of the normalized termination resistance is described by Eq. (5.3) and plotted in Figure 5.2. The peak absorption coefficient is maximized when the normalized termination resistance at resonance equals one, which, according to Figure 6.5, would occur with four to five resonators for the tested configuration. According to the behavior described by Eq. (5.3) and plotted in Figure 5.2, the peak absorption coefficient decreases as the nor-

malized termination resistance at resonance moves away from one, which is exactly the behavior observed in Figure 6.4. Therefore, the change in the peak absorption coefficient as the number of resonators increases is well explained by this analysis.

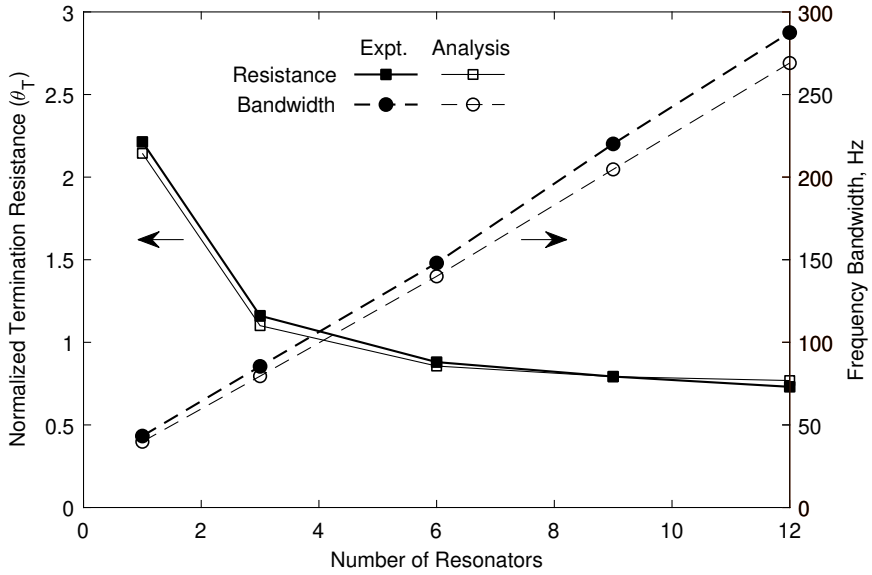

Figure 6.5: Normalized termination resistance at resonance and absorption frequency bandwidth of various numbers of half-wave resonators measured in the two-sided impedance tube and calculated using the simplified analytical expressions developed in Section 5.2.

Figure 6.5 also compares the measured absorption frequency bandwidth of the various numbers of half-wave resonators to the corresponding values predicted by the simplified analytical expression given by Eq. (5.37). Equation (5.37) predicts that the absorption frequency bandwidth varies as $BW \propto (\sigma + \theta_{0,\text{eff}})$, and Figure 6.5 indicates that the measured bandwidth indeed follows this trend reasonably closely as the number of resonators increases. Therefore, the change in the absorption frequency bandwidth as the number of resonators increases is also well explained by the simplified analytical expressions developed in Section 5.2.

6.5.2 Effect of the Number of Injectors on the Resonance Frequency

The resonance frequency also increases as the number of resonators increases. This observation has not been reported elsewhere, including by Park and Sohn [11], who conducted

similar experiments. For this analysis, it is assumed that the length correction at the area discontinuity between a resonator and the impedance tube, $\Delta L_{1,2}$, is not a function of the number of resonators. However, the normalized reactance at the inlet end of each resonator, χ_L, which is described by the imaginary part of Eq. (5.19), modifies the length correction at the inlet of each resonator, and the resulting length correction is given by

$$\Delta L_L = \Delta L_{1,2} - \frac{(1-\sigma)\tan(kL_e)}{k[1+(1-\sigma)^2\tan^2(kL_e)]} \tag{6.3}$$

The second term in this expression describes the effect of the acoustic oscillations within the cavity surrounding the extension of the resonators into the impedance tube on the length correction at the inlet end of the resonators, so the term vanishes if $L_e = 0$. The extension length of the multiple stainless steel resonators shown in Figure 4.14 is 30.68 mm. The acoustic oscillations within the cavity cause the length correction at the inlet end of the resonators to decrease as the open area ratio increases for this configuration. Thus, the analysis predicts that the resonance frequency increases as the number of resonators increases, and indeed, this trend is observed in the measurements shown in Figure 6.4.

6.5.3 Sound Power Dissipation and Transmission of Multiple Injectors

The power dissipation coefficients of various numbers of half-wave resonators measured in the two-sided impedance tube are shown in Figure 6.6, and the power transmission coefficients of the same configurations are shown in Figure 6.7. For a single half-wave resonator, the fraction of the incident sound power that is dissipated at resonance is several times greater than the fraction that is transmitted; however, as the number of resonators increases, the peak power dissipation coefficient decreases, and the peak power transmission coefficient increases. The measured power absorption, dissipation, and transmission coefficients at resonance are plotted as functions of the number of resonators in Figure 6.8. The analytical estimates for the power absorption, dissipation, and transmission coefficients at

resonance given by Eqs. (5.32)–(5.34) are also plotted in Figure 6.8. The simplified analytical expressions show reasonable agreement with the measured data, which confirms that the expressions are sufficiently accurate to obtain a proper physical understanding of the acoustic damping mechanisms. A more accurate prediction of the power dissipation and transmission coefficients is provided by the numerical model described in Section 5.3; the comparison between the numerical model and the experimental results is presented in Section 6.7.

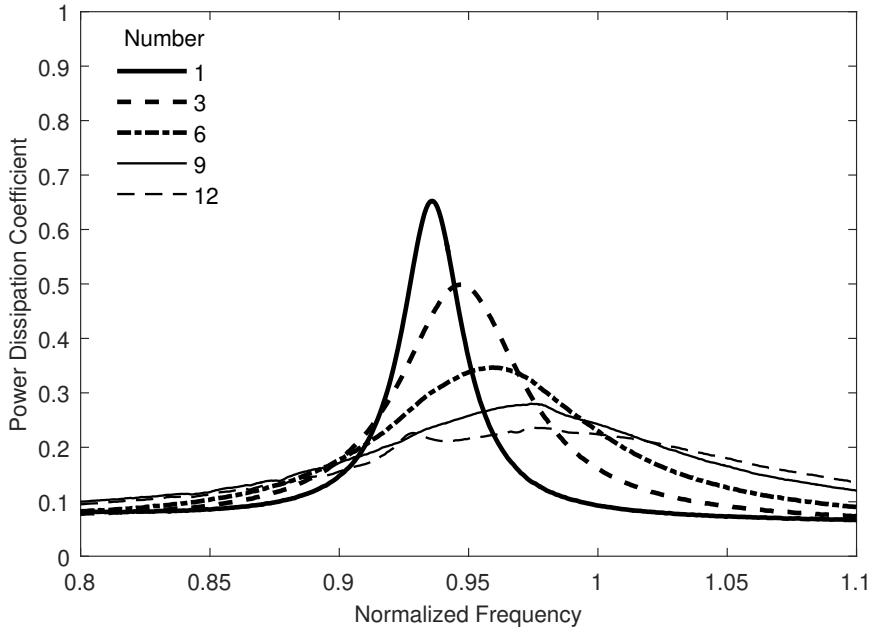

Figure 6.6: Power dissipation coefficients of various numbers of half-wave resonators measured in the two-sided impedance tube.

6.6 Effect of the Position of the Injectors

The effect of the position and distribution of the propellant injectors on the injector faceplate was measured using various configurations of half-wave resonators, as shown in Figure 6.9. The configurations are designated by the total number of resonators and the positions of the resonators on the "inner," "outer," or "both" rings.

Figure 6.10 shows the absorption coefficients of each of these configurations measured in the two-sided impedance tube. Park and Sohn [11] found that the spatial distribution

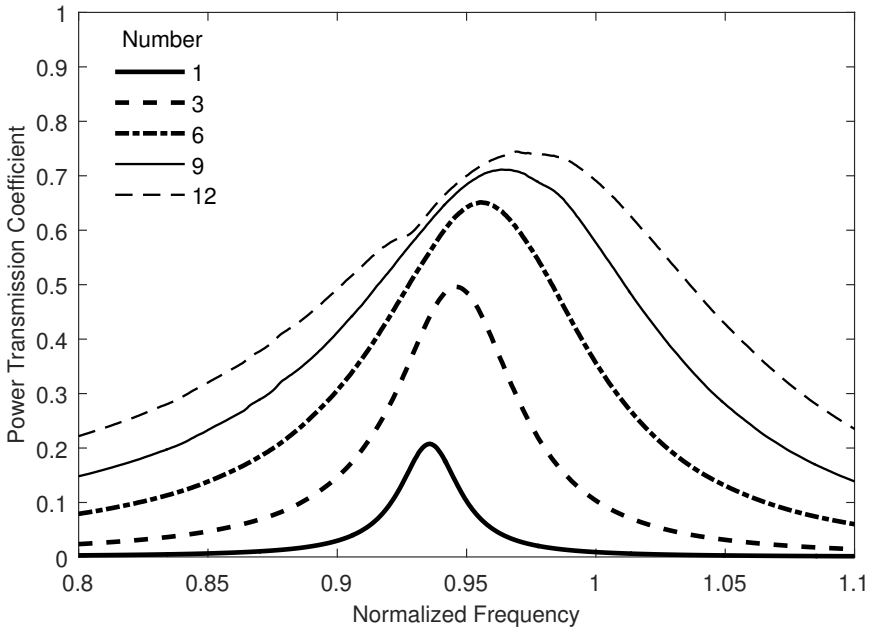

Figure 6.7: Power transmission coefficients of various numbers of half-wave resonators measured in the two-sided impedance tube.

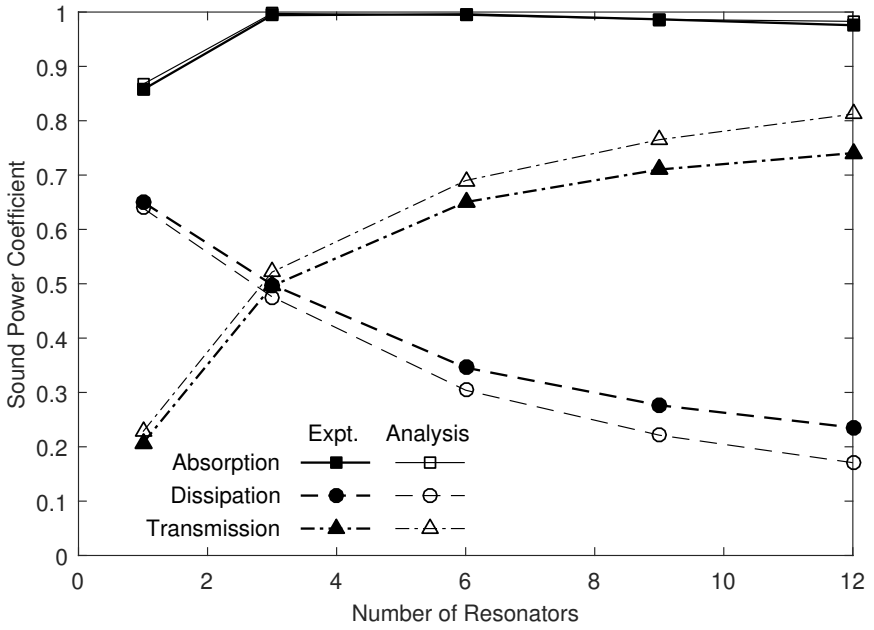

Figure 6.8: Power absorption, dissipation, and transmission coefficients of various numbers of half-wave resonators at resonance in the two-sided impedance tube.

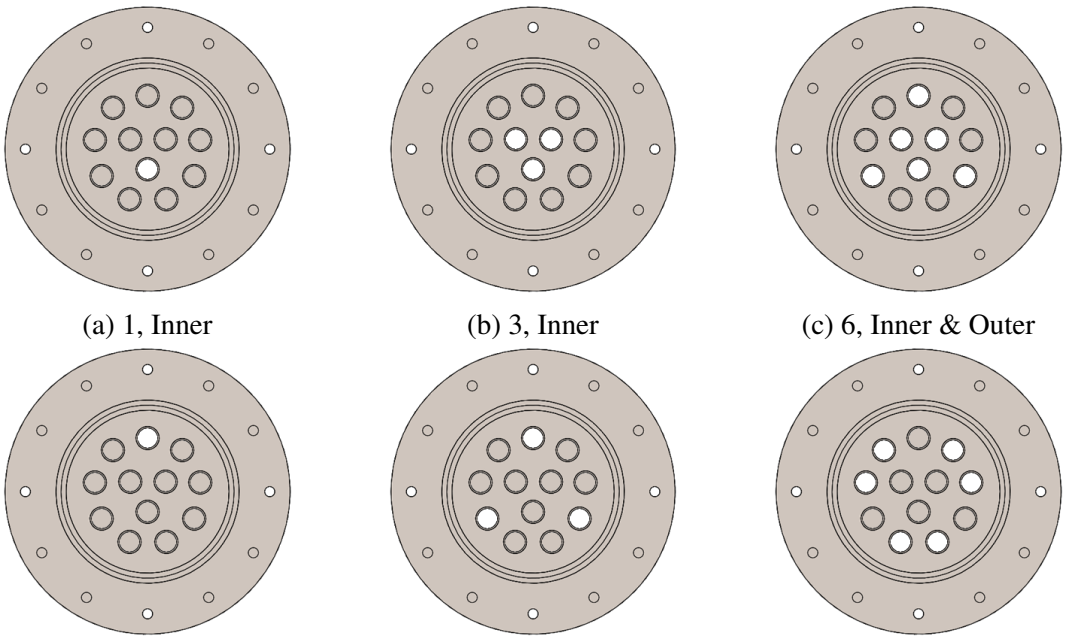

(a) 1, Inner (b) 3, Inner (c) 6, Inner & Outer

(d) 1, Outer (e) 3, Outer (f) 6, Outer

Figure 6.9: Number and positions of the half-wave resonators.

of resonators has a negligible effect on the absorption coefficient for plane-wave propagation. The current results also show that the peak absorption coefficient and the absorption frequency bandwidth are nearly identical for a given number of resonators, regardless of the position of the resonators. However, the current results indicate that the position of the resonators has a non-negligible effect on the resonance frequency, and the direction of this effect depends on the number of resonators. The resonance frequency of a single half-wave resonator mounted in the outer ring (Figure 6.9d) is lower than the resonance frequency of the same resonator mounted in the inner ring (Figure 6.9a), but the resonance frequency of three half-wave resonators mounted in the outer ring (Figure 6.9e) is higher than the resonance frequency of the same three resonators mounted in the inner ring (Figure 6.9b).

The acoustic pressure and particle velocity of a plane wave is constant throughout the cross-section, so the position of a resonator within the cross-section of the impedance tube should theoretically have no effect on the measured acoustic properties in the plane wave regime. However, evanescent higher-order modes are formed to satisfy the boundary conditions at an area discontinuity, and these evanescent modes are responsible for the length

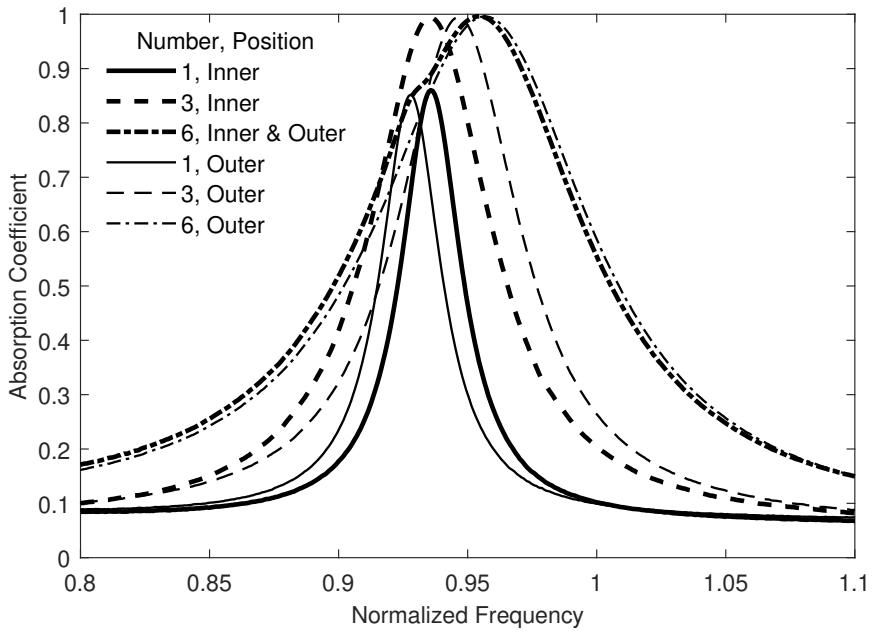

Figure 6.10: Absorption coefficients of various numbers of half-wave resonators in different positions measured in the two-sided impedance tube.

correction at the area discontinuity. The expression for the length correction given by Eq. (5.6) was developed assuming that the ducts forming the area discontinuity are concentric [145]. The evanescent higher-order modes that are required to satisfy the boundary conditions at an area discontinuity between non-concentric ducts are different than those required at an area discontinuity between concentric ducts, so it stands to reason that the length correction at an area discontinuity is a function of the position of the resonator within the cross-section. However, these effects are due to higher-order modes and cannot be adequately described using the plane wave assumptions. A more complete analysis of the effect of the position and distribution of the propellant injectors on the injector faceplate is provided in Chapter 10, which is dedicated to the discussion of the effects of higher-order modes.

6.7 Validation of the Numerical Model

In this section, the numerical model described in Section 5.3 (and developed in detail in Appendix C) is validated by comparing the predictions to the measured results for propellant

injectors with realistic geometric features and multiple half-wave resonators.

6.7.1 Numerical Model for a Single Propellant Injector

The predicted power absorption, dissipation, and transmission coefficients of the injectors with different geometric features are compared to the measurements as shown in Figures 6.11, 6.12, and 6.13, respectively. The predicted power absorption, dissipation, and transmission coefficients are close to the measured results for each injector. The errors between the predicted and measured results for the absorption coefficient are summarized in Table 6.2. The percentage error between the numerical model and the measured data is less than 0.5% for the resonance frequency, less than 2.5% for the peak absorption coefficient, and less than 5.5% for the absorption frequency bandwidth. These errors are relatively small, so the numerical model is judged to perform reasonably well for a single injector with and without an inlet protrusion and a recess.

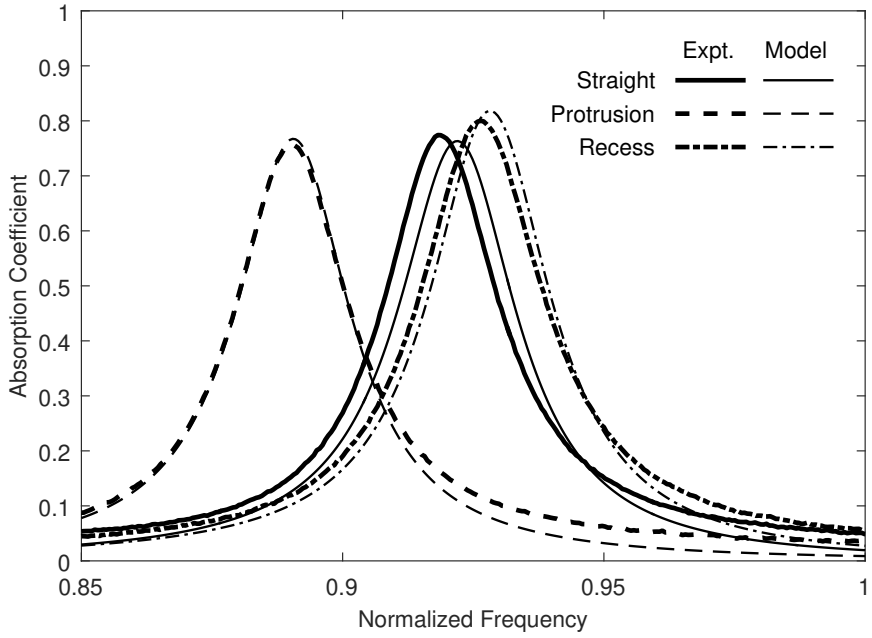

Figure 6.11: Comparison between the numerical model prediction and the measured absorption coefficients for the injectors with different geometric features.

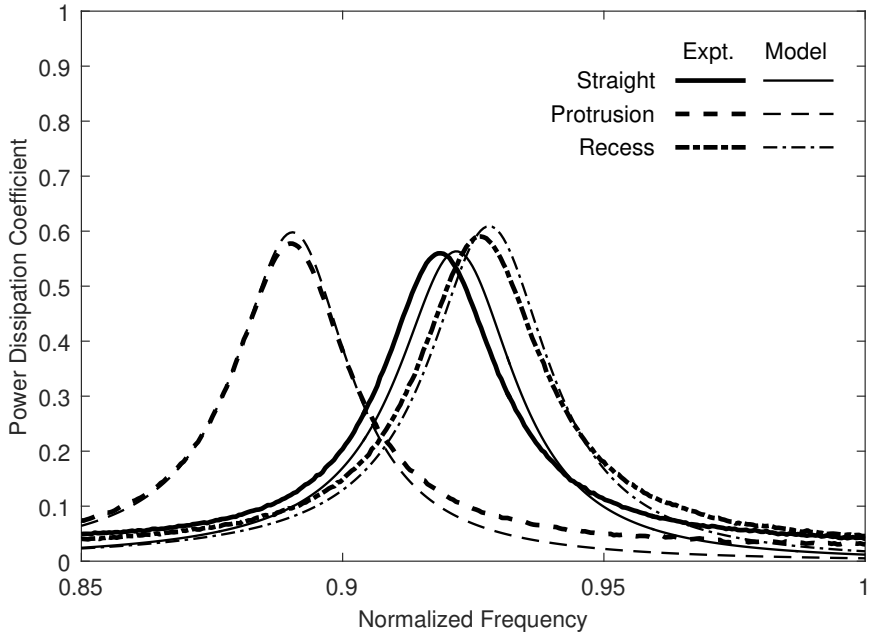

Figure 6.12: Comparison between the numerical model prediction and the measured power dissipation coefficients for the injectors with different geometric features.

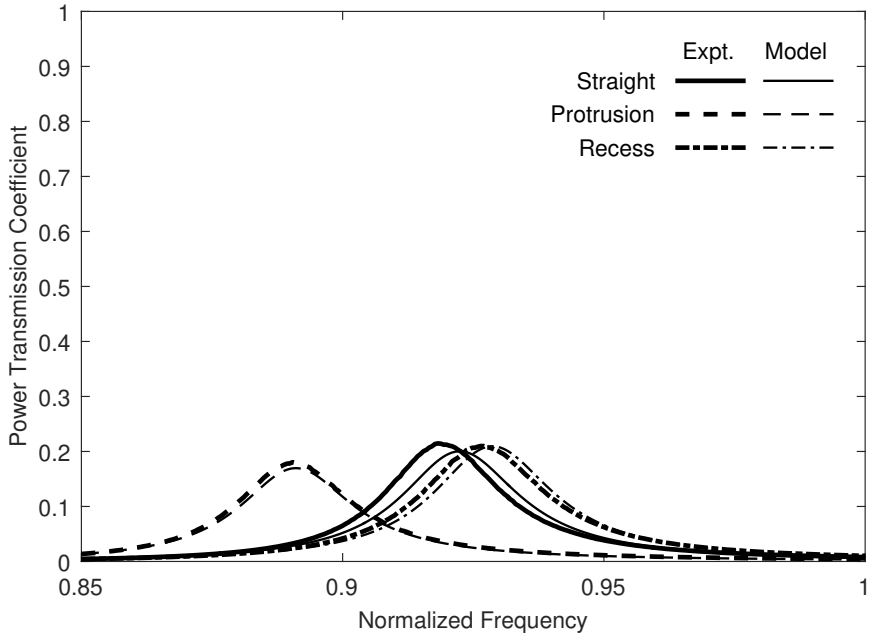

Figure 6.13: Comparison between the numerical model prediction and the measured power transmission coefficients of the injectors with different geometric features.

Table 6.2: Percentage errors between the numerical model and the measured data for the injectors with different geometric features.

Injector	Resonance	Peak Absorption	Bandwidth
Straight	0.43%	-1.4%	-0.94%
Protrusion	0.14%	1.3%	-3.3%
Recess	0.28%	2.2%	-5.3%

6.7.2 Numerical Model for Multiple Half-Wave Resonators

The numerical model described in Section 5.3 (and developed in detail in Appendix C) can also be applied to multiple propellant injectors. The predicted absorption coefficients of different numbers of half-wave resonators are compared to the corresponding measurements in order to validate the numerical model for multiple injectors, and the results are shown in Figure 6.14. The errors between the predicted and measured values are summarized in Table 6.3. The percentage error between the numerical model and the measured data is 1.1% or less for the resonance frequency and peak absorption coefficient. Additionally, the percentage error is less than 10% for the absorption frequency bandwidth. These errors are reasonably small, and the model conservatively underpredicts the absorption frequency bandwidth. Therefore, the numerical model is judged to perform acceptably well for multiple half-wave resonators.

Table 6.3: Percent errors between the numerical model and the measured data for different numbers of half-wave resonators.

Number	Resonance	Peak Absorption	Bandwidth
1	0.16%	0.52%	-8.2%
3	-0.44%	0.49%	-9.6%
12	-1.1%	-1.1%	-7.1%

The numerical model applies existing expressions from the literature for the length correction, $\Delta L_{1,2}$, the resistance correction, $\theta_{1,2}$, and the attenuation coefficient, β. These ex-

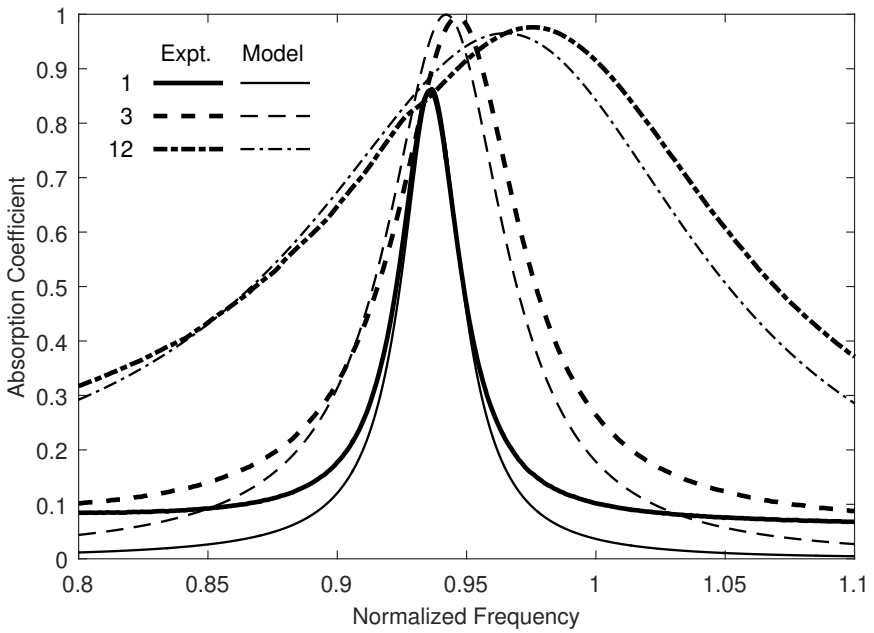

Figure 6.14: Comparison between the numerical model prediction and the measured absorption coefficients of different numbers of half-wave resonators.

pressions could be empirically adjusted to account for surface roughness and other effects, which could force the numerical model to better fit the measured data. However, in order to keep the numerical model as general as possible, these expressions are not adjusted, and the numerical model is still judged to be sufficiently accurate.

6.8 Summary

In this chapter, the effects of geometric parameters on the acoustic damping of propellant injectors were investigated in quiescent air at ambient conditions in the linear acoustic regime for the plane wave mode. The effects of the geometric parameters and the contributions of the physical mechanisms responsible for the acoustic damping are summarized below.

Effect of the Geometric Features

A straight cylindrical injector, which represents the main body of a propellant injector, was shown to behave like an ideal half-wave resonator: it has a high peak absorption coeffi-

cient and a relatively narrow absorption frequency bandwidth. Table 6.4 summarizes the measured effects of the other geometric features of propellant injectors on the resonance frequency and the normalized resistance at resonance. It was shown that the peak absorption coefficient is a function of the normalized resistance at resonance and is governed by the $\chi_T = 0$ curve plotted in Figure 5.2. Additionally, the absorption frequency bandwidth was shown to increase approximately linearly with the normalized resistance based on Eq. (5.37). In a real propellant injector, the liquid propellant injected through the fuel holes into the annulus has a significantly higher impedance than the gaseous oxidizer, and the "recess" injector includes a hard wall where the liquid propellant would be. Therefore, it was suggested that the "recess" injector is likely the best model for the acoustic damping of an operating propellant injector.

Table 6.4: Effect of realistic geometric features on the acoustic properties of a propellant injector.

Geometric Feature	Resonance Frequency	Normalized Resistance
Inlet Protrusion	Decreases	Slightly Increases
Recess	Increases	Slightly Decreases
Annulus	Slightly Decreases	Negligible
Fuel Holes	Increases	Increases

Effect of the Open Area Ratio

As the open area ratio increases, the resonance frequency of a propellant injector was found to increase because the length correction at the area discontinuity between the injector and the impedance tube (or combustion chamber) decreases. The experiments and analysis also showed that the termination impedance of the impedance tube (or combustion chamber) is approximately inversely proportional to the open area ratio, and the absorption coefficient was shown to be a function of the termination impedance through Eq. (5.3). Finally, the absorption frequency bandwidth was shown to increase approximately linearly with the

open area ratio based on Eq. (5.37).

Effect of the Number of Injectors

The open area ratio is also a function of the number of injectors, but the measurements showed that there are subtle differences between varying the diameter of the impedance tube (or combustion chamber) and varying the number of injectors. It was shown that the length correction at the simple area discontinuity between the outlet ends of the injectors and the impedance tube (or combustion chamber) is not a function of the number of injectors. However, the length correction at the area discontinuity with the side branch formed by the extension of the inlet ends of the injectors into the impedance tube was shown to vary with the number of injectors based on Eq. (6.3). Thus, the resonance frequency was found to depend on the boundary condition at the inlet ends of the injectors. The experiments and analysis also showed that the termination impedance of the impedance tube (or combustion chamber) is approximately inversely proportional to the number of injectors, but the input impedance of each injector was shown to depend on the boundary condition at the inlet end, too. Finally, the absorption frequency bandwidth was shown to increase approximately linearly with the number of injectors based on Eq. (5.37), although the relationship is not exactly linear if the input impedance varies.

Effect of the Position of the Injectors

The position of the injectors on the injector faceplate should theoretically have no effect on the acoustic damping in the plane wave regime. The position indeed was found to have a negligible effect on the peak absorption coefficient and the absorption frequency bandwidth, but the resonance frequency was found to be affected by the position due to the formation of evanescent higher-order modes at the area discontinuity between the injectors and the impedance tube (or combustion chamber). The role of the evanescent higher-order modes on the effect of position is discussed in more detail in Chapter 10.

Analytical and Numerical Models

The analytical expressions developed in Section 5.2 were shown to be useful for gaining a physical understanding of the effects of the open area ratio and the number of injectors. The numerical model for one or more propellant injectors developed in Section 5.3 was shown to accurately predict the power absorption, dissipation, and transmission coefficients measured experimentally.

Acoustic Damping Mechanisms

For the experiments discussed in this chapter, it was shown that the physical mechanisms responsible for the acoustic damping are viscothermal losses in the acoustic boundary layer and acoustic radiation from the open end of the injectors opposite the incident acoustic waves. The viscothermal dissipation was modeled by the Kirchhoff wavenumber, and the resulting contribution to the acoustic damping was measured directly by the power dissipation coefficient. The acoustic radiation was modeled by the radiation impedance, and the resulting contribution to the acoustic damping was measured directly by the power transmission coefficient. The acoustic radiation accounts for the transmission of sound power and does not actually represent a power dissipation process, but the radiation contributes to the acoustic damping of the propellant injectors because the transmitted sound power is removed from the combustion chamber.

CHAPTER 7
EFFECT OF BIAS FLOW

7.1 Overview

In this chapter, the effects of bias flow on the acoustic damping of propellant injectors are investigated for the following geometric parameters:

- Geometric features of the injectors
- Number of injectors

The experiments presented in this chapter are conducted in the two-sided impedance tube using the 3D-printed propellant injectors with unique geometric features (see Figures 4.10–4.12) and multiple stainless steel half-wave resonators (see Figure 4.14). The experiments are conducted at different mean flow rates at ambient temperature in the linear acoustic regime for the plane wave mode. The primary physical mechanisms responsible for the acoustic damping in the experiments described in this chapter include:

- Viscous and thermal losses in the acoustic boundary layer
- Acoustic radiation from the open end of the injectors opposite the incident acoustic waves
- Dissipation due to turbulence
- Conversion of acoustic energy to vorticity at the open ends of the injectors

The outline of this chapter is as follows: First, in Section 7.2, the simplified analytical expressions for the acoustic damping of half-wave resonators near resonance that were developed in Chapter 5 in the absence of flow are extended to include bias flow. Considerations for including the effects of bias flow in the numerical model are also discussed in

Section 7.3. Next, in Sections 7.4–7.5, the effects of bias flow on the acoustic damping are investigated experimentally using three of the propellant injectors with different geometric features and multiple half-wave resonators, and the measured results are compared to the simplified analytical expressions. Finally, a discussion of underdamping, overdamping, and optimal damping is included in Section 7.6 based on the measurements of the acoustic damping of multiple half-wave resonators with bias flow.

7.2 Analytical Expressions in the Presence of Flow

In Section 5.2, simplified expressions for the acoustic damping and resonance frequency were derived for half-wave resonators in a quiescent medium to provide an understanding of the acoustic damping mechanisms. In this section, similar derivations are performed for half-wave resonators in the presence of bias flow.

7.2.1 Effect of Flow on the Resonance Frequency

The resonance frequency of a half-wave resonator in the absence of flow is given by Eq. (2.8). Acoustic waves are convected by a mean flow, so the resonance frequency of a resonator changes due to the presence of bias flow. The propagation speeds of the acoustic waves in the upstream and downstream directions are described by $c^- = c - \overline{U}$ and $c^+ = c + \overline{U}$, respectively, where $\overline{U}$ is the velocity of the mean flow in the resonator [24]. The time-of-flight required for an acoustic wave to make a round trip in the upstream and downstream directions in a half-wave resonator of effective length L_{eff} is given by

$$t = \frac{L_{\text{eff}}}{c + \overline{U}} + \frac{L_{\text{eff}}}{c - \overline{U}} \tag{7.1}$$

which can be written in terms of the Mach number as

$$t = \frac{L_{\text{eff}}}{c(1 + M)} + \frac{L_{\text{eff}}}{c(1 - M)} \tag{7.2}$$

The fundamental resonance frequency is given by the inverse of the time-of-flight:

$$f_0 = \frac{c}{2L_{\text{eff}}}(1 - M^2) \tag{7.3}$$

The fundamental resonance frequency of a half-wave resonator without flow can be written as $f_0 = c/(2L_{\text{eff}})$, so Eq. (7.3) shows that convection of the acoustic waves by the mean flow modifies the resonance frequency of a half-wave resonator by the factor $(1 - M^2)$.

7.2.2 Normalized Resistance at the Inlet and Outlet of a Duct

Bias flow modifies not only the resonance frequency, but also the normalized resistance of a half-wave resonator. A number of studies have shown that the acoustic resistance of an orifice, resonator, or open end of a pipe increases monotonically with the velocity of the bias flow. For example, Ingard and Ising [54] found that the specific acoustic resistance of an orifice increases linearly with the velocity of the bias flow above some nonzero velocity, as shown earlier in Figure 2.16. Ingard and Singhal [33] showed that the flow losses at the open end of a pipe with a mean flow are significantly greater than the losses due to acoustic radiation, and the normalized resistance at the outlet end of the pipe is approximately equal to the Mach number at relatively low frequencies and Mach numbers. Bechert [42] and Salikuddin and Ahuja [43] demonstrated that the sound dissipation mechanism at the outlet of a pipe with mean flow is the conversion of acoustic energy into the kinetic energy of fluctuating vortices, which shed from the edge of the pipe and convect downstream. Howe [52] developed a theory for the dissipation of sound at the exit of a pipe with mean flow by applying the Kutta condition and calculating the dissipation due to the conversion of acoustic energy into the kinetic energy of the vortices. Substitution of Eq. (3.29) from Ref. [52] into Eq. (3.61) in the current work reveals that the normalized impedance at the

outlet end of a pipe with a mean flow is given by

$$\zeta = M + \left[\frac{1}{4}(ka)^2 + jk\Delta L\right] \tag{7.4}$$

The term in square brackets is identical to Eq. (2.4), which describes the normalized radiation impedance of an unflanged pipe in the absence of flow. Therefore, Howe's theory [52] predicts that the normalized resistance at the outlet end of a pipe increases by an amount equal to the Mach number of the mean flow.

Ingard and Singhal [33] showed that losses also occur at the inlet end of a pipe with mean flow, but the losses at the inlet are less than those at the outlet. For this simplified analysis, the flow losses at a contraction are neglected based on the recommendation of Davies [24], and the additional losses due to flow at an expansion are represented by a normalized resistance, θ_F. The form of the normalized resistance due to flow is assumed to be

$$\theta_F = \begin{cases} 0, & M < M_F \\ M - M_F, & M \geq M_F \end{cases} \tag{7.5}$$

where the constant M_F is the Mach number at which the flow losses become non-negligible. The slope of θ_F is theoretically unity based on the result of Howe's theory [52] given by Eq. (7.4). The constant M_F is included based on the experimental results of Ingard and Singhal [33], who found that the normalized resistance increases with Mach number only when the mean flow exceeds some nonzero Mach number. This constant must be determined empirically and may vary depending on the particular configuration.

7.2.3 Impedance Near Resonance in the Presence of Flow

In Section 5.2, a simplified expression for the impedance of the half-wave resonator shown in Figure 5.1 was obtained at frequencies near resonance in a quiescent medium. The resulting expression was helpful for understanding the mechanisms that contribute to the

acoustic damping of half-wave resonators in the absence of flow. In this section, a similar derivation is performed for half-wave resonators with bias flow.

In the absence of flow, the normalized input impedance of a straight cylinder of length L is given by Eq. (5.14). In the presence of flow, the corresponding expression is

$$\zeta_0 = \theta_F + \frac{\zeta_L + j\tan(\overline{k}L)}{1 + j\zeta_L\tan(\overline{k}L)} \tag{7.6}$$

where θ_F is the normalized resistance due to the mean flow given by Eq. (7.5), ζ_L is the normalized impedance of the open end of the resonator at $z = -L$ given by Eq. (5.19), and $\overline{k} = (k^+ + k^-)/2$ is the mean of the upstream and downstream wavenumbers. The flow losses at the inlet end of the resonator at $z = -L$ are neglected based on the recommendation of Davies [24], so ζ_L is assumed to be unmodified by the presence of flow. The outlet end of the resonator at $z = 0$ forms a flow expansion with the impedance tube, so the normalized resistance due to the mean flow at the area expansion, θ_F, is added directly to the normalized input impedance of the resonator.

In general, the wavenumber is complex due to the viscothermal losses in the acoustic boundary layer at the walls of the resonator. Kirchhoff [119, 120] obtained a solution for the complex wavenumber of the plane wave mode in the absence of flow, and Weng and Bake [121] incorporated the convective effects of a uniform mean flow into the Kirchhoff wavenumber. Their result is given by Eq. (3.18), which is repeated here:

$$k^{\pm} = \frac{\omega/c}{1 \pm M} + \frac{(1-j)\beta}{(1 \pm M)^{3/2}} \tag{7.7}$$

The attenuation coefficient, β, given by Eq. (3.17) is of the order $\beta \sim (\omega/c)(\delta/a)$, where $\delta = \sqrt{2\nu/\omega}$ is the thickness of the acoustic boundary layer. The wide duct assumption used in the derivation of the Kirchhoff wavenumber requires that $\delta/a \ll 1$, which is satisfied for the injectors used in these experiments. Therefore, $\beta \ll \omega/c$, so the real part of the Kirchhoff wavenumber in terms of β can be neglected compared to the real part in terms of

ω/c. The mean wavenumber is then derived as

$$\overline{k} \approx \frac{\omega/c}{1-M^2} - j\beta\left[\frac{(1+M)^{3/2}+(1-M)^{3/2}}{2(1-M^2)^{3/2}}\right] \tag{7.8}$$

The term in square brackets can be approximated by a Taylor series expansion at $M = 0$, so Eq. (7.8) can be rewritten, neglecting terms of order higher than M^2, as

$$\overline{k} \approx \frac{\omega/c}{1-M^2} - j\beta(1+1.875M^2) \tag{7.9}$$

Thus, the magnitudes of both the real and imaginary parts of the complex wavenumber increase due to bias flow.

Following the procedure outlined in Section 5.2.5, let $\omega = \omega_0 + \Delta\omega$ near resonance, where ω_0 is the resonance frequency of the half-wave resonator. If the length correction, ΔL, is neglected in Eq. (7.3), then the resonance frequencies of a half-wave resonator with mean flow are given by

$$\omega_0 = \frac{n\pi c}{L}(1-M^2) \tag{7.10}$$

The tangent of the complex argument $\overline{k}L$ can be approximated as

$$\tan(\overline{k}L) \approx \frac{\Delta\omega L}{c(1-M^2)} - \frac{j\beta L(1+1.875M^2)}{1-\left(\frac{\Delta\omega L}{c(1-M^2)}\right)^2} \tag{7.11}$$

Substituting Eq. (7.11) into Eq. (7.6) and making the appropriate order-of-magnitude approximations yields

$$\zeta_0 \approx \left[\theta_F + \theta_L + \beta L(1+1.875M^2)\right] + j\left[\chi_L + \frac{\Delta\omega L}{c(1-M^2)}\right] \tag{7.12}$$

Therefore, the effective normalized input resistance and reactance of the resonator are given

by

$$\begin{aligned} \theta_{0,\text{eff}} &\approx \theta_F + \theta_L + \beta L(1 + 1.875M^2) + \theta_{1,2} \\ \chi_{0,\text{eff}} &\approx \chi_L + \frac{\Delta\omega L}{c(1-M^2)} + \chi_{1,2} \end{aligned} \tag{7.13}$$

Finally, the normalized termination resistance and reactance near resonance are approximated by $\theta_T \approx \theta_{0,\text{eff}}/\sigma$ and $\chi_T \approx \chi_{0,\text{eff}}/\sigma$, respectively, based on Eq. (5.11). The details of the steps leading to the above approximations are discussed in Section 5.2.5.

7.2.4 Sound Power Coefficients in the Presence of Flow

In the absence of flow, the normalized termination resistance and reactance uniquely determine the absorption coefficient, as expressed by Eq. (5.3). In the presence of a mean flow, the absorption coefficient is a function of the Mach number, too. If the incident acoustic waves propagate in the direction opposite the mean flow, then the absorption coefficient can be written as

$$A = \frac{4\left[\theta_T - M_T(\theta_T(\theta_T - M_T) + \chi_T^2 + 1)\right]}{(1-M_T)^2\left[(1+\theta_T)^2 + \chi_T^2\right]} \tag{7.14}$$

where M_T is the Mach number of the flow in the impedance tube. If, instead, the incident acoustic waves propagate in the same direction as the mean flow, then M_T is negative in Eq. (7.14). In the experiments presented in this chapter, the Mach number of the flow in the impedance tube is sufficiently low that $M_T^2 \ll 1$, so the absorption coefficient is approximately

$$A \approx \frac{4\left[\theta_T - M_T(\theta_T^2 + \chi_T^2 + 1)\right]}{(1-2M_T)\left[(1+\theta_T)^2 + \chi_T^2\right]} \tag{7.15}$$

Figure 7.1 shows the absorption coefficient as a function of the normalized termination resistance at resonance ($\chi_T = 0$) for different values of the Mach number. The maximum absorption coefficient at $\theta_T = 1$ is unchanged by the presence of bias flow. At values of the normalized termination resistance other than one, the absorption coefficient increases with Mach number if the incident acoustic waves and bias flow are in the same direc-

tion ($M_T < 0$), but the absorption coefficient decreases with Mach number if the incident acoustic waves and bias flow are in opposite directions ($M_T > 0$).

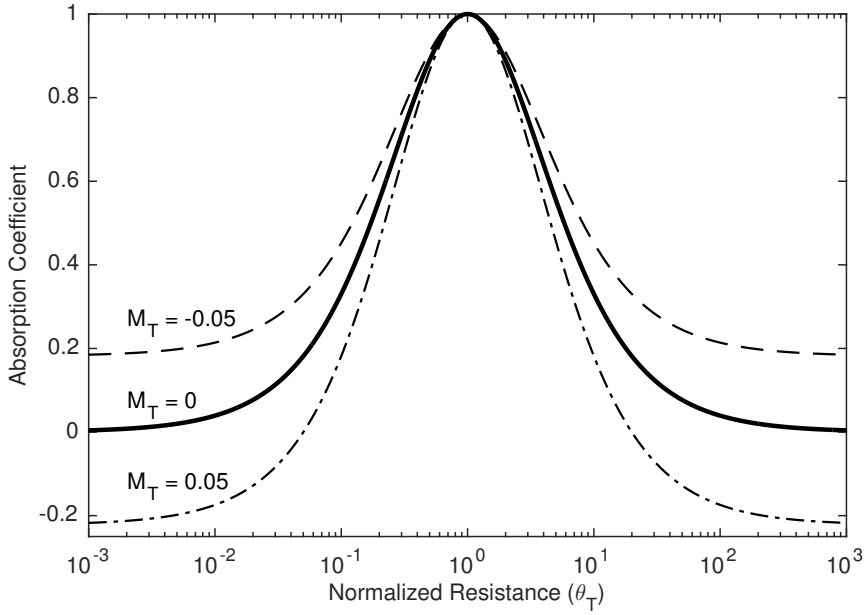

Figure 7.1: Absorption coefficient versus normalized termination resistance at resonance for different values of the Mach number.

Alternatively, the absorption coefficient can be written in terms of the effective normalized input impedance and the Mach number in the resonator. Substitution of $M_T = \sigma M$, $\theta_T = \theta_{0,\text{eff}}/\sigma$, and $\chi_T = \chi_{0,\text{eff}}/\sigma$ into Eq. (7.15) results in the expression

$$A \approx \frac{4\sigma\left[\theta_{0,\text{eff}} - M(\theta_{0,\text{eff}}^2 + \chi_{0,\text{eff}}^2 + \sigma^2)\right]}{(1-2\sigma M)\left[(\sigma+\theta_{0,\text{eff}})^2 + \chi_{0,\text{eff}}^2\right]} \tag{7.16}$$

The orders of the individual terms in Eq. (7.13) are $\theta_F \sim M$, $\theta_L \sim \sigma$, $\beta L \sim \pi\delta/a$, and $\theta_{1,2} \sim \pi\delta/L$ at the fundamental resonance frequency of the half-wave resonator. The open area ratio and Mach number are relatively small for the experiments presented in this chapter, and the thickness of the acoustic boundary layer is significantly smaller than the radius and length of the resonator, so the effective normalized input resistance, $\theta_{0,\text{eff}}$, is typically considerably smaller than one for the half-wave resonators. Therefore, the terms $M\theta_{0,\text{eff}}^2$ and $M\sigma^2$ in Eq. (7.16) can be neglected compared to $\theta_{0,\text{eff}}$, and a simpler expression

for the absorption coefficient is given by

$$A \approx \frac{4\sigma(\theta_{0,\text{eff}} - M\chi_{0,\text{eff}}^2)}{(1-2\sigma M)\left[(\sigma+\theta_{0,\text{eff}})^2 + \chi_{0,\text{eff}}^2\right]} \tag{7.17}$$

which is valid for low Mach numbers and small open area ratios. It is possible to obtain an analytical expression for the absorption frequency bandwidth from Eq. (7.17), but the resulting expression is too cumbersome to provide a physical understanding of the mechanisms that affect the bandwidth.

As discussed in Section 5.2.6, the effective normalized input resistance of the resonator can be decomposed into two components, $\theta_{0,\text{eff}} = \theta_{0,\text{eff},D} + \theta_{0,\text{eff},T}$, where $\theta_{0,\text{eff},D}$ is the part of the resistance that governs dissipation, and $\theta_{0,\text{eff},T}$ is the part of the resistance that governs transmission. These components are assumed to be $\theta_{0,\text{eff},D} \approx \theta_F + \beta L(1+1.875M^2) + \theta_{1,2}$ and $\theta_{0,\text{eff},T} \approx \theta_L$ based on Eq. (7.13). Estimates of the power dissipation and transmission coefficients are then given by splitting Eq. (7.17) into

$$D^{\Pi} \approx \frac{4\sigma(\theta_{0,\text{eff},D} - M\chi_{0,\text{eff}}^2)}{(1-2\sigma M)\left[(\sigma+\theta_{0,\text{eff}})^2 + \chi_{0,\text{eff}}^2\right]} \tag{7.18}$$

and

$$T^{\Pi} \approx \frac{4\sigma\theta_{0,\text{eff},T}}{(1-2\sigma M)\left[(\sigma+\theta_{0,\text{eff}})^2 + \chi_{0,\text{eff}}^2\right]} \tag{7.19}$$

These analytical expressions for the sound power coefficients in the presence of flow are compared to the experimental measurements in subsequent sections, and they are shown to be useful for providing a physical understanding of the damping mechanisms of half-wave resonators with bias flow.

7.3 On the Numerical Model in the Presence of Flow

The analytical expressions for the sound power coefficients of half-wave resonators developed in the previous section are intended to provide an understanding of the acoustic damp-

ing mechanisms in the presence of flow, but they are not expected to predict the acoustic damping of propellant injectors with perfect quantitative accuracy. In Chapter 6, the analytical expressions developed in Section 5.2 in the absence of flow were shown to agree reasonably well with the corresponding measurements. However, the numerical model described in Section 5.3 (and developed in detail in Appendix C) was required to achieve close quantitative accuracy compared to the measured sound power coefficients. Additionally, only the numerical model could accurately predict the acoustic damping of propellant injectors with realistic geometric features.

As described in Appendix C, the numerical model for the acoustic damping of propellant injectors in the absence of flow was developed using the transfer matrix approach proposed by Munjal [148]. Munjal [148] also presented equations for the conservation of mass, momentum, and energy at a discontinuity in a duct with mean flow, and he expressed these equations as a transfer matrix of the form defined in Appendix C. Munjal included an empirical constant in the energy equation to account for the acoustic losses at the area discontinuity due to the mean flow. However, the numerical model using Munjal's transfer matrix formulation in the presence of flow suffers from the same limitations as the simplified analytical expressions developed in Section 7.2. For example, Munjal's equations do not account for the coupling between the acoustic waves and the hydrodynamic waves shed from the area discontinuity, which may lead to errors in the resonance frequency predicted by the numerical model for the reasons discussed in Section 7.4.3. Therefore, the numerical model described in Section 5.3 is not extended to include bias flow because the resulting model is no more accurate than the simplified analytical expressions derived in Section 7.2.

A higher-fidelity numerical model grounded more closely in theory would be required to accurately predict the acoustic damping of half-wave resonators with bias flow. For example, Howe [36, 52, 53] applied the Kutta condition to develop a theory for the sound power dissipation at the exit of a pipe with a mean flow, so an accurate numerical model could be developed following a similar theoretical treatment at an area expansion in a circu-

lar duct. Crighton [51] stated that "[The Kutta condition] is the analytical step that in many cases describes the conversion—almost total—of acoustic energy in an incident sound wave to energy of vortical motion on a shear layer," so the accuracy of the numerical model is predicated on the application of the Kutta condition. Boij and Nilsson [62] also discussed the importance of the Kutta condition on the accuracy of their numerical model for the scattering and absorption of acoustic waves at an area expansion in a rectangular duct. In most of the models described in the literature, the incident acoustic waves propagate in the same direction as the mean flow, but the opposite is true for the experiments in this work. Dupère and Dowling [68] modeled the case in which the acoustic waves propagate in the opposite direction as the mean flow at an area expansion, and they applied their model to predict the absorption coefficient of a half-wave resonator with bias flow. Unfortunately, there were a number of errors in Ref. [68], so their results could not be reproduced. Therefore, there are no known models in the literature that accurately predict the acoustic damping of half-wave resonators with bias flow, but it is beyond the scope of this work to develop such an involved numerical model.

7.4 Effect of the Geometric Features in the Presence of Flow

7.4.1 Normalized Resistance of Unique Injectors in the Presence of Flow

The acoustic properties of the "straight," "protrusion," and "recess" propellant injectors were measured using the two-sided experimental facility, HOTMESS, to investigate the effects of the bias flow velocity on injectors with different geometric features. Figure 7.2 shows the normalized termination resistance, θ_T, at resonance for each injector as a function of the Mach number of the mean flow in the main body of the injector. The normalized resistance at resonance of the "protrusion" injector is only plotted at velocities up to Mach 0.1 because its reactance does not cross the zero axis at higher velocities, so its resonance frequency is undefined above Mach 0.1. The normalized resistance of each injector increases monotonically with the bias flow velocity, but the normalized resistance increases

more quickly with Mach number for the "protrusion" and "recess" injectors than for the "straight" injector. The main difference between these injectors is that the "protrusion" and "recess" injectors include an inlet protrusion, which has a cross-sectional area equal to about 51% of the area of the main body of the injector. Continuity requires that the Mach number of the mean flow through the inlet protrusion be roughly twice the Mach number of the flow through the main body of the injector if the flow is assumed to be incompressible. Previous studies on orifices [54] and the open ends of pipes [33, 52] with bias flow showed that the increase in the normalized resistance is linearly related to the Mach number, so the relative differences between the injectors were expected.

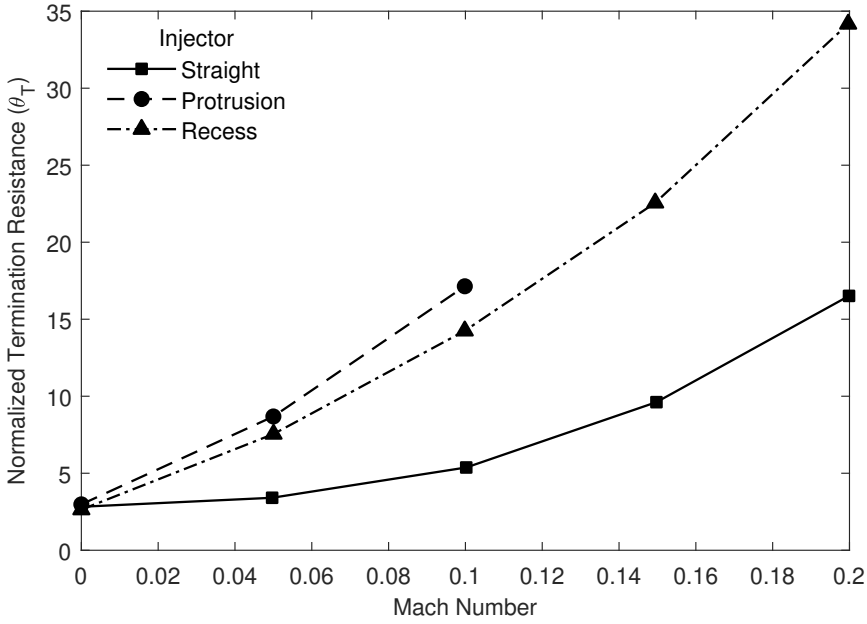

Figure 7.2: Normalized termination resistance at resonance as a function of the bias flow Mach number in the main body of the injector for the propellant injectors with different geometric features.

However, the measured increase in the normalized resistance of the propellant injectors shown in Figure 7.2 is not quite linear with respect to the Mach number. There are several notable differences between these measurements and previous studies that may account for this nonlinear relationship. Howe's theory [52] for the acoustic losses at the open end of a pipe with mean flow was developed for a pipe open to the ambient air and not for

a flow expansion in a duct, so the duct walls on the downstream side of the impedance tube may have an effect on the acoustic losses. In addition, the viscous losses across an orifice are small, but the viscothermal losses in the acoustic boundary layer at the walls of the injector are non-negligible. The viscothermal losses increase with Mach number based on the simplified expression given by Eq. (7.13), and the increase is even greater if the boundary layer becomes turbulent. For example, Peters, et al. [22] showed that the acoustic attenuation in a turbulent boundary layer is significant and can be approximately modeled by adding the eddy viscosity to the kinematic viscosity. Additionally, the change in cross-sectional area from the impedance tube to the injector is large, so losses may occur due to the generation of turbulence at the inlet of the injector. However, the acoustic properties measured in these experiments are insufficient to prove conclusively if these explanations are correct.

7.4.2 Absorption Coefficient of Unique Injectors in the Presence of Flow

Straight Injector

Figure 7.3 shows the absorption coefficient of the "straight" injector at different Mach numbers of the mean flow through the injector. As the Mach number of the mean flow increases, the peak absorption coefficient decreases and the absorption frequency bandwidth increases. The behavior of the peak absorption coefficient is related to the normalized resistance at resonance; this relationship is plotted in Figure 7.1. In the absence of flow, the normalized termination resistance of the "straight" injector is greater than one at resonance, so as the resistance increases with Mach number, the peak absorption coefficient decreases.

Inlet Protrusion

Figure 7.4 shows the absorption coefficient of the "protrusion" injector at different Mach numbers of the mean flow through the injector. The Mach number is measured in the main body of the injector, so the Mach number of the flow through the inlet protrusion is ap-

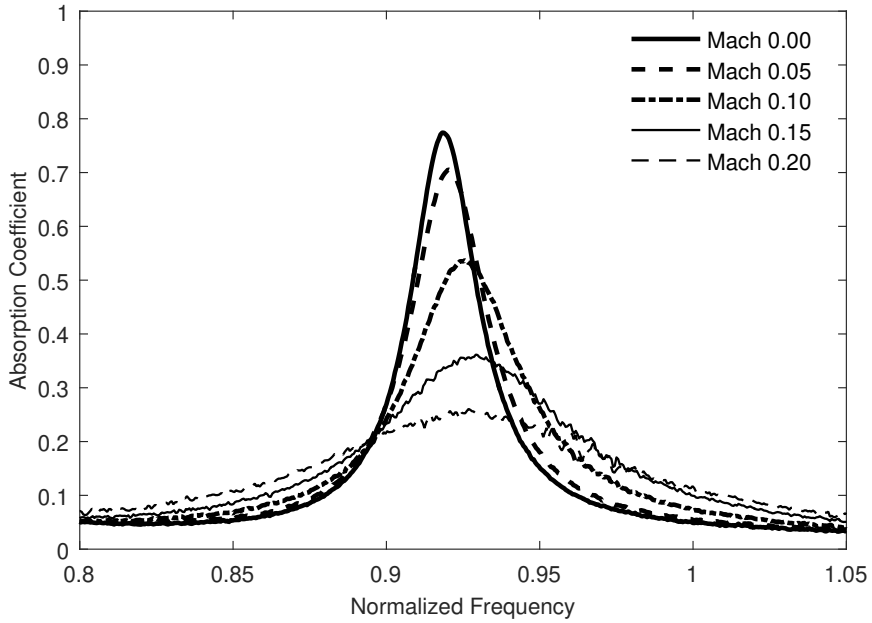

Figure 7.3: Absorption coefficient of the "straight" injector at different bias flow Mach numbers in the main body of the injector.

proximately twice the listed Mach number. The resonance frequency of the "protrusion" injector is lower than that of the "straight" injector at all flow rates for the reasons discussed in Section 6.2. As the bias flow Mach number increases, the peak absorption coefficient of the "protrusion" injector decreases more quickly than that of the "straight" injector. This corresponds to the behavior of the normalized resistance at resonance, which increases more quickly with Mach number for the "protrusion" injector than for the "straight" injector. These results show that the inlet protrusion, which has a relatively minor effect on the acoustic damping in a quiescent medium (besides shifting the resonance frequency), has a major effect on the behavior of the acoustic damping in the presence of bias flow.

Recess

Figure 7.5 shows the absorption coefficient of the "recess" injector at different Mach numbers of the mean flow through the injector. The Mach number is measured in the main body of the injector, so the Mach number of the flow through the inlet protrusion is approximately twice the listed Mach number. The recess increases the resonance frequency

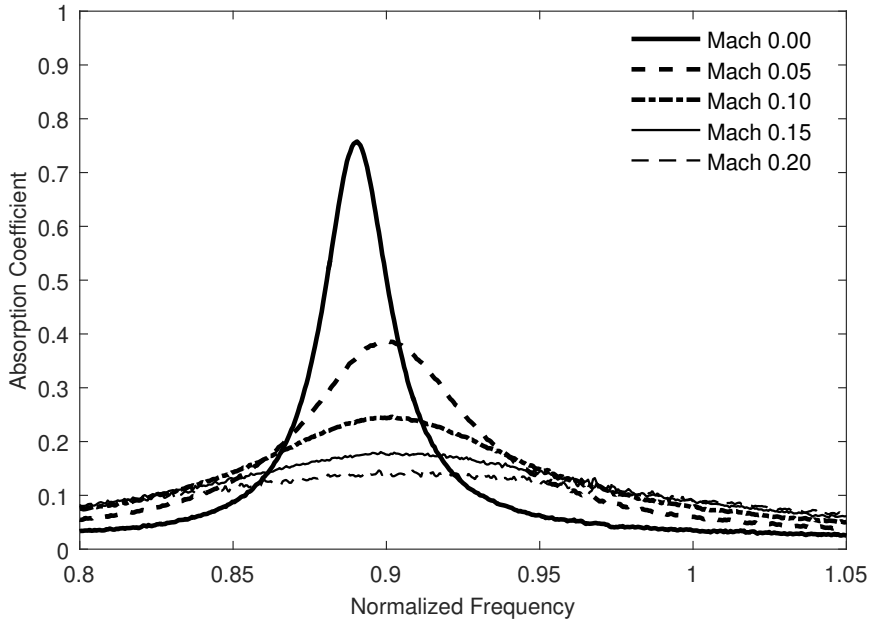

Figure 7.4: Absorption coefficient of the "protrusion" injector at different bias flow Mach numbers in the main body of the injector.

of the injector at all flow rates for the reasons discussed in Section 6.2. However, the peak absorption coefficient and the normalized resistance at resonance of the "recess" and "protrusion" injectors are similar at each bias flow Mach number. These results indicate that major effect of the recess is to shift the resonance frequency, but the effect of the recess on the acoustic damping is less than that of the inlet protrusion for nonzero bias flow.

Absorption Frequency Bandwidth of Unique Injectors in the Presence of Flow

Figure 7.6 shows the ratio of the absorption frequency bandwidth with mean flow to the absorption frequency bandwidth with no flow for each injector. The bandwidth increases monotonically with increasing Mach number for each injector, but the bandwidth of the "protrusion" and "recess" injectors increases more quickly with Mach number than the bandwidth of the "straight" injector. The behavior of the absorption frequency bandwidth is qualitatively similar to that of the normalized resistance for each injector. In the absence of flow, the absorption frequency bandwidth varies linearly with the normalized resistance according to the approximate analytical expression given by Eq. (5.37), and a similar trend

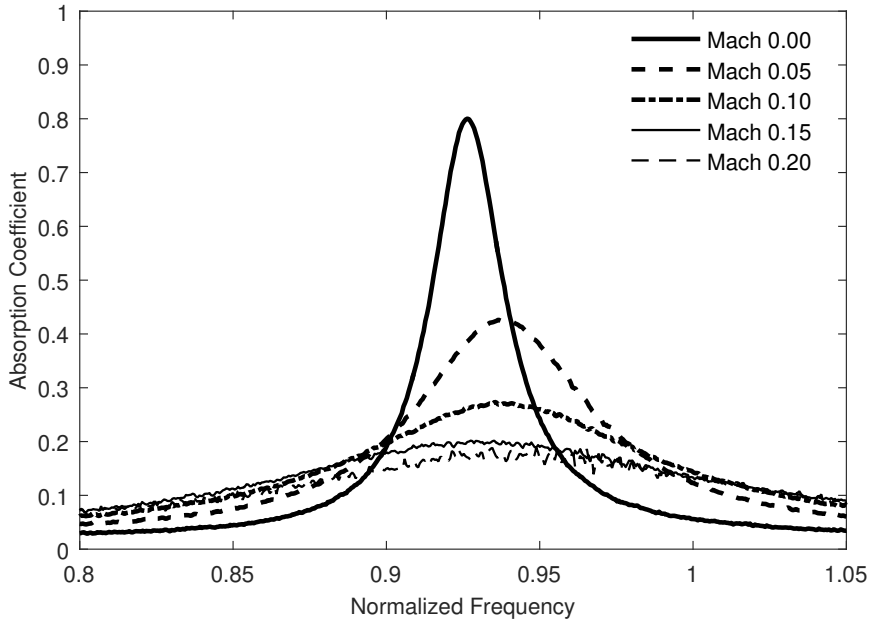

Figure 7.5: Absorption coefficient of the "recess" injector at different bias flow Mach numbers in the main body of the injector.

is observed in the presence of flow for the relatively low Mach numbers measured here.

7.4.3 Resonance Frequency of Unique Injectors in the Presence of Flow

Convection Effects on the Resonance Frequency

Figure 7.7 shows the percentage change in the resonance frequency of each injector as a function of the Mach number of the mean flow in the main body of the injector with respect to the resonance frequency for zero flow. The resonance frequency of a half-wave resonator with bias flow is given by Eq. (7.3), which demonstrates that the resonance frequency theoretically varies with $(1 - M^2)$ due to the convection effects of the mean flow, where M is the Mach number of the flow inside the resonator. The theoretical percentage change in the resonance frequency is plotted in Figure 7.7 as the $(1 - M_{\text{body}}^2)$ curve, where M_{body} is the Mach number of the flow in the main body of the injector. Whereas Eq. (7.3) predicts that the resonance frequency decreases monotonically with increasing Mach number, the measured resonance frequency of each injector increases slightly at low Mach numbers before decreasing at higher Mach numbers. The resonance frequency of the "straight"

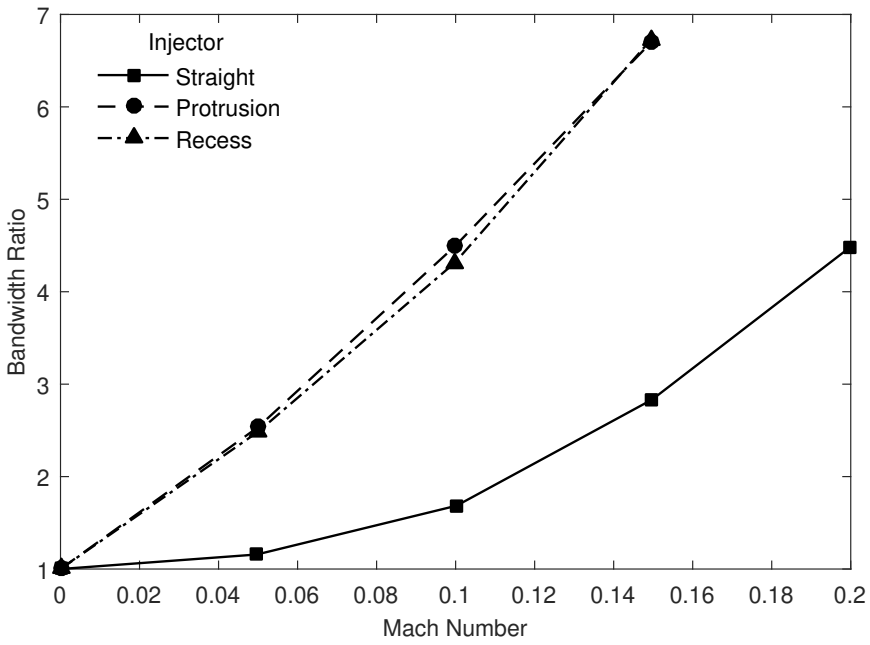

Figure 7.6: Ratio of the absorption frequency bandwidth with mean flow to the absorption frequency bandwidth with no flow as a function of the bias flow Mach number in the main body of the injector for the propellant injectors with different geometric features.

injector remains greater than the theoretical curve at all measured nonzero Mach numbers, but the resonance frequency of the "recess" injector is less than the theoretical curve at the highest measured Mach numbers. In fact, the resonance frequency of the "recess" injector approximately follows the $(1 - M_{\text{inlet}}^2)$ curve at Mach numbers above 0.1, where M_{inlet} is the Mach number of the flow through the inlet protrusion.

However, this result appears to contradict the time-of-flight argument used to derive the theoretical change in the resonance frequency due to convection effects. The length of the inlet protrusion is short compared to the main body of the injector, so the time-of-flight of the acoustic waves in the inlet protrusion is too small to have such a significant effect on the resonance frequency of the injector. Instead, the majority of the time-of-flight of the acoustic waves inside the "recess" injector is spent in the main body of the injector, in which the Mach number of the mean flow is M_{body}. One possible explanation for why the resonance frequency of the "recess" injector approximately follows the $(1 - M_{\text{inlet}}^2)$ curve is that the mean flow may separate as it passes through the inlet protrusion and does not

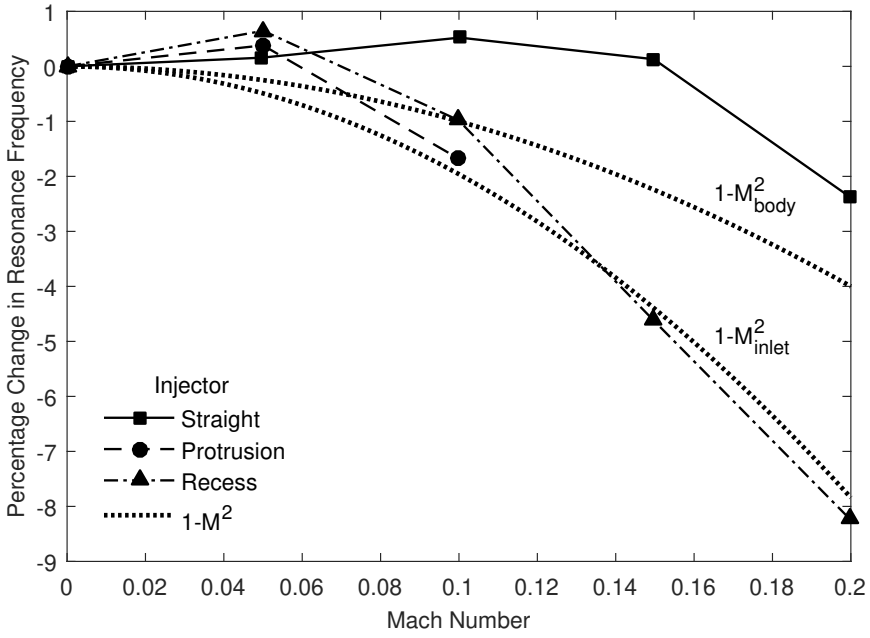

Figure 7.7: Percentage change in resonance frequency as a function of the bias flow Mach number in the main body of the injector for the propellant injectors with different geometric features.

quickly reattach; instead, the mean flow may form a sort-of jet in the main body of the injector. If this occurs, the centerline velocity of the mean flow in the main body of the injector would be closer to M_{inlet} than to M_{body}, and thus M_{inlet} should be used to estimate the time-of-flight and the resonance frequency.

Effect of Flow on the End Corrections

It is hypothesized that the measured resonance frequencies of the "straight" injector at all Mach numbers and the "protrusion" and "recess" injectors at low Mach numbers exceed the theoretical predictions because the length corrections at the open ends of the injectors decrease at certain bias flow conditions. Davies [24, 69] found that the length correction at the open end of a pipe scales with $(1 - M^2)$, but this factor is too small to account for the relatively large differences between the measured and theoretical resonance frequencies. Additionally, if the length correction were only dependent on Mach number, then it would not explain why the resonance frequencies of the "protrusion" and "recess" injectors only

exceed theory at low Mach numbers. Peters, et al. [22] showed experimentally that the length correction at the open end of a pipe is a function of the mean flow Strouhal number, which is defined as $St = ka/M$. Boij [63] calculated the length correction at an area discontinuity in a circular duct with mean flow using the experimental data obtained by Ronneberger [71] and found that there is a minimum in the length correction at Strouhal numbers of the order $St \sim 1$, as shown in Figure 2.17. Furthermore, Boij applied the numerical model developed by Boij and Nilsson [62] and reproduced similar Strouhal-number dependence of the length correction. Boij [63] also provided an explanation for the effect: The Strouhal number is the ratio of the characteristic frequencies—or the inverse of the characteristic time scales—of the acoustic waves and the hydrodynamic waves. When $St \sim 1$, the time scales of the acoustic and hydrodynamic waves are of the same order, so there is significant interaction between the incident acoustic waves and the vortices shed from the area expansion. This coupling between the acoustic and hydrodynamic waves induces changes in the length correction, but it is difficult to obtain a simple expression for the length correction in this Strouhal number regime [49].

The mean flow Strouhal number is of the order $St \sim 1$ at the resonance frequencies of the injectors at the Mach numbers under consideration. The length corrections at the inlet and outlet of each injector are related to the resonance frequency by Eq. (7.3), where the effective length is $L_{\text{eff}} = L + \Delta L_{\text{in}} + \Delta L_{\text{out}}$. An estimate of the length correction at one open end is given by $\Delta L = (\Delta L_{\text{in}} + \Delta L_{\text{out}})/2$. Equation (7.3) can be rearranged to show that

$$\Delta L = \frac{1}{2}\left[\frac{c}{2f_0}(1 - M^2) - L\right] \tag{7.20}$$

where f_0 is the measured resonance frequency. Figure 7.8 shows the measured length correction of the "straight" injector normalized by its radius as a function of the Strouhal number. The length correction of the single half-wave resonator shown in Figure 4.13 is also plotted to confirm the results. The limiting values of the normalized length corrections for no flow ($St \to \infty$) are indicated by the points at the right side of the plot. The length

correction reaches a minimum at a Strouhal number very close to one, which matches the results obtained by Boij [63]. This decrease in the length correction corresponds to an increase in the resonance frequency. These results, which are supported by the literature, provide an explanation for the differences between the measured and theoretical resonance frequencies of the injectors.

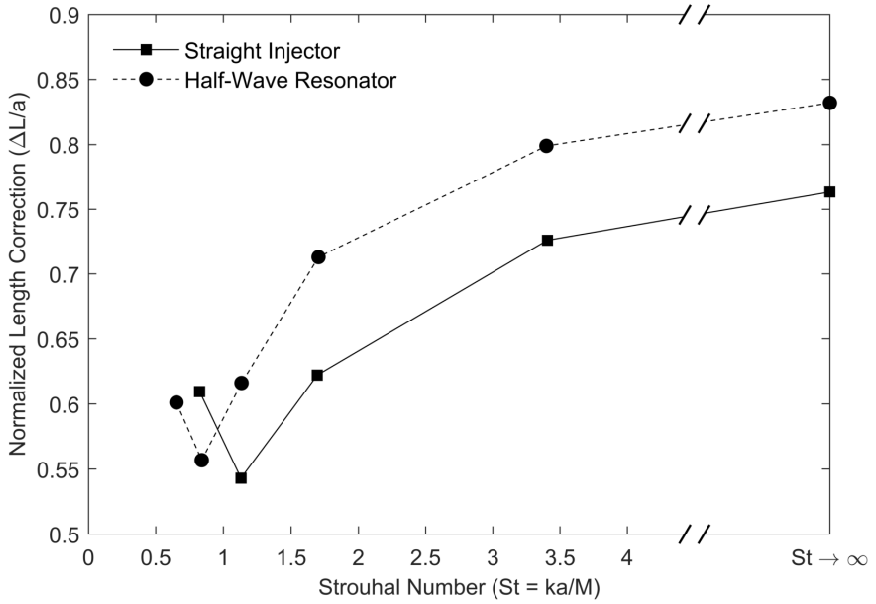

Figure 7.8: Normalized length correction as a function of Strouhal number for the "straight" injector shown in Figure 4.12 and the single half-wave resonator shown in Figure 4.13.

7.5 Effect of the Number of Injectors in the Presence of Flow

7.5.1 Normalized Resistance of Multiple Injectors in the Presence of Flow

The acoustic properties of multiple stainless steel half-wave resonators were measured using HOTMESS to investigate the effects of the bias flow velocity on multiple injectors. Figure 7.9 shows the normalized termination resistance, θ_T, at resonance for different numbers of half-wave resonators as a function of the Mach number of the mean flow in the resonators. According to Eq. (5.11), the normalized termination resistance is related to the effective normalized input resistance of each resonator by $\theta_T = \theta_{0,\text{eff}}/\sigma$. If S_1 is the

cross-sectional area of the impedance tube and S_2 is the open area of a single resonator, then the combined open area ratio of the N resonators is given by $\sigma = N(S_2/S_1)$. Therefore, $\theta_T \propto \theta_{0,\text{eff}}/N$, and thus the normalized termination resistance decreases as the number of resonators increases, as discussed in Section 6.5. In addition, the normalized termination resistance does not vary as strongly with Mach number as the number of resonators increases.

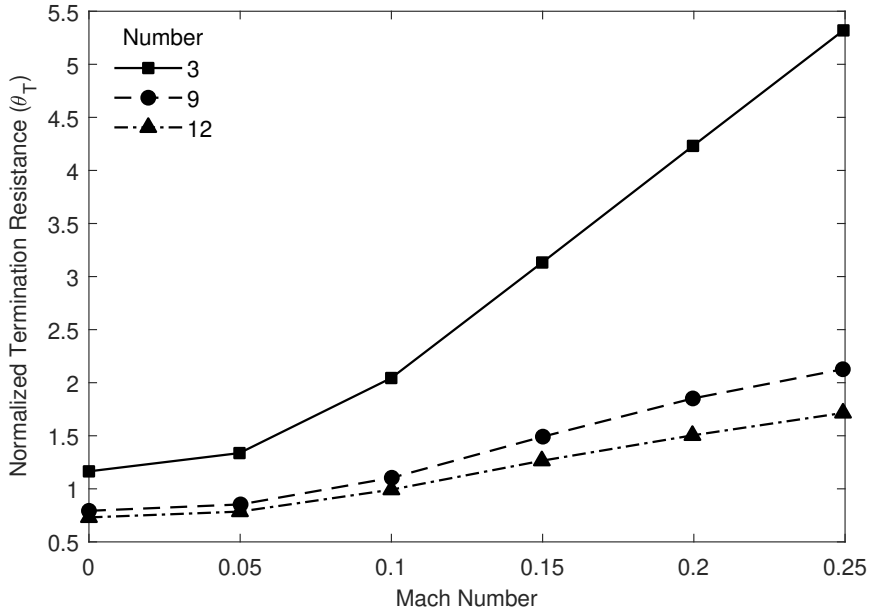

Figure 7.9: Normalized termination resistance at resonance as a function of the bias flow Mach number in the resonators for different numbers of half-wave resonators.

The measured increase in the normalized termination resistance of the resonators shown in Figure 7.9 is approximately linear with respect to the Mach number above a certain Mach number, which is consistent with previous studies on orifices [54] and the open ends of pipes [33, 52] with bias flow. The results of these previous studies suggest that the additional normalized input resistance due to the flow losses, θ_F, can be approximated by Eq. (7.5). Figure 7.10 shows the difference between the normalized input resistance with flow and in the absence of flow for different numbers of half-wave resonators; this difference defines θ_F. The normalized input resistances of three, nine, and twelve resonators nearly collapse on top of one another. Equation (7.5) is fit to the measurements, and the

Mach number of the bias flow through the resonators at which flow losses become non-negligible, M_F, is found to be approximately 0.059 (or 20 m/s for these conditions). The slope of the normalized input resistance with respect to Mach number is indeed approximately unity at Mach numbers greater than M_F.

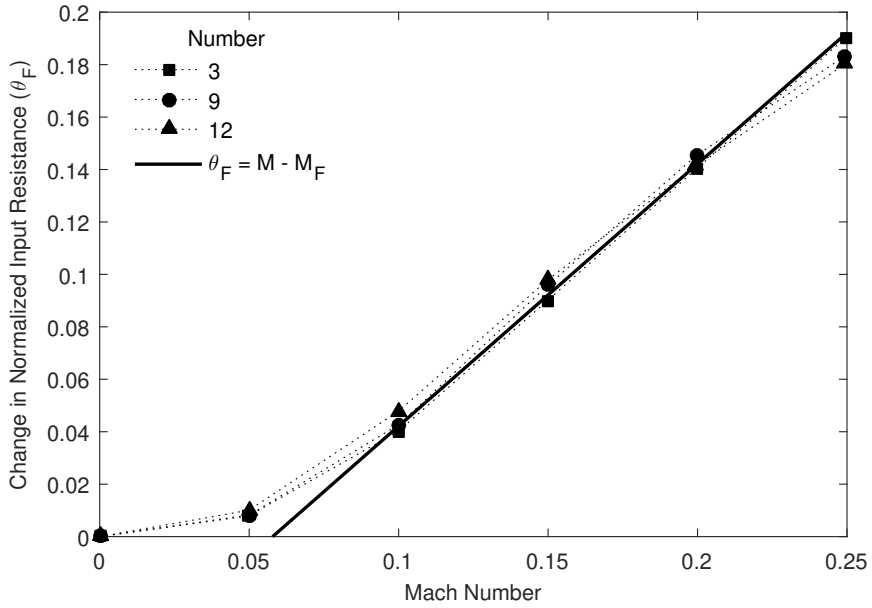

Figure 7.10: Change in the normalized input resistance at resonance as a function of the bias flow Mach number in the resonators for different numbers of half-wave resonators.

One interesting observation is that the normalized resistance of the multiple half-wave resonators increases linearly with Mach number, but the relationship between the resistance and the Mach number shown in Figure 7.2 for the propellant injectors with different geometric features is nonlinear, even for the "straight" injector. Several possible reasons for the nonlinear relationship were suggested in Section 7.4.1, including viscothermal losses in the acoustic boundary layer at the walls of the injector and losses due to the generation of turbulence at the injector inlet. However, these phenomena do not appear to have a significant effect on multiple resonators. The area ratio between the multiple resonators and the impedance tube is less severe than the area ratio between a single injector and the impedance tube, and the multiple resonators are more widely distributed throughout the cross-section of the impedance tube. This will likely result in lower losses due to any tur-

bulence generated at the inlets of the resonators. Thus, it is likely that flow losses generated by the extreme change in cross-sectional area between a single injector and the impedance tube are responsible for the additional losses that cause the normalized resistance to increase nonlinearly with Mach number for a single injector. Additional work is required to prove these points conclusively.

7.5.2 Sound Power Coefficients of Multiple Injectors in the Presence of Flow

As shown in Figure 7.9, the normalized termination resistance of three half-wave resonators at resonance is slightly greater than one for zero flow, and it increases with increasing Mach number. Thus, based on the behavior of the absorption coefficient as a function of the normalized termination resistance at resonance plotted in Figure 7.1, it is expected that the peak absorption coefficient will decrease with increasing Mach number. This is exactly what is observed in the present experiments as seen in Figure 7.11a, which shows the absorption coefficient of the three half-wave resonators at different Mach numbers of the mean flow through the resonators. Conversely, the normalized termination resistance of the twelve half-wave resonators at resonance shown in Figure 7.9 is less than one for zero flow, and it increases with increasing Mach number to a value greater than one at the highest measured Mach numbers. Thus, based on the behavior of the absorption coefficient as a function of the normalized termination resistance at resonance plotted in Figure 7.1, it is expected that the peak absorption coefficient will first increase with Mach number until it reaches a maximum at the Mach number at which the normalized termination resistance at resonance is equal to one, beyond which it will decrease with increasing Mach number. This is exactly what is observed in the present experiments as seen in Figure 7.11b, which shows the absorption coefficient of the twelve half-wave resonators at different Mach numbers of the mean flow through the resonators. Figure 7.11 also shows that the absorption frequency bandwidth increases monotonically with increasing Mach number for both three and twelve half-wave resonators. Thus, for the three half-wave resonators, bias flow

degrades the absorption coefficient very close to resonance but enhances the absorption coefficient at frequencies away from resonance. However, the behavior of the absorption coefficient for twelve half-wave resonators demonstrates that, if the open area ratio is sufficiently large, bias flow can enhance the acoustic damping by increasing both the peak value and the frequency bandwidth of the absorption coefficient.

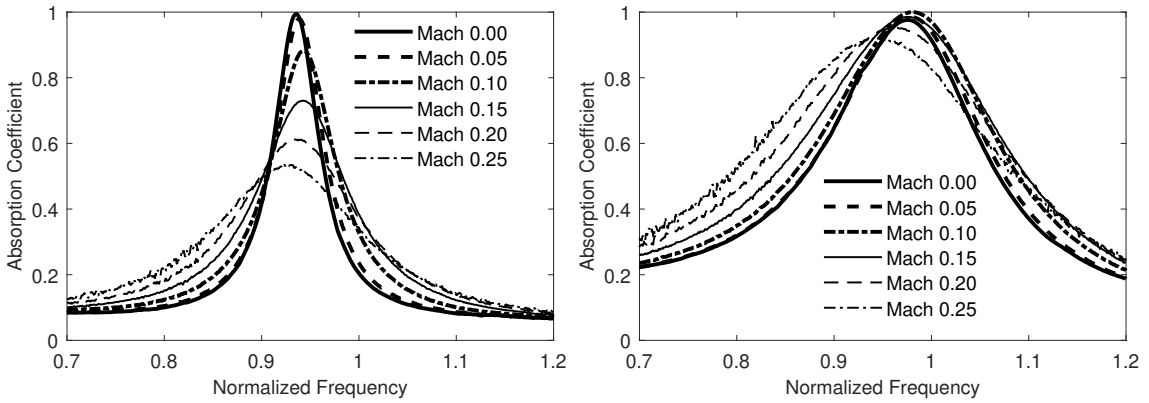

(a) Three half-wave resonators

(b) Twelve half-wave resonators

Figure 7.11: Absorption coefficient of three and twelve half-wave resonators at different bias flow Mach numbers in the resonators.

Figure 7.12 shows the power dissipation coefficients of three and twelve half-wave resonators at different Mach numbers of the mean flow through the resonators. At low Mach numbers, the peak dissipation coefficient of three half-wave resonators shown in Figure 7.12a increases with Mach number because there are additional dissipation mechanisms due to the bias flow, such as the conversion of acoustic waves into hydrodynamic waves at the outlet ends of the resonators, that increase with increasing Mach number. However, the peak dissipation coefficient reaches a maximum at Mach 0.1, and at higher Mach numbers, the peak dissipation coefficient decreases with Mach number. This seemingly presents a paradox because the dissipation mechanisms due to the bias flow increase in strength as the Mach number increases, which is the reason that the normalized termination resistance shown in Figure 7.9 increases monotonically with Mach number. However, as the normalized termination resistance increases further above one, a greater fraction of the incident sound power is reflected from the resonators. At flow rates greater than Mach 0.1, the peak

dissipation coefficient decreases because there is less sound power entering the resonators to be dissipated. On the other hand, the dissipation coefficient of twelve half-wave resonators increases monotonically with Mach number, as shown in Figure 7.12b. For twelve resonators, as the Mach number increases, the dissipation mechanisms due to the bias flow grow in strength, and the normalized termination resistance of the twelve resonators shown in Figure 6.5 remains relatively close to one; thus, the reflection coefficient remains relatively small, and a large fraction of the incident sound power enters the resonators and is dissipated.

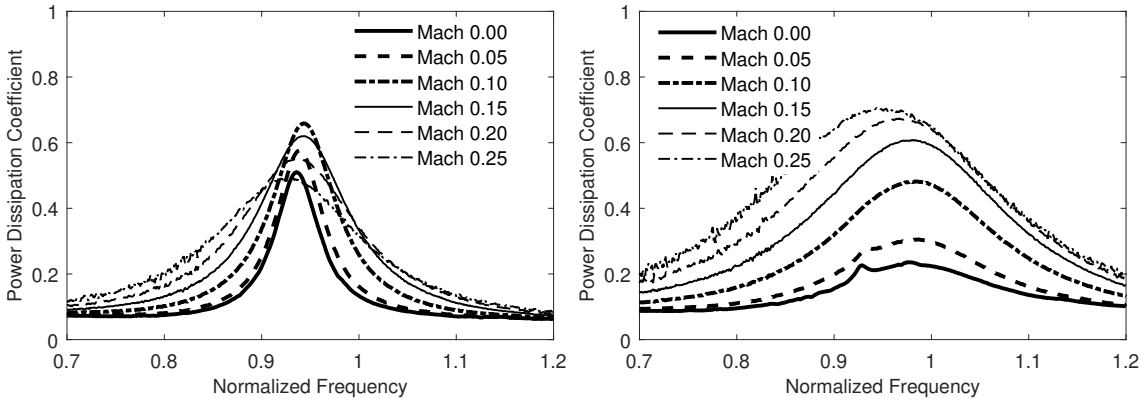

(a) Three half-wave resonators (b) Twelve half-wave resonators

Figure 7.12: Dissipation coefficient of three and twelve half-wave resonators at different bias flow Mach numbers in the resonators.

Figure 7.13 shows the power transmission coefficients of three and twelve half-wave resonators at different Mach numbers of the mean flow through the resonators. For both three and twelve resonators, the power transmission coefficient decreases monotonically with increasing Mach number because some fraction of the acoustic energy that would be transmitted from the resonators into the impedance tube in the absence of flow is instead dissipated by the conversion of the acoustic energy into the kinetic energy of hydrodynamic waves that shed from the open ends of the resonators.

The power absorption, dissipation, and transmission coefficients of the three half-wave resonators at resonance are reasonably well-predicted by the simplified analytical expressions given by Eqs. (7.17)–(7.19), as shown in Figure 7.14. For example, the simplified

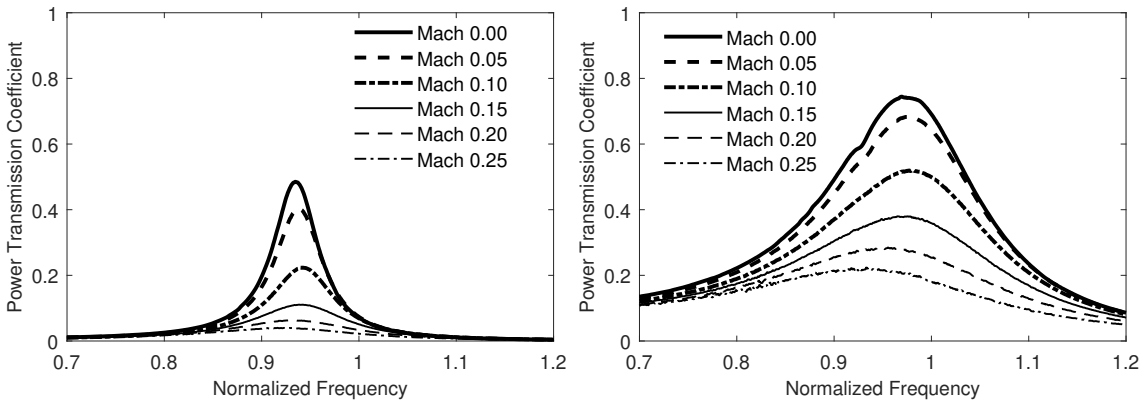

(a) Three half-wave resonators

(b) Twelve half-wave resonators

Figure 7.13: Power transmission coefficient of three and twelve half-wave resonators at different bias flow Mach numbers in the resonators.

expressions correctly predict the maximum in the dissipation coefficient at Mach 0.1 and the monotonic decrease in the power transmission coefficient with increasing Mach number. However, the quantitative accuracy of the simplified expressions is not as good for twelve resonators as for three resonators, even in the absence of flow, so the analytical results for twelve resonators are not shown. Regardless, these simplified expressions are useful for understanding the physical mechanisms responsible for the sound power absorption, dissipation, and transmission.

7.5.3 Resonance Frequency of Multiple Injectors in the Presence of Flow

Figure 7.15 shows the percentage change in the resonance frequency of different numbers of half-wave resonators with respect to the Mach number of the mean flow in the resonators. The theoretical resonance frequency of the half-wave resonators varies with $(1 - M^2)$ according to Eq. (7.3), where M is the Mach number of the flow inside the resonators. The resonance frequencies of the different numbers of resonators are greater than the theoretical curve at all measured nonzero Mach numbers; similar behavior was also observed for the "straight" injector. The mean flow Strouhal numbers at the resonance frequencies of the multiple resonators are of the order $St \sim 1$ for the range of Mach numbers at which the measurements were conducted. Based on the results of Boij [63] and the measurements

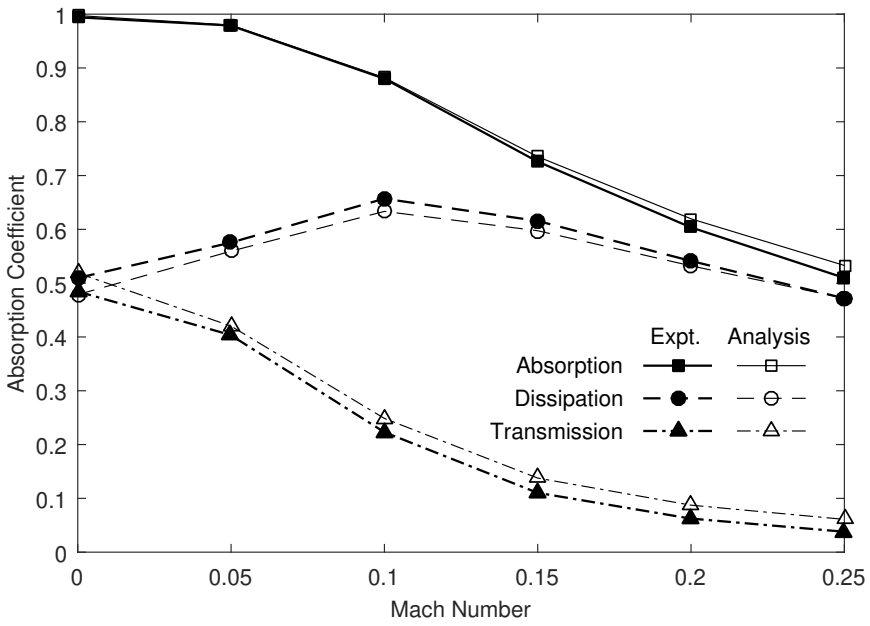

Figure 7.14: Power absorption, dissipation, and transmission coefficients of three half-wave resonators at resonance as a function of the bias flow Mach number in the resonators.

shown in Figure 7.8, the difference between the measured resonance frequencies and the theoretical prediction is likely caused by a decrease in the length correction at the open ends of the resonators at Strouhal numbers near one.

7.6 Discussion of Underdamping and Overdamping

In the previous section, the peak absorption coefficient of twelve half-wave resonators shown in Figure 6.4 was observed to vary non-monotonically with Mach number. This behavior of the absorption coefficient is often classified as *underdamped*, *overdamped*, or *optimally damped* in the literature. Laudien, et al. [6] and Förner, et al. [84–86] described the absorption coefficient as *underdamped* (or *normally damped*) when the peak absorption coefficient is less than one and the absorption frequency bandwidth is relatively narrow; conversely, they described the absorption coefficient as *overdamped* when the peak absorption coefficient is less than one and the absorption frequency bandwidth is relatively wide. Finally, *optimal damping* refers to the case in which the peak absorption coefficient reaches the maximum value of one. For the results shown in Figure 7.11b, as the Mach

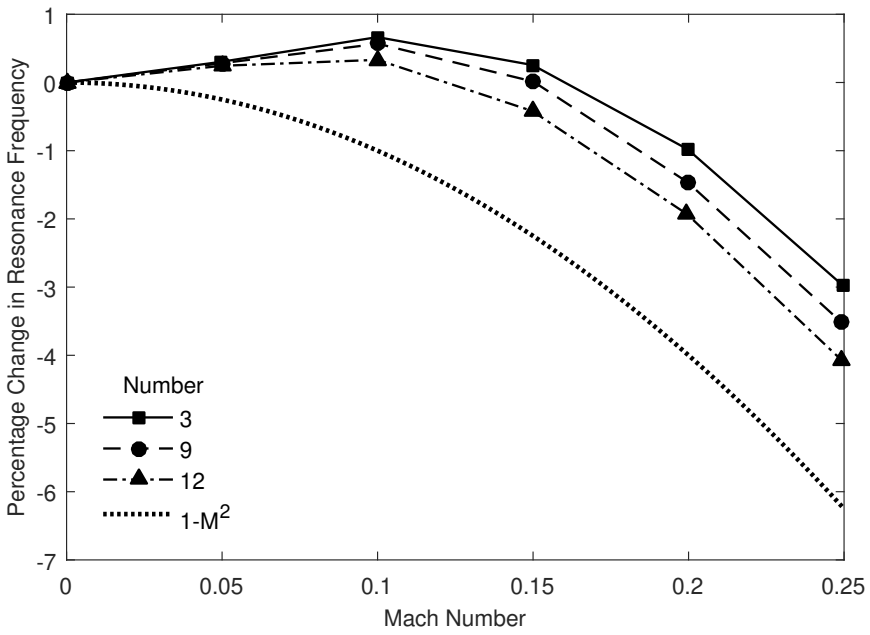

Figure 7.15: Percentage change in resonance frequency as a function of the bias flow Mach number in the resonators for different numbers of half-wave resonators.

number increases, the acoustic damping mechanisms also increase. The absorption coefficient progresses from underdamped at zero flow to optimally damped at Mach 0.1 to overdamped at even higher Mach numbers. These terms seem to be useful for describing the qualitative behavior of the absorption coefficient. However, the quantitative definitions of these terms are not consistent in the literature; in fact, the quantitative definitions of Laudien, et al. [6] and Förner, et al. [84–86] are opposites. In the author's knowledge, this inconsistency has not been previously pointed out in the literature. The reasons for the inconsistent definitions are discussed below based on the results presented in the current work.

Underdamping, *overdamping*, and *optimal damping* are typically defined quantitatively based on the value of the normalized termination resistance, θ_T, at resonance, which was already shown to uniquely determine the peak value of the absorption coefficient according to Eq. (7.15). If $\theta_T = 1$ at resonance, then the absorption coefficient is maximized, and both Laudien, et al. [6] and Förner, et al. [84–86] define this condition as *optimal damping*. However, their definitions of *underdamping* and *overdamping* differ, as described below.

Both groups of authors classified the damping behavior of resonators based on the changes in the normalized termination impedance and the absorption frequency bandwidth, but they studied the effects of different independent variables. For this discussion, recall that the normalized termination resistance is given by $\theta_T = \theta_{0,\text{eff}}/\sigma$, and the absorption frequency bandwidth is proportional to $BW \propto \sigma + \theta_{0,\text{eff}}$.

Laudien, et al. [6] studied these parameters by varying the open area ratio using different numbers of resonators. As the open area ratio, σ, increases, the effective normalized input impedance, $\theta_{0,\text{eff}}$, of each resonator remains nearly constant; thus, the normalized termination impedance decreases and the absorption frequency bandwidth increases with increasing open area ratio (see Figure 6.5). Since they only varied the open area ratio, Laudien, et al. observed that the absorption frequency bandwidth is inversely related to the normalized termination impedance. For this reason, Laudien, et al. defined *underdamping* by the condition $\theta_T > 1$ and *overdamping* by the condition $\theta_T < 1$ at resonance.

Förner, et al. [84–86] studied the absorption parameters by varying the incident sound pressure level; alternatively, they would have obtained the same results by varying the bias flow Mach number, as was done in this chapter. As the Mach number (or incident sound pressure level) increases, the effective normalized input impedance of each resonator also increases, which is predicted by Eq. (7.13) and shown in Figure 7.10. Thus, both the normalized termination impedance and the absorption frequency bandwidth increase with increasing Mach number, so Förner, et al. observed that the absorption frequency bandwidth is directly related to the normalized termination impedance. For this reason, Förner, et al. defined *underdamping* by the condition $\theta_T < 1$ and *overdamping* by the condition $\theta_T > 1$ at resonance, which is the opposite of Laudien, et al. [6].

Neither set of definitions is incorrect, but neither set of definitions completely classifies the damping behavior of the half-wave resonators. The absorption coefficient is a function of both the resistance and the reactance, so it is unreasonable to expect that the behavior of the absorption coefficient could be classified solely based on the normalized termination

resistance at resonance. This attempt, however, has led to opposing definitions in the published literature [6, 84–86]. Even though *underdamping* and *overdamping* seem to be useful terms for describing the qualitative behavior of the absorption coefficient, these terms are not used in the current work because of the inconsistencies in their quantitative definitions. In the author's knowledge, this is the first time that these inconsistencies have been pointed out and explained.

7.7 Summary

In this chapter, the effects of bias flow on the acoustic damping of propellant injectors were investigated at different mean flow rates at ambient temperature in the linear acoustic regime for the plane wave mode. The effects of bias flow and the contributions of the physical mechanisms responsible for the acoustic damping are summarized below.

Experimental Results

The normalized resistance of an injector at resonance was found to increase monotonically with the Mach number of the bias flow through the injector. The increase in resistance was found to be greater for the "protrusion" and "recess" injectors than for the "straight" injector due to the increased velocity through the inlet protrusion. The relationship between the resistance and Mach number is expected to be linear at high Mach numbers based on theoretical and experimental results in the literature; indeed, it was found to be linear above a certain Mach number for multiple half-wave resonators, but it was found to be nonlinear for the single injectors. The experiments also showed that the absorption frequency bandwidth of the injectors increases monotonically with Mach number, and the peak absorption coefficient either increases or decreases with Mach number based on the value of the normalized termination resistance at resonance. This behavior of the absorption coefficient is often classified as underdamped, overdamped, or optimally damped based on the normalized termination resistance at resonance, but there are opposing quantitative definitions of

these terms in the literature, so the use of these terms is not recommended.

A simple time-of-flight argument was used to show that the resonance frequency of a half-wave resonator theoretically varies with $(1 - M^2)$, where M is the Mach number of the bias flow inside the resonator. However, it was found that the measured resonance frequency exceeds the theoretical prediction for many of the experimental conditions. It was hypothesized that the length corrections at the open ends of the injectors decrease near a mean flow Strouhal number close to one. There is good support for this hypothesis in the literature [63], and the experiments presented in this chapter suggested that the length correction indeed reaches a minimum near $St \sim 1$.

Analytical and Numerical Models

The simplified expression for the impedance of a half-wave resonator near resonance derived in Chapter 5 in the absence of flow was extended to include bias flow. The resulting expressions for the sound power coefficients were shown to be reasonably accurate, and they provide a physical understanding of the damping mechanisms of a half-wave resonator with bias flow. A numerical model for the acoustic damping was not developed because the transfer matrix approach fails to account for the coupling between the acoustic and hydrodynamic waves. It is beyond the scope of this work to develop such a theory for the acoustic damping of half-wave resonators with bias flow.

Acoustic Damping Mechanisms

For the experiments discussed in this chapter, it was shown that the primary physical mechanisms responsible for the acoustic damping are viscothermal losses in the acoustic boundary layer, acoustic radiation from the open end of the injectors opposite the incident acoustic waves, dissipation due to turbulence, and the conversion of acoustic energy to vorticity at the open ends of the injectors. The viscothermal losses in the acoustic boundary layer and the acoustic radiation from the open end were shown to be present for half-wave resonators

regardless of the presence or absence of flow. The new acoustic damping mechanisms introduced by bias flow were found to be dissipation due to turbulence and the conversion of acoustic energy to vorticity at the open ends of the resonators. Theoretical and experimental works in the literature suggest that the normalized resistance due to the conversion of acoustic energy to vorticity at the outlet of an injector is linearly related to the Mach number above a certain Mach number. A linear relationship was measured for multiple resonators, but a nonlinear relationship was measured for a single propellant injector. Dissipation due to turbulence generated in the acoustic boundary layer or at the inlet of the injector may account for this nonlinear relationship.

CHAPTER 8
EFFECT OF TEMPERATURE

8.1 Overview

In this chapter, the effects of temperature on the acoustic damping of propellant injectors are investigated. The experiments presented in this chapter are conducted in the two-sided impedance tube using the single stainless steel half-wave resonator (see Figure 4.13) and multiple stainless steel half-wave resonators (see Figure 4.14). The experiments are conducted at different mean flow rates and elevated temperatures in the linear acoustic regime for the plane wave mode. Because the experiments are conducted at elevated temperatures, the acoustic measurements are made using the pressure transducers and water-cooled adapters instead of the microphones. The physical mechanisms responsible for the acoustic damping in the experiments described in this chapter include:

- Viscous and thermal losses in the acoustic boundary layer
- Acoustic radiation from the open end of the injectors opposite the incident acoustic waves
- Dissipation due to turbulence
- Conversion of acoustic energy to vorticity at the open ends of the injectors
- Acoustic attenuation within the bulk fluid

The outline of this chapter is as follows: First, in Section 8.2, the acoustic dissipation mechanisms at elevated temperatures are discussed, and the acoustic attenuation within the fluid itself is compared to the attenuation in the acoustic boundary layer. The temperatures and frequencies at which the attenuation within the fluid is important in the half-wave resonators are plotted for different conditions. Next, selected experimental measurements of

the absorption coefficients of half-wave resonators at different temperatures are presented in Section 8.3. The effects of temperature and temperature gradients are discussed based on the results of the experiments. Finally, in Section 8.4, a method for incorporating the effects of temperature in the numerical model described in Chapter 5 is briefly discussed.

8.2 Acoustic Dissipation Mechanisms at High Temperatures

8.2.1 Dissipation at the Walls and Within the Fluid

In duct acoustics, the viscothermal dissipation at the walls of the duct is typically much larger than the dissipation within the duct fluid itself, so the losses within the fluid are commonly neglected [75]. However, measurements acquired by Lahiri, et al. [74] suggested that this might be a poor assumption at elevated temperatures and pressures, so Lahiri, et al. [41] analyzed the dissipation mechanisms within fluid itself at different temperatures and pressures. The following discussion is a summary of the analysis performed by Lahiri, et al., and the reader is encouraged to consult Ref. [41] for additional details and equations.

Lahiri, et al. [41] first considered the acoustic losses at the walls of the duct. They used the attenuation coefficient obtained by Kirchhoff [119, 120], which is given by Eq. (3.17), to account for the viscothermal dissipation at the walls in the absence of flow. However, if there is a mean flow through the duct, the attenuation coefficient at the wall is modified by convection effects and the presence of a turbulent flow boundary layer [22, 32, 34, 36, 37]. Allam and Åbom [38] showed that the model derived by Howe [37] accurately accounts for these effects. Following Lahiri, et al. [41], let $\beta^{\pm}_{\text{wall}}$ represent the attenuation coefficient at the wall in the upstream and downstream directions, and define the average attenuation coefficient at the wall as $\bar{\beta}_{\text{wall}} = (\beta^{+}_{\text{wall}} + \beta^{-}_{\text{wall}})/2$. Note that α is commonly used to represent the attenuation coefficient, whereas β is used in this work to avoid confusion with the wavenumber parameter defined in Eq. (3.13).

Next, Lahiri, et al. [41] considered the acoustic loss mechanisms within the fluid itself, including the viscosity, thermal conductivity, and molecular relaxation. They presented

expressions for the classical absorption coefficient, β_{cl}, which accounts for losses due to viscosity and thermal conductivity, the absorption coefficient due to rotational relaxation, β_{rot}, and the absorption coefficients due to the vibrational relaxation of nitrogen, $\beta_{\text{vib,N}}$, and oxygen, $\beta_{\text{vib,O}}$. The exact expressions that they presented are specific to air that is assumed to be composed primarily of nitrogen and oxygen, but the attenuation coefficients due to vibrational relaxation depend on the concentration of water vapor in the air. The overall attenuation coefficient due to dissipation mechanisms within the fluid itself is given by $\beta_{\text{fluid}} = \beta_{\text{cl}} + \beta_{\text{rot}} + \beta_{\text{vib,N}} + \beta_{\text{vib,O}}$.

Lahiri, et al. [41] showed that the attenuation due to vibrational relaxation increases significantly at high temperatures, so the acoustic losses within the fluid cannot be neglected at high temperatures. They also showed that the vibrational relaxation, and thus the attenuation within the fluid, depends strongly on the concentration of water vapor in the air.

8.2.2 Application to Half-Wave Resonators

Lahiri, et al. [41] considered the acoustic losses within the fluid to be non-negligible if they are at least of the same order of magnitude as the losses at the wall, which they expressed by the criterion

$$\frac{\beta_{\text{fluid}}}{\bar{\beta}_{\text{wall}}} \geq 10^{-1} \tag{8.1}$$

Furthermore, Lahiri, et al. [41] plotted contours depicting the temperatures and frequencies at which this criterion is met for a duct with a specific diameter, Mach number, and concentration of water vapor. Their procedure is applied to the half-wave resonators studied in the current work. Figures 8.1–8.4 show the temperatures and frequencies at which the acoustic losses within the fluid are non-negligible compared to the losses at the wall of a 6.275-mm diameter resonator for concentrations of water vapor of 0.07%, 0.10%, 0.25%, and 0.50%, respectively. In each figure, different curves are plotted through the temperatures and frequencies at which the equality holds in Eq. (8.1) for mean flow Mach numbers of 0.0, 0.1, 0.2, and 0.3. The shaded region represents the temperatures and frequencies at which the

inequality expressed by Eq. (8.1) is met for zero mean flow. The labeled square markers indicate the resonance frequencies of the twelve half-wave resonators at the measured temperature conditions.

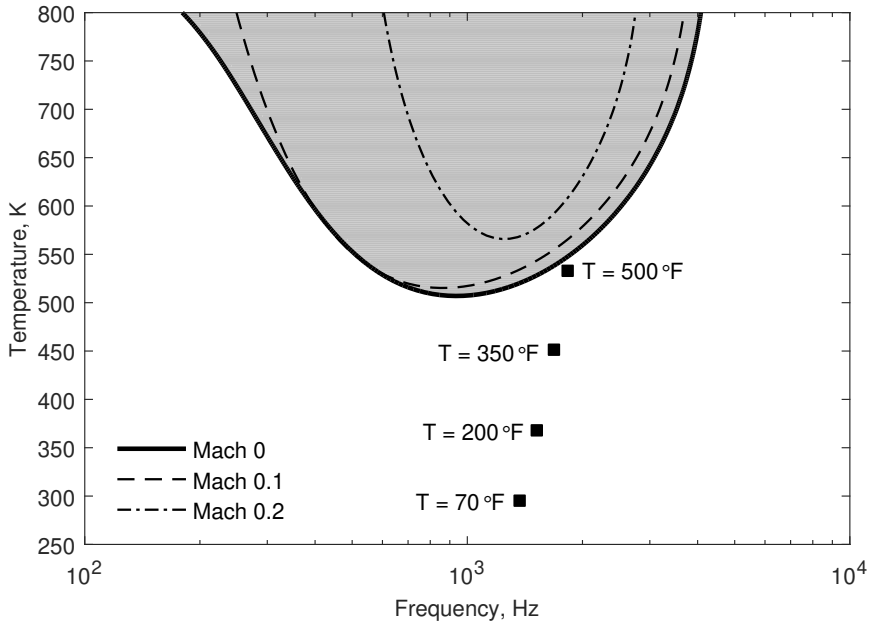

Figure 8.1: Temperatures and frequencies (shaded region) in which the attenuation in the bulk fluid is at least 10% of the attenuation in the acoustic boundary layer for a 6.275-mm diameter resonator at a constant concentration of water vapor of h = 0.07%.

Figures 8.1–8.4 show that at frequencies near the resonance frequency of the half-wave resonators given by the solid symbols, the acoustic losses within the fluid itself become important at elevated temperatures. As the Mach number increases, the acoustic losses at the wall increase due to the turbulent boundary layer, so the acoustic losses within the fluid do not become important compared to the acoustic losses at the wall until even higher temperatures. A comparison between the figures shows that the concentration of water vapor also has a significant effect on the magnitude of the acoustic losses within the fluid. At low concentrations of water vapor, such as h = 0.07%, the acoustic losses within the fluid can be neglected at the resonance frequencies of the half-wave resonators for each of the measured temperatures. However, if h = 0.10% or h = 0.25%, the acoustic losses within the fluid are non-negligible compared to the acoustic losses at the walls at the highest

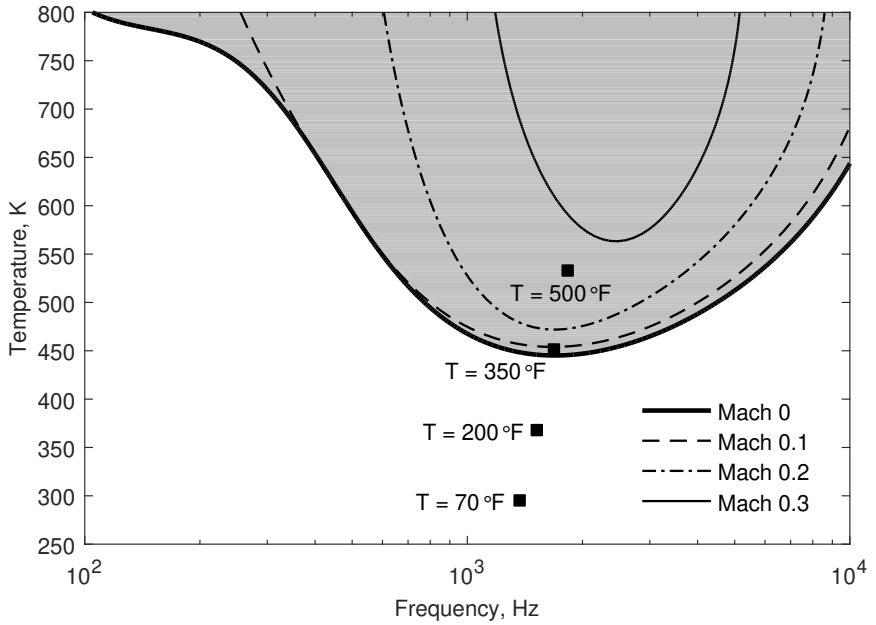

Figure 8.2: Temperatures and frequencies (shaded region) in which the attenuation in the bulk fluid is at least 10% of the attenuation in the acoustic boundary layer for a 6.275-mm diameter resonator at a constant concentration of water vapor of $h = 0.10\%$.

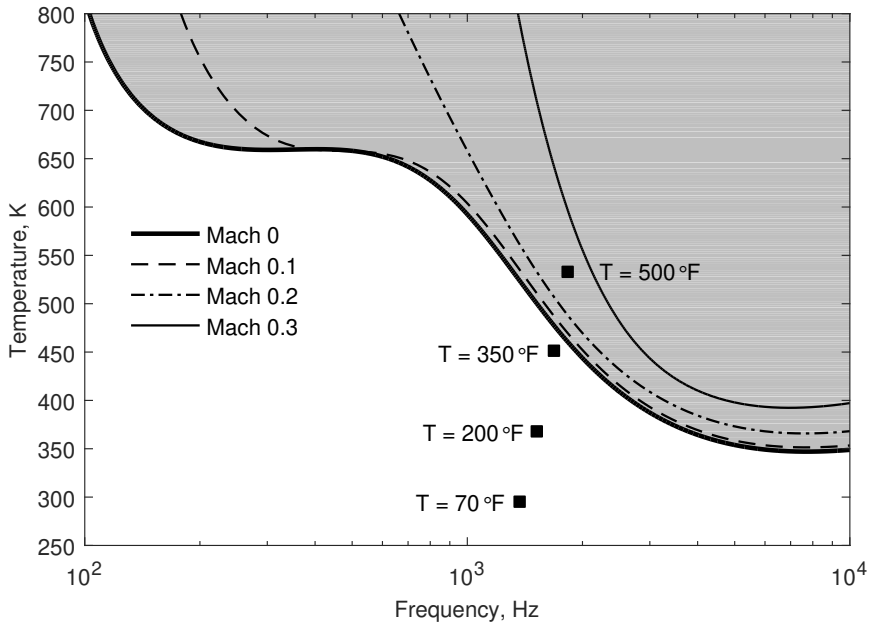

Figure 8.3: Temperatures and frequencies (shaded region) in which the attenuation in the bulk fluid is at least 10% of the attenuation in the acoustic boundary layer for a 6.275-mm diameter resonator at a constant concentration of water vapor of $h = 0.25\%$.

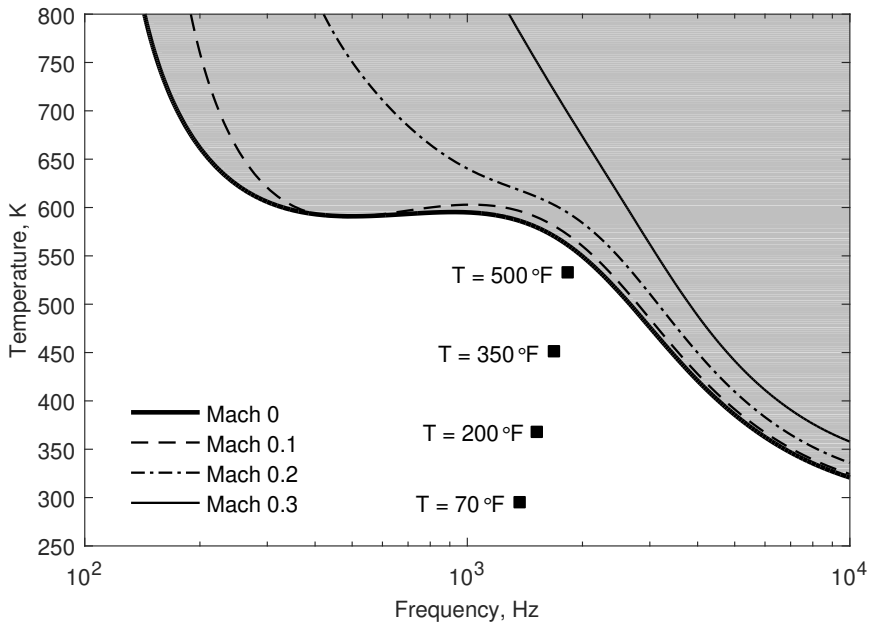

Figure 8.4: Temperatures and frequencies (shaded region) in which the attenuation in the bulk fluid is at least 10% of the attenuation in the acoustic boundary layer for a 6.275-mm diameter resonator at a constant concentration of water vapor of h = 0.50%.

measured temperatures. At still higher concentrations of water vapor, such as h = 0.50%, the acoustic losses within the fluid are only important at higher temperatures or frequencies than those measured in the current work.

Unfortunately, the experimental facility does not include any transducers to measure the humidity of the mean flow through HOTMESS, so the concentration of water vapor in the experiments is not known to accurately determine the acoustic losses within the fluid. For this reason, the frequencies and temperatures at which the acoustic losses within the fluid are non-negligible compared to the losses in the acoustic boundary layer are shown at several concentrations of water vapor in Figures 8.1–8.4. Unless otherwise noted, the acoustic results presented in this work are post-processed using the Weng-Bake wavenumber given by Eq. (3.19), which does not include the acoustic losses within the fluid; thus, the concentration of water vapor is not required.

8.3 Acoustic Measurements at High Temperatures

The attenuation within the fluid was analyzed in the previous section. In this section, selected experimental measurements at different temperatures are presented to investigate the effect of this dissipation mechanism on the absorption coefficients of the half-wave resonators. These experiments are conducted with bias flow through the resonators because nonzero mean flow is required to maintain high temperatures in the test section of HOTMESS. First, the effect of temperature is shown using three and twelve half-wave resonators because these configurations represent the conditions in a combustion chamber better than a single resonator. Next, the effect of a temperature gradient is discussed based on selected configurations.

8.3.1 Effect of Temperature

Figure 8.5 shows the absorption coefficients of three half-wave resonators arranged in the "3, Inner" configuration shown in Figure 6.9b. The experiments were conducted at different temperatures with a Mach 0.2 mean flow through the resonators. The absorption coefficient is plotted as a function of the normalized frequency, which is defined in Eq. (6.1), to correct for the effect of temperature on the resonance frequency. The temperature varies from room temperature to over 500°F (260°C), but there is minimal variation in the magnitude of the absorption coefficient over this range of temperatures. The absorption frequency bandwidth increases slightly with temperature, but the normalized frequency and magnitude of the peak absorption coefficient remain nearly identical for each of these temperatures.

Figure 8.6 shows the absorption coefficients of twelve half-wave resonators at different temperatures with a Mach 0.1 mean flow through the resonators. Once again, the temperature varies from room temperature to 500°F (260°C), but there is minimal variation in the absorption coefficient over this range of temperatures. It appears that, except for the change in resonance frequency captured by the normalized frequency, the effect of temperature on

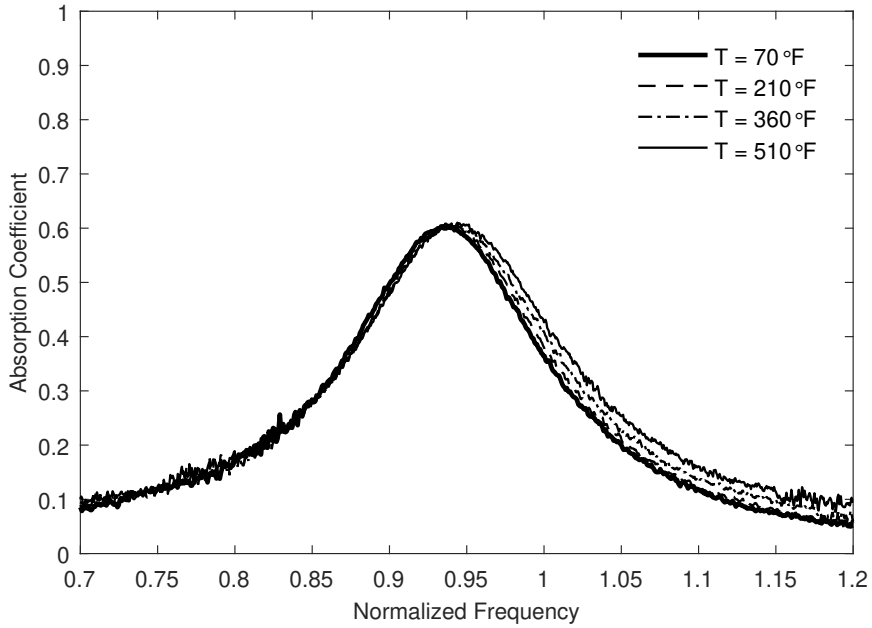

Figure 8.5: Absorption coefficient of three half-wave resonators at different temperatures with a Mach 0.2 mean flow through the resonators.

the acoustic damping of the tested half-wave resonator configurations is negligible up to at least 500°F (260°C). This is confirmed by the plots shown in Figures 8.1–8.4, in which the measured data points mostly fall below the region in which the attenuation within the bulk fluid is at least 10% of the attenuation in the acoustic boundary layer.

8.3.2 Effect of Temperature Gradient

Even though a single temperature is reported for each of the measured conditions in the results discussed above, the reported temperature is the mean of the values recorded by the thermocouples upstream and downstream of the test section. In reality, the temperature of the mean flow through HOTMESS was not constant. The temperature at the upstream thermocouple was consistently higher than the temperature at the downstream thermocouple because heat is transferred from the mean flow to the water-cooled adapters for the pressure transducers. In some cases, the temperature gradient between the upstream and downstream thermocouples is significant. For example, at the highest temperature measured for a single half-wave resonator with a mean flow of Mach 0.1 through the resonator,

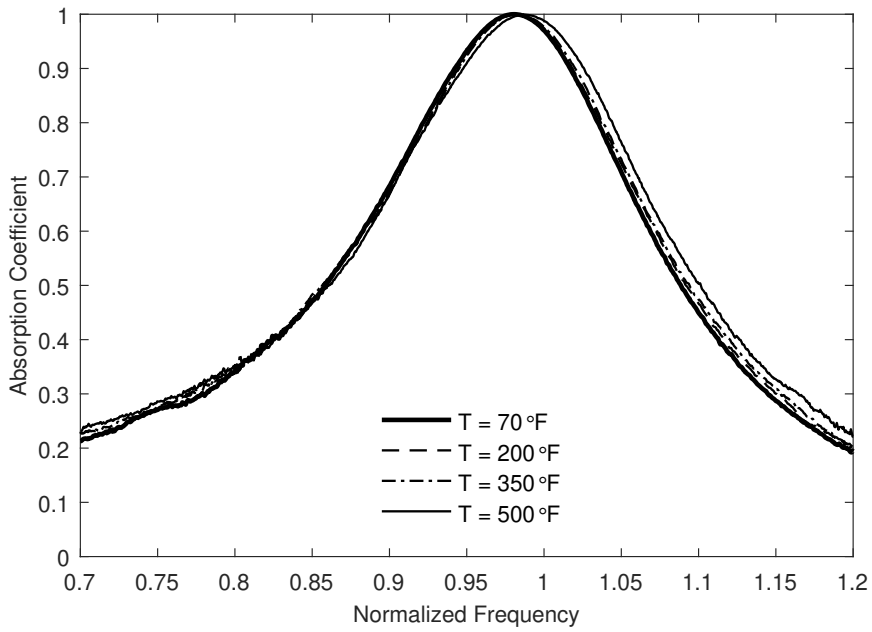

Figure 8.6: Absorption coefficient of twelve half-wave resonators at different temperatures with a Mach 0.1 mean flow through the resonators.

the temperature at the upstream thermocouple was approximately 580°F (304°C), whereas the temperature at the downstream thermocouple was approximately 315°F (157°C). Similarly, at the highest temperature measured for the twelve half-wave resonators with a mean flow of Mach 0.1 through them, the temperature varied from approximately 550°F (288°C) at the upstream thermocouple to 450°F (232°C) at the downstream thermocouple.

In addition to the axial temperature gradient, which is measured by the thermocouples upstream and downstream of the test section, there may also exist a temperature gradient within the cross-section of the impedance tube, especially at low velocities. For the one- and three-resonator configurations with a mean flow of Mach 0.1 through the resonators, the mean flow through the impedance tube is less than Mach 0.005, which is nearly stagnant. At these conditions, it is reasonable to assume that the warmer air rises within the impedance tube cross-section. The impedance tube is mounted horizontally, so the cross-section of the impedance tube is oriented perpendicular to the ground; thus, a temperature gradient within the cross-section is likely to be vertical with respect to the ground. However, as the thermocouples were not distributed throughout the cross-section of HOTMESS, the vertical

temperature gradient could not be measured directly.

At low velocities, the single resonator configuration depicted in Figure 8.7a is likely to experience the effects of a vertical temperature gradient within the cross-section of HOTMESS. Figure 8.8 shows the absorption coefficients of this single half-wave resonator at different temperatures with a Mach 0.1 mean flow through the resonator. As the temperature increases, the normalized resonance frequency decreases, even though the normalized frequency theoretically accounts for the effect of temperature. However, the temperature used to compute the normalized frequency is the mean of the upstream and downstream thermocouple measurements, which is not necessarily equal to the local temperature in the resonator. If a vertical temperature gradient exists within the cross-section of the impedance tube, then lower-temperature air would sink to the point within the cross-section closest to the ground, which is where the single resonator is mounted, as shown in Figure 8.7a. Thus, the actual temperature in the resonator would be lower than the mean of the upstream and downstream thermocouple measurements due to the vertical temperature gradient. Since the resonance frequency is directly proportional to temperature, the observed decrease in the normalized resonance frequency with increasing mean temperature is consistent with the existence of a vertical temperature gradient within the impedance tube.

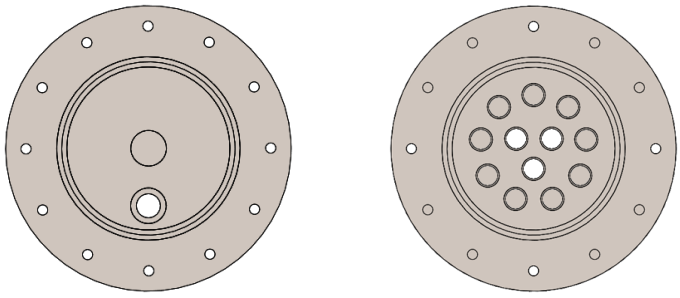

(a) Single Resonator, Outer (b) Three Resonators, Inner

Figure 8.7: Number and positions of the half-wave resonators.

At low velocities, three half-wave resonators arranged in the configuration depicted in Figure 8.7b may also experience the effects of a vertical temperature gradient within the cross-section of HOTMESS. Figure 8.9 shows the absorption coefficients of these three

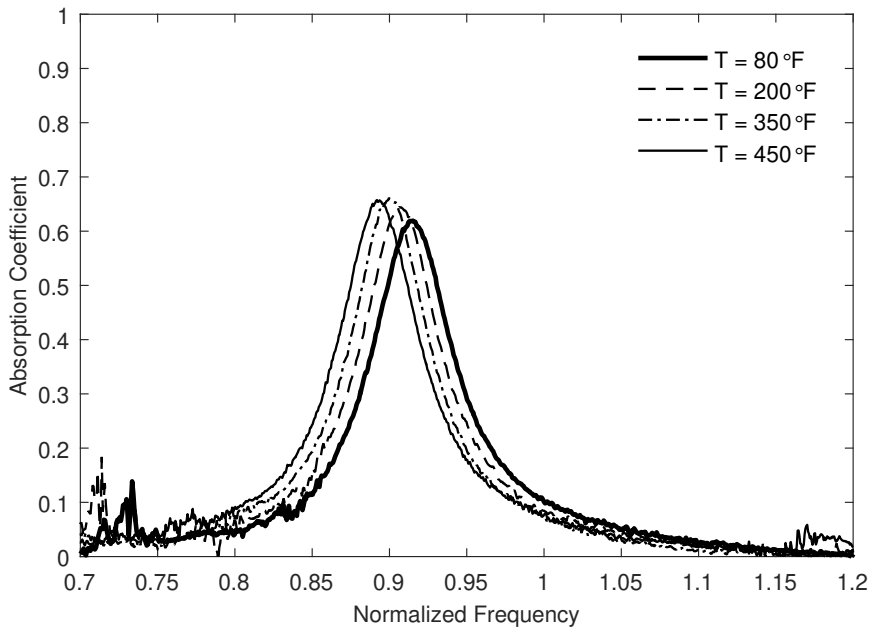

Figure 8.8: Absorption coefficient of one half-wave resonator at different temperatures with a Mach 0.1 mean flow through the resonator.

half-wave resonators at different temperatures with a Mach 0.1 mean flow through the resonators. The temperature appears to have a large effect on the absorption coefficient of three resonators with a Mach 0.1 mean flow through them even though temperature has a negligible effect for a Mach 0.2 mean flow based on Figure 8.5. The apparent effect of temperature shown in Figure 8.9 is likely caused by a vertical temperature gradient within the impedance tube. If, indeed, there is a vertical temperature gradient in the impedance tube, then the two resonators mounted higher (further from the ground) within the cross-section would have a higher resonance frequency than the one resonator mounted lower (closer to the ground) within the cross-section. In addition, the two higher-mounted resonators would be expected to provide more absorption than the single lower-mounted resonator. As the temperature increases, the absorption coefficient indeed splits into two peaks, and the peak absorption coefficient of the higher-frequency peak is greater than that of the lower-frequency peak. Thus, the results are consistent with the hypothesis that the apparent effect of temperature is actually the result of a vertical temperature gradient within the cross-section of the impedance tube, and this temperature gradient is shown to have a

significant effect on the resonance frequency and the peak absorption coefficient.

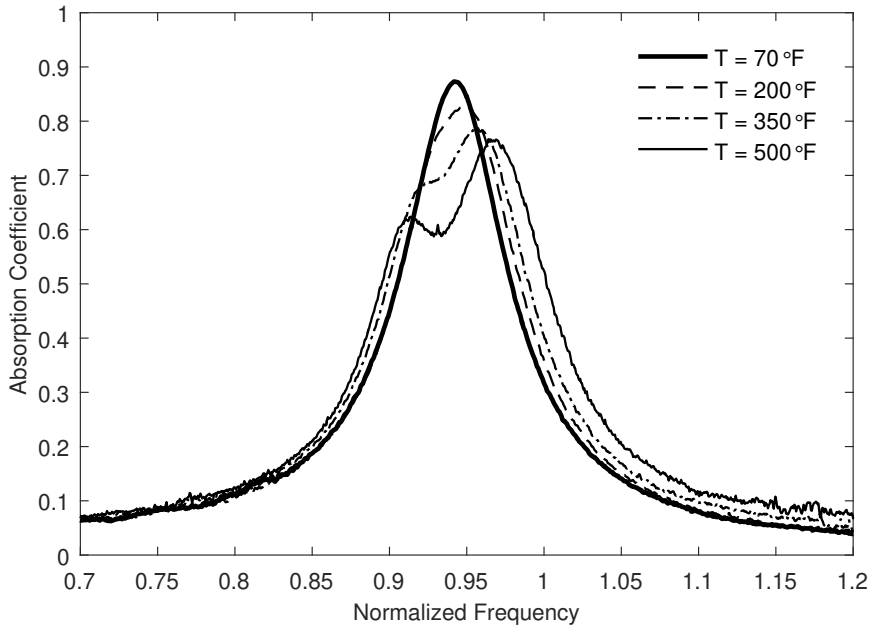

Figure 8.9: Absorption coefficient of three half-wave resonators at different temperatures with a Mach 0.1 mean flow through the resonators.

8.4 On the Numerical Model at High Temperatures

No numerical model was developed for the effects of temperature on the acoustic damping because the temperature was found to have little effect on the amount of acoustic damping up to at least 500°F (260°C), which was the upper limit of the present experiments. However, it would be a straightforward matter to incorporate the acoustic damping mechanisms within the fluid into the numerical model. In fact, Lahiri, et al. [41] provided expressions for the wavenumber due to the combined losses at the wall and within the fluid, so this wavenumber could be substituted into the numerical model for mean flow to include the effects of temperature.

The effect of a temperature gradient is more challenging to incorporate into the numerical model. To a first approximation, the effect of the axial temperature gradient could be included in the model by allowing the temperature in each region of the model to be a different constant value. For example, the upstream thermocouple measurement could be

set as the temperature in side A of the two-sided impedance tube, the downstream thermocouple measurement could be set as the temperature in side B, and the mean of the two measurements could be set as the temperature in the resonator. Properties such as the density, speed of sound, and the cut-on frequencies of the higher order modes would then vary between the different duct regions in the model. However, this method is only an approximation because it assumes that the temperature changes occur instantaneously across the area discontinuities, and it does not take into consideration the temperature gradients within each individual duct section. To truly incorporate the axial temperature gradient within each duct section into the model, wavenumber models for the propagation of acoustic waves through an axial temperature gradient would have to be used. Similarly, it would be challenging to incorporate the vertical temperature gradient into the numerical model because the current wavenumber models assume that the temperature is constant across the cross-section.

8.5 Summary

In this chapter, the effects of temperature on the acoustic damping of propellant injectors were investigated at different mean flow rates and elevated temperatures in the linear acoustic regime for the plane wave mode. The effects of temperature and the contributions of the physical mechanisms responsible for the acoustic damping are summarized below.

Experimental and Numerical Results

The acoustic dissipation mechanisms at elevated temperatures were discussed, and the acoustic attenuation within the fluid itself was compared to the attenuation in the acoustic boundary layer. The temperatures and frequencies at which the attenuation within the fluid is non-negligible in the half-wave resonators were plotted for different Mach numbers and concentrations of water vapor. The attenuation within the fluid was shown to become more important as the temperature increases.

The absorption coefficients of several half-wave resonator configurations at different temperatures were presented. The effect of temperature on the acoustic damping was shown to be negligible up to at least 500°F (260°C). However, some measurements at low Mach numbers suggested that a vertical temperature gradient existed within the cross-section of the impedance tube, which affected the resonance frequency and absorption coefficient of the resonators.

No numerical model was developed for the effect of temperature, but the effects of temperature could be incorporated into the numerical model by using a wavenumber that includes the damping mechanisms within the fluid. Methods for incorporating the temperature gradient into the numerical model were also briefly discussed.

Acoustic Damping Mechanisms

For the experiments discussed in this chapter, it was shown that the physical mechanisms responsible for the acoustic damping are viscothermal losses in the acoustic boundary layer, acoustic radiation from the open end of the injectors opposite the incident acoustic waves, dissipation due to turbulence, the conversion of acoustic energy to vorticity at the open ends of the injectors, and attenuation within the bulk fluid itself. The viscothermal losses in the acoustic boundary layer and the acoustic radiation from the open end were shown to be present for half-wave resonators at all flow and temperature conditions. The dissipation due to turbulence and the conversion of acoustic energy to vorticity at the open ends of the injectors were found to become important when there is nonzero mean flow. The new acoustic damping mechanism introduced by high temperatures was found to be the attenuation within the fluid itself, which occurs because the vibrational relaxation of the molecules in air becomes increasingly significant as the temperature increases. However, at temperatures up to at least 500°F (260°C), which was the upper limit of the present experiments, the attenuation within the fluid was found to be less significant than the other acoustic damping mechanisms.

CHAPTER 9
EFFECT OF HIGH AMPLITUDE

9.1 Overview

In this chapter, the effects of high incident sound amplitudes on the acoustic damping of propellant injectors are investigated for the following geometric parameters:

- Geometric features of the injectors
- Number of injectors

The experiments presented in this chapter are conducted in the two-sided impedance tube using the 3D-printed propellant injectors with unique geometric features (see Figures 4.10–4.12) and multiple stainless steel half-wave resonators (see Figure 4.14). The experiments are conducted in quiescent air at ambient conditions in both the linear and nonlinear acoustic regimes for the plane wave mode. Unlike the experiments discussed in previous chapters, in which broadband excitation was used to measure all frequencies simultaneously, single-frequency sinusoidal excitation is used to achieve high amplitudes in the experiments presented in this chapter. The acoustic amplitudes of the sound waves incident on the injectors are expressed in terms of sound pressure level (SPL) and fall in the range of 110–155 dB. The experiments are conducted at a relatively small number of frequencies close to the resonance frequencies of the injectors. The physical mechanisms responsible for the acoustic damping in the experiments described in this chapter include:

- Viscous and thermal losses in the acoustic boundary layer
- Acoustic radiation from the open end of the injectors opposite the incident acoustic waves

- Dissipation due to turbulence
- Conversion of acoustic energy to vorticity at the open ends of the injectors

The outline of this chapter is as follows: First, a brief justification is given in Section 9.2 for applying the experimental methodology developed for linear wave propagation to high amplitudes. Next, in Sections 9.3–9.4, the effects of high incident sound amplitudes on the acoustic damping are investigated using three of the propellant injectors with different geometric features and multiple half-wave resonators. Selected results from the particle image velocimetry (PIV) measurements of the flow field at the open end of the injectors opposite the incident acoustic waves are then presented in Section 9.5 to show the flow features that are formed at high amplitudes. Next, the dissipation mechanisms responsible for the acoustic losses in the flow field are discussed, and methods are developed in Sections 9.6–9.7 to calculate the nonlinear sound power dissipation from the acoustic and PIV measurements. Finally, in Section 9.8, the values of the nonlinear sound power dissipation calculated from the acoustic and PIV measurements are compared to one another quantitatively, and possible explanations for the differences between the acoustic and PIV measurements are discussed.

9.2 Nonlinear Wave Propagation

It is well established that at low sound amplitudes, the assumptions used to derive the linear acoustic wave equation are generally valid, and acoustic properties are independent of amplitude [20]. However, at high amplitudes, the governing equations for the acoustic propagation become nonlinear, and some acoustic properties can be shown to vary with amplitude [20]. The definition of what constitutes “low” and “high” amplitudes is problem-dependent and separates the linear and nonlinear acoustic regimes.

At very high amplitudes, the propagation speed of an acoustic wave varies with amplitude. The variation in the propagation speed causes a single-frequency acoustic wave to

eventually steepen into a shock wave. Kinsler, et al. [20] described the distance over which this nonlinear steepening occurs by the discontinuity distance

$$L_{\text{nonlinear}} = \left[\left(\frac{\gamma + 1}{2} \right) M_a k \right]^{-1} \tag{9.1}$$

where γ is the ratio of specific heats, $M_a = u/c$ is the acoustic Mach number based on the particle velocity, and k is the wavenumber. In the experiments presented in this chapter, the highest incident sound pressure level in the impedance tube is 155 dB, and the highest frequency under consideration is less than 2000 Hz. At these conditions, the discontinuity distance is approximately 3.6 m, which is shorter than the discontinuity distance at the other amplitudes and frequencies measured in this work. As shown in Table 4.2, the farthest distance between the microphones and the test article in HOTMESS is 338 mm, so the discontinuity distance is more than an order of magnitude greater than the propagation distance between the microphones and the test article. Therefore, nonlinear steepening due to propagation in the impedance tube is neglected in these experiments, and the acoustic measurement methodology described in Chapter 3 is assumed to remain reasonably accurate for the experiments at high amplitudes.

9.3 Effect of the Geometric Features at High Amplitudes

9.3.1 Normalized Resistance of Unique Injectors at High Amplitudes

The acoustic properties of the "straight," "protrusion," and "recess" propellant injectors were measured using the two-sided experimental facility, HOTMESS, to investigate the effects of high incident sound amplitudes on injectors with different geometric features. Figure 9.1 shows the normalized termination resistance, θ_T, at resonance of each injector as a function of the incident sound pressure level in the impedance tube. At low incident sound amplitudes, the resistance does not vary significantly with amplitude, but at higher amplitudes, the resistance increases monotonically with increasing amplitude. This

behavior is qualitatively similar to that of orifices [54] and Helmholtz and quarter-wave resonators [6] at high amplitudes.

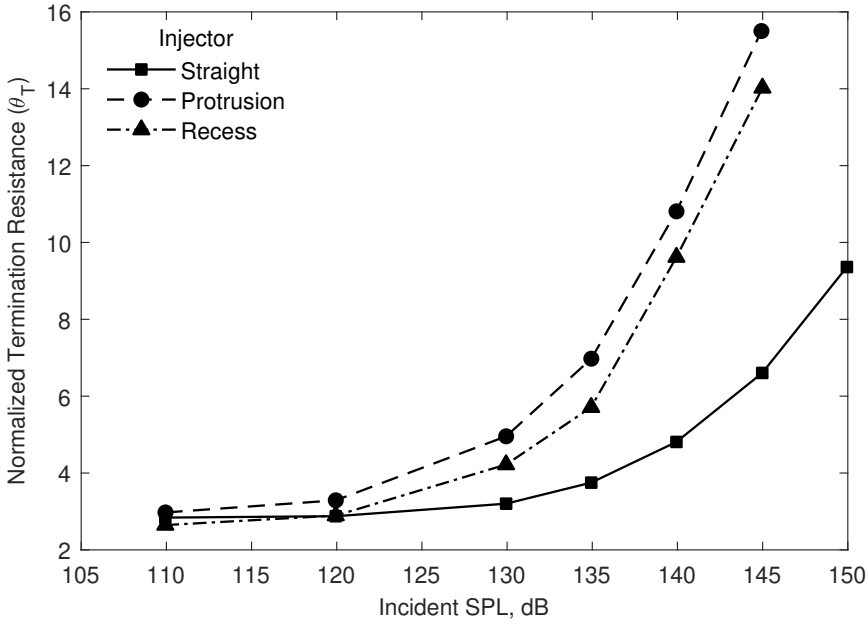

Figure 9.1: Normalized termination resistance at resonance as a function of incident amplitude for the propellant injectors with different geometric features.

It is commonly accepted that the amplitude at which the resistance begins to increase characterizes the boundary between the linear and nonlinear acoustic regimes [20]. Figure 9.1 shows that nonlinearities begin to occur at a lower amplitude for the "protrusion" and "recess" injectors than for the "straight" injector. Additionally, the resistance of the "protrusion" and "recess" injectors increases more quickly with amplitude than the resistance of the "straight" injector. The main difference between these injectors is that the "protrusion" and "recess" injectors include an inlet protrusion, which has a cross-sectional area equal to about 51% of the area of the main body of the injector. Due to this reduction in the cross-sectional area, continuity requires that, for a fixed incident SPL, the particle velocity through the inlet protrusion be approximately twice the particle velocity through the main body of the injector. The particle velocity at the end of the "protrusion" and "recess" injectors is thus expected to be roughly twice the particle velocity at the end of the "straight" injector at the same incident amplitude.

At high acoustic amplitudes, Ingard and Ising [54] found that the resistance of an orifice increases approximately linearly with the particle velocity. Atig, et al. [89] also showed that the resistance of the open end of a cylindrical tube increases with the particle velocity. Additionally, experimental evidence exists for the formation of vortices at an orifice or the open end of a tube at high amplitudes, and the strength of the resulting vortices and the acoustic resistance both increase with particle velocity [96]. These studies suggest that the normalized resistance of the injectors increases at high amplitudes due to the conversion of acoustic energy into the kinetic energy of vortices, and this increase is primarily caused by the resulting increase in the particle velocity—and thus the strength of the vortices—at the open end. This hypothesis is examined qualitatively in Section 9.5 and quantitatively in Section 9.8.

9.3.2 Absorption Coefficient of Unique Injectors at High Amplitudes

Straight Injector

Figure 9.2 shows the absorption coefficient of the "straight" injector at different incident sound pressure levels. The curve labeled "Broadband" was measured using broadband excitation in the linear acoustic regime. The change in the absorption coefficient with amplitude is minimal up to almost 130 dB, but as the amplitude increases further, the peak absorption coefficient decreases and the absorption frequency bandwidth increases. The behavior of the peak absorption coefficient is related to the normalized resistance at resonance; this relationship is plotted in Figure 5.2. At low amplitudes, the normalized termination resistance of the "straight" injector is greater than one at resonance, so as the resistance increases with amplitude, the peak absorption coefficient decreases.

Inlet Protrusion

Figure 9.3 shows the absorption coefficient of the "protrusion" injector at different incident sound pressure levels. The inlet protrusion has several effects on the acoustic damping of

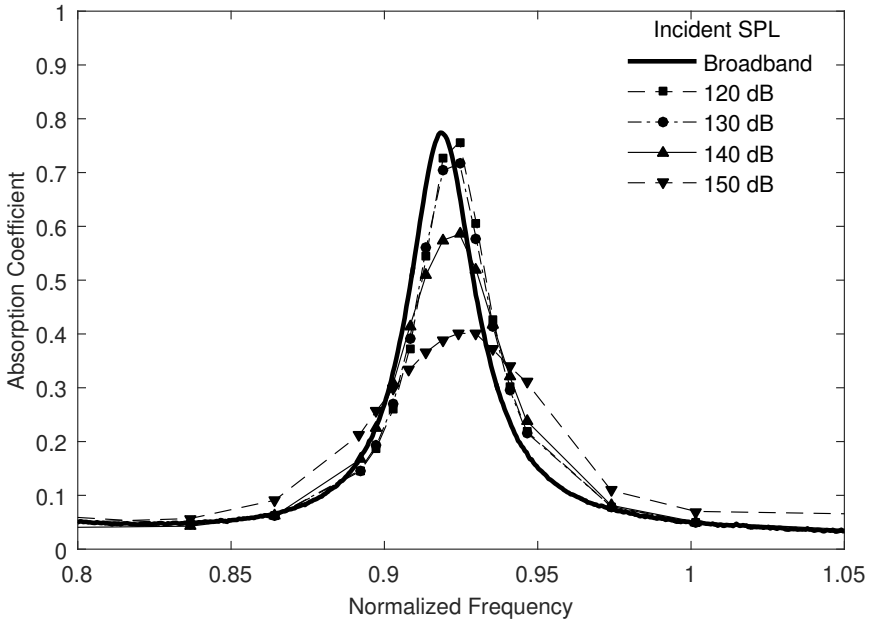

Figure 9.2: Absorption coefficient of the "straight" injector at different incident amplitudes.

the injector at both low and high amplitudes. The resonance frequency of the "protrusion" injector is lower than that of the "straight" injector at all amplitudes, as discussed in Section 6.2. As the amplitude increases, the peak absorption coefficient of the "protrusion" injector decreases more quickly than that of the "straight" injector. This corresponds to the behavior of the normalized resistance at resonance, which increases more quickly with amplitude for the "protrusion" injector than for the "straight" injector. These results show that the inlet protrusion, which has a relatively minor effect on the acoustic damping at low amplitudes (besides shifting the resonance frequency), has a major effect on the acoustic damping at high amplitudes.

Recess

Figure 9.4 shows the absorption coefficient of the "recess" injector at different incident sound pressure levels. The recess increases the resonance frequency at all amplitudes, as discussed in Section 6.2. However, the peak absorption coefficient and the normalized resistance at resonance of the "recess" and "protrusion" injectors are very similar at each incident amplitude. These results indicate that major effect of the recess is to shift the

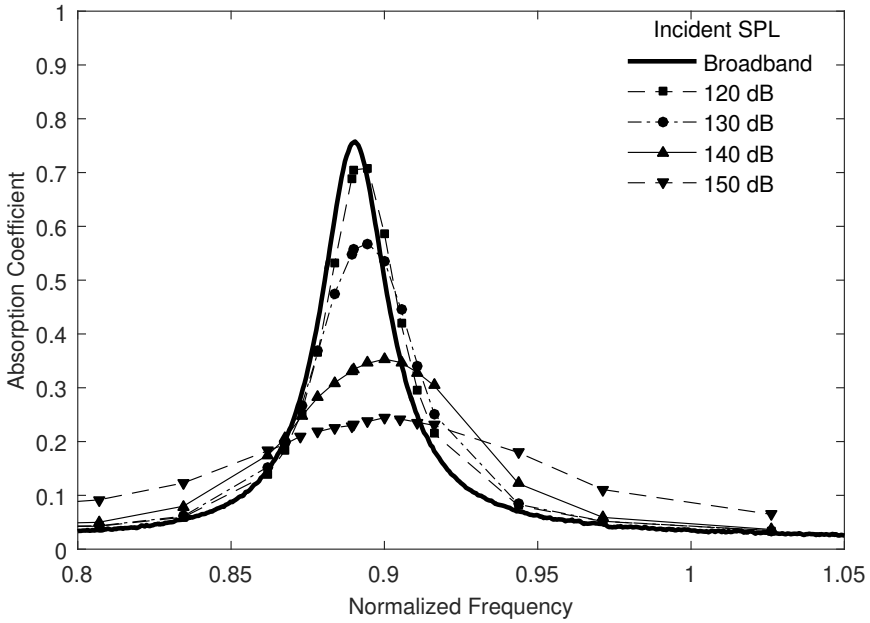

Figure 9.3: Absorption coefficient of the "protrusion" injector at different incident amplitudes.

resonance frequency, but the recess has little other effect on the acoustic damping at high amplitudes.

Absorption Frequency Bandwidth of Unique Injectors at High Amplitudes

Figure 9.5 shows the absorption frequency bandwidth of each injector as a function of the incident sound pressure level in the impedance tube. At low amplitudes, the absorption frequency bandwidth is nearly constant, but at higher amplitudes, the bandwidth increases monotonically with increasing amplitude. The simplified analytical expression for the bandwidth given by Eq. (5.37) predicts that the bandwidth scales with the normalized resistance at resonance, and indeed, the behavior of the bandwidth is similar to that of the measured normalized resistance. The normalized resistance and absorption frequency bandwidth of the "protrusion" and "recess" injectors at high amplitudes are greater than those of the "straight" injector.

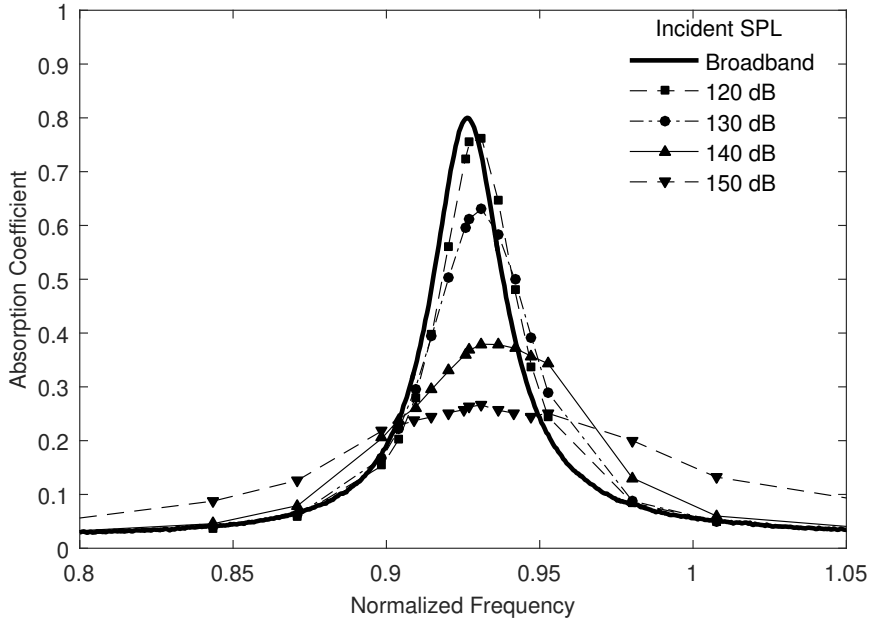

Figure 9.4: Absorption coefficient of the "recess" injector at different incident amplitudes.

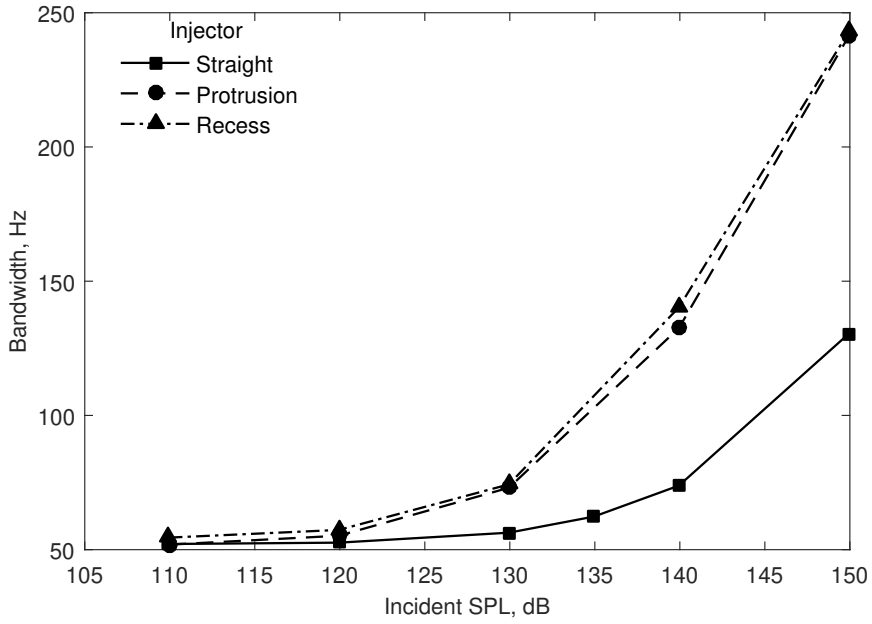

Figure 9.5: Absorption frequency bandwidth as a function of incident amplitude for the propellant injectors with different geometric features.

9.3.3 Resonance Frequency of Unique Injectors at High Amplitudes

Figure 9.6 shows the percentage change in the resonance frequency of each injector as a function of the incident sound pressure level in the impedance tube. The percentage change in the resonance frequency is evaluated with respect to the resonance frequency at an incident SPL of 110 dB. At SPLs greater than about 120 dB, the resonance frequency starts decreasing with increasing amplitude, and this decrease is more significant for the "protrusion" and "recess" injectors than for the "straight" injector. The behavior of the resonance frequency as a function of incident SPL is qualitatively similar to the behavior of the resonance frequency as a function of the mean flow velocity, which is shown in Figure 7.7. Park and Sohn [16] showed numerically that the length correction of a half-wave resonator increases—and thus the resonance frequency decreases—at high amplitudes, which they attributed to the formation of a jet flow at the open ends of the resonator. This same trend is observed in the current experiments.

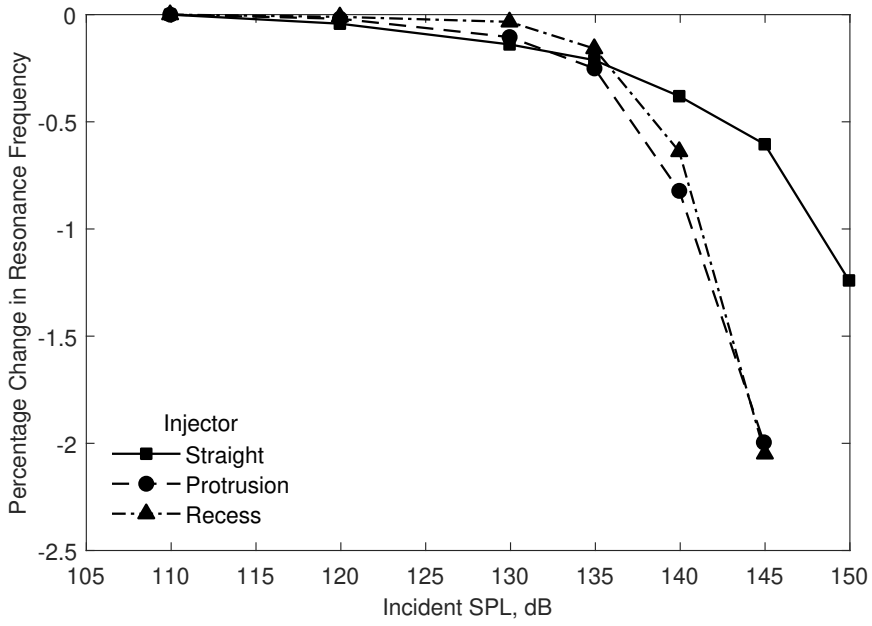

Figure 9.6: Percentage change in the resonance frequency as a function of incident amplitude for the propellant injectors with different geometric features.

Recall that the resonance frequency is defined as the frequency at which the reactance

is zero. In the linear acoustic regime, the peak absorption frequency and the resonance frequency are nearly identical. However, as the amplitude increases, the peak absorption frequency does not change significantly (and may even increase slightly), but the resonance frequency decreases, so the difference between the peak absorption frequency and the resonance frequency increases.

9.4 Effect of the Number of Injectors at High Amplitudes

9.4.1 Normalized Resistance of Multiple Injectors at High Amplitudes

The acoustic properties of multiple stainless steel half-wave resonators were measured using HOTMESS to investigate the effects of high amplitudes on multiple injectors. Figure 9.7 shows the normalized termination resistance, θ_T, at resonance for different numbers of half-wave resonators as a function of the incident sound pressure level in the impedance tube. As the number of resonators increases, the amplitude of the onset of the nonlinear acoustic regime also increases. The continuity equation requires that the volume velocity remain constant across the area discontinuity between the impedance tube and the half-wave resonators, which means that the particle velocity in each resonator varies inversely with the number of resonators. At high amplitudes, the acoustic resistance of an orifice or open end of a tube is known to be a function of the particle velocity [54, 89]. Thus, as the number of resonators increases, the particle velocity in each resonator at a given incident sound pressure level decreases, so the normalized resistance varies less strongly with the incident amplitude.

9.4.2 Sound Power Coefficients of Multiple Injectors at High Amplitudes

As shown in Figure 9.7, the normalized termination resistance of three half-wave resonators at resonance is slightly greater than one at low amplitudes, and it increases with incident SPL at high amplitudes. Thus, based on the behavior of the absorption coefficient as a function of the normalized termination resistance at resonance plotted in Figure 5.2, it is ex-

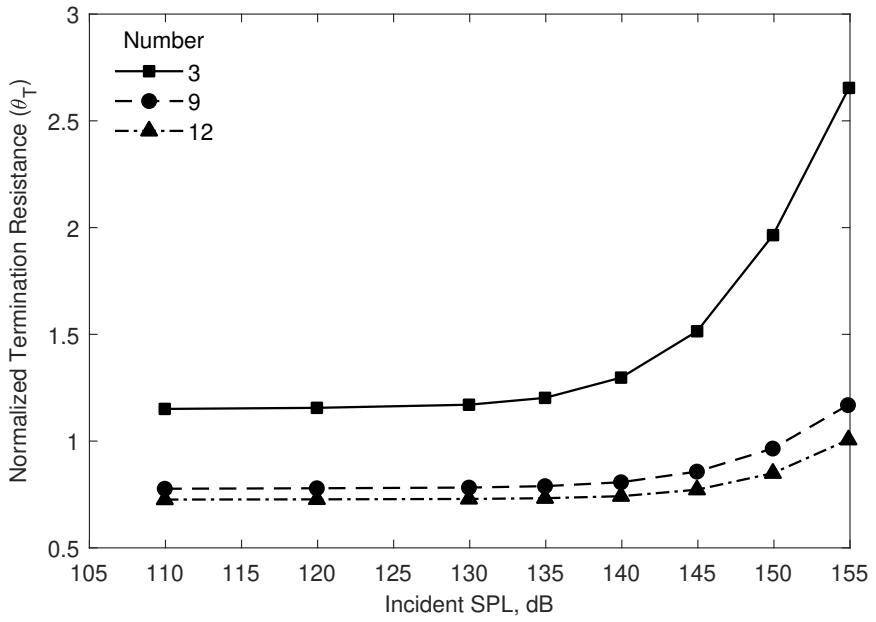

Figure 9.7: Normalized termination resistance at resonance as a function of incident amplitude for different numbers of half-wave resonators.

pected that the peak absorption coefficient will decrease with increasing incident SPL. This is exactly what is observed in the present experiments as seen in Figure 9.8a, which shows the absorption coefficient of the three half-wave resonators at different incident SPLs. Conversely, the normalized termination resistance of the twelve half-wave resonators at resonance shown in Figure 9.7 is less than one at low amplitudes, and it increases with incident SPL at high amplitudes until it is almost exactly equal to one at an incident SPL of 155 dB. Thus, based on the behavior of the absorption coefficient as a function of the normalized termination resistance at resonance plotted in Figure 5.2, it is expected that the peak absorption coefficient will increase with incident SPL and reach its maximum at 155 dB. This is exactly what is observed in the present experiments as seen in Figure 9.8b, which shows the absorption coefficient of the twelve half-wave resonators at different incident SPLs. However, the increase is small because the peak absorption coefficient of the twelve half-wave resonators is already close to its maximum value at low amplitudes. Figure 9.8 also shows that the absorption frequency bandwidth increases slightly with increasing incident SPL. Thus, for the three half-wave resonators, high incident SPLs degrade the absorption

coefficient very close to resonance but slightly enhance the absorption coefficient at frequencies away from resonance. For the twelve half-wave resonators, high incident SPLs slightly enhance the absorption coefficient at all frequencies. However, the change in the absorption coefficient with increasing SPL is relatively small for twelve resonators, so as the number of resonators increases, the acoustic damping of the resonators becomes more invariant to changes in the amplitude of the incident acoustic waves.

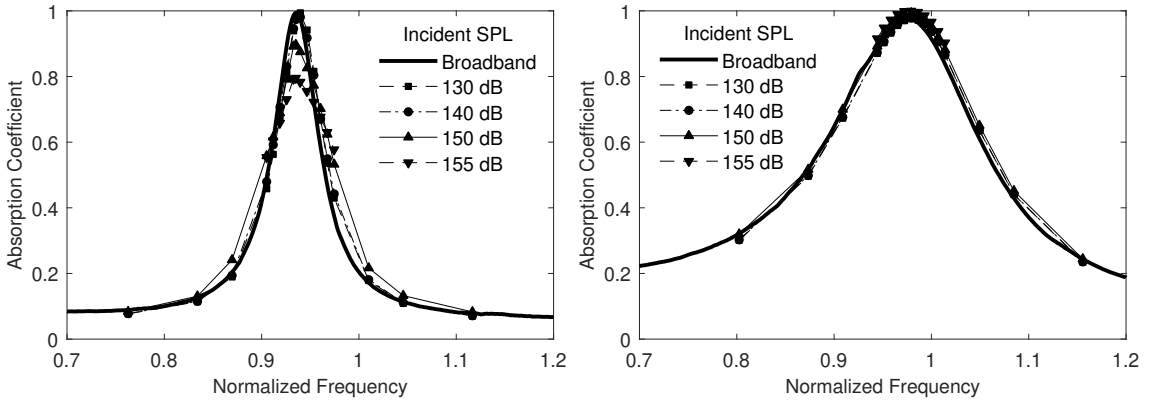

(a) Three half-wave resonators

(b) Twelve half-wave resonators

Figure 9.8: Absorption coefficient of three and twelve half-wave resonators at different incident amplitudes.

Figure 9.9 shows the power dissipation coefficients of three and twelve half-wave resonators at different incident SPLs. At sufficiently high amplitudes, the power dissipation coefficients near resonance increase with increasing incident SPL because there are additional dissipation mechanisms at high amplitudes, such as the conversion of acoustic energy into vorticity at the open ends of the resonators, which are not present in the linear acoustic regime. However, Figure 9.10 shows that the power transmission coefficients of three and twelve half-wave resonators decrease with increasing incident SPL at frequencies near resonance. The power transmission coefficients decrease because some fraction of the acoustic energy that would be transmitted from the resonators into the impedance tube at low amplitudes is instead converted into vorticity at high amplitudes. For the twelve resonators, there is little change in the absorption coefficient shown in Figure 9.8b because the increase in the power dissipation coefficient and the decrease in the power transmission

coefficient nearly offset each other. For the three resonators, though, the absorption coefficient shown in Figure 9.8a decreases with increasing incident SPL because the decrease in the power transmission coefficient is greater than the increase in the power dissipation coefficient.

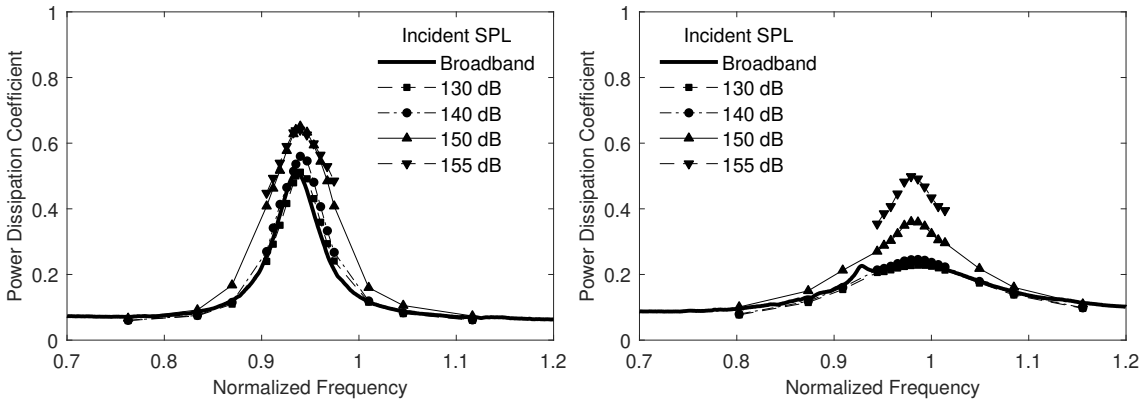

(a) Three half-wave resonators (b) Twelve half-wave resonators

Figure 9.9: Power dissipation coefficient of three and twelve half-wave resonators at different incident amplitudes.

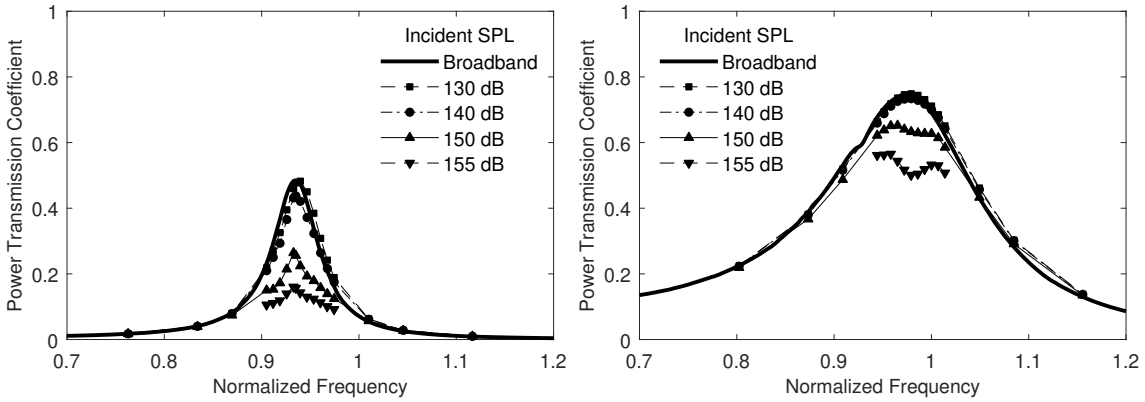

(a) Three half-wave resonators (b) Twelve half-wave resonators

Figure 9.10: Power dissipation coefficient of three and twelve half-wave resonators at different incident amplitudes.

9.4.3 Resonance Frequency of Multiple Injectors at High Amplitudes

Figure 9.11 shows the percentage change in the resonance frequency of different numbers of half-wave resonators as a function of the incident sound pressure level in the impedance

tube. The percentage change in the resonance frequency is evaluated with respect to the resonance frequency at an incident SPL of 110 dB. It is seen that, at high amplitudes, the resonance frequency of multiple resonators decreases with increasing amplitude. The behavior of the resonance frequency as a function of amplitude appears to be qualitatively similar to the behavior of the resonance frequency as a function of the mean flow velocity shown in Figure 7.15. Park and Sohn [16] showed numerically that, at high amplitudes, the length correction of a half-wave resonator increases—and thus the resonance frequency decreases—due to the formation of a jet flow at the open ends of the resonator. At a given incident SPL, the velocity of the jet emanating from each resonator increases as the number of resonators decreases. Thus, the change in resonance frequency is expected to be more significant if there are fewer resonators. This is exactly what is observed in the present experiments as seen in Figure 7.15 (except at the highest incident SPL of 155 dB).

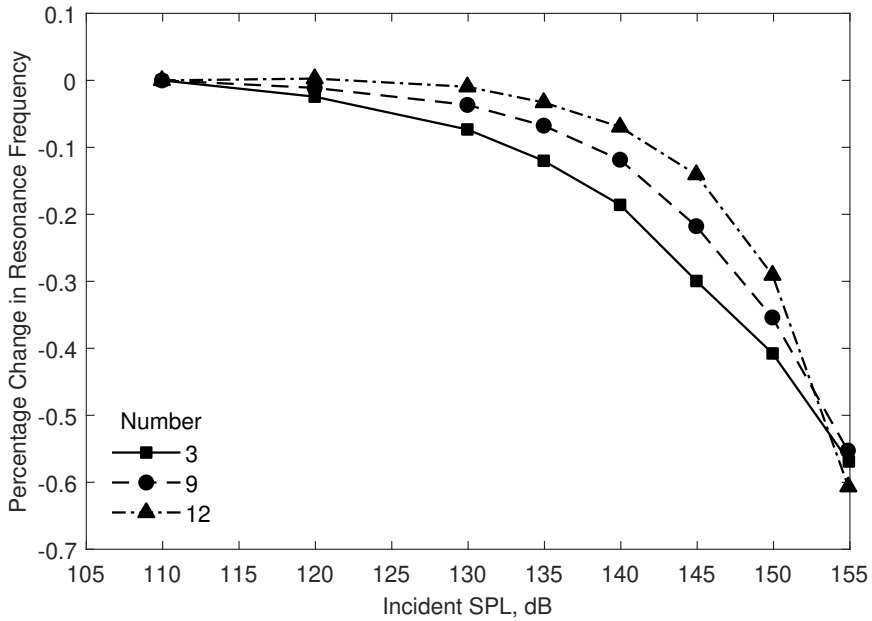

Figure 9.11: Percentage change in the resonance frequency as a function of incident amplitude for different numbers of half-wave resonators.

9.5 Particle Image Velocimetry Measurements

In the previous sections, the acoustic damping of propellant injectors was shown to vary with the incident SPL at high amplitudes. This change in the acoustic damping was attributed without proof to the conversion of acoustic energy into the kinetic energy of vortices at the open ends of the injectors. As discussed in this section, the existence of vortices was confirmed experimentally using particle image velocimetry (PIV) measurements of the flow fields at the inlet ends of the "straight," "protrusion," and "recess" injectors at incident SPLs of 130 dB, 140 dB, and 150 dB. Selected results from the PIV measurements are presented in this section to demonstrate the effects of the geometric features of the injectors at different amplitudes.

As described in Section 4.4, the PIV measurements were conducted using the 101.6-mm diameter one-sided impedance tube to provide optical access to the inlet ends of the injectors. The velocities were measured at every point on a two-dimensional rectangular grid bisecting the inlet end of each injector, as shown in Figure 9.12, where the origin of the spatial grid is defined as the center of the open end of the injector. The grid spacing in the y-direction, Δy, and the z-direction, Δz, are both constant. The velocity vector at grid point (i, j) is labeled as $\mathbf{v}(i, j)$, and it has components $v_y(i, j)$ and $v_z(i, j)$ in the y- and z-directions, respectively.

In reality, the flow field at the open end of an injector is three-dimensional. Since the geometry of each propellant injector is axisymmetric, the flow field is also assumed to be axisymmetric. Therefore, the grid points in either the upper or lower half-plane could be neglected because it is assumed that $v_y(i, -j) = -v_y(i, j)$ and $v_z(i, -j) = v_z(i, j)$. However, all grid points are included in the analysis to minimize experimental errors by averaging the results over both half-planes. The velocities measured at grid points in the upper half-plane are assumed to be representative of the flow field at angles $0^\circ < \theta < 180^\circ$ in the three-dimensional upper half-space, and the velocities measured at grid points in the

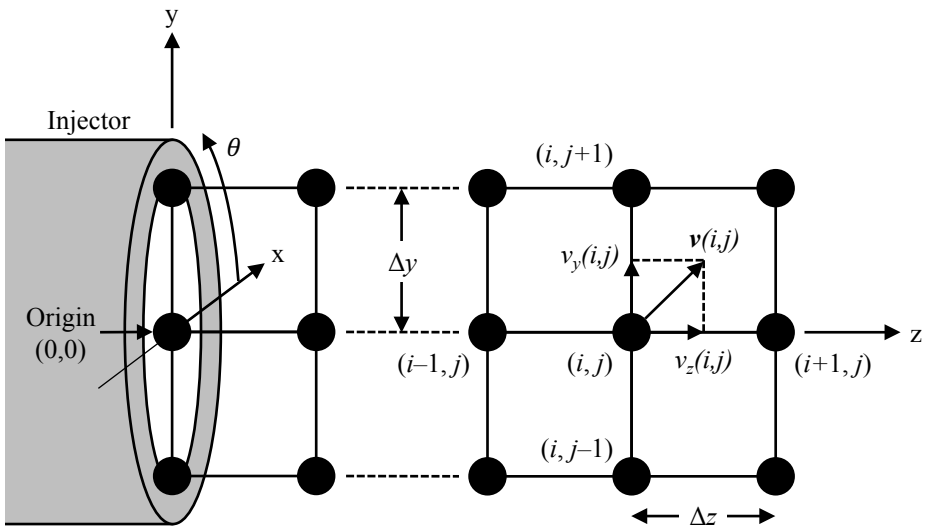

Figure 9.12: Representative two-dimensional spatial grid for the PIV measurements at the open end of an injector.

lower half-plane are assumed to be representative of the flow field at angles $-180^\circ < \theta < 0^\circ$ in the three-dimensional lower half-space.

9.5.1 PIV Measurements for the Straight Injector

PIV measurements of the velocity flow field at the inlet end of the "straight" injector were conducted at its linear resonance frequency of 1660 Hz for incident SPLs of 130 dB, 140 dB, and 150 dB. Figure 9.13 shows the velocity and vorticity fields outside the open end of the "straight" injector at 1660 Hz and an incident SPL of 140 dB. The flow fields are plotted from the time $0.0T$ in steps of $0.2T$ until $1.0T$, where T is the acoustic period. The white rectangle at the left side of each plot represents the inner dimensions of the open end of the injector, and the gray rectangles represent the wall thickness of the injector. Positive values of vorticity correspond to counterclockwise rotation, and negative values correspond to clockwise rotation. The magnitude and direction of the velocity at each point can be difficult to distinguish in Figure 9.13, so Figure 9.14 shows the corresponding axial particle velocity profiles at various distances downstream of the open end of the "straight" injector at an incident SPL of 140 dB. The velocity profiles are plotted starting at a distance

of $z = 1.5$ mm from the open end of the injector because the PIV measurements closer to the open end may be contaminated by optical glare from the injector.

Although there is some vorticity present in the measured flow field shown in Figure 9.13, the magnitude of the vorticity is relatively small, and it is confined to the region immediately surrounding the open end of the injector. The largest-magnitude vorticity occurs near the walls of the injector at $0.6T$. This vorticity is generated during outflow and is indicative of some flow separation at the open end of the injector, which may account for the increase in the normalized termination resistance of the "straight" injector at 140 dB compared to the linear acoustic regime, as shown in Figure 9.1. At a lower incident SPL of 130 dB, the PIV measurements indicate that the magnitude of the vorticity is significantly smaller than at 140 dB, but the flow field at 130 dB is not shown because the experimental uncertainties in the PIV measurements become more significant at low velocities. Even at an incident SPL of 140 dB, there are random patches of vorticity distributed throughout the flow field shown in Figure 9.13 that are likely due to experimental uncertainties. Similarly, the asymmetry and jaggedness of the axial velocity profiles shown in Figure 9.14 near the open end of the injector are likely due to experimental uncertainties in the PIV measurements. Ignoring these uncertainties, however, the axial particle velocity oscillates roughly sinusoidally about the zero mean during a single acoustic period, and the particle velocity amplitude decreases with distance from the open end of the injector. These characteristics describe an acoustic flow field, so the measured velocity flow field provides evidence that the acoustic losses downstream of the open end of the injector are relatively small at an incident SPL of 140 dB.

Figure 9.15 shows the velocity and vorticity fields outside the open end of the "straight" injector at 1660 Hz and an incident SPL of 150 dB, and Figure 9.16 shows the axial particle velocity profiles at various distances from the open end. The axial particle velocity profile at a distance of $z = 1.5$ mm from the open end indicates that inflow occurs at $0.0T$ and $0.2T$, and outflow occurs at $0.4T$, $0.6T$, and $0.8T$. Vorticity is ejected from the open end of

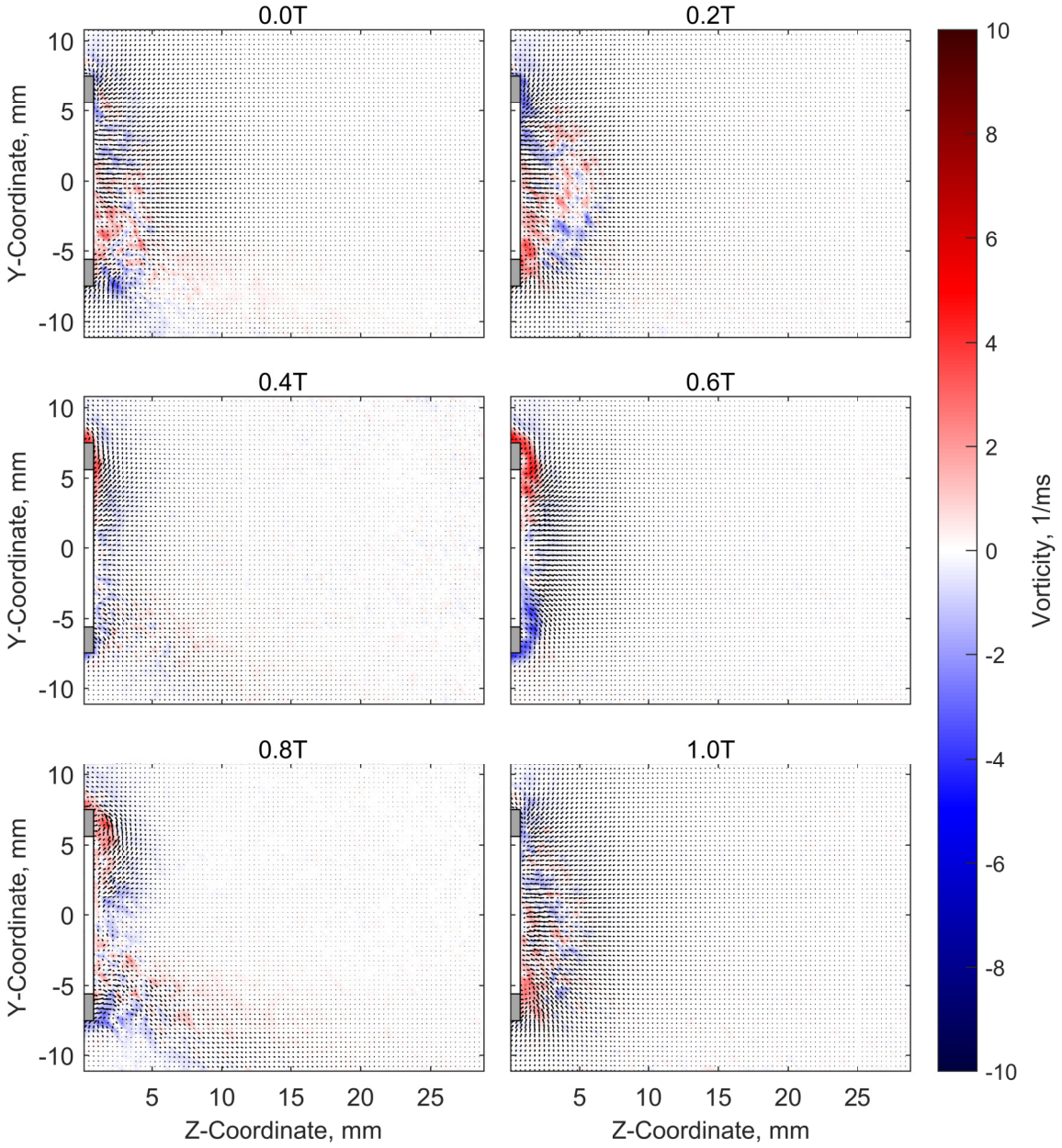

Figure 9.13: Velocity (arrows) and vorticity (colors) flow field outside the open end of the "straight" injector at an incident SPL of 140 dB.

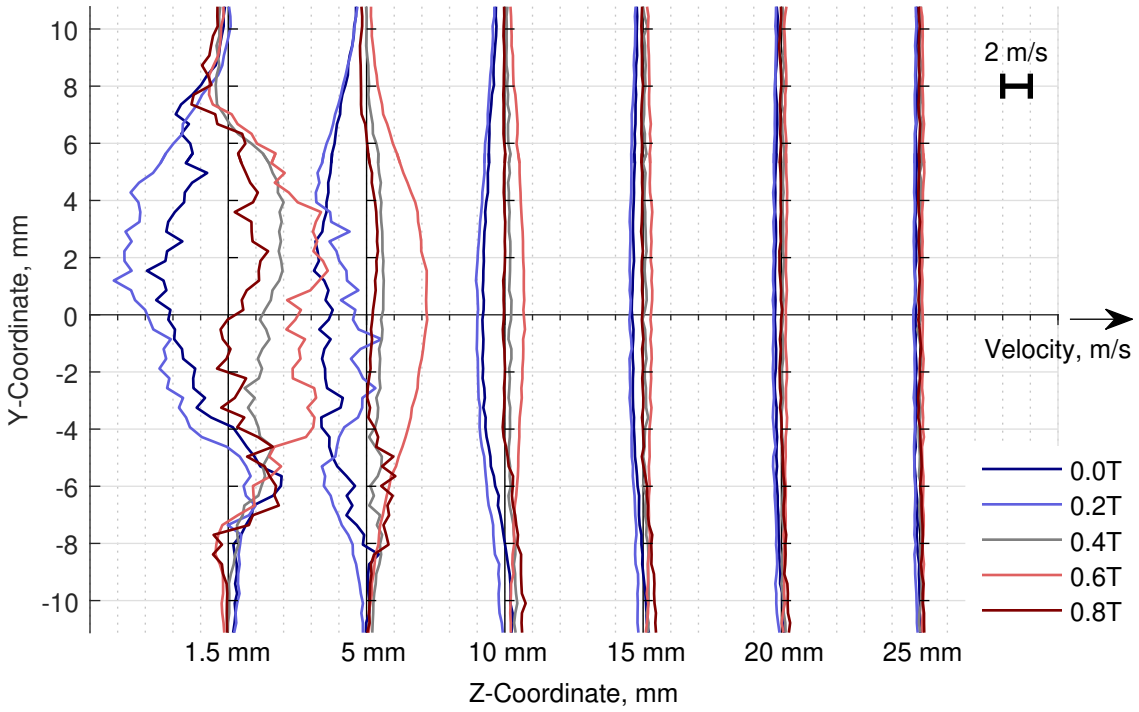

Figure 9.14: Velocity profiles at various distances downstream of the open end of the "straight" injector at an incident SPL of 140 dB.

the injector during the outflow cycle, as shown in the vorticity field at $0.6T$ in Figure 9.15. The vorticity is organized into counter-rotating primary and secondary ring vortices, which are shown most clearly in the vorticity fields at $0.6T$ and $0.8T$. However, these vortices remain near the open end of the injector during the inflow cycle, and they weaken over time. During the next outflow cycle, the primary vortex that remains in the flow field at $0.4T$ from the previous acoustic cycle is pushed downstream between $0.4T$ and $0.6T$ by the newly ejected vorticity. Note that the flow field is measured in a two-dimensional plane bisecting the open end of the injector, but the real flow field is three-dimensional and axisymmetric. Therefore, the vortices above and below the z-axis that appear to have different signs of vorticity are actually ring vortices in three-dimensional space.

Figures 9.16 shows that a steady jet is also formed at the open end of the "straight" injector at an incident SPL of 150 dB. This is evident because the axial particle velocity profiles downstream of the open end no longer oscillate about the zero mean. Sufficiently far downstream, the velocity is directed outward from the open end throughout the acoustic

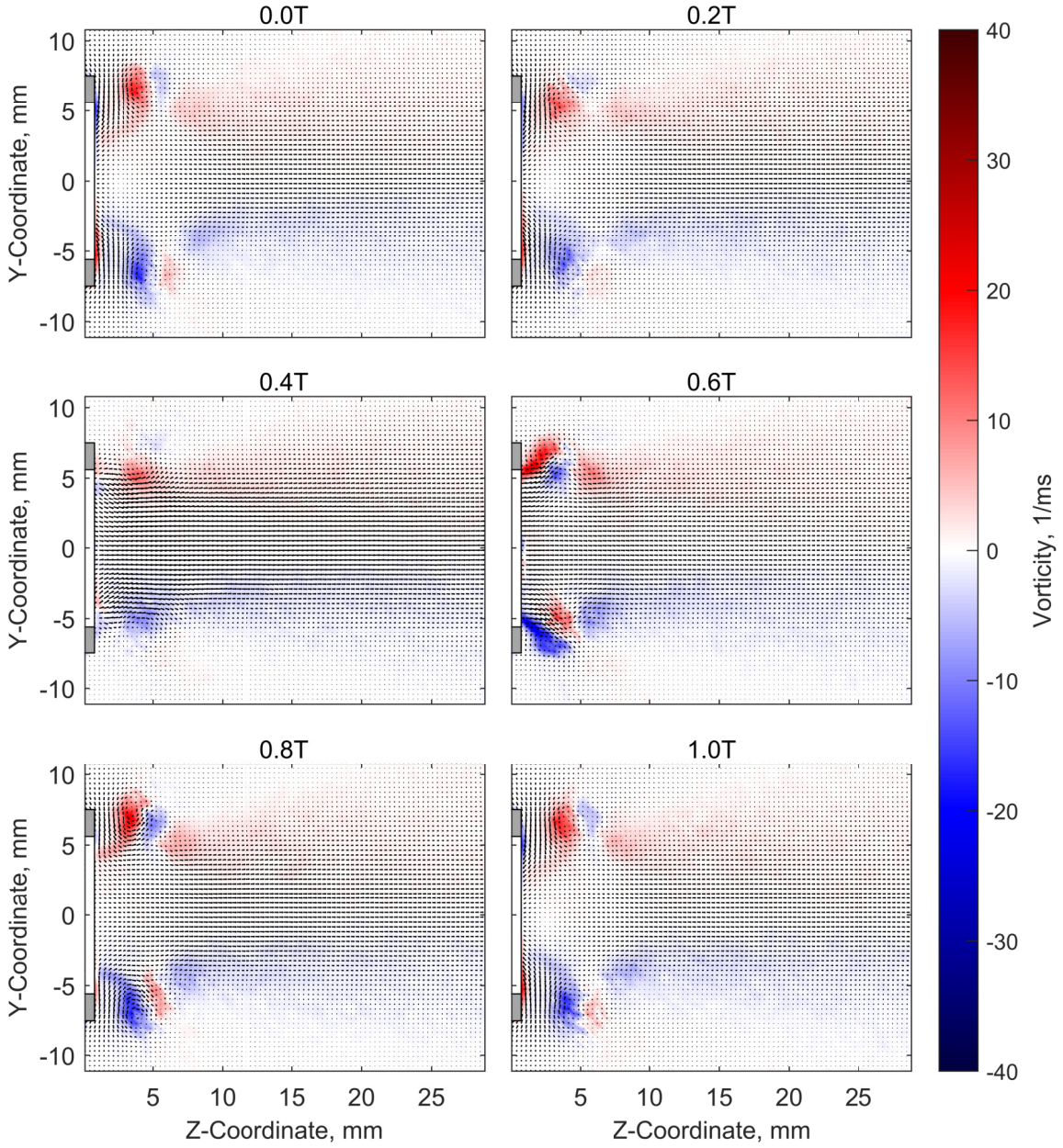

Figure 9.15: Velocity (arrows) and vorticity (colors) flow field outside the open end of the "straight" injector at an incident SPL of 150 dB.

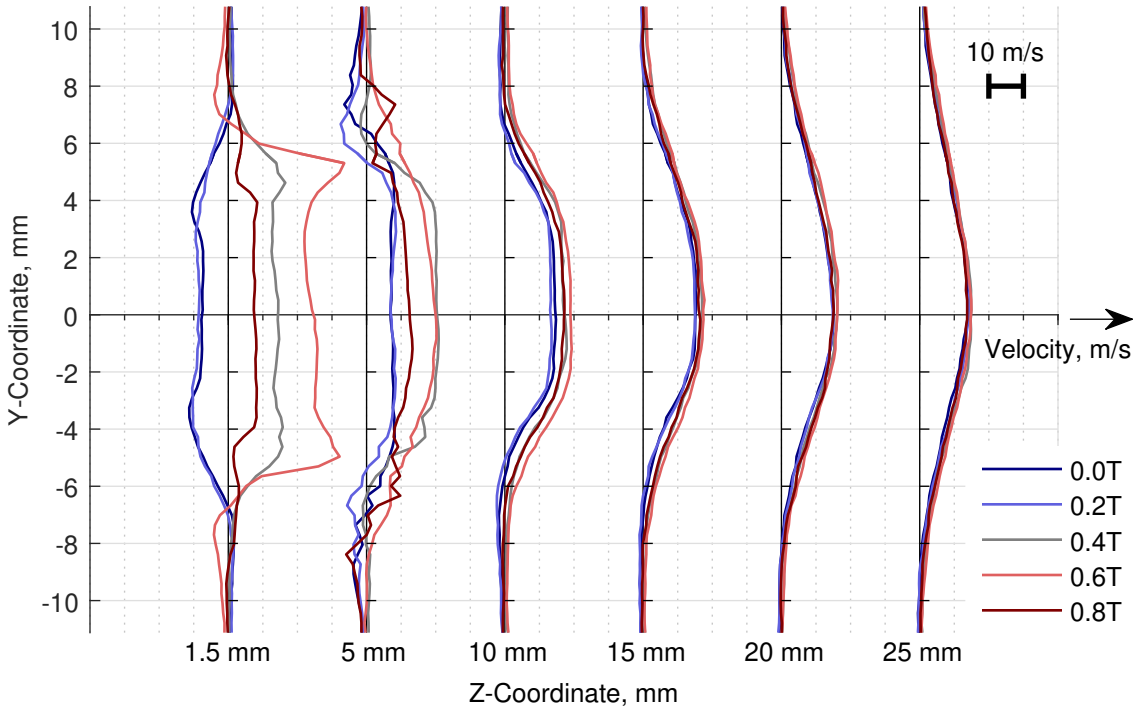

Figure 9.16: Velocity profiles at various distances downstream of the open end of the "straight" injector at an incident SPL of 150 dB.

cycle, and the velocity profiles resemble a mean jet flow. Figure 9.15 shows that there is nonzero vorticity in the shear layer surrounding this jet flow. There is no mean flow through the impedance tube, so the jet is generated by the high-amplitude acoustic oscillations. This phenomenon has previously been observed for orifices at high amplitudes [77] and is called a *synthetic jet*. Glezer and Amitay [149] stated that synthetic jets are "produced by the interactions of a train of vortices that are typically formed by alternating momentary ejection and suction of fluid across an orifice such that the net mass flux is zero." This exactly describes the flow field at the open end of the "straight" injector at an incident SPL of 150 dB.

The strength of the vortices and the magnitude of the particle velocity at the open end of the injector are significantly greater at an incident SPL of 150 dB than 140 dB (note the difference in the color scales between Figures 9.13 and 9.15 and also the difference in the velocity scales between Figures 9.14 and 9.16). The normalized termination resistance of the "straight" injector shown in Figure 9.1 was also found to be greater at 150 dB than

at 140 dB, so there is at least qualitative agreement between the increase in the resistance and the increase in the strength of the vortices and jet at the open end. A quantitative comparison between the acoustic and PIV measurements is given later in Section 9.8.

9.5.2 PIV Measurements for the Recess Injector

PIV measurements of the velocity flow field at the inlet end of the "recess" injector were conducted at its linear resonance frequency of 1680 Hz for incident SPLs of 130 dB, 140 dB, and 150 dB. Similar PIV measurements of the flow field at the inlet end of the "protrusion" injector were also conducted; however, the flow fields for the "protrusion" injector are not shown here because they are similar to those of the "recess" injector, and the "recess" injector is the more realistic injector based on the discussion in Section 6.2. Figure 9.17 shows the velocity and vorticity fields outside the open end of the "recess" injector at 1680 Hz and an incident sound pressure level of 130 dB, and Figure 9.18 shows the axial particle velocity profiles at various distances from the open end. Note that the flow field is measured outside the inlet end of the "recess" injector, which is the open end of the injector with the inlet protrusion. The inner radius of the open end of the "recess" injector is smaller than the inner radius of the "straight" injector because of the inlet protrusion, so the white and gray rectangles at the left side of each plot in Figure 9.17 are sized accordingly.

Qualitatively, the flow field at the open end of the "recess" injector at 130 dB shown in Figure 9.17 is similar to the flow field at the open end of the "straight" injector at 140 dB shown in Figure 9.13. In both flow fields, the magnitude of the vorticity is relatively small, and the largest-magnitude vorticity occurs near the walls of the injector during the outflow cycle. The results shown in Figure 9.1 indicate that the normalized resistance of the "recess" injector at 130 dB is also very close to the normalized resistance of the "straight" injector at 140 dB. The fact that these two different configurations have similar values of resistance and qualitatively similar flow fields supports the hypothesis that the acoustic losses at high amplitudes are due to the conversion of acoustic energy into vorticity. Quan-

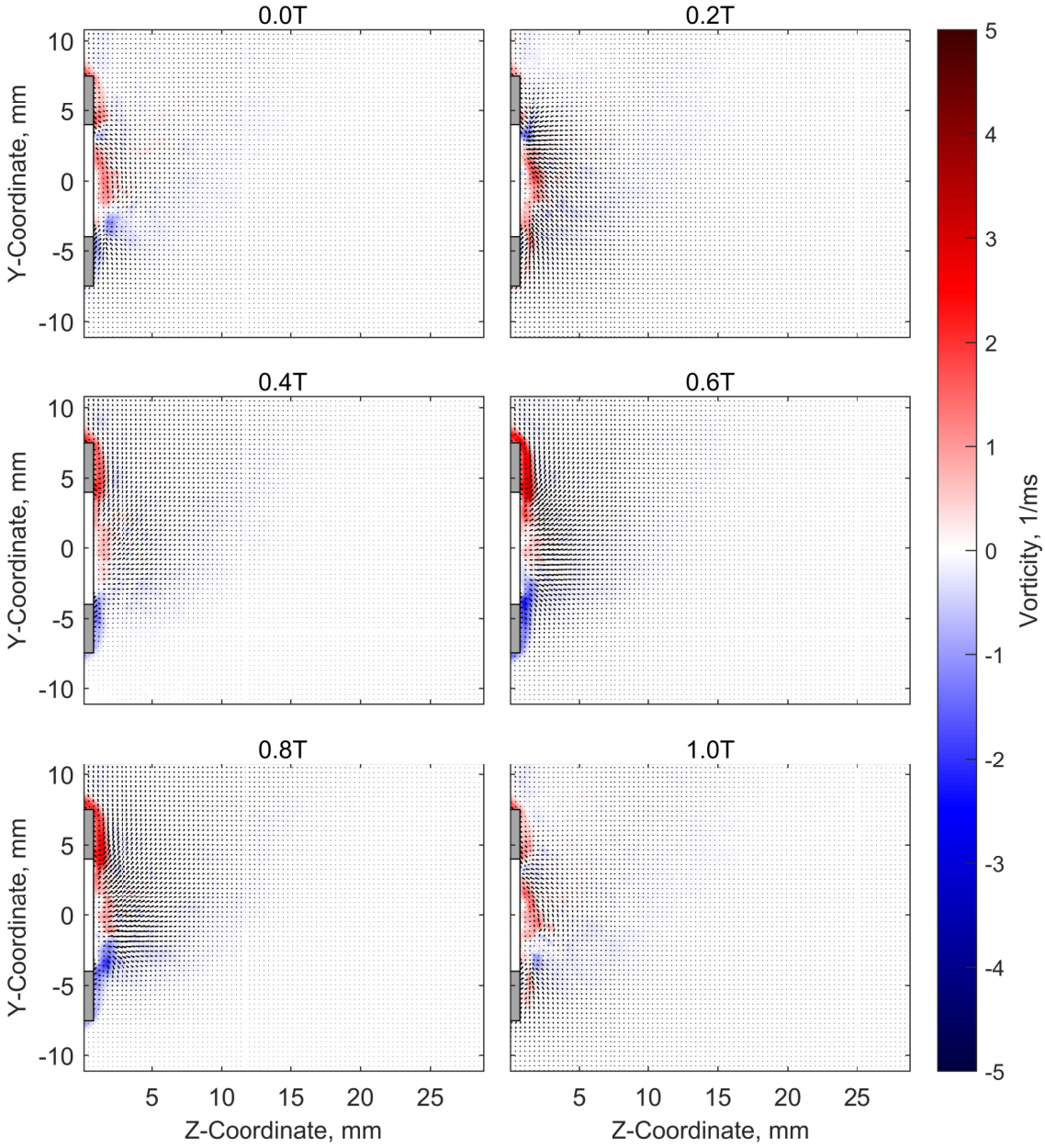

Figure 9.17: Velocity (arrows) and vorticity (colors) flow field outside the open end of the "recess" injector at an incident SPL of 130 dB.

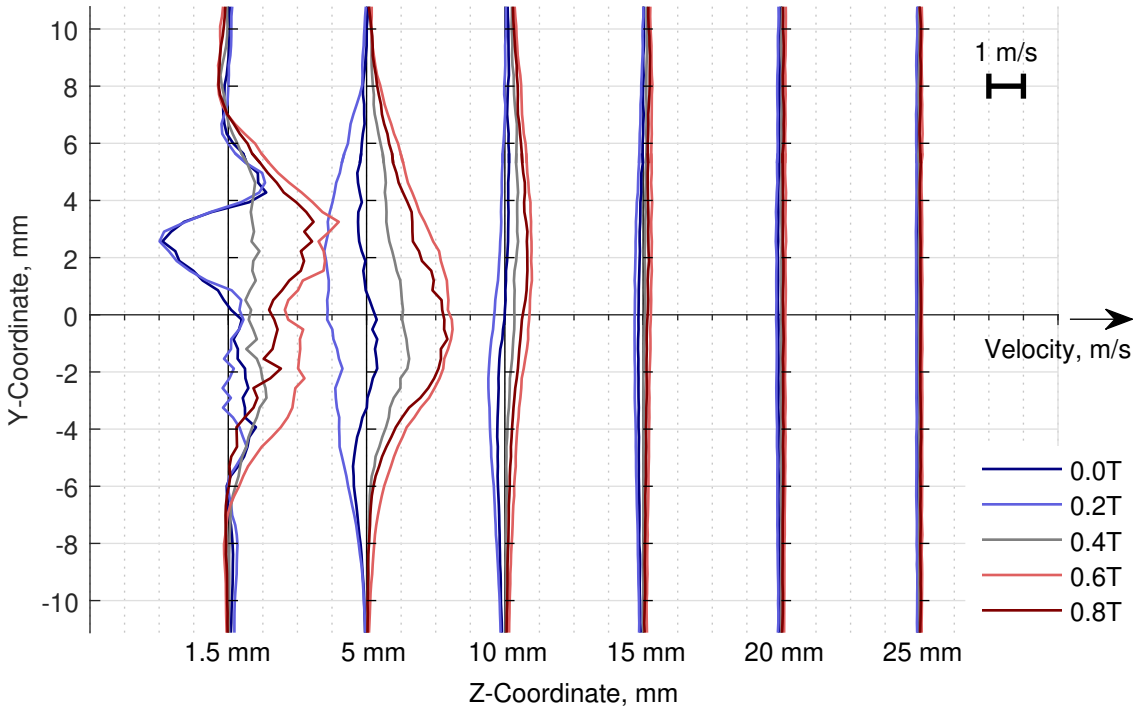

Figure 9.18: Velocity profiles at various distances downstream of the open end of the "recess" injector at an incident SPL of 130 dB.

titatively, the axial particle velocity profiles for the "recess" injector at 130 dB shown in Figure 9.18 and the "straight" injector at 140 dB shown in Figure 9.14 are of the same order of magnitude but are not identical. However, experimental uncertainties in the PIV measurements become more significant at the relatively low velocities shown in these figures. For example, the asymmetry and jaggedness of the axial particle velocity profiles shown in Figure 9.18 near the open end of the injector are likely caused by experimental uncertainties in the PIV measurements. Thus, it is difficult to perform a quantitative comparison between PIV measurements at low velocities.

Figure 9.19 shows the velocity and vorticity fields outside the open end of the "recess" injector at 1680 Hz and an incident SPL of 150 dB, and Figure 9.20 shows the axial particle velocity profiles at various distances from the open end. PIV measurements were also conducted for the "recess" injector at an incident SPL of 140 dB, but the results are not shown because the flow fields at 140 dB and 150 dB are qualitatively similar. Note that the flow fields are measured outside the inlet end of the "recess" injector, which is the open end

of the injector with the inlet protrusion. The axial particle velocity profile at a distance of $z =$ 1.5 mm from the open end indicates that inflow occurs at $0.0T$ and $0.2T$, and outflow occurs at $0.4T$, $0.6T$, and $0.8T$. However, the particle velocity is not uniform over the area of the open end of the injector; the velocity at the center of the open end is always directed outward, and inflow only occurs closer to the edges of the injector. Vorticity is ejected from the open end of the injector during the outflow cycle, as shown in the vorticity field at $0.6T$ in Figure 9.19. The vorticity is organized into a single ring vortex, which is shown clearly in the vorticity field at $0.8T$. As time progresses, the distance between the ring vortex and the end of the injector increases, so the vortex sheds from the open end of the injector and convects downstream. A new ring vortex then forms during the next outflow cycle. The measurement window is large enough that vortices from multiple acoustic cycles are visible in the flow field at any snapshot in time.

Figure 9.20 shows that a jet is also formed at the open end of the "recess" injector at an incident SPL of 150 dB. This is evident because the mean axial particle velocity downstream of the open end of the injector is nonzero and directed away from the open end. However, the particle velocity does not converge to a single time-invariant value at each location; instead, the particle velocity increases significantly above the mean velocity as the ring vortex convects downstream. The jet axis and the convection direction of the vortices are angled slightly above the z-axis. One possible explanation for this phenomenon is that the high-amplitude acoustic oscillations raise the temperature of the air in the injector, which in turn decreases the density of the jet flow compared to the ambient density, causing the jet to convect upward relative to the ground. This would not be unprecedented, as Bies and Wilson [73] found that high-amplitude acoustic waves cause the temperature in a Helmholtz resonator to increase.

There are a number of differences between the flow fields at the open end of the "recess" injector and the open end of the "straight" injector at an incident sound pressure level of 150 dB. Qualitatively, the vortices shed from the open end of the "recess" injector and

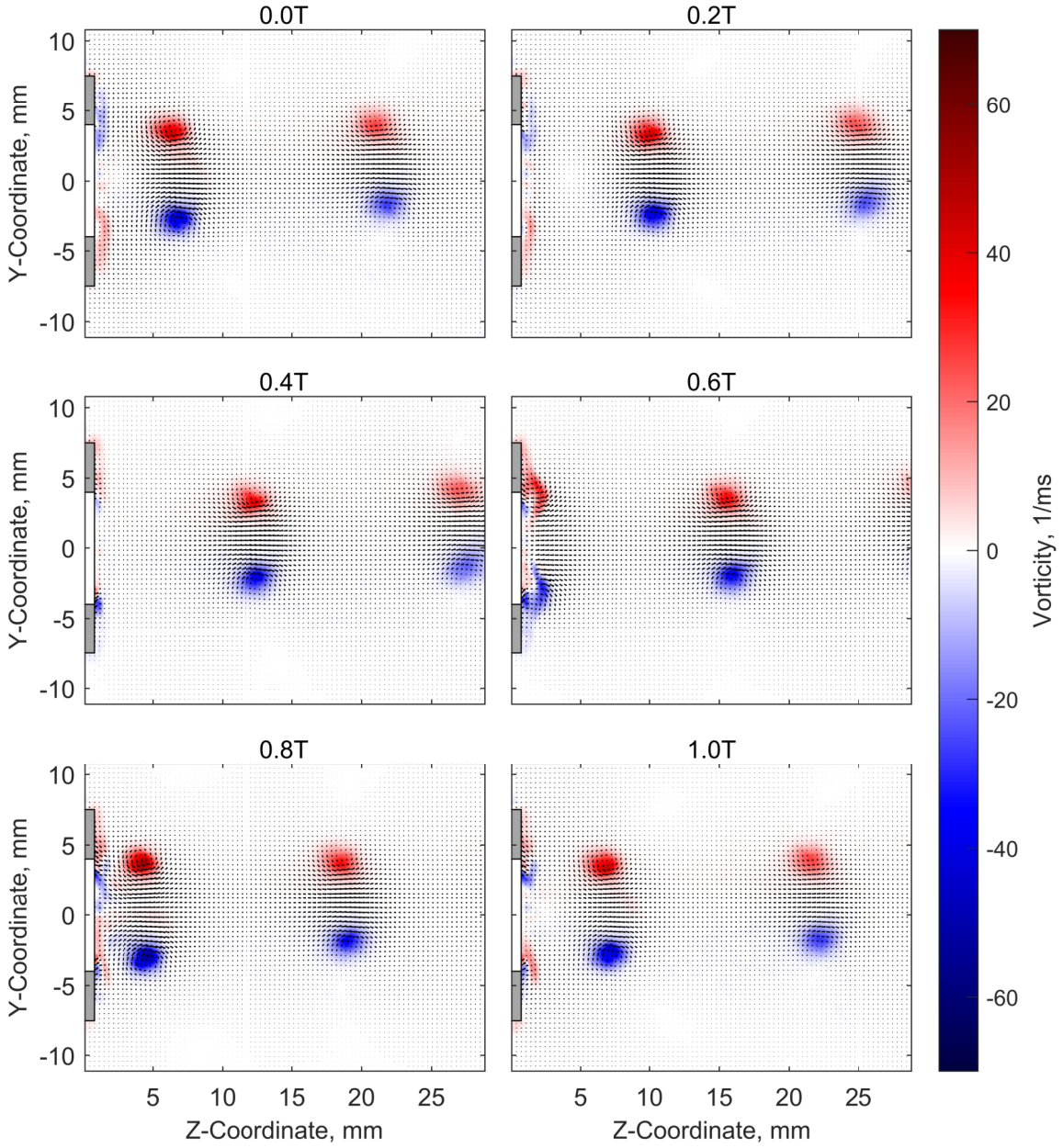

Figure 9.19: Velocity (arrows) and vorticity (colors) flow field outside the open end of the "recess" injector at an incident SPL of 150 dB.

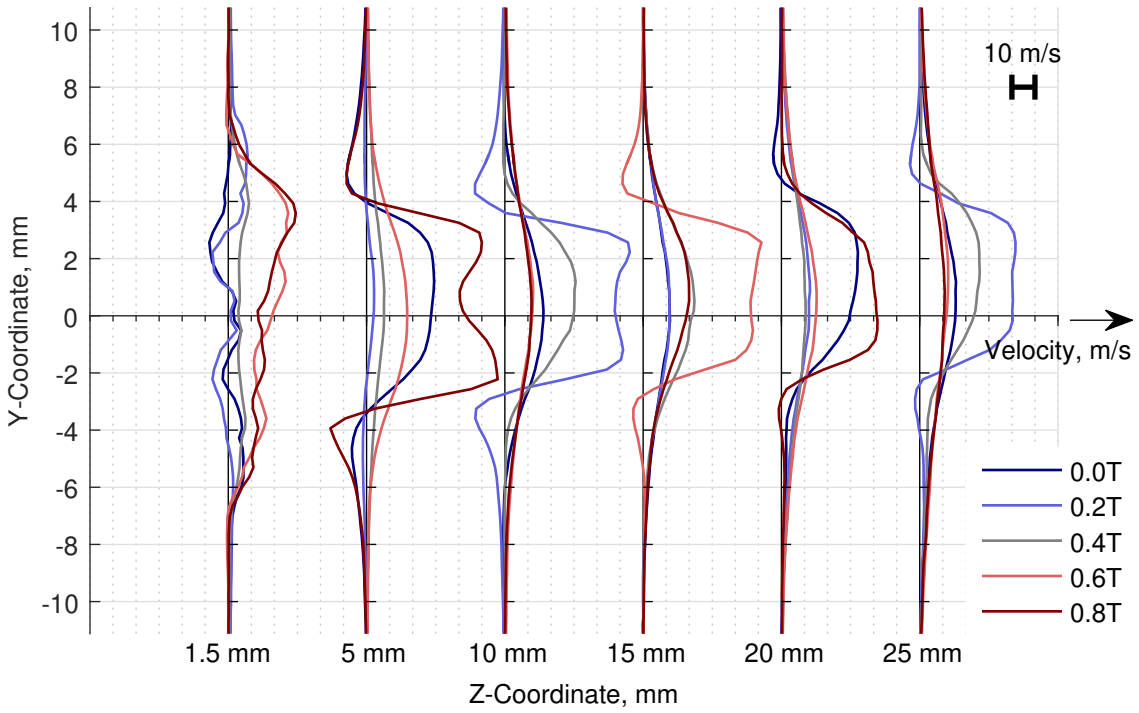

Figure 9.20: Velocity profiles at various distances downstream of the open end of the "recess" injector at an incident SPL of 150 dB.

convect downstream, as shown in Figure 9.19, whereas the vortices remain attached to the open end of the "straight" injector during a single acoustic period, as shown in Figure 9.15. Quantitatively, a comparison of Figures 9.19 and 9.20 to Figures 9.15 and 9.16 indicates that the magnitudes of the particle velocity and vorticity are considerably greater at the open end of the "recess" injector than at the open end of the "straight" injector. Similarly, Figure 9.1 shows that the normalized resistance of the "recess" injector at resonance is significantly greater than that of the "straight" injector at 150 dB. (The normalized resistance at resonance of the "recess" injector at 150 dB is not shown in Figure 9.1 because its reactance does not cross the zero axis, so its resonance frequency is undefined, but the resistance of the "recess" injector increases more quickly with amplitude than that of the "straight" injector.) Therefore, there is at least qualitative agreement between the increase in resistance and the increase in the strength of the vortices and jet at the open end. A quantitative comparison between the acoustic and PIV measurements is given later in Section 9.8.

9.6 Sound Power Dissipation: Acoustic Measurements

Measurements of the acoustic damping of propellant injectors at high amplitudes were presented in Sections 9.3–9.4, and the qualitative characteristics of the flow field at the open end of an injector were discussed in Section 9.5. The overarching goal of this chapter is to quantitatively compare the values of the nonlinear sound power dissipation calculated from the acoustic and PIV measurements. First, the nonlinear sound power dissipation must be determined from each set of measurements. The purpose of this section is to develop a method for estimating the nonlinear sound power dissipation from the acoustic measurements presented in Section 9.3.

The total sound power dissipated by a propellant injector is measured directly in the two-sided impedance tube, but at high amplitudes, the measured dissipation coefficient, $D^{\Pi} = D^{\Pi}_{\text{linear}} + D^{\Pi}_{\text{nonlinear}}$, includes both linear and nonlinear dissipation mechanisms. The nonlinear dissipation coefficient, $D^{\Pi}_{\text{nonlinear}}$, cannot be measured directly, so it must be calculated from the measurements. Based on Eqs. (5.11) and (5.33), the total dissipation coefficient can be expressed as

$$D^{\Pi} = \frac{4\theta_D}{\left|1+\zeta_T\right|^2} \tag{9.2}$$

where ζ_T is the measured normalized termination impedance, and θ_D is the part of the normalized termination resistance that describes the dissipation. Since the dissipation coefficient is comprised of linear and nonlinear terms at high amplitudes, it stands to reason that θ_D can also be decomposed into linear and nonlinear terms such that $\theta_D = \theta_{D,\text{linear}} + \theta_{D,\text{nonlinear}}$. Substitution of this decomposition into Eq. (9.2) yields

$$D^{\Pi} = D^{\Pi}_{\text{linear}} + D^{\Pi}_{\text{nonlinear}} = \frac{4\theta_{D,\text{linear}}}{\left|1+\zeta_T\right|^2} + \frac{4\theta_{D,\text{nonlinear}}}{\left|1+\zeta_T\right|^2} \tag{9.3}$$

Equation (9.3) can then be solved for the nonlinear dissipation coefficient to show that

$$D^{\Pi}_{\text{nonlinear}} = D^{\Pi} - \frac{4\theta_{D,\text{linear}}}{\left|1+\zeta_T\right|^2} \tag{9.4}$$

where D^{Π} and ζ_T are measured directly using the two-sided impedance tube, but the normalized termination resistance associated with the linear dissipation mechanisms, $\theta_{D,\text{linear}}$, remains to be determined. According to the simplified analytical expression for the dissipation coefficient derived in Eq. (5.33), the most significant linear dissipation mechanisms are viscothermal losses in the acoustic boundary layer at the walls of the injector and viscous losses at the area discontinuity between the injector and the impedance tube. These are the only significant dissipation mechanisms at low amplitudes. Therefore, $\theta_{D,\text{linear}}$ can be calculated directly from the acoustic measurements at low amplitudes since Eq. (9.2) can be rearranged to find that

$$\theta_{D,\text{linear}} = \frac{D^{\Pi}_{\text{linear}}}{4}\left|1+\zeta_{T,\text{linear}}\right|^2 \tag{9.5}$$

where D^{Π}_{linear} and $\zeta_{T,\text{linear}}$ are measured directly using the two-sided impedance tube at a low incident SPL. The result of Eq. (9.5) is then substituted into Eq. (9.4), so the nonlinear dissipation coefficient is calculated directly from the acoustic measurements provided that measurements are conducted at both low and high incident SPLs.

The nonlinear dissipation coefficient given by Eq. (9.4) is a normalized quantity. However, the sound power dissipated by nonlinear dissipation mechanisms is required for the quantitative comparison between the acoustic and PIV measurements. This nonlinear dissipated sound power is given by

$$\Pi_D = \Pi_I D^{\Pi}_{\text{nonlinear}} \tag{9.6}$$

where Π_I is the incident sound power in the impedance tube given by Eq. (3.56).

9.7 Sound Power Dissipation: PIV Measurements

In the previous section, a method was developed for calculating the nonlinear sound power dissipation from the acoustic measurements. The sound power dissipated due to losses in the flow field at the open ends of the injectors can also be calculated from the PIV measurements. There are several mechanisms by which sound power is dissipated at the open end of an injector, including dissipation due to the Coriolis force when acoustic waves interact with vorticity, the conversion of the acoustic energy into the kinetic energy of vortices, and the formation of a steady jet. The methods for calculating the sound power dissipated by each of these mechanisms are developed in the following sections.

9.7.1 Dissipation by the Coriolis Force

As shown in Figures 9.15 and 9.19, acoustic energy is converted into vorticity at the open end of an injector at high incident SPLs. The acoustic losses due to the generation of these vortices are considered later in Section 9.7.3. Once the vortices are present in the flow field, the interaction between the acoustic waves and the vorticity may act as an additional sound power dissipation—or generation—mechanism. This interaction between the acoustic waves and the vorticity already present in the flow field is considered in this section.

Powell [150] developed a theory of vortex sound in which he showed that sound is generated by vorticity, and he identified the primary sound generation mechanism as the Coriolis force term. Howe [36, 52, 53] showed that the Coriolis term can act as either a sound source or sound sink when acoustic waves propagate through a turbulent flow field. He further showed that the rate at which acoustic energy is dissipated by vorticity is given by

$$\Pi_\Omega = \rho \iiint_V (\mathbf{\Omega} \times \mathbf{v}) \cdot \mathbf{u} \mathrm{d}V \tag{9.7}$$

where Π_Ω is the sound power dissipated by the vorticity, $\mathbf{v}$ is the velocity of the flow field, $\mathbf{u}$ is the acoustic particle velocity, $\mathbf{\Omega} = \nabla \times \mathbf{v}$ is the vorticity, and the integration

is performed over the volume, V. The density of the medium, ρ, is assumed to remain constant throughout the flow field. If Π_Ω is negative, then sound power is produced by the interaction between the acoustic waves and vorticity.

Following Buick, et al. [93], Eq. (9.7) can be rewritten on the discrete grid shown in Figure 9.12 as

$$\Pi_\Omega = \rho \sum_{i,j} [\mathbf{\Omega}(i,j) \times \mathbf{v}(i,j)] \cdot \mathbf{u}(i,j) V(i,j) \tag{9.8}$$

The velocity of the flow field at each point, $\mathbf{v}(i,j)$, is measured directly using PIV, and the vorticity at each point, $\mathbf{\Omega}(i,j)$, is evaluated using the `curl` function in MATLAB. The flow field is measured in a two-dimensional plane, but the actual flow field is three-dimensional. Therefore, the volume represented by each grid point (i,j) is equal to the volume of the solid of revolution formed by a rectangle of dimensions $\Delta y \times \Delta z$ centered at point (i,j) revolved by 180° about the z-axis, or

$$\begin{aligned} V(i,j) &= \frac{1}{2}\left[\pi\left(y_j + \frac{\Delta y}{2}\right)^2 - \pi\left(y_j - \frac{\Delta y}{2}\right)^2\right]\Delta z \\ &= \pi y_j \Delta y \Delta z \end{aligned} \tag{9.9}$$

where y_j is the y-coordinate of the grid points with index j. In some of the PIV measurements, the vortices and jet convect downstream from the open end of the injector at a shallow angle relative to the outward normal direction. In these cases, the z-axis is redefined in the direction of the jet axis, and y_j is defined relative to the angled z-axis.

The acoustic particle velocity, $\mathbf{u}(i,j)$, which appears in Eq. (9.8), cannot be measured directly. Skulina [90] presented two different methods for obtaining the acoustic particle velocity at the open end of a tube. The first method is to measure the flow field at a low incident acoustic amplitude using PIV and then extrapolate this flow field to high amplitudes. However, it is difficult to obtain accurate measurements of the flow field at low velocities using PIV, and any errors at low amplitude are amplified by the extrapolation to high amplitude. The second method, which is used in this work, is to calculate the theoretical acoustic

flow field induced by an oscillating circular piston at the open end of the tube.

9.7.2 Acoustic Particle Velocity

Flow Field Radiated by a Circular Piston

There is no general closed-form solution for the flow field radiated by an oscillating circular piston at points in the near field, so the acoustic particle velocity field is calculated as a superposition of monopole point sources. The complex velocity potential amplitude of a monopole point source at a single frequency is adapted from Pierce [151] as

$$\Phi = -\frac{Q}{4\pi r} e^{-jkr} \tag{9.10}$$

where Q is the monopole source strength, k is the wavenumber, and r is the distance from the point source to the receiver. The velocity is related to the velocity potential by $\hat{\mathbf{u}} = \nabla\Phi$, so the acoustic particle velocity induced by a point source in the frequency domain is

$$\hat{\mathbf{u}}(r, f) = \frac{Q}{4\pi}\left(\frac{jk}{r} + \frac{1}{r^2}\right) e^{-jkr}\hat{\mathbf{r}} \tag{9.11}$$

where $\hat{\mathbf{r}}$ is the unit vector pointing from the point source towards the receiver.

The open end of a propellant injector with inner radius a can be modeled as a circular piston of radius a. The acoustic particle velocity at any grid point (i, j) in Figure 9.12 is then approximated by the superposition of a large but finite number of point sources of equal strength distributed in an evenly spaced rectangular grid on a circular piston of radius a centered at the origin in the x-y plane. The distance between a point source at coordinates $(x_s, y_s, 0)$ and the grid point (i, j) at $(0, y_j, z_i)$ is given by

$$r(i, j|s) = \sqrt{x_s^2 + (y_j - y_s)^2 + z_i^2} \tag{9.12}$$

and the unit vector pointing from the source towards the grid point is

$$\hat{\mathbf{r}}(i,j|s) = \frac{-x_s\hat{\mathbf{x}} + (y_j - y_s)\hat{\mathbf{y}} + z_i\hat{\mathbf{z}}}{r(i,j|s)} \tag{9.13}$$

where $\hat{\mathbf{x}}$, $\hat{\mathbf{y}}$, and $\hat{\mathbf{z}}$ are the unit vectors aligned with the x-, y-, and z-axes, respectively. The acoustic particle velocity amplitude induced by a circular piston is given by the sum of Eq. (9.11) over the monopole point sources:

$$\hat{\mathbf{u}}(i,j,f) = \frac{Q}{4\pi}\sum_s \left(\frac{jk}{r(i,j|s)} + \frac{1}{r^2(i,j|s)}\right) e^{-jkr(i,j|s)}\hat{\mathbf{r}}(i,j|s) \tag{9.14}$$

The time-varying acoustic particle velocity at point (i,j) at a single frequency is given by

$$\mathbf{u}(i,j,t) = \Re\left[\hat{\mathbf{u}}(i,j,f)e^{j\omega t+\phi}\right] \tag{9.15}$$

where $\Re$ designates the real part, and ϕ is an unknown phase angle.

The flow field induced by each point source is described by a velocity potential, so the flow field radiated by an oscillating circular piston is an irrotational potential flow because it is the superposition of potential flows.

Linear Least Squares Fit of PIV Measurements

Equation (9.15) describes the particle velocity induced by the piston, which is assumed to model the theoretical acoustic particle velocity field at the open end of an injector. A linear least-squares approach is employed to determine the monopole source strength, Q, and the phase angle, ϕ, that minimize the error $\|v_z(i,j) - u_z(i,j)\|^2$ between the measured velocity field, $v_z(i,j) = \mathbf{v}(i,j)\cdot\hat{\mathbf{z}}$, and the piston velocity field, $u_z(i,j) = \mathbf{u}(i,j)\cdot\hat{\mathbf{z}}$, in the z-direction. Only the velocity components in the z-direction are included in the least squares computation because the piston is assumed to radiate primarily in the z-direction.

To employ a linear least-squares approach, the system of equations must be expressed

in the matrix form $\mathbf{Ay} = \mathbf{b}$, where $\mathbf{y}$ is a function of only the unknown monopole source strength and phase angle. Let $\hat{g}(i,j,f) = (1/Q)\hat{\mathbf{u}}(i,j,f) \cdot \hat{\mathbf{z}}$ for simplicity of notation. Using Euler's formula and the trigonometric identities

$$\begin{aligned} \cos(\omega t + \phi) &= \cos(\omega t)\cos(\phi) - \sin(\omega t)\sin(\phi) \\ \sin(\omega t + \phi) &= \sin(\omega t)\cos(\phi) + \cos(\omega t)\sin(\phi) \end{aligned} \tag{9.16}$$

the acoustic particle velocity in the z-direction at point (i,j) at a single frequency can be written as

$$\begin{aligned} u_z(i,j,t) = Q\cos(\phi)\{\Re[\hat{g}(i,j,f)]\cos(\omega t) - \Im[\hat{g}(i,j,f)]\sin(\omega t)\} - \\ Q\sin(\phi)\{\Re[\hat{g}(i,j,f)]\sin(\omega t) + \Im[\hat{g}(i,j,f)]\cos(\omega t)\} \end{aligned} \tag{9.17}$$

where $\Im$ designates the imaginary part. The linear least squares problem can now be written in the matrix form $\mathbf{Ay} = \mathbf{b}$ as

$$\begin{bmatrix} \vdots & \vdots \\ \Re[\hat{g}(i,j,t)]\cos(\omega t) - & \Re[\hat{g}(i,j,t)]\sin(\omega t) + \\ \Im[\hat{g}(i,j,t)]\sin(\omega t) & \Im[\hat{g}(i,j,t)]\cos(\omega t) \\ \vdots & \vdots \end{bmatrix} \begin{bmatrix} Q\cos(\phi) \\ Q\sin(\phi) \end{bmatrix} = \begin{bmatrix} \vdots \\ v_z(i,j,t) \\ \vdots \end{bmatrix} \tag{9.18}$$

where each row represents a unique grid point (i,j) and time t. The solution to the unknown vector is given by $\mathbf{y} = (\mathbf{A}^T\mathbf{A})^{-1}\mathbf{A}^T\mathbf{b}$, from which the values of Q and ϕ that best model the acoustic particle velocity are obtained.

9.7.3 Dissipation Due to the Formation of Vortices

In Section 9.7.1, it was shown that acoustic energy can be dissipated by the Coriolis force term in the interaction between acoustic waves and vorticity. However, the vortices that

form at the open ends of the injectors have kinetic energy, which was not considered in Section 9.7.1. The incident acoustic waves provide the only source of energy in the system, so the energy required to create these vortices must come from the incident acoustic energy. The kinetic energy of the vortices is eventually dissipated into heat by viscosity and thermal conduction [36], so the generation of vortices at the open ends of the injectors represents a sound power dissipation mechanism.

Kinetic Energy of the Flow Field

Quantitatively, the kinetic energy of the flow at any grid point (i, j) in the flow field at a snapshot in time is given by

$$E_k(i, j, t) = \frac{1}{2}\rho V(i, j)|\mathbf{v}(i, j, t)|^2 \tag{9.19}$$

However, this definition includes the kinetic energy of the acoustic particle velocity field, which should not be counted as sound power dissipation. The kinetic energy of the non-acoustic flow field is given by first subtracting the acoustic particle velocity field from the measured flow field such that

$$E_k(i, j, t) = \frac{1}{2}\rho V(i, j)|\mathbf{v}(i, j, t) - \mathbf{u}(i, j, t)|^2 \tag{9.20}$$

The acoustic energy dissipated by the formation of vortices is equal to the kinetic energy of the non-acoustic flow field that forms during one acoustic period. Since the acoustic oscillations are continuous, however, the measured flow field contains vortices that were generated during the preceding acoustic periods. Two different flow regimes have been observed: the vortices may remain attached to the open end of the injector throughout the acoustic period, as shown in Figure 9.15, or the vortices may shed from the open end of the injector and convect downstream, as shown in Figure 9.19. Different procedures are used to estimate the energy of the vortices formed during one period depending on the behavior

of the flow.

Attached Vortices

If the vortices remain attached to the open end of the injector, the kinetic energy of the vortices formed during a single acoustic period are evaluated in a measurement region close to the open end of the injector. The kinetic energy given by Eq. (9.20) is first summed over the j-index (y-coordinate) to obtain the kinetic energy, $E_k(i,t) = \sum_j E_k(i,j,t)$, as a function of the i-index (z-coordinate). The kinetic energy of the vortices formed during a single acoustic period is then given by the sum of $E_k(i,t)$ over the appropriate i-indices close to the open end of the injector. The starting i-index is selected as the grid point closest to the open end of the injector for which the PIV measurements are not contaminated by optical glare from the injector, and the ending i-index is selected as the grid point at which $E_k(i,t)$ falls to within a small percentage of the mean kinetic energy far downstream of the injector.

Figure 9.21 shows the kinetic energy field, $E_k(i,j,t)$, and the sum of the energy over the j-index, $E_k(i,t)$, for the "straight" injector at an incident SPL of 150 dB at a single snapshot in time. The shaded region in Figure 9.21b is the region in which the kinetic energy is summed to obtain the kinetic energy of the attached vortices formed during a single acoustic period. Note that the kinetic energy $E_k(i,j,t)$ at each grid point tends to increase with distance from the z-axis because grid points farther from the z-axis represent larger three-dimensional volumes than grid points closer to the z-axis.

Convected Vortices

If the vortices shed from the open end of the injector and convect downstream, the measured flow field contains vortices from multiple acoustic cycles. Again, the kinetic energy given by Eq. (9.20) is first summed over the j-index (y-coordinate) to obtain the kinetic energy, $E_k(i,t) = \sum_j E_k(i,j,t)$, as a function of the i-index (z-coordinate). Local maxima in the

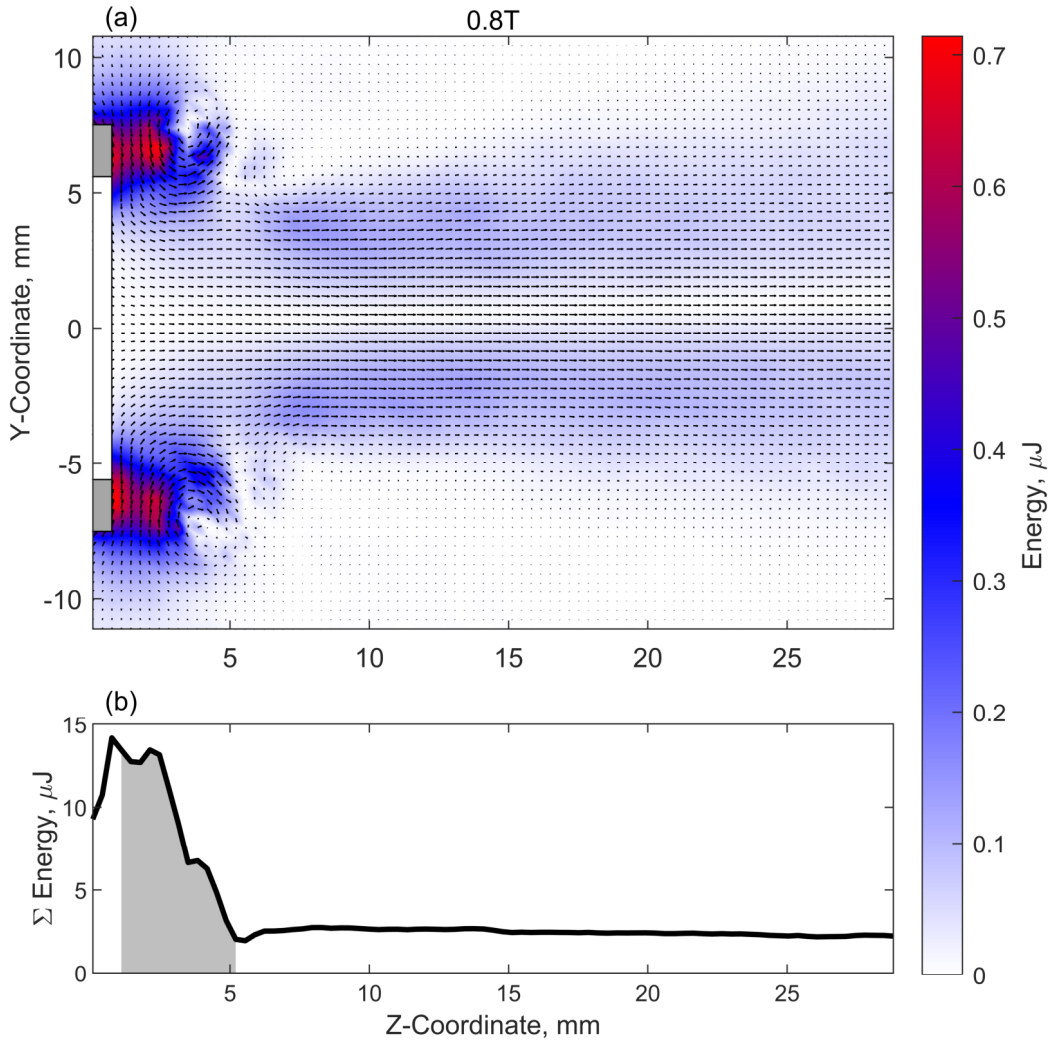

Figure 9.21: (a) Velocity (arrows) and energy (colors) flow field outside the open end of the "straight" injector at an incident SPL of 150 dB; (b) Sum of the kinetic energy over the y-coordinate, where the shaded region corresponds to one acoustic period for attached vortices.

kinetic energy field occur in regions immediately surrounding the vortices, so the i-indices of the local minima of $E_k(i,t)$ are considered to be the boundaries between the vortices shed during successive acoustic periods. The kinetic energy of the vortices formed during a single acoustic period is then given by the sum of $E_k(i,t)$ over the appropriate i-indices. If one local minimum is found in $E_k(i,t)$, then the starting i-index is the grid point closest to the end of the injector not contaminated by optical glare, and the ending i-index is the local minimum. If multiple local minima are found in $E_k(i,t)$, then the starting and ending i-indices that result in the largest kinetic energy are selected.

Figure 9.22 shows the kinetic energy field, $E_k(i,j,t)$, and the sum of the energy over the j-index, $E_k(i,t)$, for the "recess" injector at an incident SPL of 150 dB at a single snapshot in time. The shaded region in Figure 9.22b is the region in which the kinetic energy is summed to obtain the kinetic energy of the shed vortices formed during a single acoustic period. Note that there is a second peak in the kinetic energy further downstream, which is localized to the region surrounding the vortices formed during the previous acoustic period.

Calculation of the Sound Power Dissipation

In a single snapshot of the flow field, the total kinetic energy of the vortices that are formed during a single acoustic period is evaluated as

$$E_k(t) = \sum_{i=i_{\text{start}}}^{i_{\text{end}}} E_k(i,t) \tag{9.21}$$

This value is a function of time: it is minimized during inflow because no vortices are formed outside the injector during inflow, but it is maximized during outflow when the vortices are fully formed. The energy of formation of the vortices, E_V, is given by this maximum value:

$$E_V = \max_t [E_k(t)] \tag{9.22}$$

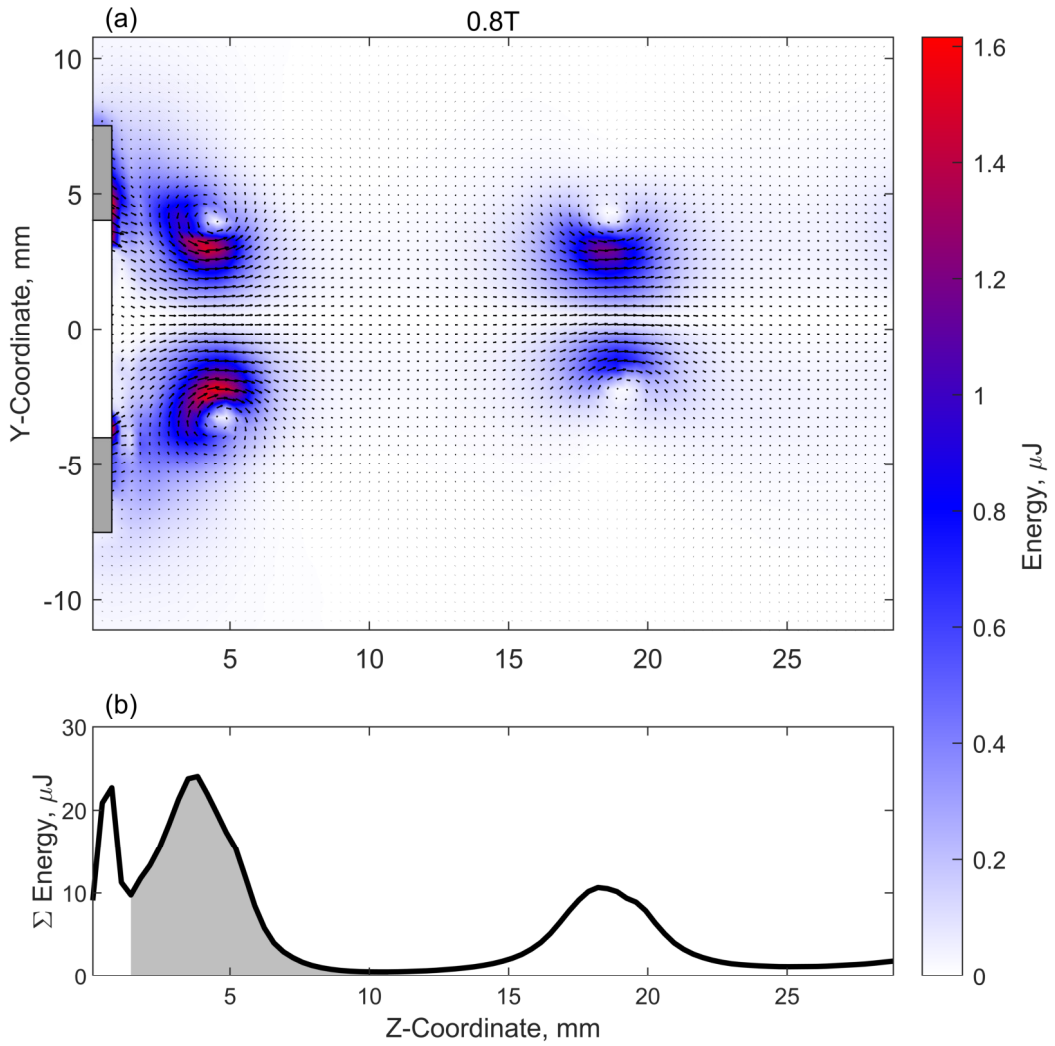

Figure 9.22: (a) Velocity (arrows) and energy (colors) flow field outside the open end of the "recess" injector at an incident SPL of 150 dB; (b) Sum of the kinetic energy over the y-coordinate, where the shaded region corresponds to one acoustic period for shed and convected vortices.

Therefore, the mean sound power dissipated by the formation of the vortices is given by

$$\langle \Pi_V \rangle = \frac{E_V}{T} \tag{9.23}$$

where T is the time period of one acoustic cycle. This quantity is reported as a mean value because the power dissipated by the formation of the vortices at any instant in time fluctuates over an acoustic cycle.

9.7.4 Dissipation Due to the Formation of a Jet

As shown in Figure 9.16, for example, a steady jet may form downstream of the open end of an injector at high amplitudes. The kinetic energy field shown in Figure 9.21 proves that this steady jet has nonzero kinetic energy. The energy required to create the steady jet must come from the incident acoustic energy, but since the acoustic oscillations are continuous, the jet measured at a single snapshot in time is formed by the acoustic energy of the current and preceding acoustic oscillations. A crude numerical integration is performed to estimate the kinetic energy of the jet corresponding to a single acoustic period. First, a reference line parallel to the y-axis is defined at $z = 10$ mm, which is sufficiently far downstream that the jet is approximately steady. The velocity at each grid point on the line at $z = 10$ mm is multiplied by the time step between successive snapshots to estimate the distance that the jet travels during that time step. A new reference curve is defined through the resulting points, and the kinetic energy is summed within the region between the original and propagated reference curves. This process is repeated for every measured time step over the acoustic period to find the kinetic energy of the jet corresponding to a single acoustic period.

The energy of formation of the jet, E_J, is given directly by the sum of the kinetic energy over the snapshots in time during one acoustic period. Therefore, the mean sound power dissipated by the formation of the jet is given by

$$\langle \Pi_J \rangle = \frac{E_J}{T} \tag{9.24}$$

9.8 Quantitative Comparison Between the Acoustic and PIV Measurements

The overarching goal of this chapter is to quantitatively compare the values of the nonlinear sound power dissipation calculated from the acoustic measurements and the PIV measurements of the flow field at the open end of the injectors. The building blocks for performing such a comparison were developed in Sections 9.6–9.7, so the quantitative comparison is now presented in this section.

9.8.1 Calculation of the Sound Power Dissipation

In Section 9.3.1, it was hypothesized that the increase in the normalized resistance at high amplitudes shown in Figure 9.1 is due to the conversion of acoustic energy into the kinetic energy of vortices and jets at the open ends of the injectors. Quantitative evidence for this hypothesis is now presented. Table 9.1 lists the nonlinear sound power dissipation, in milliwatts, obtained from the acoustic and PIV measurements for each injector at an incident sound pressure level of 150 dB. The columns labeled "Vortices" and "Jet" contain the sound power dissipated by the formation of the vortices, $\langle \Pi_V \rangle$, and jet, $\langle \Pi_J \rangle$, respectively, and are calculated using the methods described in Sections 9.7.3 and 9.7.4. The column labeled "Coriolis" contains the sound power dissipated by the interaction of the acoustic waves with vorticity due to the Coriolis force term, Π_Ω, which is described in Section 9.7.1. The column labeled "Acoustic" contains the nonlinear sound power dissipation estimated from the acoustic measurements, Π_D, using the method developed in Section 9.6. The final column is the ratio of the acoustic losses calculated from the PIV measurements to the nonlinear dissipation estimated from the acoustic measurements reported as a percentage, which is given by the expression

$$\frac{\langle \Pi_V \rangle + \langle \Pi_J \rangle + \Pi_\Omega}{\Pi_D} \times 100\% \tag{9.25}$$

The measurements at incident SPLs of 130 dB and 140 dB are not included in the table because there is greater uncertainty in the PIV measurements of the flow field at low velocities, which translates to additional uncertainty in the sound power dissipation calculations.

Table 9.1: Nonlinear sound power dissipation, in milliwatts, calculated from the acoustic and PIV measurements at an incident sound pressure level of 150 dB.

Injector		Vortices		Jet		Coriolis			Acoustic		Percent
Straight	(	191 mW	+	85 mW	+	5.5 mW	)	÷	1960 mW	=	14%
Protrusion	(	337 mW	+	92 mW	+	22 mW	)	÷	1420 mW	=	32%
Recess	(	430 mW	+	86 mW	+	61 mW	)	÷	1590 mW	=	36%

The acoustic losses calculated from the PIV measurements at the open end of each injector account for only part of the nonlinear sound power dissipation estimated from the acoustic measurements, although the results are at least of the same order of magnitude. The dissipation due to the formation of the vortices is the largest dissipation mechanism in the flow field for each injector at 150 dB. The dissipation due to the formation of vortices is greater for the "protrusion" and "recess" injectors than for the "straight" injector because of the inlet protrusion. The dissipation due to the formation of the jet is the next-largest dissipation mechanism, and its magnitude is very similar for each of the three injectors. The dissipation due to the Coriolis force is negligible for the "straight" injector and small for the "protrusion" and "recess" injectors.

Buick, et al. [93] performed a similar comparison between the sound power dissipation calculated from acoustic and PIV measurements at the open end of a tube at high amplitudes. They found that the PIV measurements underpredicted the measured acoustic losses by at least an order of magnitude. However, they only included the dissipation due to the Coriolis force in their calculations. The current results show that the formation of the vortices and jet account for a significantly greater percentage of the acoustic losses than the Coriolis force, but the losses calculated from the PIV measurements still underpredict the nonlinear dissipation estimated from the acoustic measurements. There are several possi-

ble explanations for the differences between the measurements, which are discussed in the following sections.

Losses at the Other Open End of the Injectors

The PIV measurements are only conducted at the inlet end of the injectors, but vortices are also formed at the other open end of the injectors, so the total acoustic losses in the flow field are greater than what is reported in Table 9.1. However, the total sound power dissipated at both ends of the injectors is not necessarily equal to twice the value of the acoustic losses at the inlet end. For example, the magnitude of the vorticity at the other end of the injectors is likely different than the magnitude of the vorticity at the measured end. The PIV measurements show that the vortices are stronger for the injectors with the smaller-diameter inlet protrusion than for the "straight" injector with the larger-diameter opening. Since the radius of the other open end of the "protrusion" and "recess" injectors is larger than the radius of the inlet protrusion, the dissipation due to the formation of vortices at the other end of these injectors is likely smaller than the dissipation at the measured end. Additionally, a steady jet is directed outward from the measured end of the injectors, but it is unknown whether a steady jet of similar velocity exists at the other open end of the injector. It is also unknown how the dissipation due to the Coriolis force varies between the two ends of the injectors, but the Coriolis losses at the measured end are small compared to the total losses, so the Coriolis losses at the other end are not expected to be significant, either.

The losses in the flow field at the other end of each injector are estimated based on several assumptions. It is assumed that the dissipation due to the formation of vortices at the other end of each injector (the end without the inlet protrusion) is equal to the dissipation due to the formation of vortices at the measured end of the "straight" injector (the injector without the inlet protrusion). Additionally, the losses due to the formation of the jet and the Coriolis losses are assumed to be equal at both ends of each injector. Under these as-

sumptions, the total losses in the flow fields at both open ends of the injectors can account for no more than approximately 30% of the nonlinear acoustic losses for the "straight" injector and 60% of the nonlinear acoustic losses for the "protrusion" and "recess" injectors. These rough estimates should be confirmed by PIV measurements of the flow fields at the other ends of the injectors, but they indicate that it is unlikely that the nonlinear dissipation calculated from the acoustic and PIV measurements would exactly agree.

Differences Between Experimental Setups

A possible reason for the differences between the acoustic and PIV measurements is that the measurements were conducted in different experimental facilities. Specifically, the acoustic measurements were conducted in the two-sided impedance tube in order to obtain reflection, transmission, and dissipation measurements, but the PIV measurements were conducted using the 101.6-mm diameter one-sided impedance tube for the reasons given in Section 4.4. In Section 6.4, the absorption coefficient of an injector was shown to differ between the one-sided and two-sided impedance tubes due to the difference in the boundary condition at the injector inlet. However, the change in the absorption coefficient is on the order of a few percent, so the differences between the experimental facilities cannot explain the much larger differences between the acoustic and PIV measurements.

9.8.2 Additional Sound Power Dissipation Mechanisms

The most likely explanation for the differences between the acoustic and PIV measurements is that there are other nonlinear sound power dissipation mechanisms that are significant at high amplitudes in addition to the losses at the open ends of the injectors. Several of these additional dissipation mechanisms are discussed in more detail below.

Structural Vibration

One apparent dissipation mechanism is the structural vibration of the impedance tube, injector mounting plate, or injector. Peerlings [152] showed that the mechanical vibrations induced by the sound sources can propagate along the impedance tube, which causes the microphones to vibrate and induces errors in the measured acoustic properties. Additionally, the high-amplitude acoustic oscillations can excite the structural responses of the impedance tube or test section, and the energy transfer from the acoustic oscillations to the structural vibration would be measured as sound power dissipation. The magnitude of the structural vibrations in HOTMESS is unknown, but it could potentially be measured in future work using accelerometers mounted to the impedance tube walls and the test article.

Scattering to Higher Harmonics

Bodén [153] and Förner, et al. [86] analyzed the scattering of a high-amplitude incident acoustic wave to higher harmonics for Helmholtz and quarter-wave resonators. At high amplitudes, they found that some fraction of the incident sound power at the fundamental resonance frequency is scattered by the resonator into reflected and transmitted sound power at higher integer harmonics. Although the scattered sound power is reflected or transmitted by the resonator, the linear acoustic measurement methodology used in this work assumes that there is no scattering between frequencies, and thus the scattered sound power would be measured as dissipation. A preliminary analysis was conducted using selected measurements to estimate the fraction of incident sound power that is scattered to higher harmonics at high amplitudes for the injectors. Although some evidence of scattering to higher harmonics was found, it accounts for no more than a few percent of the measured nonlinear sound power dissipation of the injectors.

Nonlinear Steepening in the Resonator

Nonlinear losses may also occur due to nonlinear steepening of the high-amplitude acoustic waves inside the injectors. At very high amplitudes, a single-frequency acoustic wave steepens as it propagates, which generates higher-frequency harmonics. The attenuation coefficient due to viscothermal losses in the acoustic boundary obtained by Kirchhoff [119, 120] is given by Eq. (3.17), which shows that the attenuation coefficient is proportional to $\sqrt{\omega}$. Therefore, the viscothermal attenuation of these higher-frequency harmonics in the acoustic boundary layer is greater than the attenuation of the fundamental half-wave resonance frequency. In Section 9.2, nonlinear propagation effects were shown to be relatively small at the sound pressure levels measured in the impedance tube. However, the injectors are tested near their resonance frequencies, so the amplitude inside the injectors can be significantly higher than the amplitude in the impedance tube. Using Eq. (9.1), the discontinuity distance inside the injectors is estimated to be of the same order as the length of the injectors, so nonlinear steepening effects are likely non-negligible inside the injectors. Ilinskii, et al. [102] found that the losses due to harmonic generation accounted for 10% to 20% of the nonlinear acoustic dissipation for the resonators they modeled. Although these specific values are not meant to apply generally to all resonators, they suggest that the losses due to nonlinear steepening cannot be neglected at high amplitudes.

Turbulent Acoustic Boundary Layer

In a pipe with a mean flow, Peters, et al. [22] showed that the attenuation in the turbulent boundary layer is significant and can be approximately modeled by adding the eddy viscosity to the kinematic viscosity. Merkli and Thomann [154] found that boundary layer in an oscillating pipe flow—such as the acoustic boundary layer at the walls of a half-wave resonator—transitions to turbulence at a Reynolds number of $Re \approx 400$. They defined the Reynolds number as

$$Re = \frac{\sqrt{2}\hat{u}\delta}{\nu} \tag{9.26}$$

where $\hat{u}$ is the amplitude of the acoustic particle velocity, ν is the kinematic viscosity, and $\delta = \sqrt{2\nu/\omega}$ is the thickness of the acoustic boundary layer. The Reynolds number increases with increasing acoustic particle velocity, so the boundary layer can become turbulent at high amplitudes. Ilinskii, et al. [102] showed that the additional dissipation due to the turbulent boundary layer in an oscillating flow can be modeled using the eddy viscosity, too. Howe [35–37] developed a detailed theoretical model for the acoustic damping in a mean flow turbulent boundary layer, which agrees well with many experiments [22] and is the most widely accepted model in the current literature [38]. It is assumed that this model can be applied to an oscillating flow turbulent boundary layer if the acoustic particle velocity is used in the model instead of the mean flow velocity.

The Reynolds number depends on the acoustic particle velocity inside the injector, but the particle velocities of the acoustic waves propagating in each direction inside the injector are not measured directly. However, the particle velocities of the incident, reflected, and transmitted acoustic waves in the impedance tube can be determined from the acoustic measurements, and the velocities inside the injector can be calculated based on the continuity of volume velocity. The Reynolds number of the oscillating flow in the "straight" injector at an incident sound pressure level of 150 dB is estimated to be slightly less than 400, which is the transition to turbulence criterion given by Merkli and Thomann [154]. At these conditions, Howe's model [37] predicts that the attenuation coefficient due to losses in the acoustic boundary layer increases by 10% to 15% compared to the linear viscothermal losses. This estimate suggests that dissipation due to turbulence in the acoustic boundary layer cannot completely account for the differences between the acoustic and PIV measurements, but nonetheless, it is a non-negligible dissipation mechanism at high amplitudes.

9.9 Summary

In this chapter, the effects of high amplitudes on the acoustic damping of propellant injectors were investigated in quiescent air at ambient conditions in both the linear and nonlinear acoustic regimes for the plane wave mode. The effects of high amplitudes and the contributions of the physical mechanisms responsible for the acoustic damping are summarized below.

Acoustic Measurements

Nonlinear acoustic propagation effects were shown to be small in the impedance tube at the amplitudes and frequencies of interest, so the linear acoustic measurement methodology was applied to measure the acoustic damping of propellant injectors at high amplitudes. The experiments presented in this chapter showed that, at high amplitudes, the normalized resistance of an injector at resonance increases monotonically with increasing amplitude, which characterizes the nonlinear acoustic regime. The increase in resistance was found to be greater for the "protrusion" and "recess" injectors than for the "straight" injector due to the increased particle velocity through the orifice-like inlet protrusion. The amplitude was shown to have less of an effect on the resistance as the number of injectors increases because the particle velocity through each injector varies inversely with the number of injectors. The experiments showed that, in the nonlinear acoustic regime, the absorption frequency bandwidth of the injectors increases with amplitude, and the peak absorption coefficient either increases or decreases with increasing amplitude based on the value of the normalized resistance. The resonance frequency was found to decrease with increasing amplitude at high amplitudes. These effects were primarily attributed to the formation of vortices and a steady jet at the open ends of the injectors, as described below.

PIV Measurements

Particle image velocimetry (PIV) measurements were conducted at the inlet end of each propellant injector. At lower amplitudes, the measurements showed that the magnitudes of the velocity and vorticity at the open end are relatively small, and nonzero vorticity is localized at the walls of the injector. At high amplitudes, the measurements showed that vortices and a steady jet are formed at the open end of the injectors. It was found that the vortices either remain attached to the open end throughout the acoustic period or shed from the open end and convect downstream. The experiments showed that the strength of the vortices at the open end increases with amplitude and is greater for the "recess" injector than for the "straight" injector at the same amplitude, which is similar to the measured behavior of the normalized resistance.

Quantitative Comparison Between Acoustic and PIV Measurements

The nonlinear sound power dissipation of an injector was compared between the acoustic and PIV measurements to test the hypothesis that the increase in acoustic resistance at high amplitudes is due to the conversion of acoustic energy into vorticity at the open ends. Numerical methods were developed to calculate the dissipation due to the Coriolis force term and the losses due to the formation of vortices and a jet at the open end. However, these dissipation mechanisms were found to account for no more than 30% to 60% of the nonlinear acoustic losses of the "straight" and "recess" injectors at an incident SPL of 150 dB. It was suggested that the excess losses in the acoustic measurements may be caused by additional nonlinear dissipation mechanisms, including structural vibration of the experimental facility, scattering to higher harmonics, nonlinear steepening inside the injector, and the generation of turbulence in the acoustic boundary layer at high amplitudes. The PIV measurements were conducted at only one end of the injectors using the one-sided impedance, whereas the acoustic measurements were conducted in the two-sided impedance tube. In future studies, PIV measurements of the flow field should be conducted

at both open ends of the injectors in the two-sided impedance tube using optical windows.

Acoustic Damping Mechanisms

For the experiments discussed in this chapter, it was shown that the primary physical mechanisms responsible for the acoustic damping are viscothermal losses in the acoustic boundary layer, acoustic radiation from the open end of the injectors opposite the incident acoustic waves, and the conversion of acoustic energy to vorticity at the open ends of the injectors. The viscothermal losses in the acoustic boundary layer and the acoustic radiation from the open end were shown to be present for half-wave resonators at all flow, temperature, and amplitude conditions. The new acoustic damping mechanism introduced by high amplitudes was found to be the conversion of acoustic energy to vorticity at the open ends of the resonators. The experiments showed that, although this nonlinear acoustic damping mechanism is significant, it cannot completely account for the measured increase in the acoustic resistance at high amplitudes. It was suggested that the high-amplitude particle velocity in the resonator may generate turbulence in the acoustic boundary layer, so dissipation due to turbulence may also be important at high amplitudes. Furthermore, structural vibration of the experimental facility, scattering to higher harmonics, and nonlinear steepening of the acoustic waves inside the resonator may also contribute to the acoustic damping at high amplitudes.

CHAPTER 10
HIGHER-ORDER MODES

10.1 Overview

In this chapter, the effects of higher-order modes on the acoustic damping of propellant injectors are investigated for the following geometric parameters:

- Number of injectors
- Position and distribution of the injectors on the injector faceplate

The experiments presented in this chapter are conducted in the two-sided impedance tube using the single stainless steel half-wave resonator (see Figure 4.13) and multiple stainless steel half-wave resonators (see Figure 4.14). The experiments are conducted in quiescent air at ambient conditions in the linear acoustic regime. The ($\pm$1,0), ($\pm$2,0), and (0,1) modes are measured in addition to the plane wave mode. The physical mechanisms responsible for the acoustic damping in the experiments described in this chapter include:

- Viscous and thermal losses in the acoustic boundary layer
- Acoustic radiation from the open end of the injectors opposite the incident acoustic waves

The outline of this chapter is as follows: First, the mode-matching method is presented in Section 10.2 as a way to analytically predict the reflection and transmission of higher-order modes at an area discontinuity. A numerical model for the scattering matrix of half-wave resonators for higher-order modes is then developed in Section 10.3 based on the mode-matching method. This is followed by a detailed discussion in Section 10.4 on the length correction at an area discontinuity. Both the mode-matching method and COMSOL are applied to calculate the length correction of one or more resonators as a function

of their position within the cross-section of the impedance tube, and the relationship between the length correction and the excitation of evanescent higher-order modes within the impedance tube is discussed. Next, in Section 10.5, selected experimental measurements of the acoustic damping of propellant injectors for higher-order modes are presented. These results include the higher-order scattering matrices and sound power coefficients of one or more half-wave resonators. The numerical model for higher-order modes is validated in Section 10.6 based on a comparison between the predicted and experimental results. Finally, in Section 10.7, the numerical model is used to investigate the acoustic effects of the side branch formed by the extension of the resonators into the impedance tube.

10.2 Mode-Matching Method

The numerical model for the acoustic damping of a propellant injector for the plane wave mode was described in Section 5.3 (and developed in detail in Appendix C). As discussed in Section 6.7, this model accurately predicts the acoustic damping of propellant injectors for the plane wave mode. One building block of this numerical model is the transfer matrix for the reflection and transmission of the plane wave mode at an area discontinuity in a duct. This transfer matrix is specific to the plane wave mode, so the same formulation cannot be used to predict the reflection or transmission of higher-order modes at an area discontinuity. This section contains a description of an analytical method for calculating the reflection and transmission of higher-order modes at a simple area discontinuity in a duct based on the boundary and continuity conditions at the discontinuity. This type of analytical method is referred to as a mode-matching method. Miles [104] was the first to develop a higher-order mode-matching method to calculate the reflection and transmission of sound at an area discontinuity in a circular duct. The method originally presented by Miles [104] was further developed by El-Sharkawy and Nayfey [105] and Selamet and Ji [31, 109]. The mode-matching method is derived in detail in Appendix D based on these prior contributions, and a summary of the method is provided below.

The mode-matching method is based on the application of the boundary and continuity conditions at an area discontinuity in a duct. The conditions at the area discontinuity are continuity of acoustic pressure and continuity of particle velocity in the union between the ducts and vanishing particle velocity on the hard wall surrounding the discontinuity. The expression for the acoustic pressure field in a circular duct given by Eq. (3.5) is substituted into these continuity and boundary conditions, and the orthogonality relationship between mode shapes given by Eq. (3.10) is employed to simplify the resulting expressions. This produces a system of infinitely many equations in infinitely many unknowns because the acoustic pressure field in each duct is given by the summation of infinitely many higher-order modes. The number of modes is truncated, and the system is solved for the scattering matrix of the area discontinuity. The transfer matrix formulation, which was used in the development of the numerical model for the plane wave mode described in Section 5.3, was not used for higher-order modes because its solution may not be exact or even unique. The steps described above are presented in detail in Appendix D.

The mode-matching method has several applications that are discussed later in this chapter. In Section 10.3, the mode-matching method is extended to more complex area discontinuities, such as an area discontinuity involving multiple ducts with a side branch, and is used to develop a numerical model for the higher-order scattering matrix of one or more half-wave resonators. Then, in Section 10.4, the mode-matching method is used to calculate the effect of the position of half-wave resonators on the length correction at an area discontinuity in a duct.

10.3 Numerical Model for Higher-Order Modes

The mode-matching method described in the previous section can be extended to more complex area discontinuities to develop a numerical model for the acoustic damping of half-wave resonators for higher-order modes. For simplicity, the realistic geometric features of a propellant injector are not included in the numerical model. The model is developed

for multiple straight cylindrical half-wave resonators with a side branch at one end, which describes the geometry of the test article shown in Figure 4.14. The numerical model for the acoustic damping of a propellant injector for the plane wave mode described in Section 5.3 (and developed in detail in Appendix C) is expressed in terms of transfer matrices, but the transfer matrix formulation has disadvantages for higher-order modes, as discussed in Section 10.2. Instead, the numerical model for higher-order modes is developed by applying the mode-matching method to the area discontinuities at both ends of the half-wave resonators and solving the resulting system of equations for the overall scattering matrix of the resonators. The numerical model for higher-order modes is derived in detail in Appendix E, and a summary of the derivation is provided below.

First, the mode-matching method described in Section 10.2 (and developed in detail in Appendix D) is applied to area discontinuities involving multiple duct sections and a side branch formed by the extension of the smaller duct sections into the larger duct section. These applications of the mode-matching method are required to calculate the reflection and transmission of sound from both ends of the multiple half-wave resonators in the test article shown in Figure 4.14. The mode-matching method requires that the mode shapes in each duct section be known. The mode shapes in the cylindrical duct sections, including the half-wave resonators and the impedance tube, are given by Eq. (3.8). However, the side branch formed by the extension of the half-wave resonators into the impedance tube has an irregular geometry, so its mode shapes are calculated using the commercially available software package COMSOL Multiphysics®. Then, the system of equations generated by the application of the mode-matching method to the area discontinuities at both ends of the half-wave resonators is truncated and assembled into a scattering matrix form. The solution to this system of equations produces the higher-order scattering matrix for the test article. The steps described above are presented in detail in Appendix E. The validation of the numerical model for higher-order modes is provided in Section 10.6.

10.4 Effect of Higher-Order Evanescent Modes on the Length Correction at an Area Discontinuity

In Section 6.6, it was shown that the position of half-wave resonators within the cross-section of the impedance tube has a non-negligible effect on the resonance frequency, which was attributed without proof to the formation of higher-order evanescent modes at the area discontinuity between the resonators and the impedance tube. The effect of these higher-order evanescent modes on the length correction—and thus the resonance frequency—of half-wave resonators is now analyzed in depth using the mode-matching method described in Section 10.2 (and developed in detail in Appendix D).

10.4.1 Effect of the Position of the Resonators

In Section 6.6, the effect of the position and distribution of propellant injectors on the injector faceplate was discussed based on measurements of the plane wave absorption coefficient for various configurations of half-wave resonators. Figure 10.1 depicts several of these configurations of half-wave resonators, which are designated by the number of resonators and the positions of the resonators on the "inner" or "outer" ring. Some of the results presented in Section 6.6 are repeated here for further analysis. Figure 10.2 shows the absorption coefficients of each of the configurations measured in the two-sided impedance tube. The resonance frequency of a single half-wave resonator mounted in the outer ring (Figure 10.1b) is lower than the resonance frequency of the same resonator mounted in the inner ring (Figure 10.1a), but the resonance frequency of three half-wave resonators mounted in the outer ring (Figure 10.1d) is higher than the resonance frequency of the same three resonators mounted in the inner ring (Figure 10.1c). Thus, the length correction at the area discontinuity between the resonators and the impedance tube is found to be a function of both the number and the positions of the resonators. An explanation for the observed changes in the resonance frequency as a function of position in Figure 10.2 is

provided in the following sections.

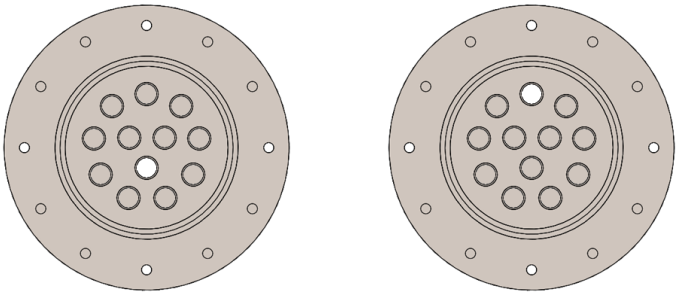

(a) 1, Inner (b) 1, Outer

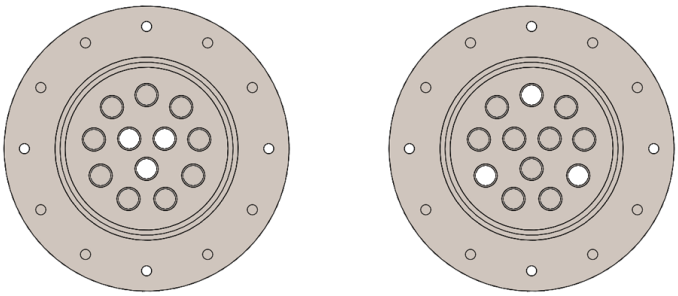

(c) 3, Inner (d) 3, Outer

Figure 10.1: Number and positions of the half-wave resonators.

10.4.2 Calculation of the Length Correction

First, methods for calculating the length correction at the area discontinuity between the resonators and the impedance tube are presented in this section. The length correction can be obtained by calculating the resonance frequency using commercially available software or by determining the amplitudes of the forward- and rearward-propagating waves on either side of the discontinuity. These methods, which are described in more detail below, provide additional physical understanding about the phenomena that affect the length correction—and thus the resonance frequency—of the resonators.

Method 1: Length Correction via the Resonance Frequency

The resonance frequencies of one and three half-wave resonators are calculated using the eigenfrequency analysis in the commercially available software package COMSOL

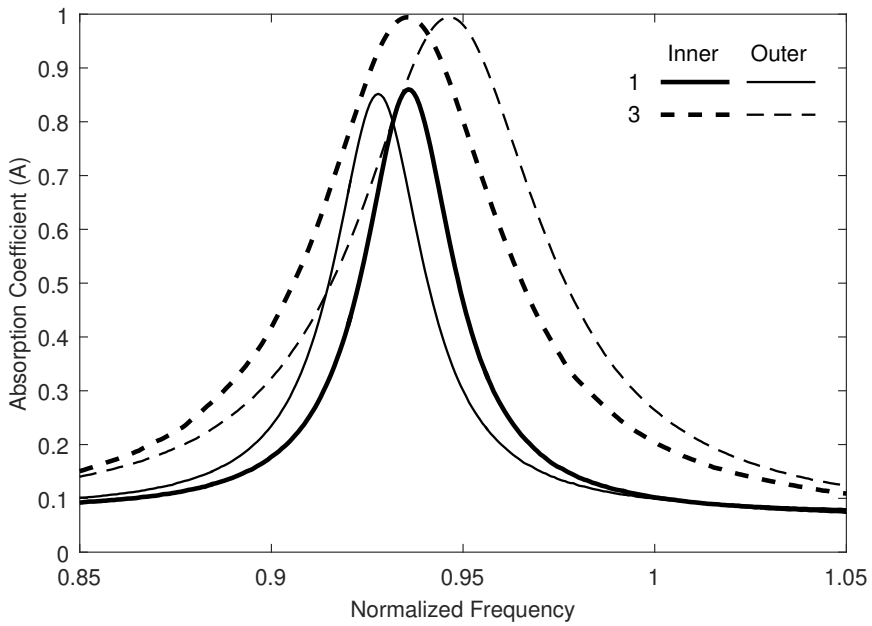

Figure 10.2: Absorption coefficients of various numbers of half-wave resonators in different positions measured in the two-sided impedance tube.

Multiphysics® for the configurations shown in Figure 10.3. These configurations are representative of one and three half-wave resonators mounted to one side of the impedance tube, such as the configurations shown in Figures 10.1b and 10.1d, respectively. The diameter of the impedance tube is 101.6 mm, and the diameter of each resonator is 12.55 mm, as specified in Figure 4.14. The medium is specified as air with $\rho = 1.2$ kg/m^3 and $c = 343$ m/s. A sound-soft boundary condition is applied to the free end of the resonators, so the length correction at the free end is zero. The specific impedance boundary condition $z = \rho c$ is applied to the opposite end of the impedance tube to minimize reflections. To further eliminate errors that may be caused by spurious reflections from the downstream end of the impedance tube, the length of the impedance tube was systematically increased until the calculated resonance frequency was found to be independent of the length.

The length correction of a half-wave resonator is uniquely determined from the resonance frequency by rearranging Eq. (2.8) to show that

$$\Delta L = \frac{c}{2f_0} - L \tag{10.1}$$

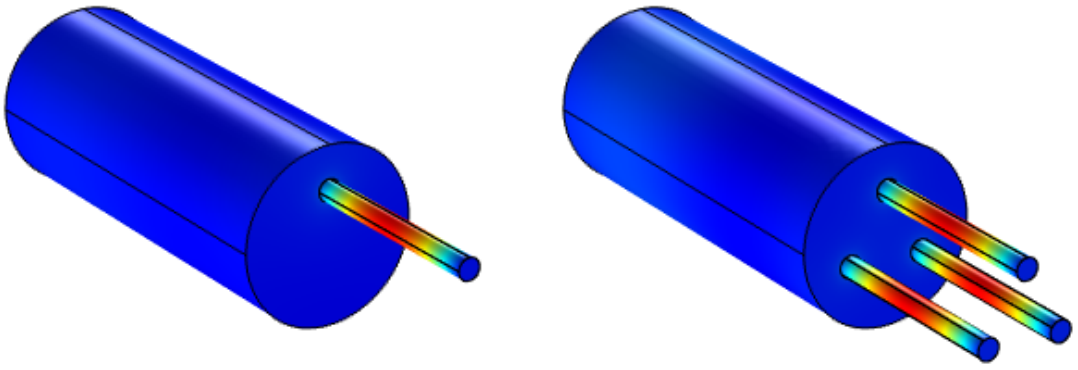

(a) One resonator (b) Three resonators

Figure 10.3: COMSOL models of the area discontinuity between the impedance tube and one and three resonators.

where the resonance frequency, f_0, is the eigenfrequency computed by COMSOL. Since the length correction at the free end of the resonators is zero, the result given by Eq. (10.1) is the length correction at the area discontinuity between the resonators and the impedance tube.

Method 2: Length Correction via Mode Decomposition

Alternatively, the length correction at the area discontinuity between the resonators and the impedance tube can be determined if the amplitudes of the forward- and rearward-propagating plane waves on either side of the discontinuity are known. The amplitudes of the acoustic waves can be obtained using COMSOL or the mode-matching method described in Section 10.2. The solution to the mode-matching method directly provides the amplitudes of the acoustic waves propagating in each direction on either side of the area discontinuity. The eigenfrequency analysis in COMSOL computes the acoustic pressure mode shape at the resonance frequency, as indicated by the colors in Figure 10.3. The pressure amplitude at each node in the finite element mesh is exported from COMSOL, and the nodes are sorted by their locations in the resonators or the impedance tube. From these computational results, there exist a number of linearly independent nodes in space at

which the pressure amplitude is known, so the amplitudes of the forward- and rearward-propagating acoustic waves in both the resonators and the impedance tube are decomposed using Eq. (3.27). The length correction at the area discontinuity is then given by [31]

$$\Delta L_{1,2} = \frac{(\hat{a}^{+}_{2,00} + \hat{a}^{-}_{2,00}) - (\hat{a}^{+}_{1,00} + \hat{a}^{-}_{1,00})}{jk(\hat{a}^{+}_{2,00} - \hat{a}^{-}_{2,00})} \tag{10.2}$$

where $\hat{a}_{1,00}$ and $\hat{a}_{2,00}$ are the amplitudes of the forward- and rearward-propagating plane waves in the impedance tube ($\hat{a}^{\pm}_{1,00}$) and the resonators ($\hat{a}^{\pm}_{2,00}$), respectively.

10.4.3 Application to the Half-Wave Resonators

The two methods described above were applied to study the effect of the position of the half-wave resonators on the length correction at an area discontinuity. Figure 10.4 shows the computed length correction at the area discontinuity between a single 12.55-mm diameter resonator and the 101.6-mm diameter impedance tube normalized by the radius of the resonator. The normalized length correction is plotted as a function of the offset distance between the centerlines of the resonator and the impedance tube as a fraction of the impedance tube radius. The range of offset distances spans from 0% (concentric) to 85% of the impedance tube radius in steps of 5% radius; larger offset distances are physically impossible because the radius of the resonator would protrude beyond the impedance tube. The length correction calculated using the COMSOL eigenfrequency analysis and Eq. (10.1) is nearly identical to the length correction calculated using the COMSOL mode decomposition and Eq. (10.2). The length correction obtained using the analytical mode-matching method and Eq. (10.2) is slightly less than the length correction computed using COMSOL, but the methods all predict that the length correction of a single resonator increases as its offset distance from the center of the duct increases.

Figure 10.5 shows the normalized length correction of three resonators instead of one resonator. The three resonators are spaced 120° degrees apart and each have the same

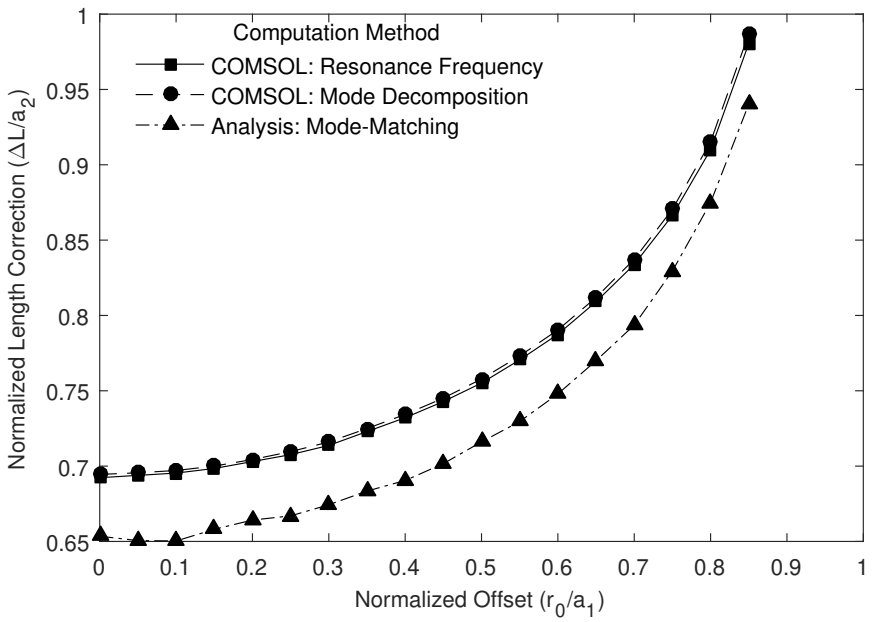

Figure 10.4: Normalized length correction of a single resonator as a function of its offset distance from the centerline of the duct.

offset distance relative to the center of the impedance tube. The range of offset distances spans from 15% to 85% of the impedance tube radius in steps of 5% radius; smaller offset distances are physically impossible because the three resonators would overlap. Again, the length correction obtained using the analytical mode-matching method is slightly less than the length correction computed from the COMSOL eigenfrequency analysis or the COMSOL mode decomposition, which produce nearly identical results. The methods all show that the length correction of three resonators with equal angular spacing reaches a minimum at an offset distance of approximately 55% of the impedance tube radius.

The offset distance between the centerlines of the resonators and the impedance tube for the "inner" configurations shown in Figures 10.1a and 10.1c is 24.9% of the impedance tube radius, and the offset distance for the "outer" configurations shown in Figures 10.1b and 10.1d is 65.8% of the impedance tube radius. Table 10.1 compares the length corrections of these configurations computed using the analytical mode-matching technique with the measured length corrections. The mode-matching technique is shown to provide a reasonably accurate prediction of the length correction. Therefore, in the following section,

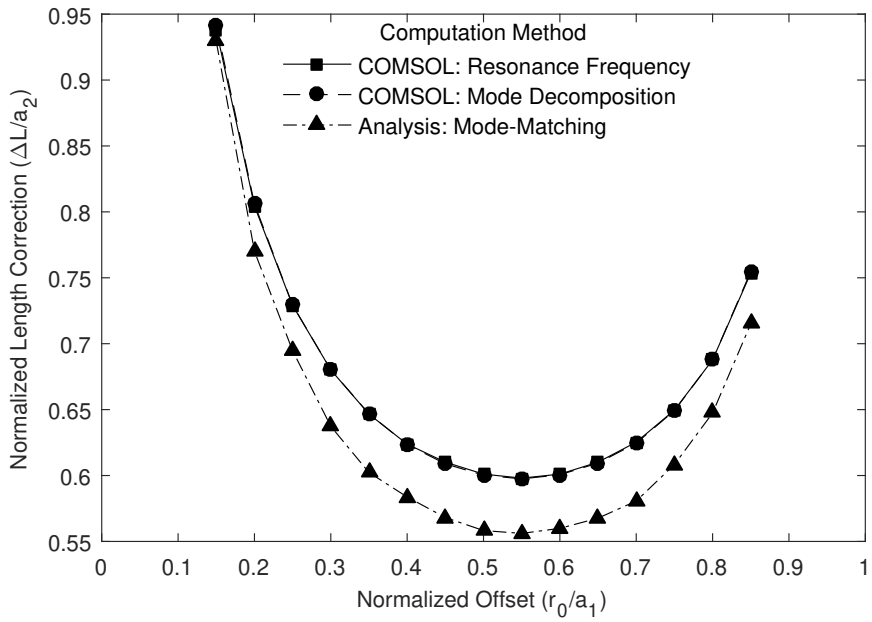

Figure 10.5: Normalized length correction of three equally distributed resonators as a function of their offset distance from the centerline of the duct.

the mode-matching technique is used to provide a physical explanation of the phenomena that cause the length correction to vary with the positions of the resonators.

Table 10.1: Measured and predicted length corrections of the resonators for the configurations shown in Figure 10.1.

Configuration	Normalized Offset (r_0/a_1)	Mode-Matching $(\Delta L/a_2)$	Experiment $(\Delta L/a_2)$	Percent Error
1, Inner	24.9%	0.665	0.687	-3.1%
1, Outer	65.8%	0.768	0.777	-1.2%
3, Inner	24.9%	0.695	0.683	1.8%
3, Outer	65.8%	0.569	0.562	1.3%

10.4.4 The Role of Evanescent Modes

Karal [144] was the first to represent the effects of the higher-order evanescent modes formed at an area discontinuity as a length correction. His results suggest that the length correction depends on the number and amplitudes of the evanescent modes that are excited

at the discontinuity. Eriksson [108] showed that specific higher-order modes in an expansion chamber could be suppressed or excited based on the locations of the inlet and outlet relative to the nodes and antinodes of the mode shapes, and Selamet and Ji [109] used the mode-matching technique to calculate which higher-order modes are excited by offset inlets and outlets. Their results suggest that higher-order modes, even below their cutoff frequencies, are either excited or suppressed based on the locations of the resonators relative to the shapes of the modes in the impedance tube. The relative amplitudes of the higher-order evanescent modes formed at the area discontinuity between the impedance tube and one and three half-wave resonators at various offset distances are calculated below, and the relationship between the energy of the evanescent modes and the length correction is discussed.

Evanescent Modes: Single Resonator Versus Three Resonators

Figure 10.6 shows the relative amplitudes of the higher-order evanescent modes formed at the area discontinuity between a single resonator and the impedance tube for offset distances of 0%, 40%, and 80% of the impedance tube radius. The modes are computed using the mode-matching method described in Section 10.2, and the amplitudes are normalized by the amplitude of the plane wave mode. The circumferential mode orders are plotted along the horizontal axis, and the radial mode orders are plotted along the vertical axis. The first 121 modes in order of increasing cut-on frequency were computed, so white squares represent modes that were not considered in the analysis. The color scale is logarithmic so that modes with non-negligible amplitudes can be distinguished from one another.

The center of the impedance tube is a node for modes with nonzero circumferential mode order and an antinode for every pure radial $(0, n)$ mode. Therefore, only the radial modes are excited when the resonator and the impedance tube are concentric. If the resonator is offset from the center of the impedance tube, then the configuration is asymmetric with respect to the circumferential mode shapes, and modes with nonzero circumferential

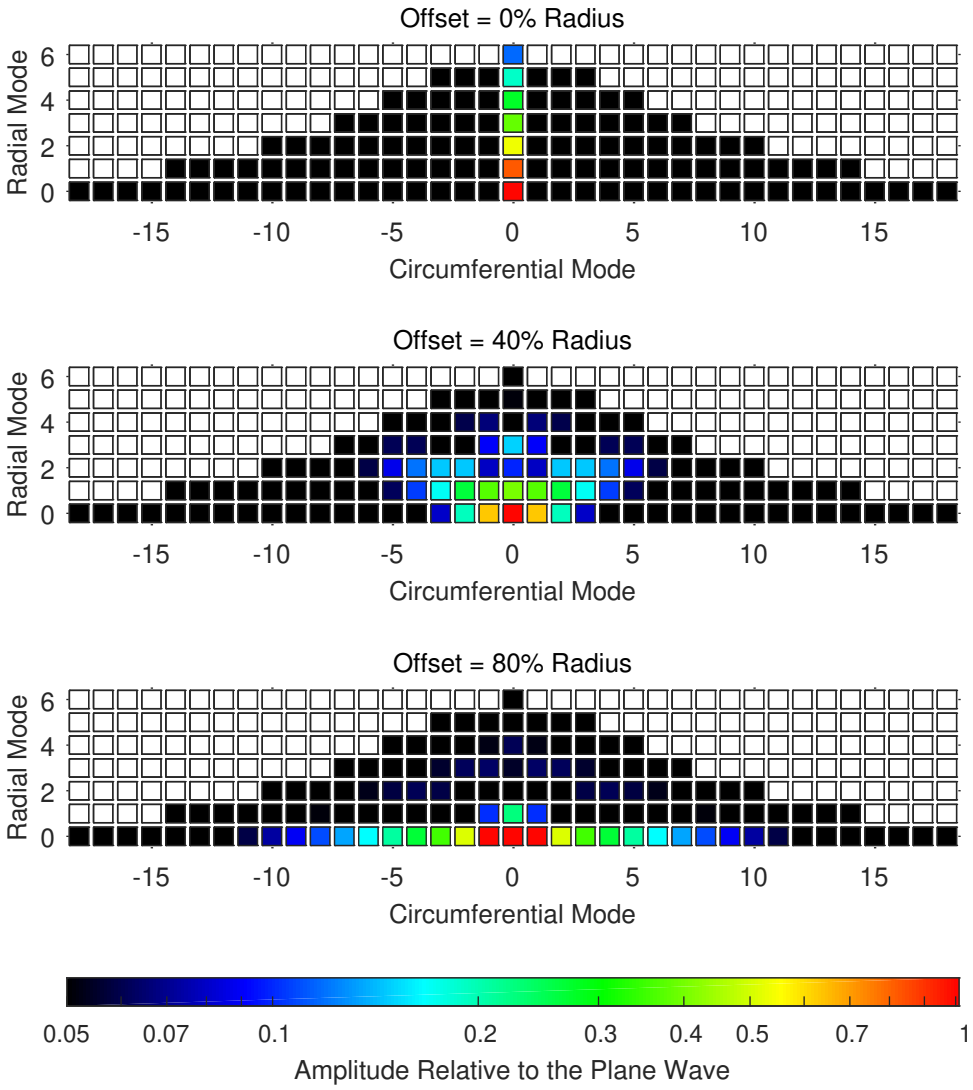

Figure 10.6: Calculated relative amplitudes of the evanescent modes formed at the area discontinuity between one 12.55-mm diameter resonator and the 101.6-mm diameter impedance tube for various offset distances between the centerlines of the ducts.

mode orders are also excited. The first several circumferential, radial, and combined modes are excited when the resonator is offset by 40% of the impedance tube radius. The antinode of every pure circumferential $(m, 0)$ mode is at the outer radius of the impedance tube, so the number of excited circumferential modes increases as the location of the resonator approaches the outer radius of the impedance tube.

Figure 10.7 shows the relative amplitudes of the higher-order evanescent modes formed at the area discontinuity between three resonators and the impedance tube. The modes are computed using the same method as for the single resonator above. The smallest computed offset distance for the three resonators is 15% of the impedance tube radius, at which only the first few pure radial $(0, n)$ modes are significantly excited. At offset distances of 50% and 85% of the impedance tube radius, an interesting pattern emerges: the only modes that are excited have circumferential mode orders, m, that are integer multiples of three. This is because of the symmetry of the three-resonator configuration, in which the three resonators are each spaced 120° apart. The $(1, n)$ and $(2, n)$ modes are not excited because the integrated effect of the three equally spaced resonators is zero for these mode shapes. However, the integrated effect of the three equally spaced resonators is additive for the $(3, n)$ mode and all successive modes with circumferential mode orders that are integer multiples of three.

Energy of Evanescent Modes

Although the exact value of the length correction can be calculated using the mode-matching method described in Section 10.2 and Eq. (10.2), Ingard [155] showed that the length correction is directly related to the kinetic energy contained within the evanescent modes formed at the area discontinuity between the resonator and the duct. Specifically, the kinetic energy in the evanescent modes can be written as $E_k = \frac{1}{2}mu^2$, where u is an effective acoustic particle velocity, the effective mass is given by $m = \rho S \Delta L$, and ΔL is the length correction. This energy formulation provides a more direct physical understanding

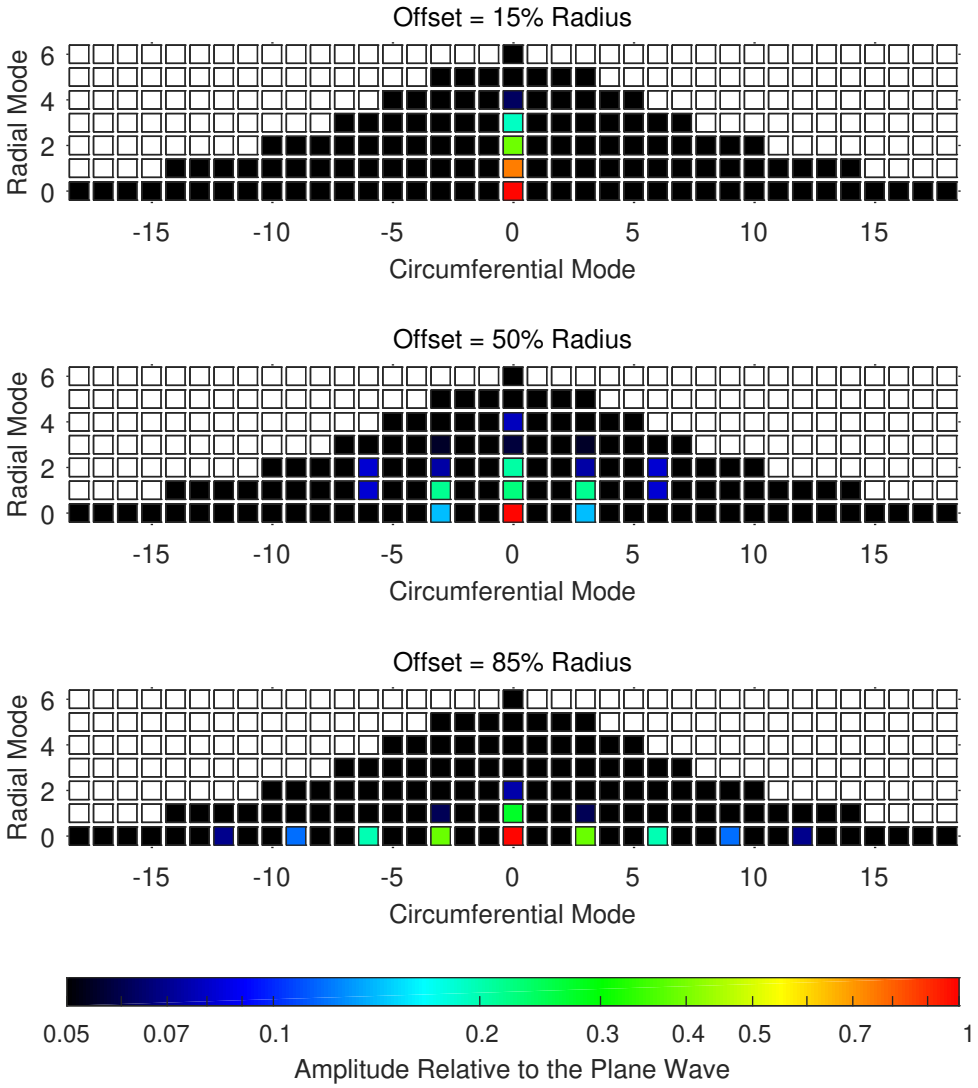

Figure 10.7: Calculated relative amplitudes of the evanescent modes formed at the area discontinuity between three equally distributed 12.55-mm diameter resonators and the 101.6-mm diameter impedance tube for various offset distances between the centerlines of the ducts.

of the length correction and shows that the length correction is related to the mass reactance [155]. Evanescent modes do not propagate energy axially along the duct; instead, their energy is stored close to the area discontinuity and decays exponentially in the axial direction. Therefore, the sound power of an evanescent mode calculated using Eq. (3.37) is purely imaginary. The sound power contained within all of the evanescent modes is computed by applying Eq. (3.37) to each higher-order evanescent mode and summing the imaginary components of all of the modes.

The filled symbols labeled as "ΔL" in Figure 10.8 are the normalized length corrections of one and three resonators as a function of their offset distances computed using the mode-matching method and Eq. (10.2). The open symbols labeled as "Power" in Figure 10.8 represent the total sound power of the calculated higher-order evanescent modes scaled by the length correction at the smallest offset distance. These results demonstrate that the length correction of resonators indeed scales with the sound power—or kinetic energy—contained within the higher-order evanescent modes formed at the area discontinuity.

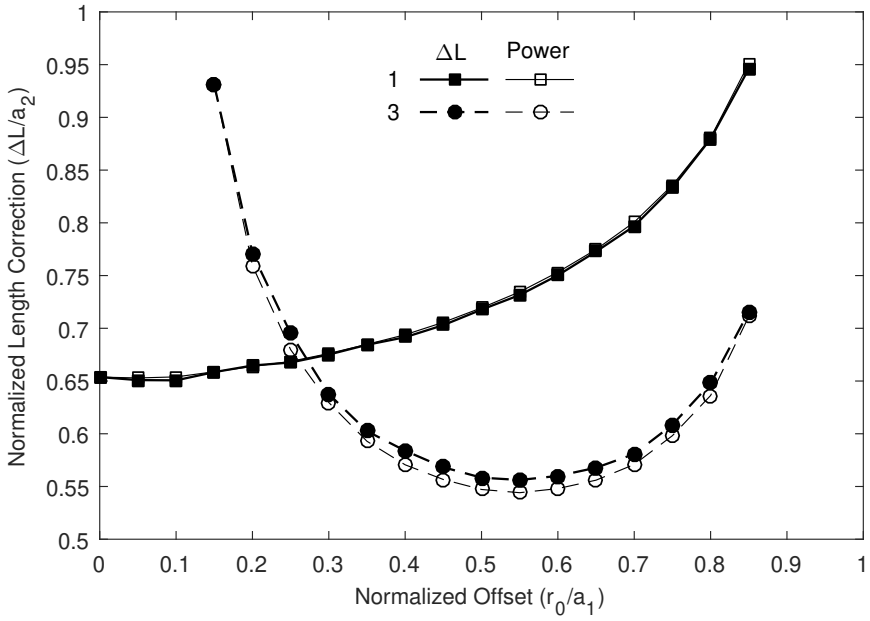

Figure 10.8: Calculated normalized length correction and scaled power of the evanescent modes at an area discontinuity between one or three resonators and the impedance tube as a function of their offset distances from the centerline of the tube.

These results provide a physical explanation for the observed change in the resonance frequencies of half-wave resonators as a function of their position within the cross-section of the impedance tube, as shown in Figure 10.2. As the offset distance between the centerlines of a single resonator and the impedance tube increases, the resonator excites additional circumferential evanescent modes, and the total energy of the evanescent modes increases. This increase in energy implies that the effective mass (or mass reactance) increases, and thus the length correction at the area discontinuity increases. Therefore, the resonance frequency of a single resonator closer to the outer radius of the impedance tube is lower than the resonance frequency of a single resonator closer to the center. Conversely, as the offset distance between the centerlines of three resonators and the impedance tube increases, the resonators first become less effective at exciting radial modes before becoming significantly more effective at exciting circumferential modes, so there is a minimum in the total energy of the evanescent modes at some offset distance. For the particular configurations tested, this explains why the resonance frequency of three resonators installed in the outer ring is greater than the resonance frequency of three resonators in the inner ring.

10.5 Measurements of the Acoustic Damping of Higher-Order Modes

The effect of evanescent higher-order modes on the resonance frequency of half-wave resonators was discussed in the previous section. In this section, measurements of the effect of propagating higher-order modes on the acoustic damping of the resonators is presented. The scattering matrices of one or more half-wave resonators were measured using the two-sided experimental facility, HOTMESS, to investigate the acoustic damping of resonators for higher-order modes. The scattering matrix, which is defined in Eq. (3.28), is a block matrix comprised of four blocks; the blocks on the diagonal are the upstream and downstream reflection matrices, and the off-diagonal blocks are the transmission matrices. The reflection and transmission matrices, which are defined in Eqs. (3.29) and (3.31), respectively, are $N \times N$ matrices, where N is the number of propagating modes. Each column

of the reflection and transmission matrices represents a particular incident mode, and each row represents a particular reflected or transmitted mode. The scattering matrix represents the most complete characterization of the acoustic properties of a test article. The sound power coefficients can then be calculated from the scattering matrix using the expressions developed in Section 3.7.

10.5.1 Scattering Matrix of a Single Half-Wave Resonator

The scattering matrix of the single half-wave resonator shown in Figure 4.13 was measured using HOTMESS. The resonator was installed such that side B of the two-sided impedance tube represents the combustion chamber and side A represents the upstream ducting. Figure 10.9 shows the absolute values of the pressure reflection matrices on side B for the half-wave resonator installed at the center of the impedance tube and at an offset distance of 70% of the impedance tube radius. Figure 10.10 shows the absolute values of the pressure transmission matrices from side B to side A for the same configurations. Figures 10.9 and 10.10 represent only half of the scattering matrix, but they still contain a considerable amount of data. The reflection and transmission matrices are plotted for the first five cut-on modes; the sixth cut-on mode—the first radial mode—was measured, but it is not plotted because the resonator has no resonance frequencies between the cut-on frequencies of the (0,1) and (3,0) modes.

Reflection Matrix in Figure 10.9

In Figure 10.9, the absolute value of the pressure reflection coefficients are plotted as functions of the normalized frequency defined in Eq. (6.1). The layout of the grid of plots in Figure 10.9 is a visual representation of the pressure reflection matrix defined in Eq. (3.29). Each column corresponds to a particular incident mode, which is designated by the mode order (m, n) and the subscript "In." Each row corresponds to a particular reflected mode, which is designated by the mode order (m, n) and the subscript "R." Therefore, the plots

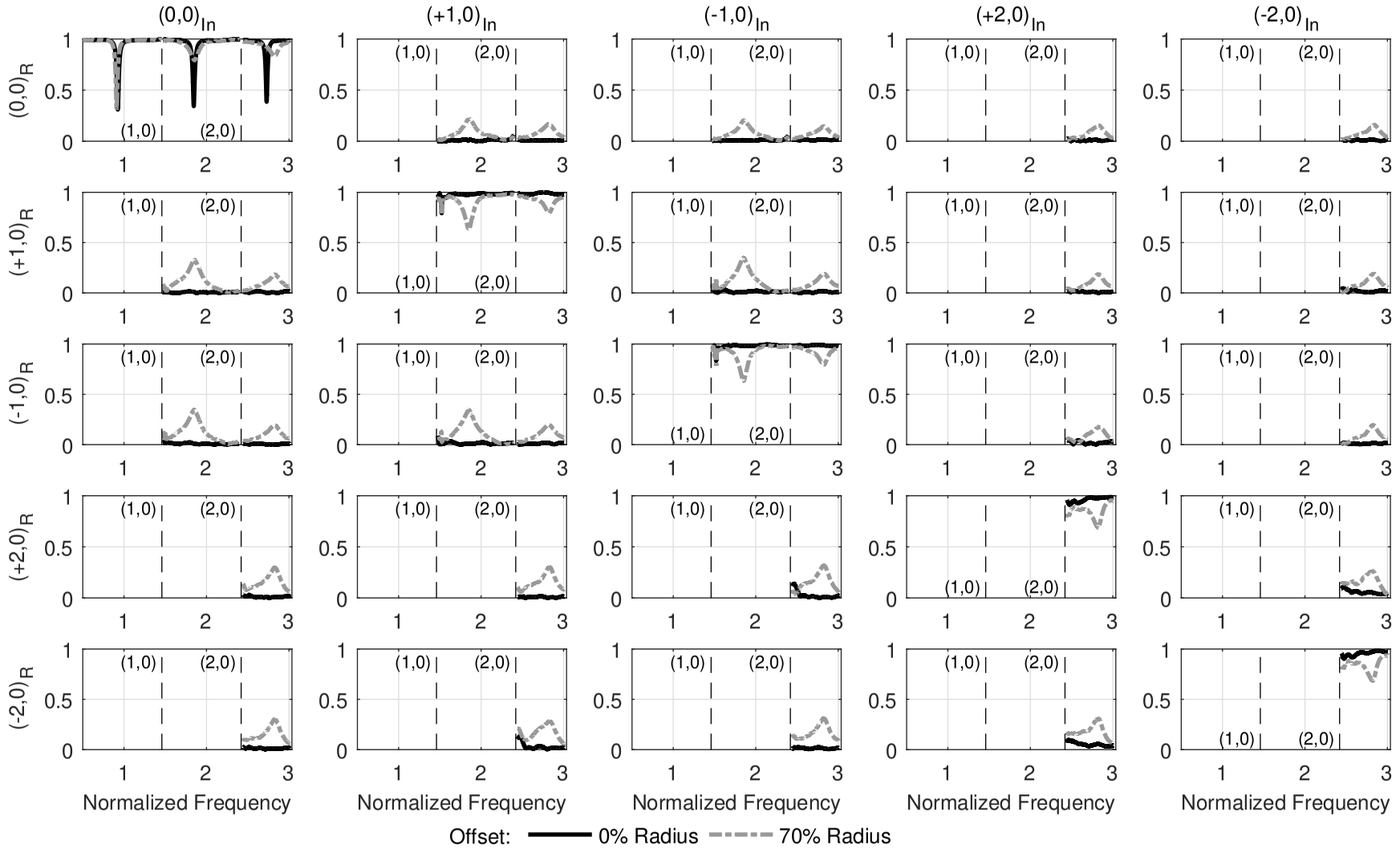

Figure 10.9: Absolute value of the pressure reflection matrix of a single half-wave resonator at various offset distances from the center of the impedance tube.

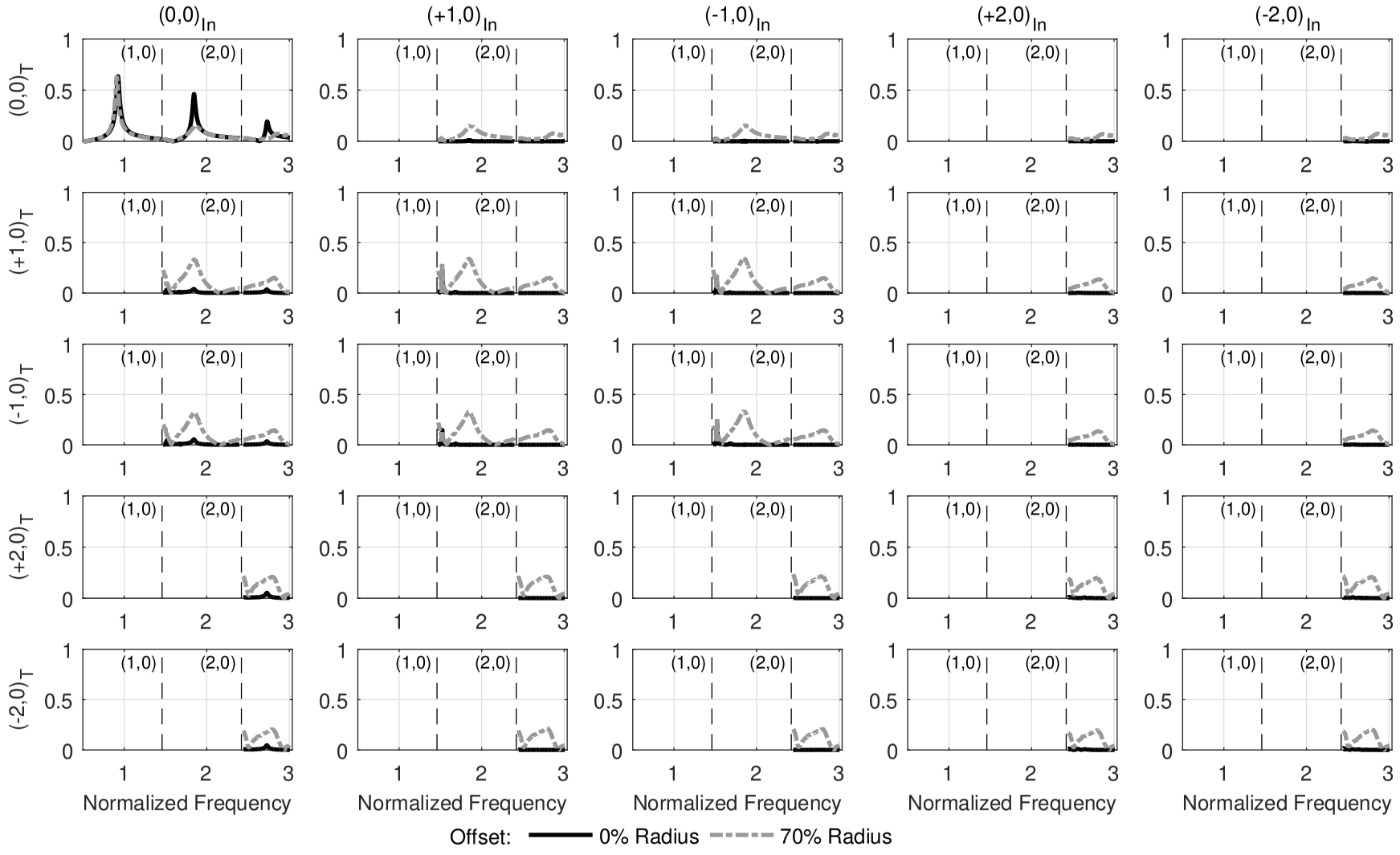

Figure 10.10: Absolute value of the pressure transmission matrix of a single half-wave resonator at various offset distances from the center of the impedance tube.

along the diagonal represent the pure reflection coefficients of an incident mode reflected as the same mode, whereas the off-diagonal plots represent the scattering coefficients from one incident mode into a different reflected mode. For example, the plot in the first row and first column shows the absolute value of the pressure reflection coefficient of the (0,0) incident mode into the (0,0) reflected mode; this represents the pure reflection coefficient for the plane wave mode. Similarly, the plot in the first row and second column shows the absolute value of the pressure reflection coefficient of the (+1,0) incident mode into the (0,0) reflected mode; this represents scattering from the first circumferential mode into the plane wave mode. The reflection coefficients involving higher-order modes are only plotted above the cut-on frequencies of the higher-order modes.

First, consider the plots along the diagonal in Figure 10.9, which show the pure reflection coefficients from an incident mode into the same reflected mode. The valleys in the pure reflection coefficients correspond to peaks in the absorption coefficient and occur at the resonance frequencies of the half-wave resonator. Thus, the first valley in the plot of the plane wave reflection coefficient occurs at the fundamental resonance frequency of the half-wave resonator, and the subsequent valleys occur at the first and second integer harmonics. The differences in the depths of the valleys of the two curves plotted in the first row and first column of Figure 10.9 indicate that the position of the resonator within the cross-section of the impedance tube has a significant effect on the plane wave reflection coefficient at the integer harmonics. These integer harmonics are at frequencies above the cut-on frequency of the first higher-order mode. Likewise, the other plots along the diagonal in Figure 10.9 show that the position of the resonator has a significant effect on the pure reflection coefficients of the higher-order modes. For example, the offset resonator has distinct valleys in the pure reflection coefficients of the ($\pm$1,0) and ($\pm$2,0) modes near the resonance frequencies, but the centered resonator has no valleys in the pure reflection coefficients of the ($\pm$1,0) and ($\pm$2,0) modes because the center of the impedance tube is a pressure node for all pure circumferential higher-order modes.

Next, consider the off-diagonal plots in Figure 10.9, which show the scattering coefficients from one incident mode into a different reflected mode. The peaks in the off-diagonal plots indicate that nonzero scattering occurs between each pair of modes near the resonance frequencies of the offset half-wave resonator. The scattering is nonzero for the offset resonator because the configuration is asymmetric with respect to the mode shapes of the (1,0) and (2,0) modes. However, no scattering occurs between the circumferential and plane wave modes for the centered resonator because the center of the impedance tube is a pressure node for the (1,0) and (2,0) modes.

Transmission Matrix in Figure 10.10

In Figure 10.10, the absolute value of the pressure transmission coefficients are plotted as functions of the normalized frequency defined in Eq. (6.1). The layout of the grid of plots in Figure 10.10 is a visual representation of the pressure transmission matrix defined in Eq. (3.31). Each column corresponds to a particular incident mode, which is designated by the mode order (m, n) and the subscript "In." Each row corresponds to a particular transmitted mode, which is designated by the mode order (m, n) and the subscript "T." Therefore, the plots along the diagonal represent the pure transmission coefficients of an incident mode transmitted as the same mode, whereas the off-diagonal plots represent the scattering coefficients from one incident mode into a different transmitted mode.

Figure 10.10 shows that the single half-wave resonator only transmits sound near its resonance frequencies, which is evident because the peaks in the transmission coefficients occur near the fundamental resonance frequency and the integer harmonics. The position of the resonator also has a significant effect on the transmission coefficients at frequencies higher than the cut-on frequency of the first higher-order mode. For example, the transmission coefficient of the plane wave mode shows that the peak values at the integer harmonics are different for the centered and offset resonators. Additionally, the other plots in Figure 10.10 indicate that the centered resonator does not transmit higher-order modes,

but the offset resonator both transmits and scatters higher-order modes.

10.5.2 Absorption Coefficient of a Single Half-Wave Resonator

The reflection and transmission matrices shown in Figures 10.9 and 10.10 contain so much information that it is difficult to evaluate the acoustic damping performance of the half-wave resonators based on these results. Thus, the sound power coefficients are examined for the cases studied. Figure 10.11 shows the absorption coefficients for the incident (0,0), (1,0), and (2,0) modes for a single half-wave resonator located at the center of the impedance tube and at an offset distance of 70% of the impedance tube radius. For higher-order modes, the absorption coefficient defined in Eq. (3.45) is the fraction of the sound power in a particular incident mode that is not reflected as any mode.

Figure 10.11 shows that the absorption coefficients of the centered resonator and the offset resonator are similar for the plane wave mode at frequencies below the cut-on frequency of the first higher-order mode; the only significant difference is the change in the resonance frequency as a function of position, which was previously shown in Figure 10.2. However, the absorption coefficients of the centered resonator and the offset resonator are significantly different at frequencies higher than the cut-on frequency of the first higher-order mode for each of the incident modes. As shown in Figures 10.11b and 10.11c, the centered resonator provides negligible absorption for the (1,0) and (2,0) incident modes because it is located at a pressure node of all pure circumferential modes, but the offset resonator has nonzero peaks in the absorption coefficient for the (1,0) and (2,0) incident modes at its resonance frequencies. Interestingly, the position of the resonator even has an effect on the absorption coefficient for the plane wave mode at frequencies higher than the cut-on frequency of the first higher-order mode. For example, Figure 10.11a shows that the peak absorption of the centered resonator is greater than that of the offset resonator at the first and second integer harmonics for the (0,0) incident mode. Previous studies have found that the position of the resonator has little to no effect for the plane wave mode [11], but

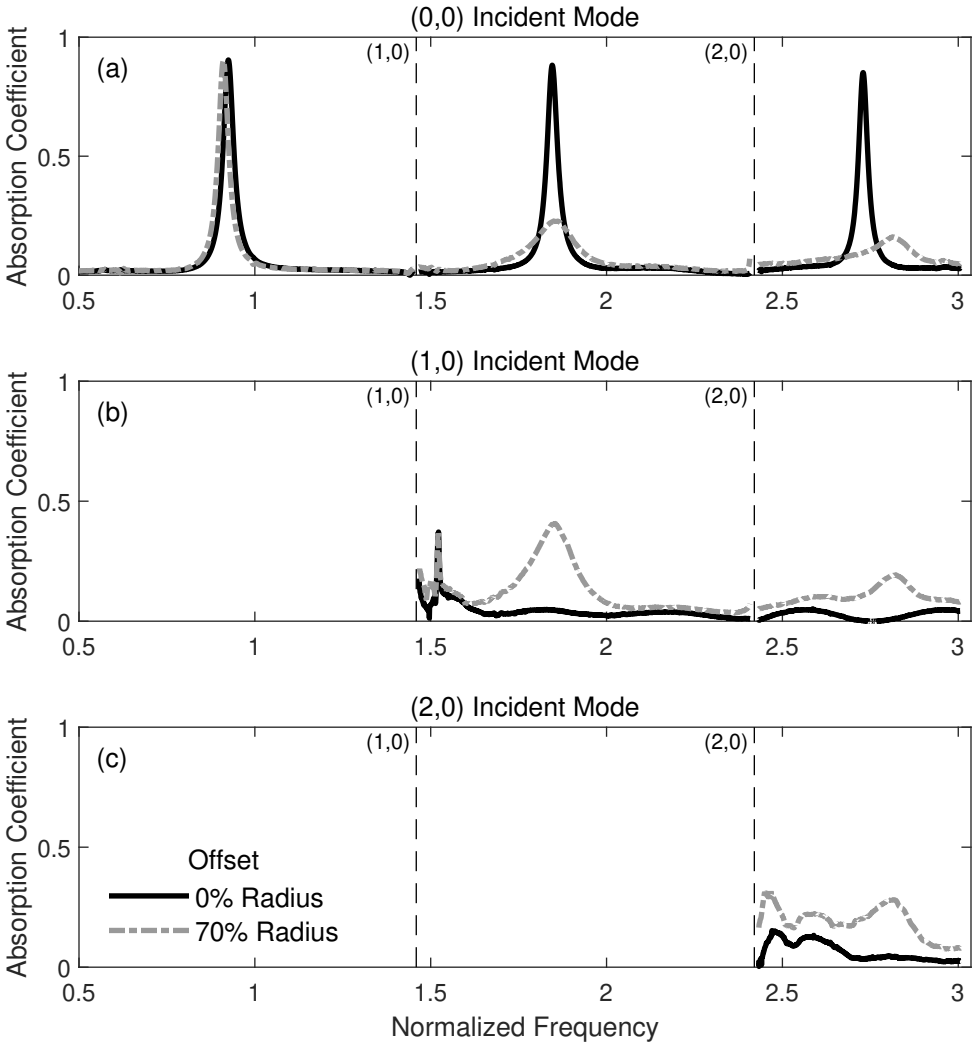

Figure 10.11: Absorption coefficient of a single half-wave resonator at various offset distances from the center of the impedance tube.

the current results show that this is only true at frequencies below the cut-on frequency of the first higher-order mode.

10.5.3 Sound Power Coefficients of Three Half-Wave Resonators

The sound power coefficients of different configurations of multiple resonators were also measured using HOTMESS. Figure 10.12 shows the absorption coefficients of the incident (0,0), (1,0), and (2,0) modes for three resonators distributed in the inner and outer rings in the configurations shown in Figures 10.1c and 10.1d, respectively. The resonance frequencies of the resonators vary as a function of their offset distance, which was previously shown in Figure 10.2. The offset distance of the three resonators has little other effect on the absorption coefficient of the plane wave mode for the fundamental resonance and first harmonic. However, as shown in Figure 10.12a, there are two peaks in the plane wave absorption coefficient near the second harmonic for the three resonators mounted in the inner ring, but there is only one peak for the resonators mounted in the outer ring. This phenomenon is due to the side branch formed by the extension of the resonators into the upstream side of the impedance tube and is discussed in more detail in Section 10.7. For the (1,0) and (2,0) incident modes shown in Figures 10.12b and 10.12c, the peak absorption coefficient of the three resonators mounted in the outer ring appears to be greater than that of the three resonators mounted in the inner ring. This is attributed to the fact that the magnitudes of the circumferential mode shapes increase with increasing distance from the center of the duct.

Figure 10.13 shows the total power transmission coefficients of the incident (0,0), (1,0), and (2,0) modes for the same three-resonator configurations. There are peaks in the total power transmission coefficient at most of the same frequencies at which there are peaks in the absorption coefficient. However, as shown in Figures 10.13a and 10.13b, there is little to no power transmission for the (0,0) and (1,0) incident modes at the first harmonic of the fundamental resonance frequency, so the sound power is nearly entirely dissipated

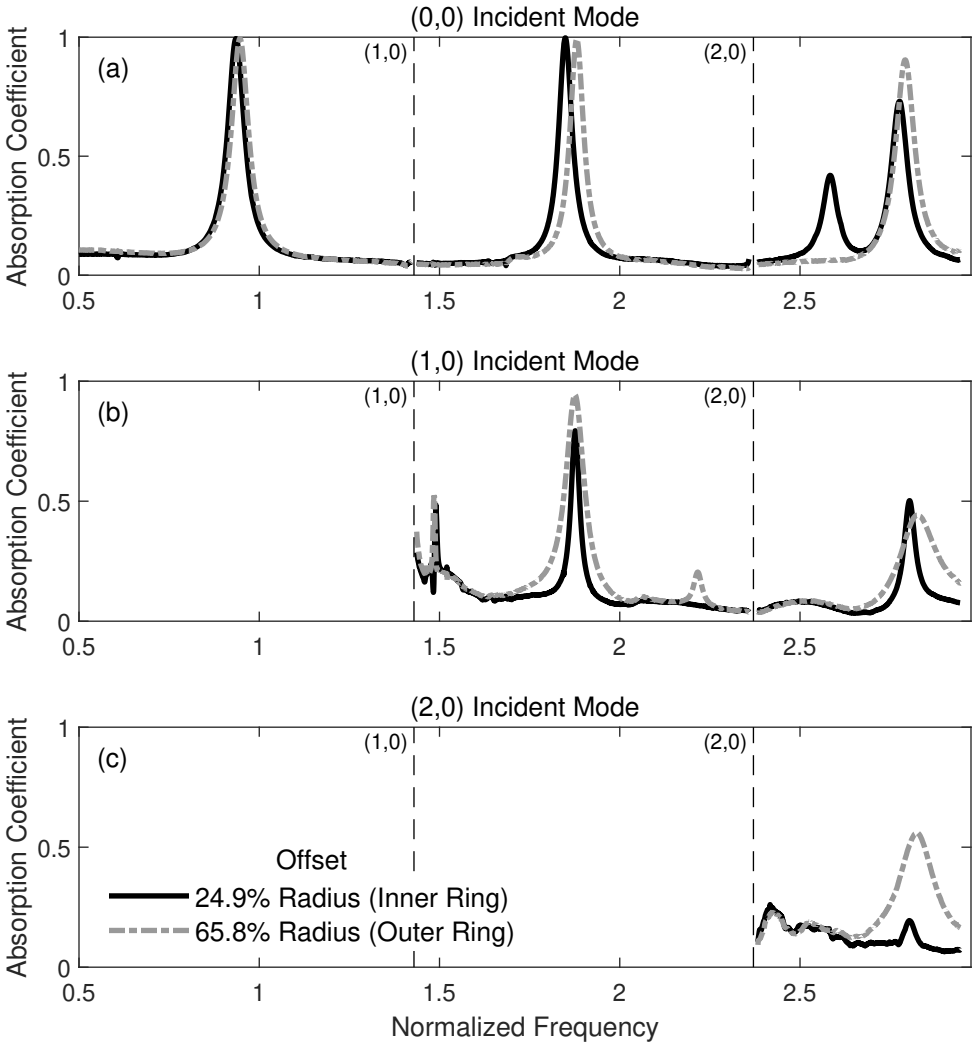

Figure 10.12: Absorption coefficient of three half-wave resonators at various offset distances from the center of the impedance tube.

by the three resonators at the first harmonic. This phenomenon is due to the side branch formed by the extension of the resonators into the upstream side of the impedance tube and is discussed in more detail in Section 10.7.

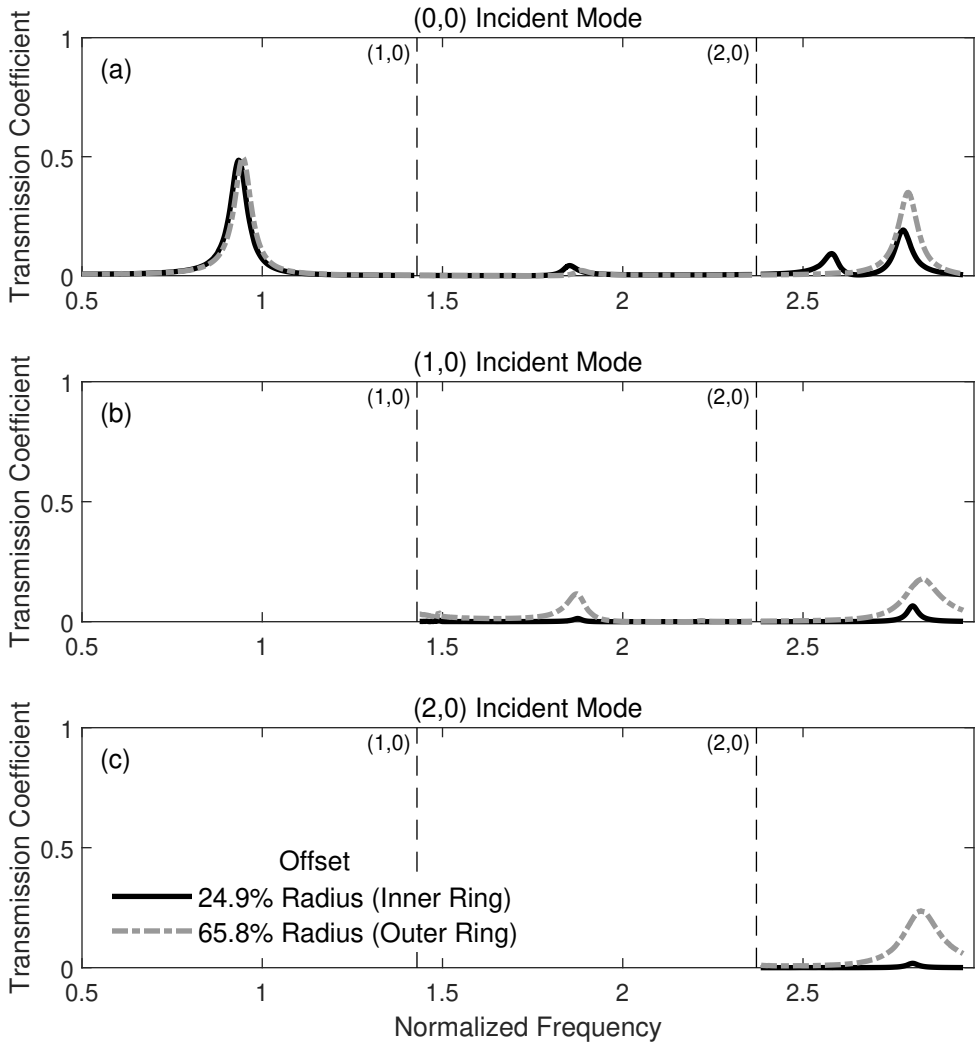

Figure 10.13: Total power transmission coefficient of three half-wave resonators at various offset distances from the center of the impedance tube.

10.6 Validation of the Numerical Model for Higher-Order Modes

The numerical model for higher-order modes described in Section 10.3 (and developed in detail in Appendix E) is useful for interpreting the experimental results presented in the previous section. First, the numerical model is validated by comparing the model predictions

to the experimental results. Each validation case is performed using $N = 121$ modes in the impedance tube, which is a reasonable compromise between computational efficiency and convergence. Figure 10.14 shows the computed and measured absolute values of the pressure reflection matrices for one half-wave resonator at an offset distance of 65.8% radius, which is the configuration shown in Figure 10.1b. Overall, the numerical model accurately computes the shapes of both the pure reflection coefficients and the scattering coefficients for a single resonator. The only significant differences between the model and the experimental results occur at frequencies just above the cut-on frequencies of the higher-order modes, but the modal decomposition method is known to be inaccurate near these frequencies [110]. Additionally, there are a few sharp peaks or valleys in the numerical model at the discrete normalized frequencies $\tilde{f} = 1.38$ and $\tilde{f} = 2.21$ that are not observed in the experiment. These discrete peaks or valleys are seen in the plots in the first three rows and first three columns of Figure 10.14. At all other frequencies, however, the numerical model accurately predicts the experimental results.

Figure 10.15 shows the computed and measured absolute values of the pressure reflection matrices for three half-wave resonators at an offset distance of 65.8% radius, which is the configuration shown in Figure 10.1d. Overall, the numerical model accurately computes the reflection matrix for three resonators, too. Again, the only significant differences between the model and experiment occur at frequencies just above the cut-on frequencies of the higher-order modes at which the modal decomposition method is known to be inaccurate [110]. Additionally, as seen in the plots in the second and third rows and columns of Figure 10.15, there are sharp peaks or valleys in the pure reflection and scattering coefficients between the (+1,0) and (–1,0) modes computed by the numerical model at the discrete normalized frequency $\tilde{f} = 2.22$. At all other frequencies, however, the numerical model accurately predicts the experimental results.

It is observed that there is significant scattering between the (+1,0) and (–2,0) modes and also between the (–1,0) and (+2,0) modes at frequencies near the second harmonic;

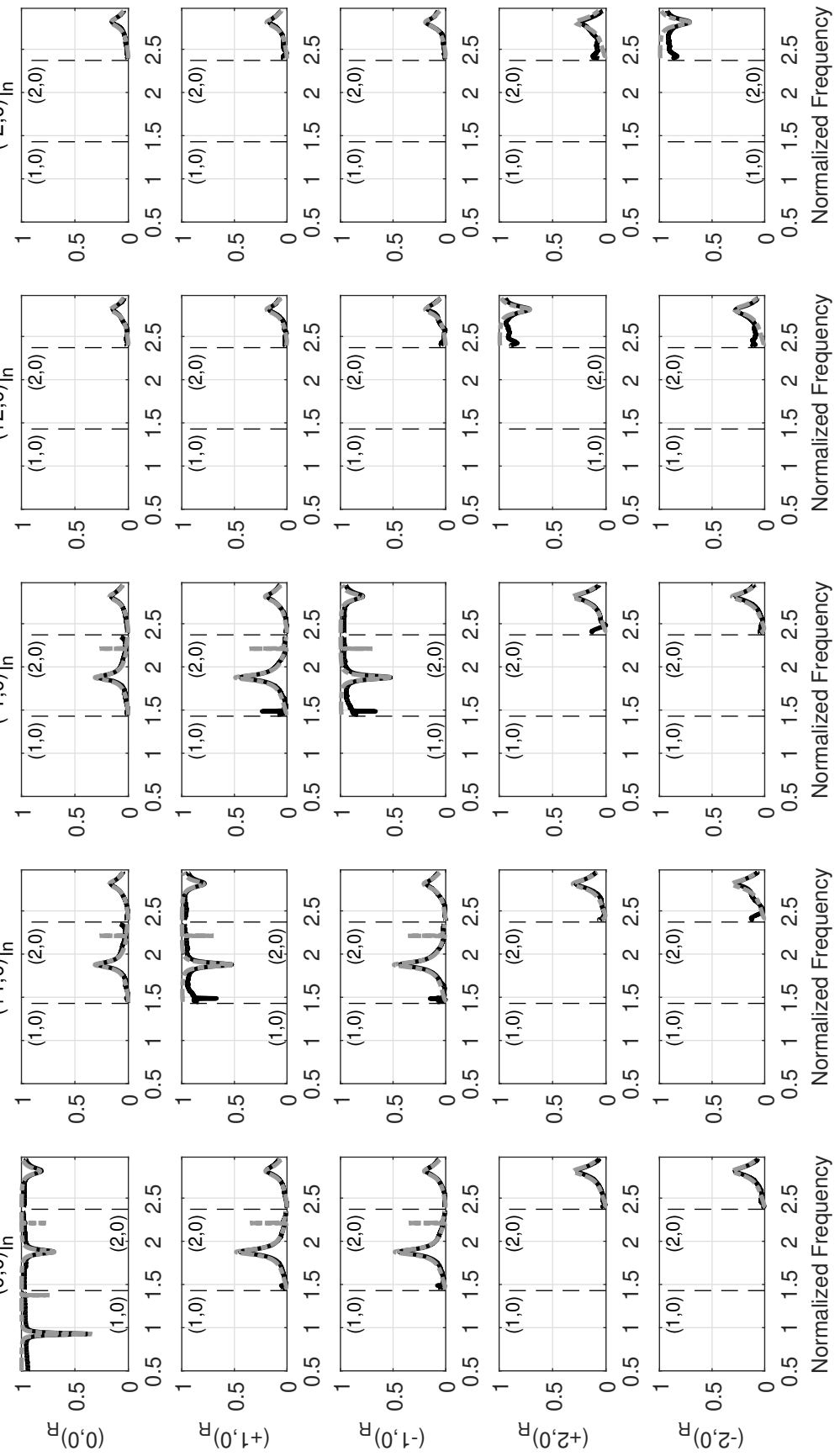

Figure 10.14: Absolute value of the pressure reflection matrix of one half-wave resonator at an offset distance of 65.8% radius (the "1, outer" configuration shown in Figure 10.1b).

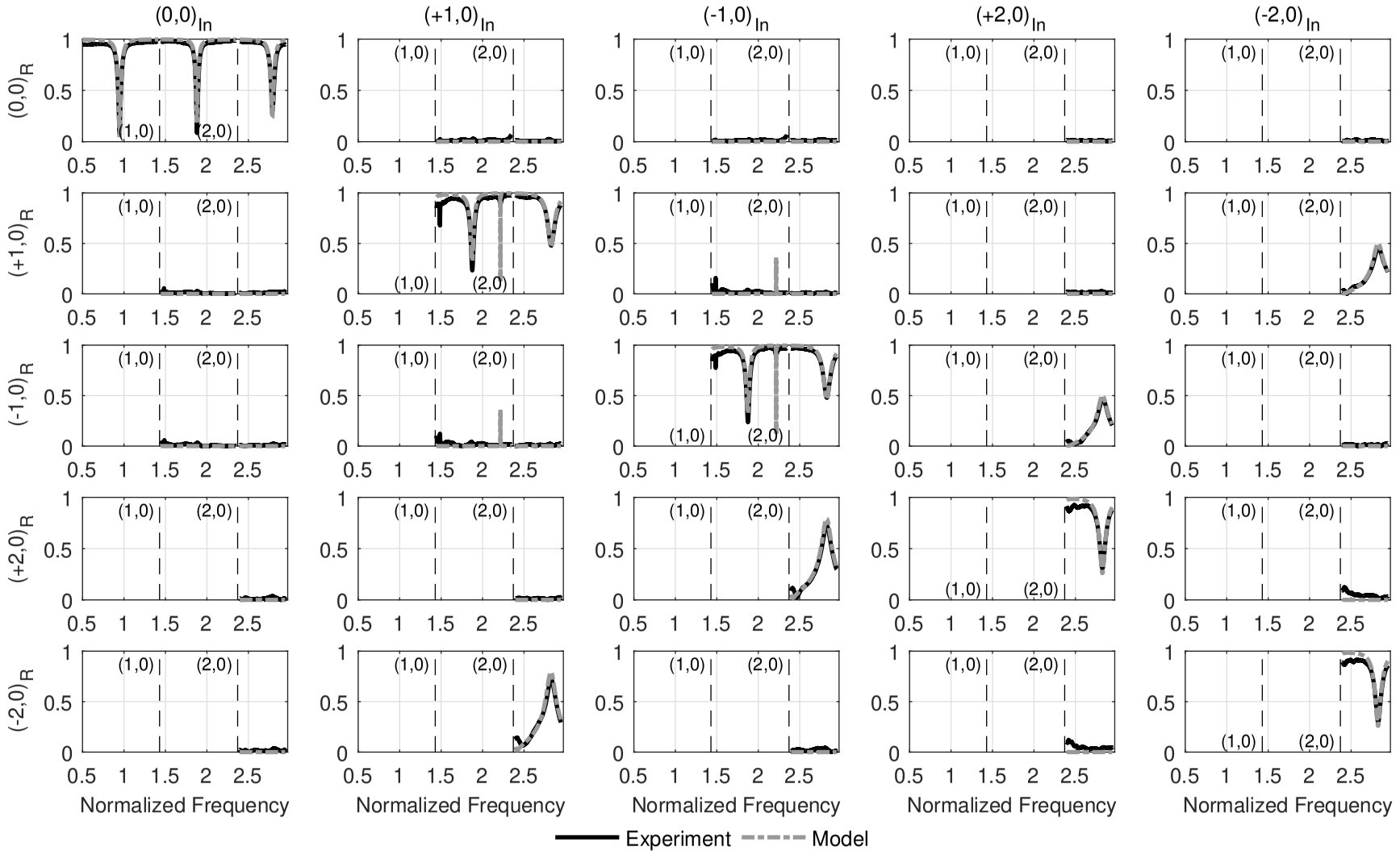

Figure 10.15: Absolute value of the pressure reflection matrix of three half-wave resonators at an offset distance of 65.8% radius (the "3, outer" configuration shown in Figure 10.1d).

this is indicated by the peaks in the scattering coefficient near $\tilde{f} = 2.8$ in the following plots: the fifth row and second column, the fourth row and third column, the third row and fourth column, and the second row and fifth column. The other off-diagonal plots show that there is minimal scattering between the remaining pairs of modes. The numerical model is shown to accurately predict this peculiar scattering pattern between the (+1,0) and (–2,0) modes and between the (–1,0) and (+2,0) modes. Note that this scattering pattern is due to the positions of the resonators with respect to the spinning mode shapes, but it would be difficult to predict this scattering pattern in advance without the numerical model.

The scattering matrices provide the most complete validation of the numerical model, but parameters such as the absorption coefficient, which characterizes the acoustic damping, provide a simpler quantitative comparison between the numerical model and the experiments. Figure 10.16 shows the computed and measured absorption coefficients of twelve half-wave resonators for the incident (0,0), (1,0), and (2,0) modes. The twelve-resonator configuration is the most challenging case for the numerical model because it includes multiple resonators in both the inner and outer rings. Overall, Figure 10.16 shows that the absorption coefficient predicted by the numerical model compares reasonably to with the experimental results. However, there are some differences between the model and the experiments. For example, as shown in Figures 10.16a and 10.16b, the model underpredicts the peak values of the absorption coefficients for the (0,0) and (1,0) incident modes at the first harmonic near the normalized frequency $\tilde{f} = 1.9$. The model also underpredicts the peak value of the absorption coefficient for the (2,0) incident mode at the second harmonic near the normalized frequency $\tilde{f} = 2.8$, as shown in Figure 10.16c. Conversely, Figure 10.16a shows that the model overpredicts the sharpness of the peak at the normalized frequency $\tilde{f} = 2.6$ for the (0,0) incident mode. Finally, the model underpredicts the measured absorption coefficient near the cut-on frequencies of higher-order modes and at frequencies away from the resonance frequencies. Some of these differences between the model and the experimental results are likely due to viscothermal losses within the side

branch and at the area discontinuities, which are neglected in the numerical model. Despite these minor differences, Figure 10.16 indicates that the numerical model performs reasonably well compared to experiment, even for the challenging twelve-resonator configuration.

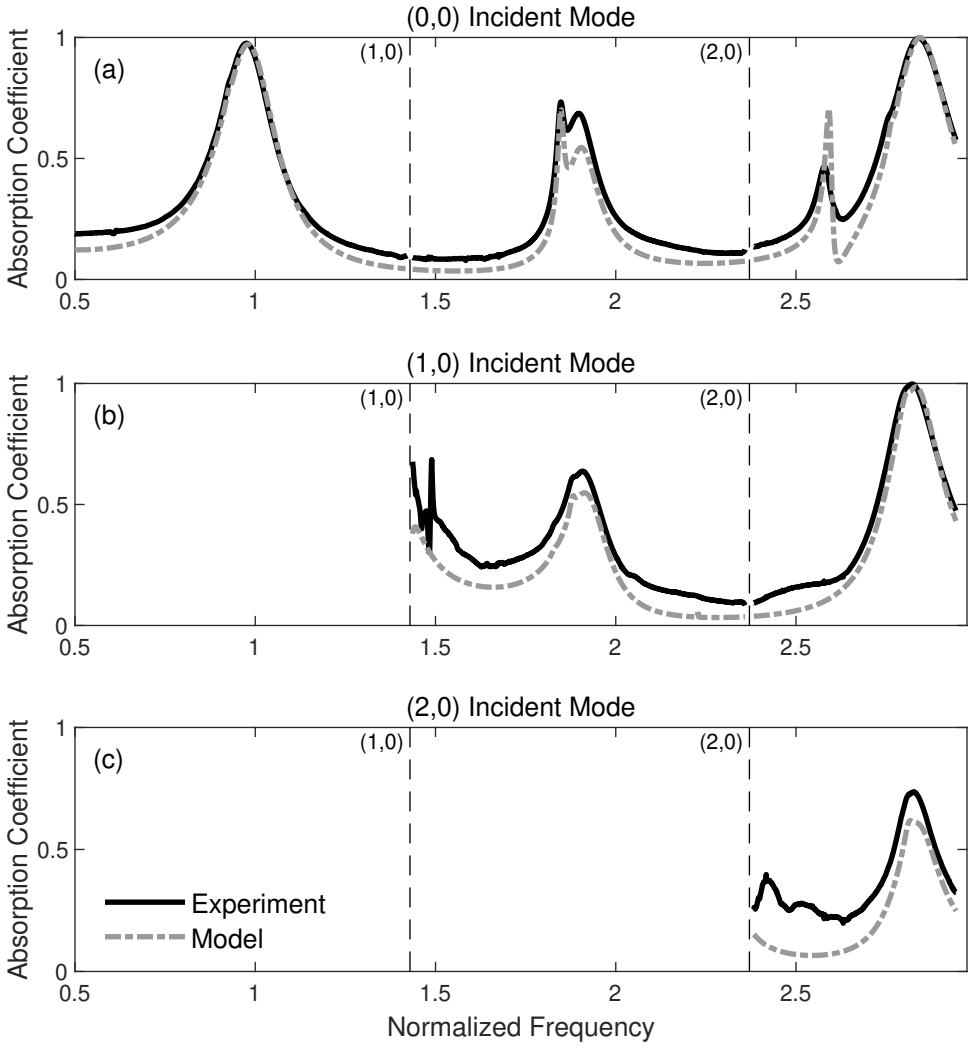

Figure 10.16: Absorption coefficient of twelve half-wave resonators.

10.7 Effect of the Side Branch

The sound power coefficients of the three-resonator configurations shown in Figures 10.12 and 10.13 include several phenomena which were attributed without proof to effects of the side branch formed by the extension of the resonators into the impedance tube. For example, Figure 10.12a shows that the configuration of three resonators mounted in the

outer ring has only a single absorption peak at the second harmonic for the (0,0) incident mode, but the configuration of three resonators mounted in the inner ring has two peaks for the (0,0) mode near the second harmonic. Additionally, Figures 10.13a and 10.13b show that the sound power transmission near the first harmonic is negligible for both three-resonator configurations.

In this section, the numerical model for higher-order modes described in Section 10.3 (and developed in detail in Appendix E) is applied to the configuration consisting of three half-wave resonators in the inner ring shown in Figure 10.1c. In addition, this numerical model is applied to the same configuration assuming that the resonators do not extend into side A of the impedance tube, which means that there is no side branch. The effect of the side branch is studied by comparing the results of the numerical models with and without the extension of the resonators into the impedance tube. Figures 10.17 and 10.18 show the absorption coefficients of the three half-wave resonators for the (0,0) incident mode on side B and side A, respectively, of the two-sided impedance tube. The experimental measurements are compared to the numerical model for the experimental geometry and the numerical model without the side branch.

10.7.1 Multiple Absorption Peaks Due to the Side Branch

Figures 10.17 and 10.18 show that for three half-wave resonators mounted in the inner ring, there are two peaks in the absorption coefficients near the second harmonic for both the experimental results and the numerical model for the test geometry. However, the numerical model without the side branch (that is, no extension of the resonators into the impedance tube) predicts only one peak in the absorption coefficient near the second harmonic, as seen in both Figures 10.17 and 10.18. (Note that the numerical model overpredicts the sharpness of the two absorption peaks, which is likely because the model does not include viscothermal losses within the side branch and at the area discontinuities.) These results prove that the dual peaks near the second harmonic are indeed an effect of the side branch.

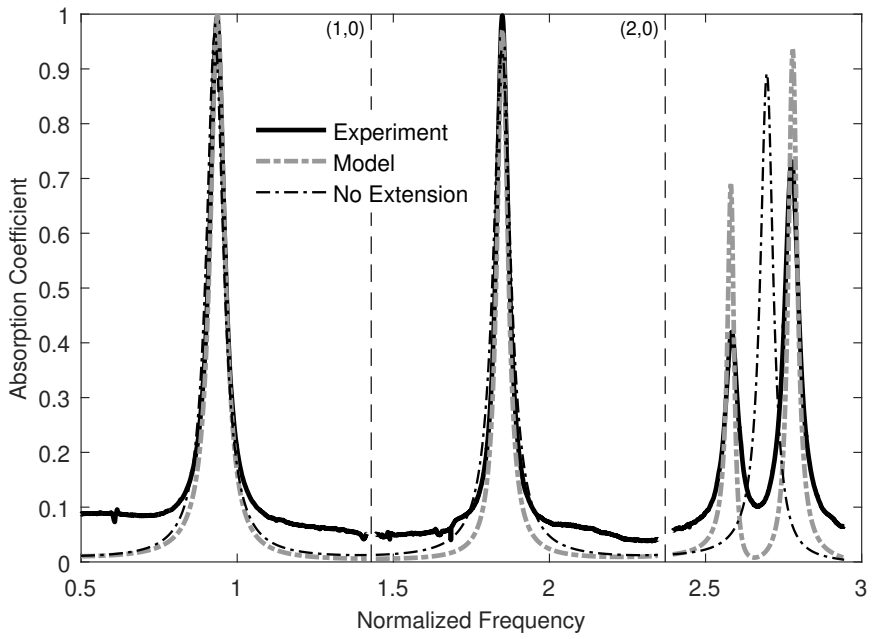

Figure 10.17: Absorption coefficient on side B for three half-wave resonators at an offset distance of 24.9% radius (see Figure 10.1c). The "No Extension" curve is the numerical model without a side branch.

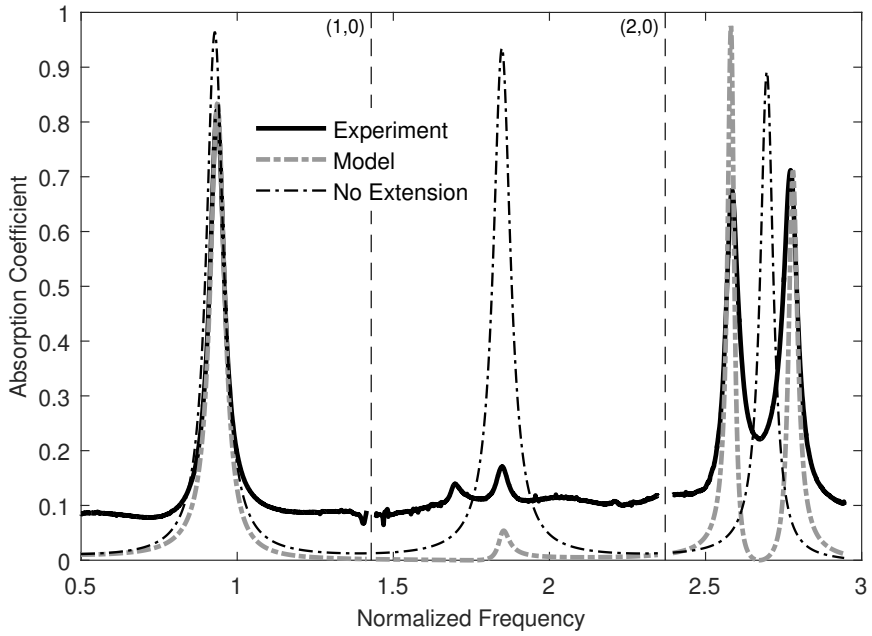

Figure 10.18: Absorption coefficient on side A for three half-wave resonators at an offset distance of 24.9% radius (see Figure 10.1c). The "No Extension" curve is the numerical model without a side branch.

The mechanism that causes the dual peaks is investigated by calculating the amplitudes of the modes in the side branch using the numerical model, which reveals that the (0,1)-like mode in the side branch is excited at frequencies corresponding to the dual peaks. This also explains why there is a difference between the absorption coefficients of three resonators mounted in the inner versus the outer rings, as shown earlier in Figure 10.12. The pressure node of the (0,1)-like mode in the side branch is aligned with the outer ring of resonators, so the resonators in the outer ring do not interact significantly with the (0,1)-like mode in the side branch. Therefore, the three resonators mounted in the outer ring have only a single absorption peak at the second harmonic for the (0,0) incident mode, whereas the three resonators mounted in the inner ring have two peaks near the second harmonic due to their interaction with the (0,1)-like mode in the side branch.

10.7.2 One-Way Absorption Due to the Side Branch

A comparison between Figures 10.17 and 10.18 indicates that the side branch also has a significant effect on the absorption coefficient near the first harmonic of these half-wave resonators. The experimental results and numerical model for the experimental geometry show that the peak absorption coefficient at the first harmonic is nearly unity on side B, as seen in Figure 10.17, but the absorption coefficient near the first harmonic is negligible on side A, as seen in Figure 10.18. Conversely, the absorption coefficient predicted by the numerical model without the side branch is identical on sides A and B, so the difference in the experimental results is evidently due to the side branch. The side branch has the boundary conditions of a quarter-wave resonator, and its fundamental quarter-wave resonance frequency is close to the first harmonic of the half-wave resonators. Near the quarter-wave resonance frequency, the input impedance of the side branch is small, so sound power is more easily transmitted from side A of the impedance tube into the side branch than between side A of the impedance tube and the resonators. Since little sound power is transmitted from side A into the resonators at their first harmonic, the resonators provide

little absorption on side A. However, the side branch has a small effect on the sound power transmitted between side B of the impedance tube and the resonators, so the resonators still provide significant absorption on side B at their first harmonic. Therefore, the presence of the side branch on only one side of the half-wave resonators creates a one-way absorption device at certain frequencies.

10.8 Summary

In this chapter, the effects of higher-order modes on the acoustic damping of propellant injectors were investigated in quiescent air at ambient conditions in the linear acoustic regime for the (0,0), ($\pm$1,0), ($\pm$2,0), and (0,1) modes. The effects of the higher-order modes and the contributions of the physical mechanisms responsible for the acoustic damping are summarized below.

Effect of Position on the Length Correction

A mode-matching method was presented for calculating the acoustic reflection and transmission of higher-order modes at an area discontinuity in a duct. The mode-matching method was applied to calculate the length correction at the area discontinuity between one or more offset half-wave resonators and the impedance tube. Furthermore, the length correction was shown to be directly related to the energy of the evanescent modes formed at the area discontinuity. The amplitudes of the evanescent modes and the length correction at the area discontinuity were found to depend on the number of resonators, the position of the resonators, and the symmetry of the configuration with respect to the mode shapes, so there is no simple formula for the length correction at a general area discontinuity. However, the methods developed in this chapter can be applied to calculate the length correction at any area discontinuity.

Experimental Results

The measured scattering matrices and sound power coefficients were presented for several configurations of half-wave resonators. The position of the resonators within the cross-section of the impedance tube was shown to have a significant effect on the scattering coefficients. In general, the resonators were shown to be most effective at providing acoustic damping if they are mounted near the pressure antinodes of the higher-order modes. Many other interesting results could be discussed in future works based on these measurements of higher-order modes.

Numerical Model

A numerical model for the higher-order scattering matrix of half-wave resonators was developed by applying the mode-matching method to the area discontinuities between the open ends of the resonators and the impedance tube. The model was shown to accurately predict the scattering matrix and sound power coefficients of one or more half-wave resonators for higher-order modes. The numerical model was applied to investigate the effect of the side branch formed by the extension of the resonators into the impedance tube. For the resonators measured in this chapter, the excitation of modes within the side branch causes an additional absorption peak to appear, and the resonators provide one-way absorption at certain frequencies because the side branch acts like a quarter-wave resonator. Such a one-way absorption device may be useful in applications beyond providing acoustic damping in a rocket engine.

Acoustic Damping Mechanisms

For the experiments discussed in this chapter, it was shown that the physical mechanisms responsible for the acoustic damping are viscothermal losses in the acoustic boundary layer and acoustic radiation from the open end of the injectors opposite the incident acoustic waves. These are the same acoustic damping mechanisms discussed in Chapter 6, in which

the effects of geometric parameters were investigated in quiescent air at ambient conditions in the linear acoustic regime for the plane wave mode. Thus, no fundamentally different acoustic damping mechanisms were found to be introduced by higher-order modes, but the acoustic damping was shown to vary with the positions of the resonators relative to the shapes of the higher-order modes.

CHAPTER 11
CONCLUSIONS AND FUTURE RESEARCH

11.1 Conclusions

The objective of this work was to investigate the acoustic damping of propellant injectors in order to gain an understanding of the physical mechanisms governing their acoustic damping. The acoustic damping of the injectors was quantified using the absorption coefficient, which is the fraction of the incident sound power that is not reflected from the injectors. The effects of realistic geometric parameters and operating conditions on the absorption coefficient were measured experimentally. In addition, the sound power dissipation and transmission coefficients were measured to separate the effects of the physical mechanisms responsible for the acoustic damping. A new experimental facility called the Heated, Optimized Tube for Multimodal Evaluation of Sound Scattering (HOTMESS) was developed to measure the acoustic scattering matrix of a test article under mean flow, high temperature, high amplitude, and higher-order mode propagation conditions. HOTMESS is currently the only known experimental facility in the world that is capable of measuring the acoustic scattering matrix—and hence the sound power reflection, transmission, dissipation, and absorption coefficients—of a test article under all of these conditions. Although the motivation for this work stemmed from propellant injectors in a rocket engine, the results are applicable, more generally, to any end-mounted half-wave resonators in a duct. In fact, since the propellant injectors were shown to nominally behave like half-wave resonators, straight cylindrical half-wave resonators were used in place of injectors with realistic geometric features in some of the experiments.

Absorption Coefficient Parameters

The behavior of the absorption coefficient can be described based on the resonance frequency, peak absorption coefficient, and absorption frequency bandwidth. However, the normalized resistance—not the peak absorption coefficient—was found to vary monotonically with the parameters under test. It was shown that the absorption coefficient is a function of the normalized termination resistance and reactance measured in the impedance tube and that the peak absorption coefficient is maximized when the normalized termination resistance at resonance is equal to one. Thus, the results of the experiments conducted in this work are reported below in terms of the resonance frequency, absorption frequency bandwidth, and normalized termination resistance.

Effect of Geometric Parameters

Geometric Features: A straight cylindrical injector, which represents the main body of a propellant injector, was shown to behave like an ideal half-wave resonator: it has a high peak absorption coefficient and a relatively narrow absorption frequency bandwidth. The experiments conducted in quiescent air at ambient conditions in the linear acoustic regime showed that the main effect of an inlet protrusion, which forms an area contraction at the inlet of the injector, is to decrease the resonance frequency. Similarly, the experiments showed that the main effect of a recess, which forms an area expansion at the outlet of the injector, is to increase the resonance frequency. The effects of an annulus and fuel holes were also measured, but these features would be filled with liquid propellant in an operating propellant injector. Therefore, it was suggested that the measurements of the injector containing an inlet protrusion and a recess were the most realistic for the acoustic damping of an operating propellant injector.

Open Area Ratio and Number of Injectors: The open area ratio is defined in this work as the ratio of the open area of the injectors to the cross-sectional area of the combustion

chamber. This ratio is a function of the diameters of the injectors, the diameter of the combustion chamber, and the number of injectors. It was shown analytically and experimentally that as the open area ratio increases, the normalized termination resistance decreases, and the absorption frequency bandwidth increases. If the open area ratio increases because the diameter of the injectors increases, then the resonance frequency was found to increase. If, instead, the open area ratio increases because the number of injectors increases, then the behavior of the resonance frequency was found to vary depending on the extension length of the injectors into the impedance tube (or combustion chamber).

Position: For the plane wave mode, the position of the injectors within the cross-section of the impedance tube (or combustion chamber) was shown to affect the resonance frequency but not the normalized termination resistance or absorption frequency bandwidth. It was found that the change in the resonance frequency is directly related to the energy of the higher-order evanescent modes that are excited at the area discontinuity between the injectors and the combustion chamber.

Effect of Operating Conditions

Bias Flow: The normalized resistance and absorption frequency bandwidth of the propellant injectors were shown to increase monotonically with the velocity of the bias flow through the injectors. Some of the experimental results displayed a linear relationship between the normalized resistance and the Mach number above a certain Mach number, whereas other results displayed a nonlinear relationship. The experiments showed that the resonance frequency generally decreases with increasing bias flow velocity, but the resonance frequency was found to increase at velocities corresponding to a mean flow Strouhal number of about one. Since the velocity through the inlet protrusion is greater than the velocity in the main body of the injector, the acoustic properties were found to vary more strongly with the bias flow Mach number for the injectors with an inlet protrusion.

Temperature: The resonance frequency of the propellant injectors is directly proportional to the speed of sound and thus increases with increasing temperature. The effect of temperature on the acoustic damping of the propellant injectors was otherwise shown to be negligible up to at least 500°F (260°C), which was the highest temperature measured in the experiments. However, temperature gradients within the cross-section of the impedance tube (or combustion chamber) were found to have a non-negligible effect on the resonance frequency and absorption coefficient of the injectors.

Amplitude: At low amplitudes, the acoustic properties—including the resonance frequency, absorption frequency bandwidth, and normalized resistance—are known to be independent of amplitude, and the current measurements confirmed this. However, the experiments at high amplitudes showed that the normalized resistance and absorption frequency bandwidth of the propellant injectors increase monotonically with amplitude and that the resonance frequency decreases with increasing amplitude at high incident sound pressure levels. The difference between the low-amplitude and high-amplitude behavior characterizes the linear and nonlinear acoustic regimes. It was shown that the acoustic particle velocity increases through the inlet protrusion, so the measured acoustic properties were found to vary more strongly with amplitude for the injectors with an inlet protrusion.

Higher-Order Modes: The position of the injectors within the cross-section of the impedance tube (or combustion chamber) was shown to have a significant effect on the acoustic damping of higher-order modes. The propellant injectors were shown to be most effective at providing acoustic damping if they are located near the pressure antinodes of the higher-order modes. The scattering between modes was found to depend on the position of the injectors with respect to the shapes of the modes.

Analytical and Numerical Models

Simplified analytical expressions for the normalized impedance and sound power coefficients of a half-wave resonator near resonance were derived to provide an understanding of the physical mechanisms responsible for the acoustic damping. A numerical model was also developed based on transfer matrices to predict the acoustic damping of propellant injectors with realistic geometric features in quiescent air at ambient conditions in the linear acoustic regime for the plane wave mode. For higher-order modes, the mode-matching method for the reflection and transmission of sound at an area discontinuity in a duct was applied to develop a numerical model for the scattering matrix and sound power coefficients of half-wave resonators. The numerical models for the plane wave mode and for higher-order modes were shown to agree well with the experimental results. The mode-matching method was also applied to analytically calculate the amplitudes of the higher-order evanescent modes and the length correction at an area discontinuity in a duct.

Acoustic Damping Mechanisms

The following physical mechanisms were investigated for their role in the acoustic damping of propellant injectors: viscous and thermal losses in the acoustic boundary layer, acoustic radiation from the open end of the injectors opposite the incident acoustic waves, dissipation due to turbulence, the conversion of acoustic energy to vorticity at the open ends of the injectors, and attenuation within the fluid itself. Viscothermal losses in the acoustic boundary layer and acoustic radiation from the open end of the injectors were shown to be present at all flow, temperature, and amplitude conditions, and they are well-described by simple analytical expressions. Attenuation within the fluid itself was shown to be negligible up to at least 500°F (260°C), which was the highest measured temperature in the experiments. The experiments showed that the conversion of acoustic energy to vorticity becomes significant as the mean flow velocity or the particle velocity increases. The flow field at the open end of each propellant injector opposite the incident acoustic waves was

measured at high amplitudes using particle image velocimetry (PIV), which revealed that vortices and a steady jet formed at high incident sound pressure levels. The kinetic energy of the vortices and jet was compared to the measured dissipated acoustic energy, and the conversion of acoustic energy to vorticity was shown to account for no more than 60% of the nonlinear dissipation at high amplitudes. A number of other dissipation mechanisms, including dissipation due to turbulence in the acoustic boundary layer, were proposed to account for the difference.

11.2 Recommendations for Future Research

This work made significant contributions to the understanding of the acoustic damping mechanisms of propellant injectors. However, there are some unanswered questions arising from the experiments that could form the basis for future research.

Geometric Features: In a real combustion chamber, there is uncertainty in the exact frequency of the combustion instability, so both a high peak value and wide frequency bandwidth of the absorption coefficient are required to prevent combustion instabilities. Propellant injectors nominally behave like narrowband half-wave resonators, but the frequency bandwidth of multiple injectors could be increased by designing injectors with several different lengths. Such configurations should be investigated experimentally for their potential to provide both a high peak value and wide frequency bandwidth of the absorption coefficient. In addition, the effects of coupling between multiple injectors should be measured.

Bias Flow: Theoretically, the normalized resistance at the open end of a propellant injector increases linearly with the bias flow Mach number due to the conversion of acoustic energy into vorticity. This dissipation mechanism should be verified experimentally by measuring the flow fields at the open ends of the injectors with bias flow using PIV. The kinetic energy of the hydrodynamic waves should be calculated from the flow field mea-

surements to determine the quantitative relationship between the normalized resistance and the Mach number. If there are additional power dissipation mechanisms that cannot be explained by the PIV measurements, then computational modeling may be useful for evaluating the dissipation mechanisms inside the injectors, such as dissipation due to turbulence in the boundary layer or at the inlet.

Temperature: The effect of temperature on the acoustic damping of the propellant injectors was found to be negligible up to 500°F (260°C). The acoustic damping should be measured at even higher temperatures representative of a combustion chamber to determine the temperature at which attenuation within the fluid becomes important compared to attenuation within the acoustic boundary layer. The attenuation within the fluid depends strongly on the concentration of water vapor, so the experimental facility should be instrumented to measure the humidity of the flow through the impedance tube.

Amplitude: Typically, the increase in the resistance of a resonator at high amplitudes is attributed to the formation of vortices at the open ends. However, the PIV measurements at the open ends of the propellant injectors at high amplitudes indicated that the conversion of acoustic energy to vorticity accounts for no more than 60% of the increase in dissipation. Additional PIV measurements should be conducted in the two-sided impedance tube to measure the flow fields at both ends of the injectors while simultaneously acquiring acoustic measurements. If these measurements do not reveal the source of the excess dissipation, then additional experiments should be conducted to measure the structural vibration of the impedance tube, scattering to higher harmonics, and the generation of turbulence in the acoustic boundary layer. Computational modeling may be useful for elucidating the dissipation mechanisms inside the injectors, such as nonlinear steepening and dissipation due to turbulence in the acoustic boundary layer. Furthermore, experimental measurements should be conducted at high incident sound pressure levels to understand possible changes in the dissipation mechanisms and flow fields at the open ends of the injectors due to the

combined effects of mean flow and fluctuating particle velocity. In particular, these experiments should investigate the regimes at which the particle velocity is much less than, on the order of, and much greater than the mean flow velocity.

Higher-Order Modes: In this work, a numerical model for the scattering matrix of half-wave resonators was developed by applying the mode-matching method to the area discontinuities between the open ends of the resonators and the impedance tube. This model holds considerable potential to analyze and design innovative acoustic damping devices for particular higher-order modes. For example, the numerical model could be employed to intelligently distribute propellant injectors of varying lengths at different locations on the injector faceplate to optimize acoustic damping for multiple higher-order modes. There are also numerous additional applications for the experimental facility, HOTMESS, which was developed as part of the current work. For example, HOTMESS is the only known experimental facility in the world that could be used to measure the acoustic properties of perforated liners under heated grazing flow conditions for higher-order modes in a circular duct.

Appendices

APPENDIX A
UNCERTAINTY ANALYSIS

In this appendix, the uncertainty in the experimental results is estimated by propagating the experimental uncertainties through the acoustic measurement methodology presented in Chapter 3. The outline of this appendix is as follows: First, the definitions and background material necessary for the uncertainty analysis are presented, and a brief survey of the literature on the influence of errors on acoustic measurements in impedance tubes is provided. Next, the sources of experimental uncertainty are discussed, and the methodology for performing the uncertainty analysis using a Monte Carlo simulation is described. Finally, the results of the Monte Carlo simulation for several representative acoustic measurements are presented.

A.1 Background

A.1.1 Definitions

This uncertainty analysis is performed using the framework outlined by Coleman and Steele [156]. A brief overview of the essential terminology based on Ref. [156] is given here. Measurements are subject to *systematic* or *bias error*, β, which is the fixed component of the error that remains constant between measurements, and *random error*, ε, which is the random component of the error that varies between measurements. The value of a measured variable X is given by

$$X = X_{\text{true}} + \beta_X + \varepsilon_X \tag{A.1}$$

where X_{true} is the true value of the variable. All experiments are subject to systematic and random errors, so the true value of a variable can never be measured with absolute certainty. Instead, the uncertainty, U_X, is defined based on the level of confidence that the true value

of X falls within the interval

$$\overline{X} - U_X \leq X_{\text{true}} \leq \overline{X} + U_X \tag{A.2}$$

where $\overline{X}$ is the sample mean. In this work, U_X is defined such that the true value of X would fall within $\overline{X} \pm U_X$ approximately 95 times out of 100, so Eq. (A.2) defines the *95% confidence interval*.

The purpose of any uncertainty analysis is to propagate the uncertainties in the experimental measurements through the data reduction equations in order to estimate the uncertainty in the final results. First, the uncertainty in the measured variables must be defined. Recall that each measured variable is subject to bias errors and random errors. It is assumed that the random errors of the measured variable X are drawn from a Gaussian parent distribution, which has a *true mean*, μ_X, and *true standard deviation*, σ_X. For a normally-distributed random variable, 95% of the population lies within $\mu_X \pm 1.96\sigma_X$. Infinitely many samples are required to determine the true mean and true standard deviation of the Gaussian parent distribution with absolute certainty, but the number of experimental measurements is finite, so the *sample mean*, $\overline{X}$, and *sample standard deviation*, $S_{X,R}$, are calculated from this finite number of samples. Coleman and Steele [156] showed that the approximate 95% confidence estimate of the random uncertainty of the variable X is given by $U_{X,R} = 2S_{X,R}$ if the number of samples is greater than ten. Therefore, the random uncertainty of the measured variable X is estimated directly from the sample standard deviation of a sufficiently large number of measurements of X.

The bias error remains constant between measurements, so it cannot be estimated directly from multiple measurements of X because the same constant error is present in every measurement. Instead, the bias uncertainty is obtained from the manufacturer's specifications or calibration uncertainty. According to the example given by Coleman and Steele [156], a manufacturer may specify that a thermocouple is accurate to within ± 1.0°C. Cole-

man and Steele [156] assumed that the bias error is drawn from a Gaussian parent distribution of possible bias errors, and the manufacturer's specification describes the 95% confidence estimate of the bias uncertainty. For this example, the 95% confidence estimate of the bias uncertainty is $U_{X,B} = 1.0°\text{C}$. The sample standard deviation of the assumed distribution is then $S_{X,B} = U_{X,B}/2$, so $S_{X,B} = 0.5°\text{C}$ for this example.

The combined 95% confidence estimate of the random and bias uncertainties of the measured variable X is given by [156]

$$U_X = \kappa S_X \tag{A.3}$$

where the coverage factor, κ, is approximated by $\kappa \approx 2$ if the number of samples is greater than ten, and S_X is the combined sample standard deviation defined by $S_X^2 = S_{X,B}^2 + S_{X,R}^2$. This uncertainty, U_X, defines the 95% confidence interval in Eq. (A.2).

A.1.2 Literature Survey

A number of authors have studied the influence of experimental errors on the acoustic measurements in an impedance tube, and some of the applicable studies are summarized here. Bodén and Åbom [157] studied the influence of errors on the two-microphone method, and Åbom and Bodén [158] extended the error analysis to the two-microphone method with flow. One of their main results was to define the range of separation distances between the microphones for which the two-microphone method is accurate. Schultz, et al. [159] analyzed the uncertainty in the two-microphone method using both a linear small-perturbation technique and a Monte Carlo method. They showed that realistic experimental uncertainties produce nonlinear perturbations in the two-microphone method. The small-perturbation technique fails to predict these nonlinear perturbations, so they recommended that the Monte Carlo method should be used to perform the uncertainty analysis. The acoustic measurement methodology for higher-order modes is considerably more complex

than the two-microphone method, so the experimental uncertainties are expected to produce nonlinear perturbations in the results. Sack, et al. [115] applied the Monte Carlo method to estimate the uncertainty in the acoustic measurements of higher-order modes. However, they only considered uncertainties in the transfer functions and in the temperature and velocity measurements for an open duct, but they neglected uncertainties in the sensor positions, the magnitude and phase mismatches between the sensors, and the precision of the static transducers. In this work, the sources of experimental uncertainty are discussed in detail, and the Monte Carlo method is applied to estimate the uncertainty in the acoustic measurement methodology for an open duct and several representative injector configurations at different conditions.

A.2 Methodology

A.2.1 Experimental Uncertainties

First, the sources of uncertainty in the experiments must be considered before the uncertainties can be propagated through the acoustic measurement methodology. Table A.1 lists the sources and values of the experimental uncertainties that are considered in this uncertainty analysis. The bias uncertainties for each component are specified by the machine shop or the manufacturer. The random temporal variations in the temperature and pressure in the impedance tube are measured directly during the experiment, so the values of these random uncertainties are calculated directly from the sample standard deviation of the measurements. The magnitude and phase mismatches between the PCB 378A14 microphones are corrected using a sensor-switching technique, which is performed using the two-microphone method in the 28.5-mm diameter impedance tube. The uncertainty in the sensor-switching technique is quantified by performing the procedure multiple times. The magnitude and phase mismatches between the PCB 113B28 pressure transducers are quantified using the sensor-switching technique, but the corrections are not applied to the pressure transducers because their magnitude and phase responses also depend on the recessed

water-cooled adapters.

Table A.1: Summary of the experimental bias and random uncertainties.

Element	Error source	Value
Microphones	Axial position	$\pm$ 0.002 in
	Azimuthal position	$\pm$ 1 deg
Temperature	Thermocouple bias error	$\pm$ 2.2°C or 0.75% meas.
	NI-9211 bias error	$\pm$ 2.11°C
	Random temporal variations	Measured during experiment
Pressure	Ambient sensor bias error	$\pm$ 0.01% FS (FS = 1200 psia)
	Ambient temporal variations	Measured during experiment
	Initium bias error	$\pm$ 0.05% FS (FS = 1 psig)
	Scanner bias error	$\pm$ 0.03% FS (FS = 1 psig)
	Random temporal variations	Measured during experiment
Transfer functions	Calibrator bias error	$\pm$ 0.2 dB
	Magnitude mismatch	Measured by sensor-switching
	Phase mismatch	Measured by sensor-switching
	Noise	See Eqs. (A.4)–(A.8)

There exist other experimental uncertainties that are not listed in Table A.1 because they are at least an order of magnitude lower than the listed uncertainties for each element. These negligible sources of uncertainty include analog-to-digital conversion in each of the input DAQs, digital noise in the NI-9234 microphone input modules, offset and gain errors in the NI-9211 temperature input modules, and the line pressure error in the pressure tubing. The calibrator stability is not included because any magnitude errors between the microphones are corrected using the sensor-switching technique.

Additionally, there are several sources of uncertainty that are not included in this uncertainty analysis because they are not easy to quantify, so it is possible that these uncertainties are non-negligible. Temperature gradients inside the impedance tube introduce uncertainty in the measured resonance frequency and other acoustic properties, but the gradients cannot be accurately measured using the existing instrumentation in HOTMESS. Similarly, Peerlings [152] showed that the sound sources induce vibrations in their mounting structures, which can propagate along the impedance tube to the microphone section if the sections

are rigidly connected. These structural vibrations cause the microphones to vibrate at the source excitation frequencies, so the measured response of each microphone is the sum of the acoustic and mechanical oscillations. Therefore, structural vibrations introduce additional uncertainties into the acoustic measurements, but the error is difficult to quantify. Finally, the recessed water-cooled adapters affect the magnitude and phase measurements of the PCB 113B28 pressure transducers, but the random uncertainties in the magnitude and phase due to the installation effects of the different water-cooled adapters cannot be easily measured using the existing experimental facilities.

A.2.2 Multivariate Uncertainty Analysis of the Transfer Functions

The random noise in the microphone signals introduces another source of uncertainty into the transfer function measurements between the microphones in addition to the magnitude and phase mismatches. In general, the real and imaginary components of the uncertainty in the complex-valued transfer functions may be correlated. Schultz, et al. [160] applied a multivariate uncertainty analysis to estimate the uncertainty in the transfer functions if both the input and output signals are corrupted by uncorrelated noise. They denoted the measured input signal by x, the measured output signal by y, and the uncorrelated input and output noise signals by m and n, respectively. Therefore, G_{xx} and G_{yy} are the auto-spectral densities of the measured input and output signals, respectively, G_{xy} is the cross-spectral density between the measured input and output signals, and G_{mm} and G_{nn} are the auto-spectral densities of the input and output noise signals, respectively. In this work, the input signal is the reference microphone measurement, and the output signals are the measurements at the other microphones. The auto-spectral densities of the noise signals are obtained by measuring the microphone signals in the impedance tube with no sound source excitation.

Schultz, et al. [160] gave the expression for the covariance matrix of the spectral com-

ponents of the input and output signals as

$$\mathbf{\Sigma}(G_{xx}, G_{yy}, C_{xy}, Q_{xy}) = \frac{1}{N}\begin{bmatrix} G_{mm}(2G_{xx} - G_{mm}) & 0 & G_{mm}C_{xy} & G_{mm}Q_{xy} \\ 0 & G_{nn}(2G_{yy} - G_{nn}) & G_{nn}C_{xy} & G_{nn}Q_{xy} \\ G_{mm}C_{xy} & G_{nn}C_{xy} & \psi/2 & 0 \\ G_{mm}Q_{xy} & G_{nn}Q_{xy} & 0 & \psi/2 \end{bmatrix} \tag{A.4}$$

where $G_{xy} = C_{xy} + jQ_{xy}$, $\psi = G_{nn}G_{xx} + G_{mm}G_{yy} - G_{mm}G_{nn}$, and N is the number of averages used to compute the power spectral densities from the measured signals. The transfer function between a pair of microphones is given by Eq. (3.26) and is repeated here:

$$H_{xy} = \frac{G_{xy}}{G_{xx}} \tag{A.5}$$

Alternatively, the real and imaginary components of the transfer function can be expressed as

$$\begin{bmatrix} H_R \\ H_I \end{bmatrix} = \begin{bmatrix} \Re(H_{xy}) \\ \Im(H_{xy}) \end{bmatrix} = \begin{bmatrix} \frac{C_{xy}}{G_{xx}} \\ \frac{Q_{xy}}{G_{xx}} \end{bmatrix} \tag{A.6}$$

The Jacobian matrix for the transfer function is then given by [160]

$$\mathbf{J}_H = \begin{bmatrix} \frac{\partial H_R}{\partial G_{xx}} & \frac{\partial H_R}{\partial G_{yy}} & \frac{\partial H_R}{\partial C_{xy}} & \frac{\partial H_R}{\partial Q_{xy}} \\ \frac{\partial H_I}{\partial G_{xx}} & \frac{\partial H_I}{\partial G_{yy}} & \frac{\partial H_I}{\partial C_{xy}} & \frac{\partial H_I}{\partial Q_{xy}} \end{bmatrix} = \begin{bmatrix} -\frac{C_{xy}}{G_{xx}^2} & 0 & \frac{1}{G_{xx}} & 0 \\ -\frac{Q_{xy}}{G_{xx}^2} & 0 & 0 & \frac{1}{G_{xx}} \end{bmatrix} \tag{A.7}$$

Finally, the covariance matrix of the real and imaginary components of the transfer function is given by [160]

$$\mathbf{\Sigma}(H_R, H_I) = \mathbf{J}_H \mathbf{\Sigma}(G_{xx}, G_{yy}, C_{xy}, Q_{xy}) \mathbf{J}_H^{-1} \tag{A.8}$$

The complex quantities are propagated through the multivariate uncertainty analysis in rectangular form instead of polar form because the magnitude and phase axes are constrained

to finite ranges, whereas the real and imaginary axes have infinite extent [160].

In general, the 95% confidence region of two correlated variables forms an ellipse in the two-dimensional space defined by the variables. If the off-diagonal elements of the covariance matrix are nonzero, then the major and minor axes of the ellipse are not aligned with the coordinate axes. The 95% confidence estimate of the uncertainty of each variable is given by Eq. (A.3), where the sample standard deviation of each variable is equal to the square root of the diagonal element of the covariance matrix corresponding to that variable. However, the coverage factor, κ, is not equal to two for multiple variables; instead, the coverage factor can be calculated using the expressions given by Schultz, et al. [160], for example.

A.2.3 Monte Carlo Method

The experimental uncertainties are propagated through the acoustic measurement methodology using a Monte Carlo method. The Monte Carlo method is advantageous because it is conceptually straightforward, it does not require the propagation of partial derivatives through least-squares solutions to matrix equations, and it is not subject to the linear assumptions of a small-perturbation uncertainty analysis based on Taylor series approximations [156, 159]. However, the Monte Carlo method is computationally expensive because it requires a large number of iterations for the statistical properties of the output variables to converge. For example, Schultz, et al. [159] used 25 000 samples to compute the 95% confidence intervals for the two-microphone method, and Sack, et al. [115] found that the uncertainty estimates for higher-order modes converged after 200 000 to 400 000 samples. In this work, 100 000 iterations were found to produce sufficiently good convergence of the uncertainty estimates of the acoustic properties.

Figure A.1 shows a flowchart of the Monte Carlo method. The flowchart is adapted from similar flowcharts presented by Coleman and Steele [156] and Schultz, et al. [159]. The inputs to the Monte Carlo method are the measured values of the input variables, the

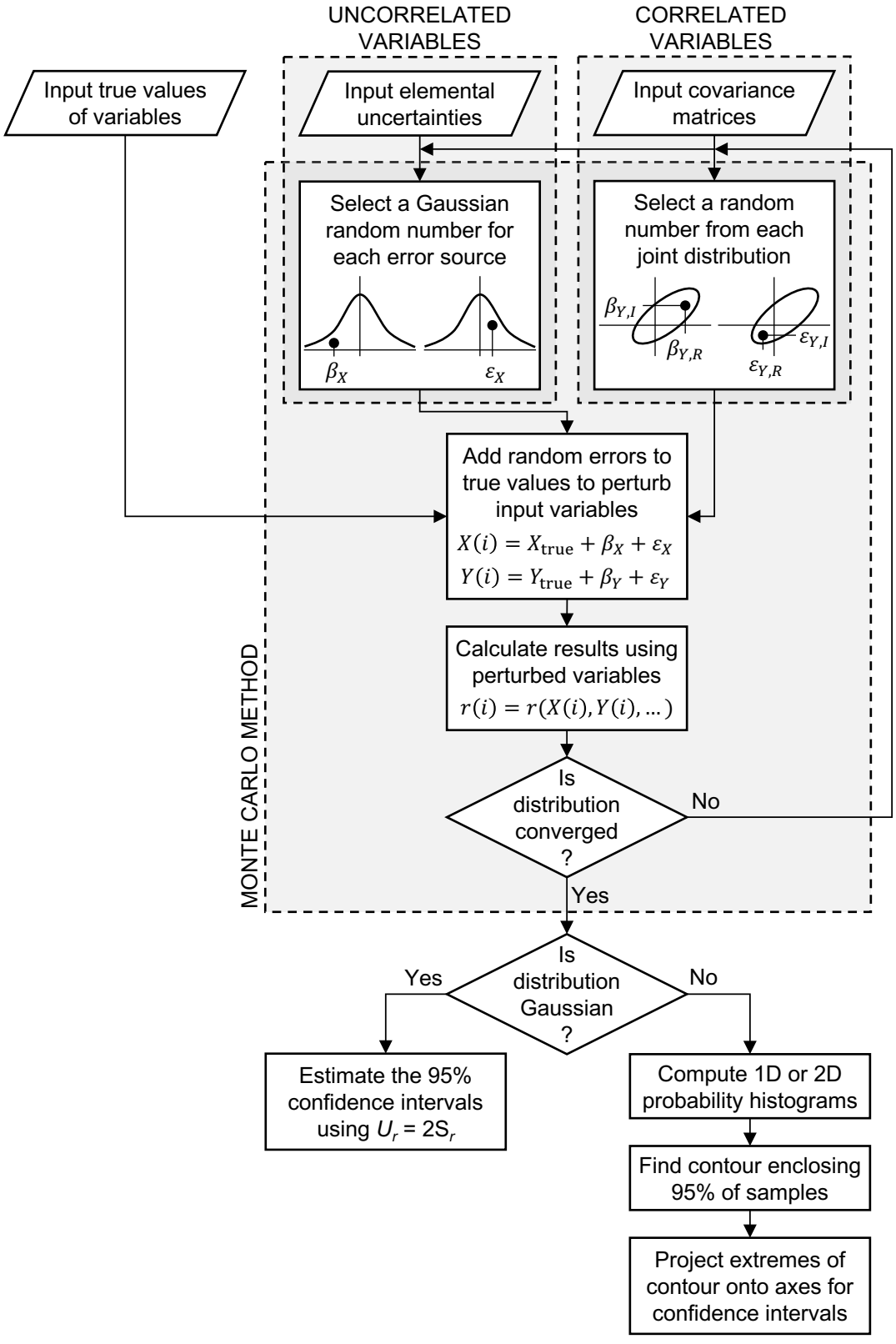

Figure A.1: Flowchart of the Monte Carlo method (adapted from Refs. [156] and [159]).

elemental uncertainties for each error source, and the covariance matrices of the correlated variables. For example, consider two measured variables, X and Y, where X is an uncorrelated variable (such as the temperature), and $Y = Y_R + jY_I$ is a complex variable (such as the transfer function between microphones) with correlated real and imaginary parts. For the Monte Carlo method, the measured values of the variables are assumed to be the their true values, X_{true} and Y_{true}. The elemental bias and random uncertainties for X are given by $U_{X,B}$ and $U_{X,R}$, respectively, and the covariance matrix between the real and imaginary parts of Y is $\mathbf{\Sigma}(Y_R, Y_I)$.

The bias and random uncertainties of each uncorrelated variable are assumed to have Gaussian distributions, so a normally-distributed random number is generated for each elemental error source. For example, the bias error for X, β_X, is randomly selected from a Gaussian distribution with standard deviation $S_{X,B} = U_{X,B}/2$, and the random error for X, ε_X, is randomly selected from a Gaussian distribution with standard deviation $S_{X,R} = U_{X,R}/2$. The error for each pair of correlated variables is randomly selected from their joint distribution, which is specified by their covariance matrix. For example, the real and imaginary errors for Y are selected from the joint distribution specified by the covariance matrix $\mathbf{\Sigma}(Y_R, Y_I)$. The randomly generated errors are then added to the measured values—or true values—of the input variables to perturb the input variables. For example, the perturbed value of X for iteration i of the Monte Carlo simulation is given by $X(i) = X_{\text{true}} + \beta_X + \varepsilon_X$. If a single error source affects multiple input variables, then the same randomly generated error is added to each of the input variables. For example, the bias error of an input DAQ applies a constant offset to each of the channels passing into the DAQ, so the same randomly generated number for the bias error of the DAQ is added to each of the input channels.

The perturbed input variables are then passed into the data reduction equations, and the results are saved. For example, if the data reduction procedure is described by the single equation $r = r(X, Y)$, then the perturbed output variable for iteration i of the Monte

Carlo simulation is given by $r(i) = r(X(i), Y(i))$. In reality, the acoustic measurement methodology is significantly more involved than a single equation of two variables, but the data reduction equations can be treated as a black box in the Monte Carlo method: the perturbed input variables are passed into the black box, and the perturbed output variables come out of the black box. This entire process is repeated for a large number of iterations until the statistical properties of the output variables converge. If an output variable has a normal distribution, then its 95% confidence interval is estimated using Eq. (A.3). If the output variable does not have a normal distribution, however, its 95% confidence interval cannot be computed from its standard deviation; instead, the confidence interval must be computed numerically. The procedures for estimating the 95% confidence intervals of the output variables are described in the following section.

A.2.4 Confidence Intervals

In this section, selected results for both uncorrelated and correlated output variables with Gaussian and non-Gaussian distributions are presented to demonstrate the methods for computing the 95% confidence intervals.

Gaussian Distribution

Figure A.2 shows the distribution of the power dissipation coefficient of the (0,0) mode in the open duct at 2500 Hz measured using the microphones. The distribution was calculated from 100 000 iterations of the Monte Carlo method and is plotted as a histogram. The resulting distribution is approximately Gaussian, so the sample mean and sample standard deviation are computed directly from the values of the samples, and the 95% confidence interval is estimated using Eq. (A.3). The black circular marker in Figure A.2 indicates the true measured value of the dissipation coefficient, and the arrows and dashed lines indicate the 95% confidence interval around the true value.

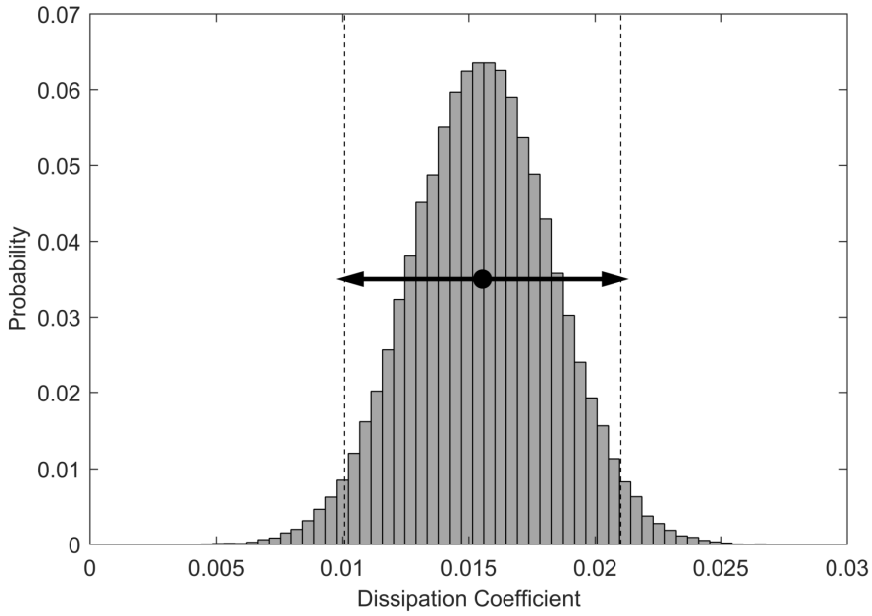

Figure A.2: True value and 95% confidence interval for the dissipation coefficient of the (0,0) mode in the open duct at 2500 Hz measured using the microphones.

Non-Gaussian Joint Distribution

Figure A.3 shows the distribution of the complex pressure transmission coefficient of the (0,0) mode in the open duct at 1000 Hz measured using the microphones. The distribution was calculated from 100 000 iterations of the Monte Carlo method and is plotted as a smoothed two-dimensional histogram on the real and imaginary axes. The resulting distribution is not Gaussian, because a joint-normal distribution in two-dimensional space would be elliptical. Therefore, the distribution cannot be represented by the sample mean and sample covariance matrix, so the uncertainty cannot be calculated using Eq. (A.3). Instead, the 95% confidence interval is estimated using the numerical method described by Schultz, et al. [159]. First, outliers that are more than 2.5 times the interquartile range below the first quartile or above the third quartile in both the real and imaginary axes are removed. The two-dimensional histogram of the probability is then computed. The value of each bar in the histogram is equal to the number of samples that fall within a particular bin in real and imaginary space divided by the total number of samples from the Monte Carlo method. Next, the contours of constant probability are computed, and the contour

that contains 95% of the samples is found by interpolation. Finally, the extreme values of the contour are projected onto the real and imaginary axes to find the 95% confidence intervals in real and imaginary space. The white circular marker shown in Figure A.3 is the true measured value of the pressure transmission coefficient, and the color scale represents the probability. The thick black curve is the contour of constant probability that contains 95% of the samples, and the arrows and dashed lines indicate the 95% confidence intervals projected onto the real and imaginary axes. Alternatively, the extreme values of the contour could be projected onto the magnitude and phase axes.

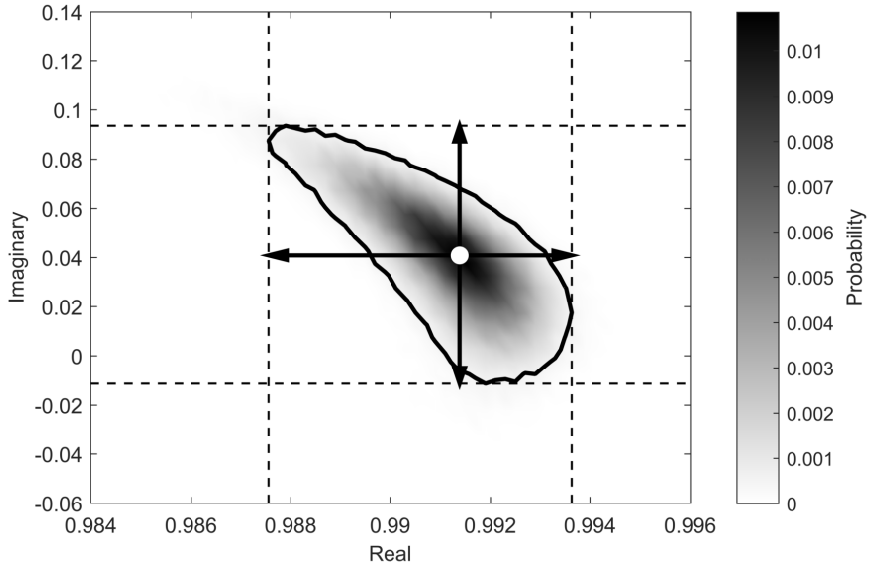

Figure A.3: True value and 95% confidence region for the complex pressure transmission coefficient of the (0,0) mode in the open duct at 1000 Hz measured using the microphones.

Figure A.4 shows the distribution of the complex pressure transmission coefficient of the (1,0) mode in the open duct at 2500 Hz measured using the microphones. The distribution forms a boomerang shape, which was also observed by Schultz, et al. [159] for the uncertainty of the resistance and reactance calculated using the two-microphone method. This distribution is definitely not Gaussian, so the contour of constant probability enclosing 95% of the samples is computed using the same procedure as above, and the extreme values of the contour are projected onto the real and imaginary axes. The boomerang shape is due to the nonlinear propagation of errors through the acoustic measurement methodology for

higher-order modes. These nonlinearities could not be modeled using the classical small-perturbation techniques based on Taylor series expansions, which demonstrates that the Monte Carlo method is required to accurately propagate uncertainties through the acoustic measurement methodology. Interestingly, the sample mean computed from the results of the Monte Carlo simulation falls outside the 95% confidence interval due to the irregular shape of the distribution. Note that the white circular marker shown in Figure A.3 is the true measured value of the pressure transmission coefficient, not the sample mean.

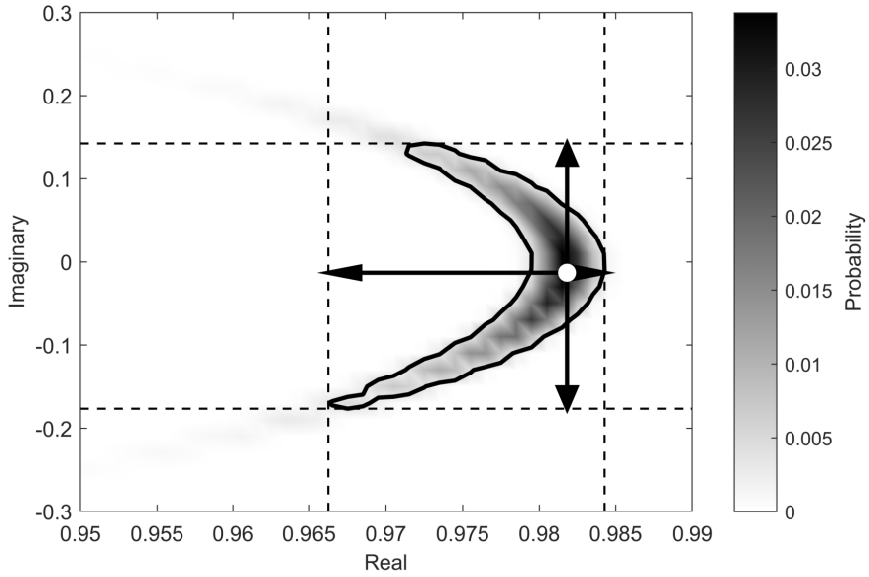

Figure A.4: True value and 95% confidence region for the complex pressure transmission coefficient of the (1,0) mode in the open duct at 2500 Hz measured using the microphones.

A.3 Applications of the Uncertainty Analysis

A.3.1 Open Duct: Microphones Versus Pressure Transducers

First, an uncertainty analysis was performed on the experimental measurements of an open duct to compare the performance of the PCB 378A14 microphones to the PCB 113B28 pressure transducers. No test section was installed in HOTMESS for these measurements; instead, the two sides of the impedance tube were joined together to form a continuous 101.6-mm (4-in) diameter duct between the microphone sections. Sack, et al. [115] also

performed an uncertainty analysis for an empty duct because its sound power coefficients are known theoretically. The power reflection coefficient from the open duct is theoretically zero, but in practice, some fraction of the sound power is dissipated by thermoviscous losses in the acoustic boundary layer at the walls of the duct. However, the acoustic measurements were processed using the Weng-Bake wavenumber model [121] given by Eq. (3.19), which accounts for the thermoviscous losses in the acoustic boundary layer at the walls of the duct. Therefore, the measured power transmission coefficient of the open duct is theoretically one, and the power dissipation coefficient is theoretically zero. Any deviation from these values is indicative of errors in the experiments or wavenumber model.

Figure A.5 shows a comparison between the measurements of the power transmission coefficient of the (0,0) mode in the open duct using the microphones and the pressure transducers. Both sets of measurements demonstrate that the power transmission coefficient of the open duct lies within a few percent of the theoretical value of one. However, the pressure transducer measurements are significantly "noisier" than the microphone measurements. One reason for this is that the magnitude and phase mismatches between the microphones are corrected using the sensor-switching technique, but the magnitude and phase mismatches between the pressure transducers are not corrected. Additionally, the nominal sensitivity of the microphones is significantly greater than the nominal sensitivity of the pressure transducers, so the microphones have a significantly lower noise floor—and thus a higher signal-to-noise ratio—than the pressure transducers. Regardless, the pressure transducer measurements do not deviate from the microphone measurements by more than approximately 2% except at a few discrete frequencies, so the pressure transducers are judged to provide acceptable measurements of the acoustic properties, albeit with some additional "noise."

The Monte Carlo method described in Section A.2 was applied to the experimental measurements of the open duct to compare the uncertainties in the measurements using the microphones and the pressure transducers. The experimental measurements were pro-

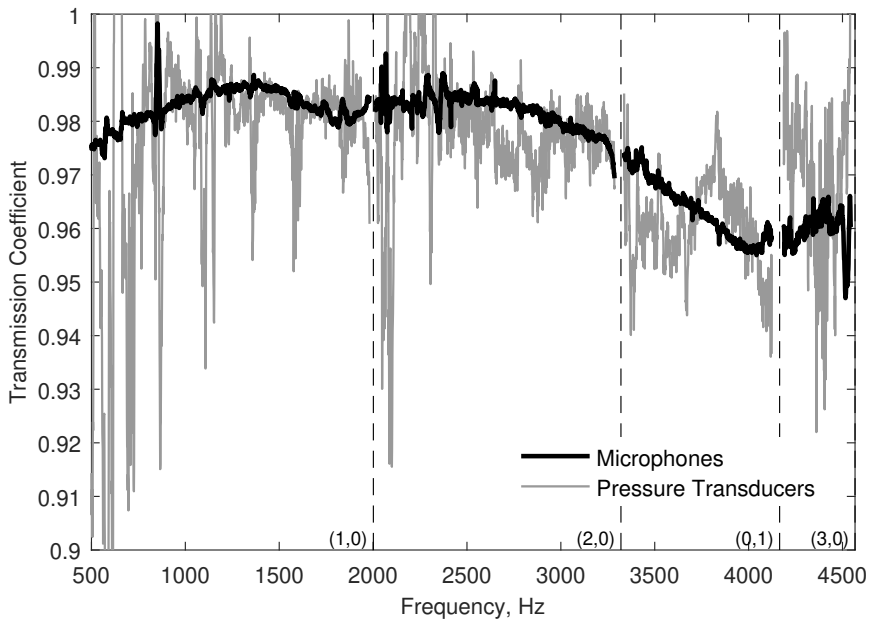

Figure A.5: Comparison of the power transmission coefficients of the (0,0) mode in the open duct measured using the microphones and pressure transducers.

cessed with a frequency bandwidth of 1 Hz, but the Monte Carlo method was only performed at discrete frequencies ranging from 1000 Hz to 4500 Hz in steps of 100 Hz due to the high computational cost of the simulation. Figure A.6 shows the calculated 95% confidence interval around the mean dissipation coefficient of the (0,0) mode in the open duct measured using the microphones. The experimental measurement, which has a frequency bandwidth of 1 Hz, is also plotted. The 95% confidence interval is greatest near the cut-on frequencies of the higher-order modes, but the modal decomposition method is known to be inaccurate near these frequencies [110]. Away from the cut-on frequencies of the higher-order modes, the 95% confidence interval is relatively small, but the uncertainty grows as the number of propagating modes increases. Sack, et al. [115] attributed this growth to decreasing overdetermination in the number of sound sources and microphones.

Figure A.7 shows the calculated 95% confidence interval around the mean dissipation coefficient of the (0,0) mode in the open duct measured using the pressure transducers. The experimental measurement, which has a frequency bandwidth of 1 Hz, is also plotted. The uncertainty in the pressure transducer measurements is greater than the uncertainty in the

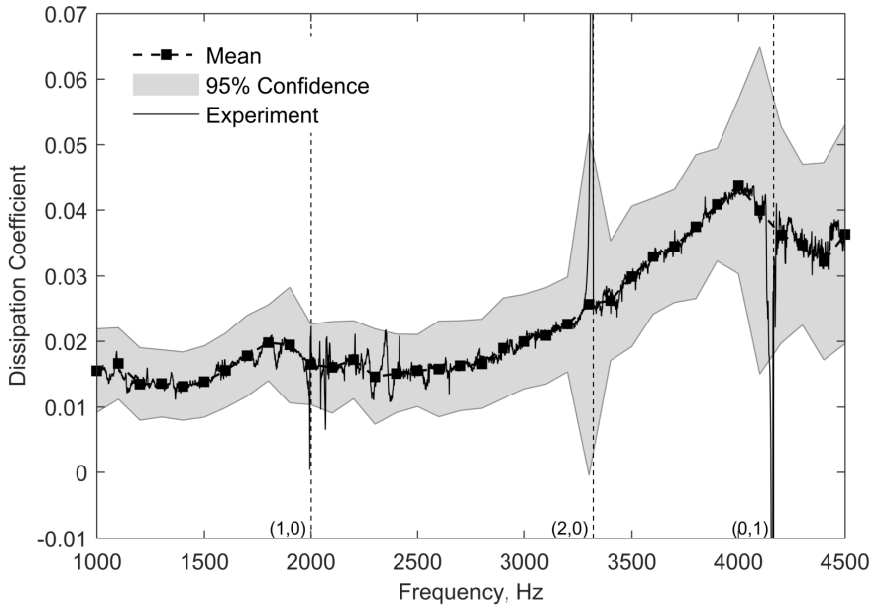

Figure A.6: Estimate of the 95% confidence interval for the dissipation coefficient of the (0,0) mode in the open duct measured using the microphones.

microphone measurements (note that the scale of the y-axis differs between Figures A.6 and A.7) because the magnitude and phase mismatches between the pressure transducers are not corrected, and the pressure transducers have a lower nominal sensitivity—and thus a lower signal-to-noise ratio—than the microphones. The 95% confidence interval for the dissipation coefficient measured by the pressure transducers spikes at certain frequencies due to the magnitude and phase mismatches between the transducers because these mismatches are functions of frequency. Because the pressure transducers introduce greater uncertainty into the measurements than the microphones, the pressure transducers are only used to conduct high-temperature measurements, and the microphones are used for all other measurements. However, the uncertainty in the pressure transducer measurements is low enough to provide quality acoustic measurements.

A.3.2 Uncertainty Analysis of a Straight Injector

The Monte Carlo method was also applied to the experimental measurements of the "straight" injector in quiescent air at ambient conditions in the linear acoustic regime for the plane

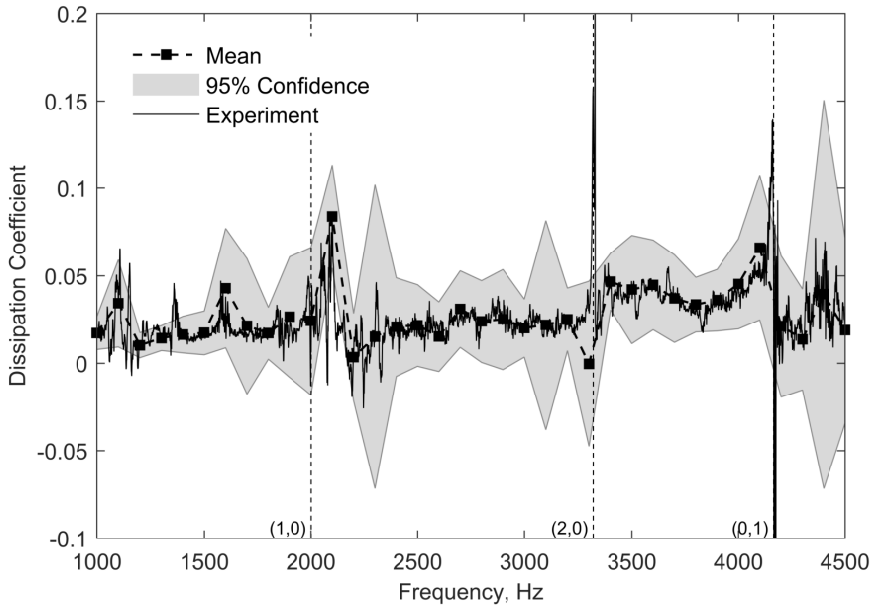

Figure A.7: Estimate of the 95% confidence interval for the dissipation coefficient of the (0,0) mode in the open duct measured using the pressure transducers.

wave mode. These measurements were conducted using the microphones. This configuration represents a baseline case for the acoustic measurements of the propellant injectors. Figure A.8 shows the calculated 95% confidence interval around the mean absorption coefficient of the "straight" injector. The experimental result, which has a frequency bandwidth of 1 Hz, is also plotted. The Monte Carlo method was performed at discrete frequencies in the neighborhood of the fundamental resonance frequency of the "straight" injector. Within ± 5 Hz of the resonance frequency, the Monte Carlo method was performed at frequency steps of 1 Hz, but the frequency density decreased further away from the resonance frequency. The 95% confidence interval for the mean absorption coefficient of the "straight" injector is so small that it is difficult to see at most frequencies shown in Figure A.8, so the 95% confidence interval at the peak absorption coefficient is shown in greater detail for frequencies between 1660 Hz and 1670 Hz. The uncertainty near the peak absorption coefficient is exceedingly small, which provides high confidence in the accuracy of the experimental results.

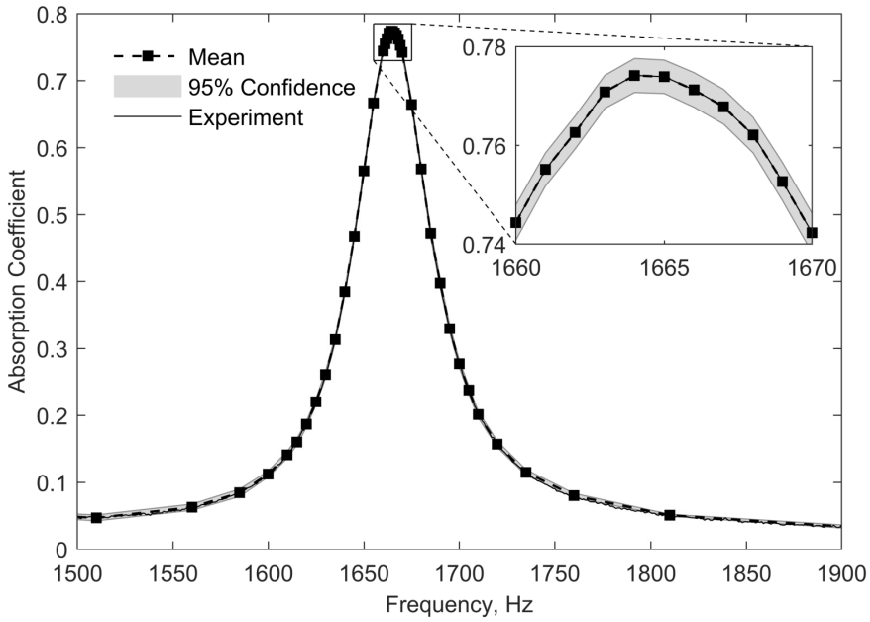

Figure A.8: Estimate of the 95% confidence interval for the plane-wave absorption coefficient of the "straight" injector in quiescent air measured using the microphones.

A.3.3 Uncertainty Analysis in Heated Flow

In this final illustrative example, the Monte Carlo method was applied to the experimental measurements of three half-wave resonators in the linear acoustic regime at a temperature of 500°F (260°C) with a Mach 0.2 mean flow through the resonators. These measurements were conducted using the pressure transducers. This configuration was selected as an illustrative example because it is expected to have the highest uncertainty of any of the acoustic measurements in the plane wave regime. Figure A.9 shows the calculated 95% confidence interval around the mean absorption coefficient of the three half-wave resonators. The experimental result, which has a frequency bandwidth of 1 Hz, is also plotted. Within $\pm$50 Hz of the resonance frequency, the Monte Carlo method was performed at frequency steps of 10 Hz, but the frequency density decreased further away from the resonance frequency. The 95% confidence interval for the absorption coefficient is significantly greater for heated-flow conditions using the pressure transducers than for the baseline configuration shown in Figure A.8. The uncertainty is greatest at frequencies further away from the

peak absorption frequency, so it appears that the uncertainty increases as the absorption coefficient decreases. The 95% confidence interval at the peak absorption coefficient is also shown in greater detail for frequencies between 1720 Hz and 1820 Hz. Although the uncertainty near the peak absorption coefficient is greater for heated flow conditions using the pressure transducers than for quiescent conditions using the microphones, the uncertainty is still relatively small, which provides confidence in the accuracy of the experimental results measured using the pressure transducers near the resonance frequencies of the resonators.

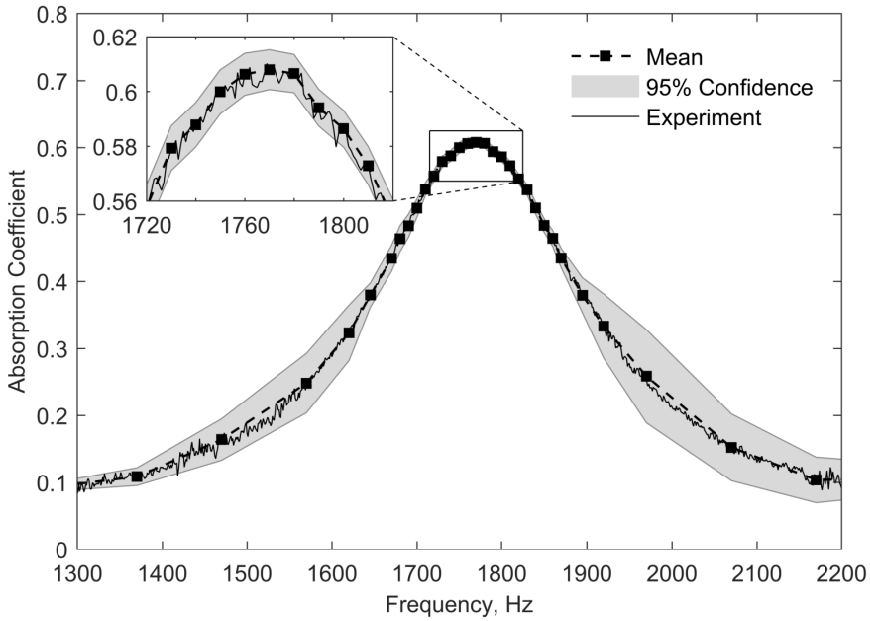

Figure A.9: Estimate of the 95% confidence interval for the plane-wave absorption coefficient of three half-wave resonators at 500°F with a Mach 0.2 mean flow through the resonators measured using the pressure transducers.

APPENDIX B

EVALUATION OF THE WAVENUMBER MODELS

B.1 Dissipative Versus Non-Dissipative Wavenumbers

In this appendix, the wavenumber models presented in Section 3.4 are compared to one another using the acoustic measurements of an open duct. The wavenumber models used in this work are the non-dissipative wavenumber given by Eq. (3.12), the Kirchhoff wavenumber given by Eq. (3.15), and the Weng-Bake wavenumber given by Eq. (3.19). The wavenumber comparison is performed using the open duct because its sound power coefficients are known theoretically. The power reflection coefficient from the open duct section is theoretically zero, but in practice, some fraction of the sound power is dissipated by thermoviscous losses in the acoustic boundary layer at the walls of the duct. The non-dissipative wavenumber does not account for these thermoviscous losses, so it is expected that the dissipation coefficient will be nonzero and the power transmission coefficient will be less than one if the acoustic measurements are post-processed using the non-dissipative wavenumber. The Kirchhoff wavenumber accounts for the thermoviscous losses in the acoustic boundary layer for the plane wave mode, and the Weng-Bake wavenumber extends the Kirchhoff model to higher-order modes. If these wavenumber models accurately account for the dissipation, then the dissipation coefficient should be zero and the power transmission coefficient should be one if the acoustic measurements are post-processed using these wavenumbers. Any deviation from these theoretical values indicates that there are additional sources of dissipation in HOTMESS which are not modeled by these wavenumbers, and it quantifies the dissipation error made throughout the measurements.

Figure B.1 shows the power transmission coefficients of the (0,0), (1,0), (2,0) and (0,1) incident modes in both directions between sides A and B of the two-sided impedance tube

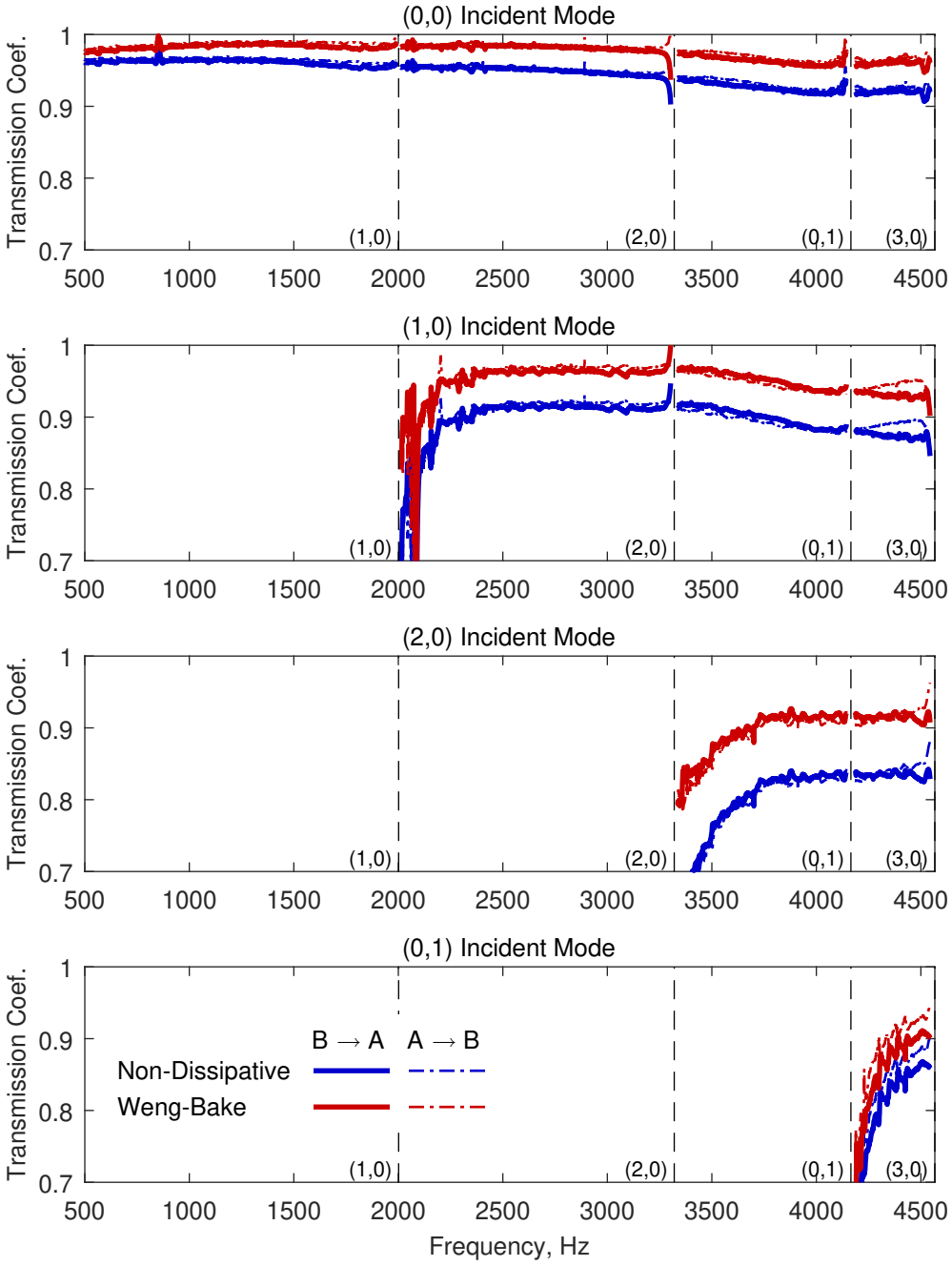

Figure B.1: Comparison of the power transmission coefficients of the (0,0), (1,0), (2,0) and (0,1) modes in the open duct using different wavenumber models.

calculated using the non-dissipative and Weng-Bake wavenumbers. The plotted curves are from the same experimental measurement that was post-processed using the different wavenumber models. Note that the Weng-Bake wavenumber reduces to the Kirchhoff wavenumber for the plane wave mode [121], so the Kirchhoff wavenumber is not shown. As expected, the power transmission coefficients in both directions are nearly identical at most frequencies. The greatest differences between the two directions occur above the cut-on frequency of the (0,1) mode, but the uncertainty in the measurements increases as the number of propagating modes increases, as discussed in Appendix A. The measured power transmission coefficient of each higher-order mode is significantly less than one near its cut-on frequency, but the modal decomposition method is known to be inaccurate near cut-on [110]. The power transmission coefficient calculated using the non-dissipative wavenumber is less than one for all modes at all frequencies, but the Weng-Bake wavenumber, which accounts for the thermoviscous losses in the acoustic boundary layer for higher-order modes, shifts the power transmission coefficient considerably closer to the theoretical value of one. However, even the Weng-Bake wavenumber does not completely account for the acoustic losses. The deviation between the measured and theoretical values of the power transmission coefficient increases with the order of the incident mode, even at frequencies away from cut-on.

Sack, et al. [115] also performed a comparison between different wavenumber models based on measurements of an empty duct, but they used the wavenumber equation derived by Dokumaci [123] instead of the model proposed by Weng and Bake [121]. Dokumaci's equation must be solved iteratively using a root-finding algorithm, whereas Weng and Bake derived an analytical solution that closely matches Dokumaci's solution in a wide duct with a uniform mean flow. The measurements of the transmission coefficient presented in this work compare well with those of Sack, et al. [115]. Note that Sack, et al. plotted the magnitude of the pressure transmission coefficient, whereas Figure B.1 shows the power transmission coefficient, which is proportional to the square of the magnitude of the pres-

sure transmission coefficient based on Eqs. (3.41) and (3.42). The results of Sack, et al. and the current results suggest that there are additional dissipation mechanisms that are not included in the dissipative wavenumber models. These errors apply to all of the acoustic results presented in this work because the post-processing was performed using the Weng-Bake wavenumber model unless otherwise noted.

B.2 Accounting for the Excess Dissipation

One dissipation mechanism that is not modeled by the Weng-Bake wavenumber is the attenuation within the fluid itself. The losses within the fluid are typically neglected in duct acoustics because they are small compared to the attenuation at the walls of the duct [75], but Lahiri, et al. [41] showed that the attenuation due to vibrational relaxation within the fluid is significant at high temperatures. Even at lower temperatures, the attenuation within the fluid becomes relatively more important compared to the attenuation at the walls as the diameter of the duct increases. The attenuation in the bulk fluid of the 101.6-mm diameter impedance tube was calculated using the methodology presented by Lahiri, et al. [41] assuming a constant concentration of water vapor of $h = 0.15\%$, which is a reasonable estimate for the concentration of water vapor present in these experiments based on the mean ambient temperature and relative humidity in the experimental facility. Figure B.2 shows contours of the attenuation due to losses within the fluid relative to the attenuation in the acoustic boundary layer at the walls of the impedance tube for these conditions. The contours are plotted as functions of the frequency and temperature. The shaded region represents the temperature and frequency range in which the dissipation within the fluid is at least 10% as large as the dissipation in the acoustic boundary layer. The measurements in the open duct were conducted at a temperature of approximately 300 K, so the losses within the fluid are non-negligible compared to the losses at the walls of the impedance tube at most frequencies of interest. In addition, the relative importance of the attenuation within the fluid increases with frequency in the measured frequency range.

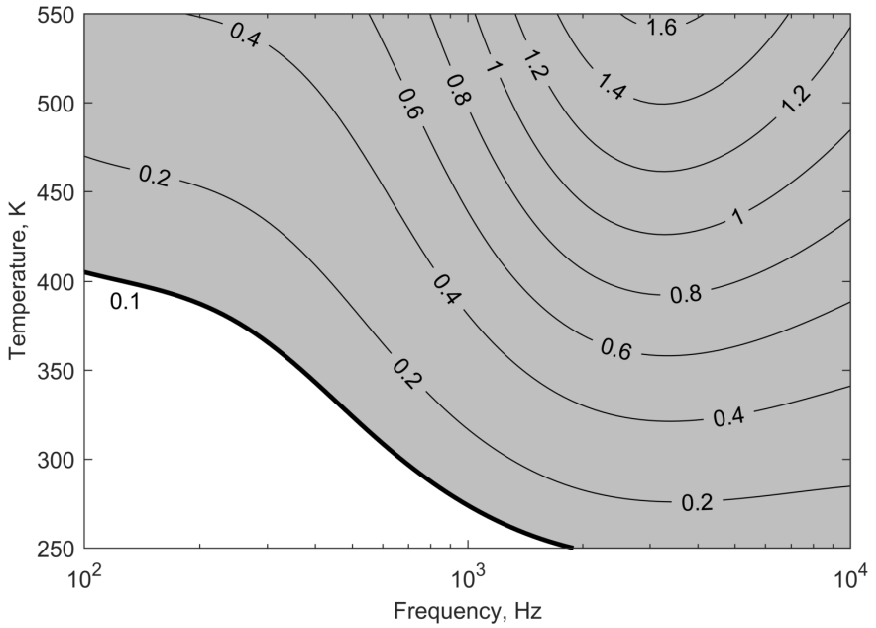

Figure B.2: Contours of the relative attenuation in the bulk fluid compared to the attenuation in the acoustic boundary layer for the 101.6-mm diameter impedance tube at a constant concentration of water vapor of $h = 0.15\%$.

The attenuation coefficient within the fluid itself was calculated using the equations given by Lahiri, et al. [41] and was added to the Kirchhoff attenuation coefficient given by Eq. (3.17) to form a new wavenumber model for the plane wave mode. Figure B.3 shows the dissipation coefficients of the (0,0) mode in both directions in the open duct calculated using the non-dissipative wavenumber, the Kirchhoff wavenumber, and the Kirchhoff wavenumber plus the attenuation within the fluid itself. The inclusion of the fluid losses may improve the accuracy of the results, particularly at higher frequencies, based on these calculations using an assumed concentration of water vapor. The relatively small magnitude of the dissipation coefficient compares reasonably well with others' experimental results, such as those of Heuwinkel, et al. [161]. However, even the calculated fluid losses do not completely account for the measured dissipation.

Peerlings [162] compared measurements from several different experimental facilities and found that the measured dissipation coefficient consistently exceeds the dissipation predicted by the Kirchhoff model. Furthermore, he showed that the losses within the fluid

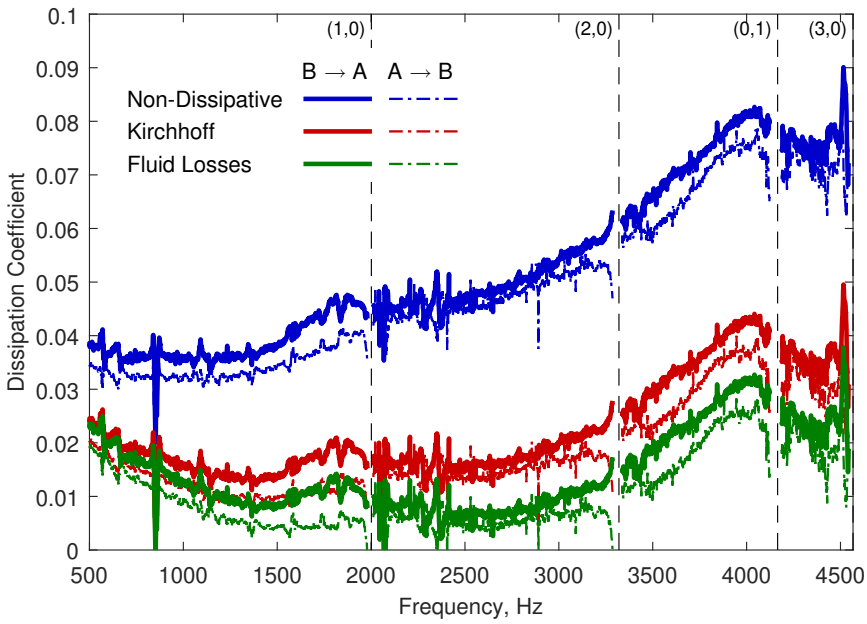

Figure B.3: Comparison of the dissipation coefficients of the (0,0) mode in the open duct using different wavenumber models.

cannot completely account for this excess dissipation. The current measurements shown in Figure B.3 support these findings. Numerous other investigators have measured excess dissipation that could not be explained by the Kirchhoff model, too, and Peerlings presented a review of the literature on these experimental measurements. Based on the results of these studies, Peerlings concluded that the excess dissipation is caused by imperfections in the walls of the impedance tube, namely, acoustic transmission through the walls and additional losses due to the surface roughness of the walls. These dissipation mechanisms likely account for the excess dissipation measured in the current experiments, too.

APPENDIX C

DEVELOPMENT OF A NUMERICAL MODEL FOR PLANE WAVES

In this appendix, the development of the numerical model for the acoustic damping of a propellant injector for the plane wave mode is presented. First, the transfer matrix formulations are related to one another so that the results derived by Munjal [148] may be employed. Next, the transfer matrices of a straight cylindrical duct and an area discontinuity with a side branch are derived. These building blocks are then combined into the numerical model for the transfer matrix of a propellant injector. Finally, the transfer matrix is rearranged into a scattering matrix, from which the reflection and transmission coefficients are obtained. Note that the numerical model described in this section does not include the effects of flow or combustion because a quiescent medium with constant properties is assumed.

C.1 Relationship Between Transfer Matrices

Munjal [148] defined the transfer matrix by the relation

$$\begin{bmatrix} \hat{p}(z_1) \\ \hat{u}(z_1) \end{bmatrix} = \mathbf{Tr}_{p,u} \begin{bmatrix} \hat{p}(z_0) \\ \hat{u}(z_0) \end{bmatrix} \tag{C.1}$$

where $\hat{p}(z)$ and $\hat{u}(z)$ are the acoustic pressure and particle velocity amplitudes, respectively, at the axial location z, and $\mathbf{Tr}_{p,u}$ is the 2×2 transfer matrix that relates the acoustic pressure and particle velocity between the arbitrary locations z_0 and z_1. Alternatively, a transfer matrix in terms of the amplitudes of the propagating acoustic waves can be defined by the

relation

$$\begin{bmatrix} \hat{a}^+(z_1) \\ \hat{a}^-(z_1) \end{bmatrix} = \mathbf{Tr} \begin{bmatrix} \hat{a}^+(z_0) \\ \hat{a}^-(z_0) \end{bmatrix} \tag{C.2}$$

where $\hat{a}^+(z)$ and $\hat{a}^-(z)$ are the amplitudes of the acoustic waves propagating in the positive and negative axial directions, respectively, at the axial location z, and $\mathbf{Tr}$ is the 2×2 transfer matrix that relates these amplitudes.

From Eq. (3.5), the acoustic pressure amplitude of the plane wave mode at a single frequency in the absence of flow is given by $\hat{p}(z) = \hat{a}^+e^{-jkz} + \hat{a}^-e^{jkz}$, and from Eq. (3.47), the particle velocity amplitude under the same assumptions is given by $\hat{u}(z) = \hat{b}^+e^{-jkz} - \hat{b}^-e^{jkz}$, where $\hat{b}^\pm = \hat{a}^\pm/(\rho c)$ based on Eq. (3.48). These relations can be written in matrix form as

$$\begin{bmatrix} \hat{p}(z) \\ \hat{u}(z) \end{bmatrix} = \begin{bmatrix} 1 & 1 \\ \frac{1}{\rho c} & -\frac{1}{\rho c} \end{bmatrix} \begin{bmatrix} \hat{a}^+(z) \\ \hat{a}^-(z) \end{bmatrix} \tag{C.3}$$

and the inverse is given by

$$\begin{bmatrix} \hat{a}^+(z) \\ \hat{a}^-(z) \end{bmatrix} = \begin{bmatrix} \frac{1}{2} & \frac{\rho c}{2} \\ \frac{1}{2} & -\frac{\rho c}{2} \end{bmatrix} \begin{bmatrix} \hat{p}(z) \\ \hat{u}(z) \end{bmatrix} \tag{C.4}$$

Therefore, the transfer matrix in terms of the pressure amplitudes of the propagating waves can be obtained from the transfer matrix in terms of the pressure and velocity by

$$\mathbf{Tr} = \begin{bmatrix} \frac{1}{2} & \frac{\rho c}{2} \\ \frac{1}{2} & -\frac{\rho c}{2} \end{bmatrix} \mathbf{Tr}_{p,u} \begin{bmatrix} 1 & 1 \\ \frac{1}{\rho c} & -\frac{1}{\rho c} \end{bmatrix} \tag{C.5}$$

and the reverse operation is given by

$$\mathbf{Tr}_{p,u} = \begin{bmatrix} 1 & 1 \\ \frac{1}{\rho c} & -\frac{1}{\rho c} \end{bmatrix} \mathbf{Tr} \begin{bmatrix} \frac{1}{2} & \frac{\rho c}{2} \\ \frac{1}{2} & -\frac{\rho c}{2} \end{bmatrix} \tag{C.6}$$

C.2 Transfer Matrix of a Straight Cylinder

For the plane wave mode at a single frequency in the absence of flow, the expression for the transfer matrix between points z_0 and z_1 in a straight cylinder is obtained directly from Eq. (3.5) as

$$\begin{bmatrix} \hat{a}^+(z_1) \\ \hat{a}^-(z_1) \end{bmatrix} = \begin{bmatrix} e^{-jk(z_1-z_0)} & 0 \\ 0 & e^{jk(z_1-z_0)} \end{bmatrix} \begin{bmatrix} \hat{a}^+(z_0) \\ \hat{a}^-(z_0) \end{bmatrix} \tag{C.7}$$

This transfer matrix is designated as $\mathbf{Tr}|_{z_0}^{z_1}$. The attenuation due to viscothermal losses within the acoustic boundary layer is incorporated into the transfer matrix using the complex Kirchhoff wavenumber given by Eq. (3.15). This transfer matrix is one of the building blocks for the numerical model for a propellant injector.

C.3 Transfer Matrix of an Area Discontinuity

To analyze the acoustic reflection and transmission at an area discontinuity between two ducts, Davies [24] proposed that the smaller-diameter duct should be extended into the larger-diameter duct by an amount equal to the length correction, $\Delta L_{1,2}$, to form an area discontinuity with a side branch. In general, there are two types of area discontinuities: a flow expansion, as shown in Figure C.1, or a flow contraction, as shown in Figure C.2. An area discontinuity is classified as a flow expansion or contraction based on the direction of the mean flow, which is assumed to travel in the positive axial direction. Even though there is no mean flow for the numerical model developed in this chapter, this terminology is adopted for consistency with future chapters. The incident acoustic wave of amplitude a_1^- travels in the negative axial direction, so the incident wave sees an area contraction at a flow expansion and an area expansion at a flow contraction. In general, the smaller-diameter duct may physically extend into the larger-diameter duct by the length L_e. For the analysis, the length of the smaller-diameter duct is then extended by the length correction $\Delta L_{1,2}$ further into the larger-diameter duct. The length of the side branch, which is labeled

as “Region 3” in Figures C.1 and C.2, is equal to the sum of the physical extension and the length correction.

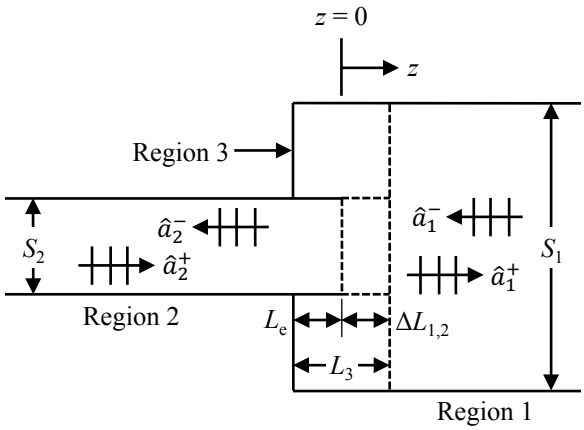

Figure C.1: Flow expansion with a side branch (the flow direction is in the positive axial direction).

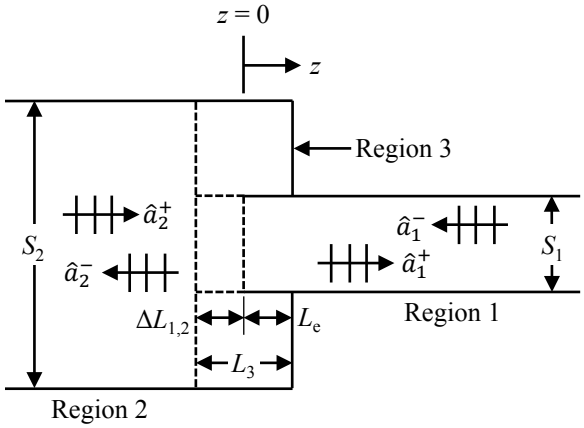

Figure C.2: Flow contraction with a side branch (the flow direction is in the positive axial direction).

It is assumed that all three regions (the two ducts and the side branch) contain the same quiescent medium with constant properties. The boundary conditions for the area discontinuities shown in Figures C.1 and C.2 can be simplified from those given by Munjal [148] since there is no mean flow. Neglecting entropy changes at the area discontinuity,

conservation of energy requires that

$$p_1 = p_2 = p_3, \quad \text{at } z = (-1)^n \Delta L_{1,2} \tag{C.8}$$

conservation of mass requires that

$$u_1 S_1 = u_2 S_2 + (-1)^n u_3 S_3, \quad \text{at } z = (-1)^n \Delta L_{1,2} \tag{C.9}$$

and conservation of momentum requires that

$$p_1 S_1 = p_2 S_2 + (-1)^n p_3 S_3, \quad \text{at } z = (-1)^n \Delta L_{1,2} \tag{C.10}$$

where $n = 0$ for the flow expansion shown in Figure C.1, and $n = 1$ for the flow contraction shown in Figure C.2. In addition, the termination of the side branch is an impermeable hard wall, so

$$u_3 = 0, \quad \text{at } z = (-1)^{n+1} L_e \tag{C.11}$$

The origin of the coordinate system, $z = 0$, is defined at the physical boundary between regions 1 and 2 in Figures C.1 and C.2 before the smaller-diameter duct is extended by $\Delta L_{1,2}$. However, Eqs. (C.8)–(C.10) are applied at $z = (-1)^n \Delta L_{1,2}$, which is the boundary between regions 1, 2, and 3 after the smaller-diameter duct is extended. Equation (C.7) can be used to calculate the transfer matrix between $z = 0$ and $z = (-1)^n \Delta L_{1,2}$, which effectively translates the origin of the coordinate system to $z = (-1)^n \Delta L_{1,2}$ and simplifies the algebra. At the translated origin, the normalized impedance of the side branch is obtained by applying the boundary condition given by Eq. (C.11) to find

$$\zeta_3 = \frac{p_3}{\rho c u_3} = j \cot[(-1)^n k_3 L_3] \tag{C.12}$$

where $L_3 = L_e + \Delta L_{1,2}$. Equation (C.12) is an extension of Eq. (5.17) to the general

case of either a flow expansion or contraction. Equations (C.8), (C.10), and (C.12) can be combined into

$$u_3 = j(-1)^{n+1}\frac{p_1}{\rho c}\frac{|S_1 - S_2|}{S_3}\tan(k_3 L_3) \tag{C.13}$$

which is then substituted into Eq. (C.9) to show that

$$u_2 = j\frac{p_1}{\rho c}\frac{|S_1 - S_2|}{S_2}\tan(k_3 L_3) + \frac{S_1}{S_2}u_1 \tag{C.14}$$

Equations (C.8) and (C.14) are in the form of a pressure and velocity transfer matrix. However, the resistance correction due to viscous losses at the area discontinuity has not yet been considered. Note that the resistance correction given by Eq. (5.8) only applies to an area discontinuity with a large planar wall surface at the discontinuity, which is the case if the extension length, L_e, is zero, and the difference between the areas of the ducts is relatively large. Munjal [148] showed that a lumped resistance such as this correction term could be included directly in the transfer matrix:

$$\begin{bmatrix} \hat{p}_2 \\ \hat{u}_2 \end{bmatrix} = \begin{bmatrix} 1 & \rho c\frac{S_1}{S_2}\theta_{1,2} \\ j\frac{|S_1 - S_2|}{\rho c S_2}\tan(k_3 L_3) & \frac{S_1}{S_2} \end{bmatrix} \begin{bmatrix} \hat{p}_1 \\ \hat{u}_1 \end{bmatrix} \tag{C.15}$$

The transfer matrix in Eq. (C.15) can be transformed to a transfer matrix in terms of the pressure amplitudes using Eq. (C.5). Finally, the transfer matrix given by Eq. (C.7) is applied again to translate the origin from $z = (-1)^n \Delta L_{1,2}$ back to $z = 0$. The resulting expression for the transfer matrix of the area discontinuities shown in Figures C.1 and C.2

is given by

$$\begin{bmatrix} \hat{a}_2^+(0) \\ \hat{a}_2^-(0) \end{bmatrix} = \begin{bmatrix} e^{j(-1)^n k_2 \Delta L_{1,2}} & 0 \\ 0 & e^{j(-1)^{n+1} k_2 \Delta L_{1,2}} \end{bmatrix} \begin{bmatrix} \frac{1}{2} & \frac{1}{2} \\ \frac{1}{2} & -\frac{1}{2} \end{bmatrix} \begin{bmatrix} 1 & \frac{S_1}{S_2}\theta_{1,2} \\ j\frac{|S_1 - S_2|}{S_2}\tan(k_3 L_3) & \frac{S_1}{S_2} \end{bmatrix} \begin{bmatrix} 1 & 1 \\ 1 & -1 \end{bmatrix} \begin{bmatrix} e^{j(-1)^{n+1} k_1 \Delta L_{1,2}} & 0 \\ 0 & e^{j(-1)^n k_1 \Delta L_{1,2}} \end{bmatrix} \begin{bmatrix} \hat{a}_1^+(0) \\ \hat{a}_1^-(0) \end{bmatrix} \quad \text{(C.16)}$$

where this transfer matrix is designated as $\mathbf{Tr}_{1\to 2}$, and the ρc terms have been canceled out because it is assumed that the medium and properties are identical in each of the three regions. Note that the wavenumber may be different in each region since the Kirchhoff wavenumber is a function of the radius of the duct. This transfer matrix is another one of the building blocks for the numerical model for a propellant injector.

C.4 Length Correction at an Area Discontinuity

The transfer matrix given by Eq. C.16 depends on the length correction, $\Delta L_{1,2}$, due to the evanescent modes at the area discontinuity between the two waveguides. There are a number of expressions in the literature for this length correction. In this discussion of length corrections, the subscript 1 refers to the larger-diameter duct, and the subscript 2 refers to the smaller-diameter duct, so a_1 is the radius of the larger duct, and a_2 is the radius of the smaller duct. Davies [24], Kergomard and Garcia [145], and Peat [70] each developed formulas for the length correction at a simple area discontinuity between two cylindrical waveguides. A simple area discontinuity is of the type shown in Figure 5.3, in which the smaller duct does not physically extend into the larger duct. The expression for the length correction given by Kergomard and Garcia [145] is an involved function of the frequency and the radii of the two waveguides that form the discontinuity, but in the low-frequency limit ($ka \ll 1$), their length correction can be approximated using Eq. (5.6).

Alternatively, the expression for the length correction developed by Peat [70] is given by

$$\frac{\Delta L_{1,2}}{a_2} = \frac{8}{3\pi} \sum_{i=0}^{5} \sum_{j=0}^{5} A_{ij} T_i \left(\frac{2ka_1 - 3.9}{3.3} \right) T_j \left(\frac{2(a_2/a_1) - 1.1}{0.9} \right) \tag{C.17}$$

for Helmholtz numbers $0.3 \leq ka_1 \leq 3.6$ and radius ratios $0.1 \leq a_2/a_1 \leq 1$. However, Peat stated that there is no significant variation in the length correction for Helmholtz numbers in the range $0 \leq ka_1 \leq 0.3$. Equation (C.17) is a finite approximation of a double Chebyshev series, where T_i and T_j are Chebyshev polynomials of the first kind of degree i and j, respectively. The coefficients A_{ij} are given in Ref. [70] and are also listed in Appendix F. The coefficients A_{i0} and A_{0j} are multiplied by one-half when performing the double Chebyshev series summation, and A_{00} is multiplied by one-fourth [163]. Note that the expressions developed by Kergomard and Garcia [145] and Peat [70] give similar results for the length correction at a simple area discontinuity between two cylindrical waveguides.

A number of authors [164–166] have developed formulas for the length correction of an extended inlet or outlet in which the smaller-diameter duct physically extends into the larger-diameter duct, as shown in Figure C.1 and C.2. Peat [164] developed an expression for the length correction of an extended inlet or outlet that extends by a length of $L_e/a_1 \geq 0.5$ into the larger duct. The expression is of the same form as Eq. (C.17) but with different values of the coefficients A_{ij}, which are given in Ref. [164] and are also listed in Appendix F. For shorter extended inlets and outlets with extension lengths in the range $0 \leq L_e/a_1 \leq 0.5$, his length correction is given by [164]

$$\Delta L_{1,2} = \Delta L_{1,2}\big|_{(L_e/a_1=0.5)} - \left(\Delta L_{1,2}\big|_{(L_e/a_1=0.5)} - \Delta L_{1,2}\big|_{(L_e/a_1=0)} \right)^{-\xi L/a_1} \tag{C.18}$$

where $\Delta L_{1,2}\big|_{(L_e/a_1=0)}$ is the length correction for a simple area discontinuity ($L_e/a_1 = 0$), $\Delta L_{1,2}\big|_{(L_e/a_1=0.5)}$ is the length correction for an extended inlet or outlet with $L_e/a_1 = 0.5$, and

$$\xi = 16.9 - 40.4(a_2/a_1) + 73.8(a_2/a_1)^2 - 1.2ka_1 - 1.3ka_2 \tag{C.19}$$

For additional accuracy, the effect of the wall thickness of the extended inlet or outlet on the length correction must be considered. This problem was studied by Chaitanya and Munjal [167], but their calculations were performed for a specific range of geometries which are not representative of the present problem. Instead, the length correction given by Peat [164] is multiplied by a factor obtained from an interpolation of the data presented by Ando [25] to account for the effect of the wall thickness. The values used to perform the interpolation are extracted from Figure 3 in Ref. [25] and are tabulated in Appendix F. This method implicitly assumes that the effect of the wall thickness on the length correction is the same for an extended inlet or outlet within a duct as for the open end of a pipe radiating into the ambient air.

For the numerical model, the expressions developed by Peat, namely Eqs. (C.17)–(C.19), are used to calculate the length correction, and the length correction of an extended inlet or outlet is multiplied by the factor obtained from an interpolation of the data presented by Ando [25] to account for the effect of wall thickness. The numerical coefficients used for these length corrections are listed in Appendix F.

C.5 Development of the Transfer Matrix of a Propellant Injector

The building blocks required for the numerical model of a propellant injector were developed in previous sections, and they can now be put together. Each geometric feature of the injector is modeled as a straight cylindrical duct, and adjacent geometric features form area discontinuities where they meet. Figure C.3 shows a schematic of the straight cylindrical duct sections that comprise the numerical model for the "recess" injector, and Table C.1 relates the numbered regions to the geometric features of the "recess" injector. The numerical models for the "straight" and "protrusion" injectors are simplifications of the model for the "recess" injector: the "protrusion" injector does not include region 2, and the "straight" injector does not include regions 2 and 4. The dimensions of each region are given in Figure 4.10 for the set of plastic injectors with unique geometric features. By comparison with

Figure 4.12, region 1 in Figure C.3 corresponds to side B of the two-sided impedance tube, and region 6 corresponds to side A. The shaded region in Figure C.3 represents the outer dimensions of the injector, and L_e is the distance that the injector physically extends into side A of the two-sided impedance tube.

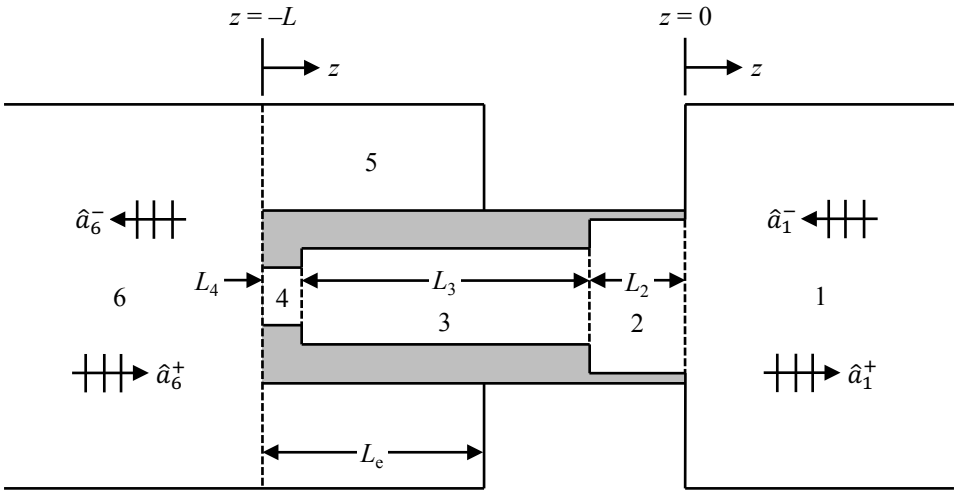

Figure C.3: Schematic of the duct sections in the numerical model for the "recess" injector (not to scale).

Table C.1: Relationship between the numbered duct sections in Figure C.3 and the geometric features of the "recess" injector.

Number	Geometric Feature
1	Impedance tube (side B)
2	Recess
3	Main body
4	Inlet protrusion
5	Impedance tube surrounding the injector
6	Impedance tube (side A)

The transfer matrix between two points in a straight cylindrical tube given by Eq. (C.7) and the transfer matrix of an area discontinuity with a side branch given by Eq. (C.16) provide the building blocks required to construct the numerical model of a propellant injector. The overall transfer matrix of the "recess" injector is constructed from these component

transfer matrices as

$$\mathbf{Tr}_{\text{recess}} = [\mathbf{Tr}_{4\to6}]\left[\mathbf{Tr}\big|_{-(L_2+L_3)}^{-L}\right][\mathbf{Tr}_{3\to4}]\left[\mathbf{Tr}\big|_{-L_2}^{-(L_2+L_3)}\right][\mathbf{Tr}_{2\to3}]\left[\mathbf{Tr}\big|_{0}^{-L_2}\right][\mathbf{Tr}_{1\to2}] \tag{C.20}$$

such that

$$\begin{bmatrix}\hat{a}_6^+(-L)\\ \hat{a}_6^-(-L)\end{bmatrix} = \mathbf{Tr}_{\text{recess}}\begin{bmatrix}\hat{a}_1^+(0)\\ \hat{a}_1^-(0)\end{bmatrix} \tag{C.21}$$

Note that the overall transfer matrices of the "straight" and "protrusion" injectors are simplifications of Eq. (C.20).

The numerical model can also be applied to multiple propellant injectors with a slight modification to the transfer matrix of an area discontinuity given by Eq. (C.16). For a flow expansion (see Figure C.1, for example) between duct 1 and multiple injectors, S_2 is replaced by NS_2 in Eq. (C.16), where N is the number of injectors. For a flow contraction (see Figure C.2, for example) between duct 2 and multiple injectors, S_1 is replaced by NS_1 in Eq. (C.16). These modifications affect the transfer matrices $\mathbf{T}_{1,2}$ and $\mathbf{T}_{4,6}$ in Eq. (C.20). These transfer matrices describe the change in the amplitudes of the acoustic waves across the area discontinuities between the impedance tube and the injectors.

C.6 Development of the Scattering Matrix of a Propellant Injector

The transfer matrix of a propellant injector can be rewritten as a scattering matrix, which is consistent with the experiments conducted in this work. The scattering matrix, as defined in Eq. (3.33), relates the acoustic pressure of the inward- and outward-propagating waves on both sides of the test article, so it is simply a reordering of the transfer matrix defined in Eq. (C.2). In terms of the scattering matrix, Eq. (C.21) can be written as

$$\begin{bmatrix}\hat{a}_6^-(-L)\\ \hat{a}_1^+(0)\end{bmatrix} = \mathbf{S}_{\text{recess}}\begin{bmatrix}\hat{a}_6^+(-L)\\ \hat{a}_1^-(0)\end{bmatrix} \tag{C.22}$$

where $\mathbf{S}_{\text{recess}}$ is the overall scattering matrix of the "recess" injector. If the transfer matrix is expressed as

$$\mathbf{Tr} = \begin{bmatrix} a & b \\ c & d \end{bmatrix} \tag{C.23}$$

then the scattering matrix is given by

$$\mathbf{S} = \frac{1}{a} \begin{bmatrix} c & ad - bc \\ 1 & -b \end{bmatrix} \tag{C.24}$$

The advantage of the scattering matrix is that the elements of the matrix are the reflection and transmission coefficients. By inspection, the pressure reflection coefficient on side B of the two-sided impedance tube is given by the element $R_{B\to B} = S_{2,2}$, and the pressure transmission coefficient from side B to side A is given by the element $T_{B\to A} = S_{1,2}$. The power reflection, transmission, dissipation, and absorption coefficients can then be calculated from the pressure reflection and transmission coefficients using Eqs. (3.58), (3.60), (3.44), and (3.45), respectively. For the assumptions used in developing the numerical model, the power reflection and transmission coefficients are simply given by the squares of the pressure reflection and transmission coefficients, respectively.

APPENDIX D
HIGHER-ORDER MODE-MATCHING METHOD

In this appendix, an analytical method is developed to calculate the reflection and transmission of sound at a simple area discontinuity in a duct based on the boundary and continuity conditions at the discontinuity. This type of analytical method is referred to as a mode-matching method. The mode-matching method requires the calculation of a large number of higher-order evanescent modes that are formed at the area discontinuity to satisfy the boundary conditions. In Appendix C, the reflection and transmission of sound at a simple area discontinuity were considered for the plane wave mode only, and the effects of the higher-order evanescent modes were included in the analysis using an empirical model for the length correction at the area discontinuity. No empirical models are required for the mode-matching method developed in this appendix, so this method is purely analytical.

Miles [104] was the first to develop a higher-order mode-matching method to calculate the reflection and transmission of sound at an area discontinuity in a circular duct. The following discussion is based on the method originally presented by Miles [104] and further developed by El-Sharkawy and Nayfey [105] and Selamet and Ji [31, 109].

D.1 Application of the Boundary and Continuity Conditions

Figure D.1 depicts the example problem of an area discontinuity in a circular duct. The subscript 1 represents the larger duct, and the subscript 2 represents the smaller duct. The area S_1 is the cross-sectional area of the larger duct, S_2 is the cross-sectional area of the smaller duct and thus the area of the union between the ducts, and $S_1 - S_2$ is the area of the wall at the discontinuity. In general, the center of the smaller duct can be offset from the center of the larger duct by the distance r_0.

The conditions at the area discontinuity are continuity of acoustic pressure at every

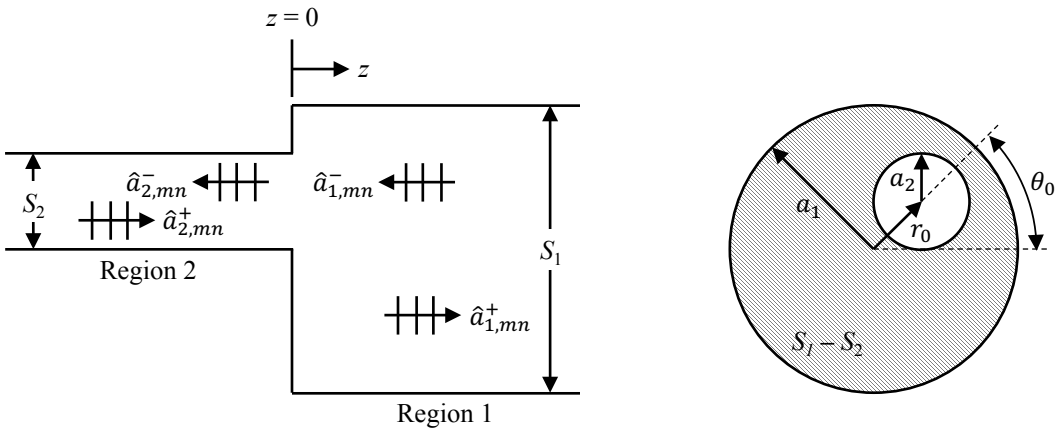

Figure D.1: Area discontinuity between two offset ducts.

point in the union between the ducts [104, 105],

$$p_1|_{z=0} = p_2|_{z=0}, \quad \text{on } S_2 \tag{D.1}$$

continuity of particle velocity at every point in the union between the ducts,

$$u_1|_{z=0} = u_2|_{z=0}, \quad \text{on } S_2 \tag{D.2}$$

and vanishing particle velocity at the wall surrounding the discontinuity

$$u_1|_{z=0} = 0, \quad \text{on } S_1 - S_2 \tag{D.3}$$

Substitution of the expression for the acoustic pressure field at a single frequency in a circular duct given by Eq. (3.5) into the pressure continuity condition of Eq. (D.1) yields

$$\sum_{m=-\infty}^{\infty} \sum_{n=0}^{\infty} (\hat{a}^+_{1,mn} + \hat{a}^-_{1,mn}) \Psi_{1,mn} = \sum_{m=-\infty}^{\infty} \sum_{n=0}^{\infty} (\hat{a}^+_{2,mn} + \hat{a}^-_{2,mn}) \Psi_{2,mn}, \quad \text{on } S_2 \tag{D.4}$$

Multiplication by $\Psi^*_{2,\mu\nu}$ and integration over the area S_2 produces

$$\sum_{m=-\infty}^{\infty}\sum_{n=0}^{\infty}(\hat{a}^+_{1,mn}+\hat{a}^-_{1,mn})\iint\limits_{S_2}\Psi_{1,mn}\Psi^*_{2,\mu\nu}dS = S_2(\hat{a}^+_{2,\mu\nu}+\hat{a}^-_{2,\mu\nu}) \tag{D.5}$$

where the orthogonality relationship between mode shapes given by Eq. (3.10) has been applied to simplify the resulting expression.

Similarly, substitution of the expression for the particle velocity field at a single frequency in a circular duct given by Eq. (3.47) into the velocity continuity condition of Eq. (D.2), multiplication of the resulting expression by $\Psi^*_{1,\mu\nu}$, and integration over the area S_2 yields

$$\begin{aligned}\sum_{m=-\infty}^{\infty}\sum_{n=0}^{\infty}(\hat{a}^+_{1,mn}-\hat{a}^-_{1,mn})\alpha_{1,mn}\iint\limits_{S_2}\Psi_{1,mn}\Psi^*_{1,\mu\nu}dS \\ = \sum_{m=-\infty}^{\infty}\sum_{n=0}^{\infty}(\hat{a}^+_{2,mn}-\hat{a}^-_{2,mn})\alpha_{2,mn}\iint\limits_{S_2}\Psi_{2,mn}\Psi^*_{1,\mu\nu}dS\end{aligned} \tag{D.6}$$

Substitution of the expression for the particle velocity field into the vanishing velocity condition of Eq. (D.3), multiplication by $\Psi^*_{1,\mu\nu}$, and integration over the area $S_1 - S_2$ yields

$$\sum_{m=-\infty}^{\infty}\sum_{n=0}^{\infty}(\hat{a}^+_{1,mn}-\hat{a}^-_{1,mn})\alpha_{1,mn}\iint\limits_{(S_1-S_2)}\Psi_{1,mn}\Psi^*_{1,\mu\nu}dS = 0 \tag{D.7}$$

The integral on the left-hand side of Eq. (D.6) is integrated over the area S_2, and the left-hand side of Eq. (D.7) is identical to the left-hand side of Eq. (D.6) except that the integral is integrated over $S_1 - S_2$. If these two integrals are added together, then they can be rewritten as a single integral over the area S_1. The summation of Eqs. (D.6) and (D.7) produces

$$S_1(\hat{a}^+_{1,\mu\nu}-\hat{a}^-_{1,\mu\nu})\alpha_{1,\mu\nu} = \sum_{m=-\infty}^{\infty}\sum_{n=0}^{\infty}(\hat{a}^+_{2,mn}-\hat{a}^-_{2,mn})\alpha_{2,mn}\iint\limits_{S_2}\Psi_{2,mn}\Psi^*_{1,\mu\nu}dS \tag{D.8}$$

where the orthogonality relationship between mode shapes given by Eq. (3.10) has been

applied to simplify the resulting expression.

D.2 Solution to the System of Equations

D.2.1 Truncation of the Number of Modes

Equations (D.5) and (D.8) represent a system of infinitely many equations for the infinitely many unknown amplitudes of the modes on either side of the area discontinuity. The infinite sum must be truncated to a finite number of modes in order to solve the system of equations. Hudde and Letens [168] showed that the number of modes considered on either side of the area discontinuity should not necessarily be equal, but instead, the order of the neglected terms due to truncation should be equal. For a large number of modes, Hudde and Letens proposed that the ratio of the number of modes in each duct be equal to the ratio of the radii of the ducts, or

$$\frac{N_1}{N_2} = \frac{a_1}{a_2} \tag{D.9}$$

where N_1 and N_2 are the number of modes considered in ducts 1 and 2, respectively. The numerical values of N_1 and N_2 are selected based on the number of modes required for convergence of a specific metric, such as the amplitude of the plane wave mode.

There are several choices for selecting which modes are considered in the ducts on either side of the area discontinuity. Selamet and Ji [31, 109] truncated the summations over the circumferential mode order, m, and the radial mode order, n, separately. However, experience in the current work suggests that better convergence is obtained if the modes are instead truncated in order of increasing cut-on frequency. The cut-on frequency of each mode is directly related to its eigenvalue through Eq. (3.14), so this method of truncating the number of modes requires the added step of computing the eigenvalues of a large number of modes using Eq. (3.9) and ordering the modes by increasing eigenvalue. The separate summations over m and n in Eqs. (D.5) and (D.8) are thus replaced by a single summation over the first N cut-on modes.

D.2.2 Scattering Matrix Solution to the Mode-Matching Method

The mode-matching method can be applied to construct the scattering matrix of the area discontinuity analytically. The higher-order scattering matrix of the area discontinuity between the two ducts shown in Figure D.1 is defined by the relation

$$\begin{bmatrix} \hat{\mathbf{a}}_2^- \\ \hat{\mathbf{a}}_1^+ \end{bmatrix} = \mathbf{S}_{1,2} \begin{bmatrix} \hat{\mathbf{a}}_2^+ \\ \hat{\mathbf{a}}_1^- \end{bmatrix} \tag{D.10}$$

where the vectors $\hat{\mathbf{a}}_1^{\pm}$ contain the N_1 modal amplitudes of the forward- and rearward-propagating modes in duct 1, and the vectors $\hat{\mathbf{a}}_2^{\pm}$ contain the N_2 modal amplitudes of the forward- and rearward-propagating modes in duct 2. To construct the scattering matrix, Eqs. (D.5) and (D.8) are first rearranged so that terms involving $\hat{a}_1^+$ and $\hat{a}_2^-$ are on the left-hand side and terms involving $\hat{a}_1^-$ and $\hat{a}_2^+$ are on the right-hand side, which corresponds with the form of the scattering matrix defined in Eq. (D.10). Equations (D.5) and (D.8) can then be written in matrix form as

$$\begin{bmatrix} -S_2\mathbf{I}_{N_2} & \mathbf{X}_{2,1} \\ \mathbf{X}_{1,2}\mathbf{A}_2 & S_1\mathbf{A}_1 \end{bmatrix} \begin{bmatrix} \hat{\mathbf{a}}_2^- \\ \hat{\mathbf{a}}_1^+ \end{bmatrix} = \begin{bmatrix} S_2\mathbf{I}_{N_2} & -\mathbf{X}_{2,1} \\ \mathbf{X}_{1,2}\mathbf{A}_2 & S_1\mathbf{A}_1 \end{bmatrix} \begin{bmatrix} \hat{\mathbf{a}}_2^+ \\ \hat{\mathbf{a}}_1^- \end{bmatrix} \tag{D.11}$$

where $\mathbf{I}_{N_i}$ is the $N_i \times N_i$ identity matrix, $\mathbf{A}_i$ is an $N_i \times N_i$ diagonal matrix with the values $\alpha_{i,mn}$ along the diagonal, and i represents either duct 1 or duct 2. The modal coupling matrix $\mathbf{X}_{2,1}$ is an $N_2 \times N_1$ matrix defined by

$$\mathbf{X}_{2,1} = \begin{bmatrix} \iint_{S_2} \Psi_{2,00}^* \Psi_{1,00} dS & \cdots & \iint_{S_2} \Psi_{2,00}^* \Psi_{1,mn} dS \\ \vdots & & \vdots \\ \iint_{S_2} \Psi_{2,\mu\nu}^* \Psi_{1,00} dS & \cdots & \iint_{S_2} \Psi_{2,\mu\nu}^* \Psi_{1,mn} dS \end{bmatrix} \tag{D.12}$$

and $\mathbf{X}_{1,2}$ is an $N_1 \times N_2$ matrix given by $\mathbf{X}_{1,2} = \mathbf{X}_{2,1}^H$, where the superscript H represents the complex conjugate (or Hermitian) transpose. The integrals in Eq. (D.12) can be evaluated

by numerically integrating the products of the mode shape functions over the area S_2, where the mode shape functions are given by Eq. (3.8).

Equation (D.11) can also be expressed compactly as

$$\mathbf{S}_{\text{out}}\hat{\mathbf{a}}_{\text{out}} = \mathbf{S}_{\text{in}}\hat{\mathbf{a}}_{\text{in}} \tag{D.13}$$

where the subscripts "in" and "out" designate the incoming and outgoing modes, respectively. Both $\mathbf{S}_{\text{out}}$ and $\mathbf{S}_{\text{in}}$ are square $(N_1 + N_2) \times (N_1 + N_2)$ matrices, so the scattering matrix is given by

$$\mathbf{S}_{1,2} = \mathbf{S}_{\text{out}}^{-1}\mathbf{S}_{\text{in}} \tag{D.14}$$

D.2.3 Transfer Matrix Solution to the Mode-Matching Method

Alternatively, the truncated mode-matching method could be expressed in terms of the higher-order transfer matrix, which is defined by the relation

$$\begin{bmatrix} \hat{\mathbf{a}}_2^+ \\ \hat{\mathbf{a}}_2^- \end{bmatrix} = \mathbf{Tr}_{1,2} \begin{bmatrix} \hat{\mathbf{a}}_1^+ \\ \hat{\mathbf{a}}_1^- \end{bmatrix} \tag{D.15}$$

This transfer matrix formulation is used in the numerical model of the acoustic damping of propellant injectors for the plane wave mode developed in Section 5.3, and transfer matrices would be useful for constructing a numerical model for higher-order modes. If Eqs. (D.5) and (D.8) are rewritten in the transfer matrix form

$$\mathbf{Tr}_2\hat{\mathbf{a}}_2 = \mathbf{Tr}_1\hat{\mathbf{a}}_1 \tag{D.16}$$

then $\mathbf{Tr}_2$ is an $(N_1 + N_2) \times 2N_2$ matrix, and $\mathbf{Tr}_1$ is an $(N_1 + N_2) \times 2N_1$ matrix. If region 1 is larger than region 2, as shown in Figure D.1, and thus more modes are considered in region 1 than in region 2 based on Eq. (D.9), then neither $\mathbf{Tr}_1$ nor $\mathbf{Tr}_2$ is a square matrix. The system of equations given by Eq. (D.16) is overdetermined for the transfer matrix $\mathbf{Tr}_{1,2}$

from region 1 to region 2, but the system is underdetermined for the inverse transfer matrix from region 2 to region 1. Therefore, the transfer matrix formulation may not produce an exact or even a unique solution, so the scattering matrix formulation is used instead.

APPENDIX E

DEVELOPMENT OF A NUMERICAL MODEL FOR HIGHER-ORDER MODES

E.1 Overview of the Numerical Model for Higher-Order Modes

In this appendix, the numerical model for the acoustic damping of a propellant injector for the plane wave mode developed in Appendix C is extended to higher-order modes. For simplicity, the realistic geometric features of a propellant injector are not included in the numerical model, but the model is developed for multiple straight cylindrical half-wave resonators with a side branch at one end, which describes the geometry of the test article shown in Figure 4.14. Figure E.1 shows a schematic of the duct sections that make up the numerical model. The side branch is designated by the letter C, and the resonators are designated by the index $\xi = \{1, \ldots, \Xi\}$, where Ξ is the number of resonators. Only two resonators are shown in Figure E.1, but the figure is intended to represent an arbitrary number of resonators in the numerical model. The resonators all have the same length, L, and they extend into side A of the impedance tube by the length L_e.

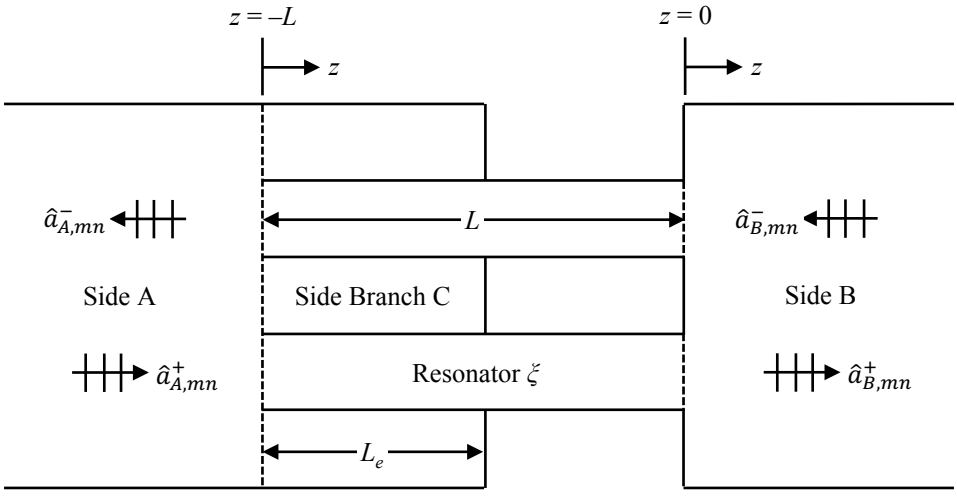

Figure E.1: Schematic of the duct sections in the numerical model for multiple half-wave resonators with a side branch at one end (not to scale).

In Appendix C, the numerical model for the plane wave mode is expressed in terms of transfer matrices, but the transfer matrix formulation has disadvantages for higher-order modes, which are discussed in Appendix D. Instead, the numerical model for higher-order modes is developed based on the mode-matching method. In the following sections, the mode-matching method is applied to each of the area discontinuities shown in Figure E.1, and the resulting system of equations is then solved to obtain the overall scattering matrix of the test article. However, the mathematics are simplified if the reference origin of the acoustic waves is defined at a different axial coordinate in each duct section. The pressure amplitudes of the propagating waves in each duct are given by

$$\hat{p}^{\pm}_{mn}(z,f) = \hat{a}^{\pm}_{mn}(f)e^{\mp k^{+}_{mn}(z-z_0)} \tag{E.1}$$

where z_0 is the reference origin. Table E.1 lists the reference origins used in the numerical model for the forward- and rearward-propagating waves in each duct section.

Table E.1: Reference origin for the acoustic waves in each duct section defined in Figure E.1.

Duct Section	Acoustic Waves	Reference Origin
Side B	$\hat{p}^{\pm}_{B,mn}$	$z_0 = 0$
Resonator ξ ($+z$ direction)	$\hat{p}^{+}_{\xi,mn}$	$z_0 = -L$
Resonator ξ ($-z$ direction)	$\hat{p}^{-}_{\xi,mn}$	$z_0 = 0$
Side Branch C	$\hat{p}^{\pm}_{C,mn}$	$z_0 = -L$
Side A	$\hat{p}^{\pm}_{A,mn}$	$z_0 = -L$

E.2 Mode-Matching Method for Multiple Ducts

The mode-matching method developed in Appendix D is extended to include multiple smaller duct sections so that it can be applied to the area discontinuity at $z = 0$ in Figure E.1 between side B of the two-sided impedance tube and multiple resonators. The

continuity conditions at the area discontinuity are continuity of acoustic pressure and continuity of particle velocity in the union between each resonator and the impedance tube, and the boundary condition is that the particle velocity is zero on the wall surrounding the discontinuity [104, 105]. Following the same methodology as in Section D.1, the pressure continuity condition leads to expressions of the form

$$\sum_{m=-\infty}^{\infty}\sum_{n=0}^{\infty}(\hat{a}^{+}_{B,mn}+\hat{a}^{-}_{B,mn})\iint_{S_\xi}\Psi_{B,mn}\Psi^{*}_{\xi,\mu\nu}dS = S_\xi(\hat{a}^{+}_{\xi,\mu\nu}e^{-jk_{\xi,\mu\nu}L}+\hat{a}^{-}_{\xi,\mu\nu}) \tag{E.2}$$

for each resonator, where the subscript B designates side B of the impedance tube, and the subscript ξ designates the resonator. Similarly, the velocity continuity and boundary conditions lead to the expression

$$S_B(\hat{a}^{+}_{B,\mu\nu}-\hat{a}^{-}_{B,\mu\nu})\alpha_{B,\mu\nu} = \sum_{\xi=1}^{\Xi}\sum_{m=-\infty}^{\infty}\sum_{n=0}^{\infty}(\hat{a}^{+}_{\xi,mn}e^{-jk_{\xi,mn}L}-\hat{a}^{-}_{\xi,mn})\alpha_{\xi,mn}\iint_{S_\xi}\Psi_{\xi,mn}\Psi^{*}_{B,\mu\nu}dS \tag{E.3}$$

where Ξ is the number of resonators. The exponential terms arise because the reference origin of the forward-propagating acoustic waves in the resonators is at $z=-L$, but the area discontinuity is at $z=0$. The Weng-Bake wavenumber given by Eq. (3.19) is used for $k_{\xi,mn}$ to account for viscothermal dissipation in the acoustic boundary layer of the resonators.

E.3 Mode-Matching Method for Ducts with a Side Branch

The mode-matching method is further extended to include a side branch so that it can be applied to the area discontinuity at $z=-L$ in Figure E.1 between side A of the two-sided impedance tube, multiple resonators, and the side branch formed by the extension of the resonators into the impedance tube. The continuity conditions at the area discontinuity are continuity of acoustic pressure and continuity of particle velocity, which apply in the union between each resonator and the impedance tube and also in the union between the

side branch and the impedance tube [104, 105]. Following the same methodology as in Section D.1, the pressure continuity condition between each resonator and the impedance tube leads to expressions of the form

$$\sum_{m=-\infty}^{\infty}\sum_{n=0}^{\infty}(\hat{a}^{+}_{A,mn}+\hat{a}^{-}_{A,mn})\iint\limits_{S_\xi}\Psi_{A,mn}\Psi^{*}_{\xi,\mu\nu}dS = S_\xi(\hat{a}^{+}_{\xi,\mu\nu}+\hat{a}^{-}_{\xi,\mu\nu}e^{-jk_{\xi,\mu\nu}L}) \tag{E.4}$$

for each resonator, where the subscript A designates side A of the impedance tube, and the subscript ξ designates the resonator. Similarly, the pressure continuity condition between the side branch and the impedance tube leads to the expression

$$\sum_{m=-\infty}^{\infty}\sum_{n=0}^{\infty}(\hat{a}^{+}_{A,mn}+\hat{a}^{-}_{A,mn})\iint\limits_{S_C}\Psi_{A,mn}\Psi^{*}_{C,\mu\nu}dS = S_C(\hat{a}^{+}_{C,\mu\nu}+\hat{a}^{-}_{C,\mu\nu}) \tag{E.5}$$

where the subscript C designates the side branch, and the area of the side branch is given by $S_C = S_A - \Xi S_\xi$. Additionally, the velocity continuity conditions lead to the expression

$$\begin{aligned} S_A(\hat{a}^{+}_{A,\mu\nu}-\hat{a}^{-}_{A,\mu\nu})\alpha_{A,\mu\nu} = &\sum_{\xi=1}^{\Xi}\sum_{m=-\infty}^{\infty}\sum_{n=0}^{\infty}(\hat{a}^{+}_{\xi,mn}-\hat{a}^{-}_{\xi,mn}e^{-jk_{\xi,mn}L})\alpha_{\xi,mn}\iint\limits_{S_\xi}\Psi_{\xi,mn}\Psi^{*}_{A,\mu\nu}dS \\ &+\sum_{m=-\infty}^{\infty}\sum_{n=0}^{\infty}(\hat{a}^{+}_{C,mn}-\hat{a}^{-}_{C,mn})\alpha_{C,mn}\iint\limits_{S_C}\Psi_{C,mn}\Psi^{*}_{A,\mu\nu}dS \end{aligned} \tag{E.6}$$

The exponential terms arise because the reference origin of the rearward-propagating acoustic waves in the resonators is at $z = 0$, but the area discontinuity is at $z = -L$. Again, $k_{\xi,mn}$ is the Weng-Bake wavenumber given by Eq. (3.19).

The final boundary condition is that the side branch terminates in a hard wall, so the particle velocity at $z = L_e - L$ in Figure E.1 is zero. Substitution of the expression for the particle velocity field into this boundary condition, multiplication by $\Psi^{*}_{C,\mu\nu}$, and integration

over the area S_C results in the expression

$$\hat{a}^{+}_{C,mn} e^{-jk_{C,mn}L_e} - \hat{a}^{-}_{C,mn} e^{jk_{C,mn}L_e} = 0 \tag{E.7}$$

Therefore, the amplitudes of either the forward- or rearward-propagating waves in the side branch can be expressed in terms of the other and substituted into Eqs. (E.4)–(E.6). The non-dissipative wavenumber given by Eq. (3.12) is used for $k_{C,mn}$ because there is no analytical formulation for a dissipative wavenumber in the irregular geometry of the side branch. This means that viscothermal losses in the side branch are not modeled, which may introduce errors between the numerical model and the experiments.

E.4 Mode Shapes in the Side Branch

In the development of Eqs. (E.4)–(E.7), it is implicitly assumed that the mode shapes in each duct section are orthogonal. The impedance tube and the resonators are cylinders, so their mode shapes are described analytically by Eq. (3.8) and are shown to be orthogonal by Eq. (3.10). The side branch, however, is formed by the extension of twelve cylinders into the impedance tube, and there is no simple analytical expression for the mode shapes in this irregular geometry. Therefore, the mode shapes in the side branch are calculated numerically using COMSOL. The computed mode shapes for the side branch are indeed found to be orthogonal, so the assumption stated above holds true.

For cylindrical ducts, each circumferential mode is doubly degenerate, which implies that there exist two distinct mode shapes with the same eigenvalue and cut-on frequency. In this work, the circumferential modes are described by clockwise- and counterclockwise-spinning solutions; for example, the $(+1, 0)$ and $(-1, 0)$ modes spin in opposite directions but they have the same eigenvalue and cut-on frequency. Alternatively, the circumferential modes could be formulated as standing modes with orthogonal nodal lines; this standing-wave form is computed by COMSOL. Figures E.2a and E.2b show the degenerate (1,0)-like

and (2,0)-like modes, respectively, in the side branch. These mode shapes are similar to the mode shapes of the (1,0) and (2,0) modes in the cylindrical duct, but the resonators slightly modify the positions of the nodal lines. The first two radial-like mode shapes in the side branch are shown in Figure E.3. The (0,1)-like mode shape is almost identical to the (0,1) mode in a cylindrical duct, but the (0,2)-like mode shape is significantly modified by the presence of the resonators.

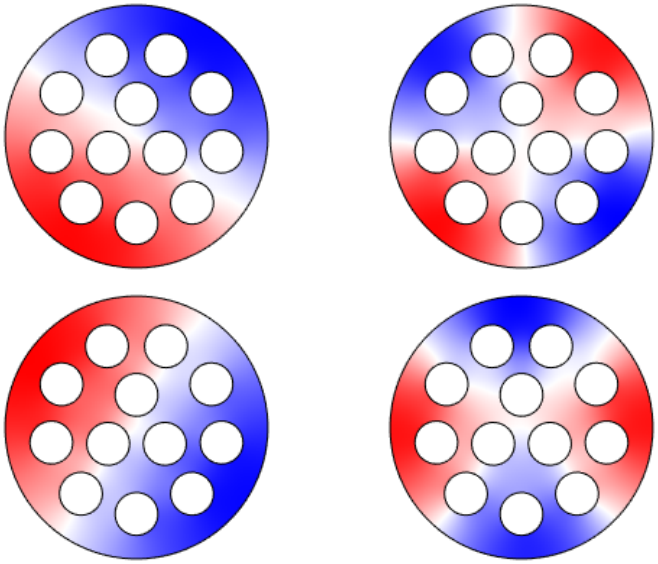

(a) (1,0)-like modes (b) (2,0)-like modes

Figure E.2: Degenerate circumferential mode shapes in the side branch formed by the extension of the resonators into the impedance tube.

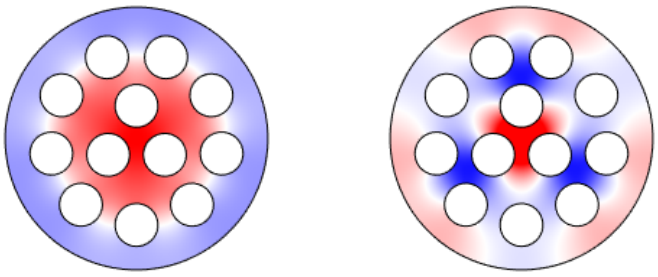

(a) (0,1)-like mode (b) (0,2)-like mode

Figure E.3: Radial mode shapes in the side branch formed by the extension of the resonators into the impedance tube.

Figure E.4 shows the split (3,0)-like mode shapes computed by COMSOL in the side

branch. These modes are not degenerate; instead, they have distinct eigenvalues and hence distinct cut-on frequencies due to the symmetry of the resonators about the nodal lines of the circular (3,0) mode. Using terminology adapted from Oschwald, et al. [29], the mode shown in Figure E.4a is designated as the (3σ,0) mode because its pressure antinodes are preferentially aligned with the resonators, whereas the mode shown in Figure E.4b is designated as the (3π,0) mode because its nodal lines are preferentially aligned with the resonators.

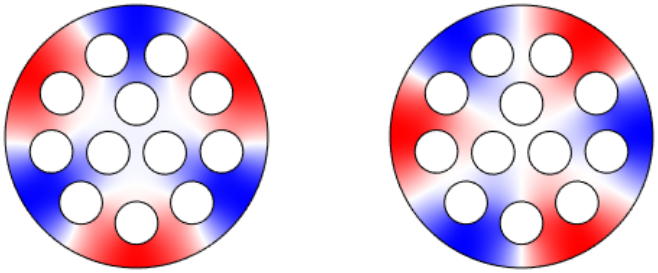

(a) (3σ,0) mode (b) (3π,0) mode

Figure E.4: Split (3,0)-like mode shapes in the side branch formed by the extension of the resonators into the impedance tube.

E.5 Scattering Matrix Solution to the Numerical Model for Higher-Order Modes

E.5.1 Truncation of the Number of Modes

The infinite system of equations given by Eqs. (E.2)–(E.7) describes the acoustic reflection and transmission of higher-order modes for the configuration of multiple resonators shown schematically in Figure E.1. In order to solve the system of equations, however, the number of modes in each duct section must be truncated. The number of modes in each side of the impedance tube should be identical, so $N_A = N_B = N$. The number of modes in the other duct sections are truncated based on the criterion suggested by Hudde and Letens [168]. The ratio between the number of modes in each resonator and in the impedance tube is related to the ratio of their radii by

$$\frac{N_\xi}{N} = \frac{a_\xi}{a_B} \tag{E.8}$$

where N_ξ is the number of modes in resonator ξ. Furthermore, the number of modes in the side branch should be truncated such that [107]

$$\frac{N_C}{N} = \frac{a_A - a_C}{a_A} \tag{E.9}$$

where N_C is the number of modes in the side branch. The numerical value of N is selected based on the number of modes required for convergence of a specific metric, such as the scattering matrix for the cut-on modes.

E.5.2 Matrix Solution to the System of Equations

After the number of modes in Eqs. (E.2)–(E.7) are truncated according to the above criteria, the system of equations can then be written in the block matrix form

$$\begin{bmatrix} \mathbf{0}_{N_\Xi,N} & \mathbf{X}_{\xi,B} & -S_\xi \mathbf{E}_\xi & -S_\xi \mathbf{I}_{N_\Xi} & \mathbf{0}_{N_\Xi,N_C} \\ \mathbf{0}_{N,N} & S_B \mathbf{A}_B & -\mathbf{X}_{B,\xi}\mathbf{A}_\xi \mathbf{E}_\xi & \mathbf{X}_{B,\xi}\mathbf{A}_\xi & \mathbf{0}_{N,N_C} \\ \mathbf{X}_{\xi,A} & \mathbf{0}_{N_\Xi,N} & -S_\xi \mathbf{I}_{N_\Xi} & -S_\xi \mathbf{E}_\xi & \mathbf{0}_{N_\Xi,N_C} \\ \mathbf{X}_{C,A} & \mathbf{0}_{N_C,N} & \mathbf{0}_{N_C,N_\Xi} & \mathbf{0}_{N_C,N_\Xi} & -S_C(\mathbf{I}_{N_C} + \mathbf{E}_C) \\ S_A \mathbf{A}_A & \mathbf{0}_{N,N} & \mathbf{X}_{N,N_\Xi}\mathbf{A}_\xi & -\mathbf{X}_{N,N_\Xi}\mathbf{A}_\xi \mathbf{E}_\xi & \mathbf{X}_{A,C}\mathbf{A}_C(\mathbf{I}_{N_C} - \mathbf{E}_C) \end{bmatrix} \begin{bmatrix} \hat{\mathbf{a}}_A^- \\ \hat{\mathbf{a}}_B^+ \\ \hat{\mathbf{a}}_\xi^+ \\ \hat{\mathbf{a}}_\xi^- \\ \hat{\mathbf{a}}_C^+ \end{bmatrix}$$
$$= \begin{bmatrix} \mathbf{0}_{N_\Xi,N} & -\mathbf{X}_{\xi,B} \\ \mathbf{0}_{N,N} & S_B \mathbf{A}_B \\ -\mathbf{X}_{\xi,A} & \mathbf{0}_{N_\Xi,N} \\ -\mathbf{X}_{C,A} & \mathbf{0}_{N_C,N} \\ S_A \mathbf{A}_A & \mathbf{0}_{N_A,N} \end{bmatrix} \begin{bmatrix} \hat{\mathbf{a}}_A^+ \\ \hat{\mathbf{a}}_B^- \end{bmatrix} \tag{E.10}$$

where $\hat{\mathbf{a}}_A^\pm$ and $\hat{\mathbf{a}}_B^\pm$ are vectors of the N modal amplitudes in sides A and B of the impedance tube, $\hat{\mathbf{a}}_C^+$ is the vector of the N_C forward-propagating modal amplitudes in the side branch, and $\hat{\mathbf{a}}_\xi^\pm = [\hat{\mathbf{a}}_{1,mn}^\pm, \ldots, \hat{\mathbf{a}}_{\Xi,mn}^\pm]^T$ are vectors of the $N_\Xi = \Xi N_\xi$ modal amplitudes in all of the resonators. The matrix terms in Eq. (E.10) are defined in Table E.2, where i and j represent

any of the duct sections.

Table E.2: Definitions of the matrices in Eq. (E.10).

Matrix	Dimensions	Definition
$\mathbf{0}_{N_i,N_j}$	$N_i \times N_j$	Zero matrix
$\mathbf{I}_{N_i}$	$N_i \times N_i$	Identity matrix
$\mathbf{A}_i$	$N_i \times N_i$	diag$(\alpha_{i,mn})$
$\mathbf{E}_i$	$N_i \times N_i$	diag$(e^{-jk_{i,mn}L})$
$\mathbf{X}_{i,j}$	$N_i \times N_j$	Eq. (D.12)

Some of the definitions given in Table E.2 are slightly modified for the matrices involving the subscript ξ to account for multiple resonators. For example,

$$\mathbf{A}_\xi = \text{diag}(\alpha_{1,mn}, \ldots, \alpha_{\Xi,mn}) \tag{E.11}$$

and

$$\mathbf{E}_\xi = \text{diag}(e^{-jk_{1,mn}L}, \ldots, e^{-jk_{\Xi,mn}L}) \tag{E.12}$$

are $N_\Xi \times N_\Xi$ matrices. The modal coupling matrix $\mathbf{X}_{\xi,i}$ is given by

$$\mathbf{X}_{\xi,i} = \begin{bmatrix} \mathbf{X}_{1,i} \\ \vdots \\ \mathbf{X}_{\Xi,i} \end{bmatrix} \tag{E.13}$$

and $\mathbf{X}_{i,\xi} = \mathbf{X}_{\xi,i}^H$, where the superscript H represents the complex conjugate (or Hermitian) transpose.

E.5.3 Scattering Matrix of Half-Wave Resonators for Higher-Order Modes

To solve for the scattering matrix, Eq. (E.10) can be expressed compactly as

$$\mathbf{S}_{\text{out}}\hat{\mathbf{a}}_{\text{out}} = \mathbf{S}_{\text{in}}\hat{\mathbf{a}}_{\text{in}} \tag{E.14}$$

where the subscripts "in" and "out" designate the incoming and outgoing modes, respectively. The matrix $\mathbf{S}_{\text{out}}$ is an invertible square matrix, so the scattering matrix solution is given by

$$\mathbf{S} = \mathbf{S}_{\text{out}}^{-1}\mathbf{S}_{\text{in}} \tag{E.15}$$

where $\mathbf{S}$ is a $(2N + 2N_{\Xi} + N_C) \times 2N$ matrix. In general, this scattering matrix includes modes that are modeled to obtain good convergence but are not actually cut-on at the frequency under consideration. In addition, the scattering matrix of the test article is typically defined according to the relationship given by Eq. (3.28), which does not include modes in the resonators or side branch. Therefore, the number of elements in $\mathbf{S}$ can be truncated so that only the scattering coefficients corresponding to the reflection and transmission of the cut-on modes in sides A and B of the impedance tube are retained.

APPENDIX F
FORMULAS FOR THE LENGTH CORRECTION AT AN AREA DISCONTINUITY

In this appendix, several expressions from the literature for the length correction at an area discontinuity are provided. The length correction at an area discontinuity can be calculated using the mode-matching method as discussed in Section 10.4. However, the expressions presented in this appendix are used in the numerical model for the acoustic damping of propellant injectors for the plane wave mode developed in Appendix C because they are simpler than the full mode-matching method.

An area discontinuity is formed between two ducts of different diameters. Even in the plane wave regime, evanescent higher-order modes are formed at the area discontinuity, and the effects of these evanescent modes can be modeled by adding a length correction to the smaller-diameter duct. In this appendix, the subscript 1 refers to the larger-diameter duct, and the subscript 2 refers to the smaller-diameter duct, so a_1 is the radius of the larger duct, and a_2 is the radius of the smaller duct.

F.1 Peat's Length Correction

The expression for the length correction at an area discontinuity developed by Peat [70] is given by

$$\frac{\Delta L_{1,2}}{a_2} = \frac{8}{3\pi} \sum_{i=0}^{5} \sum_{j=0}^{5} A_{ij} T_i \left(\frac{2ka_1 - 3.9}{3.3} \right) T_j \left(\frac{2(a_2/a_1) - 1.1}{0.9} \right) \tag{F.1}$$

for Helmholtz numbers $0.3 \leq ka_1 \leq 3.6$ and radius ratios $0.1 \leq a_2/a_1 \leq 1$. There is no significant variation in the length correction for Helmholtz numbers in the range $0 \leq ka_1 \leq 0.3$ according to Peat. Eq. (C.17) is a finite approximation of a double Chebyshev series,

where T_i and T_j are Chebyshev polynomials of the first kind of degree i and j, respectively. Chebyshev polynomials of the first kind are defined recursively by

$$\begin{aligned} T_0(x) &= 1 \\ T_1(x) &= x \\ T_{n+1}(x) &= 2xT_n(x) - T_{n-1}(x), \quad n \geq 1 \end{aligned} \tag{F.2}$$

The coefficients A_{ij} are listed in Table F.1 for a simple area discontinuity in which $L_e = 0$, and the coefficients A_{ij} are listed in Table F.2 for an extended inlet or outlet with an extension length of $L_e/a_1 \geq 0.5$. The coefficients A_{i0} and A_{0j} are multiplied by one-half when performing a double Chebyshev series summation, and A_{00} is multiplied by one-fourth [163].

Table F.1: Coefficients of the double Chebyshev series for a simple area discontinuity (Ref. [70]).

i \ j	0	1	2	3	4	5
0	1.7263	−1.0062	0.0476	0.1115	−0.0167	0.0009
1	0.2549	−0.1287	−0.0419	0.0579	−0.0104	−0.0049
2	0.1298	−0.0659	−0.0215	0.0316	−0.0062	−0.0033
3	0.0602	−0.0311	−0.0097	0.0157	−0.0034	−0.0019
4	0.0310	−0.0162	−0.0046	0.0083	−0.0020	−0.0010
5	0.0155	−0.0082	−0.0022	0.0043	−0.0011	−0.0006

For short extended inlets and outlets with extension lengths in the range $0 \leq L_e/a_1 \leq 0.5$, the end correction is given by [164]

$$\Delta L_{1,2} = \Delta L_{1,2}\big|_{(L_e/a_1=0.5)} - \left(\Delta L_{1,2}\big|_{(L_e/a_1=0.5)} - \Delta L_{1,2}\big|_{(L_e/a_1=0)}\right)^{-\xi L/a_1} \tag{F.3}$$

where $\Delta L_{1,2}\big|_{(L_e/a_1=0)}$ is the length correction for a simple area discontinuity ($L_e/a_1 = 0$), $\Delta L_{1,2}\big|_{(L_e/a_1=0.5)}$ is the length correction for an extended inlet or outlet with $L_e/a_1 = 0.5$,

Table F.2: Coefficients of the double Chebyshev series for an extended inlet or outlet with an extension length of $L_e/a_1 \geq 0.5$ (Ref. [164]).

i \ j	0	1	2	3	4	5
0	1.3402	−0.7586	0.0198	0.0651	0.0041	−0.0001
1	0.1402	−0.0641	−0.0284	0.0230	0.0017	−0.0016
2	0.0652	−0.0305	−0.0119	0.0098	0.0013	−0.0007
3	0.0271	−0.0132	−0.0040	0.0034	0.0008	−0.0003
4	0.0129	−0.0065	−0.0015	0.0014	0.0004	−0.0001
5	0.0061	−0.0032	−0.0005	0.0005	0.0002	0.0000

and

$$\xi = 16.9 - 40.4(a_2/a_1) + 73.8(a_2/a_1)^2 - 1.2ka_1 - 1.3ka_2 \tag{F.4}$$

F.2 Ando's Length Correction

Ando [25] computed the effect of wall thickness on the end correction of a pipe radiating into the ambient air. Figure F.1 shows the measured end correction normalized by the inner radius of the pipe, $\Delta L/a_{\text{in}}$, as a function of the Helmholtz number in terms of the outer radius, ka_{out}, for several different wall thickness ratios, $a_{\text{out}}/a_{\text{in}}$.

In the present work, the effect of the wall thickness on the end correction of a pipe is modeled using a multiplicative factor obtained from the data plotted in Figure F.1. It is assumed that this factor is the same for an extended inlet or outlet within a duct as for a pipe radiating into the ambient air. Under this assumption, the end correction of an extended inlet or outlet with finite wall thickness is given by

$$\Delta L_{1,2} = F(ka_{\text{out}}, a_{\text{out}}/a_{\text{in}})\Delta L_{1,2}\big|_{(a_{\text{out}}/a_{\text{in}}=1)} \tag{F.5}$$

where $\Delta L_{1,2}\big|_{(a_{\text{out}}/a_{\text{in}}=1)}$ is the end correction for zero wall thickness given by Peat [70, 164], and F is the multiplicative factor that accounts for the effect of the wall thickness.

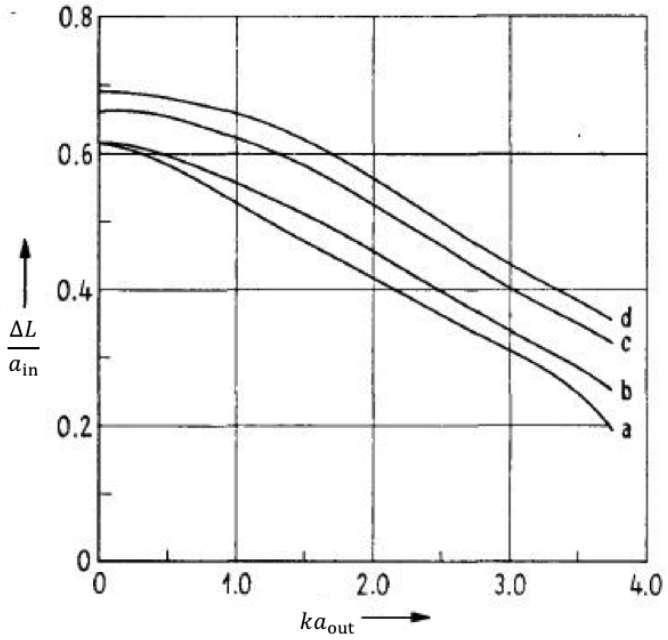

Figure F.1: End correction as a function of Helmholtz number for wall thickness ratios $a_{\text{out}}/a_{\text{in}}$ of (a) 1.00, (b) 0.85, (c) 0.75, and (d) 0.70 (Ref. [25]).

The results obtained by Ando [25] were extracted from the plot shown in Figure F.1 using a computer program, and the end corrections for each wall thickness ratio were normalized by the end correction for a wall thickness ratio of $a_{\text{out}}/a_{\text{in}} = 1$ to produce the multiplicative factor. The multiplicative factor at any Helmholtz number and wall thickness ratio is calculated by interpolating (or extrapolating) the data in Table F.3.

Table F.3: Multiplicative factor for the effect of wall thickness on the end correction of a pipe as a function of the Helmholtz number and wall thickness ratio (extracted from Ref. [25]).

ka_{out}	$a_{\text{out}}/a_{\text{in}}$			
	1.0	0.85	0.75	0.70
0.0	1.0	1.0004	1.0748	1.1243
0.1	1.0	1.0059	1.0856	1.1300
0.2	1.0	1.0118	1.0934	1.1367
0.3	1.0	1.0158	1.1066	1.1488
0.4	1.0	1.0191	1.1146	1.1583
0.5	1.0	1.0243	1.1260	1.1713
0.6	1.0	1.0298	1.1347	1.1845
0.7	1.0	1.0353	1.1425	1.1973
0.8	1.0	1.0419	1.1543	1.2144
0.9	1.0	1.0489	1.1668	1.2324
1.0	1.0	1.0562	1.1797	1.2479
1.1	1.0	1.0620	1.1933	1.2633
1.2	1.0	1.0672	1.2046	1.2794
1.3	1.0	1.0727	1.2149	1.2921
1.4	1.0	1.0780	1.2258	1.3036
1.5	1.0	1.0821	1.2334	1.3156
1.6	1.0	1.0860	1.2405	1.3252
1.7	1.0	1.0892	1.2459	1.3324
1.8	1.0	1.0924	1.2499	1.3398
1.9	1.0	1.0942	1.2540	1.3465
2.0	1.0	1.0946	1.2583	1.3523
2.1	1.0	1.0950	1.2628	1.3583
2.2	1.0	1.0953	1.2672	1.3637
2.3	1.0	1.0956	1.2719	1.3677
2.4	1.0	1.0959	1.2769	1.3720
2.5	1.0	1.0963	1.2822	1.3765
2.6	1.0	1.0968	1.2868	1.3813
2.7	1.0	1.0972	1.2912	1.3886
2.8	1.0	1.0977	1.2959	1.3974
2.9	1.0	1.0977	1.2995	1.4055
3.0	1.0	1.0985	1.3027	1.4133
3.1	1.0	1.0993	1.3074	1.4230
3.2	1.0	1.1041	1.3218	1.4416
3.3	1.0	1.1107	1.3391	1.4637
3.4	1.0	1.1299	1.3724	1.5036
3.5	1.0	1.1527	1.4158	1.5533
3.6	1.0	1.1949	1.4930	1.6388
3.7	1.0	1.2571	1.5999	1.7576

APPENDIX G

DERIVATION OF THE MODE NORMALIZATION FACTOR

In this appendix, the expression for the mode normalization factor, C_{mn}, given by Eq. (3.11) is derived based on the orthonormality of the mode shape functions. The mode shape function describes the variation of the acoustic pressure across the cross-section of the duct. The mode shape functions for a duct with a circular cross-section are given by Eq. (3.8) and are repeated here:

$$\Psi_{mn}(r,\theta) = C_{mn} J_m(\kappa_{mn} r) e^{-jm\theta} \tag{G.1}$$

where C_{mn} is a normalization factor, J_m is the Bessel function of the first kind of order m, and κ_{mn} is the eigenvalue of mode (m,n). The eigenvalues κ_{mn} are given by the roots of Eq. (3.9), which is repeated here:

$$J'_m(\kappa_{mn} a) = 0 \tag{G.2}$$

where J'_m is the first derivative of the Bessel function of the first kind of order m, and a is the radius of the duct. The normalization factor is defined in Eq. (3.10), which is also repeated here:

$$\frac{1}{S}\int_S \Psi_{mn}\Psi^*_{\mu\nu} dS = \begin{cases} 1, & (m,n) = (\mu,\nu) \\ 0, & (m,n) \neq (\mu,\nu) \end{cases} \tag{G.3}$$

where S is the cross-sectional area of the duct, and $*$ denotes the complex conjugate.

The value of the normalization factor for mode (m,n) is calculated by substituting Eq. (G.1) into Eq. (G.3) for the case $(m,n) = (\mu,\nu)$, which yields

$$\frac{1}{\pi a^2}\int_0^{2\pi}\int_0^a C_{mn}^2 J_m^2(\kappa_{mn} r) e^{jm\theta} e^{-jm\theta} r\, dr\, d\theta = 1 \tag{G.4}$$

in polar coordinates. The cross-sectional area of the circular duct is $S = \pi a^2$. Since the product of the exponential terms in Eq. (G.4) is unity, the integrand is constant with respect to the azimuthal coordinate θ, and Eq. (G.4) simplifies to

$$\frac{2C_{mn}^2}{a^2} \int_0^a J_m^2(\kappa_{mn} r) r dr = 1 \tag{G.5}$$

The solution to the definite integral in Eq. (G.5) is obtained using a table of integrals. From the *Handbook of Mathematical Functions* compiled by Abramowitz and Stegun [169, Eq. (11.4.5)],

$$\int_0^1 J_m(\alpha_\mu t) J_m(\alpha_\nu t) t dt = \begin{cases} 0, & (\mu \neq \nu,\, m > -1) \\ \frac{1}{2} J_m'(\alpha_\mu)^2, & (\mu = \nu,\, c_2 = 0,\, m > -1) \\ \frac{1}{2\alpha_\mu^2} \left(\frac{c_1^2}{c_2^2} + \alpha_\mu^2 - m^2 \right) J_m^2(\alpha_\mu), & (\mu = \nu,\, c_2 \neq 0,\, m \geq -1) \end{cases} \tag{G.6}$$

where $\{\alpha_1, \alpha_2, ...\}$ are the positive roots of the equation

$$c_1 J_m(x) + c_2 x J_m'(x) = 0 \tag{G.7}$$

and c_1 and c_2 are real constants.

The definite integral in Eq. (G.5) has different limits of integration than the definite integral on the left-hand side of Eq. (G.6). To change the limits of integration in Eq. (G.5), a normalized radius is defined as $r' = r/a$. Note that $r dr = a^2 r' dr'$, so Eq. (G.5) can be rewritten in terms of the normalized radius as

$$2C_{mn}^2 \int_0^1 J_m^2(\kappa_{mn} a r') r' dr' = 1 \tag{G.8}$$

and the limits of integration now match those of Eq. (G.6). The integrand on the left-hand side of Eq. (G.6) is of the same form as the integrand in Eq. (G.8) if $\alpha_\mu = \alpha_\nu = \kappa_{mn} a$,

which implies that $\mu = \nu$ in Eq. (G.8). The values $\kappa_{mn}a$ are the positive roots of Eq. (G.2), and the values α_μ are the positive roots of Eq. (G.7). These equations are of the same form if $c_1 = 0$ and $c_2 \neq 0$ in Eq. (G.7).

Since $\mu = \nu$ and $c_2 \neq 0$, the conditions for the third solution in Eq. (G.6) are satisfied except for $m \geq -1$. In general, the circumferential mode order, m, can be positive or negative. However, the circumferential mode order is always an integer, and the identity $J_{-m}(x) = (-1)^m J_m(x)$ is satisfied for Bessel functions of integer orders [170, Eq. (9.1.5)]. Thus, $J_m^2(x) = J_{-m}^2(x)$, so the normalization factor of the (m, n) mode is identical to the normalization factor of the $(-m, n)$ mode, and Eq. (G.8) can be evaluated for $m \geq 0$ only. All three conditions for the third solution in Eq. (G.6) are now satisfied, and the solution to the definite integral is substituted into Eq. (G.8) to produce

$$\frac{C_{mn}^2}{\kappa_{mn}a}\left(\kappa_{mn}a - m^2\right) J_m^2(\kappa_{mn}a) = 1 \tag{G.9}$$

The solution for the mode normalization factor is then

$$C_{mn} = \left[\left(1 - \left(\frac{m}{\kappa_{mn}a}\right)^2\right) J_m^2(\kappa_{mn}a)\right]^{-1/2} \tag{G.10}$$

REFERENCES

[1] D. T. Harrje and F. H. Reardon, *Liquid Propellant Rocket Combustion Instability*. Washington, D.C.: National Aeronautics and Space Administration, 1972.

[2] F. E. C. Culick and V. Yang, "Overview of combustion instabilities in liquid-propellant rocket engines," in *Liquid Rocket Engine Combustion Instability*, V. Yang and W. Anderson, Eds., ser. Progress in Astronautics and Aeronautics. Washington, D.C.: AIAA, 1995, vol. 169, ch. 1, pp. 3–37.

[3] J. C. Oefelein and V. Yang, "Comprehensive review of liquid-propellant combustion instabilities in F-1 engines," *Journal of Propulsion and Power*, vol. 9, no. 5, pp. 657–677, 1993.

[4] C. L. Oberg, "Combustion stabilization with acoustic cavities," *Journal of Spacecraft and Rockets*, vol. 8, no. 12, pp. 1220–1225, 1971.

[5] R. B. Keller Jr., "Liquid rocket engine combustion stabilization devices," National Aeronautics and Space Administration, Report NASA-SP-8113, 1974.

[6] E. Laudien, R. Pongratz, R. Pierro, and D. Preclik, "Experimental procedures aiding the design of acoustic cavities," in *Liquid Rocket Engine Combustion Instability*, V. Yang and W. Anderson, Eds., ser. Progress in Astronautics and Aeronautics. Washington, D.C.: AIAA, 1995, vol. 169, ch. 14, pp. 377–399.

[7] D. Zhao and X. Y. Li, "A review of acoustic dampers applied to combustion chambers in aerospace industry," *Progress in Aerospace Sciences*, vol. 74, pp. 114–130, 2015.

[8] H. Kim and C. H. Sohn, "Experimental study of the role of gas-liquid scheme injector as an acoustic resonator in a combustion chamber," *Journal of Mechanical Science and Technology*, vol. 20, no. 6, pp. 896–904, 2006.

[9] C. H. Sohn, I. S. Park, S.-K. Kim, and H. J. Kim, "Acoustic tuning of gas-liquid scheme injectors for acoustic damping in a combustion chamber of a liquid rocket engine," *Journal of Sound and Vibration*, vol. 304, no. 3–5, pp. 793–810, 2007.

[10] C. H. Sohn and I. S. Park, "Effects of inlet blockage of gas-liquid scheme injector on acoustic tuning for acoustic damping in a combustion chamber," *Journal of Mechanical Science and Technology*, vol. 22, no. 2, pp. 330–337, 2008.

[11] J. H. Park and C. H. Sohn, "On optimal design of half-wave resonators for acoustic damping in an enclosure," *Journal of Sound and Vibration*, vol. 319, no. 3–5, pp. 807–821, 2009.

[12] S. H. Kim, Y. J. Kim, and C. H. Sohn, "Acoustic damping of gas-liquid scheme injectors with a recess in a subscale combustor," *Journal of Mechanical Science and Technology*, vol. 28, no. 9, pp. 3813–3823, 2014.

[13] S. V. Lympany and K. K. Ahuja, "Sound damping by injector tubes and surrounding ducting used in liquid rocket combustors," 22nd AIAA/CEAS Aeroacoustics Conference, Lyon, France, Conference Paper, 2016.

[14] H. Kim and C. H. Sohn, "Experimental study of acoustic damping induced by gas-liquid scheme injectors in a combustion chamber," *Journal of Mechanical Science and Technology*, vol. 21, no. 1, pp. 153–161, 2007.

[15] S. V. Lympany and K. K. Ahuja, "Acoustic damping of propellant injectors with through-flow in liquid rocket combustors," 23rd AIAA/CEAS Aeroacoustics Conference, Denver, Colorado, Conference Paper, 2017.

[16] I. S. Park and C. H. Sohn, "Nonlinear acoustic damping induced by a half-wave resonator in an acoustic chamber," *Aerospace Science and Technology*, vol. 14, no. 6, pp. 442–450, 2010.

[17] T. L. Acker and C. E. Mitchell, "Combustion zone—acoustic cavity interactions in rocket combustors," *Journal of Propulsion and Power*, vol. 10, no. 2, pp. 235–243, 1994.

[18] G. Searby, M. Habiballah, A. Nicole, and E. Laroche, "Prediction of the efficiency of acoustic damping cavities," *Journal of Propulsion and Power*, vol. 24, no. 3, pp. 516–523, 2008.

[19] S.-K. Kim, H. S. Choi, H. J. Kim, Y. S. Ko, and C. H. Sohn, "Finite element analysis for acoustic characteristics of combustion stabilization devices," *Aerospace Science and Technology*, vol. 42, pp. 229–240, 2015.

[20] L. E. Kinsler, A. R. Frey, A. B. Coppens, and J. V. Sanders, *Fundamentals of Acoustics*, 2nd. John Wiley and Sons, Inc., 1999.

[21] Y. Nomura, I. Yamamura, and S. Inawashiro, "On the acoustic radiation from a flanged circular pipe," *Journal of the Physical Society of Japan*, vol. 15, no. 3, pp. 510–517, 1960.

[22] M. C. A. M. Peters, A. Hirschberg, A. J. Reijnen, and A. P. J. Wijnands, "Damping and reflection coefficient measurements for an open pipe at low Mach and low Helmholtz numbers," *Journal of Fluid Mechanics*, vol. 256, pp. 499–534, 1993.

[23] H. Levine and J. Schwinger, "On the radiation of sound from an unflanged circular pipe," *Physical Review*, vol. 73, no. 4, pp. 383–406, 1948.

[24] P. O. A. L. Davies, "Practical flow duct acoustics," *Journal of Sound and Vibration*, vol. 124, no. 1, pp. 91–115, 1988.

[25] Y. Ando, "On the sound radiation from semi-infinite circular pipe of certain wall thickness," *Acta Acustica united with Acustica*, vol. 22, no. 4, pp. 219–225, 1969.

[26] C. H. Sohn and J. H. Park, "A comparative study on acoustic damping induced by half-wave, quarter-wave, and Helmholtz resonators," *Aerospace Science and Technology*, vol. 15, no. 8, pp. 606–614, 2011.

[27] D. T. Blackstock, *Fundamentals of Physical Acoustics*. New York: John Wiley and Sons, Inc., 2000.

[28] H. J. Kim, J. P. Cha, J. K. Song, and Y. S. Ko, "Geometric and number effect on damping capacity of Helmholtz resonators in a model chamber," *Journal of Sound and Vibration*, vol. 329, no. 16, pp. 3266–3279, 2010.

[29] M. Oschwald, Z. Farago, G. Searby, and F. Cheuret, "Resonance frequencies and damping of a combustor acoustically coupled to an absorber," *Journal of Propulsion and Power*, vol. 24, no. 3, pp. 524–533, 2008.

[30] U. Ingard, "On the theory and design of acoustic resonators," *Journal of the Acoustical Society of America*, vol. 25, no. 6, pp. 1037–1061, 1953.

[31] A. Selamet and Z. L. Ji, "Circular asymmetric Helmholtz resonators," *Journal of the Acoustical Society of America*, vol. 107, no. 5, pp. 2360–2369, 2000.

[32] U. Ingard and V. K. Singhal, "Sound attenuation in turbulent pipe flow," *The Journal of the Acoustical Society of America*, vol. 55, no. 3, pp. 535–538, 1974.

[33] U. Ingard and V. K. Singhal, "Effect of flow on the acoustic resonances of an open-ended duct," *Journal of the Acoustical Society of America*, vol. 58, no. 4, pp. 788–793, 1975.

[34] D. Ronneberger and C. D. Ahrens, "Wall shear stress caused by small amplitude perturbations of turbulent boundary-layer flow: an experimental investigation," *Journal of Fluid Mechanics*, vol. 83, no. 3, pp. 433–464, 1977.

[35] M. S. Howe, "The interaction of sound with low Mach number wall turbulence, with application to sound propagation in turbulent pipe flow," *Journal of Fluid Mechanics*, vol. 94, no. 4, pp. 729–744, 1979.

[36] M. S. Howe, "On the absorption of sound by turbulence and other hydrodynamic flows," *IMA Journal of Applied Mathematics*, vol. 32, pp. 187–209, 1984.

[37] M. S. Howe, "The damping of sound by wall turbulent shear layers," *Journal of the Acoustical Society of America*, vol. 98, no. 3, pp. 1723–1730, 1995.

[38] S. Allam and M. Åbom, "Investigation of damping and radiation using full plane wave decomposition in ducts," *Journal of Sound and Vibration*, vol. 292, no. 3–5, pp. 519–534, 2006.

[39] E. Dokumaci, "On attenuation of plane sound waves in turbulent mean flow," *Journal of Sound and Vibration*, vol. 320, no. 4–5, pp. 1131–1136, 2009.

[40] M. Knutsson and M. Åbom, "The effect of turbulence damping on acoustic wave propagation in tubes," *Journal of Sound and Vibration*, vol. 329, no. 22, pp. 4719–4739, 2010.

[41] C. Lahiri, K. Knobloch, F. Bake, and L. Enghardt, "Attenuation of sound in wide ducts with flow at elevated pressure and temperature," *Journal of Sound and Vibration*, vol. 333, no. 15, pp. 3440–3458, 2014.

[42] D. W. Bechert, "Sound absorption caused by vorticity shedding, demonstrated with a jet flow," *Journal of Sound and Vibration*, vol. 70, no. 3, pp. 389–405, 1980.

[43] M. Salikuddin and K. K. Ahuja, "Acoustic power dissipation on radiation through duct terminations: experiments," *Journal of Sound and Vibration*, vol. 91, no. 4, pp. 479–502, 1983.

[44] C. L. Morfey, "Acoustic energy in non-uniform flows," *Journal of Sound and Vibration*, vol. 14, no. 2, pp. 159–170, 1971.

[45] M. S. Howe, "Contributions to the theory of aerodynamic sound, with application to excess jet noise and the theory of the flute," *Journal of Fluid Mechanics*, vol. 71, no. 4, pp. 625–673, 1975.

[46] R. M. Munt, "The interaction of sound with a subsonic jet issuing from a semi-infinite cylindrical pipe," *Journal of Fluid Mechanics*, vol. 83, no. 4, pp. 609–640, 1977.

[47] R. M. Munt, "Acoustic transmission properties of a jet pipe with subsonic jet flow: I. the cold jet reflection coefficient.," *Journal of Sound and Vibration*, vol. 142, no. 3, pp. 413–436, 1990.

[48] A. M. Cargill, "The radiation of high frequency sound out of a jet pipe," *Journal of Sound and Vibration*, vol. 83, no. 3, pp. 313–337, 1982.

[49] A. M. Cargill, "Low frequency acoustic radiation from a jet pipe—a second order theory," *Journal of Sound and Vibration*, vol. 83, no. 3, pp. 339–354, 1982.

[50] S. W. Rienstra, "A small strouhal number analysis for acoustic wave—jet flow-pipe interaction," *Journal of Sound and Vibration*, vol. 86, no. 4, pp. 539–556, 1983.

[51] D. G. Crighton, "The kutta condition in unsteady flow," *Annual Review of Fluid Mechanics*, vol. 17, pp. 411–445, 1985.

[52] M. S. Howe, "Attenuation of sound in a low Mach number nozzle flow," *Journal of Fluid Mechanics*, vol. 91, no. 2, pp. 209–229, 1979.

[53] M. S. Howe, "The dissipation of sound at an edge," *Journal of Sound and Vibration*, vol. 70, no. 3, pp. 407–411, 1980.

[54] U. Ingard and H. Ising, "Acoustic nonlinearity of an orifice," *Journal of the Acoustical Society of America*, vol. 42, no. 1, pp. 6–17, 1967.

[55] U. Ingard, "Absorption characteristics of nonlinear acoustic resonators," *Journal of the Acoustical Society of America*, vol. 44, no. 4, pp. 1155–1156, 1968.

[56] K. K. Ahuja, R. J. Gaeta, and M. D'Agostino, "Acoustic absorption characteristics of an orifice with a mean bias flow," National Aeronautics and Space Administration, GTRI Report A5004/2000-4, 2000.

[57] D. Yang and A. S. Morgans, "A semi-analytical model for the acoustic impedance of finite length circular holes with mean flow," *Journal of Sound and Vibration*, vol. 384, pp. 294–311, 2016.

[58] C. Lahiri and F. Bake, "A review of bias flow liners for acoustic damping in gas turbine combustors," *Journal of Sound and Vibration*, vol. 400, pp. 564–605, 2017.

[59] A. Cummings, "Sound transmission at sudden area expansions in circular ducts, with superimposed mean flow," *Journal of Sound and Vibration*, vol. 38, no. 1, pp. 149–155, 1975.

[60] A. Cummings and H. Haddad, "Sudden area changes in flow ducts: further thoughts," *Journal of Sound and Vibration*, vol. 54, no. 4, pp. 611–612, 1977.

[61] S. Boij and B. Nilsson, "Reflection of sound at area expansions in a flow duct," *Journal of Sound and Vibration*, vol. 260, no. 3, pp. 477–498, 2003.

[62] S. Boij and B. Nilsson, "Scattering and absorption of sound at flow duct expansions," *Journal of Sound and Vibration*, vol. 289, no. 3, pp. 577–594, 2006.

[63] S. Boij, "Flow effects on the acoustic end correction of a sudden in-duct area expansion," *Journal of the Acoustical Society of America*, vol. 126, no. 3, pp. 995–1004, 2009.

[64] G. Kooijman, P. Testud, Y. Aurégan, and A. Hirschberg, "Multimodal method for scattering of sound at a sudden area expansion in a duct with subsonic flow," *Journal of Sound and Vibration*, vol. 310, no. 4–5, pp. 902–922, 2008.

[65] A. Kierkegaard, S. Boij, and G. Efraimsson, "Simulations of the scattering of sound waves at a sudden area expansion," *Journal of Sound and Vibration*, vol. 331, no. 5, pp. 1068–1083, 2012.

[66] H. Bodén, L. Zhou, J. A. Cordioli, A. A. Medeiros, and A. M. N. Spillere, "On the effect of flow direction on impedance eduction results," 22nd AIAA/CEAS Aeroacoustics Conference, Lyon, France, Conference Paper, 2016.

[67] A. Scarpato, N. Tran, S. Ducruix, and T. Schuller, "Modeling the damping properties of perforated screens traversed by a bias flow and backed by a cavity at low strouhal number," *Journal of Sound and Vibration*, vol. 331, pp. 276–290, 2012.

[68] I. D. J. Dupère and A. P. Dowling, "The absorption of sound near abrupt axisymmetric area expansions," *Journal of Sound and Vibration*, vol. 239, no. 4, pp. 709–730, 2001.

[69] P. O. A. L. Davies, "Plane wave reflection at flow intakes," *Journal of Sound and Vibration*, vol. 115, no. 3, pp. 560–564, 1987.

[70] K. S. Peat, "The acoustical impedance at discontinuities of ducts in the presence of a mean flow," *Journal of Sound and Vibration*, vol. 127, no. 1, pp. 123–132, 1988.

[71] D Ronneberger, "Theoretische und experimentelle untersuchung der schallausbreitung durch querschnittssprünge und lochplatten in strömungskanälen (theoretical and experimental investigation of sound propagation at sudden area changes and diaphragms in flow ducts)," DFG-Abschlussbericht, Drittes Physikalisches Institut der Universität Göttingen, Tech. Rep., 1987.

[72] C. H. Sohn and H. C. Cho, "Numerical analysis of acoustic characteristics in gas turbine combustor with spatial non-homogeneity," *KSME International Journal*, vol. 18, no. 8, pp. 1461–1469, 2004.

[73] D. A. Bies and O. B. Wilson Jr., "Acoustic impedance of a Helmholtz resonator at very high amplitude," *Journal of the Acoustical Society of America*, vol. 29, no. 6, pp. 711–714, 1957.

[74] C. Lahiri, K. Knobloch, F. Bake, and L. Enghardt, "Acoustic measurements of perforated liners in hot and pressurized flow," ASME Turbo Expo: Turbine Technical Conference and Exposition, San Antonio, Texas, Conference Paper, 2013.

[75] P. E. Doak and P. G. Vaidya, "Attenuation of plane wave and higher order mode sound propagation in lined ducts," *Journal of Sound and Vibration*, vol. 12, no. 2, pp. 201–224, 1970.

[76] L. J. Sivian, "Acoustic impedance of small orifices," *Journal of the Acoustical Society of America*, vol. 7, no. 2, pp. 94–101, 1935.

[77] U. Ingard and S. Labate, "Acoustic circulation effects and the nonlinear impedance of orifices," *Journal of the Acoustical Society of America*, vol. 22, no. 2, pp. 211–218, 1950.

[78] G. B. Thurston and C. E. Martin Jr., "Periodic fluid flow through circular orifices," *Journal of the Acoustical Society of America*, vol. 25, no. 1, pp. 26–31, 1953.

[79] G. B. Thurston, L. E. Hargrove, and B. D. Cook, "Nonlinear properties of circular orifices," *Journal of the Acoustical Society of America*, vol. 29, no. 9, pp. 992–1001, 1957.

[80] R. L. Panton and A. L. Goldman, "Correlation of nonlinear orifice impedance," *Journal of the Acoustical Society of America*, vol. 60, no. 6, pp. 1390–1396, 1977.

[81] B. Sturtevant, "Nonlinear gas oscillations in pipes. part 2. experiment," *Journal of Fluid Mechanics*, vol. 63, no. 1, pp. 97–120, 1974.

[82] T. H. Melling, "The acoustic impedance of perforates at medium and high sound pressure levels," *Journal of Sound and Vibration*, vol. 29, no. 1, pp. 1–65, 1973.

[83] K. K. Ahuja and J. Gaeta R. J., "Active control of liner impedance by varying perforate orifice geometry," Langley Research Center, Report NASA CR-2000-210633, 2000.

[84] K. H. Förner, "Nonlinear aeroacoustics characterization of resonators," Thesis, 2017.

[85] K. Förner, M. A. Temiz, W. Polifke, I. L. Arteaga, and A. Hirschberg, "On the nonlinear influence of the edge geometry on vortex shedding in Helmholtz resonators," The 22nd International Congress on Sound and Vibration, Conference Paper, 2015.

[86] K. Förner, J. Tournadre, P. Martínez-Lera, and W. Polifke, "Scattering to higher harmonics for quarter-wave and Helmholtz resonators," *AIAA Journal*, vol. 55, no. 4, pp. 1194–1204, 2017.

[87] J. H. M. Disselhorst and L. Van Wijngaarden, "Flow in the exit of open pipes during acoustic resonance," *Journal of Fluid Mechanics*, vol. 99, no. 2, pp. 293–319, 1980.

[88] M. C. A. M. Peters and A. Hirschberg, "Acoustically induced periodic vortex shedding at sharp edged open channel ends: simple vortex models," *Journal of Sound and Vibration*, vol. 161, no. 2, pp. 281–299, 1993.

[89] M. Atig, J.-P. Dalmont, and J. Gilbert, "Termination impedance of open-ended cylindrical tubes at high sound pressure level," *Comptes Rendus - Academie des Sciences Paris Serie 2b Mecanique*, vol. 332, no. 4, pp. 299–304, 2004.

[90] D. J. Skulina, "Study of nonlinear acoustic flows at the open end of a tube using particle image velocimetry," Thesis, 2005.

[91] R. Macdonald, D. Skulina, M. Campbell, J.-C. Valiere, D. Marx, and H. Bailliet, "PIV and POD applied to high amplitude acoustic flow at a tube termination," 10ème Congrès Français d'Acoustique, Lyon, France, Conference Paper, 2010.

[92] D. Marx, H. Bailliet, and J.-C. Valière, "Analysis of the acoustic flow at an abrupt change in section of an acoustic waveguide using particle image velocimetry and proper orthogonal decomposition," *Acta Acustica united with Acustica*, vol. 94, no. 1, pp. 54–65, 2008.

[93] J. M. Buick, M. Atig, D. J. Skulina, D. M. Campbell, J. P. Dalmont, and J. Gilbert, "Investigation of non-linear acoustic losses at the open end of a tube," *Journal of the Acoustical Society of America*, vol. 129, no. 3, pp. 1261–1272, 2011.

[94] A. Cummings and W. Eversman, "High amplitude acoustic transmission through duct terminations: theory," *Journal of Sound and Vibration*, vol. 91, no. 4, pp. 503–518, 1983.

[95] A. Cummings, "Acoustic nonlinearities and power losses at orifices," *AIAA Journal*, vol. 22, no. 6, pp. 786–792, 1984.

[96] M. Salikuddin and W. H. Brown, "Non-linear effects in finite amplitude wave propagation through ducts and nozzles," *Journal of Sound and Vibration*, vol. 106, no. 1, pp. 71–106, 1986.

[97] C. K. W. Tam, K. A. Kurbatskii, K. K. Ahuja, and R. J. Gaeta, "A numerical and experimental investigation of the dissipation mechanisms of resonant acoustic liners," *Journal of Sound and Vibration*, vol. 245, no. 3, pp. 545–557, 2001.

[98] B. Sturtevant and J. J. Keller, "Subharmonic nonlinear acoustic resonances in open tubes. part II: experimental investigation of open-end boundary condition," *Journal of Applied Mathematics and Physics*, vol. 29, no. 3, pp. 473–485, 1978.

[99] P. K. Tang, D. T. Harrje, and W. A. Sirignano, "Experimental verification of the energy dissipation mechanism in acoustic dampers," *Journal of Sound and Vibration*, vol. 26, no. 2, pp. 263–267, 1973.

[100] W. Chester, "Resonant oscillations of a gas in an open-ended tube," *Proceedings of the Royal Society A: Mathematical, Physical and Engineering Sciences*, vol. 377, no. 1771, pp. 449–467, 1981.

[101] L. Van Wijngaarden, "On the oscillations near and at resonance in open pipes," *Journal of Engineering Mathematics*, vol. 2, no. 3, pp. 225–240, 1968.

[102] Y. A. Ilinskii, B. Lipkens, and E. A. Zabolotskaya, "Energy losses in an acoustical resonator," *The Journal of the Acoustical Society of America*, vol. 109, no. 5, pp. 1859–1870, 2001.

[103] T. Shimizu, D. Hori, S. Yoshida, S. Tachibana, S. Matsuyama, J. Shinjo, Y. Mizobuchi, and K. Kobayashi, "On acoustic damping of a cylindrical chamber in resonant modes," *Fluid Dynamics Research*, vol. 44, no. 4, pp. 1–20, 2012.

[104] J. Miles, "The reflection of sound due to a change in cross section of a circular tube," *Journal of the Acoustical Society of America*, vol. 16, no. 1, pp. 14–19, 1944.

[105] A. I. El-Sharkawy and A. H. Nayfeh, "Effect of an expansion chamber on the propagation of sound in circular ducts," *Journal of the Acoustical Society of America*, vol. 63, no. 3, pp. 667–674, 1978.

[106] J.-G. Ih and B.-H. Lee, "Analysis of higher-order mode effects in the circular expansion chamber with mean flow," *Journal of the Acoustical Society of America*, vol. 77, no. 4, pp. 1377–1388, 1985.

[107] M. Åbom, "Derivation of four-pole parameters including higher order mode effects for expansion chamber mufflers with extended inlet and outlet," *Journal of Sound and Vibration*, vol. 137, no. 3, pp. 403–418, 1990.

[108] L. J. Eriksson, "Effect of inlet/outlet locations on higher order modes in silencers," *Journal of the Acoustical Society of America*, vol. 72, no. 4, pp. 1208–1211, 1982.

[109] A. Selamet and Z. L. Ji, "Acoustic attenuation performance of circular expansion chambers with offset inlet/outlet: I. analytical approach," *Journal of Sound and Vibration*, vol. 213, no. 4, pp. 601–617, 1998.

[110] M. Åbom, "Modal decomposition in ducts based on transfer function measurements between microphone pairs," *Journal of Sound and Vibration*, vol. 135, no. 1, pp. 95–114, 1989.

[111] W. R. Watson and M. G. Jones, "Impedance eduction in ducts with higher-order modes and flow," 15th AIAA/CEAS Aeroacoustics Conference, Miami, Florida, Conference Paper, 2009.

[112] T. Schultz, L. N. Cattafesta III, and M. Sheplak, "Modal decomposition method for acoustic impedance testing in square ducts," *Journal of the Acoustical Society of America*, vol. 120, no. 6, pp. 3750–3758, 2006.

[113] M. Akoum and J. M. Ville, "Measurement of the reflection matrix of a discontinuity in a duct," *Journal of the Acoustical Society of America*, vol. 103, no. 5, pp. 2463–2468, 1998.

[114] A. Sitel, J.-M. Ville, and F. Foucart, "Multiload procedure to measure the acoustic scattering matrix of a duct discontinuity for higher order mode propagation conditions," *The Journal of the Acoustical Society of America*, vol. 120, no. 5, pp. 2478–2490, 2006.

[115] S. Sack, M. Åbom, and G. Efraimsson, "On acoustic multi-port characterisation including higher order modes," *Acta Acustica united with Acustica*, vol. 102, no. 5, pp. 834–850, 2016.

[116] C. L. Morfey, "Sound transmission and generation in ducts with flow," *Journal of Sound and Vibration*, vol. 14, no. 1, pp. 37–55, 1971.

[117] J. M. Tyler and T. G. Sofrin, "Axial flow compressor noise studies," SAE Technical Paper No. 620532, 1962.

[118] P. M. Morse and K. U. Ingard, *Theoretical Acoustics*. McGraw-Hill Inc., 1968.

[119] G. Kirchhoff, "Ueber den einfluss der wärmeleitung in einem gase auf die schallbewegung," *Annalen der Physik*, vol. 210, no. 6, pp. 177–193, 1868.

[120] G. Kirchhoff, "On the influence of thermal conduction in a gas on sound propagation," in, R. B. Lindsay, Ed., ser. Benchmark Papers in Acoustics. Dowden, Hutchinson & Ross, Stroudsburg, PA, 1974, vol. 4, ch. 1, pp. 7–19.

[121] C. Weng and F. Bake, "Analytical model for boundary layer attenuation of acoustic modes in rigid circular ducts with uniform flow," *Acta Acustica united with Acustica*, vol. 102, no. 6, pp. 1138–1141, 2016.

[122] R. E. Beatty Jr., "Boundary layer attenuation of higher order modes in rectangular and circular tubes," *Journal of the Acoustical Society of America*, vol. 22, no. 6, pp. 850–854, 1950.

[123] E. Dokumaci, "On the effect of viscosity and thermal conductivity on sound propagation in ducts: a re-visit to the classical theory with extensions for higher order modes and presence of mean flow," *Journal of Sound and Vibration*, vol. 333, no. 21, pp. 5583–5599, 2014.

[124] J. Y. Chung and D. A. Blaser, "Transfer function method of measuring in-duct acoustic properties. I. theory," *Journal of the Acoustical Society of America*, vol. 68, no. 3, pp. 907–913, 1980.

[125] C. J. Moore, "Measurement of radial and circumferential modes in annular and circular fan ducts," *Journal of Sound and Vibration*, vol. 62, no. 2, pp. 235–256, 1979.

[126] R. Penrose, "On best approximate solutions of linear matrix equations," *Mathematical Proceedings of the Cambridge Philosophical Society*, vol. 52, no. 1, pp. 17–19, 1956.

[127] J. Z. Hearon, "Generalized inverses and solutions of linear systems," *Journal of Research of the National Bureau of Standards—B. Mathematical Sciences*, vol. 72B, no. 4, pp. 303–308, 1968.

[128] M. Åbom, "Measurement of the scattering-matrix of acoustical two-ports," *Mechanical Systems and Signal Processing*, vol. 5, no. 2, pp. 89–104, 1991.

[129] M. L. Munjal and A. G. Doige, "Theory of a two source-location method for direct experimental evaluation of the four-pole parameters of an aeroacoustic element," *Journal of Sound and Vibration*, vol. 141, no. 2, pp. 323–333, 1990.

[130] M. Åbom, "A note on the experimental determination of acoustical two-port matrices," *Journal of Sound and Vibration*, vol. 155, no. 1, pp. 185–188, 1992.

[131] A. Holmberg, M. Åbom, and H. Bodén, "Accurate experimental two-port analysis of flow generated sound," *Journal of Sound and Vibration*, vol. 330, no. 26, pp. 6336–6354, 2011.

[132] C. Lahiri, "Acoustic performance of bias flow liners in gas turbine combustors," Thesis, 2014.

[133] K. Knobloch, C. Lahiri, L. Enghardt, F. Bake, and D. Peitsch, "Hot-Acoustic-Testrig (HAT) - a unique facility for thermoacoustic research," ASME Turbo Expo:

Turbine Technical Conference and Exposition, Vancouver, British Columbia, Canada, Conference Paper, 2011.

[134] E. R. Rademaker, S. T. Idzenga, H. N. Huisman, R. J. Nijboer, and S. L. Sarin, "A new facility for hot stream acoustic liner testing," National Aerospace Laboratory NLR, Amsterdam, The Netherlands, Report NLR-TP-2003-202, 2003.

[135] R. Kabral, H. Bodén, and T. Elnady, "Determination of liner impedance under high temperature and grazing flow conditions," 20th AIAA/CEAS Aeroacoustics Conference, Atlanta, Georgia, Conference Paper, 2014.

[136] C. H. Gerhold, R. H. Cabell, and M. C. Brown, "Development of an experimental rig for investigation of higher order modes in ducts," 12th AIAA/CEAS Aeroacoustics Conference, Cambridge, Massachusetts, Conference Paper, 2006.

[137] C. Gerhold, M. Jones, M. Brown, and B. Howerton, "Report on recent upgrades to the curved duct test rig at NASA Langley Research Center," 17th AIAA/CEAS Aeroacoustics Conference, Portland, Oregon, Conference Paper, 2011.

[138] A. Sitel, J.-M. Ville, and F. Foucart, "Experimental facility for measurement of acoustic transmission matrix and acoustic power dissipation of duct discontinuity in higher order modes propagation conditions," *Acta Acustica united with Acustica*, vol. 89, no. 4, pp. 586–594, 2003.

[139] D. A. Belsley, E. Kuh, and R. E. Welsch, *Regression Diagnostics: Identifying Influential Data and Sources of Collinearity*. New York: John Wiley and Sohns, Inc., 1980, pp. 100–104.

[140] "Standard test method for impedance and absorption of acoustical materials using a tube, two microphones and a digital frequency analysis system," ASTM International, Standard ASTM E1050-12, 2012.

[141] D. B. Hann and C. A. Greated, "Measurement of acoustic particle velocity using particle image velocimetry techniques," *Acta Acustica united with Acustica*, vol. 83, no. 2, pp. 354–358, 1997.

[142] D. B. Hann and C. A. Greated, "The measurement of flow velocity and acoustic particle velocity using particle-image velocimetry," *Measurement Science and Technology*, vol. 8, no. 12, pp. 1517–1522, 1997.

[143] D. Rockliff, "Application of particle image velocimetry to the measurement of nonlinear effects generated by high-intensity acoustic fields," Thesis, 2002.

[144] F. C. Karal, "The analogous acoustical impedance for discontinuities and constrictions of circular cross section," *Journal of the Acoustical Society of America*, vol. 25, no. 2, pp. 327–334, 1953.

[145] J. Kergomard and A. Garcia, "Simple discontinuities in acoustic waveguides at low frequencies: critical analysis and formulae," *Journal of Sound and Vibration*, vol. 114, no. 3, pp. 465–479, 1987.

[146] J. W. S. B. Rayleigh, *The Theory of Sound, Vol. 2*, 2nd. New York: MacMillan, 1896.

[147] S. Allam and M. Åbom, "A new type of muffler based on microperforated tubes," *Journal of Vibration and Acoustics*, vol. 133, no. 3, pp. 031 005–1–8, 2011.

[148] M. L. Munjal, *Acoustics of Ducts and Mufflers*, 2nd. West Sussex, United Kingdom: John Wiley & Sons, Inc., 2014.

[149] A. Glezer and M. Amitay, "Synthetic jets," *Annual Review of Fluid Mechanics*, vol. 34, pp. 503–529, 2002.

[150] A. Powell, "Theory of vortex sound," *Journal of the Acoustical Society of America*, vol. 36, no. 1, pp. 177–195, 1964.

[151] A. D. Pierce, *Acoustics: An Introduction to Its Physical Principles and Applications*. Melville, New York: Acoustical Society of America, 1989.

[152] L. Peerlings, "Methods and techniques for precise and accurate in-duct aero-acoustic measurements: application to the area expansion," Licentiate Thesis, 2015.

[153] H. Bodén, "One-sided multi-port techniques for characterisation of in-duct samples with nonlinear acoustic properties," *Journal of Sound and Vibration*, vol. 331, no. 13, pp. 3050–3067, 2012.

[154] P. Merkli and H. Thomann, "Transition to turbulence in oscillating pipe flow," *Journal of Fluid Mechanics*, vol. 68, no. 3, pp. 567–575, 1975.

[155] K. U. Ingard, *Notes on Acoustics*. Hingham, Massachusetts: Infinity Science Press, 2008.

[156] H. W. Coleman and W. G. Steele, *Experimentation and Uncertainty Analysis for Engineers*, 2nd. New York: John Wiley and Sons, Inc., 1999.

[157] H. Bodén and M. Åbom, "Influence of errors on the two-microphone method for measuring acoustic properties in ducts," *Journal of the Acoustical Society of America*, vol. 79, no. 2, pp. 541–549, 1986.

[158] M. Åbom and H. Bodén, "Error analysis of two-microphone measurements in ducts with flow," *Journal of the Acoustical Society of America*, vol. 83, no. 6, pp. 2429–2438, 1988.

[159] T. Schultz, M. Sheplak, and L. N. Cattafesta III, "Uncertainty analysis of the two-microphone method," *Journal of Sound and Vibration*, vol. 304, no. 1–2, pp. 91–109, 2007.

[160] T. Schultz, M. Sheplak, and L. N. Cattafesta III, "Application of multivariate uncertainty analysis to frequency response function estimates," *Journal of Sound and Vibration*, vol. 305, no. 1–2, pp. 116–133, 2007.

[161] C. Heuwinkel, L. Enghardt, and I. Röhle, "Experimental investigation of the acoustic damping of perforated liners with bias flow," 13th AIAA/CEAS Aeroacoustics Conference (28th AIAA Aeroacoustics Conference), Rome, Italy, Conference Paper, 2007.

[162] L. Peerlings, "Assessing precision and accuracy in acoustic scattering matrix measurements," Doctoral Thesis, 2015.

[163] N. K. Basu, "On double chebyshev series approximation," *SIAM Journal on Numerical Analysis*, vol. 10, no. 3, pp. 496–505, 1973.

[164] K. S. Peat, "The acoustical impedance at the junction of an extended inlet or outlet duct," *Journal of Sound and Vibration*, vol. 150, no. 1, pp. 101–110, 1991.

[165] A. J. Torregrosa, A. Broatch, R. Payri, and F. González, "Numerical estimation of end corrections in extended-duct and perforated-duct mufflers," *Journal of Vibration and Acoustics*, vol. 121, no. 3, pp. 302–308, 1999.

[166] Z. Kang and Z. Ji, "Acoustic length correction of duct extension into a cylindrical chamber," *Journal of Sound and Vibration*, vol. 310, no. 4, pp. 782–791, 2008.

[167] P. Chaitanya and M. L. Munjal, "Effect of wall thickness on the end corrections of the extended inlet and outlet of a double-tuned expansion chamber," *Applied Acoustics*, vol. 72, no. 1, pp. 65–70, 2011.

[168] H. Hudde and U. Letens, "Scattering matrix of a discontinuity with a nonrigid wall in a lossless circular duct," *Journal of the Acoustical Society of America*, vol. 78, no. 5, pp. 1826–1837, 1985.

[169] Y. L. Luke, "Integrals of bessel functions," in *Handbook of Mathematical Functions with Forumlas, Graphs, and Mathematical Tables*, M. Abramowitz and I. A. Stegun, Eds., 10th, ser. Applied Mathematics Series. Washington, D.C.: National Bureau of Standards, 1972, vol. 55, ch. 11, pp. 479–491.

[170] F. W. J. Olver, "Bessel functions of integer order," in *Handbook of Mathematical Functions with Forumlas, Graphs, and Mathematical Tables*, M. Abramowitz and I. A. Stegun, Eds., 10th, ser. Applied Mathematics Series. Washington, D.C.: National Bureau of Standards, 1972, vol. 55, ch. 9, pp. 355–389.

VITA

Shane Vincent Lympany was born in Raleigh, North Carolina on October 4, 1992, and grew up in the nearby small town of Fuquay-Varina. Shane attended Fuquay-Varina Elementary, Middle, and High Schools, and he enrolled at the Georgia Institute of Technology in the fall of 2010 as an undergraduate student to study aerospace engineering. When he is asked why he chose aerospace engineering, he responds that he was born on the anniversary of the launch of Sputnik, in the state that was first in flight, to parents who first met an airport, so he had no other choice! In reality, Shane read Jim Lovell's book *Lost Moon* (now *Apollo 13*) in the third grade, and from then on, he aspired to be an aerospace engineer like the engineers in Mission Control.

Shane graduated with a Bachelor of Science in Aerospace Engineering from Georgia Tech in May 2014, and he obtained his Master of Science in Aerospace Engineering in May 2016. During his tenure as a student at Georgia Tech, Shane performed research in the Vibration and Wave Propagation Laboratory under the direction of Prof. Massimo Ruzzene and in the Aerospace, Transportation, and Advanced Systems Laboratory at the Georgia Tech Research Institute under the direction of Prof. Krish Ahuja. Shane also completed one internship at LORD Corporation and five cooperative program rotations at Gulfstream Aerospace Corporation. After completing his Doctor of Philosophy in Aerospace Engineering, Shane will move to Asheville, North Carolina to begin work as an aeroacoustics research engineer for Blue Ridge Research and Consulting, LLC.